

Wake Structures of Simplified Automotive Geometries Using Numerical Methods

Dissertation submitted in partial fulfilment
Of the requirements for the degree of
Doctor of Philosophy at Monash University

Shaun A. Johnson
B.Eng. Mech & Sp (Hons)

Department of Mechanical Engineering
Monash University
Victoria, Australia

October 2005

Statement of Originality

This thesis contains no material that has been accepted for the award of a degree or diploma in this or any other university. To the best of the candidate's knowledge and belief, this thesis contains no material previously published or written by another person except where due reference is made in the text of the thesis.

Shaun Johnson

October, 2005.

Summary

In vehicle aerodynamics, a significant proportion of vehicle drag is due to the large separated region in the wake. Although earlier studies have characterised the effect of vehicle geometric parameters on the body drag, the complex wake structure is still not well understood. Even for simple geometries, small geometric modifications have a significant effect on wake structures. One aim of this thesis was to examine the wake structures of a simplified automotive geometry known as the *Ahmed body*. The effect of the angle of the slant surface and the vehicle aspect ratio (body width/characteristic body length) was examined.

This study was undertaken using computational fluid dynamics simulations to examine the wake structures. Solution strategies were developed to model complex turbulent flow with both unsteady and steady simulations. Comparisons with experimental data show that the simulations capture the observed change in the wake structures as the slant angle is varied.

Analysis of the drag and lift forces on the Ahmed body compare well with experimental data, especially on the rear portion of the body. Discrepancies were mainly due to an over prediction of the contribution from the front portion.

Four flow regimes were identified from the drag and lift forces, and from the flow visualisations in the analysis of the wake structures. In Region I, the flow is attached to the slant surface, while a small stable separation bubble forms on the slant surface in Region II. In Region III, a large separation bubble is present on the slant surface with strong C-pillar vortices present. When the flow is completely separated from the slant surface, this is identified with Region IV.

The most significant effect found from varying the body aspect ratio is the change in location of the critical slant angle where the wake structures change from a wake dominated by the C-pillar vortices (Region III), to a large separation bubble encompassing the slant and rear surface (Region IV).

The change in location of critical slant angle represents the location of maximum coefficient of drag for a given aspect ratio, which results in a lower peak coefficient of

drag. The critical slant angle ranged from 34° for the low aspect ratio bodies (narrow) to 25° for the high aspect ratio bodies.

The structure of the C-pillar vortex emanating from the top corners of the slant was examined to determine how the slant angle and aspect ratio affect the vortex structure. Simulations showed that as the slant angle approaches the critical slant angle, vortex breakdown occurs in the C-pillar vortex. Increasing the slant angle moved the location of vortex breakdown closer to the formation point of the vortex. Simulations indicated that the mechanism for the transition to a fully separated wake structure above the critical slant angle is due to the flow field near the formation point exceeding the swirl parameter criteria for a stable vortex, and as a result, the C-pillar vortex fails to develop.

The flow field for the Ahmed body was analysed using the momentum equation to locate the sources of drag in the wake. By evaluating the separate contributions from integrating the momentum equation over control volumes, the structures associated with different sources of drag were identified. This method is better suited to identifying sources of drag (especially vortex drag) rather than for calculating the overall drag of a body. The analysis showed that the reduction in drag at the critical slant angle is due to a reduction in vortex drag, which contributes up to 33% of the total drag on the Ahmed body.

Inside the C-pillar vortex, pressure loss inside the vortex is the main source of drag. The C-pillar vortex also creates a region of high vortex drag on the inside edge of the vortex. Past the end of the body, the main sources of drag occur in the shear layers of the separation bubble. For flows with two counter-rotating streamwise vortices present in the far wake, drag is primarily associated with pressure losses in the vortex core.

The time-averaged flow fields from the unsteady simulations were similar to steady state fields helping to support the novel approaches used for time-independent simulations. The visualisations of the wake structures provided an insight into the unsteady nature of the wake structures. For flow attached to the slant surface the vortex shedding past the end of the body occurs along the vehicle centreline. When the flow is separated from the top of the slant surface, the shear layer emanating from the top of the slant surface is unstable with vortices shed downstream. This is

considerably different to the time-averaged flow, which shows the separation bubble reattaches to the slant surface. The C-pillar vortex exhibited signs of bubble-type breakdown with a spiral tail breakdown over the slant surface. This location moves towards the top of the slant surface and the wake after breakdown is highly unsteady. When the Ahmed body was past the critical slant angle, there was large-scale shedding from the separation bubble and the structures are more coherent.

The frequency analysis indicated the dominant shedding frequency occurred at the bottom of the rear surface. Simulations suggested that the dominant shedding frequency increases with slant angle. However, the frequency spectra are considerably more complex when the wake has separated from the top of the slant surface and C-pillar vortices are breaking down.

These results indicate that the structure of the C-pillar vortex is more complex than previously thought. Near the critical slant angle, vortex breakdown occurs leading to total separation of the wake. This is a significant development since a clear explanation is provided for the transition to a large separated wake. Simulations indicate that drag for given frontal area is higher for the low aspect ratio bodies. Previously, the aspect ratio of a vehicle has not been considered to have a significant effect.

Publications

S.A. Johnson, K. Hourigan, and M.C. Thompson., *Effect of aspect ratio on the wake structures of simplified automotive geometries*. 5th International Colloquium on Bluff Body Aerodynamics and Applications, 2004, Ottawa, Canada

S.A. Johnson, K. Hourigan, and M.C. Thompson., *Low Frequency Structures in the wake of Elliptical Cylinders*. European Journal of Mechanics B/Fluids, 2003, Vol. 22, no. 5/6.

L. Mununga, K. Hourigan, and M.C. Thompson and S.A. Johnson, *Numerical investigations of discharge flow and circulation flow in unbaffled mixing vessels agitated by a plain disk*, in 2nd International Conference on Heat Transfer, fluid Mechanics and Thermodynamics, 2003, Victoria Falls, Zambia.

S.A. Johnson, K. Hourigan, and M.C. Thompson., *Low Frequency Unsteadiness in the Wake of Elliptical Cylinders*. in Conference on Bluff Bodies and Vortex Induced Vibration 3, 2002, Port Douglas, Australia.

S.J. Wordly, R. Lyddy-Meaney and S.A. Johnson, *Design and development of an aerodynamic package for the Monash – PLM Formula SAE Racer*, in Young Automotive and Transport Executives Conference, 2002, Melbourne, Victoria.

S. A. Johnson, K. Hourigan, and M.C. Thompson. *Flow Past Elliptical Cylinders at Low Reynolds Numbers*. in 14th Australasian Fluid Mechanics Conference. 2001. Adelaide, Australia.

S.A. Johnson, C.E. Nash, B.P. Osborne and P. Teakle, *Solid Fuel Rocket Testing at The University of Queensland*, 4th Australian Space Research Conference, 2001.

Table of Contents

Statement of Originality	2
Summary	3
Publications	6
Table of Contents	7
Nomenclature	13
Chapter 1 Introduction	Error! Bookmark not defined.
Chapter 2 Literature Review	20
2.1 Wake Structures of Simplified Automotive Geometries	20
2.2 The Ahmed Body	83
2.3 The use of CFD for research on automotive vehicles	96
2.3.1 Linear Methods	97
2.3.2 Non Linear Methods	99
2.4 Vortex Breakdown	111
2.4.1 Introduction	111
2.4.2 Delta Wings	114
2.4.3 Transition from attached flow to separated flow on delta wings	114
2.4.4 Criteria for vortex Breakdown	116
2.4.4.1 Helix angle	116
2.4.4.2 Swirl Parameter	117
Chapter 3 Methods	25
3.1 Numerical Method	25
3.1.1 Continuity Equation	26
3.1.2 Momentum Equation	27
3.1.3 Energy Equation	27
3.1.4 Navier-Stokes Equations	28
3.1.5 Integral forms of the general transport equations	29
3.1.6 Discretisation of equations	29
3.1.7 Turbulence	31
3.1.8 Turbulence models	33
3.1.9 $k\epsilon$ Turbulence Model	34
3.1.10 $k\omega$ turbulence model	35
3.1.11 Reynolds Stress Model	36
3.1.12 Wall Boundary Conditions	37
3.2 Geometry	39

3.3	Grid Setup.....	40
3.3.1	Mesh Generation Procedure.....	42
3.3.2	Geometry Creation.....	42
3.3.3	Meshing.....	43
3.3.3.1	Edge Meshing.....	43
3.3.3.2	Face Meshing.....	44
3.3.3.3	Boundary Layer.....	44
3.3.4	Zone Assignment.....	45
3.4	Model Setup.....	47
3.4.1.1	Model initialisation.....	47
3.4.1.2	Convergence Criteria.....	48
3.5	Grid Resolution study.....	52
3.5.1.1	Domain Resolution.....	53
3.5.1.2	Face Mesh Resolution.....	54
3.5.1.3	Volume Resolution.....	55
3.5.1.4	Boundary Layer Resolution.....	56
3.5.1.5	Final Mesh Design.....	57
3.6	Further model resolution and validation studies.....	58
3.6.1.1	Turbulence models.....	59
3.6.1.1.1	kε-realizable turbulence model.....	60
3.6.1.1.2	kω-SST turbulence model.....	62
3.6.1.1.3	Reynolds Stress Model turbulence model.....	63
3.6.1.1.4	Turbulence model comparison.....	68
3.6.1.2	Under Relaxation.....	69
3.6.1.3	Time dependent simulations.....	72
3.6.1.4	Symmetry conditions.....	77
3.6.2	Conclusion.....	79
Chapter 4	Effect of Slant Angle.....	119
4.1	Introduction.....	119
4.2	Body forces.....	119
4.2.1	Total body drag and lift forces.....	119
4.2.2	Lift to Drag Ratio.....	120
4.2.3	Drag and lift from individual surfaces.....	121
4.2.4	Normal force on the slant surface.....	124
4.2.5	Conclusion.....	126
4.3	Wake Structures.....	126
4.3.1	Introduction.....	126
4.3.2	Region I.....	128

4.3.3 Region II	129
4.3.4 Region III	130
4.3.5 Region IV	134
4.3.6 Surface Pressure Near Slant Surface.....	134
4.3.7 Rear separation bubble size.....	138
4.3.8 Conclusion	141
4.4 Experimental Comparison	142
4.4.1 Wake structures near slant surface.....	142
4.4.2 Wake structures in the body wake.	146
4.4.3 Surface Pressure.....	150
4.4.4 Surface Topology.....	152
4.5 Conclusion	153
Chapter 5 Effect of Aspect Ratio	156
5.1 Introduction.....	156
5.2 Body forces.....	158
5.2.1 Low AR.....	158
5.2.1.1 Overall Forces	158
5.2.1.2 Lift to drag ratio.....	159
5.2.1.3 Breakdown of surface.....	160
5.2.1.4 C_N (slant surface).....	161
5.2.2 High AR.....	163
5.2.2.1 Overall Forces	163
5.2.2.2 Lift to drag ratio.....	164
5.2.2.3 Break down of forces from different surfaces	165
5.2.2.4 C_N slant.....	166
5.2.3 Effect of Aspect Ratio.....	168
5.3 Wake Structures.....	172
5.3.1 Low AR bodies	172
5.3.1.1 Region I	172
5.3.1.2 Region II.....	174
5.3.1.3 Region III.....	176
5.3.1.4 Region IV	179
5.3.2 High AR bodies.....	180
5.3.2.1 Region I	180
5.3.2.2 Region II.....	182
5.3.2.3 Region III.....	185
5.3.2.4 Region IV	187
5.4 Effect of aspect ratio	191
5.4.1 Change in downwash	191

5.4.2	Portion of slant surface with separated flow.....	196
5.4.3	Separation bubble size	198
5.4.4	Downstream effects	205
5.5	Conclusion	207
Chapter 6	C-Pillar Vortex Structure.....	211
6.1	Introduction.....	211
6.2	Vortex core location	212
6.3	Methods	217
6.4	Standard Ahmed body	217
6.4.1	Location of vortex core.....	218
6.4.2	C-pillar Vortex Size	220
6.4.3	Pressure Profiles along Vortex Core.....	222
6.4.4	Core Axial velocity	227
6.4.5	Core Vorticity	228
6.4.6	Swirl parameter.....	228
6.4.7	Helix Angle.....	230
6.4.8	Core Gradient.....	231
6.5	Effect of Aspect Ratio on Vortex Breakdown.....	234
6.5.1	Low Aspect Ratio Bodies	234
6.5.1.1	Core Position	234
6.5.1.2	Core radius.....	235
6.5.1.3	Core Pressure.....	237
6.5.1.4	Core Axial velocity.....	240
6.5.1.5	Core vorticity.....	241
6.5.1.6	Swirl parameter	242
6.5.1.7	Helix angle.....	243
6.5.1.8	Core Gradient	244
6.5.2	High Aspect Ratio Bodies.....	245
6.5.2.1	Core Location	245
6.5.2.2	Core Radius	246
6.5.2.3	Pressure.....	247
6.5.2.4	Axial Velocity	249
6.5.2.5	Vorticity.....	250
6.5.2.6	Swirl Velocity.....	251
6.5.2.7	Helix angle.....	251
6.5.2.8	Core Gradient	253
6.5.3	Effect of Aspect Ratio on the C-pillar Vortex	254
6.5.3.1	Location of C-pillar vortex	254
6.5.3.2	Radius of vortex	255

6.5.3.3	Pressure of vortex	256
6.5.3.4	Location of vortex breakdown.....	257
6.5.4	Mechanism for change of α_c	259
6.6	Conclusion	261
Chapter 7	Wake Analysis	264
7.1	Introduction.....	264
7.2	Method.....	265
7.2.1	Momentum Theory	265
7.2.2	Implementation	267
7.2.3	Resolution study.....	269
7.2.3.1	Grid Density	269
7.2.3.2	Domain limits	271
7.2.4	Comparison with Surface Forces	274
7.3	Results.....	276
7.3.1	Standard Ahmed body.....	276
7.3.1.1	Change in C_D in X direction	276
7.3.1.2	C_D of slant and rear surfaces using the momentum equation. .	277
7.3.1.3	Effect of slant angle.....	278
7.3.1.4	Spatial analysis	284
7.3.2	Effect of AR on drag structures	291
7.3.2.1	Drag calculations on the slant and rear surface	291
7.3.2.2	Streamwise change in momentum equation with AR	293
7.3.2.3	Wake visualisations	297
7.4	Conclusion	300
Chapter 8	Unsteady Simulations.....	303
8.1	Introduction.....	303
8.2	Time averaged simulations	306
8.2.1	Introduction.....	306
8.2.2	$\alpha=10^\circ$, AR=1.75	307
8.2.3	$\alpha=22^\circ$, AR=1.75	307
8.2.4	$\alpha=25^\circ$, AR=1.75	308
8.2.5	$\alpha=28^\circ$, AR=1.75	309
8.2.6	$\alpha=30^\circ$, AR=1.75	310
8.2.7	$\alpha=35^\circ$, AR=1.75	311
8.2.8	Conclusion	311
8.3	Body Forces	312
8.4	Unsteady Simulations	317

8.4.1 $\alpha=10^\circ$, AR=1.75	318
8.4.2 $\alpha=22^\circ$, AR=1.75	320
8.4.3 $\alpha=25^\circ$, AR=1.75	324
8.4.4 $\alpha=28^\circ$, AR=1.75	326
8.4.5 $\alpha=30^\circ$, AR=1.75	329
8.4.6 $\alpha=35^\circ$, AR=1.75	331
8.5 Frequency analysis.....	333
8.5.1 $\alpha=10^\circ$, AR=1.75	334
8.5.2 $\alpha=22^\circ$, AR=1.75	338
8.5.3 $\alpha=25^\circ$, AR=1.75	341
8.5.4 $\alpha=30^\circ$, AR=1.75	344
8.5.5 $\alpha=35^\circ$, AR=1.75	347
8.6 Conclusion	350
Chapter 9 Conclusion.....	355
9.1 Strategy for numerical simulations.....	355
9.2 Effect of slant angle	357
9.3 Effect of Aspect Ratio	359
9.4 Structure of C-pillar vortex and vortex breakdown.....	361
9.5 Sources of drag in the wake.....	362
9.6 Unsteady wake structures	364
9.7 Future Work.....	365
References.....	368
Movies	378

Nomenclature

α	Slant angle
α_c	Critical Slant Angle
φ	sweep back angle
γ	helix angle
Γ_0	circulation at the outer limits of the vortex
τ_{ij}	viscous stress components
ρ	fluid density
μ	dynamic viscosity
ε	rate of dissipation of turbulence
μ_t	eddy viscosity
u^+	dimensionless velocity
y^+	dimensionless wall distance
Δt	time step
U_∞	Free stream velocity
\dot{m}	mass flow rate
Γ	circulation
ω	vorticity
$ \omega_z $	Absolute streamwise vorticity
$\ \omega\ $	Vorticity magnitude
C_D	Coefficient of Drag
C_L	Coefficient of Lift
C_N	Coefficient of Normal Force
C_P	Coefficient of static pressure
C_{TP}	Coefficient of total pressure
C_{DP}	Coefficient of dynamic pressure
C_{PL}	Coefficient of pressure loss
C_{LVL}	Coefficient of Longitudinal velocity Loss
C_{VD}	Coefficient of vortex drag
C-pillar	the pillar that joins the rear window to the rear side window

P_{ref}	reference pressure
P_t	total pressure
R_{ij}	Reynolds stress tensor
Re	Reynolds Number
Ro	Rossby number
r_c	radius of the vortex where maximum swirl velocity occurs
S*	critical swirl parameter
St	Strouhal number
U_∞	Free stream velocity
St	Strouhal number
V_x	axial component of velocity in a vortex
V_r	radial component of velocity in a vortex
V_x, V_y, V_z	components in the velocity
$V_{\theta \max N}$	Maximum radial component of velocity in a vortex
$V_{X(\text{axis})}$	axial component of velocity in a vortex
A	Cross sectional area
AOA	angle of attack
AR	Aspect Ratio (body width/characteristic body length)
CV	Control Volume
CFD	Computational Fluid Dynamics
DES	Detached Eddy Simulation
DNS	Direct Numerical Simulation
EWf	enhanced wall function
F	Force
FL	First Length
FFT	Fast Fourier Transform
GC	Ground Clearance
H	Height
IA	iteration-averaged
k	kinetic energy of turbulence
LD	Lift/Drag ratio
LDA	Laser-Doppler Anemometer
LES	Large Eddy Simulation

LL	Last Length
NOI	number of intervals
NDU	Non Dimensional Unit
P	Pressure
PIV	Particle-Image Velocimetry
R	Radius
RANS	Reynolds Averages Navier Stokes
RSM	Reynolds Stress Model
RT	Residual Truncation
S	swirl parameter
SL	Slant Length
SR	succession ratio
SST	Shear Stress Turbulence
SWF	standard wall function
t	time
TA	iteration-averaged
UR	Under Relaxation
URANS	Unsteady Reynolds Averages Navier Stokes
W	Width
U, V, W	Componentsof velocity
X, Y, Z	Axis System

Chapter 1 Introduction

The aerodynamics of automotive geometries is a field of research that has become more complex and diverse through the evolution of the automobile. The realisation that performance, handling, comfort and fuel economy are all dependent on the external flow means that more aerodynamic emphasis is placed on vehicle styling. Increasing world energy requirements have placed a greater importance on vehicle energy loss, which is primarily due to rolling resistance and aerodynamic drag.

It is now well established that a significant proportion of vehicle drag is due to the large separated region in the wake. Although researchers [5-11] have characterised the effect of vehicle geometric parameters on the body drag, the complex wake structure is still not well understood. An area of research that appears to be lacking is relating how flow structures affect the body forces and why these effects occur. Even for simple geometries, small geometric modifications have a significant effect on wake structures [5, 10]. In the last decade, the advent of better experimental techniques and more importantly, increased resolution and accuracy of Computational Fluid Dynamics (CFD) simulations, have promoted better understanding of wake structures. This has led to improved design of vehicles with improved fuel economy and handling.

The focus of this research is the numerical study of the flow over a simplified automotive geometry in ground effect. The body described as the Ahmed body was initially used by Ahmed et al. [5] for examining the effect of slant angle flow structures and has been used as a basis for many numerical and experimental investigations. Even though the effect of the slant angle has been investigated, the vehicle aspect ratio (body width/characteristic body length) was examined to gain a better insight into the wake structures.

This research stems from initial work done by Janssen and Hucho [10] in the development of the Volkswagen Golf I, which showed that small geometric changes of the slant angle of the rear window had a dramatic effect on the wake structures and drag. High drag was associated with the presence of the streamwise vortices emanating from the C-pillar region of the car. This caused a paradigm shift in the philosophy of vehicle aerodynamics since it was generally perceived that attached

flow had lower drag. Significant improvements of drag reduction observed from small styling changes were of considerable interest to manufactures and led to increased investment in vehicle aerodynamics research [12].

Although the change from high drag to low drag has been demonstrated and examined on multiple geometries, the physical mechanism for this transition is not yet understood and surprisingly few researchers have paid attention to this phenomenon. The present study proposes that the transition is linked to vortex breakdown, which has been investigated in the aerospace industry on geometries such as delta wings and finite span wings.

One of the primarily objectives of vehicle design is the reduction of drag on the body. Although the contributions of drag on the Ahmed body from various regions have been identified due to pressure and viscous losses, hardly any studies have been undertaken to establish the link between these forces and the different flow structures as well as their effects on drag. Much of previous experimental and numerical research has examined the time-averaged flow structures of the wake, although the flow structures are highly unsteady. Only recently have the unsteady wake structures of automotive geometries been investigated. Research on simplified geometries such the Ahmed body allows for an enhanced understanding of the unsteady wake and how geometric parameters affect these structures. The growing knowledge of the unsteady flow field on the Ahmed body can be used as a basis for understanding more complex flow fields.

Having highlighted the areas that require further research, the primary objectives of this thesis include:

1. Development of a numerical grid and strategy for the numerical simulations to ensure the data produced is valid and representative of the flow field measured and observed in experiments. The unsteady nature of the flow field at high Reynolds numbers requires an extensive grid resolution study.
2. Characterisation of the effect of the Ahmed body slant angle (α) on the body forces and the wake structures. This is undertaken to provide a more detailed analysis of the wake than is currently available in the literature and to compare to the experimental data available to verify the numerical simulations.

3. Characterisation of the effect of the vehicle aspect ratio on the wake structures. This parameter is investigated along with the slant angle to determine how wake structures change, and in particular, the location of the critical slant angle where the transition from high drag to low drag occurs.
4. Examination of the C-pillar vortex and how the slant angle and vehicle aspect ratio affects this structure since the literature suggests this is the critical feature.
5. Analysis of the wake flow field using momentum theory to pinpoint the structures that cause the drag on the body.
6. Examination into the unsteady wake structures for the Ahmed body. This is undertaken by examining the frequency spectrum in the wake from the flow structures and the unsteady flow visualisations.

The numerical investigation in this thesis examines the effect of geometric changes of the Ahmed body on the wake structure, provides evidence the existence of vortex breakdown in the streamwise C-pillar vortex and examines the unsteady flow field. The organisation of this thesis follows the objectives outlined and is briefly summarised below.

Chapter 2 presents a review of the relevant literature regarding simplified automotive geometries. The review examines the progression of research conducted from that by Janssen and Hucho [10] to Ahmed et al. [5]. The current experimental data using the Ahmed body is presented. This is followed by the development of numerical simulations that have used the Ahmed body for their analysis. Finally, a brief introduction of the phenomenon of vortex breakdown on delta wings is presented.

Chapter 3 presents various resolution, validation, domain size and turbulence modelling investigations to establish the capabilities of the computational software to contribute to an understanding of the flow dynamics of idealised vehicles. A brief description is presented of the formulation of the finite-volume method used to solve the governing equations of fluid flow.

Chapter 4 examines the effect of the slant angle on the Ahmed body for $1^\circ \leq \alpha < 50^\circ$. The flow structures in the wake region of an Ahmed body are examined to

analyse how these structures change with α and compared with other experimental data [13, 14]. The contribution of the drag and lift to the total body forces are examined for the different regions of the body, such as the slant and rear surface.

Chapter 5 investigates the effect of the vehicle aspect ratio on the body forces and wake structures. The aspect ratio is modified by changing the width of the body, and both narrower and wider bodies are examined. The effect of aspect ratio is quantified by examining various parameters such as the induced downwash and size of the rear separation bubble.

Chapter 6 investigates the change of the C-pillar vortex with α and aspect ratio. This study provides evidence to show that the vortex breakdown is the likely mechanism that causes the transition from high to low drag on the Ahmed body. Key features of the vortex are examined spatially along the length of the vortex above the slant surface.

Chapter 7 uses the momentum theorem used by Onorato [6] to examine which structures cause the drag. The theory is explained and then applied to the data from numerical simulations. Various α and aspect ratios are examined to pinpoint the flow structures influencing drag and how changes in geometry affect the wake.

Chapter 8 presents data from time dependent simulations to justify the use of time independent data for the parameter space study. The average flow field of time dependent simulations are compared with the mean time independent simulations. The unsteady wake structures are visualised to provide a better insight into the wake structures. Finally, the frequency spectrum of the total pressure in the wake is investigated to determine the frequencies associated with the different wake structures.

Chapter 9 summarises the major conclusions and findings from the research presented in this thesis and recommendations for future work are suggested.

Chapter 2 Literature Review

2.1 Wake Structures of Simplified Automotive Geometries

Aerodynamics of bluff bodies in ground proximity has become an increasingly important factor in vehicle design, in an effort to decrease fuel consumption and improve stability and handling. Ignoring the energy losses from transmission and energy consumption from accessories such as air conditioning, for a vehicle travelling at a constant velocity on a horizontal surface, all energy is consumed overcoming rolling resistance and aerodynamic drag. Rolling resistance increases linearly with vehicle velocity while aerodynamic drag loading increases quadratically. Thus at high velocities, most energy produced by the engine is used to overcome aerodynamic forces.

From an aerodynamic point of view, automotive vehicles are considered as bluff bodies. Drag is mainly from pressure drag as opposed to aircraft and ships, which suffer primarily from friction drag. Therefore, it is important to develop a vehicle whose basic body shape creates minimal drag and the flow structures associated with it are well understood. Buchhiem et al. [9] examined how a basic vehicle shape could be developed to produce a vehicle shape that was acceptable as a styled model for a subcompact car as outlined in Figure 2.1. To produce a model that is acceptable for industry use requires the vehicle shape to be altered from the optimal design to one that has higher drag than the original body. This emphasizes the importance of understanding the flow structures of the basic vehicle geometry as the starting point for development in order to develop a vehicle that can have the best flow characteristics possible since it is the starting point for development.

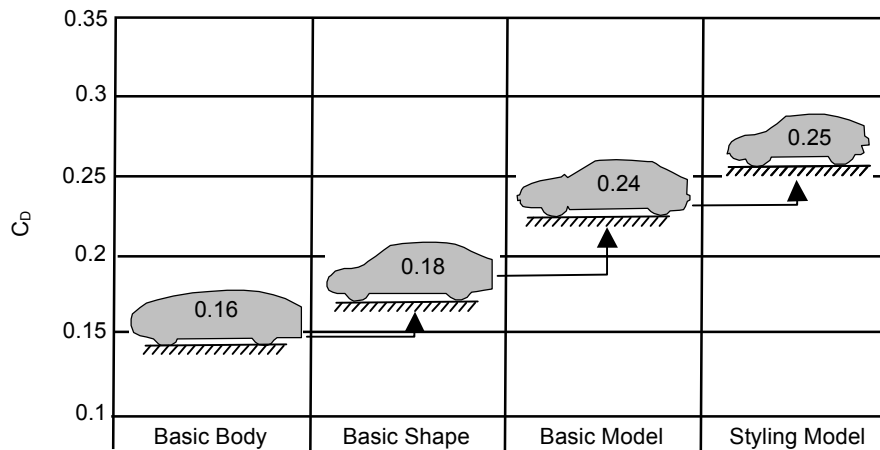


Figure 2.1 Evolution of a vehicle shape from a basic vehicle to styled model [9]

Avoiding separation is desirable to reduced drag. However, in most situations vehicles are susceptible to flow separation due to their shape being influenced by other requirements such as packaging and ergonomics. Extensive research on the wake structures produced by automotive vehicles of different rear-end shapes has sought to determine how vehicle parameters influence the separation and base drag.

Dramatic changes in the wake structures and corresponding levels of vehicle drag were first observed by Jannsen and Hucho [10] in the development of the Volkswagen Golf I by changing the slant angle (α : vertical= 0°) of the rear window as shown in Figure 2.2. They observed that the separation line was located at the top of the slanted rear surface for $\alpha < 58^\circ$ (Figure 2.2a), but moved to the bottom of the slant surface for $\alpha > 62^\circ$ (Figure 2.2b). In between these two angles, the point of separation would pulse randomly from the top to the bottom edge and vice versa. For $\alpha > 62^\circ$, two streamwise (structure parallel to free stream velocity) vortices emanated from the C-pillars (the pillar that joins the rear window to the rear side window) creating high levels of drag but when the wake separated from the top edge of the slant surface, the drag dramatically decreased. This consequently led to many studies examining the effect of the slant angle and wake structures on different bluff bodies [5, 11, 15]

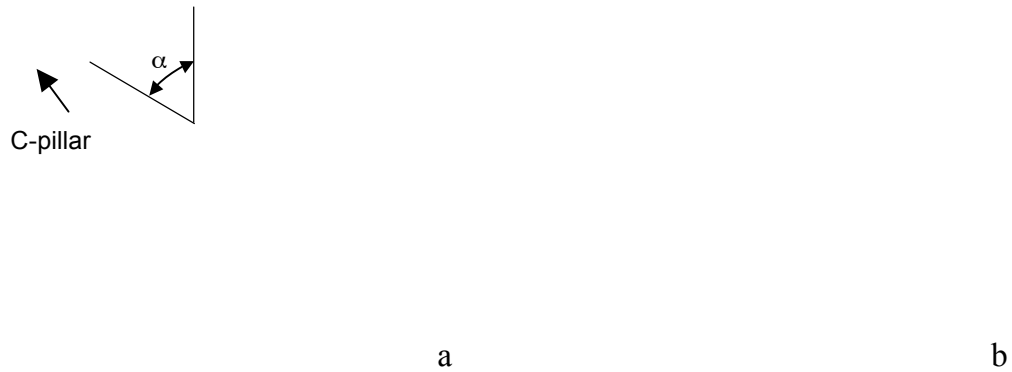


Figure 2.2 Flow visualisations on the VW Golf with a separated wake (a) and with an attached wake (b). [10]

Morel [16] examined the effects of slanting the blunt base of three dimensional axis-symmetric and rectangular cross sectional bodies. Since the critical behaviour of a slanted base could be dependent on a number of parameters (e.g. aspect ratio, fore body and after body geometry, ground proximity and Reynolds number), the first geometry examined to isolate the effect of the slant angle on the flow field was a slender axis symmetric cylinder with a slanted base as shown in Figure 2.3.

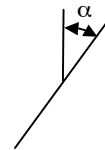
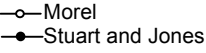


Figure 2.3 Schematic of the axis symmetric body to isolate effect of slant angle. [16]

Experiments were conducted for $Re=9.4 \times 10^4$ based on the cylinder diameter. Figure 2.4 and Figure 2.5 show the change in base pressure and drag coefficients with base slant angle. Both results show the existence of two different base flows. Pressure tap data showed the transition point at 47.5° while drag coefficient data showed the critical angle to be 45° . Experiments by Stuart and Jones showed the transition point to occur at lower angles. Of note is the difference in the base pressure in Regime II where the sharp pressure gradient across the centreline indicates different flow structures on the edges of the slant surface compared with the centreline (pressure tap 1).

	
Figure 2.4 Base pressure Vs slant angle at three pressure locations on slant surface of axis symmetric body. [16]	Figure 2.5 Drag Coefficient variation with slant angle showing two different results by two different researchers. [16]

The second body used to examine the effect of the slant angle was a vehicle of similar dimensions to basic automotive geometry in ground proximity shown in Figure 2.6 described as the Morel Body.

H

W

Figure 2.6 Schematic of the Morel Body. [16]

Experiments were conducted at $Re=1.4 \times 10^6$ based on the equivalent diameter ($\sqrt{4WH/\pi}$) with the model at two ground clearances to simulate the body in a free stream and to simulate a typical road vehicle in ground proximity. Drag and lift measurements shown in Figure 2.7 out of ground effect showed similar results to those observed for the axis symmetric cylinder with a pronounced change in lift and drag at 60° . Reducing the ground clearance did not affect the trend as the slant angle was changed. However it decreased the overall lift of the body for all slant angles and the change in drag was less pronounced at the critical angle. Flow visualisations with smoke and tufts showed a large separation bubble below the critical angle and flow attached to the slant surface with strong streamwise vortices emanating from the C-pillars above the critical angle.

Figure 2.7 The C_D and C_L variation with slant angle of the Morel body

Morel concluded, “As the aspect ratio increases, the effect of the side-edge vortices on the overall flow pattern gets progressively smaller, as only a relatively smaller portion of the base is exposed to them.” This means that the difference between the critical angles of the cylinder and the vehicle-like body was due to the change in aspect ratio of the slant surface.

Chapter 3 In 1981, Ahmed [8] conducted experiments on wake structures of typical automobile shapes. Vehicle shapes for an estate, fastback and notchback were tested by varying the upper rear end of a quarter scale model (Figure 3.33) with flow visualisation and wake surveys performed in the region behind the model. All Methods

This chapter presents various resolution, validation, domain size and turbulence modelling investigations to establish the capabilities of the computational software to contribute to an understanding of the flow dynamics of idealised vehicles. The studies focus on the Ahmed body [5], which has become almost a default standard for this type of investigation.

The Ahmed body has been widely used as a reference geometry for validation of various in-house and commercial computational fluid dynamics (CFD) simulation programs, and experimental investigations, for external aerodynamics applications. Judging by the spread in the existing computational predictions and experimental data, simulating such a seemingly simple geometry, relative to a geometrically-complex vehicle, is still complex due to intricacy of the flow structures, particularly in the wake. Since modelling of complex three-dimensional flows is still computationally expensive, in order to use numerical simulations as a tool for research on external vehicle aerodynamics it is critical to create semi-optimal grids that capture the key flow structures efficiently. Clearly, it must be ensured that results from the simulations are representative of experimental observations and measurements, especially given inherent uncertainties in modelling turbulence.

3.1 Numerical Method

Numerical experiments for this research were performed using the commercial computational fluid dynamics software *FLUENT*, version 6.1.22. This software

Chapter 3 In 1981, Ahmed [8] conducted experiments on wake structures of typical automobile shapes. Vehicle shapes for an estate, fastback and notchback were tested by varying the upper rear end of a quarter scale model (Figure 3.33) with flow visualisation and wak

Shaun Johnson

utilizes the finite-volume approach to solve the Navier-Stokes equations. An advantage of using commercial software packages is that they are usually designed to handle three-dimensional complex geometries. Fluent uses triangular/quadrilateral elements for two-dimensional geometries, and tetrahedral/hexahedral/pyramid/wedge and mixed (hybrid) elements for three-dimensional geometries. Fluent is also able to simulate various physical phenomena such as inviscid, laminar, and turbulent flows, acoustical noise, compressible flow, multiphase flow and heat transfer. This versatility and its lower-order formulation means it is not as efficient as some other special-purpose numerical methods, such as the spectral-element approach, which has been used for high-resolution studies of much simpler objects such as flows past spheres and cylinders [63-65].

In the following few sections, a brief description will be presented of the formulation of the finite-volume method used to solve the governing equations of fluid flow for a simple one-dimensional problem. A more extensive account of this summarised explanation is described by Versteeg and Malaskechera [66]. This description is included partially to aid in discussions later, but also for completeness.

The finite-volume method uses a discretized domain consisting of small finite control volumes. In each finite volume, the governing equations are integrated, which leads to equations in terms of field quantities such as velocity and pressure defined at discrete points within the cell or on the cell faces. Integration of the second-order diffusion term only reduces the order of the derivative by one; hence a finite-difference approximation is often used to further simplify the equations. The non-linear set of equations is solved using iterative methods, or by time stepping for unsteady problems. In general, the governing equations are the continuity equation, the momentum equation and the energy equation supplemented as necessary with other equations such as an equation of state.

3.1.1 Continuity Equation

The continuity equation states that the mass of a fluid is always conserved. This can be written in the following form:

Chapter 3 In 1981, Ahmed [8] conducted experiments on wake structures of typical automobile shapes. Vehicle shapes for an estate, fastback and notchback were tested by varying the upper rear end of a quarter scale model (Figure 3.33) with flow visualisation and wak

Shaun Johnson

$$\frac{\partial \rho}{\partial t} + \frac{\partial(\rho u)}{\partial x} + \frac{\partial(\rho v)}{\partial y} + \frac{\partial(\rho w)}{\partial z} = \text{div}(\rho \mathbf{u}) = 0 \quad \text{Eqn 3.1}$$

Where ρ is the fluid density and u, v, w are the velocity components in their respective directions, x, y, z . For incompressible flow, the density of the fluid is constant so only the net flow of volume across the boundaries of the element needs to be considered as written in Eqn 3.2:

$$\frac{\partial u}{\partial x} + \frac{\partial v}{\partial y} + \frac{\partial w}{\partial z} = \text{div}(\mathbf{u}) = 0 \quad \text{Eqn 3.2}$$

3.1.2 Momentum Equation

The momentum equation states that the rate of change of momentum of a fluid parcel moving with the fluid equals the sum of external forces acting on the fluid parcel (Newton's second law). The two types of forces on a fluid parcel are surface forces, which includes pressure and viscous forces, and body forces including gravity, and centrifugal and Coriolis forces (in a non-inertial frame). For the purposes of the numerical solution procedure, body forces are included as source terms in the equations and are handled separately. The three components of the vector momentum equation can be written as

$$\begin{aligned} \rho \frac{Du}{Dt} &= \frac{\partial \tau_{xx}}{\partial x} + \frac{\partial \tau_{yx}}{\partial y} + \frac{\partial \tau_{zx}}{\partial z} - \frac{\partial p}{\partial x} + S_{Mx} \\ \rho \frac{Dv}{Dt} &= \frac{\partial \tau_{xy}}{\partial x} + \frac{\partial \tau_{yy}}{\partial y} + \frac{\partial \tau_{zy}}{\partial z} - \frac{\partial p}{\partial y} + S_{My} \\ \rho \frac{Dw}{Dt} &= \frac{\partial \tau_{xz}}{\partial x} + \frac{\partial \tau_{yz}}{\partial y} + \frac{\partial \tau_{zz}}{\partial z} - \frac{\partial p}{\partial z} + S_{Mz} \end{aligned} \quad \text{Eqn 3.3}$$

where τ_{ij} are the viscous shear stress components in the i direction on the surface with normal direction j ; u, v, w are the velocity components in their respective directions x, y, z ; p is the pressure and S_{Mi} is the source term to represent the body forces. In addition, D/Dt is the *total* time derivative, including local and convective rates of change.

3.1.3 Energy Equation

The first law of thermodynamics states that the change of internal energy of a fluid parcel is equal to the sum of the work done and heat added.

$$\begin{aligned}
 & - \operatorname{div}(\rho \mathbf{u}) - \\
 \rho \frac{DE}{Dt} = & + \left[\begin{aligned} & \frac{\partial(u\tau_{xx})}{\partial x} + \frac{\partial(u\tau_{yx})}{\partial y} + \frac{\partial(u\tau_{zx})}{\partial z} \\ & + \frac{\partial(v\tau_{xy})}{\partial x} + \frac{\partial(v\tau_{yy})}{\partial y} + \frac{\partial(v\tau_{zy})}{\partial z} \\ & + \frac{\partial(w\tau_{xz})}{\partial x} + \frac{\partial(w\tau_{yz})}{\partial y} + \frac{\partial(w\tau_{zz})}{\partial z} \end{aligned} \right] \\
 & + \left[-\frac{\partial q_x}{\partial x} - \frac{\partial q_y}{\partial y} - \frac{\partial q_z}{\partial z} \right] + S_E
 \end{aligned} \tag{Eqn 3.4}$$

The first term is the rate of work done on the element by normal forces, the second term is the rate of work due to shear forces and the third term is the rate of heat addition to the element. The term S_E includes the effects of potential energy. This equation is not required for incompressible flow calculations.

3.1.4 Navier-Stokes Equations

The governing equations contain the viscous stress components (τ_{ij}) which need to be expressed in terms of other flow variables. For Newtonian fluids, the fluid is isotropic and the viscous stresses are proportional to the rate of deformation. The viscous stresses can be written as

$$\begin{aligned}
 \tau_{xy} = \tau_{yx} &= \mu \left(\frac{\partial u}{\partial y} + \frac{\partial v}{\partial x} \right) & \tau_{xx} &= 2\mu \frac{\partial u}{\partial x} + \lambda \operatorname{div}(\mathbf{u}) \\
 \tau_{xz} = \tau_{zx} &= \mu \left(\frac{\partial u}{\partial z} + \frac{\partial w}{\partial x} \right) & \tau_{yy} &= 2\mu \frac{\partial v}{\partial y} + \lambda \operatorname{div}(\mathbf{u}) \\
 \tau_{yz} = \tau_{zy} &= \mu \left(\frac{\partial v}{\partial z} + \frac{\partial w}{\partial y} \right) & \tau_{zz} &= 2\mu \frac{\partial w}{\partial z} + \lambda \operatorname{div}(\mathbf{u})
 \end{aligned} \tag{Eqn 3.5}$$

where μ is the dynamic viscosity and λ is the second viscosity, usually approximated as $\lambda = -\frac{2}{3}\mu$. For incompressible flow the second term in τ_{xx} , τ_{yy} and τ_{zz} are dropped as the volumetric deformation is zero due to volume conservation. When these expressions are substituted into the momentum equations (Eqn 3.3), the Navier-Stokes equations result

Chapter 3 In 1981, Ahmed [8] conducted experiments on wake structures of typical automobile shapes. Vehicle shapes for an estate, fastback and notchback were tested by varying the upper rear end of a quarter scale model (Figure 3.33) with flow visualisation and wak

Shaun Johnson

$$\rho \frac{Du}{Dt} = -\frac{\partial p}{\partial x} + \frac{\partial}{\partial x} \left[2\mu \frac{\partial u}{\partial x} \right] + \frac{\partial}{\partial y} \left[\mu \left(\frac{\partial u}{\partial y} + \frac{\partial v}{\partial x} \right) \right] + \frac{\partial}{\partial z} \left[\mu \left(\frac{\partial u}{\partial z} + \frac{\partial w}{\partial x} \right) \right] + S_{Mx}$$

Eqn 3.6

$$\rho \frac{Dv}{Dt} = -\frac{\partial p}{\partial x} + \frac{\partial}{\partial x} \left[\mu \left(\frac{\partial u}{\partial x} + \frac{\partial v}{\partial y} \right) \right] + \frac{\partial}{\partial y} \left[2\mu \frac{\partial v}{\partial y} \right] + \frac{\partial}{\partial z} \left[\mu \left(\frac{\partial v}{\partial z} + \frac{\partial w}{\partial y} \right) \right] + S_{My}$$

$$\rho \frac{Dw}{Dt} = -\frac{\partial p}{\partial z} + \frac{\partial}{\partial x} \left[\mu \left(\frac{\partial u}{\partial z} + \frac{\partial w}{\partial x} \right) \right] + \frac{\partial}{\partial y} \left[\mu \left(\frac{\partial v}{\partial z} + \frac{\partial w}{\partial y} \right) \right] + \frac{\partial}{\partial z} \left[2\mu \frac{\partial w}{\partial z} \right] + S_{Mz}$$

These equations are often written in the simplified form

$$\frac{\partial(\rho u)}{\partial t} + \text{div}(\rho u \mathbf{u}) = -\frac{\partial p}{\partial x} + \text{div}(\mu \text{grad} u) + S_{Mx}$$

Eqn 3.7

$$\frac{\partial(\rho v)}{\partial t} + \text{div}(\rho v \mathbf{u}) = -\frac{\partial p}{\partial y} + \text{div}(\mu \text{grad} v) + S_{My}$$

$$\frac{\partial(\rho w)}{\partial t} + \text{div}(\rho w \mathbf{u}) = -\frac{\partial p}{\partial z} + \text{div}(\mu \text{grad} w) + S_{Mz}$$

3.1.5 Integral forms of the general transport equations

The generalised form of the Navier-Stokes equations and the continuity equation is described in words by Versteeg and Malaskechera [66] as

Rate of increase of ϕ of fluid element	+	Net rate of flow of ϕ out of fluid element	=	Rate of increase of ϕ due to diffusion	+	Rate of increase of ϕ due to sources
(Rate of change)		(Convection)		(Diffusion)		(Source)

where ϕ is a general variable that can represent u, v or w and for the continuity equation, $\phi=1$. This is written as

$$\frac{\partial(\rho\phi)}{\partial t} + \text{div}(\rho\phi \mathbf{u}) = \text{div}(\Gamma \text{grad}\phi) + S_{\phi}$$

Eqn 3.8

where Γ is the diffusion coefficient and S_{ϕ} is the source term. When the generalised equation is integrated over the control volume, this gives

$$\int_{CV} \frac{\partial(\rho\phi)}{\partial t} dV + \int_{CV} \text{div}(\rho\phi \mathbf{u}) dV = \int_{CV} \text{div}(\Gamma \text{grad}\phi) dV + \int_{CV} S_{\phi} dV$$

Eqn 3.9

3.1.6 Discretisation of equations

For the finite-volume method, it is necessary to discretise the equations in order that they can be solved using numerical methods. As a brief explanation of processes used, a steady one-dimensional convection-diffusion example will be used in the absence of sources. The momentum equations from Eqn 3.3 can be simplified to

Chapter 3 In 1981, Ahmed [8] conducted experiments on wake structures of typical automobile shapes. Vehicle shapes for an estate, fastback and notchback were tested by varying the upper rear end of a quarter scale model (Figure 3.33) with flow visualisation and wak

Shaun Johnson

$$\frac{d}{dx}(\rho u \phi) = \frac{d}{dx} \left(\Gamma \frac{d\phi}{dx} \right). \quad \text{Eqn 3.10}$$

In addition, the continuity equation from Eqn 3.2 reduces to

$$\frac{d(\rho u)}{dx} = 0. \quad \text{Eqn 3.11}$$

With reference to the one-dimensional control volume in Figure 3.1, consider node P. The neighbouring nodes are referenced relative to node P and are referred as the West and East nodes. The interface between the control volumes for the west and east face are labels w and e respectively.

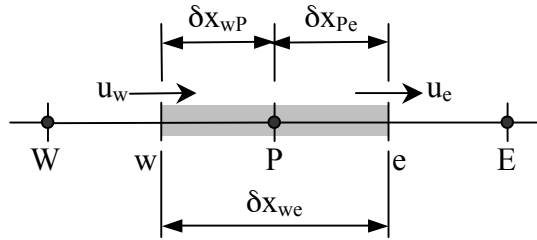


Figure 3.1 Control volume around node P for one-dimensional analysis.

The momentum equation (Eqn 3.10) and continuity equation (Eqn 3.11) are integrated over the control volume to give:

$$(\rho u A \phi)_e - (\rho u A \phi)_w = \left(\Gamma A \frac{\partial \phi}{\partial x} \right)_e - \left(\Gamma A \frac{\partial \phi}{\partial x} \right)_w \quad \text{Eqn 3.12}$$

$$(\rho u A)_e - (\rho u A)_w = 0, \quad \text{Eqn 3.13}$$

where A is the face area. By substituting $F = \rho u$ for the convective mass flux per unit area and $D = \Gamma / \delta x$ for the diffusion conductance at the cell faces, assuming the

cell face area is a constant, and using a central-difference approximation for the derivatives, allows these equations to be reduced to

$$F_e \phi_e - F_w \phi_w = D_e (\phi_E - \phi_P) - D_w (\phi_P - \phi_W) \quad \text{Eqn 3.14}$$

$$F_e - F_w = 0. \quad \text{Eqn 3.15}$$

For a fluid solving the equivalent equations is non-trivial due to the lack of an explicit equation to calculate the pressure. Instead, pressure can be determined indirectly using the continuity equation since the pressure field is coupled to the velocity field. Fluent uses the well-established iterative solution scheme, SIMPLE (Semi-Implicit Method for Pressure-Linked Equations) algorithm of Pantakar &

Spalding [67]. In this procedure, an initial guess is made of the pressure field. The momentum equations are solved and then the continuity equations are solved to create an updated guess of the pressure field. This updated pressure field is used to update the velocity field and the process is repeated until continuity is satisfied.

3.1.7 Turbulence

For laminar flow, the Navier-Stokes equations (Eqn 3.7) completely describe the flow field and can be accurately approximated using the finite-volume method using only modest computational resources. However, most flows of engineering significance are turbulent, this being a critical feature of the flow field. The Navier-Stokes equations are also assumed to represent turbulent flows; however, in this case the flows are three-dimensional and time-dependent, and involve a large range of spatial scales from the size of large-scale eddies, which depend on the largest features of the geometries involved, to the smallest scales, where coherent flow energy is dissipated as heat through viscous dissipation. Using direct numerical simulation (DNS) to simulate all length scales for high Reynolds number flows is not practical with computational resources presently available. Interestingly, Phillip Spalart from Boeing estimated the given Moore's law applies for the foreseeable future, fully-resolved direct simulations of flows over aircraft will not be possible until about 2080. In the interim turbulence models are used, which attempt to approximate the effects of turbulence on the flow. In this section, a brief description will be given of turbulence modelling especially in the context of the finite-volume method.

Above a critical Reynolds number, the flow field changes from smooth flow to one that is by nature random, chaotic and unsteady. For one modelling approach known as *Reynolds-averaging*, the flow field is decomposed into a mean value Φ and a fluctuating component $\varphi'(t)$ so that $\varphi(t) = \Phi + \varphi'(t)$. The mean value is usually taken as time-independent; however, it is also possible for it to represent a mean value that varies in time but on a time-scale that is much longer than the fluctuation time-scale. This approach is known as *unsteady Reynolds-averaging*, and when it is applied to the Navier-Stokes equations, the resultant equations are called the Unsteady Reynolds-Averaged Navier-Stokes Equations (URANS).

Chapter 3 In 1981, Ahmed [8] conducted experiments on wake structures of typical automobile shapes. Vehicle shapes for an estate, fastback and notchback were tested by varying the upper rear end of a quarter scale model (Figure 3.33) with flow visualisation and wak

Shaun Johnson

The turbulent fluctuations are three-dimensional in nature and are constructed physically of turbulent eddies with a wide range of length scales. The largest turbulent eddies are generated from the energy of the mean flow and are dominated by inertia effects. Due to their interaction with the mean flow, in general the large eddies are anisotropic. The smaller eddies are stretched by the larger eddies and the kinetic energy of the larger eddies is transferred to smaller and smaller eddies in an energy cascade. As a result, turbulent flow contains energy across a large range of frequencies/length-scales. The smallest eddy size is ultimately limited by viscosity and work is performed against the viscous stresses resulting in flow energy loss through conversion to thermal energy. The energy cascade and the associated vortex stretching and turning mechanisms that transport energy through the scales, together with the increasing effects of viscosity, mean that the small eddies are isotropic.

The effect of turbulence on the flow is included in simulations through the influence of correlations between fluctuating components on the mean flow properties. If φ is taken as the flow property, the mean component of the flow can be taken as

$$\Phi = \frac{1}{\Delta t} \int_0^{\Delta t} \varphi(t) dt \text{ or } \Phi = \frac{1}{N} \sum_{i=1}^N \varphi_i. \quad \text{Eqn 3.16}$$

Here the first expression represents a time mean and the second expression defines an ensemble mean. The first approach is useful for time-steady mean flows and is the standard conceptual view employed in steady RANS turbulence modelling. The second expression represents a mean from a statistically-representative set (ensemble) of independent instantaneous measurements or experiments, possibly taken at the same phase of a slowly-varying mean flow, e.g., at the same phase in the shedding cycle for flow past a cylinder. This viewpoint is useful for such flows, in which the time-mean is not particularly representative of the flow at any stage of the cycle.

For the time-mean, Δt is taken so that it significantly exceeds the slowest variations in the eddies, thus ensuring it should be adequate for time-averaged or steady state flows. Clearly in this case, the mean of the fluctuating component must be zero,

Chapter 3 In 1981, Ahmed [8] conducted experiments on wake structures of typical automobile shapes. Vehicle shapes for an estate, fastback and notchback were tested by varying the upper rear end of a quarter scale model (Figure 3.33) with flow visualisation and wak

Shaun Johnson

$\overline{\varphi'} = \frac{1}{\Delta t} \int_0^{\Delta t} \varphi'(t) dt = 0.$	Eqn 3.17
--	----------

If we consider the continuity equation (Eqn 3.2) and the Navier-Stokes equations (Eqn 3.7), we can replace the mean velocity terms with the terms that include fluctuating components:

$$u = U + u'; \quad v = V + v'; \quad w = W + w'. \quad \text{Eqn 3.18}$$

The continuity equation becomes

$$\text{div}(\mathbf{U}) = \mathbf{0}, \quad \text{Eqn 3.19}$$

since $\overline{\text{div}(\mathbf{u})} = \text{div}(\mathbf{U})$.

The momentum equations for incompressible flow become

$$\begin{aligned} \frac{\partial U}{\partial t} + \text{div}(UU) &= -\frac{1}{\rho} \frac{\partial P}{\partial x} + \nu \text{div}(\text{grad}U) + \left[-\frac{\partial \overline{u'^2}}{\partial x} - \frac{\partial \overline{u'v'}}{\partial y} - \frac{\partial \overline{u'w'}}{\partial z} \right], \\ \frac{\partial V}{\partial t} + \text{div}(VU) &= -\frac{1}{\rho} \frac{\partial P}{\partial y} + \nu \text{div}(\text{grad}V) + \left[-\frac{\partial \overline{u'v'}}{\partial x} - \frac{\partial \overline{v'^2}}{\partial y} - \frac{\partial \overline{u'w'}}{\partial z} \right], \\ \frac{\partial W}{\partial t} + \text{div}(WU) &= -\frac{1}{\rho} \frac{\partial P}{\partial z} + \nu \text{div}(\text{grad}W) + \left[-\frac{\partial \overline{u'v'}}{\partial x} - \frac{\partial \overline{u'w'}}{\partial y} - \frac{\partial \overline{w'^2}}{\partial z} \right]. \end{aligned} \quad \text{Eqn 3.20}$$

These are referred to as the Reynolds Averaged Navier-Stokes equations (RANS) with the correlations between fluctuating components in the extra terms referred to as the Reynolds stresses. For turbulent flow, the normal stresses are non-zero since they contain a squared term and the shear-stress terms, i.e., the correlations between *different* velocity components, are usually much larger than the viscous stresses.

3.1.8 Turbulence models

A number of different turbulent models have been proposed to tackle the problem of modelling turbulence while trying to keep the simulations from being too computationally expensive. The classic models used such as the $k\epsilon$ turbulence model and Reynolds Stress Model are based on the RANS formulation, while an alternative approach called Large Eddy Simulation (LES) uses space-filtered equations. As turbulence is unsteady, the LES turbulence approach accurately simulates the largest eddies since they have the greatest interaction with the flow, while the effect of the smaller eddies is modelled. Due to the unsteady nature of the LES model and the

large meshes required, it is computationally expensive and at the present time has limited application for investigations involving large parameter-space studies. The three models considered for the investigations reported in this thesis were all RANS models: the $k\epsilon$ turbulence model, the $k\omega$ turbulence model, and the Reynolds stress model.

3.1.9 $k\epsilon$ Turbulence Model

The $k\epsilon$ turbulence model is a two-equation model, which requires an equation for the kinetic energy of turbulence (k), and the rate of dissipation of turbulence (ϵ). Compared with other models, the $k\epsilon$ model is quite stable and robust. It is semi-empirically based on experiments using high Reynolds numbers flows to determine the *constants* in the equations.

The key assumption used in this model is that the Reynolds stresses act to cross-diffuse (or transport) mass and momentum, similar to the role of the viscous stresses. Given this, it is tempting to assume that the turbulent stress can be expressed in terms of the mean flow gradient, as is the case for the viscous stress. Of course, the standard picture of turbulence in terms of interacting eddies makes this analogy somewhat questionable, especially at the larger scales. In any case, the $k\epsilon$ model uses this *Boussinesq approximation*, which proposes that the Reynolds stresses are linked to the mean rates of deformation as follows

$$\tau_{ij} = -\rho \overline{u'_i u'_j} = \frac{2}{3} \rho k \delta_{ij} + \mu_t \left(\frac{\partial U_i}{\partial x_j} + \frac{\partial U_j}{\partial x_i} \right), \quad \text{Eqn 3.21}$$

where μ_t is the eddy viscosity, δ_{ij} is the Kronecker delta and k is the turbulent kinetic energy given by

$$k = \frac{1}{2} \left(\overline{u'^2} + \overline{v'^2} + \overline{w'^2} \right), \quad \text{Eqn 3.22}$$

The eddy viscosity coefficient is chosen as $\mu_t = \rho C_\mu \frac{k^2}{\epsilon}$ on dimensional grounds with C_μ assumed to be a constant.

The standard $k\epsilon$ model uses the additional transport equations for k and ϵ .

Chapter 3 In 1981, Ahmed [8] conducted experiments on wake structures of typical automobile shapes. Vehicle shapes for an estate, fastback and notchback were tested by varying the upper rear end of a quarter scale model (Figure 3.33) with flow visualisation and wak

Shaun Johnson

$$\frac{\partial(\rho k)}{\partial t} + \text{div}(\rho k \mathbf{U}) = \text{div} \left[\frac{\mu_t}{\sigma_k} \text{grad} k \right] + 2\mu_t E_{ij} \cdot E_{ij} - \rho \varepsilon, \quad \text{Eqn 3.23}$$

$$\frac{\partial(\rho \varepsilon)}{\partial t} + \text{div}(\rho \varepsilon \mathbf{U}) = \text{div} \left[\frac{\mu_t}{\sigma_k} \text{grad} \varepsilon \right] + C_{1\varepsilon} \frac{\varepsilon}{k} 2\mu_t E_{ij} \cdot E_{ij} - c_{2\varepsilon} \rho \frac{\varepsilon^2}{k}, \quad \text{Eqn 3.24}$$

where $E_{ij} = \text{div} \mathbf{U}$; $C_\mu = 0.09$; $\sigma_k = 1.00$; $\sigma_\varepsilon = 1.30$; $C_{1\varepsilon} = 1.44$; $C_{2\varepsilon} = 1.92$

This is described in words by Versteeg and Malaskeera [66] as

Rate of change of k or ε	+	Transport of k or ε by convection	=	Transport of k or ε by diffusion	+	Rate of production of k or ε	-	Rate of destruction of k or ε
--------------------------	---	-----------------------------------	---	----------------------------------	---	------------------------------	---	-------------------------------

The realizable kε model is a variant of the standard kε model described above with two major differences. Firstly, the variable C_μ is calculated from the formula

$$\mu_t = \rho C_\mu \frac{k^2}{\varepsilon} \quad \text{Eqn 3.25}$$

This is because in highly strained flows, the normal Reynolds Stresses can become negative which is unrealistic. The second difference is that the realizable kε model uses different sources and sink terms in the transport equation for eddy dissipation.

3.1.10 kω turbulence model

The kω turbulence model was first proposed by Kolmogorov and later modified by Wilcox [68] which has become known as the standard kω model. It is similar to the kε model in that two additional equations are used for modelling turbulence. The first term is the kinetic energy of turbulence k and the second term ω is the rate of dissipation of turbulence per unit of turbulent kinetic energy ($\omega \approx \varepsilon/k$). The main advantage over the kε model is that this model is integrated down to the wall without the use of wall functions and has shown to be robust for a wide range of boundary layer flows under a pressure gradient.

The standard kω model uses the additional transport equations for k and ω . The turbulent kinetic energy equations is given by:

$$\frac{\partial(\rho k)}{\partial t} = \text{div} \left[\frac{\mu_t}{\sigma_k} \text{grad} k \right] + \tau_{ij} E_{ij} - \rho \beta^* f_{B^*} k \omega, \quad \text{Eqn 3.26}$$

Chapter 3 In 1981, Ahmed [8] conducted experiments on wake structures of typical automobile shapes. Vehicle shapes for an estate, fastback and notchback were tested by varying the upper rear end of a quarter scale model (Figure 3.33) with flow visualisation and wak

Shaun Johnson

where β^* and f_{β^*} are parameters that are a function of Re and the cross-diffusion parameter, χ_k . The specific dissipation equation is given by:

$$\frac{\partial(\rho\omega)}{\partial t} = \text{div} \left[\frac{\mu_t}{\sigma_k} \text{grad} \varepsilon \right] + \alpha \frac{\omega}{k} \tau_{ij} E_{ij} - \rho \beta f_{\beta} \omega^2, \quad \text{Eqn 3.27}$$

where α and β are parameters that are function of Re and the vortex-stretching parameter, χ_ω . For the $k\omega$ model, the turbulent viscosity is given by:

$$\mu_t = \alpha^* \rho \frac{k}{\omega}. \quad \text{Eqn 3.28}$$

where α^* is dependent on Re.

A derivation of the standard $k\omega$ model is called the $k\omega$ Shear Stress Transport (SST) model proposed by Menter [69]. The main differences being a modified turbulent viscosity formulation to account for the transport effects of the principal turbulent shear stress. A cross-diffusion term in the ω equation and a blending function are added to change from the standard $k\omega$ model in the inner region of the boundary layer to a high-Reynolds-number version of the $k\varepsilon$ model in the outer part of the boundary layer to ensure that the model equations behave appropriately in both the near-wall and far-field zones.

3.1.11 Reynolds Stress Model

One of the main limitations of the $k\varepsilon$ turbulence model is that it assumes that turbulent viscosity is isotropic which is not realistic. The Reynolds stress model does not use the Boussinesq approximation for the Navier-Stokes equations but calculates the Reynolds stress individually. For a three-dimensional model, this equates to six additional transport equations along with the transport equation for ε . This model has proven to be more realistic for flows under high strain rates.

The equation governing the evolution of the Reynolds stress tensor $R_{ij} = \overline{u'_i u'_j}$ is

$$\frac{DR_{ij}}{Dt} = P_{ij} + D_{ij} - \varepsilon_{ij} + \Pi_{ij} + \Omega_{ij} \quad \text{Eqn 3.29}$$

where P_{ij} is the production term, D_{ij} is the diffusion term, ε_{ij} is dissipation rate, Ω_{ij} is the rotation term and Π_{ij} is the pressure-strain correlation. The production term is

Chapter 3 In 1981, Ahmed [8] conducted experiments on wake structures of typical automobile shapes. Vehicle shapes for an estate, fastback and notchback were tested by varying the upper rear end of a quarter scale model (Figure 3.33) with flow visualisation and wak

Shaun Johnson

$$P_{ij} = -\left(R_{im} \frac{\partial U_j}{\partial x_m} + R_{im} \frac{\partial U_i}{\partial x_m} \right). \quad \text{Eqn 3.30}$$

The diffusion term assumes that the rate of transport of Reynolds stresses is proportional to the Reynolds stress gradient,

$$Dij = \frac{\partial}{\partial x_m} \left(\frac{v_t}{\sigma_k} \frac{\partial R_{ij}}{\partial x_m} \right) = \text{div} \left(\frac{v_t}{\sigma_k} \text{grad}(R_{ij}) \right), \quad \text{Eqn 3.31}$$

where $v_t = C_\mu \frac{k^2}{\varepsilon}$; $C_\mu = 0.09$ and $\sigma_k = 1.0$. Isotropy is assumed for the dissipation rate

$$\varepsilon_{ij} = \frac{2}{3} \varepsilon \delta_{ij}. \quad \text{Eqn 3.32}$$

The pressure-strain term is given by

$$\Pi_{ij} = -C_1 \frac{\varepsilon}{k} \left(R_{ij} - \frac{2}{3} k \delta_{ij} \right) - C_2 \left(P_{ij} \right) - \frac{2}{3} P \delta_{ij}, \quad \text{Eqn 3.33}$$

where $C_1 = 1.8$ and $C_2 = 0.6$. The rotational term is given by

$$\Omega_{ij} = -2\omega_k \left(R_{jm} e_{ikm} + R_{im} e_{jkm} \right), \quad \text{Eqn 3.34}$$

where ω_k is the rotation vector.

For three-dimensional flow, the six Reynolds stresses equations are solved along with the equation for the dissipation rate, which is similar to that used in the $k\varepsilon$ turbulence model. The dissipation rate equation is

$$\frac{D\varepsilon}{Dt} = \text{div} \left(\frac{v_t}{\sigma_\varepsilon} \text{grad}\varepsilon \right) + C_{1\varepsilon} \frac{\varepsilon}{k} 2v_t E_{ij} \cdot E_{ij} - C_{2\varepsilon} \frac{\varepsilon^2}{k}, \quad \text{Eqn 3.35}$$

where $C_{1\varepsilon} = 1.44$ and $C_{2\varepsilon} = 1.92$.

3.1.12 Wall Boundary Conditions

Numerical simulations are significantly affected by the treatment of wall boundary conditions. For turbulence models, not only does the non-slip condition requirement have to be met, but walls are a source for turbulent kinetic energy and vorticity due to the large velocity gradients.

Chapter 3 In 1981, Ahmed [8] conducted experiments on wake structures of typical automobile shapes. Vehicle shapes for an estate, fastback and notchback were tested by varying the upper rear end of a quarter scale model (Figure 3.33) with flow visualisation and wak

Shaun Johnson

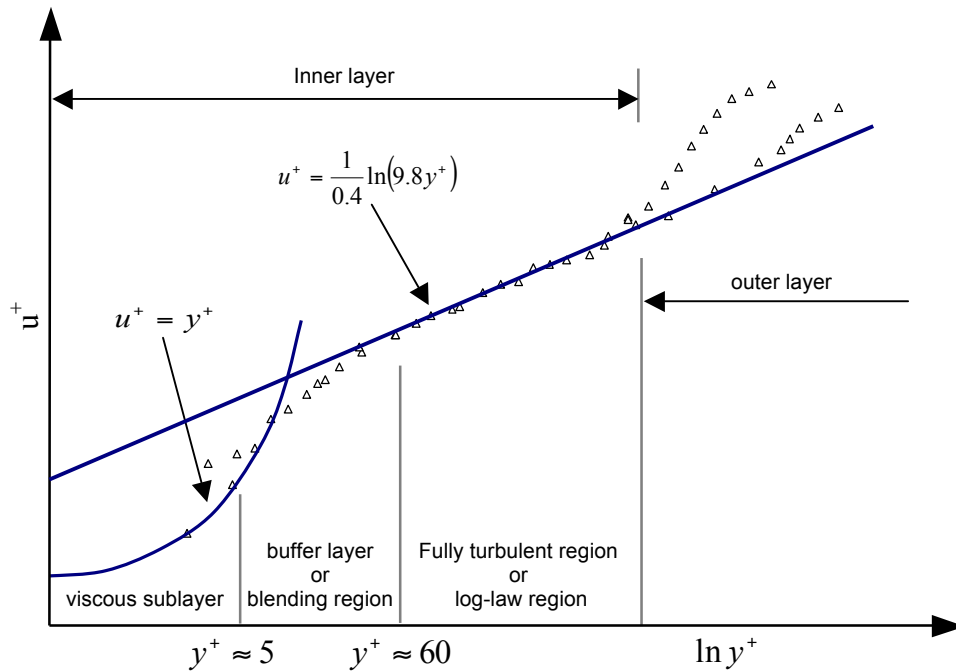


Figure 3.2 Turbulent profile taken from [70]

In Figure 3.2, the dimensionless velocity (u^+) is plotted against the log of the dimensionless wall distance (y^+) to outline the three main regions of the wall velocity profile. The dimensionless wall distance is given by:

$y^+ = \frac{\Delta y_p}{\nu} \sqrt{\frac{\tau_w}{\rho}}$	Eqn 3.36
---	-----------------

where Δy_p is the distance normal to the wall. The dimensionless velocity is calculated by:

$u^+ = \frac{U}{\left(\frac{\tau_w}{\rho}\right)^{\frac{1}{2}}}$	Eqn 3.37
--	-----------------

These three regions are the viscous sublayer, the log-law region and the outer layer. In the extremely thin viscous sublayer ($y^+ < 5$), the shear stress is dominated by the viscous stresses. In the log-law region ($60 < y^+ < 500$) where the viscous and turbulent effects are significant, the shear stress increases slowly with Δy_p . Finally in the outer layer, turbulent effects dominate the velocity profile.

Two approaches are possible to model the near wall region. To reduce grid requirements, it is possible to model the viscosity affected region by using wall functions proposed by Launder and Spalding [71]. Instead of directly simulating the inner layer near the wall, the velocity profile is modelled using semi-empirical formulas. For wall functions to be valid, the first node away from the wall should be in the region of $30 < y^+ < 60$. Wall functions are not well suited to less than ideal flows such as for severe pressure gradients or high three-dimensionality near the wall. The near-wall modelling method is to resolve the viscosity-affected region all the way to the wall, including the viscous sublayer. This requires a high local near-wall density grid so that the significantly varying velocity is resolved near the wall. In practice, this requires the first node to be at $y^+ \approx 1$. For complex three-dimensional problems this may mean trading grid density in regions of interest against the increased grid density required at the wall. In Fluent, wall functions are referred to as the standard wall function (SWF) approach while near wall modelling is referred to as using enhanced wall functions (EWF). Enhanced wall functions use a near wall modelling if $y^+ \approx 1$, otherwise standard wall functions are used. More information can be found in [70].

3.2 Geometry

The geometry used for numerical simulations was that described by Ahmed et al. [5] shown in Figure 3.36. For reference, the coordinate system, unless otherwise stated, is as indicated in Figure 3.3, with the origin at the rear of the model at the base of the rear surface on the vehicle centreline. The X direction is referred to downstream or streamwise direction while the Z direction is referred to as the spanwise direction. The XY plane at $Z=0$ is referred to as the centreline. For analysis, drag and lift measurements were computed from different regions of the body. The four regions as indicated are the slant surface, rear surface, side surface and front surface. The slant surface comprises the chamfered surface of the Ahmed body. Note that the length of this surface is kept constant. As a result, for higher slant angles, the vertical rear end of the model (labelled the rear surface) decreases in height and surface area. All surfaces that are parallel to the downstream direction are

Chapter 3 In 1981, Ahmed [8] conducted experiments on wake structures of typical automobile shapes. Vehicle shapes for an estate, fastback and notchback were tested by varying the upper rear end of a quarter scale model (Figure 3.33) with flow visualisation and wak

Shaun Johnson

referred to as the side surfaces. For models where a symmetry boundary condition was employed and only half the body is modelled, body forces are adjusted to reflect a full model.

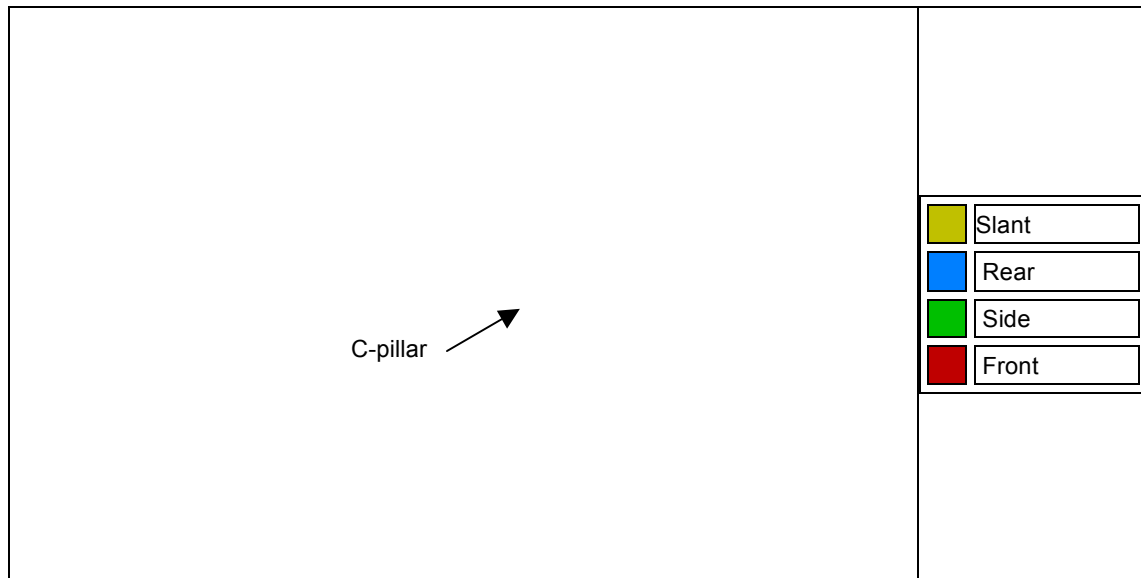


Figure 3.3 Coordinate system and origin location used in the Simulations. The four regions as indicated are the slant surface, rear surface, side surface and front surface used for analysis of body forces.

3.3 Grid Setup

The generation of efficient two-dimensional and three-dimensional meshes is a complex and difficult task. A number of steps were required to produce a grid for simulations. The pre-processor *Gambit 2.04*, which is supplied with *Fluent* was used for domain and grid generation. Instead of using the Graphical User Interface (GUI) to create the domain and grid, scripts were employed to automate grid generation using a parameterized model of the geometry. This was to ensure that different grids for different models were reproduced consistently.

The biggest problem with meshing the model was to produce an efficient mesh, which captures the key flow structures while at the same time, ensuring the mesh size does not exceed the computational resources available. Two mesh models were examined for modelling the Ahmed body.

The first mesh utilized was a tetrahedral mesh with triangular prism elements on the surface of the geometry and ground to model the boundary layer. In general, tetrahedral meshes are good for capturing complex geometries and structures. For simple geometries, more elements are required for the same level accuracy compared with hexagonal elements. However, due to their unstructured nature, it was possible to expand cells in the far field where a dense grid is not required, allowing more cells in critical regions surrounding the geometry of interest.

The second mesh examined utilized hexagonal elements, which have less diffusion and are more accurate for the same grid size. However, with hexagonal meshes, many cells are wasted in the far field since the mesh cannot be expanded in three dimensions. It is also more difficult to capture complex geometries. The Ahmed body is a relatively simple body compared with true automotive geometries but it still represents a challenge to create a hexagonal mesh to model the front surfaces of the body without an excessive number of elements in that region. It was found that using hexagonal elements created meshes which were too computationally expensive compared with the tetrahedral meshes. Modelling the viscous sub-layer proved to be difficult because on the model surface a small grid spacing is required. When these grids were stretched towards the boundaries, they created high aspect ratio elements in the simulations, which caused discontinuities in the flow field.

Various techniques were employed to reduce the grid size. These included removing the front region (Figure 3.3) of the geometry and using velocity data from tetrahedral meshes for the inlet boundary condition. This proved effective but required other simulations to calculate the velocity inlet profile. Non-conformal interfaces were used near the body to reduce mesh density in the far field where dense grids were not required. Initial investigations found that the non-conformal interfaces were very sensitive to flow gradients, causing large discontinuities in the flow field, and had to be placed far away from the body negating their effectiveness in reducing the number of elements.

Chapter 3 In 1981, Ahmed [8] conducted experiments on wake structures of typical automobile shapes. Vehicle shapes for an estate, fastback and notchback were tested by varying the upper rear end of a quarter scale model (Figure 3.33) with flow visualisation and wak

Shaun Johnson

3.3.1 Mesh Generation Procedure

The grid generation procedure for geometry creation, edge meshing, face meshing, volume meshing and zone assignment will be discussed in the following sections. The procedure for grid generation is outlined in Table 3.1.

	Step	Description
1	Geometry Creation	Import or draw the geometry for the simulation, creating faces and volumes
2	Edge meshing	mesh the edges of the mesh controlling the edge density
3	Face Mesh	Mesh the surface faces of the volume
4	Volume Meshing	For 3D models, the volumes are meshes using data from the edges and faces to control mesh density
5	Mesh examination	Check the mesh to ensure there are no highly skewed or large aspect ratio elements which could effect the simulation
6	Zone Assignment	Assign the boundary conditions to faces on the geometry
7	Mesh export	Export the mesh for computation in the solver

Table 3.1 Procedure for grid generation

3.3.2 Geometry Creation

As opposed to using the built in functions in *Gambit* to create primitive volumes or importing the geometry from an external source, the model was built “bottom up” from coordinates. These coordinates were linked together to create edges, which were stitched together to form the faces that are used to create volumes. This created a parameterised domain based on the coordinates, which were calculated from input parameters such as slant angle and body width. The vehicle surfaces were subdivided into smaller surfaces (Figure 3.3) to isolate forces from different regions of the body during simulations and to control grid refinement. The domain was subdivided into three regions to control mesh density as indicated in Figure 3.4 and are labelled the inner volume, rear volume and outer volume. Various meshing densities were used in each of these regions to control the mesh density according to the gradients expected in the flow field.

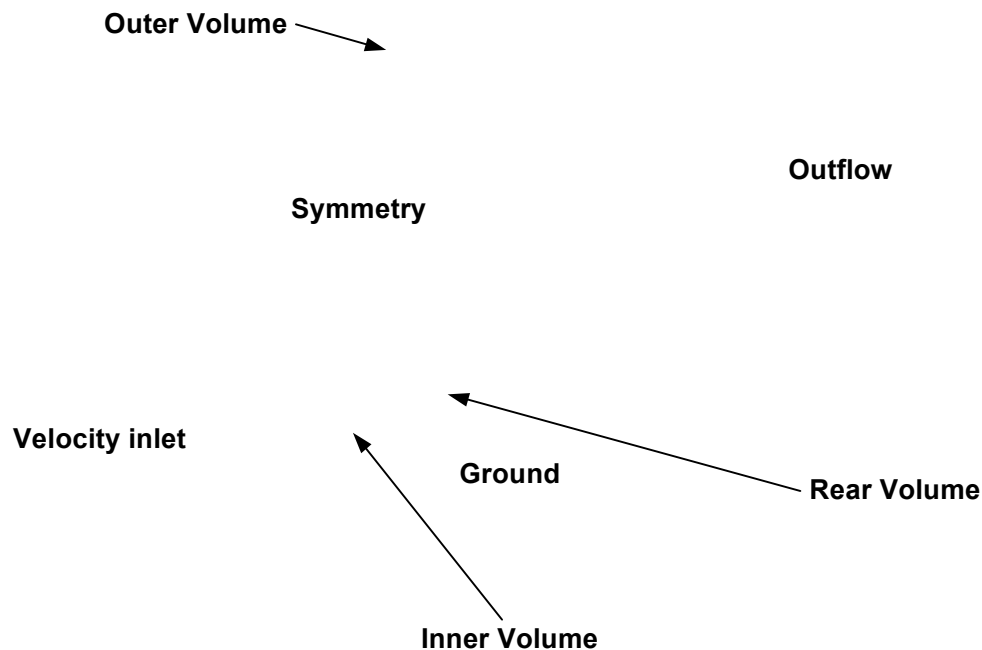


Figure 3.4: Three volumes were defined in the domain to control mesh density, labelled the Inner Volume, Rear Volume and the Outer Volume. Surfaces are removed from the outer volume to allow visualisation of the inner regions. Boundary labels indicate the different boundary conditions used on the outer volume.

3.3.3 Meshing

Meshing the model required three steps: edge meshing, face meshing and volume meshing. The objective was to reduce overall mesh size, confine small cells to areas where they were needed for expected high gradients, remove grid discontinuities and avoid skewed meshes which decrease the accuracy of the mesh. Edge meshes were graded by varying the interval size on the edge. The graded edge mesh controls the distribution of cell sizes in the face mesh, which in turn, controls the distribution of cell size in the volume mesh.

3.3.3.1 Edge Meshing

Considerable effort was undertaken to ensure the edge meshes in domain were constructed correctly to ensure smooth mesh spacing between different edges. The two parameters which affect the mesh spacing were the number of intervals (NOI) and the succession ratio (SR), which is given by the formula:

Chapter 3 In 1981, Ahmed [8] conducted experiments on wake structures of typical automobile shapes. Vehicle shapes for an estate, fastback and notchback were tested by varying the upper rear end of a quarter scale model (Figure 3.33) with flow visualisation and wak

Shaun Johnson

$$SR = \frac{l_{i+1}}{l}, \quad \text{Eqn 3.38}$$

where l_i and l_{i+1} are the lengths of consecutive intervals. The five built-in meshing schemes (refer to [72] for further details) available were not suitable since it was not possible to specify the first length and the last length of an edge. Consequently, a new meshing scheme was developed that calculated the SR and NOI given first and last interval length desired and the length of the edge. The advantage of this method was that it was possible to specify the grid density at specific locations on the geometry and allow the script to calculate the mesh spacing to match between two points. This avoided the problems of skewed grids as the geometry changed, especially for parametrised models where edge lengths change regularly.

An iterative method was used to calculate the SR and NOI. The upper limit and lower limit of the SR were predefined. The midpoint between the SR limits was calculated and for that given SR, the length of the last interval was calculated and compared with the desired last length interval spacing. If the last interval was larger, the midpoint SR became the SR upper limit, and if the last interval was shorter, the SR lower limit was replaced with the midpoint SR. This decreased the limit range of each iteration until an acceptable SR was calculated.

3.3.3.2 Face Meshing

A triangular face mesh was used on the surfaces of the body. On the sharp edges of the body such as the C-pillar edge, a finer grid was merged with the face mesh. As can be seen in Figure 3.5a, the face meshing near the centre of the side surface is quite coarse and increases in density near the C-pillar. Sizing functions were employed to ensure the SRs were controlled to avoid mesh discontinuities.

3.3.3.3 Boundary Layer

Instead of using growing equal-angle tetrahedral volumes from the body surface, a layer of triangular prisms was used on the surface to model the viscous sublayer. The first node was placed at 0.00025 non-dimensional units from the surface, which equated to a $y^+ \approx 1$ on the surface of the model. The triangular face was extruded using SR=1.2 for 17 layers to create the boundary-layer prisms. The boundary layer

Chapter 3 In 1981, Ahmed [8] conducted experiments on wake structures of typical automobile shapes. Vehicle shapes for an estate, fastback and notchback were tested by varying the upper rear end of a quarter scale model (Figure 3.33) with flow visualisation and wak

Shaun Johnson

was kept relative to the model surfaces and the tetrahedral mesh was expanded for different slant angles as can be seen in Figure 3.5. Triangular prisms were also used to model the ground boundary layer but were kept relatively coarse since testing indicated it had a negligible effect on the body. Here, 17 prism layers were used with the first node 0.00075 non-dimensional units from the wall ($y^+ \approx 1$).

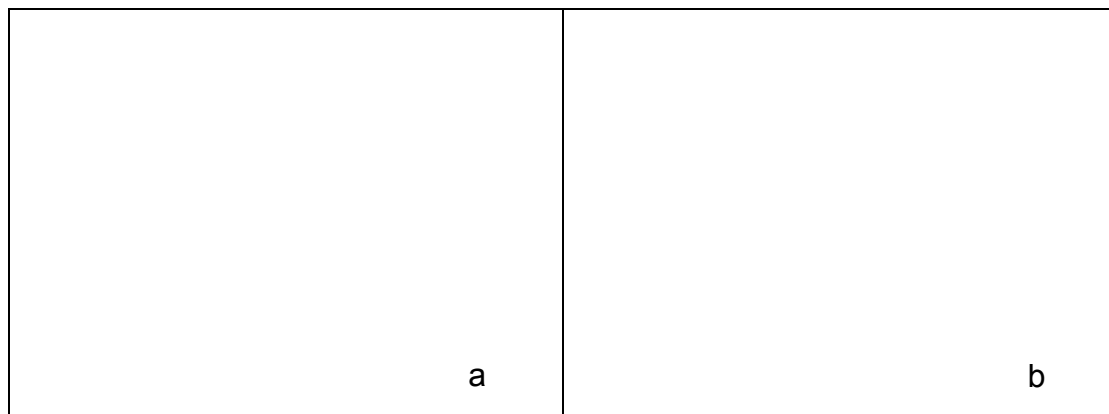


Figure 3.5 variation in mesh a) 15 b) 30

The tetrahedral meshes were defined in three major grid regions: the inner region, rear region and outer region corresponding to the different volumes in Figure 3.4. The inner region consisted of small volume cells surrounding the body. The smallest grid spacing was on the slant surface where complex flow structures were expected. Initially, the mesh was slightly coarsened on the vehicle centreline to allow higher density grids near the C-pillars and to reduce mesh size on higher AR simulations. However, it was found that the gradient in mesh density near the slant surface caused the wake to evolve into a large separation bubble. In the rear region the grid was kept relatively dense because two counter-rotating vortices were present, with the grid density decreasing further away from the body. The grid density in the outer region was kept coarse to reduce the grid size. This was acceptable since the cell gradients were not high and the purpose of having a large domain was to limit blockage effects on the model.

3.3.4 Zone Assignment

The boundary conditions and zone assignments define the physical and operational characteristics of the model at its boundaries and within specific regions of its

Chapter 3 In 1981, Ahmed [8] conducted experiments on wake structures of typical automobile shapes. Vehicle shapes for an estate, fastback and notchback were tested by varying the upper rear end of a quarter scale model (Figure 3.33) with flow visualisation and wak

Shaun Johnson

domain. The locations of the various zones are labelled in Figure 3.4. On the vehicle surface, a non-slip wall was specified and a symmetry condition was assigned to the surfaces, which are removed to allow viewing of the internal volumes since the surfaces were not critical.

The velocity inlet boundary condition defines the velocity field at the inlet without specifying the stagnation pressure. Only the velocity scalar and turbulence intensity level were specified since the velocity vector is normal to the boundary plane.

The outlet boundary is usually used in conjunction with the inlet boundary condition. This boundary was placed far downstream in a region where the gradient of the flow field was zero in the streamwise direction. The mass flux into the domain from the inlet velocity must be equal to the mass flux out of the domain through the outlet boundary condition for continuity to be satisfied. Since neither the velocity inlet nor the outflow boundary condition defines the pressure in the far field, the gauge pressure must be defined at a location in the domain. This was specified at a point with free stream conditions near the inlet boundary in the domain.

The Ahmed body and the ground were modelled using a wall boundary condition. For a non-slip wall, the parallel velocity and normal velocity must be zero. Moving walls were defined by specifying a value for the parallel velocity. To accurately model a vehicle moving down a road, the ground should be defined as a wall moving at the same velocity as the free stream. Despite this, in these simulations the ground was specified as a non-slip wall to parallel the experimental set-up. The pressure and viscous forces on wall surface were calculated by:

$F = \sum (p - p_{ref}) A_{cell} \hat{n} + \sum -\tau_w A_{cell} ,$	Eqn 3.39
---	-----------------

where A_{cell} is the area of the face, p_{ref} is the reference pressure and \hat{n} is the unit normal.

The symmetry boundary condition was used because the physical geometry of the Ahmed body and the expected pattern of the flow/thermal solution, have mirror symmetry. It is a special situation of the wall boundary condition where only the normal velocity is set to zero. Beside the symmetry plane on the vehicle centreline,

Chapter 3 In 1981, Ahmed [8] conducted experiments on wake structures of typical automobile shapes. Vehicle shapes for an estate, fastback and notchback were tested by varying the upper rear end of a quarter scale model (Figure 3.33) with flow visualisation and wak

Shaun Johnson

the outer region defined in Figure 3.4 was specified as a symmetry boundary to avoid boundary-layer blockage in the domain.

3.4 Model Setup

As mentioned previously, the commercial software *Fluent* was used to conduct the numerical simulations on the Ahmed body. Due to the complexity of the simulation program with such a vast number of parameters available for modification, a considerable time and effort was spent determining how different parameters affected the simulation results. It was found that the flow structures near the critical slant angle were difficult to model because of the high sensitivity to model parameters.

In this section, the procedure for initialising the solution will be presented as well as the approach to determine convergence.

3.4.1.1 Model initialisation

To run and process the simulations, scripts were utilised to set-up and define the model to ensure all simulations had the same configuration. The procedure for initialising the simulation is outlined in Table 3.2. Other scripts were used to run the simulations and modify various parameters such as under-relaxation factors after the simulation was initialised.

	Step	Description
1	Read Mesh File	Read in mesh file produced by <i>Gambit</i> .
2	Check grid	Check the validity of mesh file and ensure that there are no cells with a negative volume.
3	Reorder domain	Reordering the domain to improve the computational performance of the solver by rearranging the nodes, faces, and cells in memory
4	Select Node based gradient scheme	Gradient scheme is changed from cell based gradient scheme to a node based gradient scheme. This is a feature that has recently been implemented and reduces diffusion in the model, especially in tetrahedral models.
5	Set viscous model	Set appropriate turbulence model for the simulations. More Details can be found in 3.1.8.
6	Change discretisation scheme	Change simulation from 1 st order simulation to a 2 nd order simulation.
7	Set the under-relaxation factors	Modify the under-relaxation factors of the model. All parameters were scaled from default values (refer to section 3.6.1.2).
8	Define Reference Pressure Location	Define the location where the gauge pressure is zero. This is important for calculating the body forces where no pressure

Chapter 3 In 1981, Ahmed [8] conducted experiments on wake structures of typical automobile shapes. Vehicle shapes for an estate, fastback and notchback were tested by varying the upper rear end of a quarter scale model (Figure 3.33) with flow visualisation and wak

Shaun Johnson

		boundary conditions have been specified. This point is located in the free stream away from boundaries
9	Define material properties	Set the density and viscosity of the fluid in the simulations. This was set to the default values of air. Density=1.225 kg/m ³ Viscosity=1.78940x10 ⁻⁵ kg/ms
10	Set Free stream velocity	Set the bulk air velocity of the velocity-inlet boundary condition. Inlet turbulence intensity was set to 1.0 % with a length scale of 0.01.
11	Set residual monitors	Redefine residuals monitors to not check for residual convergence (Refer to 3.4.1.2 for more details).
12	Set Monitors	Monitor body forces on all body surfaces. Drag, lift and moment data is collected for each iteration.
14	Initialise the flow	Initialise the flow from a predefined velocity vector.
15	Write Case and Data File	Write the case and data to a file for computation.

Table 3.2 Procedure for initialising the simulation

3.4.1.2 Convergence Criteria

The common practice to determine solution convergence for time-independent problems is to use the residuals, which indicate how well the solution satisfies the set of discrete equations during the iterative solution procedure. Using the residuals as the sole indication of convergence requires care because convergence criteria are set relatively high by default. Apart from this, in strongly time-varying flows, such as flows involving vortex shedding, as is the case here, it is often difficult to get the residuals to decrease past certain limits without the use of extremely small under-relaxation parameters. This can slow down the solution process to unacceptable levels. As well as monitoring residuals, monitoring of the solution was also conducted using body forces since they provide a better indication of the behaviour of the flow field near the body. Drag and lift forces on the model were extracted at every iteration to monitor the simulation. For many simulations, the body force did not converge but oscillated about a mean value. In these situations, the simulations were stopped when the apparent mean body forces had reached a constant value.

For some simulations, it was found that the local-iteration-mean body forces were highly dependent on the number of iterations performed. (This, of course, is not surprising). In general, for time-averaged models, the higher the number of iterations carried out, the lower the error. For the current problem, it is found that when the iteration process is carried out for a large number of iterations the wake flow structure

does settle down to a large diffuse bubble, which is not necessarily representative of the wake structure at any time in the shedding cycle even though it may be representative of the time-mean behaviour. Of course, it is questionable whether it is really useful obtaining a time-mean flow field of a highly time-dependent quasi-periodic flow, and perhaps URANS modelling is more appropriate. For instance, the C-pillar vortex cores are much thinner than the average core widths obtained from experiments [15, 73], because of the wandering of the core position as pointed out by Bearman [74], and is evident in LES simulations [75].

Illustrated in Figure 3.6 is the drag and lift history for $\alpha=30^\circ$ for 5000 iterations. The corresponding flow structure visualisations at the locations marked on Figure 3.6 are illustrated in Figure 3.7 using iso-surfaces of zero total pressure. In the initial stages, the wake is still varying considerably. At this stage it is possible to see what appear to be C-pillar vortices after 500 iterations (Figure 3.7a).

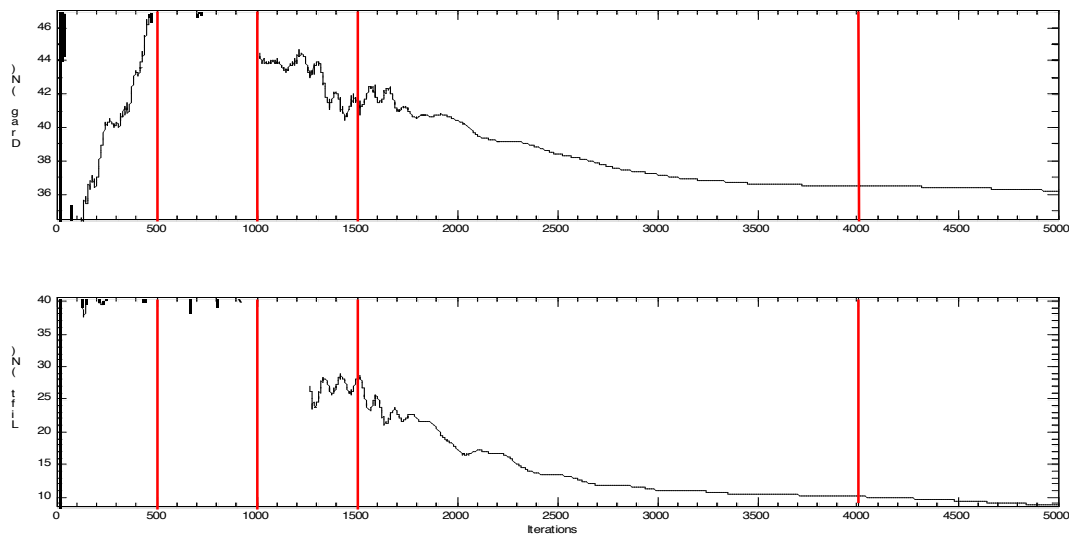


Figure 3.6 Drag and Lift iteration history for 5000 iterations for $\alpha=30^\circ$.

However, after 1500 iterations for this particular case, the C-pillar vortex disappears and a large separation bubble forms as seen in (Figure 3.7d). Interestingly, the experiments show that at 30° , the drag is bistable corresponding to a choice of high or low drag regime as shown in Figure 3.37. The converged result appears to be more consistent with the low drag regime, while the flow structures and drag

behaviour during the earlier stages of the iteration sequence when the force residuals temporarily plateau appear to be more consistent with the behaviour expected for the high-drag regime.

Ahmed et al. [5] found that at $\alpha=30^\circ$, the wake naturally evolved into the low drag regime and the high drag could only be produced by placing a splitter plate downstream on the body centreline. In contrast, experiments by Vio et al. [76] using the Ahmed body, found that the high drag regime appeared to be more stable and this indicates that stability could be very sensitive to experimental conditions. Therefore, in these simulations, it could also be possible that near $\alpha=30^\circ$, the high drag regime is also unstable and simulations naturally progresses to more stable flow field such as the low drag regime as the simulation converge. This makes it difficult to simulate the high drag regime.

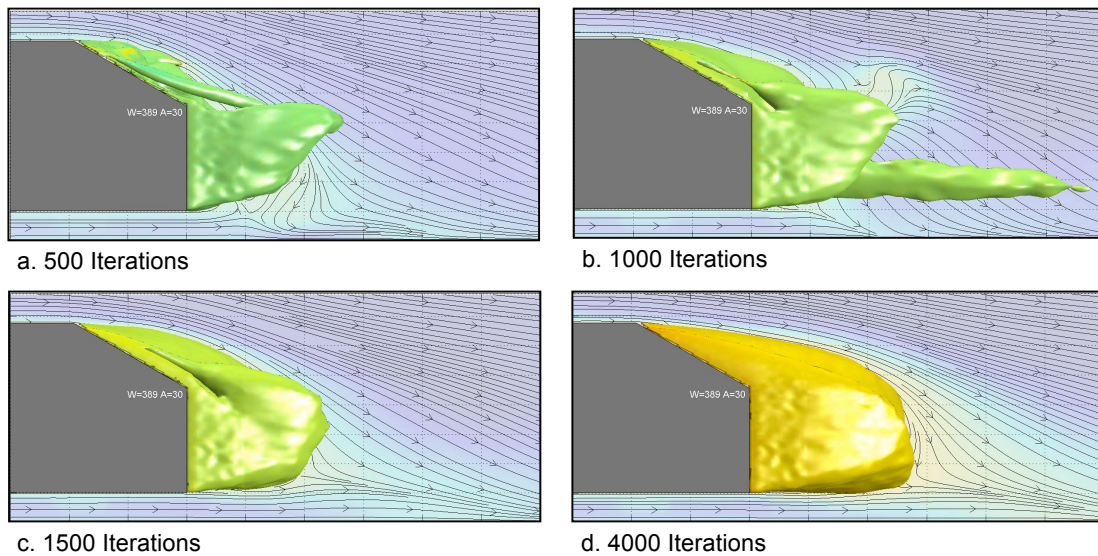


Figure 3.7 Wake structures for $\alpha=30^\circ$ for 500, 1000, 1500 and 4000 iterations using iso-surface of 0 total pressure and with streamlines on the vehicle centreline.

The residuals for this simulation are shown in Figure 3.8. After approximately 2000 iterations, the continuity and k residuals start to plateau. This coincides with the time when the drag and lift forces stop oscillating. After 2000 iterations, the drag force decrease considerably and flow visualisations observe the wake evolving from attached flow with strong C-pillar vortices into a large separation bubble.

This was unexpected since it was assumed, that running simulations for more iterations would lead to a solution with better convergence. For all simulations, residuals would decrease and then plateau at various values so it was not possible to determine a residual convergence level. Therefore, in some simulations where it appeared that the drag history was slowly decaying, a secondary stopping criterion was utilised, especially for the $k\omega$ -SST and ke-realizable turbulence models. As opposed to defining a strict convergence criterion for residuals, the residuals were monitored until one or more stopped decaying. At this point the simulation predictions were recorded. This process is referred to as Residual Truncation (RT). This method was not used for the RSM turbulence model.

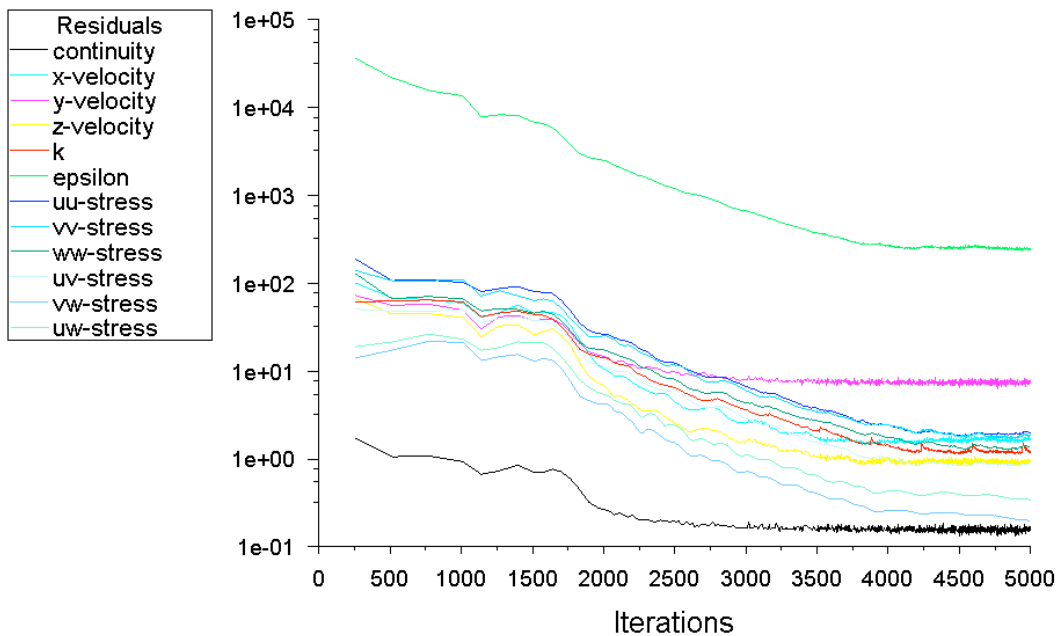


Figure 3.8 Residuals corresponding to the drag and lift iteration history in Figure 3.6 for $\alpha=30^\circ$ using RSM turbulence model

For slant angles other than $\alpha=30^\circ$ where RT was used, it could be possible that a bistable regime exists. Since Ahmed only investigated $\alpha=25^\circ$, 30° and 35° , the bistable regime could be present for $26^\circ \leq \alpha \leq 34^\circ$. As was shown by Morel [16] for an axis symmetric body, there was a variation in the critical angle at which transition occurred.

At this stage, no evidence has been supplied to justify the truncation of the simulations prior to numerical convergence and to expect that the simulation results should be representative of the typical physical state of the flow. This procedure is at best heuristic; however, it is shown later that a comparison of semi-converged steady-state results with asymptotic results from time-dependent simulations helps provide some support as to the relevance of the approach.

3.5 Grid Resolution study

Due to computational memory constraints and the complexity of the mesh, it was not feasible to conduct a brute-force full grid resolution study for the entire domain. Instead, the mesh was subdivided into regions and the separate grid resolution studies were conducted in each region to determine the resolution required for grid independence.

Simulations were conducted at $Re=2.86 \times 10^6$ (inlet velocity=40m/s). Instead of using higher slant angles near the critical angle, $\alpha=25^\circ$ was used since experimental data was available for comparison and it was in the regime where C-pillar vortex structures were present. Simulations were conducted using a $k\omega$ -SST turbulence model and the initial velocity field was set to zero. To simplify the resolution procedure, residual truncation was not used in the grid resolution study.

An initial mesh was developed that was structured with high-density regions near the body, especially on the slant surface. The flow structures and body forces gave a reasonable approximation of the experimental results. This was used as the base mesh for the investigation to determine grid independence.

The effect of domain size was examined by moving the outer boundaries and grid resolution was determined by varying the grid density in different regions. To check if grid independence was achieved, the parameter under investigation was stepped towards the most resolved solution. The drag and lift forces were compared with those from the most resolved simulation. If the drag or lift varied by more than 1% from the best resolved simulation, the grid spacing was decreased or the boundaries were extended.

Chapter 3 In 1981, Ahmed [8] conducted experiments on wake structures of typical automobile shapes. Vehicle shapes for an estate, fastback and notchback were tested by varying the upper rear end of a quarter scale model (Figure 3.33) with flow visualisation and wak

Shaun Johnson

3.5.1.1 Domain Resolution

Outlined in Table 3.3 is the domain-size study for the domain cross-section to examine the effect of blockage. The domain size was increased up to 5x5 (non-dimensional units squared) but a 4x4 domain was found to be sufficient for the simulations

Parameter	Drag (N)	Lift (N)	% Drag	% Lift
25	36.48	23.03	0.00%	0.00%
16	36.44	23.04	0.09%	0.08%
9	36.85	23.15	1.01%	0.54%
4	36.96	23.21	1.31%	0.78%
1	37.06	23.31	1.59%	1.22%

Table 3.3 Effect of domain cross section on force coefficients.

The domain outflow position was placed 4 to 12 NDU downstream from the origin (Figure 3.3). As shown in Table 3.4, the domain outflow position had negligible effect on the body forces. However, the domain outflow location was left at 7 NDU to observe the wake structures downstream.

Parameter	Drag (N)	Lift (N)	% Drag	% Lift
12	36.50	23.20	0.00%	0.00%
9	36.44	23.11	0.17%	0.35%
8	36.48	23.18	0.07%	0.08%
7	36.49	23.23	0.03%	0.14%
6	36.51	23.07	0.02%	0.52%
4	36.53	23.07	0.08%	0.54%

Table 3.4: Effect of domain outflow location on the force coefficients.

The inlet velocity profile was varied between 4 to 8 NDU upstream of the vehicle. For the simulations, the inlet profile was moved from 6 NDU to 7 NDU upstream after this test.

Parameter	Drag (N)	Lift (N)	% Drag	% Lift
8	36.10	23.36	0.00%	0.00%
7	36.21	23.28	0.31%	0.35%
6	36.52	23.18	1.17%	0.77%
5	36.94	23.34	2.33%	0.06%
4	38.43	23.62	6.45%	1.13%

Table 3.5: Effect of the inlet velocity location on force coefficients.

3.5.1.2 Face Mesh Resolution

As shown in Table 3.6, for the front surface of the Ahmed body, the face mesh spacing had a negligible effect on the drag and lift forces. Final mesh spacing was not \changed from the reference mesh.

Parameter	Drag (N)	Lift (N)	% Drag	% Lift
0.5	36.74	23.20	0.00%	0.00%
0.75	36.55	23.15	0.51%	0.23%
1	36.48	23.18	0.71%	0.10%
1.25	36.39	22.84	0.94%	1.53%

Table 3.6: Effect of face mesh spacing on the front surface on force coefficients.

Lift forces were most influenced by changing the side mesh spacing since only the viscous component of drag would change. As can be seen from Table 3.7, the mesh spacing was scaled by 0.75 from the original spacing to reduce the effect of side mesh spacing on the lift force.

Parameter	Drag (N)	Lift (N)	% Drag	% Lift
0.25	36.33	22.83	0.00%	0.00%
0.5	36.59	22.92	0.74%	0.41%
0.75	36.66	22.74	0.92%	0.40%
1	36.48	23.18	0.42%	1.52%
1.25	36.40	23.51	0.20%	2.99%

Table 3.7: Effect of mesh spacing on the side surface on forces.

The rear surfaces on the body had the largest effect on drag and lift forces was expected. Mesh spacing on the rear surface was scaled by 0.5 from the original spacing of the original mesh, significantly increasing the mesh density. Since the lift forces were most affected by changing the mesh density, it indicates that the mesh spacing in the rear region affects the flow structures. This in turn influences the forces on surfaces other than the rear surface.

Parameter	Drag (N)	Lift (N)	% Drag	% Lift
0.25	35.85	21.30	0.00%	0.00%
0.5	35.87	21.45	0.04%	0.71%
0.75	36.18	22.19	0.92%	4.17%
1	36.48	23.18	1.75%	8.80%
1.25	36.85	24.13	2.78%	13.26%

Table 3.8: Effect of face spacing on rear surface on force coefficients.

The slant surface spacing was also decreased to 0.5 of the original spacing on the slant surface as shown in Table 3.9. As the mesh spacing was already dense (0.004

Chapter 3 In 1981, Ahmed [8] conducted experiments on wake structures of typical automobile shapes. Vehicle shapes for an estate, fastback and notchback were tested by varying the upper rear end of a quarter scale model (Figure 3.33) with flow visualisation and wak

Shaun Johnson

NDU), this considerably increased the number of grid cells as the mesh face spacing was decreased to 0.003 NDU while the edge spacing was decreased to 0.001 NDU.

Parameter	Drag (N)	Lift (N)	% Drag	% Lift
0.25	37.04	24.17	0.00%	0.00%
0.5	36.91	24.09	0.34%	0.34%
0.75	36.68	23.61	0.96%	2.29%
1	36.48	23.18	1.51%	4.10%
1.25	36.38	22.79	1.77%	5.70%

Table 3.9: Effect of face spacing on the slant surface on force coefficients.

The mesh spacing on the ground surfaces was also investigated. As can be seen in Table 3.10, the mesh face spacing did not strongly influence the body forces and the mesh spacing was not reduced.

Parameter	Drag (N)	Lift (N)	% Drag	% Lift
0.5	36.55	23.10	0.00%	0.00%
0.75	36.35	22.95	0.53%	0.65%
1	36.36	22.99	0.52%	0.49%

Figure 3.9: Effect of face mesh spacing on ground surfaces on force coefficients.

3.5.1.3 Volume Resolution

The mesh density in the three different volume regions described in Figure 3.4 was examined to determine how it influenced the body forces. The resolution study of the outer-region volume in Table 3.10 showed that the mesh density had little influence on the body forces.

Parameter	Drag (N)	Lift (N)	% Drag	% Lift
0.4	36.50	23.35	0.00%	0.00%
0.7	36.58	23.24	0.22%	0.47%
0.9	36.58	23.17	0.20%	0.79%
1.0	36.48	23.18	0.07%	0.75%

Table 3.10: Effect of volume spacing of the outer region on force coefficients.

The rear volume region had a minor effect on the drag and lift forces. As indicated in Table 3.11, the mesh spacing was only decreased by 0.9 to give drag forces within 1% of mesh scaling of 0.6, the finest resolution studied. However, the volume spacing in the inner region surrounding the vehicle was decreased by 0.5 as it was the critical area surrounding the body (see Table 3.12).

Chapter 3 In 1981, Ahmed [8] conducted experiments on wake structures of typical automobile shapes. Vehicle shapes for an estate, fastback and notchback were tested by varying the upper rear end of a quarter scale model (Figure 3.33) with flow visualisation and wak

Shaun Johnson

Parameter	Drag (N)	Lift (N)	% Drag	% Lift
0.6	36.28	23.02	0.00%	0.00%
0.7	36.30	23.00	0.06%	0.06%
0.9	36.38	23.03	0.29%	0.08%
1.0	36.89	23.07	1.69%	0.24%

Table 3.11: Effect of volume spacing of rear region on force coefficients.

Parameter	Drag (N)	Lift (N)	% Drag	% Lift
0.3	36.64	23.40	0.00%	0.00%
0.5	36.67	23.37	0.10%	0.13%
0.75	37.08	23.08	1.21%	1.38%
1	37.56	23.00	2.52%	1.71%

Table 3.12: Effect of volume spacing of inner volume region on force coefficients.

In the mesh creation procedure, extra planes were placed above the slant surface to help control the mesh spacing in that region since it was the critical area of interest but they were not included in the exported mesh. The density of the mesh spacing was also decreased in this region in order to sufficiently capture the separation bubble. The initial spacing of 0.006 NDU was decreased to 0.003 NDU over the slant surface.

Parameter	Drag (N)	Lift (N)	% Drag	% Lift
0.4	36.60	23.32		
0.5	36.48	23.18	0.33%	0.60%
0.8	36.32	22.88	0.75%	1.86%
1	36.19	22.45	1.12%	3.73%

Table 3.13: Influence of volume spacing of slant surface on force coefficients.

3.5.1.4 Boundary Layer Resolution

As expected, the boundary layer prism layer was found to have a large influence on the body forces. The two parameters investigated that were the distance of the first element length (FL) from the surface and the number of prism layers used in the boundary layer mesh. Problems were encountered when reducing the spacing of the first element because on the front portion of the vehicle negative volumes were created since the mesh could not match the surface curvature. This restricted the smallest distance to 0.000025 NDU as can be seen in Table 3.14. The y^+ values were also checked and it was found for elements less than 0.000075, $y^+ \approx 1$ for the majority of the model.

Chapter 3 In 1981, Ahmed [8] conducted experiments on wake structures of typical automobile shapes. Vehicle shapes for an estate, fastback and notchback were tested by varying the upper rear end of a quarter scale model (Figure 3.33) with flow visualisation and wak

Shaun Johnson

Parameter	Drag (N)	Lift (N)	% Drag	% Lift
0.000025	35.41	22.99	0.00%	0.00%
0.00005	35.71	23.06	0.85%	0.27%
0.000075	36.48	23.18	3.02%	0.79%
0.0001	36.94	23.29	4.32%	1.27%
0.000125	36.81	23.82	3.94%	3.57%
0.00015	36.32	25.86	2.58%	12.46%

Table 3.14: Influence of boundary layer mesh - first element normal distance.

The drag approached a constant value for a prism layer count above 17 layers. Increasing the layer count severely affected the size of the mesh so 17 layers were used, since it was within an acceptable tolerance compared with 20 layers. It may have been possible to reduce the number of layers by optimising the succession ratio; however, this was not investigated.

Parameter	Drag (N)	Lift (N)	% Drag	% Lift
20	36.95	24.93	0.00%	0.00%
19	36.96	24.85	0.02%	0.34%
17	36.96	24.76	0.03%	0.67%
15	36.48	23.18	1.28%	7.03%
12	34.95	20.44	5.41%	18.00%
10	33.63	18.98	8.98%	23.86%

Table 3.15: Influence of the boundary layer mesh - effect of the number of layers.

3.5.1.5 Final Mesh Design

The final domain size used for this study is outlined in Table 3.15. It was found that the domain size did not have a significant effect on the overall drag and lift forces on the body if they were placed sufficiently far away from the model

Parameter	Value
Outer Wall Top	5
Outer Wall Side	5
Inlet velocity location	-7
Ouflow Location	7

Table 3.16: Domain dimensions of the final mesh.

The mesh resolution study required the mesh to be enhanced in some areas. In particular, the mesh resolution was increased in the wake region. The final spacing parameters for mesh generation are outlined in Table 3.17.

Region	Parameter	Mesh type	Value
Surface	front	face	0.01

Chapter 3 In 1981, Ahmed [8] conducted experiments on wake structures of typical automobile shapes. Vehicle shapes for an estate, fastback and notchback were tested by varying the upper rear end of a quarter scale model (Figure 3.33) with flow visualisation and wak

Shaun Johnson

		edge	0.005
	side-top	face	0.015
	side-side	face	0.05
	side-underside	face	0.025
	side	edge	0.015
	rear	face	0.0075
		edge	0.005
	slant	face	0.003
		edge	0.001
	ground near body	face	0.3
	ground far field	face	0.05
Volume	Outer region	volume	0.7
	Rear region	volume	0.1
	Inner region	volume	0.05
Boundary layer	first length	spacing	0.00005
	Prism layers	count	17

Table 3.17: Characteristic mesh parameters for the final mesh.

3.6 Further model resolution and validation studies

Investigations were undertaken to determine how different run-time simulation parameters affect the solution. Initial testing found the wake structures to be sensitive to choice of turbulence model. For time-independent simulations, the selection of under-relaxation parameters was also investigated. The effect of using a symmetry boundary condition on the vehicle centreline was also investigated. Both time-independent and time-dependent simulations were investigated. Initially, the results of time-independent simulations are discussed.

Simulations were conducted at various slant angles to ensure that parameter changes were independent of α . Initial investigations found that only examining one slant angle could be misleading since parameter changes were not representative for all slant angles. As was discussed in the Literature review, there is a wide spread of simulations data and it is difficult to determine their effectiveness in capturing the key flow structures if only limited slant angles are investigated. Therefore, finding model

Chapter 3 In 1981, Ahmed [8] conducted experiments on wake structures of typical automobile shapes. Vehicle shapes for an estate, fastback and notchback were tested by varying the upper rear end of a quarter scale model (Figure 3.33) with flow visualisation and wak

Shaun Johnson

parameters such as turbulence models that match experimental data such as body forces was not the objective. Of more importance, is to determine how modelling parameters affect the trends as the slant angle is varied. Therefore, for each parameter, various slant angles were investigated.

Simulations were conducted at $Re=2.86 \times 10^6$ (inlet velocity of 40m/s) in order to compare results with experimental data at the same Reynolds number. The predicted C_D values are compared with values from the data of Ahmed et al. [5]. Where there was still some variation in the force coefficients at the end of the simulation time, the C_D and C_L values given are obtained by averaging at least the last 500 iterations to calculate the mean forces.

Due to the large parameter space, it was unfeasible to complete a full study of all options available. Therefore, each parameter was progressively investigated and used as a basis for the next investigation. The initial setup used as a starting point is outlined in Table 3.18.

Parameter	Setting
Solver	Steady state
Turbulence model	$k\epsilon$ realizable with standard wall function
Initial conditions	Flow field set to 0
Time dependence	Independent
Under relaxation	Default
Symmetry plane	Yes

Table 3.18: Parameter study initial conditions.

3.6.1.1 Turbulence models

Three turbulence models were investigated to determine their feasibility to accurately model the wake structures behind the Ahmed body, and to predict the drag and lift behaviour with slant angle. The models investigated were the $k\epsilon$ -realizable model with standard wall functions, the $k\omega$ -SST turbulence model and the Reynolds-stress model (RSM) with both standard and enhanced wall functions. More advanced and complex turbulence models such as LES and DES were not considered since they are unsteady models and require a very dense mesh. While it is possible to run these models for a few discrete points in parameter space, the computational resources

available for the present work are not sufficient for the planned full parameter-space study.

3.6.1.1.1 $k\varepsilon$ -realizable turbulence model

The $k\varepsilon$ -realizable turbulence model was used as a base point as it was used by Gilliéron and Chometon [15] and thus provides a reference point for comparison. Standard wall functions were used to model the wall boundary layer. Shown in Figure 3.10 are the C_D and C_L coefficients indicated by blue diamonds. Initial results indicate that results were similar to those by Gilliéron and Chometon [15]. However, it appeared that the peak drag occurs at $\alpha=28^\circ$ as opposed to $\alpha=30^\circ$ and the drag decreases at $\alpha>30^\circ$. C_L decreases considerably above $\alpha>25^\circ$ as the flow is separated from the slant surface. These results were obtained from the steady solver.

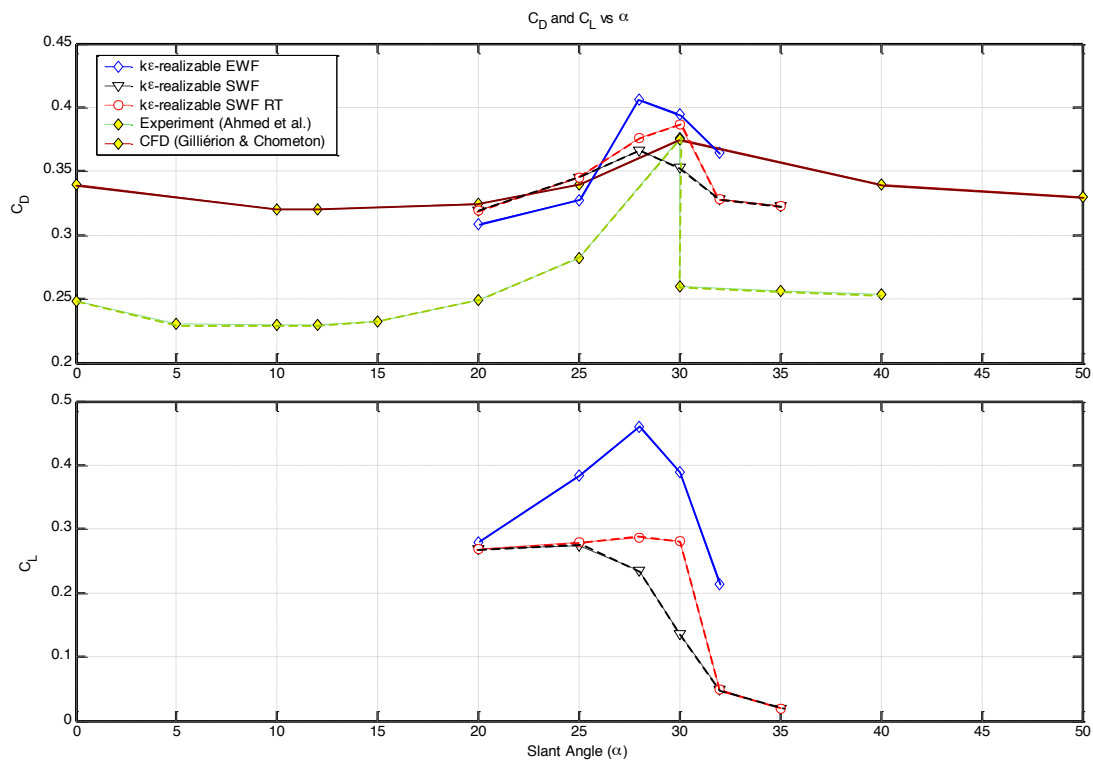


Figure 3.10 Comparison of $k\varepsilon$ -realizable model using standard wall function with other experimental and computational data.

The iteration history for various slant angles are shown in Figure 3.11 for the $k\varepsilon$ -realizable model. As can be seen, the drag history for $\alpha=20^\circ$ and $\alpha=25^\circ$ have stabilised, while for other slant angles, the drag is still decreasing. If the simulations

are run until the body force reaches a steady value, the wake evolves into a large separation bubble. Therefore, the second criteria using Residual Truncation (3.4.1.2) was used to determine solution convergence. As can be seen in Figure 3.10, the drag profile for RT indicated by black triangles follows a profile similar to those of Gilliéron and Chometon with peak drag occurring at $\alpha=30^\circ$. Differences in the drag profiles could be due to the smaller number of iterations conducted by Gilliéron and Chometon where simulations were stopped all simulations after 1600 iterations.

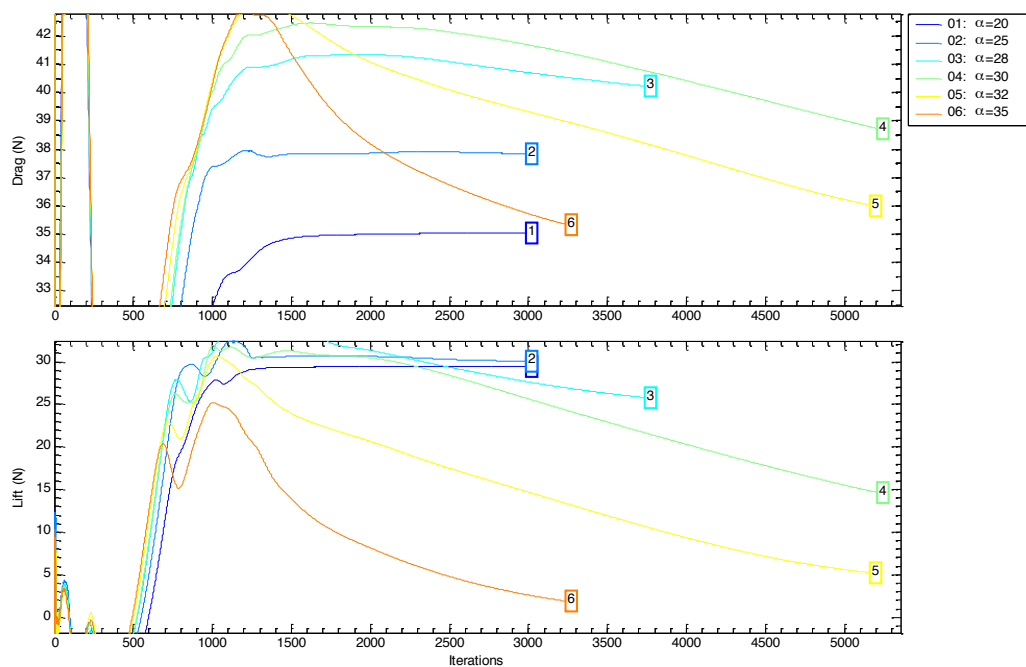


Figure 3.11 Iteration history for $k\epsilon$ -realizable turbulence model

It appears that the $k\epsilon$ -realizable turbulence model captured the drag profile as α was varied. Flow visualisations showed a similar structure to those previously observed. However, there were numerical discrepancies with this model. As was stated previously in 3.1.12, the standard wall function was used which requires the y^+ on body surfaces to be between 30 and 60. However, the grid was designed for enhanced wall functions which require $y^+ \approx 1$. Simulations were re-run using the $k\epsilon$ -realizable turbulence with enhanced wall functions indicated by blue diamonds in Figure 3.10. It can be seen that the drag profile is considerably different to using SWF with the peak drag occurring at $\alpha=28^\circ$. Flow visualisations for $\alpha=25^\circ$ showed

no separation from the slant surface which is not consistent with experimental data. Therefore, the $k\omega$ -Shear Stress Turbulence (SST) model was considered for evaluation since it does not employ wall functions and requires $y^+ \approx 1$.

3.6.1.1.2 $k\omega$ -SST turbulence model

The $k\omega$ -SST turbulence model was evaluated to simulate the wake structures behind the Ahmed body. The drag and lift profiles shown in Figure 3.12 are for different slant angles for drag history convergence (blue diamond) and for RT (black triangles) convergence. Similar problems were experienced as with the $k\epsilon$ -Realizable model, that if drag history was used as the convergence criteria, then near $\alpha=30^\circ$ the wake would evolve into a large separation bubble with lower drag. From the lift data, it is evident that this would occur for slant angles where the flow had separated from the slant surface whereas for RT data, the C_L would decrease only for $\alpha>30^\circ$. Of interest is the gradient of the profiles for $k\omega$ -SST RT profile near $\alpha=30^\circ$ indicating that the $k\omega$ -SST turbulence model matches the effect of varying α even though C_D is over predicted as compared with experimental data.

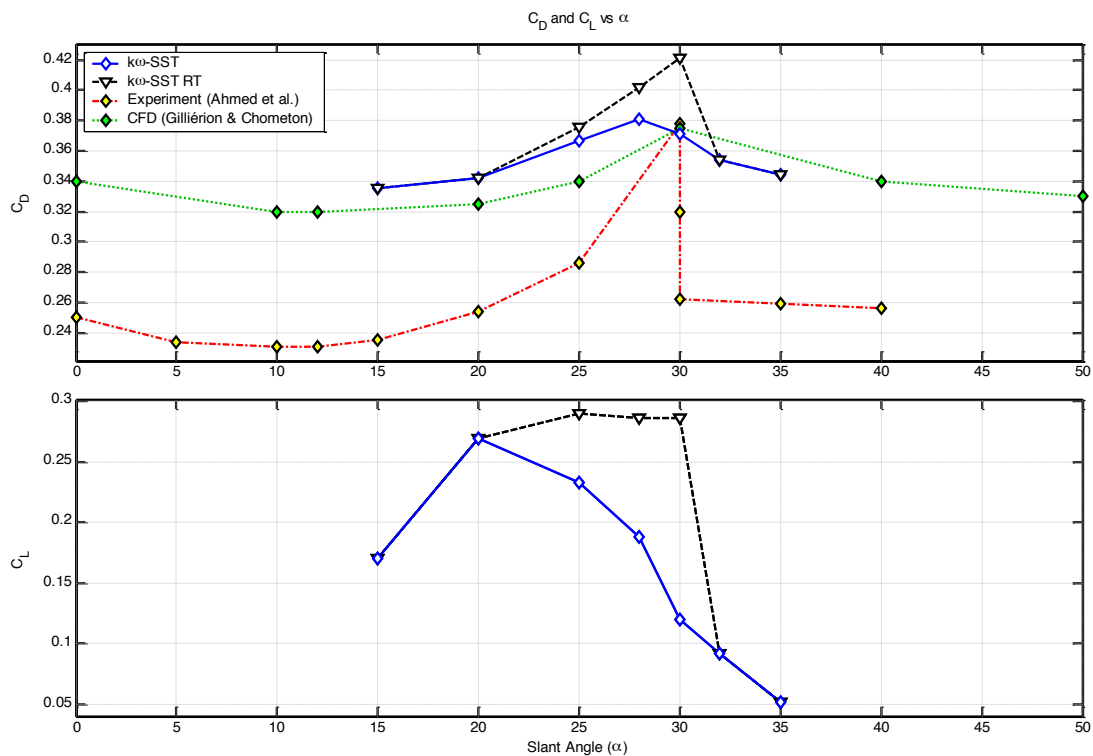


Figure 3.12 Drag and lift data using the $k\omega$ -SST turbulence model for $\alpha=15^\circ$ up to $\alpha=35^\circ$.

Chapter 3 In 1981, Ahmed [8] conducted experiments on wake structures of typical automobile shapes. Vehicle shapes for an estate, fastback and notchback were tested by varying the upper rear end of a quarter scale model (Figure 3.33) with flow visualisation and wak

Shaun Johnson

3.6.1.1.3 Reynolds Stress Model turbulence model

The use of the Reynolds Stress Model (RSM) was investigated since it is generally accepted that it is a more accurate turbulence model because it does not assume that turbulent viscosity is isotropic. Simulations conducted with the standard wall function and with enhanced wall functions with the C_D and C_L values are shown in Figure 3.13.

The drag profile using the RSM SWF (black diamonds) does not match the experimental data and was similar to the $k\varepsilon$ -Realizable and $k\omega$ -SST profiles without using RT because it did not simulate the peak drag at $\alpha=30^\circ$. The drag forces peak occurs at $\alpha=25^\circ$ just as the flow starts to separate from the slant surface and a large separation bubble is present at $\alpha=30^\circ$. However, unlike the $k\varepsilon$ -realizable and $k\omega$ -SST turbulence models, the RSM SWF drag history did not peak and then decay. The drag and lift history in Figure 3.14 shows that after an initial number of simulations, the drag and lift would increase until it reached a steady value. Therefore, it was not possible to use residual truncation to determine solution convergence. From Figure 3.13, it can be seen that the C_D profile for RSM SWF does not match the experimental data profile. It indicates that the drag peak occurs just as the flow starts to separate from the slant surface and peak drag near $\alpha=30^\circ$ was not captured using this turbulence model.

Chapter 3 In 1981, Ahmed [8] conducted experiments on wake structures of typical automobile shapes. Vehicle shapes for an estate, fastback and notchback were tested by varying the upper rear end of a quarter scale model (Figure 3.33) with flow visualisation and wak

Shaun Johnson

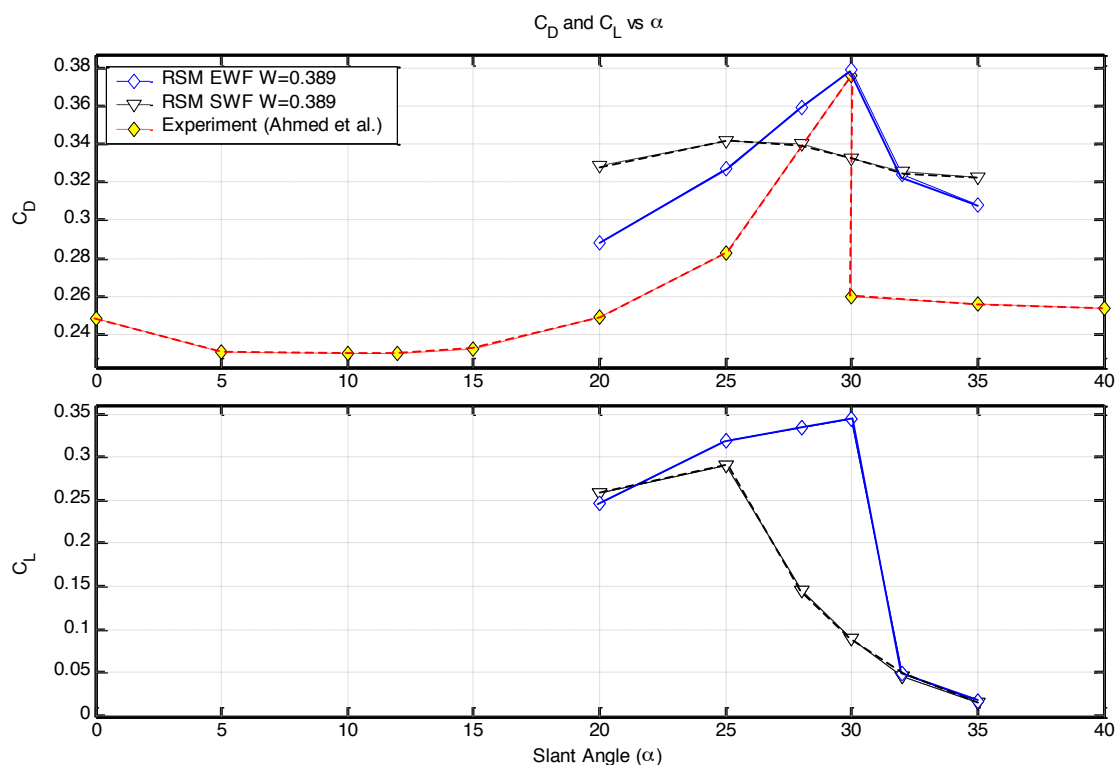


Figure 3.13 Drag profiles using RSM SWF and RSM EWF. The RSM SWF does not match experimental data with maximum drag occurring at $\alpha=25^\circ$ as opposed to $\alpha=30^\circ$.

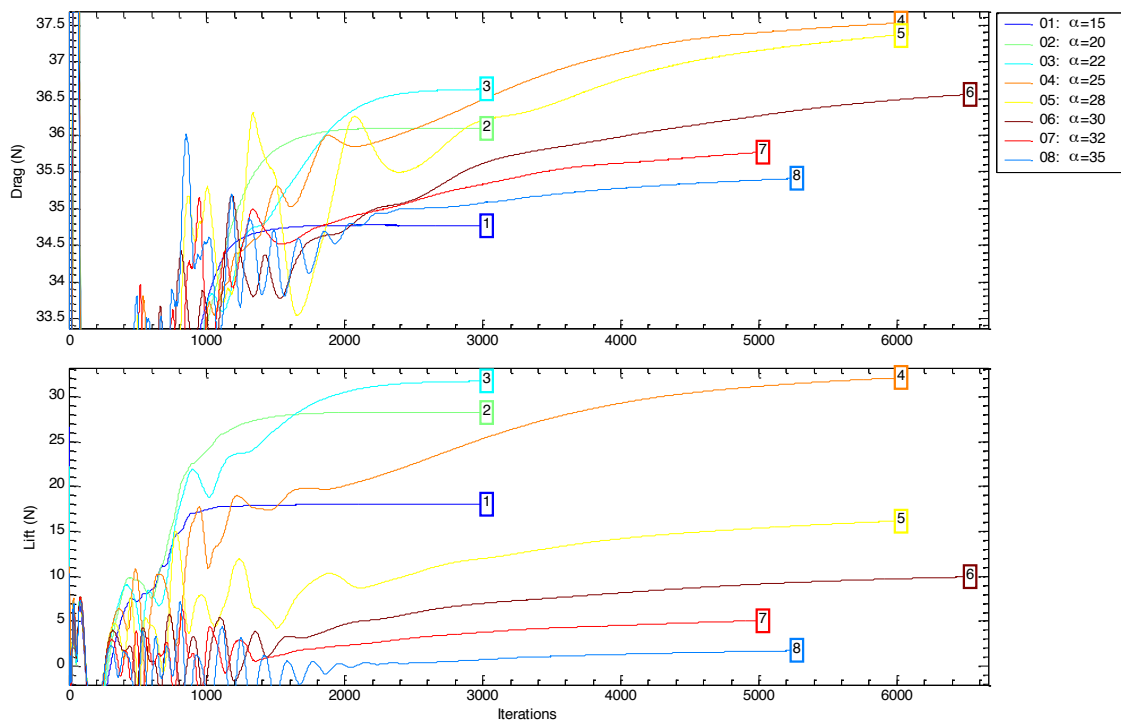


Figure 3.14 RSM SWF drag and lift history

Chapter 3 In 1981, Ahmed [8] conducted experiments on wake structures of typical automobile shapes. Vehicle shapes for an estate, fastback and notchback were tested by varying the upper rear end of a quarter scale model (Figure 3.33) with flow visualisation and wak

Shaun Johnson

In contrast, the RSM EWF (blue diamond) profile compares better with the experimental data. The peak change in drag as α varies follows the experimental profile closer with the decrease in drag and lift occurring at $\alpha > 30^\circ$. However, the iteration history for the RSM EWF in Figure 3.15 indicates that the solution has not converged to a single solution as should happen for time independent solutions but has a high frequency unsteadiness about a mean value. The C_D and C_L values were calculated by averaging the drag and lift forces respectively over the last 500 iterations to calculate a mean value

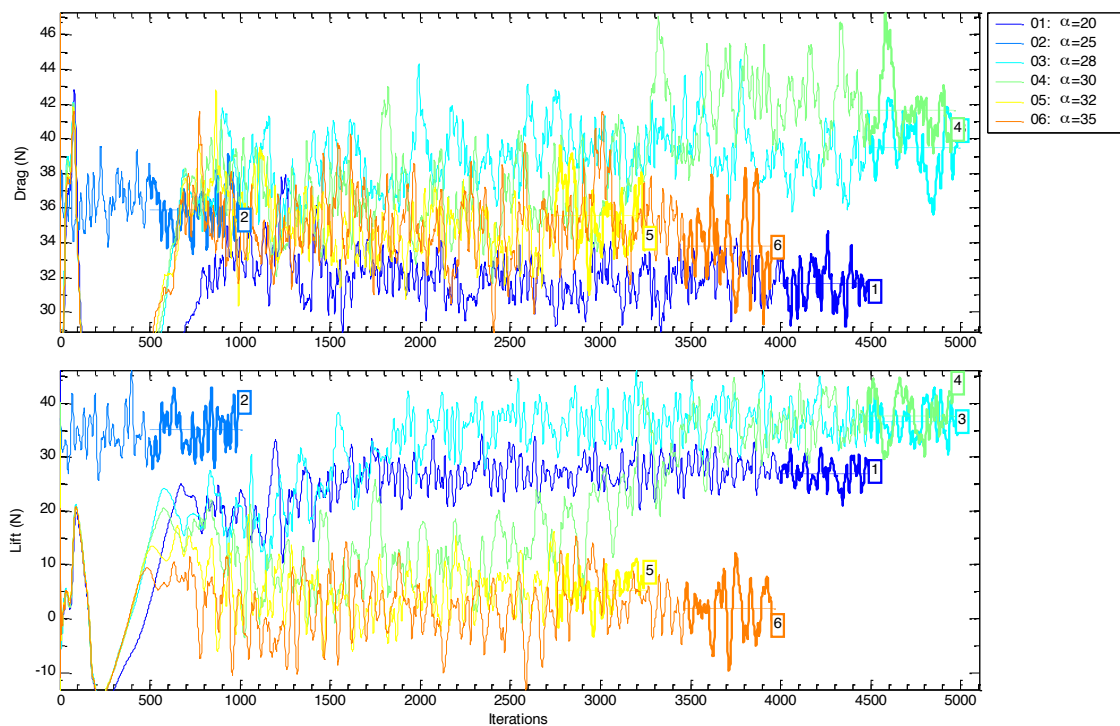


Figure 3.15 RSM EWF drag and lift history.

An orthographic projection of an instantaneous visualisation of the flow field at the rear of the Ahmed body with an iso-surface of zero u-velocity, streamlines and contours of u-velocity and on the body centreline is shown Figure 3.16. As can be seen the flow structure on the slant surface and at the vehicle rear is very unsteady and seems more akin to a time dependent rather than a time independent simulation. When the flow field is averaged over 500 iterations using every 5th iteration as in

Chapter 3 In 1981, Ahmed [8] conducted experiments on wake structures of typical automobile shapes. Vehicle shapes for an estate, fastback and notchback were tested by varying the upper rear end of a quarter scale model (Figure 3.33) with flow visualisation and wak

Shaun Johnson

Figure 3.17, the wake structures seem similar to that expected from modelling a time dependent simulation.

Figure 3.16 An orthographic projection of an instantaneous visualisation of the flow field at the rear of the Ahmed body with an iso-surface of zero u-velocity, streamlines and contours of u-velocity on the body centreline

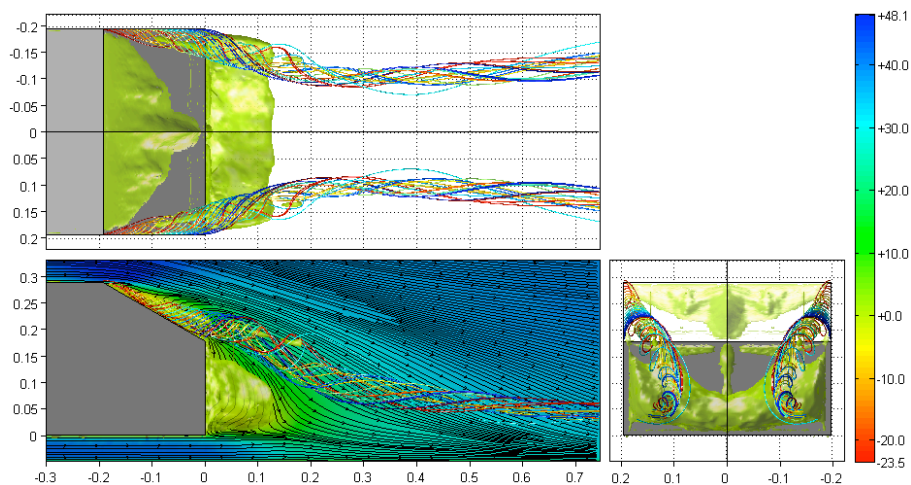


Figure 3.17 An orthographic projection of the iteration averaged (every 5 iterations over 500 iterations) flow field at the rear of the Ahmed body with an iso-surface of zero u-velocity, streamlines and contours of u-velocity on the body centreline

To ensure this phenomena was not a grid resolution issue since the kw-SST turbulence model was used in the grid resolution study, the mesh was increased to the maximum possible resolution using the resources available. In Figure 3.18, the drag history for the high density mesh was compared with the mesh calculated from the resolution study. In both cases, the drag and lift history is unsteady, but the mean drag and lift are similar.

Chapter 3 In 1981, Ahmed [8] conducted experiments on wake structures of typical automobile shapes. Vehicle shapes for an estate, fastback and notchback were tested by varying the upper rear end of a quarter scale model (Figure 3.33) with flow visualisation and wak

Shaun Johnson

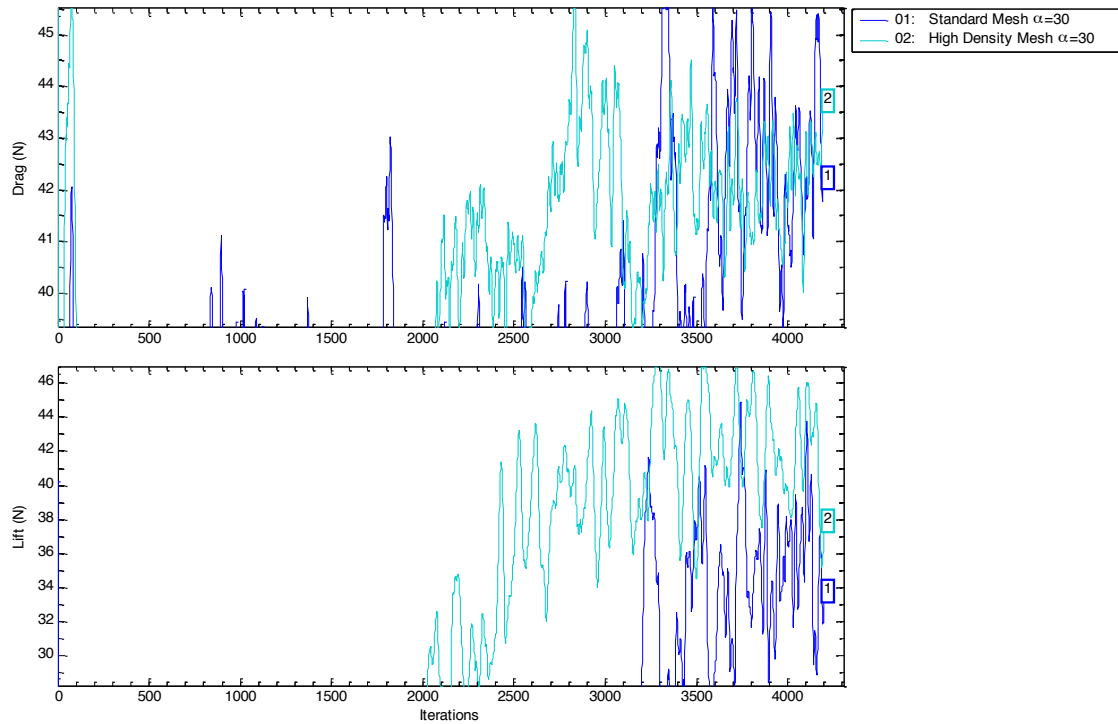


Figure 3.18 Comparison of drag and lift iteration history for $\alpha=30^\circ$ using the mesh derived from the grid resolution study and a mesh which was increased to the maximum possible size.

The RSM EWF turbulence model was also used in 2-dimensional simulation on the vehicle centreline. As can be seen in Figure 3.19, the simulations still contain a iteration unsteady component to the simulations. For 2-dimnsional simulations, a significant amount of under-relaxation was required to ensure the solution did not diverge.

Chapter 3 In 1981, Ahmed [8] conducted experiments on wake structures of typical automobile shapes. Vehicle shapes for an estate, fastback and notchback were tested by varying the upper rear end of a quarter scale model (Figure 3.33) with flow visualisation and wak

Shaun Johnson

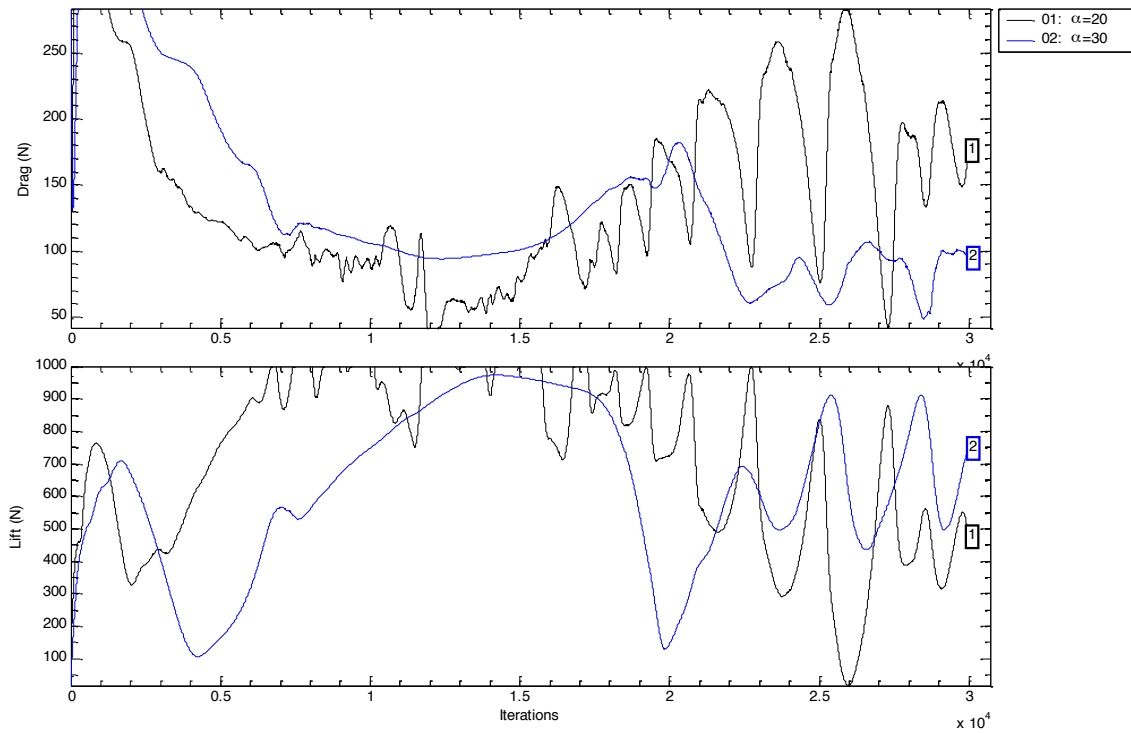


Figure 3.19 2-dimensional simulations on the body centreline using RSM EWF turbulence model

This phenomena has also been observed by Scotto d'Apollonia et al. [77] on simulations for automotive applications using the RSM turbulence model. Quasi-periodic oscillations around a constant value were observed on body forces were found to be due to local instabilities on area where the flow is inherently unsteady. The RSM turbulence model had a better correlation with wind-tunnel testing compared with the $k\epsilon$ -model.

3.6.1.1.4 Turbulence model comparison

Shown in Figure 3.20 are the drag forces using the various turbulence models on the slant surface and on all surfaces on the model. On the all body surfaces, the drag forces are over predicted by all turbulence models. However, the RSM turbulence model with enhanced wall functions appears to have the closest match to experimental data. On the slant surface, the RSM turbulence model with EWF captures the drag crisis point at $\alpha=30^\circ$ better with a sudden decrease in drag rather than a gradual reduction as was observed with the $k\omega$ -SST and $k\epsilon$ -realizable turbulence model. Further resolution studies were conducted to determine the cause of the nonphysical

unsteady nature of the RSM model with EWF. Although the RSM simulations appear promising, the results are deceptive since the time independent simulations have not converged even though a mean flow field can be created by iteration averaging the solution. Of interest, is the effect of the solution under relaxation and how time dependent simulations compare with time independent simulations.

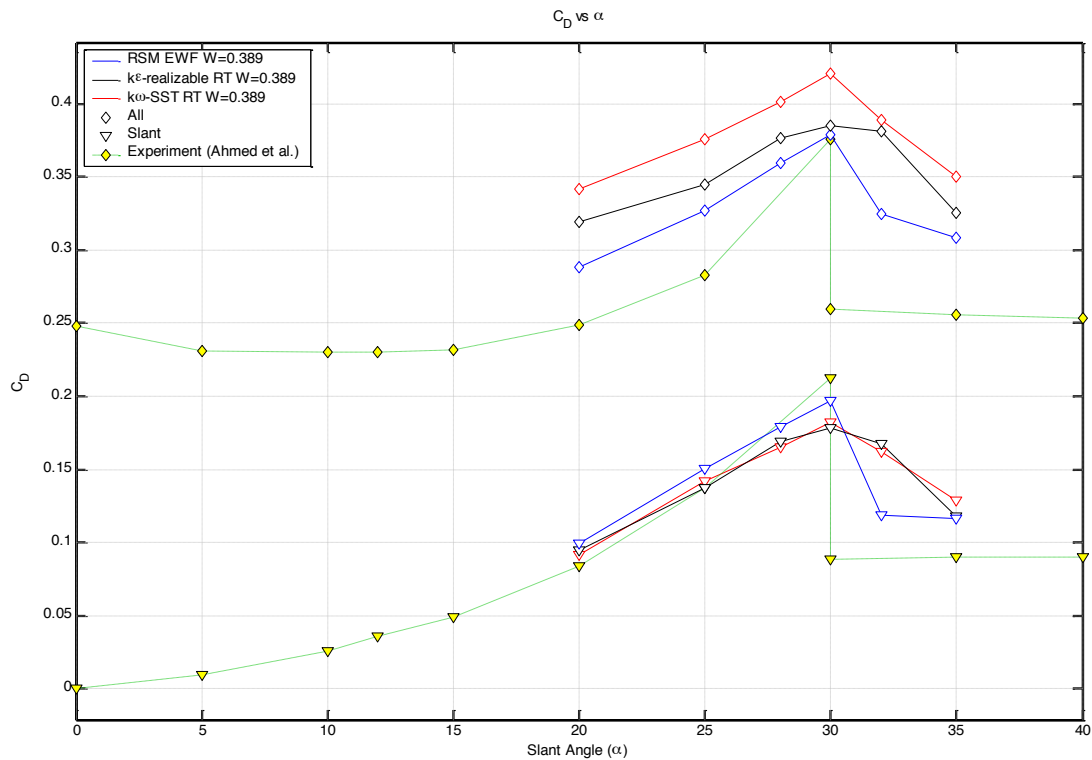


Figure 3.20 Comparison on all surfaces and just on slant surface

3.6.1.2 Under Relaxation

In order to develop a converged solution using the RSM model with EWF, the effect of under relaxation (UR) was examined. Under-relaxation factors control the amount by which the variables are allowed to change from iteration to iteration during the solution process. For each iteration, the under relaxation factor determines what portion of the new calculated value of each variable in each cell should be used to update the solution. This can be written in the following generalised form

$$\Phi_{new} = \Phi_{old} + f \times (\Phi_{new} - \Phi_{new}) \quad \text{Eqn 3.40}$$

where f is the under relaxation factor. If f is set to 0.5, then only 50% of Φ_{new} will be used to update the solution. All under relaxation parameters were scaled according

to the default values given by *Fluent*. The levels tested were 0.1, 0.5, 0.75 and 1.0 of default parameters.

The first method investigated was to restart simulations with the initial velocity field set to zero and rerun with various levels of UR. However, the drag and lift profiles did not match experimental data (Figure 3.21) with flow visualisations indicating that at $\alpha=30^\circ$, a large separation bubble had formed.

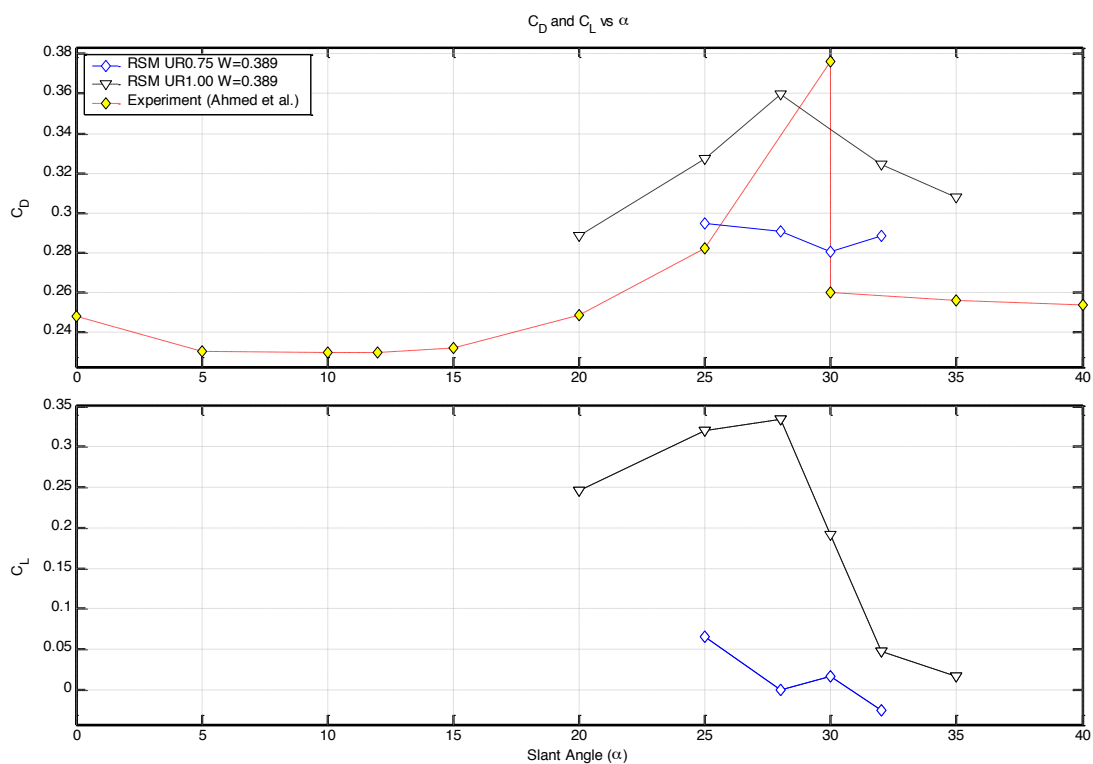


Figure 3.21 RSM SWF using decreased Under-relaxation factors. Simulations were started using zero velocity field as initial conditions.

Instead, the UR was decreased on simulations which had already run for over 3000 iterations using UR=1.00. Figure 3.22 shows the effect of decreasing the UR for $\alpha=30^\circ$. As can be seen as the UR is decreased, the period of unsteadiness increases. However, the only noticeable effects in stopping the oscillations were found using a very small UR (UR<0.1).

Chapter 3 In 1981, Ahmed [8] conducted experiments on wake structures of typical automobile shapes. Vehicle shapes for an estate, fastback and notchback were tested by varying the upper rear end of a quarter scale model (Figure 3.33) with flow visualisation and wak

Shaun Johnson

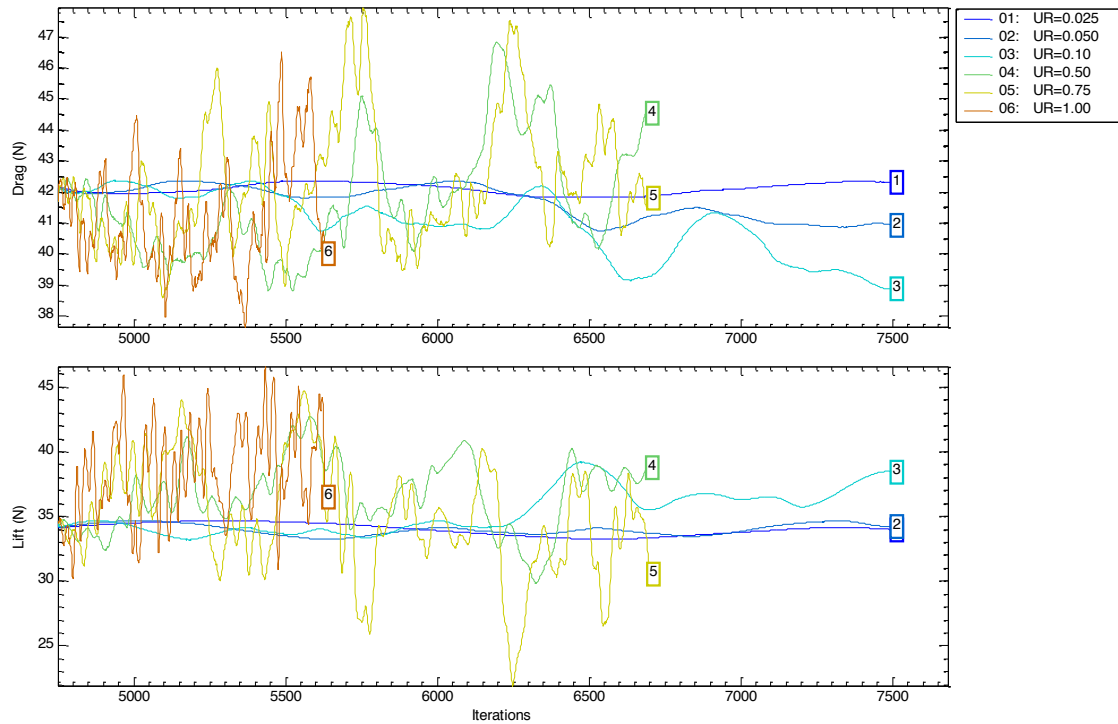


Figure 3.22 Effect of UR for after iterating for $\alpha=30^\circ$

The mean C_D and C_L for $\alpha=30^\circ$ for various UR values indicated in Figure 3.23 with error bars showing the range of the oscillations. As can be seen for $UR < 0.1$, the drag and lift forces are almost steady with very small oscillations. However flow visualisations revealed that even after running 3000 iterations using $UR=0.025$, the flow field was not the same as iteration averaging the flow field for $UR=1.0$. This indicates that although decreasing UR dampens the oscillations in the drag and lift data, it does not change the flow field to one that would be expected for a time dependent simulation.

Chapter 3 In 1981, Ahmed [8] conducted experiments on wake structures of typical automobile shapes. Vehicle shapes for an estate, fastback and notchback were tested by varying the upper rear end of a quarter scale model (Figure 3.33) with flow visualisation and wak

Shaun Johnson

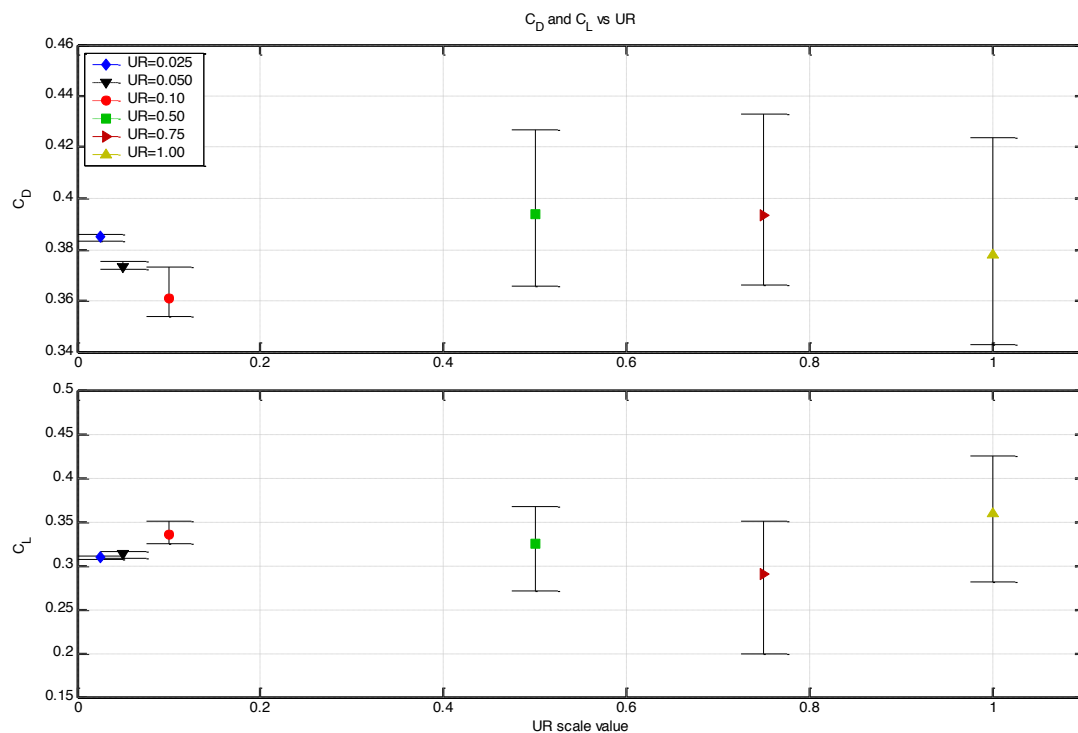


Figure 3.23 Mean CD and CL for $\alpha=30^\circ$ for various UR. Error bars indicate the range of the oscillations of the drag and lift iteration history.

3.6.1.3 Time dependent simulations

The time independent simulations appear to show that the wake structure was unsteady and therefore, difficult to converge. It was necessary undertake time dependent simulations for comparison. Since time dependent simulations are computationally expensive, limited simulations were undertaken only for $\alpha=30^\circ$ using time independent simulations as the initial velocity field to determine time step (Δt) independence. Due to the high Reynolds numbers, the initial time step was set to 0.01 and reduced by half in each simulation. Using Δt less than 0.0005 was not unfeasible due to the long computational time required. Shown in Figure 3.24 is the unsteady drag and lift history for $\alpha=30^\circ$ using different time steps. Compared with $\Delta t=0.001$ and $\Delta t=0.0005$, it can be seen that higher frequency interactions are not observed in the drag and lift history for larger Δt .

Chapter 3 In 1981, Ahmed [8] conducted experiments on wake structures of typical automobile shapes. Vehicle shapes for an estate, fastback and notchback were tested by varying the upper rear end of a quarter scale model (Figure 3.33) with flow visualisation and wak

Shaun Johnson

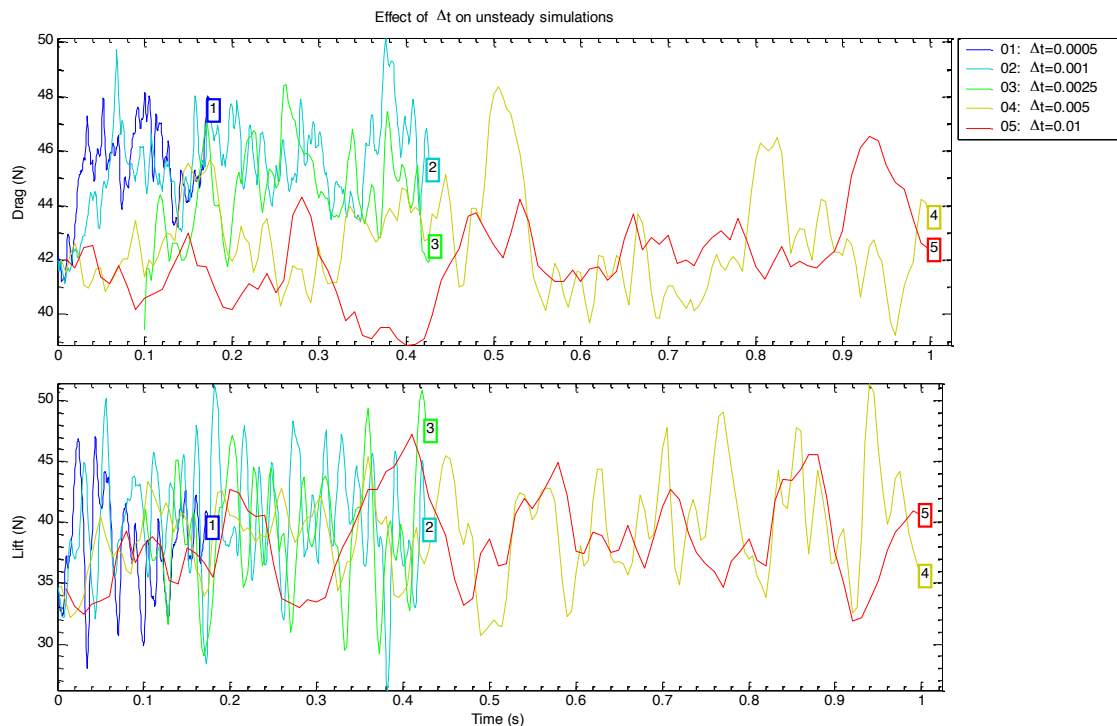


Figure 3.24 Unsteady simulations for $\alpha=30^\circ$ examining the effect of different time steps

From Figure 3.24, the drag history for $\Delta t \leq 0.0025$ is similar. The mean drag and lift forces in Figure 3.25 for different Δt indicate that the mean C_D has reached a plateau for $\Delta t \leq 0.001$. Therefore, $\Delta t = 0.001$ was used to investigate the effect of time dependent simulations for different slant angles. Although longer simulation runs were required to determine the full effects on the time-step on time dependent simulations, these results were sufficient given the large computational time required for a more thorough investigation.

Chapter 3 In 1981, Ahmed [8] conducted experiments on wake structures of typical automobile shapes. Vehicle shapes for an estate, fastback and notchback were tested by varying the upper rear end of a quarter scale model (Figure 3.33) with flow visualisation and wak

Shaun Johnson

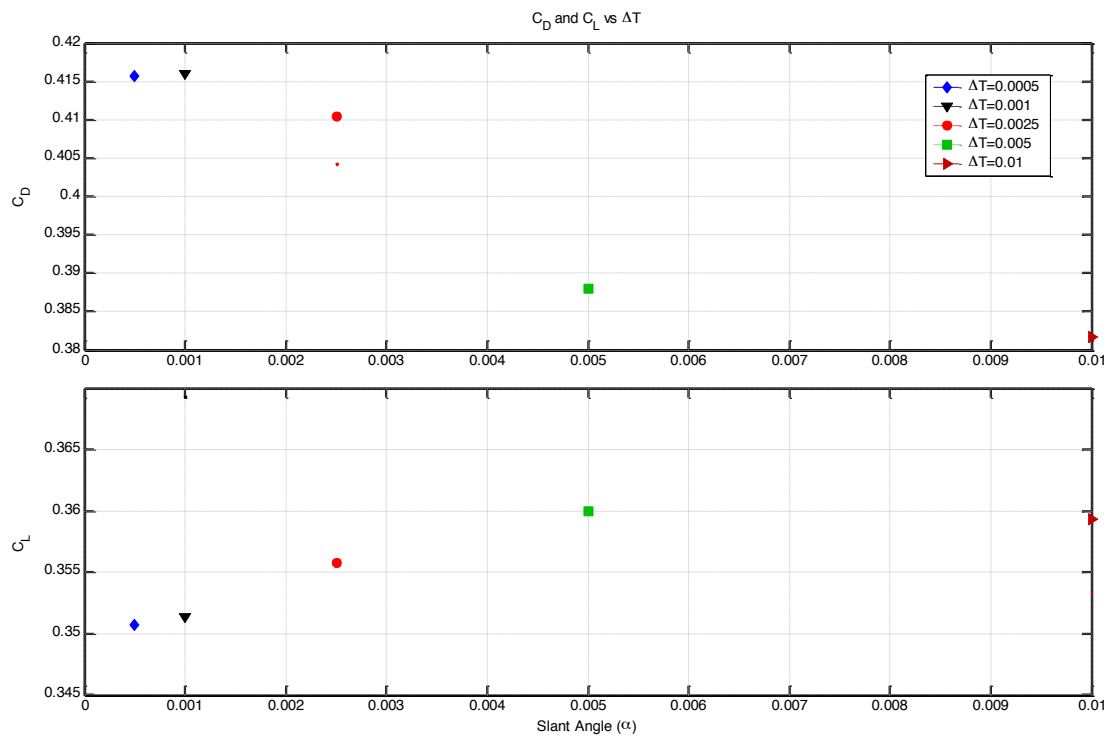


Figure 3.25 Effect of different Δt on mean C_D and C_L using time dependent simulations for $\alpha=30^\circ$.

Time dependent simulations were run for different slant angles using $\Delta t=0.001$. Shown in Figure 3.26 is the time history for the entire model run up to 0.5s. Due to divergence issues, $\alpha=25^\circ$ was only simulated for 0.1s. Although, the simulations are clearly unsteady, after 0.1s it is evident that the drag and lift forces are oscillating about a mean value.

Chapter 3 In 1981, Ahmed [8] conducted experiments on wake structures of typical automobile shapes. Vehicle shapes for an estate, fastback and notchback were tested by varying the upper rear end of a quarter scale model (Figure 3.33) with flow visualisation and wak

Shaun Johnson

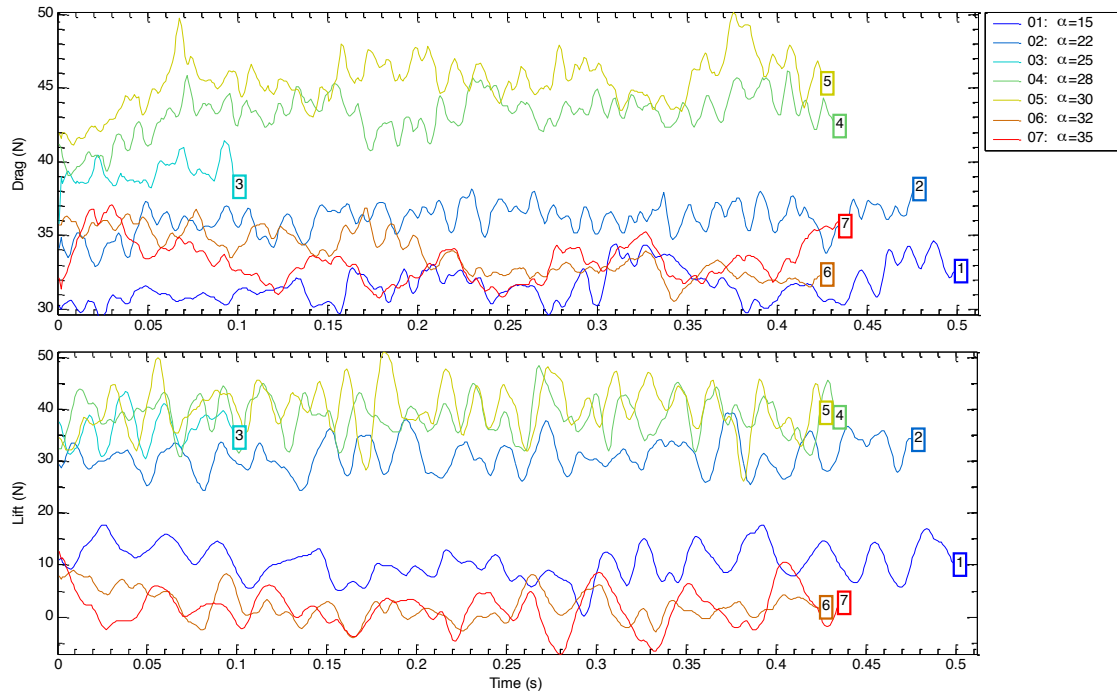


Figure 3.26 Time history for various slant angles using $\Delta t=0.001$.

Time dependent simulations were compared with time independent simulations on the full body forces and just on the slant surface as seen in Figure 3.27. For all α , there was an increase in drag on the overall body. However, there are no major changes to the drag profile as α is varied. This indicates that there is little difference in time averaging the time independent simulations compared with iteration averaging time independent simulations. This was also evident when comparing the time averaged and iteration averaged wakes structures in Figure 3.28 and Figure 3.29.

Chapter 3 In 1981, Ahmed [8] conducted experiments on wake structures of typical automobile shapes. Vehicle shapes for an estate, fastback and notchback were tested by varying the upper rear end of a quarter scale model (Figure 3.33) with flow visualisation and wak

Shaun Johnson

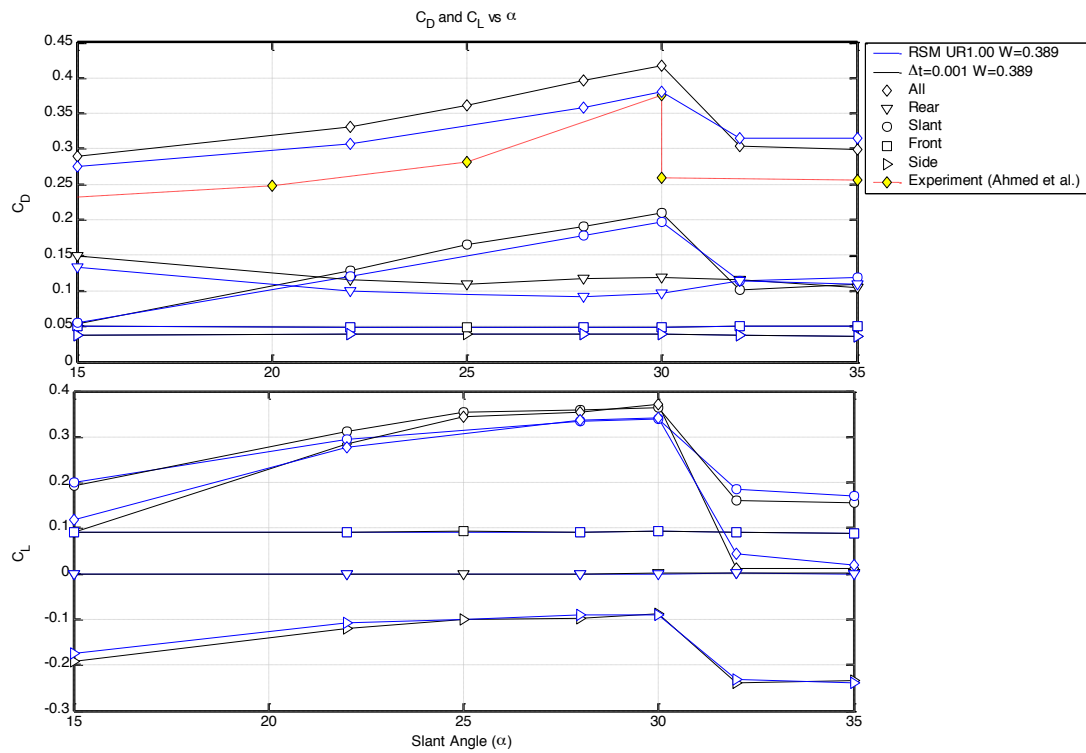


Figure 3.27 Comparison between the time independent and time dependent simulations on the different surfaces of the body at various α .

Figure 3.28 Flow structures of iteration averaged time independent simulations for $\alpha=30^\circ$. Visualisation of U overlaid with stream lines on orthogonal planes in the wake

Chapter 3 In 1981, Ahmed [8] conducted experiments on wake structures of typical automobile shapes. Vehicle shapes for an estate, fastback and notchback were tested by varying the upper rear end of a quarter scale model (Figure 3.33) with flow visualisation and wak

Shaun Johnson

Figure 3.29 Flow structures of time averaged time dependent simulations for $\alpha=30^\circ$. Visualisation of U overlaid with stream lines on orthogonal planes in the wake

3.6.1.4 Symmetry conditions

Experimental data has indicated that the flow is symmetric about $z=0$ plane and numerous computational studies have used this flow feature to reduce the computational resource requirements. An investigation was undertaken to ensure that the symmetry plane used in the simulations did not have an impact on the wake structures. Experimental results by Lienhart et al. [14] showed that the time averaged flow downstream to be symmetrical about $z=0$ ($y=0$, using their coordinate system).

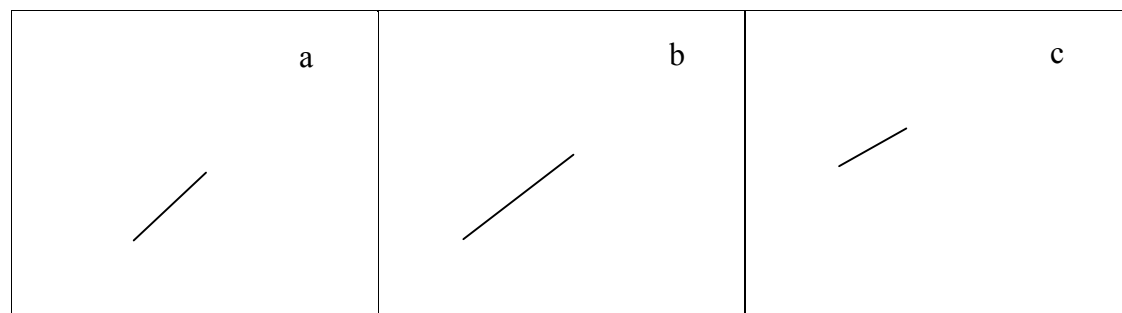


Figure 3.30 Contours of x-velocity overlaid with in plane stream lines in the YZ plane at $x=0.08$ (a), $x=0.2$ (b) and $x=0.5$ (c) for $\alpha=25^\circ$ ([14]). Full flow field indicates that the wake is symmetric about $Z=0$

Simulations of the full domain were compared with the previous results using only half the domain with a symmetry boundary condition used at $Z=0$. The drag and lift forces seen in previous simulations has been doubled to correspond with experimental forces. As shown in Figure 3.31, there are no major differences in the iteration averaged

Chapter 3 In 1981, Ahmed [8] conducted experiments on wake structures of typical automobile shapes. Vehicle shapes for an estate, fastback and notchback were tested by varying the upper rear end of a quarter scale model (Figure 3.33) with flow visualisation and wak

Shaun Johnson

C_D and C_L . The subtle differences can be attributed to the fact that these values are iteration averaged over a highly unsteady drag history.

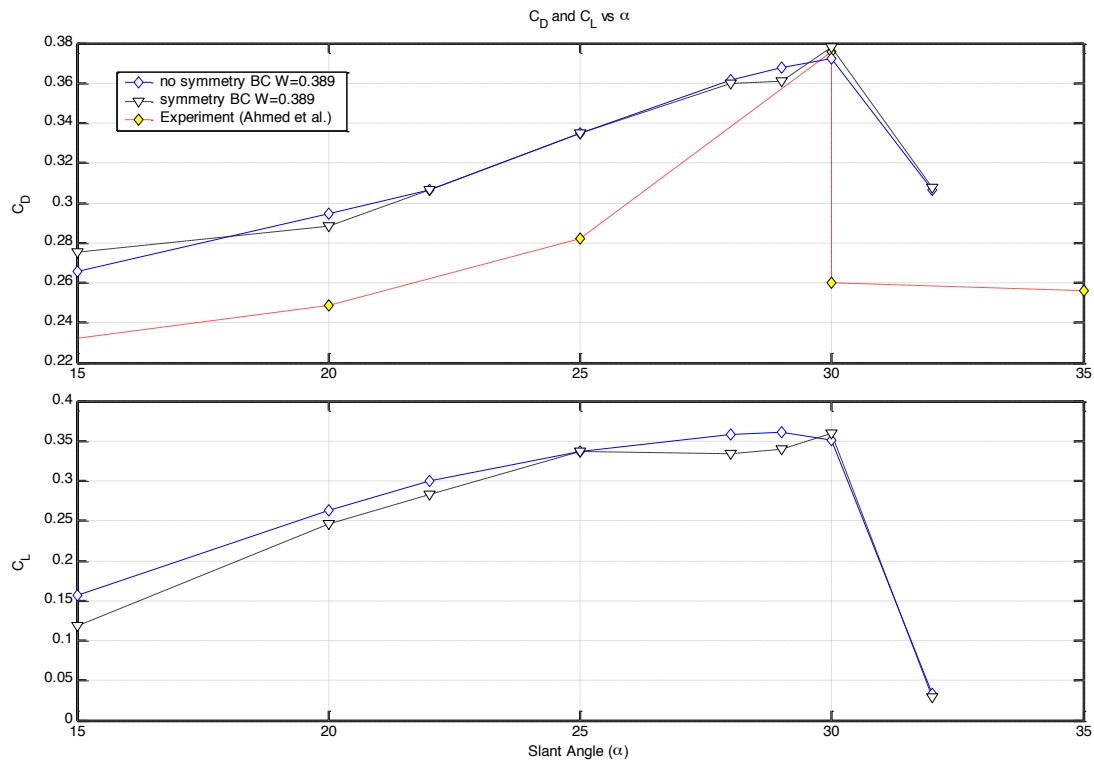


Figure 3.31 Comparison with simulations where the full body is modelled and where a symmetry plane is used.

However, flow visualisations (Figure 3.32) found slight differences in the flow field near $Z=0$ using a symmetrical boundary condition. As can be seen in Figure 3.32(b), the saddle point of the stream lines of the slant surface is slightly off centre indicating that the flow field is slightly skew in this instance. This could be a by-product from averaging the data. However the strange flow streamlines at the bottom of the slant surface in Figure 3.32a appear to be from using a symmetry boundary condition. This flow feature was not present for all other slant angles. Away from the centreline, there is little difference in the wake structures with C-pillar vortex in the same location.

Chapter 3 In 1981, Ahmed [8] conducted experiments on wake structures of typical automobile shapes. Vehicle shapes for an estate, fastback and notchback were tested by varying the upper rear end of a quarter scale model (Figure 3.33) with flow visualisation and wak

Shaun Johnson

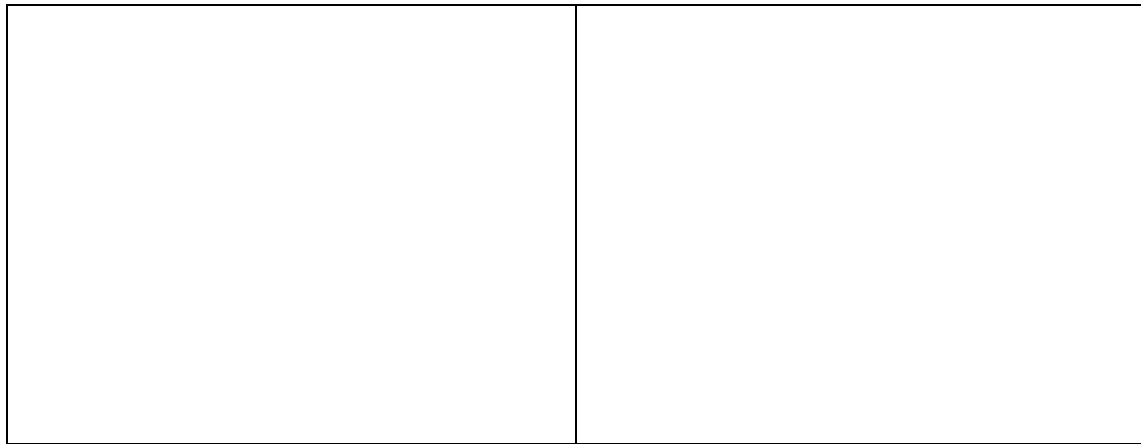


Figure 3.32 Orthographic projection of flow visualisations for symmetric (a) and non symmetric model (b) model for $\alpha=25^\circ$ near the slant surface using contours of x-velocity and stream lines

Therefore, due to good agreement between non-symmetrical and symmetrical simulations, a symmetrical boundary condition along $Z=0$ was used to reduce the computation resources required.

3.6.2 Conclusion

From the analysis of numerical simulations, it was found that the RSM turbulence was the appropriate model for simulating the flow around the Ahmed body. This is probably because this model does not assume that the turbulent viscosity is isotropic.

However, since the flow structures are unsteady, it made it difficult to find a converged solution with the time independent simulations fluctuating around a mean solution similar to the time dependent simulations. Various methods were examined to converge the time independent simulations such as reducing under-relaxation and changing the initial conditions at which solutions were started. It was found that these methods would diffuse the simulation and effect the wake structures near $\alpha=30^\circ$ causing a large separation bubble found at higher α instead of strong c-pillar vortices.

When the under relaxation was left at the default values, it was found that the time independent simulations which were iteration averaged and the time dependent simulations which were time averaged had very similar mean flow fields. Therefore, it was more computationally efficient to iteration average the time independent simulations instead of running time dependent simulations for the parameter space study.

Chapter 3 In 1981, Ahmed [8] conducted experiments on wake structures of typical automobile shapes. Vehicle shapes for an estate, fastback and notchback were tested by varying the upper rear end of a quarter scale model (Figure 3.33) with flow visualisation and wak

Shaun Johnson

To reduce computational requirements further, a symmetry at $Z=0$ was used to reduced the domain size without effecting the flow structures adversely. Experimental data also shows the averaged flow field to be symmetrical and this process has been used in other numerical experiments [15, 20].

were done with a free stream velocity of 60 m/s, using the vehicle length as the length scale, which equated to a $Re=4.29 \times 10^6$.

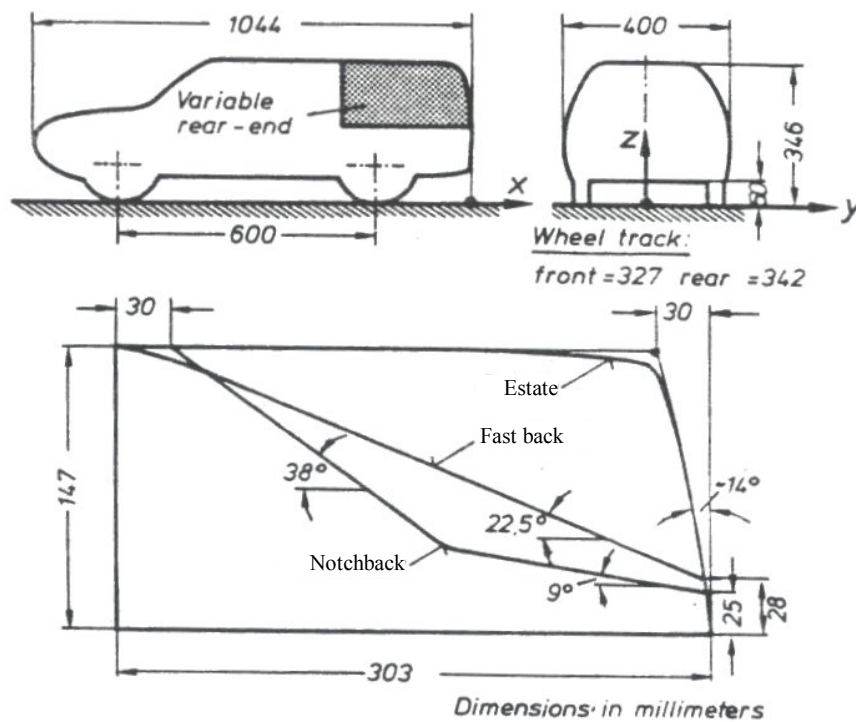


Figure 3.33 Diagram of the wind tunnel model with interchangeable estate, fastback and hatchback profiles. [8]

The wake behind the models was characterised by an oval separation bubble. In the case of the estate, the bubble consisted mainly of a recirculatory motion directed upwards, while for the fastback model, there was an overall downwash as illustrated in Figure 3.34. Ahmed concluded that a base slant angle existed for which there was no rotational motion present in the wake and this angle was the critical angle at which there would be minimum aerodynamic drag.

Chapter 3 In 1981, Ahmed [8] conducted experiments on wake structures of typical automobile shapes. Vehicle shapes for an estate, fastback and notchback were tested by varying the upper rear end of a quarter scale model (Figure 3.33) with flow visualisation and wak

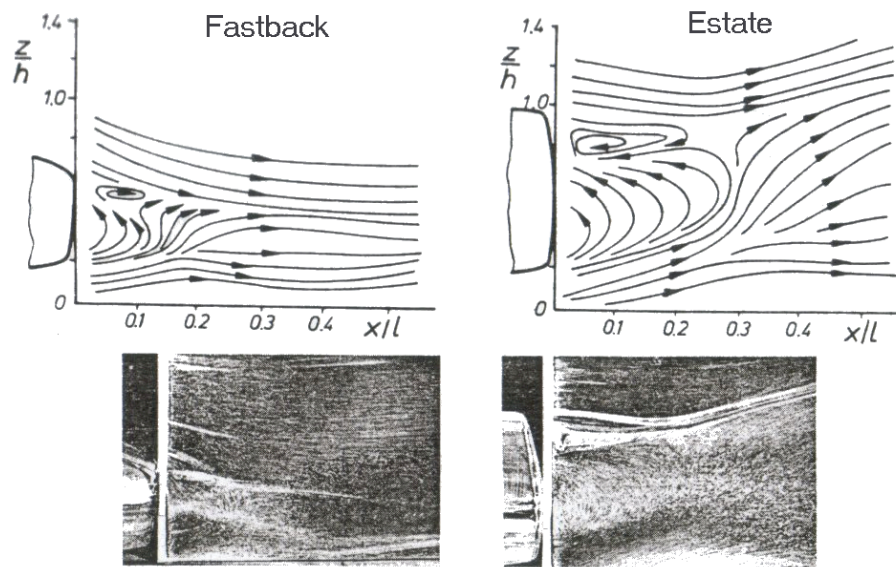


Figure 3.34 Streak lines from experiments on the symmetry plane for the fastback and estate quarter scale models. The fastback exhibits a net downwash while a net up wash exists on the estate model. [8]

The drag for the three models outlined in Table 3.19, showed that the fastback model had the lowest drag coefficient (C_D). Ahmed concluded this was due to enhanced control of the vortex drag on the fastback rather than a decrease in skin friction from using a model with less surface area. However, evaluating the vortex drag on the basis of kinetic energy of vortex motion, the vortex drag of the fastback amounted to 28% of total aerodynamic drag while only 8% for the estate model. This must imply that the pressure drag is more dominate on the estate model due to a larger rear surface.

Vehicle Shape	Estate	Fastback	Notch back
Coefficient of drag (C_D)	0.272	0.215	0.236
Coefficient of lift (C_L)	-0.148	0.210	0.155

Table 3.19 Drag and lift for various vehicle shapes

In 1983, Ahmed [7] concentrated further on research to find the critical angle of a fast back car where the C_D is a minimum. In this set of experiments, the same model was used with eight upper rear-end sections with various slant angles to model different fastback configurations. The slant angles ranged from 0° (measured from the horizontal) to 40° with the slant area kept at a constant size. In these experiments,

Chapter 3 In 1981, Ahmed [8] conducted experiments on wake structures of typical automobile shapes. Vehicle shapes for an estate, fastback and notchback were tested by varying the upper rear end of a quarter scale model (Figure 3.33) with flow visualisation and wak

Shaun Johnson

four regimes of flow were visualised as the slant angle was changed. Schematics of the flow streak lines on the symmetry plane are illustrated in Figure 3.35. For 5 degrees, the lower counter rotating structures were more predominant leading to a net up wash behind the vehicle. At 15°, both the recirculating flows were of equal strength and at 30°, the upper flow was more dominant, leading to a net down wash. However, above 30° the flow separated from the roof trailing edge resulting in an abrupt switch of the wake pattern, which now resembled flow structures similar to those observed at 5°. Ahmed concluded that the kinetic energy of the transverse flow wake could be correlated to the aerodynamic drag of the vehicle and for the optimum low drag configuration, the transverse component of the flow should be minimised.

Chapter 3 In 1981, Ahmed [8] conducted experiments on wake structures of typical automobile shapes. Vehicle shapes for an estate, fastback and notchback were tested by varying the upper rear end of a quarter scale model (Figure 3.33) with flow visualisation and wak

Shaun Johnson

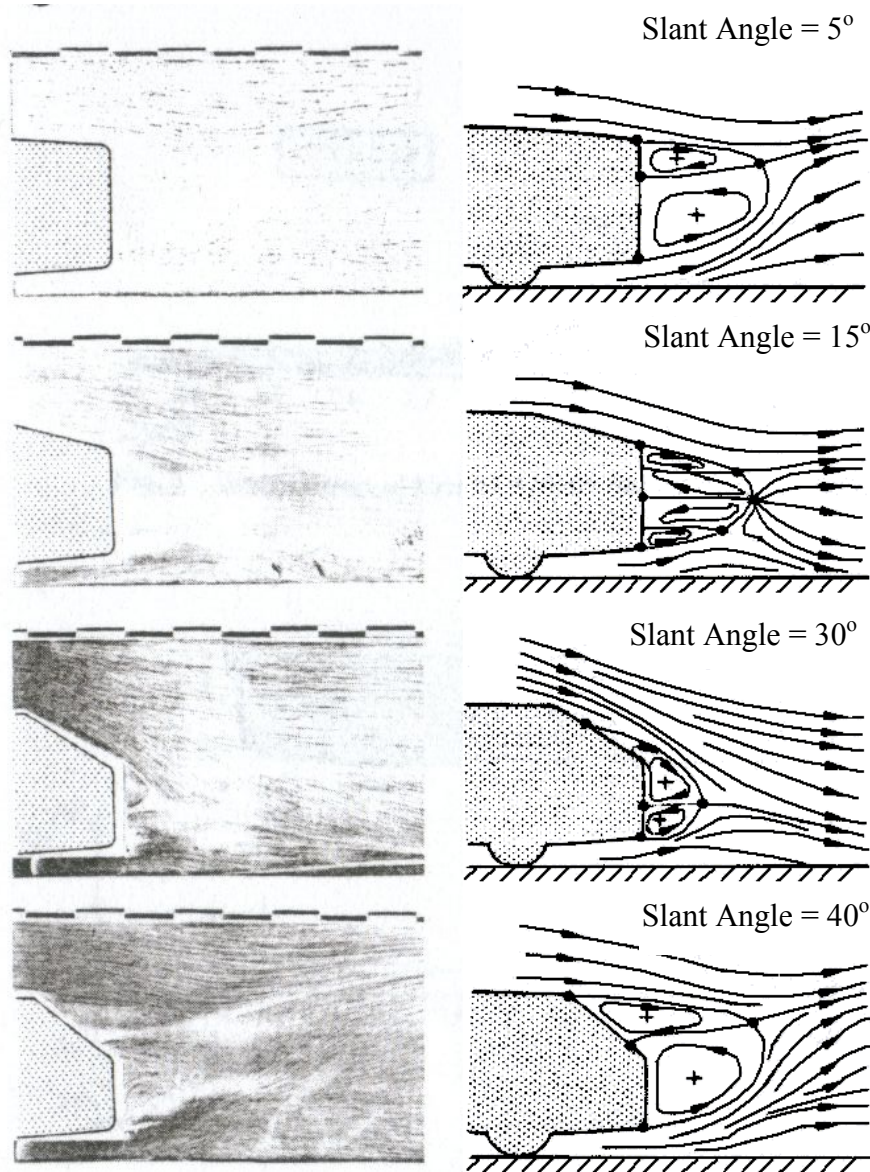


Figure 3.35 Flow patterns in the wake central plane. On the left are the Oil flow pictures for give slant angles and the proposed streamlines are shown on the right. [7]

3.7 The Ahmed Body

Instead of using the quarter scale car model, new experiments by Ahmed et al. [5] used a simplified version of the previous model similar to the Morel body. This model isolated the effect of varying the slant angle on the rear of vehicle. This new model shown in Figure 3.36 and referred to as the Ahmed body was designed to generate a strong three-dimensional displacement flow at the front, provide relatively uniform flow in the middle section and generate a large structured wake at the rear to

Chapter 3 In 1981, Ahmed [8] conducted experiments on wake structures of typical automobile shapes. Vehicle shapes for an estate, fastback and notchback were tested by varying the upper rear end of a quarter scale model (Figure 3.33) with flow visualisation and wak

Shaun Johnson

mimic a passenger automotive vehicle. Similar to the quarter scale model, the slant angle was varied between 0° and 40° keeping a constant slant area.

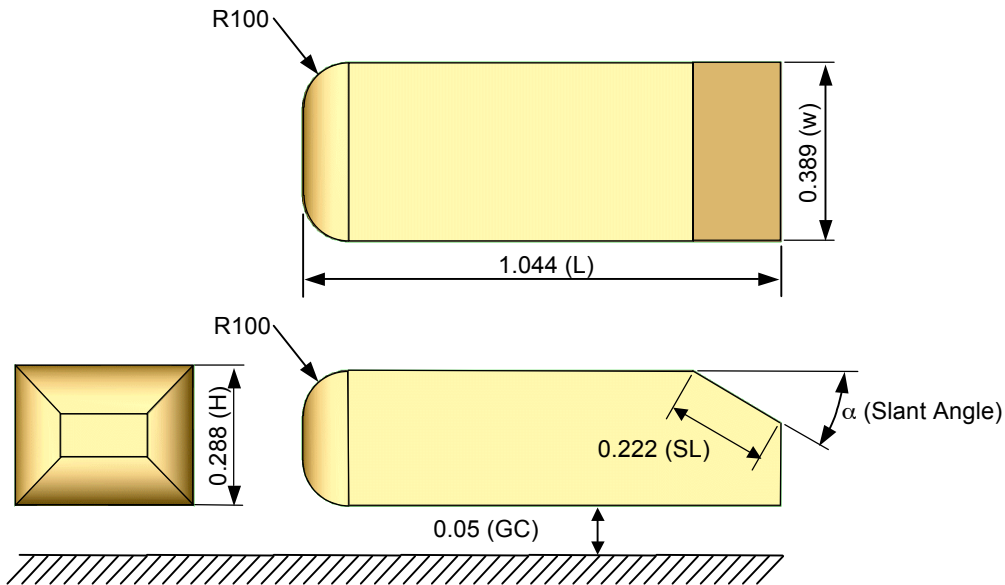


Figure 3.36 Critical dimensions of the Ahmed Reference Body. L represents the body length, W represents the body width, SL is slant length, R is the radius and GC is the body ground clearance.

The flow regimes found using the Ahmed body compared well to the previous model used even though flow visualisations were done at a different velocity (actual inlet velocity not provided).

The drag from different sections of the model was isolated to determine the effect that each section of the model had on the drag. The results shown in Figure 3.37 clearly show the increase in drag on the slant surface as slant angle is increased even though the surface area is constant. For a slant angle greater than 30° , full separation occurs and the net drag reduction is mainly due to the decrease in drag on the slant surface. Also of note, is the small contribution made by the forebody to the total drag.

Chapter 3 In 1981, Ahmed [8] conducted experiments on wake structures of typical automobile shapes. Vehicle shapes for an estate, fastback and notchback were tested by varying the upper rear end of a quarter scale model (Figure 3.33) with flow visualisation and wak

Shaun Johnson

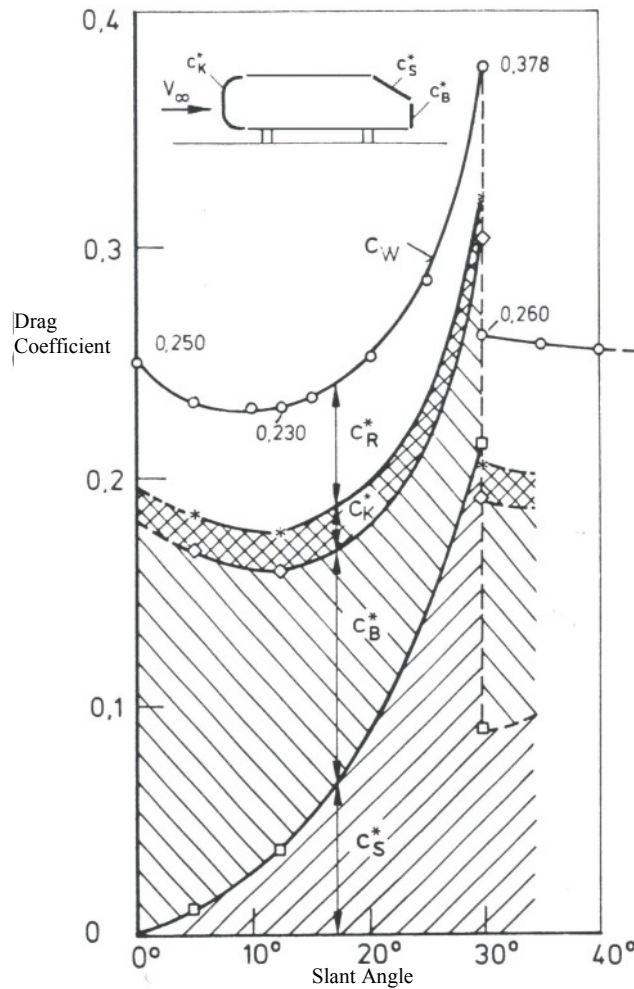


Figure 3.37 Variation in drag with base slant angle. C_K^* is the front of the body. C_B^* denotes the vertical base surface and C_S^* is the slant area as shown in the enclosed schematic. C_R^* is the difference between the measures Drag and the drag that is accounted for. This is primarily skin friction. [5]

The flow structures in the wake area were investigated with three main types of flow observed. Figure 3.38 shows the flow structures up to a slant angle of 30°. The main structures were the shear layers coming off the slant edge rolling into streamwise vortices. At the top and bottom edges of the flat vertical base, the shear layer rolled up into two recirculatory flow regions situated one above the other. The strength of the streamwise vortex was influenced by the slant angle as long as the flow remained attached.

Chapter 3 In 1981, Ahmed [8] conducted experiments on wake structures of typical automobile shapes. Vehicle shapes for an estate, fastback and notchback were tested by varying the upper rear end of a quarter scale model (Figure 3.33) with flow visualisation and wak

Shaun Johnson

a

b

Figure 3.38 Schematic of the wake structure described by Ahmed et al. [5] when the wake is attached to the slant surface (a) and the wake structures for the high drag regime (b). The streak lines indicate that the flow has separated from the top of the slant surface

At 30° , the flow began to separate from the slant surface as illustrated in Figure 3.38b. For this configuration, the flow separated at the upstream edge of the slant surface. The half elliptic region of circulatory flow was flanked by two triangular attached flow regions indicated on the surface as streak lines. These were generated by a fourth vortex whose axis was aligned with the core of the recirculation region on the slant surface with the legs merging into the stream wise vortices at the corners of the vehicle. However, in Figure 3.38b, there appears to be some discrepancy between the streak lines on the slant surface compared with the predicted flow structures. On the slant surface, the streak lines showed a streamwise rotational component whereas the schematic of the flow structures indicate that only a spanwise rotation was presented. If this were the case, the streak lines should be vertical.

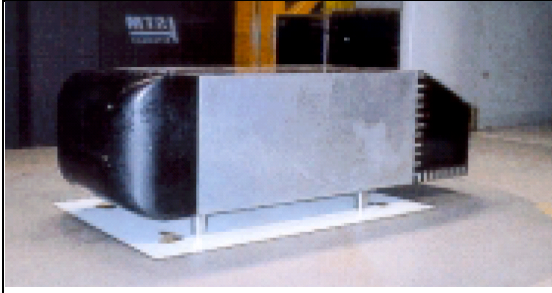
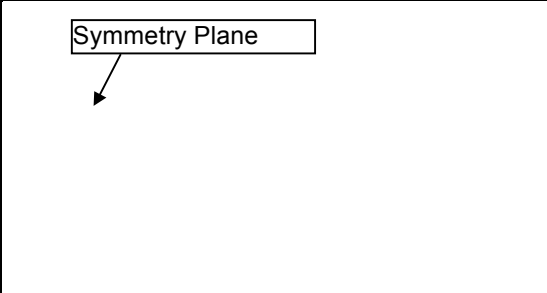
Above a 30° slant angle, the flow fully separated from slant surface and rear vertical edge. This caused the strength of the streamwise vortices to decrease. Further downstream, two larger counter rotating stream wise vortices were still

Chapter 3 In 1981, Ahmed [8] conducted experiments on wake structures of typical automobile shapes. Vehicle shapes for an estate, fastback and notchback were tested by varying the upper rear end of a quarter scale model (Figure 3.33) with flow visualisation and wak

Shaun Johnson

measurable. However their strength was decreased compared with the vortices produced for attached flow.

Lienhart et al. [13, 14] conducted experiments on the Ahmed body to provide experimental data for validation of turbulence models on automotive geometries. The two slant angles investigated were $\alpha=25^\circ$ and $\alpha=35^\circ$, which bracket the critical angle of 30° . Experiments were conducted in a $\frac{3}{4}$ open jet wind tunnel with the model placed on a fixed ground plane on stilts as illustrated in Figure 3.39. The inlet bulk velocity was reduced to 40m/s which corresponds to a $Re=2.78 \times 10^6$ based on vehicle length. Data about the flow field was collected using a laser-Doppler anemometer (LDA) on the body centreline, on the slant surface and on spanwise and streamwise slices at various locations downstream as indicated in Figure 3.40. Smoke visualisation and surface streak lines for surface topology were also conducted.

	
<p>Figure 3.39 Ahmed body model used in experiments in $\frac{3}{4}$ open jet wind tunnel. [13]</p>	<p>Figure 3.40 Schematic showing slice locations where LDA measurements were taken. [13]</p>

Smoke visualisation for $\alpha=25^\circ$ in Figure 3.41 indicates that a large unsteady separated region exists at the rear of the vehicle and that the flow is attached to the slant surface. However, as can be seen in Figure 3.42, the surface topology from the streak lines on the slant surface indicates that a separation bubble exists on the slant surface. Since the separation bubble reattaches on the slant surface, the smoke released at the rear of the model is not entrained into the slant surface separation bubble. On the side edges of the slant surface, footprints of the streamwise vortices are visible emanating from the C-pillar.

Chapter 3 In 1981, Ahmed [8] conducted experiments on wake structures of typical automobile shapes. Vehicle shapes for an estate, fastback and notchback were tested by varying the upper rear end of a quarter scale model (Figure 3.33) with flow visualisation and wak

Shaun Johnson

<p>Figure 3.41 Flow visualisation using smoke released behind body for $\alpha=25^\circ$ indicating no separation bubble on the slant surface. [13]</p>	<p>Figure 3.42 Oil streak lines on the slant surface for $\alpha=25^\circ$ indicating a small separation bubble present on the slant surface. [13]</p>

The mean velocity vectors in Figure 3.43 indicated that no separation along the line of symmetry occurred. However, a more detailed investigation close to the slant surface (Figure 3.44) indicated that a small recirculation region was present with the flow reattaching on the slant surface. Spanwise (direction perpendicular to free stream velocity) velocity vectors on a spanwise plane downstream indicated the presence of two large counter rotating trailing vortices in agreement with earlier observations.

<p>Figure 3.43 Velocity vectors on the symmetry plane for $\alpha=25^\circ$ in far wake. [13]</p>	<p>Figure 3.44 Profiles of U velocity near slant surface for $\alpha=25^\circ$. [13]</p>

For $\alpha=35^\circ$, smoke visualisations illustrated in Figure 3.45 reveal that the wake has separated completely from the slant surface and the separation bubble from the slant surface and the separation bubble from the rear have merged together. The footprint

Chapter 3 In 1981, Ahmed [8] conducted experiments on wake structures of typical automobile shapes. Vehicle shapes for an estate, fastback and notchback were tested by varying the upper rear end of a quarter scale model (Figure 3.33) with flow visualisation and wak

Shaun Johnson

of the streamwise vortices are no longer present as the streak lines in Figure 3.46 reveal that the separation bubble has an almost two dimensional structure.

<p>Figure 3.45 Flow visualisation using smoke released behind body for $\alpha=35^\circ$ indicating full separation. [13]</p>	<p>Figure 3.46 Oil streak lines on the slant surface for $\alpha=35^\circ$ indicating a full separation with no indication on c-pillar vortices. [13]</p>

Full separation is confirmed with flow field measurements at $\alpha=35^\circ$ on the vehicle centreline in Figure 3.47, showing a large single recirculation region behind the vehicle. U velocity profiles in Figure 3.48 indicate that the flow has separated from the top of slant surface.

<p>Figure 3.47 Velocity vectors on the symmetry plane for $\alpha=35^\circ$ in far wake. [13]</p>	<p>Figure 3.48 Profiles of U velocity near slant surface for $\alpha=25^\circ$. [13]</p>

Additional static pressure measurements on the rear portion of Ahmed body were incorporated later[13] to the available data. The 500 pressure taps located on one side of the vehicle provided a time-averaged pressure field on the vehicle surface. As can be seen in Figure 3.49a at $\alpha=25^\circ$, the pressure field is stronger than at $\alpha=35^\circ$ (Figure

Chapter 3 In 1981, Ahmed [8] conducted experiments on wake structures of typical automobile shapes. Vehicle shapes for an estate, fastback and notchback were tested by varying the upper rear end of a quarter scale model (Figure 3.33) with flow visualisation and wak

Shaun Johnson

3.49b) and the footprint of the vortices on the side of the slant surface can be easily identified.

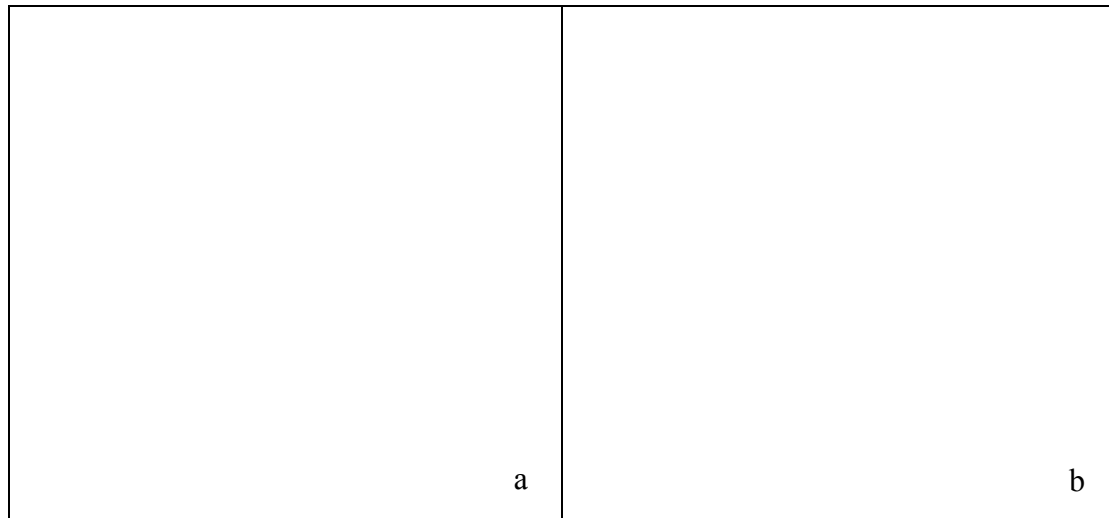


Figure 3.49 Surface pressure distribution on rear region of the Ahmed body for $\alpha=25^\circ$ (a) and $\alpha=35^\circ$. Foot print from C-pillar vortex is clearly visible at $\alpha=25^\circ$. [13]

In 2001, the thesis by Sims-Williams [17] investigated large-scale aerodynamic unsteadiness of automotive vehicles using computational and experimental methods. The main focus of this investigation was the unsteady wake structures downstream of fast vehicles including the Ahmed body ($\alpha=30^\circ$). Due to limitations with experimental equipment, the separation region was not measured.

The surface oil streak patterns for $\alpha=30^\circ$ (high drag) shown in Figure 3.50 (by Dominy [18]) showed different patterns to those observed by Ahmed et. al. Below the D shaped separation bubble was a central tail which extended to the rear of the body. Inboard of the C-pillar vortex streak marks, weak reattachment lines are visible where the flow is entrained in the C-pillar impinges onto the slant surface. These steak patterns were taken at $Re=1.5 \times 10^6$ (25m/s) whereas is it unknown at what Reynolds number streak lines by Ahmed were carried out.

Sims-Williams concluded that the transition from the high drag to low drag was not due to vortex breakdown since the swirl angle on the counter rotating structures downstream was nowhere near the required angle. Neither were there signs of rapid expansion of the vortex core or reversed flow inside the core.

Chapter 3 In 1981, Ahmed [8] conducted experiments on wake structures of typical automobile shapes. Vehicle shapes for an estate, fastback and notchback were tested by varying the upper rear end of a quarter scale model (Figure 3.33) with flow visualisation and wak

Shaun Johnson

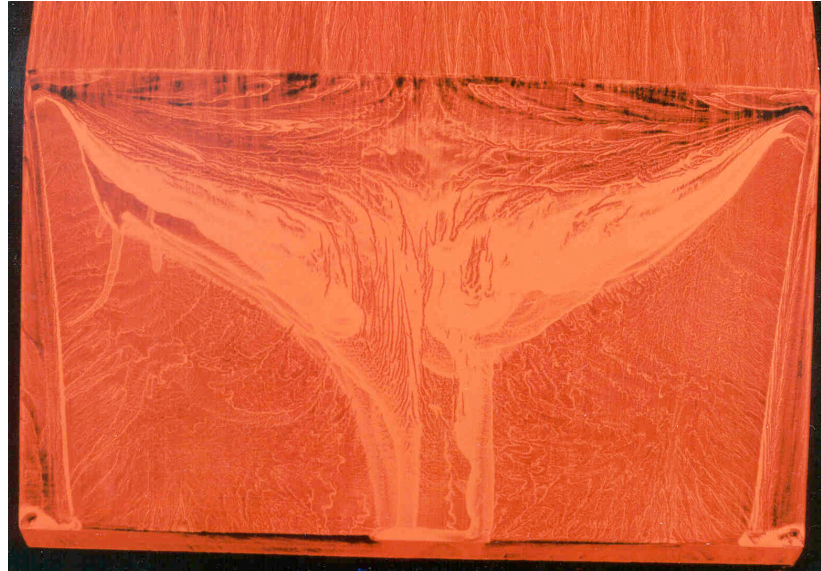


Figure 3.50 Streak patterns on the slant surface of the Ahmed body for $\alpha=30^\circ$. [17]

Besides the Ahmed body, experiments were also conducted on a two dimensional version of the Ahmed body equivalent width of 800mm and with end plates on the side of the body. Using this model, it was found that the transition from the attached flow (Figure 3.51) to separated flow (Figure 3.52) occurred at $\alpha=22.5^\circ$ as opposed to $\alpha=30^\circ$ for normal Ahmed body. It was concluded that the C-pillar vortices on the three dimensional model delayed final separation.

Chapter 3 In 1981, Ahmed [8] conducted experiments on wake structures of typical automobile shapes. Vehicle shapes for an estate, fastback and notchback were tested by varying the upper rear end of a quarter scale model (Figure 3.33) with flow visualisation and wak

Shaun Johnson

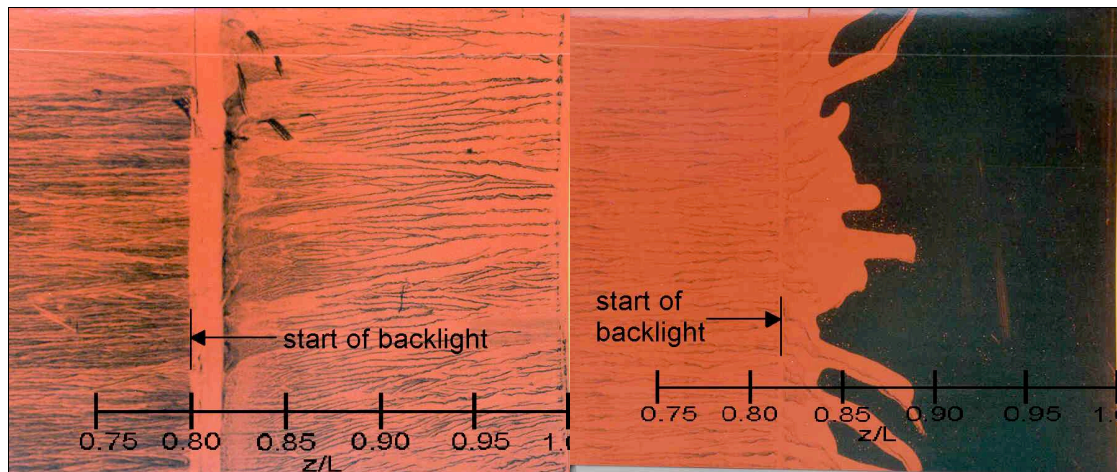


Figure 3.51 Top view of the two dimensional Ahmed body at $\alpha=20^\circ$ showing the flow is attached. [17]

Figure 3.52 Top view of the two dimensional Ahmed body at $\alpha=30^\circ$ showing the flow is separated. [17]

Experimental simulations by Drouin et al. [19] characterised the flow structures at $\alpha=25^\circ$ using particle-image velocimetry (PIV) at $Re=0.7 \times 10^6$. Instantaneous streamlines on a plane 2mm offset from the slant surface reveal that the separation bubble is unstable. However, the C-pillar vortex emanating from the top of the slant surface is quite stable. Time averaged path lines (from 200 images) in Figure 3.54 reveal a similar structure to that seen in RANS numerical simulations [15, 20].

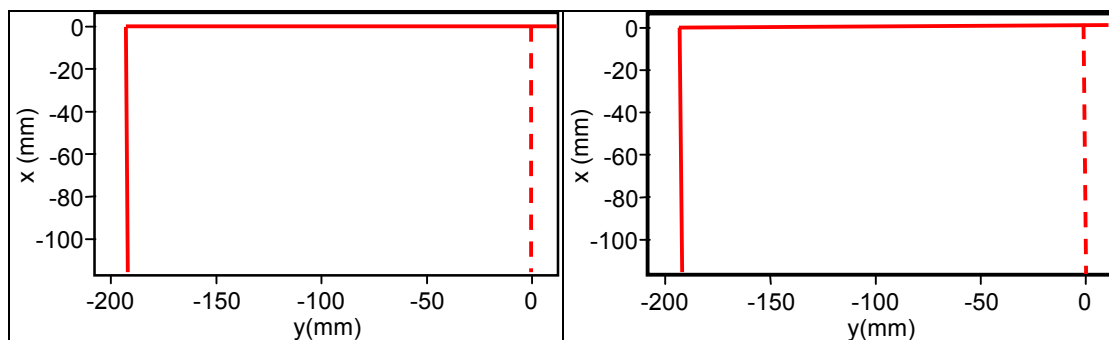


Figure 3.53 Instantaneous streamlines on slant surface ($\alpha=25^\circ$) from PIV data. [19]

Figure 3.54 Time averaged streamlines on slant surface ($\alpha=25^\circ$) from PIV data. [19]

Spohn and Gilliéron [21] extended previous research to examine in more detail the near wake flow and its unsteady behaviour. Experiments were conducted on a scale model of the Ahmed body ($\alpha=25^\circ$) in a water tunnel at 3.0×10^4 (based on vehicle length). On the forebody region of the vehicle, skin friction lines (Figure 3.55), showed the existence of a separation zone which had not been observed before in

Chapter 3 In 1981, Ahmed [8] conducted experiments on wake structures of typical automobile shapes. Vehicle shapes for an estate, fastback and notchback were tested by varying the upper rear end of a quarter scale model (Figure 3.33) with flow visualisation and wak

Shaun Johnson

earlier experiments. The focal points were linked to two counter rotating longitudinal vortices linked by transverse vortices shown schematically in Figure 3.56.

<p>Figure 3.55. Top view of surface streak lines on front region of Ahmed body. [21]</p>	<p>Figure 3.56. Proposed flow topology on the front region of the Ahmed body. [21]</p>

On the rear body region, the skin friction lines (Figure 3.57) show that the separation bubble does not to reattach to the slant surface on the body centreline. The vortices emanating from C-pillar reattach the separated flow on the edges of the slant surface. The schematic for the flow topology show in Figure 3.58 show the vortices rolling up from the edges creating an attachment line (line AC). Even with the presence of C-pillar vortices, it was still possible for recirculation bubble on slant surface and on the rear to combine. This could be a Reynolds Number effect or arise from tripping the boundary layer with the flattened solder wires on the body surface used for flow visualisation.

<p>Figure 3.57. Top view of surface streak lines on slant surface of the Ahmed body. [21]</p>	<p>Figure 3.58. Proposed flow topology on the slant surface of the Ahmed body. [21]</p>

Most numerical work simulating the Ahmed body has used the drag coefficient as guide to the accuracy of their simulations. Most have compared with the drag profile

Chapter 3 In 1981, Ahmed [8] conducted experiments on wake structures of typical automobile shapes. Vehicle shapes for an estate, fastback and notchback were tested by varying the upper rear end of a quarter scale model (Figure 3.33) with flow visualisation and wak

Shaun Johnson

as α is varied by Ahmed et al. [5]. Watkins and Vio [2] investigated the effect of vehicle spacing and its effect on drag and lift using two Ahmed Bodies with $\alpha=30^\circ$. Drag forces of one body in isolation had a $C_D=0.32$ at $Re=2.3 \times 10^6$. This is in contrast to what was reported to Ahmed et al. who reported $C_D=0.378$ at $Re=4.3 \times 10^6$. This represents a 39% change in drag over the current range in data. Even though it was not reported by Watkins and Vio, it appears that the ground clearance is higher (Figure 3.59) than the original simulations. It is possible that the different ground clearance could account for the different drag coefficients. Subsequent research by Vio et al. [22] show there is variation in the C_D with Re but not up to the Re used by Ahmed et al.[5]. The question arises of how sensitive the Ahmed body is to ground clearance and Reynolds numbers effects. Without more information, it is impossible to determine how accurate the experimental data is with variations between different experiments.



Figure 3.59 Experimental setup shows a large ground clearance used in experiments, which might be the cause of a difference C_D . (Watkins and Vio [2])

A number of other experimental data has shown a scatter in recorded drag measurements. Shown in Figure 3.60 is a graph of drag coefficient data from different experiments using the Ahmed body. Of note are the experiments by Ramm and Hummel [4] at $\alpha=28^\circ$ not showing the large peak associated with the high drag. There seems to be quite some discrepancy for $\alpha=25^\circ$, but these results other results were conducted with a moving ground plane as opposed to a stationary ground plane which has been done previously.

Chapter 3 In 1981, Ahmed [8] conducted experiments on wake structures of typical automobile shapes. Vehicle shapes for an estate, fastback and notchback were tested by varying the upper rear end of a quarter scale model (Figure 3.33) with flow visualisation and wak

Shaun Johnson

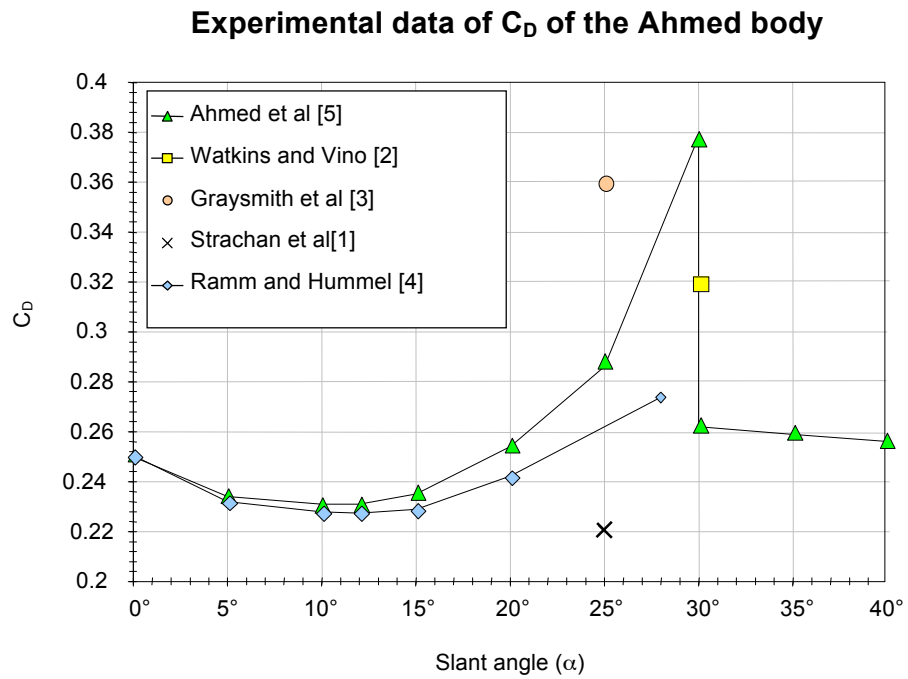


Figure 3.60 Comparison of C_D calculated by different experiments.

Chapter 3 In 1981, Ahmed [8] conducted experiments on wake structures of typical automobile shapes. Vehicle shapes for an estate, fastback and notchback were tested by varying the upper rear end of a quarter scale model (Figure 3.33) with flow visualisation and wak

Shaun Johnson

3.8 The use of CFD for research on automotive vehicles

The conventional method for automotive testing has been the use of wind tunnels and road tests for investigating the vehicle flow structures. Besides the advantage of been able to test full size vehicles and capture all the flow structures that are seen on road vehicles, wind tunnels are expensive to set up and operate, require a large amount of capital and usually have long development cycle times. Experiments are influenced by scaling effects, tunnel boundary layers, blockage effects, interference from flow intrusive probes and model supports which affect the accuracy of the simulations and data collection is limited. Road tests are an accurate simulation of the environment but are difficult to reproduce due to changing environmental effects.

In recent years, the use of computers for Computation Fluid Dynamics (CFD) has been seen as a viable approach to using wind tunnels and road tests. As computing power increases, CFD is becoming an additional tool for the vehicle aerodynamic design. CFD is in essence a digital wind tunnel in which the user has complete control of the environment simulating the flow field around the object of interest. CFD is advantageous since it is cheaper to operate, complete control of the environment is possible and far more information is available about the flow field. Complications associated with wind-tunnel blockage, uncontrolled turbulence levels and tunnel boundary layer are avoided

The main disadvantage of CFD over wind tunnel testing is the accuracy due to numerical errors from finite spatial and temporal resolution and limited accuracy of turbulence models. As computing power increases, modelling of the flow structures will become more accurate as finer grids are possible to resolve smaller scale structures in the flow. CFD is useful for parametric studies of the basic shape during early design development such as the backlight slant angle on a fastback car, while wind tunnel testing is more useful for examining small geometric changes such as detail changes to an A-pillar.

A general overview of different numerical methods available for use are shown in Table 3.20 taken from [10]. In general terms, these can be divided into linear and

Chapter 3 In 1981, Ahmed [8] conducted experiments on wake structures of typical automobile shapes. Vehicle shapes for an estate, fastback and notchback were tested by varying the upper rear end of a quarter scale model (Figure 3.33) with flow visualisation and wak

Shaun Johnson

non-linear methods. These will be examined in the following sections focusing on their application to the Ahmed and similar bodies.

Methods	Linear	Non-linear		
Code designation	Panel Method	Euler Method	RANS-method	LES/DNS-method
Simplifying assumption	Medium incompressible, inviscid and irrotational	Medium inviscid	Hypothetical modeling of turbulence	LES: Small eddies modeled DNS: none DES: Small eddies modeled with RANS BL.
Nature of resulting equation	Linear Laplace equation	Non-linear partial differential equations of first order (Euler Equation)	Non-linear partial differential equations of second order (RANS-equation)	See: RANS-method
Solution Method	Superposition of basic analytic solutions such as source, sink, dipole, vortex flows, Iterative numerical solution of resulting system of linear algebraic equations	Solution of Euler equations together with continuity –(and evtl energy-) equation. Iterative solution of resulting discretized equation with Finite Volume or Finite Element techniques	Solution of RANS-continuity and turbulence model equations with Finite Volume or Finite Element techniques	Solution of NS-and continuity equations. Techniques see Euler- and RANS-method
Grid generation	Only object surface discretisation necessary	Object surface and computational domain discretisation needed	See Euler-methods	See Euler-methods

Table 3.20 CFD methods based on Navier-Stokes equations [10]

3.8.1 Linear Methods

The Panel method and Vortex Lattice method neglect the viscous terms and impose the condition of non-rotational flow when solving the incompressible Navier Stokes equations. For streamlined flow where the flow this attached to the entire body, the potential flow method can provide some insight. However, for ground vehicles where the flow field is typically separated, they cannot be modelled unless the user has prior knowledge of the flow field.

The panel method was employed by Ahmed and Hucho [23] to calculate the velocity field and pressure distribution on a generic model of a Volkswagen Minivan without wheels or under body. As can be seen in Figure 3.61, there was a requirement to create panels for the wake surface, which was calculated from smoke visualisation conducted in a wind tunnel on a quarter-scale model. The pressure distribution in

Chapter 3 In 1981, Ahmed [8] conducted experiments on wake structures of typical automobile shapes. Vehicle shapes for an estate, fastback and notchback were tested by varying the upper rear end of a quarter scale model (Figure 3.33) with flow visualisation and wak

Shaun Johnson

Figure 3.62 of the body vertical centreline has good agreement with experimental data for the majority of the model except near the separated region.

<p>Figure 3.61 Computational grid of a generic mini van. [23]</p>	<p>Figure 3.62 Experimental and computational pressure distribution along vehicle centreline. [23]</p>

Simulations conducted by Ramm and Hummel [4] on a simplified geometry failed to accurately calculate the drag profile as the slant angle was varied. The main difference in the profile of the drag shown in Figure 3.63, was the failure of the panel method to account for the relocation of the separation point as the slant angle was varied. Viscous drag and drag on the model supports was not calculated which probably accounts for the offset of data.

Figure 3.63 Comparison of using the Panel method to predict drag forces on the Ahmed body for various slant angles. [4]

The use of the panel method is not appropriate for use for simulations in automotive applications since it cannot predict separation. For accurate calculations

Chapter 3 In 1981, Ahmed [8] conducted experiments on wake structures of typical automobile shapes. Vehicle shapes for an estate, fastback and notchback were tested by varying the upper rear end of a quarter scale model (Figure 3.33) with flow visualisation and wak

Shaun Johnson

of the wake structure, this method requires experimental data to create the grid for separated flows limiting its application for automotive vehicles. However, the panel method has been successfully used for calculating surface deformation due to wind loading on forebody components of vehicles[24] where the flow is attached.

3.8.2 Non Linear Methods

All other methods specified in Table 3.20 require spatial discretisation of the flow domain. The finite volume method is the most commonly used approach for spatial discretisation since it allows for arbitrary shaped cells to model the body geometry. However, regular shaped volumes such as hexagonal and tetrahedral are the most used commonly used for meshing volumes.

Using Direct Numerical Simulation (DNS), in theory it should be possible simulate the entire flow field around an automotive vehicle at high Re. However, to achieve accurate simulations, the grid must be small enough and time-step sufficiently small to resolve all scale structures in the flow field. However, the computational requirements for these simulations exceed the current computing power available with the exception of low Reynolds numbers simulations on simple problems. As sufficient and economical computing power become accessible, DNS will become a viable option for modelling the flow field around the car including engine cooling and under body flows.

In order to simulate the flow fields at high Reynolds numbers using current computing power, different methods such as the use of Reynolds Averaged Navier Stokes (RANS) equations, Large Eddy Simulation (LES) and Detached Eddy Simulations (DES) are utilised. In these models, the smaller scale structures and the mixing action of sub-grid eddies is modelled empirically and included through the Reynolds stress terms. In the following sections, the various methods for the simulation of simplified automotive geometries will be discussed in chronological order.

One of the first numerical simulations for the Ahmed body was conducted by Han [25] using RANS finite volume code using a k- ϵ turbulence model. A relatively

Chapter 3 In 1981, Ahmed [8] conducted experiments on wake structures of typical automobile shapes. Vehicle shapes for an estate, fastback and notchback were tested by varying the upper rear end of a quarter scale model (Figure 3.33) with flow visualisation and wak

Shaun Johnson

coarse square grid of 1.53×10^5 points was employed to model the flow field at $Re = 4.3 \times 10^6$ for $\alpha = 0^\circ$ up to 30° . The over prediction in the drag profile shown in Figure 3.64 was accounted for by the lower than expected base drag. The large drag increase at $\alpha = 30^\circ$ was captured in the simulations. However, simulations were not pursued beyond $\alpha = 30^\circ$ since Han claimed that the phenomenon of vortex breakdown was not captured in the computations.

Figure 3.64 Comparison of C_D by Han with Experimental data from Ahmed. Variation in drag compares well for all α except $\alpha > 20^\circ$. [25]

Another early study was conducted by Hashiguchi [26] to employ a DNS simulation using 1×10^6 points on a square mesh. The drag profile shown in Figure 3.65 compared remarkably well with experimental data. Even though the overall drag was unpredicted (viscous forces not computed), the change in drag on slant surface followed the experimental data indicating the C-pillar structures were modelled in the simulations. Hashiguchi believed that the two quasi steady regions in the drag history were the high and low drag regimes observed at $\alpha = 30^\circ$ (Figure 3.66). This could indicate that near the critical slant angle, numerical simulations might tend to converge to the more stable low drag wake where there is less energy in the wake.

Chapter 3 In 1981, Ahmed [8] conducted experiments on wake structures of typical automobile shapes. Vehicle shapes for an estate, fastback and notchback were tested by varying the upper rear end of a quarter scale model (Figure 3.33) with flow visualisation and wak

Shaun Johnson

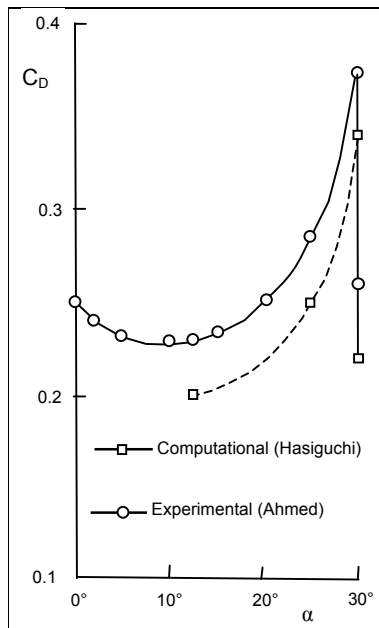


Figure 3.65. Comparison of experimental data with numerical simulations by Han. [25]

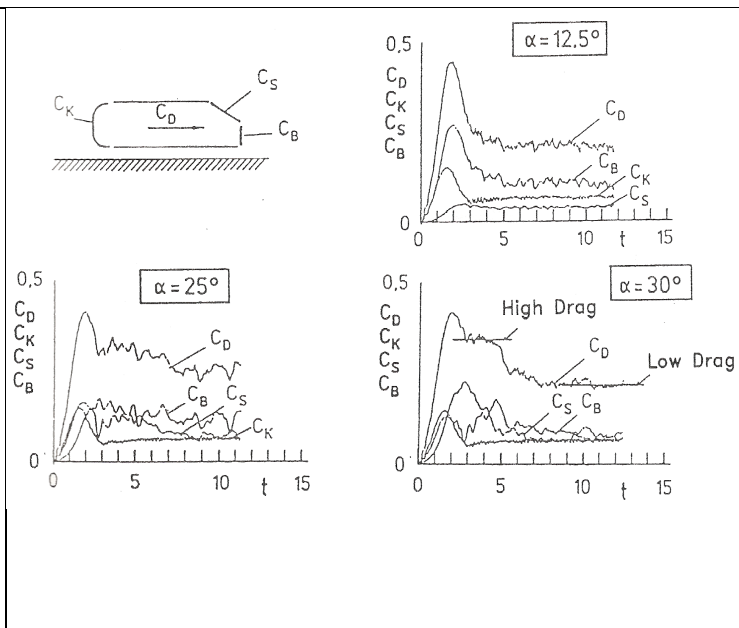


Figure 3.66. Time history from simulations for different slant angles. For $\alpha=30^\circ$, a region of high and low drag is present. [25]

A report by Makowski [27] investigated the suitability of using the commercial software *Fluent* for external aerodynamic simulations for automotive applications. For the case study, the Ahmed body at $\alpha=30^\circ$ was chosen because the high drag wake structures have represented a challenge for numerical simulation. A hybrid tetrahedral mesh was employed consisting of 190,000 tetrahedral and prism cells before refinement. Uniform triangular surface elements were used on the body surface which were extruded to create a triangular prism layer (16 layers) on the body surface to model the boundary layer. The simulation was set up to mimic experiments by Ahmed et al. [5] conducted at $Re=4.29 \times 10^6$. Simulation employed second-order accurate convective differences and the standard $k-\epsilon$ turbulence model. During the simulation, the mesh was refined using pressure gradients as the refinement criteria. Grid refinement was conducted until drag forces from the body were constant. The final refined grid had 475,000 cells.

Chapter 3 In 1981, Ahmed [8] conducted experiments on wake structures of typical automobile shapes. Vehicle shapes for an estate, fastback and notchback were tested by varying the upper rear end of a quarter scale model (Figure 3.33) with flow visualisation and wak

Shaun Johnson

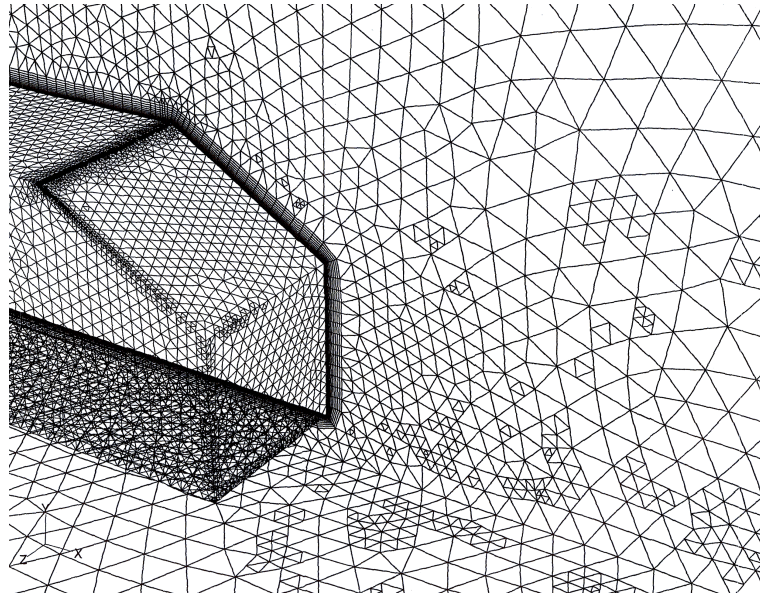


Figure 3.67 Rear region of hybrid grid after grid refinement. [27]

Flow structures on the rear of the vehicle shown in Figure 3.68 had the same features as those shown schematically by Ahmed (Figure 3.38). The pathlines indicate the presence of a strong vortex along the outboard lateral edge and partial separation above the slant surface. Contours of total pressure coefficient on the vertical plane coincident to the rear vertical surface were in agreement with experimental data. The overall drag for the Ahmed body a $\alpha=30^\circ$ compared well with experimental data. The experimental calculated value of $C_D=0.378$ correlated well with the calculated value of $C_D=0.378$. However, the density used for the calculation was 1.1767kg/ms as opposed to 1.225kg/ms , which *Fluent* uses as the default value for air. As can be seen in Table 3.19, the over-predicted fore body was compensated by the unpredicted forces on the rear of the vehicle. This discrepancy is due to an over prediction of the pressure coefficient since the isotropic $k-\epsilon$ turbulence model over-predicts the effective viscosity where turbulence is anisotropic [28]. However the use of the Reynolds Stress Model (RSM) on the same geometry by Makowski in 2000 [28] still followed the trend of over-prediction of the forebody and under-prediction of the rear body. As was seen by Han [25], drag forces using the $k-\epsilon$ model correlated well for $\alpha=30^\circ$ but not for other angles. It raises the question of how simulations for other slant angles using *Fluent* compare with experimental data.

Chapter 3 In 1981, Ahmed [8] conducted experiments on wake structures of typical automobile shapes. Vehicle shapes for an estate, fastback and notchback were tested by varying the upper rear end of a quarter scale model (Figure 3.33) with flow visualisation and wak

Shaun Johnson

Whether it is coincidence that $\alpha=30^\circ$ was used as a test case for assessment is unknown.

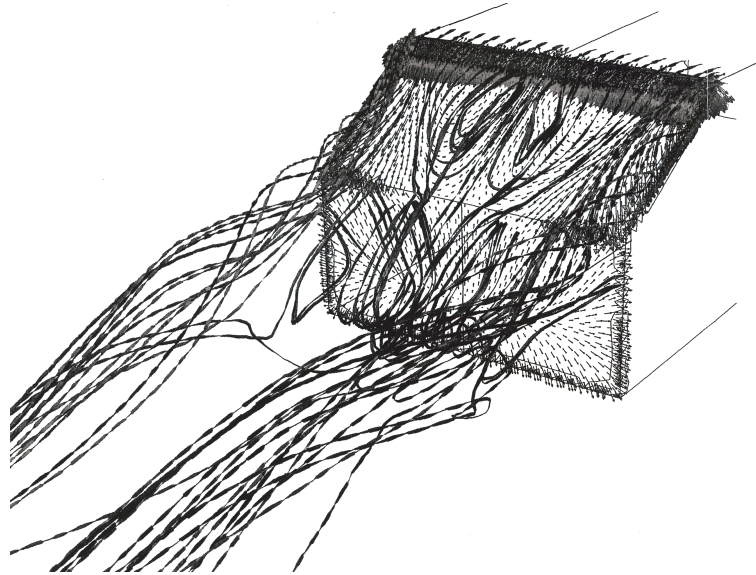


Figure 3.68 Pathlines released from slant surface for $\alpha=30^\circ$ confirming presence of c-pillar vortices and partial separation. [27]

Surface	Experiment [5]	Simulation ke[27]	Simulation RSM[28]
Forebody	0.016	0.036	0.037
Slant Surface	0.213	0.200	0.193
Vertical Base	0.092	0.098	0.083
Other	0.057	0.048	0.048
Total	0.378	0.382	0.361

Table 3.21 Breakdown of forces on different surfaces of Ahmed body. Refer to Figure 3.37 for surface location. [27]

Gilliéron [15] also conducted computational studies on the Ahmed reference body using *Fluent*. The aerodynamic drag coefficient and wake structures behind the body were compared with the experimental results for different slant angles. The simulations were conducted using Fluent 4.2 implementing a k- ϵ turbulence model. The grid consisted of prisms near the surface of the model ($y^+ \approx 30$) to capture the boundary layer with tetrahedral meshing applied to the remaining volume.

The computed drag coefficients in Figure 3.69 were higher than the experimental values. However, the computed results did indicate the same trends in drag as the slant angle was modified. For a slant angle of 30° , the C_D compared extremely well. It was postulated by Gilliéron that the difference in results was due to the over

Chapter 3 In 1981, Ahmed [8] conducted experiments on wake structures of typical automobile shapes. Vehicle shapes for an estate, fastback and notchback were tested by varying the upper rear end of a quarter scale model (Figure 3.33) with flow visualisation and wak

Shaun Johnson

estimation of the pressure drop at the base and that it might have been due to an insufficient simulation of the boundary layer.

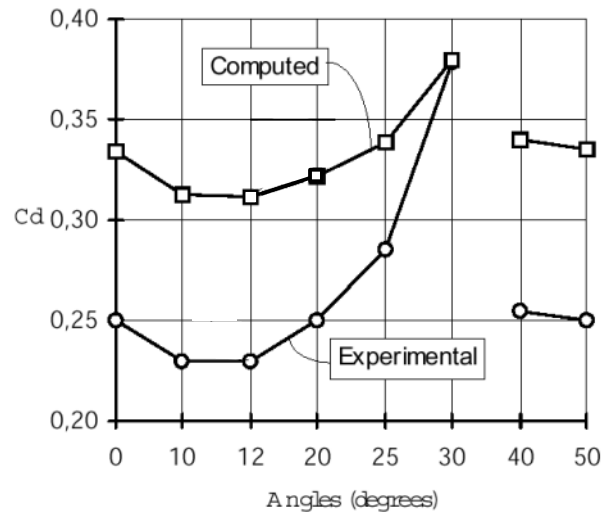


Figure 3.69 Comparison of coefficient of Drag vs. slant angle for experimental and computational results for the Ahmed reference body. [15]

The flow structures and pressure distributions from the simulations were of more interest, since it was critical to simulate the same wake structures as observed by Ahmed. The wake structures were divided up into three regions. For a slant angle less than 12° , the flows were classed as a two-dimensional base flow. Between 12° and 30° was the region where three-dimensional hatchback flow occurred and over 30° , flow reverted to a two dimensional base flow.

Chapter 3 In 1981, Ahmed [8] conducted experiments on wake structures of typical automobile shapes. Vehicle shapes for an estate, fastback and notchback were tested by varying the upper rear end of a quarter scale model (Figure 3.33) with flow visualisation and wak

Shaun Johnson

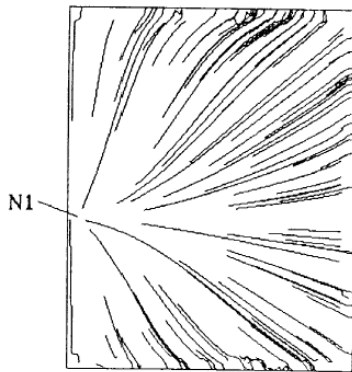


Figure 3.70 Friction lines on the vertical base and slant surface for $\alpha = 10^\circ$. Only half and experimental pressure coefficients (right) for the body is represented. [15]

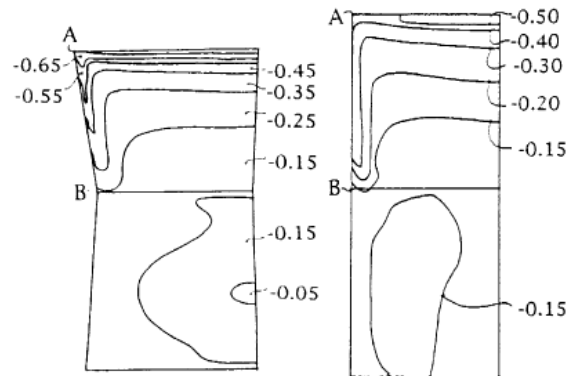


Figure 3.71 Computed pressure coefficients (left) and experimental pressure coefficients (right) for $\alpha = 12^\circ$. Note the streamwise vortex generated from point A is visible. [15]

For slant angles less than 12 degrees, the same two-dimensional base flow structures were observed as shown in Figure 3.70. The pressure coefficient distributions shown in Figure 3.71 compared well with the experimental results. However as mentioned above, it is slightly overestimated indicating a strong stream wise vortex.

The three-dimensional hatchback flow region showed considerable differences to those reported by Ahmed. As shown in Figure 3.72, there appeared to be a stream wise vortex emanating from the centre of the slant surface, which is not mentioned by Ahmed. The generation of a second streamwise vortex besides the vortex starting from Point A was also indicated in the streak line patterns in Figure 3.73. A similar streak line pattern was present in Ahmed's results (Figure 3.38), which was interpreted as a spanwise vortex.

Chapter 3 In 1981, Ahmed [8] conducted experiments on wake structures of typical automobile shapes. Vehicle shapes for an estate, fastback and notchback were tested by varying the upper rear end of a quarter scale model (Figure 3.33) with flow visualisation and wak

Shaun Johnson

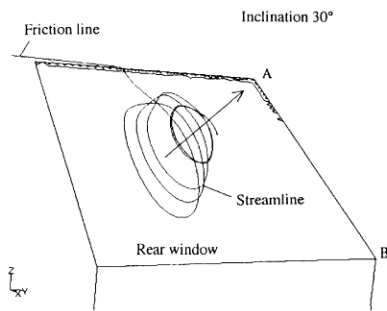


Figure 3.72 Path lines on rear window for slant angle=30°. Only half body is represented. [15]

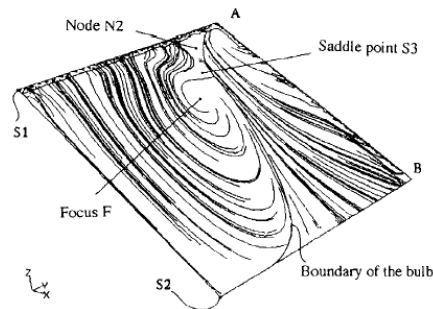


Figure 3.73 Streak lines on the slant surface at slant angle=30°. Only half body represented. [15]

Above 30°, the flow structures were the same as reported by Ahmed with total separation from the slant surface and rear edge. Again, the structures were similar to the two-dimensional base flow discussed above with no strong vortices observed downstream. In Figure 3.74, the streak lines on the rear of the Ahmed body show full separation.

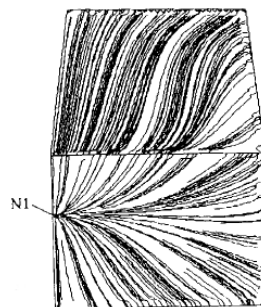


Figure 3.74 Streak lines for slant angle=40°. [15]

For the 10th joint ERCOFTAC Workshop on Refined Turbulence Modelling, the Ahmed body was used as one of the test cases for evaluating different turbulence models. Experimental data by Lienhart et al. [14] was provided for verification and comparison with various turbulence models. A number of papers were presented [29-34].

Guilmineau [30] conducted simulations for $\alpha=25^\circ$ on a three dimensional unstructured mesh at $Re=4.784 \times 10^6$. Results were obtained with steady RANS equations using the $k\omega$ -SST turbulence model. The drag coefficient obtained using this method was slightly over predicted (0.295 as compared with 0.285) as the vortex structures at the rear of the body were more intense. These initial simulations were

extended [20] using a finer mesh and comparing the $k\omega$ -SST and $R_{ij}\text{-}\omega$ turbulence model. As can be seen in Figure 3.75, the separation bubble on the slant surface for $\alpha=25^\circ$ are over predicted using both turbulence models. However, the intensity of vortex produced and wake structures, suggest that the wake is similar to that of the low drag regime after full separation has occurred.

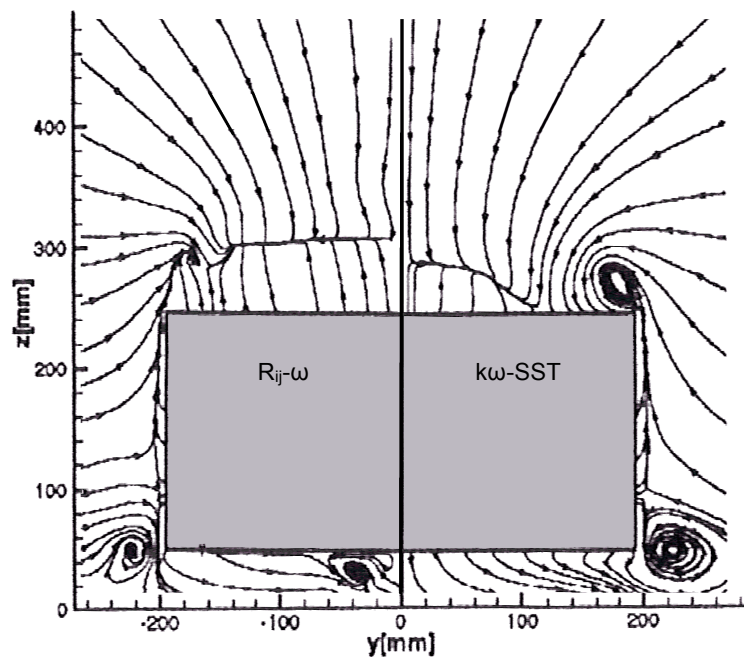


Figure 3.75. Streamlines on a surface coincident with rear surface of vehicle. Both the $k\omega$ -SST and $R_{ij}\text{-}\omega$ turbulence model show separation on the slant surface. Experimental data indicates that the separation bubble has reattached to the slant surface. [20]

Simulations using *Fluent* by Braun et. al. [31] were also conducted on a hybrid mesh (2.3×10^6 cells) model using a symmetry boundary condition on the vehicle centreline for $\alpha=25^\circ$. Results from the $k\epsilon$ -Realizable and $k\omega$ -SST turbulence model are shown in Figure 3.76. A small separation bubble occurs when using the $k\omega$ -SST turbulence while the $k\epsilon$ -realizable model remains attached on the slant surface. Overall drag ($k\epsilon$ -realizable=0.2894, $k\omega$ -SST=0.2891) for the entire body is in agreement with experimental data. However, the fore body and viscous forces are over predicted.

Chapter 3 In 1981, Ahmed [8] conducted experiments on wake structures of typical automobile shapes. Vehicle shapes for an estate, fastback and notchback were tested by varying the upper rear end of a quarter scale model (Figure 3.33) with flow visualisation and wak

Shaun Johnson

$k\epsilon$ Realisable

$k\omega$ SST

Figure 3.76 Simulated streak lines on the slant surface for $\alpha=25^\circ$ using two different turbulence models. [31]

Detached Eddy Simulations (DES) were performed by Kapadia [35] using DES and unsteady RANS ($k\epsilon$) for $\alpha=25^\circ$ using the commercial program *Cobalt*. Unsteady simulations were undertaken on an unstructured grid of 1.7×10^6 cells at $Re=2.78 \times 10^6$. Simulations required approximately 8 hours on a cluster of 256 parallel CPUs. Flow visualisations of the zero streamwise velocity isosurface shown in Figure 3.77, indicated that the DNS simulations predicted a small separation bubble on the slant surface while the RANS simulations failed to capture this flow structure. The average C_D using DES was $C_D=0.2585$ and $C_D=0.3272$ for RANS ($k\epsilon$) (exp. $C_D=2.85$). However the average C_D for DES included the transient effects at the beginning of the simulation. The time history of the C_D indicated the average C_D was more likely to be $C_D \geq 0.3$. These results appear to be in contradiction with other simulations by Kapadia [36] using *Cobalt* with a denser mesh (4.6×10^6 cells). The separation bubble on the slant surface for $\alpha=25^\circ$ did not reattach while a small separation bubble was present on the slant surface using an unsteady RANS ($k\epsilon$) simulation on the denser mesh. For the DES simulation, the average $C_D=0.283$ and $C_D=0.338$ using RANS.

Chapter 3 In 1981, Ahmed [8] conducted experiments on wake structures of typical automobile shapes. Vehicle shapes for an estate, fastback and notchback were tested by varying the upper rear end of a quarter scale model (Figure 3.33) with flow visualisation and wak

Shaun Johnson

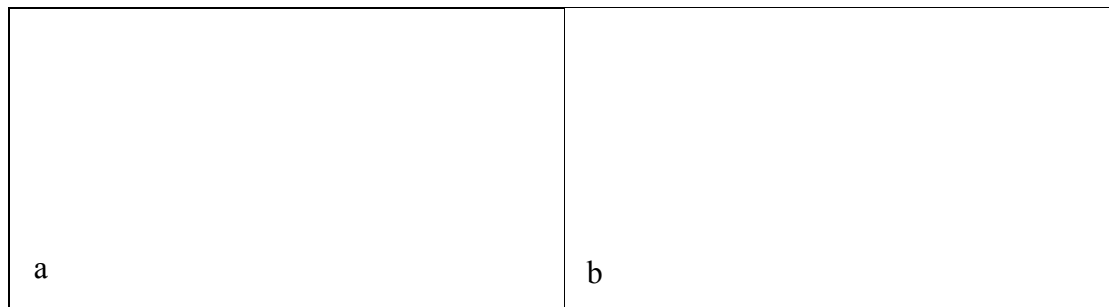


Figure 3.77 Flow visualisations of reversed flow on the rear portion of the Ahmed body for $\alpha=25^\circ$ for DES (a) and RANS ($k\epsilon$) (b). [35]



Figure 3.78 Comparison of experimental velocity field to computational velocity field using DES at $\alpha=25^\circ$. [35]

Kranjnović and Davidson [37] used Large Eddy Simulation (LES) to simulate the flow around the Ahmed body at $\alpha=25^\circ$. The Reynolds number was reduced to 7.25×10^5 ($U_\infty=10\text{m/s}$) to determine if the flow around vehicles becomes independent of Reynolds Number since most separation points are fixed. Simulations were conducted on a square mesh consisting of 9.6×10^6 cells using a time step of 1×10^{-4} (110×10^3 iterations). As was seen by Drouin et al. [19], the instantaneous flow structures in Figure 3.79 show that the separation bubble on the slant surface is quite unstable with small hairpin vortices forming. The C-pillar vortices on the side of the slant surfaces force the small vortices towards the vehicle centreline. Time averaged streamlines in Figure 3.80 indicate that the flow separates and reattaches on the front of the body. The time averaged streamlines in Figure 3.80 show the separation bubble reattaching to the slant surface and are similar to oil film visualisations at higher Re.

Chapter 3 In 1981, Ahmed [8] conducted experiments on wake structures of typical automobile shapes. Vehicle shapes for an estate, fastback and notchback were tested by varying the upper rear end of a quarter scale model (Figure 3.33) with flow visualisation and wak

Shaun Johnson

These results indicate the external vehicle flow at high Re is insensitive to the Reynolds Number

Figure 3.79 instantaneous isosurface of second invariant of the velocity gradient.

Figure 3.80 Time averaged streamlines on surface of body

As can be seen, the Ahmed body has been studied quite extensively to examine different numerical methods for predicting the flow structures and body forces on simplified automotive geometries. It appears that more complex methods such as LES [37] and DES [35] seem to produce results that capture the flow fields accurately but require massive computational resources and run at lower Re. For most cases, a sufficient understanding of the flow field can be achieved using time-averaged solutions using time averaged RANS. Shown in Figure 3.81 is a comparison of all C_D data from numerical simulations. Most models over predict the drag coefficient but capture the different flow structures as α is varied.

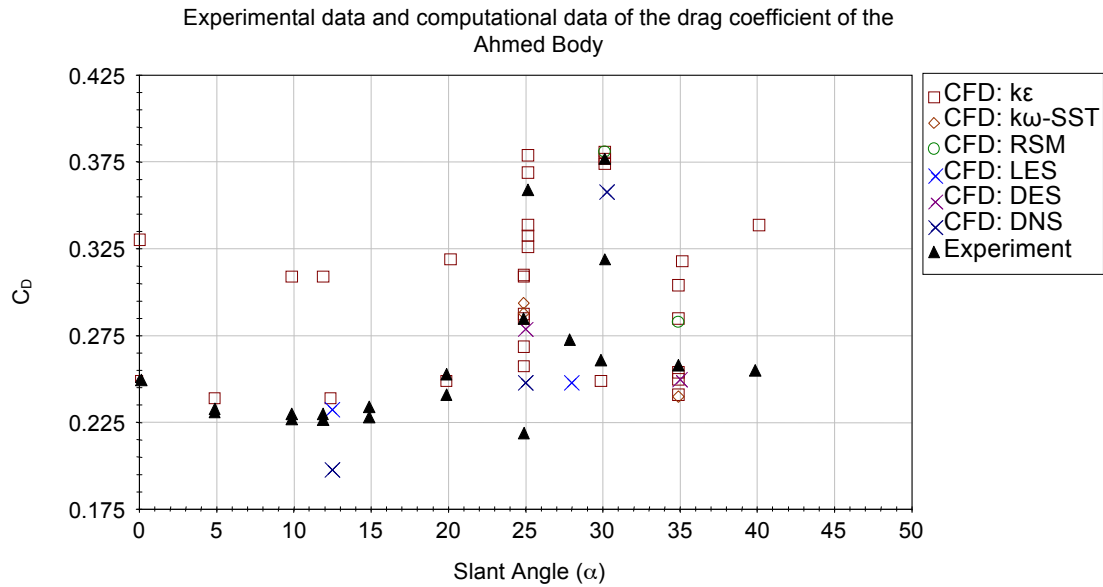


Figure 3.81 Comparison of all experimental and numerical C_D for the Ahmed body

3.9 Vortex Breakdown

3.9.1 Introduction

Flows containing vortical structures exist in natural flows such as hurricanes and tornadoes as well many engineering situations. Their presence in engineering applications such as aircraft aerodynamics, structures and the process industry has led to extensive research into the formation and breakdown of vortices, the control of these vortices to suit an application and the effect vortices have on structures subjected to vortex induced vibration.

One particular phenomenon that occurs in vortices is the abrupt enlargement of the vortex core with limited flow reversal near the vortex centreline. This is known as vortex breakdown and was first observed by Peckham and Atkinson [38] on the breakdown of tip vortices on a delta wing similar to water tunnel visualisations in Figure 3.82. This has been followed by numerous other research [39-44] on vortex breakdown in internal flows such as enclosed cylinders with rotating end walls for mixing [45] and in aircraft wake breakdowns where vortices represent a hazard to smaller aircraft[46]. Although much research has been devoted to vortex breakdown on aircraft wings and delta wings, to the author's current knowledge, this has not been extended to bluff bodies in ground effect such as automobiles. In this section,

Chapter 3 In 1981, Ahmed [8] conducted experiments on wake structures of typical automobile shapes. Vehicle shapes for an estate, fastback and notchback were tested by varying the upper rear end of a quarter scale model (Figure 3.33) with flow visualisation and wak

Shaun Johnson

research on external flows over delta wings to provide a basic understanding of vortex breakdown is presented.

Figure 3.82 Vortex breakdown over a slender delta wing visualized in a water tunnel using dye released from near the apex [43]

When separation occurs from three-dimensional bodies, the vorticity previously confined in a thin boundary layer separates from the body surface to form a vortex sheet. This shear layer rolls up to form vortical structures, which forms a nearly axisymmetric spiral structure. A streamwise vortex is generally characterised by a velocity along the vortex axis (axial component, V_x) generally in the free stream direction, and a swirling component on the plane normal to the vortex axis (swirl component, V_θ). The radial velocity away from the vortex centre (radial component, V_r) is generally small. For a delta wing, the strength of the primary streamwise vortex steadily increases until a sudden disorganisation of the vortex structure occurs. The vortex breakdown is characterised by a rapid dilation of the vortical structure, a profound alteration of the velocity field and occurrence of large fluctuations [42].

The physical mechanism that causes vortex breakdown is still in dispute due to the complex nature of the flow. Theories that have been proposed include an axis symmetric analogy of a two dimensional hydraulic jump [47], the quasi-cylindrical approximation analogous to two dimensional boundary separation [44] and hydrodynamic instability from stability theory [48]. These theories are supported to

Chapter 3 In 1981, Ahmed [8] conducted experiments on wake structures of typical automobile shapes. Vehicle shapes for an estate, fastback and notchback were tested by varying the upper rear end of a quarter scale model (Figure 3.33) with flow visualisation and wak

Shaun Johnson

some extent by experiments and simulations but thus far, no universal theory has been found to explain and tie together all the experiments and simulations.

By varying V_x and V_θ independently in slightly diverging cylindrical tube, Sarpkaya [49, 50] observed three types of breakdown of the vortex described as axisymmetric (Figure 3.83a), spiral (b) and double helix breakdown (c). This was expanded further by Falar and Leibovich [51] who found seven distinct structure types using a liquid dye tracer.

a. bubble vortex breakdown

b. spiral vortex breakdown

c. Double helix breakdown

Figure 3.83 Types of vortex breakdown observed by Falar and Leibovich [51] by varying V_x using the volume flow rate and V_θ with the vane angle.

For bubble type vortex breakdown (Figure 3.83a), a stagnation point exists on the vortex axis was visible by and abrupt expansion of the centreline dye filament creating a bubble of recirculating fluid. The axial location of the bubble was observed to be quasi-steady in location by Leibovich. Often, other types of vortex breakdown are observed such a spiral type breakdown in the wake deficit region.

The spiral type vortex breakdown (Figure 3.83b) described by Lucca-Nergo and O'Doherty [44] is characterised by a rapid deceleration of the dye filament marking

Chapter 3 In 1981, Ahmed [8] conducted experiments on wake structures of typical automobile shapes. Vehicle shapes for an estate, fastback and notchback were tested by varying the upper rear end of a quarter scale model (Figure 3.33) with flow visualisation and wak

Shaun Johnson

the swirl axis, which causes stagnation, and by an abrupt kink, followed by a corkscrew-shaped twisting of the dye.

3.9.2 Delta Wings

Both types of breakdown have been observed on simple flat delta wings with sharp leading edges have been used extensively for investigations on vortex breakdown [52]. Poission-Quinton and Erlich [53] were the first to conduct systematic investigations to determine the breakdown location as a function of sweep back angle (φ) and angle of attack (AOA) as indicated in Figure 3.84. Further experiments were subsequently carried out by numerous other researchers [42, 54-56]. The location of vortex breakdown between different experiments were varied but the overall trend in vortex breakdown location as the AOA was varied was similar. Findings from the parametric tests were summarized by Delery [42] below.

- For increasing AOA, breakdown occurs immediately downstream of the trailing edge where it is induced by compression of the flow coming from the suction side.
- For a limiting value of AOA, breakdown occurs over the wing with increasing AOA causing displacement of the breakdown location towards the delta wing leading point.
- For sharp leading edges, vortex breakdown is weakly influenced by the Reynolds number due to fixed separation points.
- For $\varphi < 75^\circ$, breakdown is dependent on AOA and φ . For $\varphi > 75^\circ$, breakdown is only dependent on AOA.

3.9.3 Transition from attached flow to separated flow on delta wings

The types of flow structures seen on Delta wing were examined by Su et al.[54] by characterising the flow topologies as the leading-edge sweep angle (φ) and angle of attack (AOA) were varied (Figure 3.84a) by observing the surface streakline patterns on the wing (Figure 3.85).

Chapter 3 In 1981, Ahmed [8] conducted experiments on wake structures of typical automobile shapes. Vehicle shapes for an estate, fastback and notchback were tested by varying the upper rear end of a quarter scale model (Figure 3.33) with flow visualisation and wak

Shaun Johnson

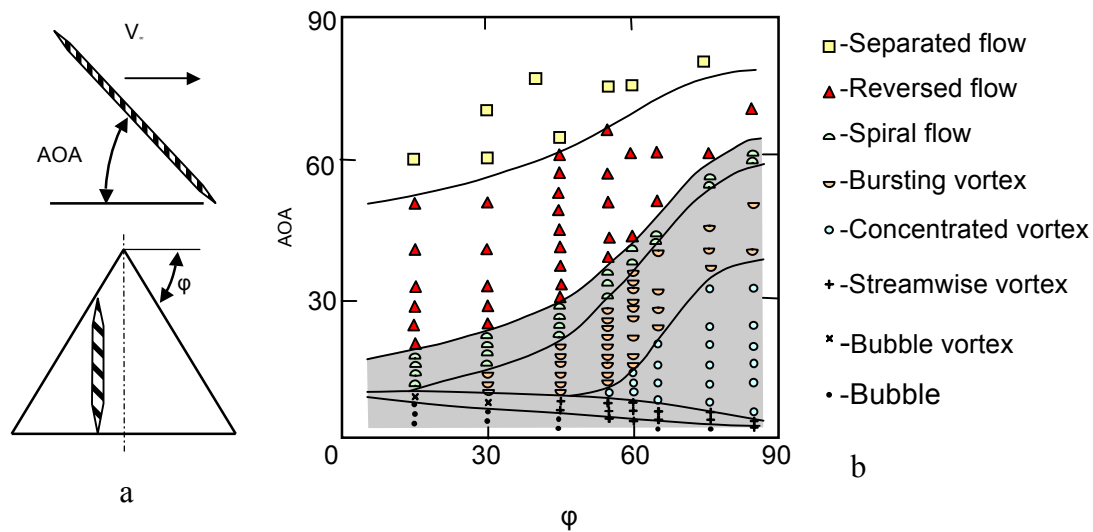


Figure 3.84 a) Geometry definition for delta wings. b) Parameter space map of Δ Vs AOA for delta wings.

The wake structures changed from a streamwise vortex, to a bursting vortex and then to spiral flow (Figure 3.85a) and eventually to separated flow (Figure 3.85 b&c) as $AOA=0 \rightarrow 90^\circ$ for a given ϕ . The transition from spiral flow to reversed flow occurs at lower AOA occurs lower ϕ . The location of vortex breakdown at a set AOA fluctuates with quasi-periodic oscillations between the two primary vortices emanating from the leading edges of the delta wing [57].

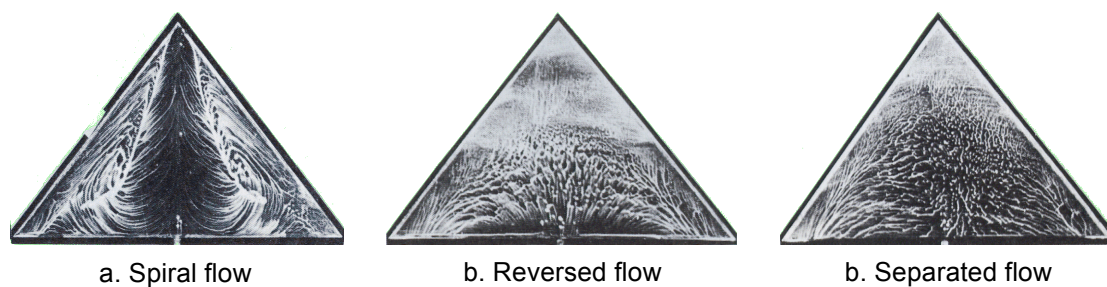


Figure 3.85 Surface streak line patterns on the top surface of the Delta wing by Su et al.[54] showing the change in wake structure from attached spiral flow (a) to separated flow (c).

Flow visualisations by Gordnier and Visbal [58] from numerical simulations for various AOA show the progression from vortex breakdown to separated flow over the delta wing. The location of the vortex breakdown occurs closer to the front of the delta wing as AOA increases from $AOA=15^\circ$ to $AOA=35^\circ$ before full separation occurs.

Chapter 3 In 1981, Ahmed [8] conducted experiments on wake structures of typical automobile shapes. Vehicle shapes for an estate, fastback and notchback were tested by varying the upper rear end of a quarter scale model (Figure 3.33) with flow visualisation and wak

Shaun Johnson

a. b. c.

Figure 3.86 Flow visualisations using iso-surface of total pressure over a delta wing ($\phi=60^\circ$) for AOA= 5° (a), 15° (b) and 40° (c) showing the progression from attached flow to vortex breakdown to separated flow.

3.9.4 Criteria for vortex Breakdown

Besides the physical mechanism, the parameter space studies enabled the researchers to determine the criteria for vortex breakdown which occur in the flow field so that particular conditions can be avoided or promoted depending on the application. Vortex breakdown is relatively independent of Reynolds number. However, the turbulence has a strong effect on the vortex breakdown position[59]. The critical parameters are usually based on the V_x and V_θ at a point in the flow. This makes the criteria ambiguous since breakdown depends on several factors such as the axial and azimuthal velocity distribution and the pressure gradients [42]. A number of parameters have been proposed to simplify the characterisation of the vortex and the criteria for vortex breakdown.

3.9.4.1 Helix angle

Hall [60] used the of definition of the helix angle (γ) defined in Eqn 3.41, as the criterion to determine if vortex breakdown occurs in highly swirling flows. It was found that if the maximum value of γ upstream of breakdown is greater than a critical value, then breakdown of the vortex is likely to occur. Hall found if the maximum value of γ upstream of breakdown did not exceed 40° , then breakdown would not occur.

$$\gamma = \tan^{-1} \left[\frac{V_\theta}{V_x} \right] \quad \text{Eqn 3.41}$$

A compilation of the measured radial distributions of the helix angle upstream of breakdown in a duct is shown in Figure 3.87 from different experiments. For

Chapter 3 In 1981, Ahmed [8] conducted experiments on wake structures of typical automobile shapes. Vehicle shapes for an estate, fastback and notchback were tested by varying the upper rear end of a quarter scale model (Figure 3.33) with flow visualisation and wak

Shaun Johnson

different types of breakdown, γ varies from $\gamma=38^\circ$ up to $\gamma=50^\circ$ making it difficult to define a set criteria of γ for vortex breakdown. Results from Kirkpatrick shows the effect of turbulence on the γ distribution upstream of the breakdown.

Figure 3.87 Measured radial distributions of helix angle upstream of breakdown for different types of breakdown [60]

3.9.4.2 Swirl Parameter

The relative importance of the V_x compared V_θ of the vortex is characterised by the swirl parameter (S) is more often as a criterion for vortex breakdown. Delery [42] defines the swirl parameter as:

$$S = \frac{\Gamma_0}{r_c V_{x(ext)}} \quad \text{Eqn 3.42}$$

where r_c is the radius of the vortex where maximum swirl velocity occurs and Γ_0 is the circulation at the outer limits of the vortex calculated using

$$\Gamma = 2\pi r V_\theta \quad \text{Eqn 3.43}$$

The swirl parameter is the inverse of the Rossby number (Ro) proposed by Spall [46]. They are both non-dimensional parameters which are a measure of a relative importance of inertial and Coriolis forces of fluid motion [44].

Breakdown is said to occur when the axial velocity is large compared with the swirl velocity. If S is modified by taking the axial velocity at the vortex core into account and taking the swirl velocity at r_c , it can be simplified to:

Chapter 3 In 1981, Ahmed [8] conducted experiments on wake structures of typical automobile shapes. Vehicle shapes for an estate, fastback and notchback were tested by varying the upper rear end of a quarter scale model (Figure 3.33) with flow visualisation and wak

$$S = \frac{V_{\theta(r_c)}}{V_{x(\text{axis})}} \quad \text{Eqn 3.44}$$

The critical criterion for breakdown, S^* was found to be $S^* \approx 1.37$. However, Bossel [61] found S^* to be as low as $S^* \approx 1.12$.

Another proposed criterion by Brown and Lopez [62] compared the relationship between the velocity vector and vorticity vectors on stream surfaces. It was found that a helix angle for the velocity that exceeds that of vorticity on some stream surfaces seems therefore to be a necessary condition for vortex breakdown to occur.

Chapter 4 Effect of Slant Angle

4.1 Introduction

As with previous numerical simulations and experiments, the effect of the slant angle on the flow structures was investigated. Simulations were conducted at $Re=2.86 \times 10^6$ with α varied between 1° and 50° . In this section, the flow structures in the wake region of an Ahmed body are examined to analyse how these structures change with α . These numerical simulations are compared with experimental data from Lienhart et al. [13, 14]. The contributions to the total body forces are examined for the different regions of the body, such as the slant surface and rear surface.

4.2 Body forces

Forces on the surfaces were examined as α is varied. The body was divided into four regions labelled front, side, rear and slant as indicated in Figure 3.3. Pressure and viscous forces have been combined together for this analysis.

4.2.1 Total body drag and lift forces

Figure 4.1 shows the (coefficient of drag) C_D and (coefficient of lift) C_L forces as a function of slant angle for the entire body. As α increases to 10° , C_D decreases to a minimum, where as experiments by Ahmed et al. [5] found the minimum C_D at $\alpha=12^\circ$. The linear increase in C_L for $\alpha \leq 12^\circ$ indicates that the flow has not separated from the slant surface. For $\alpha > 12^\circ$, C_D increases until $\alpha=30^\circ$. However, for $\alpha > 20^\circ$, the gradient of the C_D profile increases while the gradient of the C_L profile decreases. At $\alpha=30^\circ$, C_D and C_L reach a maximum and there is a discontinuity in the drag and lift profile caused by a sudden decrease in drag as α increases to $\alpha=31^\circ$. The slant angle at which the highest drag occurs before the rapid decrease in drag is labelled the *critical slant angle* (α_c). The decrease found in the simulations of $\Delta C_D=0.075$ is not as large as the drop of $\Delta C_D=0.118$ found in experiments. For $\alpha > \alpha_c$, the C_D and C_L slowly decrease as α increases. It is expected that C_D and C_L would decrease until they matched the forces at $\alpha=0^\circ$ since $\alpha=0^\circ=90^\circ$.

In comparison with experimental work by Ahmed et al. [5], C_D is over predicted for all slant angles. The C_D is typically over predicted by 10-15% over the range examined. A better agreement with the experimental measurements of C_D found as

$\alpha \rightarrow 30^\circ$. This result similar to the numerical simulations by Gilliéron and Chometon [15], where the C_D at $\alpha=30^\circ$, compared well with experiments. However, this was due to an under prediction of the C_D on the front and side surfaces compensating for the over prediction on the rear and slant surface.

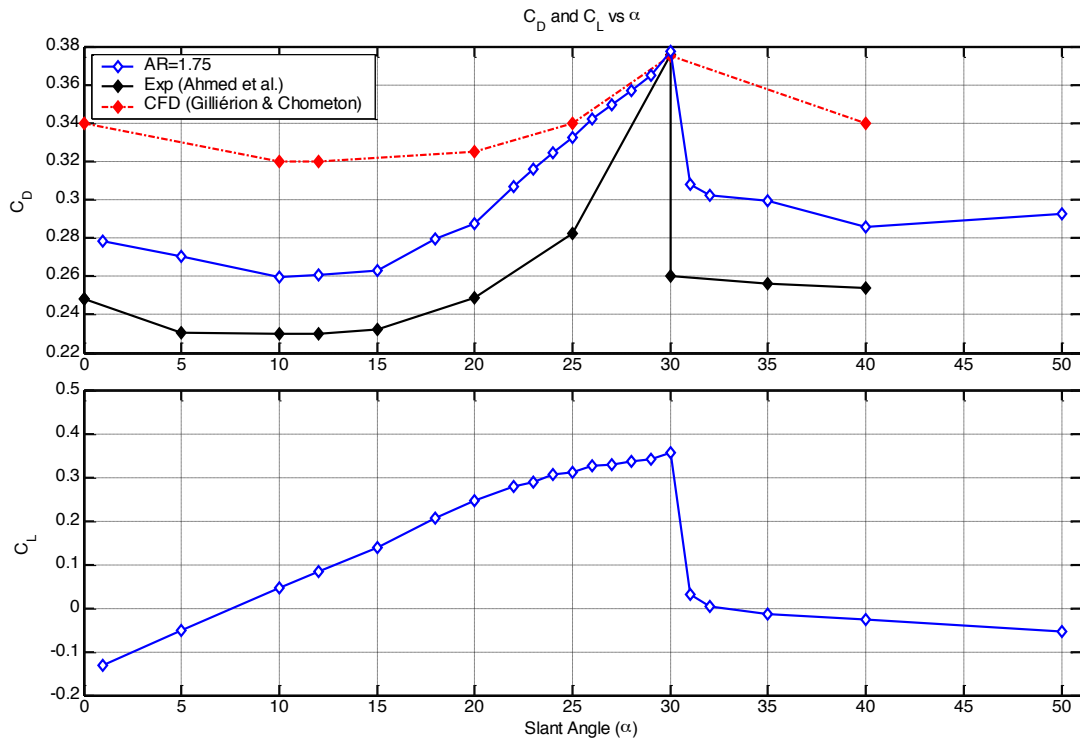


Figure 4.1 The total C_D and C_L for Ahmed body. Results are compared with experimental data [5] and numerical simulations [15]. Current simulations over predict the C_D but follow similar trends as α is varied.

4.2.2 Lift to Drag Ratio

Three distinct regions in the Lift/Drag ratio (LD) were observed as α increases (Figure 4.2). There is a linear increase in LD as α is increased to $\alpha \leq 15^\circ$. Above $\alpha > 15^\circ$, the LD ratio plateaus at $\alpha = 22^\circ$ and is virtually constant until $\alpha = \alpha_c$ after which, a rapid transition to a lower LD ratio occurs. After $\alpha = 30^\circ$, the LD ratio decreases as α increases at least until $\alpha = 50^\circ$.

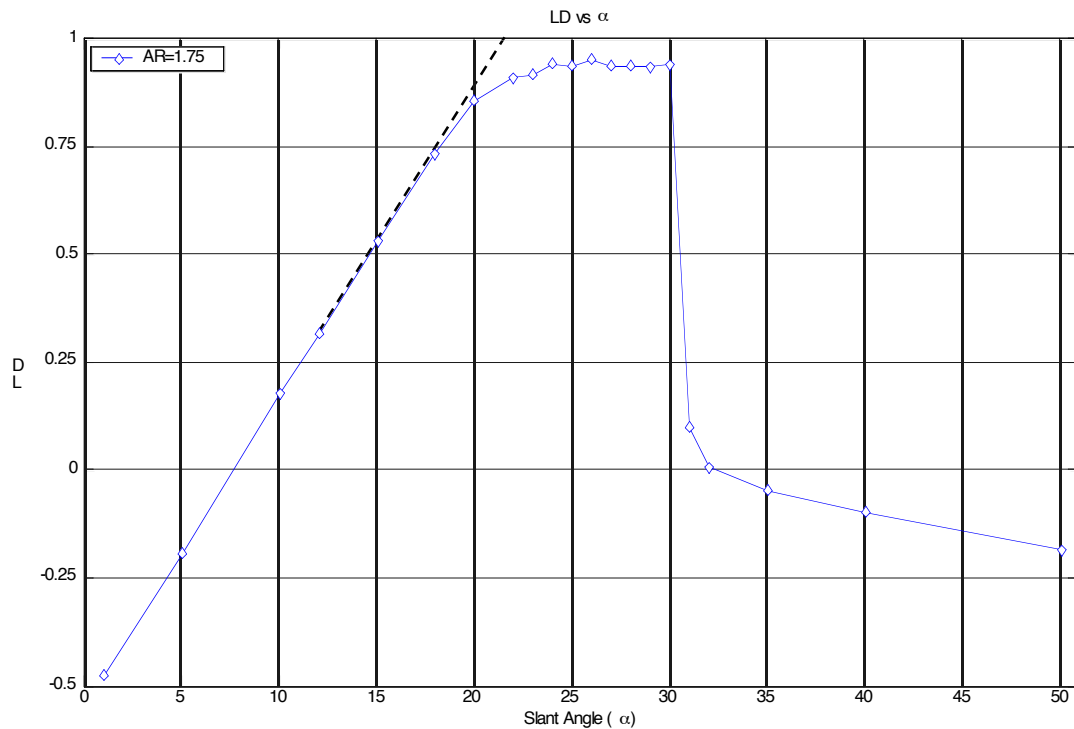


Figure 4.2 The LD ratio of the entire body. The dotted line indicates the linear increase in LD as α increases. For $22^\circ < \alpha < 25^\circ$, the LD is plateaus before considerable decrease for $\alpha > \alpha_c$.

4.2.3 Drag and lift from individual surfaces

To gain a better understanding from where the lift and drag forces originate, the drag profiles from the rear, slant, front and rear region are shown in Figure 4.3. Not surprisingly, the main variations in C_D and C_L occur on the slant and rear surface with very little variation on the front and side surfaces. The minimum C_D found in the simulations and experiments at $\alpha=12^\circ$ is not due to a minimum C_D on any particular surface. It is due to the geometric effect of changing α which reduces the C_D on the rear surface (decreasing surface area). There is a corresponding increase in C_D on the slant surface for increasing α which results in the local minimum C_D at $\alpha=12^\circ$ for the overall C_D .

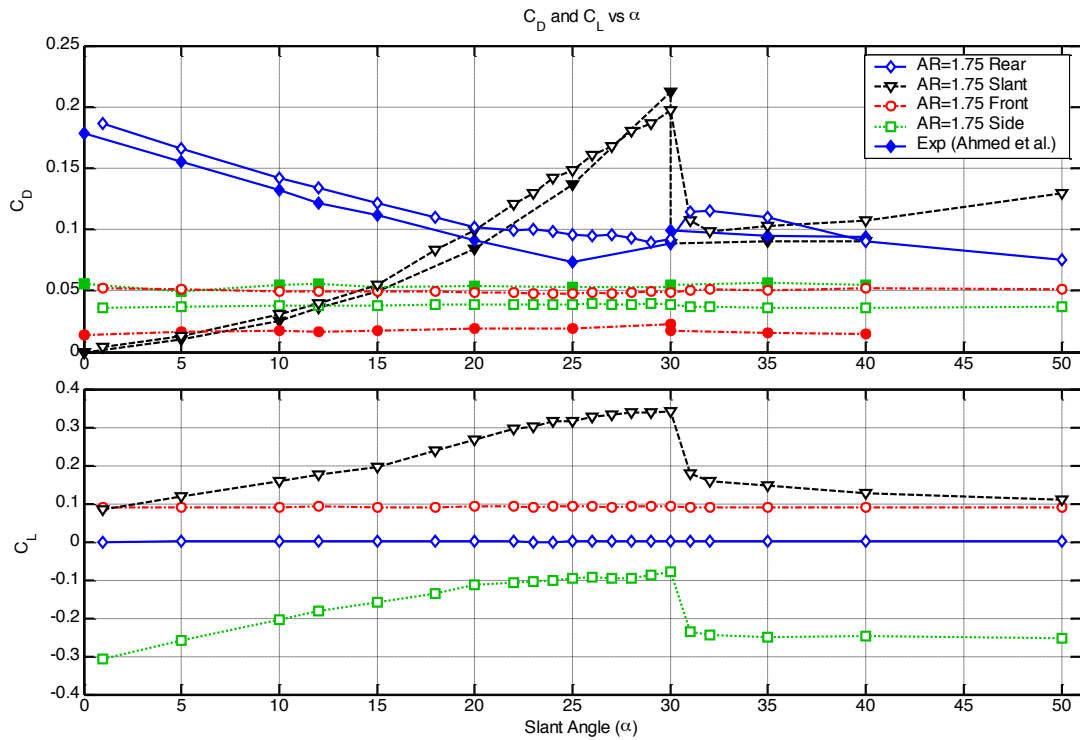


Figure 4.3 C_D and C_L for the rear, slant, front and side surfaces as indicated in Figure 3.3. The change in drag as α is varied is due to a change in the slant surface. Markers with solid fill indicate measurements from experimental data. The C_D on slant surface compares well with the trend found in experiments.

On the rear surface, the drag decreases as α increases. This is due to the effects of both the decrease in surface area of the rear surface as α increases and to changes in flow structures in the vehicle wake. Up to $\alpha=20^\circ$, there is a linear decrease in drag indicating that only the decrease in surface area is affecting the drag. It must be noted that the surface area of the rear surface ($rear\ surface\ area = (H - \sin(\alpha)L)W$, Figure 3.36) is not a linear function of α . However, between $1^\circ \leq \alpha \leq 20^\circ$, the rear surface area is virtually linear and this small difference is indistinguishable on the C_D . For $20^\circ < \alpha < 30^\circ$, the C_D for the rear surface is almost constant. This indicates that the wake structures become progressively stronger because the surface area is still decreasing. The experimental data (solid diamonds) suggest that the drag on the rear surface reaches a minimum at $\alpha=25^\circ$. However, this point is an interpolated experimental data point since the C_D of the individual surfaces were only calculated at $\alpha=12^\circ$ and $\alpha=30^\circ$ with the over all C_D used as a guide at $\alpha=25^\circ$ (Figure 3.37). This makes it difficult if the minimum C_D at $\alpha=25^\circ$ on the rear surface does exist. Numerical simulations indicate that the lowest drag on the rear surface occurs at about $\alpha=30^\circ$. At α_c , the C_D begins to increase on the rear surface. Experimental data also

indicate an increase in the C_D but not to the same extent as was observed in the simulations. This increase in C_D on the rear surface is the main reason the decrease in overall drag near $\alpha=30^\circ$ in the simulations is not as substantial as in the experiments.

The effect of the change in the surface area on the rear surface has been isolated in Figure 4.4 where the C_D is calculated using the surface area of the rear surface instead of the cross sectional area of the entire model. The figure illustrates that the wake structure behind the Ahmed body decreases up to $\alpha=20^\circ$, as the separation bubble decreases in size (Section 4.3). Then wake structures for $20^\circ > \alpha > 30^\circ$ remains relatively constant with $C_{D \text{ rear}} \approx 0.145$ until the wake transition at $\alpha_c=30^\circ$ when $C_{D \text{ rear}}$ increases.

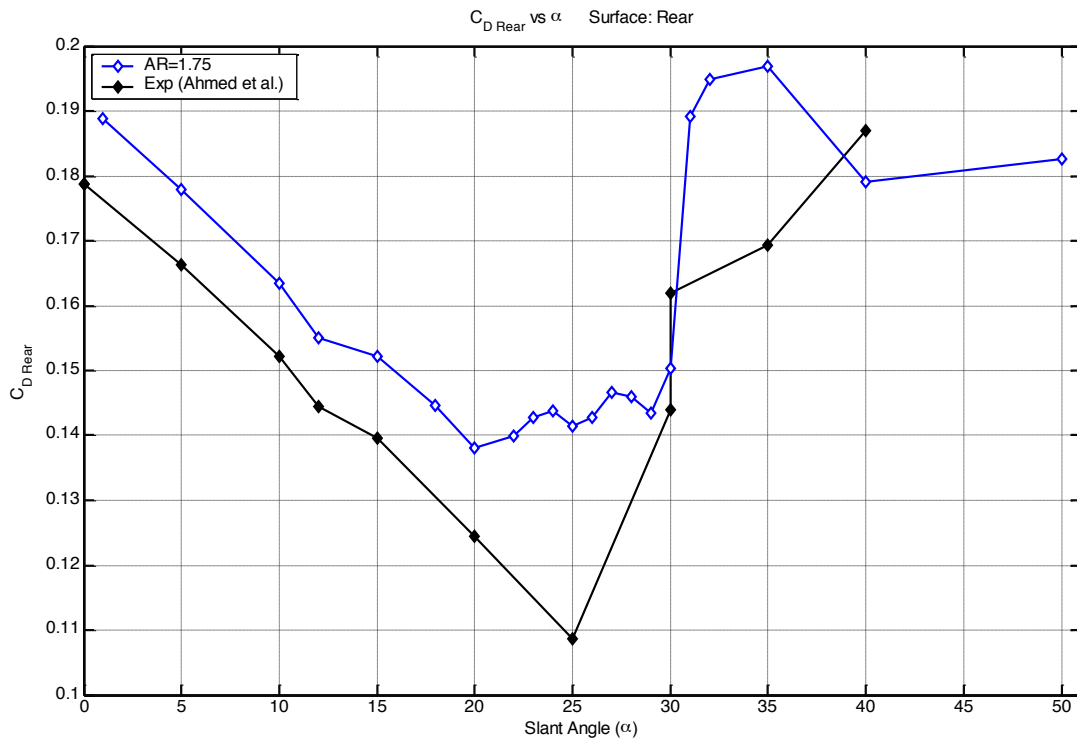


Figure 4.4 C_D of the rear surface normalised against the surface area of the rear surface. The $C_{D \text{ Rear}}$ reaches a minimum at $\alpha=20^\circ$ before slowly growing to $\alpha=30^\circ$. It is difficult to distinguish if the large difference in $C_{D \text{ Rear}}$ is real since the experimental data point is interpolated from data at $\alpha=12^\circ$ and $\alpha=30^\circ$.

On the front and side surfaces, there is little variation in C_D over the entire range of α . On the front surface, the C_D is over predicted whilst on the side surfaces, the C_D is under predicted.

In the experiments by Ahmed et al. [5], it was not possible to determine the viscous drag and the pressure drag on the individual regions since the drag from individual regions was calculated only using pressure taps. As a result, the total viscous forces

were obtained by subtracting the pressure force from the total force calculated by a force balance. In Figure 3.37, the drag of the side region included the viscous forces on the side of the body but also included the viscous force from the front, slant and rear surfaces. In the numerical simulations in this study, it was difficult to separate the pressure forces and viscous forces since the drag was calculated from finding the mean C_D for given number of iterations (Section 3.4). Consequently, the pressure and viscous forces on each surface were summed together to calculate the overall force on each region of the Ahmed body. However, it is possible to calculate the component of the viscous and pressure drag for a given iteration.

Figure 4.5 shows the breakdown of forces for $\alpha=5^\circ$ to enable comparison of the forces on different surfaces. At $\alpha=5^\circ$, the drag remains relatively constant compared with higher slant angles. When the surfaces are separated by the same method that was used in the experiments (middle column), it shows that the major difference in C_D between the experiments and numerical simulations is from the front surface. The viscous forces represented by the side surface compare well with experimental data. The pressure drag on the rear surface makes the largest contribution to the overall C_D .

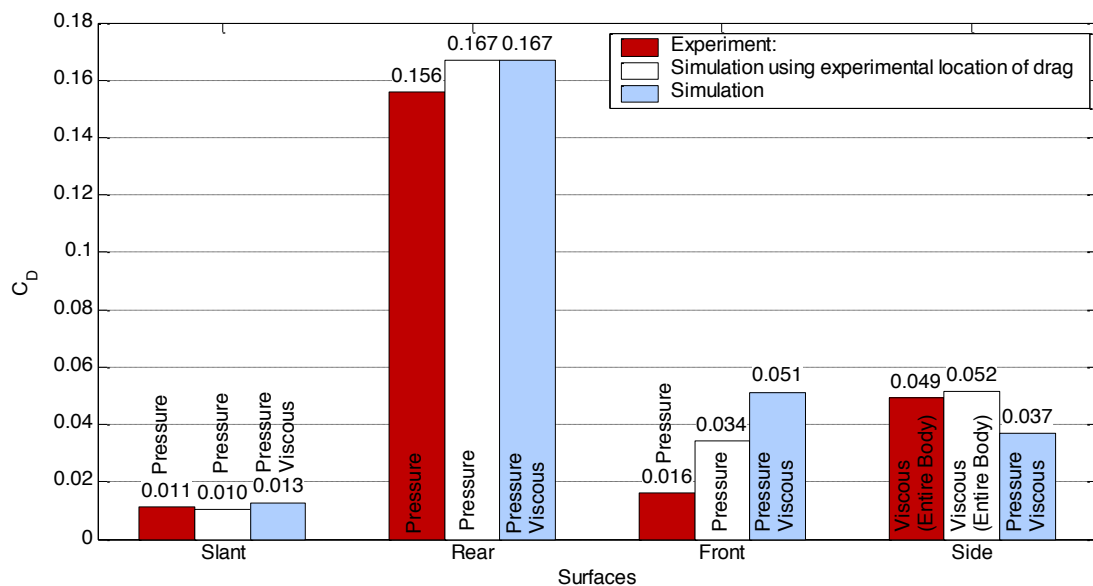


Figure 4.5 Breakdown of the forces on different regions for $\alpha=5^\circ$. The red bar and white bars represent the breakdown of the forces as used by Ahmed et al.[5] from the experiments and current numerical simulations respectively. The blue bars represent the total viscous and pressure forces on each surface from numerical simulations. The largest difference in C_D occurs on the front surface.

4.2.4 Normal force on the slant surface

On the slant surface it was found that as α increases, C_D increases up to $\alpha=30$. As with the rear surface, the changing geometry influences the C_D . To remove the effect

of increasing α on the slant surface, the force normal to the surface, the coefficient of normal force (C_N), was calculated with the following equation.

$$C_N = \frac{L \cos(\alpha)}{\frac{1}{2} \rho u_\infty^2 A} \quad \text{Eqn 4.1}$$

where L is the lift force on the slant surface, A is the cross sectional area of the Ahmed body and u_∞ is the free stream velocity. Shown in Figure 4.6 is the graph of C_N vs. α for the slant surface.

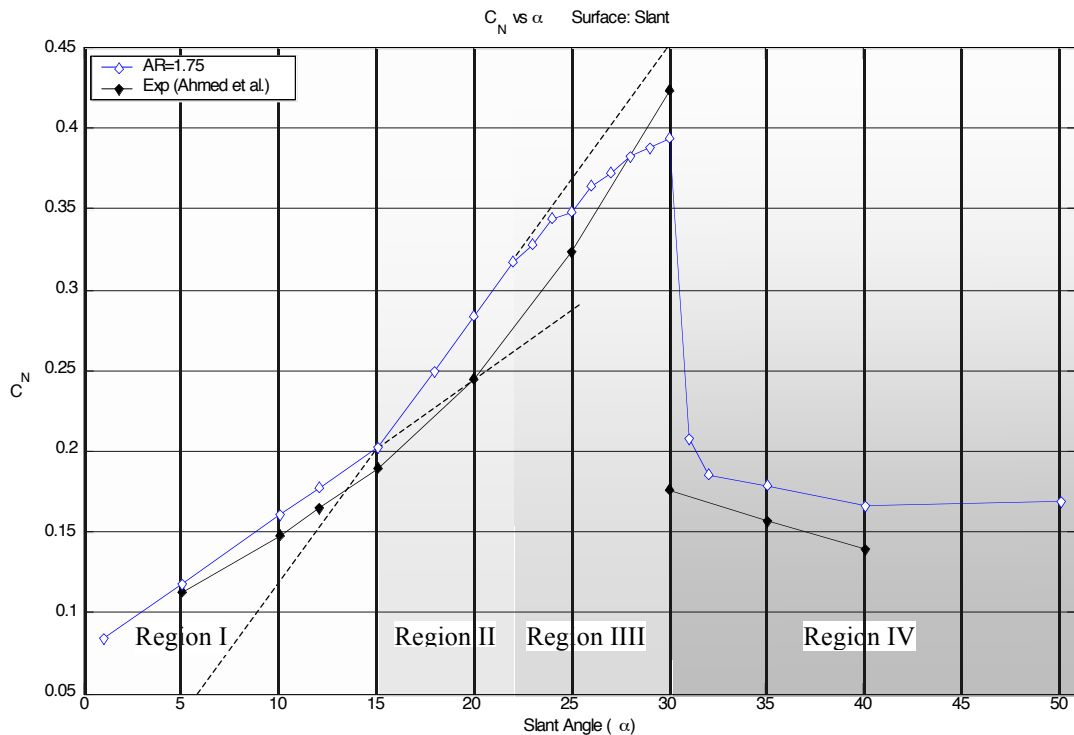


Figure 4.6 The normal force coefficient, C_N of the slant surface vs. α . Dotted lines are used to differentiate between the different regions, which are indicated by different background shades.

Up to $\alpha=22^\circ$, there is a piecewise linear relationship between C_N and α with the gradient for $15^\circ < \alpha < 22^\circ$ higher than the gradient for $\alpha < 15^\circ$. Above $\alpha=22^\circ$, the linear relationship with increasing α is lost with C_N increasing until $\alpha_c=30^\circ$, where the transition to a lower C_N occurs. After α_c , the C_N for the slant surface decreases as α increases to $\alpha=50^\circ$. From Figure 4.3 and Figure 4.6, the largest change in C_D occurs on the slant surface. This indicates that the structures over the slant surface affecting the pressure distribution on the slant surface play a critical role in affecting the wake structures and it is these structures that affect the critical slant angle at $\alpha_c=30^\circ$.

Using the changes in the C_N profile for varying alpha, four distinct regions are identified, which are used to classify the wake structures. For the standard Ahmed body, Region I is denoted by the linear increase in C_N with α up to $\alpha=15^\circ$. After that, Region II exists where there is still a linear change in C_N with α , but the gradient is higher compared with Region I. Region III occurs for $22^\circ < \alpha < \alpha_c$ where $\alpha_c=30^\circ$. In this region, the linear change in C_N with α no longer holds but C_N still increases. Region IV exists for $\alpha > \alpha_c$, where the C_N has dramatically decreased.

4.2.5 Conclusion

The effect of the slant angle on body forces has been investigated for $1^\circ < \alpha < 50^\circ$ for the Ahmed body. Relative to experiments, the overall drag was over predicted for all α but this was primarily due to over prediction of the pressure forces on the front region of the body. This is similar to simulations by Braun et al.[31] which also found the C_D was over predicted on the front surface. At $\alpha_c=30^\circ$, the total C_D compares well with experimental C_D , but this is misleading since the over prediction on front region is compensated by the under prediction on the slant and rear surfaces. However, it must be noted that these simulations have only been compared with one set of experimental data at $Re=4.3 \times 10^6$ while numerical simulations were conducted at $Re=2.86 \times 10^6$. Experiments by Watkins et al. [2] run at a lower Re , indicated that at $\alpha=30^\circ$, the C_D is significantly lower at $C_D=0.32$ compared with $C_D=0.378$ found by Ahmed. On the slant surface, the values of the drag force and especially the trends with the slant surface compared well with the limited experimental data. The normal force coefficient on the slant surface shows four distinct regions as α is varied indicating changes in the flow field in the wake region of the model.

4.3 Wake Structures

4.3.1 Introduction

Four regions were identified from the drag and lift forces, and from the flow visualisations in the analysis of the wake structures. These are defined as Region I through Region IV. They are distinguished by the change in C_N profile in Figure 4.6.

In overview, in Region I, the flow is attached to the slant surface while a small stable separation bubble forms on the slant surface in Region II. In Region III, a large separation bubble is present on the slant surface with strong C-pillar vortices present.

When the flow is completely separated from the slant surface, this is identified with region IV.

In the following section, the different flow field structures will be identified and discussed. Details about the formation and development of the c-pillar vortex are covered in Chapter 6.

Figure 4.7 3D view of the rear portion of the Ahmed body for $\alpha=30^\circ$ visualised by slices coloured by velocity magnitude/ U_∞ , iso-surface of $U/U_\infty=0$ to indicate the separation zone and path lines released from the edge of the slant surface to illustrate the C-pillar vortex.

To characterise the different regions, the wake is visualised in Figure 4.7, with the aid of slices coloured by velocity magnitude/ U_∞ , an iso-surface of $U/U_\infty=0$ to indicate the recirculation zone, and path lines released from the edge of the slant surface to highlight the C-pillar vortex. Due to the complexity of the flow structure, projections of the rear portion from a top view, side view and rear view are also used to illustrate the flow as shown in Figure 4.8.

4.3.2 Region I

Region I occurs for $0^\circ < \alpha < 15^\circ$. Figure 4.8 shows a flow visualisation for $\alpha = 10^\circ$. In this region, there is no separation bubble present on the slant surface, which can be seen by the streak lines on the slant surface. The streamlines released from the side of the slant surface indicate that the C-pillar vortex exists for small α , but it is weak.

Figure 4.8 Orthographic projection of wake structures behind the Ahmed body for $\alpha = 5^\circ$. Stream slices are contoured by velocity magnitude/ U_∞ overlaid with streak lines on each plane. Path lines are released from one side edge of the slant surface. The separated region is outlined with an iso-surface of $U/U_\infty = 0$ coloured by velocity magnitude/ U_∞ .

Behind the body, a large separation bubble is present encompassing the entire rear surface which is outlined by streak lines on the vehicle centreline and the iso-surface of $U/U_\infty = 0$ in Figure 4.8. Of note, is the horizontal direction of the streak lines on the rear surface indicating that the rotation of the rear separation bubble is circulating about the Y-axis as opposed to the Z-axis. This is most likely due to the longer shear layers on the side of the body compared with the shear layer underneath the body (Figure 4.9) dominating the recirculation region.

Figure 4.9 Orthographic projection of slices of contours of vorticity magnitude (0-1000s) overlaid with streak lines for $\alpha=10^\circ$.

4.3.3 Region II

In Region II, a small stable separation bubble forms on the slant surface. This region corresponds to the increase in the linear gradient of C_N in Figure 4.6 occurring for $15^\circ < \alpha < 22^\circ$. As shown in Figure 4.10, the flow has separated from the top of the slant surface. This separation bubble is only present in the central region of the slant surface and then reattaches again. Streak lines on the slant surface indicate two recirculation regions inside the separation bubble. On the outside edges of the slant surface, the flow remains attached. Streamlines released from the edge of the slant surface indicate that the C-pillar vortex has increased in strength relative to Region I and its footprint on the slant surface is visible by streamlines moving back towards the side edge of the slant surface. Behind the body, the separation bubble decreases in length as α increases. The streak lines patterns are considerably different to Region I revealing an unstable node on the rear surface of the Ahmed body. This indicates that a toroid vortex structure is present behind the rear body. The centres of the recirculation behind the rear of the body have moved inwards closer to the rear body.

Figure 4.10 Orthographic projection of wake structures behind the Ahmed body for $\alpha=20^\circ$. Stream slices are contoured by velocity magnitude/ U_∞ overlaid with streak lines on each plane. Path lines are released from one side edge of the slant surface. The separated region is outlined with an iso-surface of $U/U_\infty=0$ coloured by velocity magnitude/ U_∞ .

4.3.4 Region III

The linear change of C_N vs. α is no longer consistent for $22^\circ < \alpha < 30^\circ$ for Region III. The flow visualisations for $\alpha=25^\circ$ in Figure 4.11 indicate separation from the entire width of the top of the slant surface as opposed to a partial section in Region II. However at $\alpha=25^\circ$, there is still reattachment of the flow even at the body centreline.

Inside the separation bubble on the slant surface, the focus points have moved closer towards the top of the C-pillar. Also of note is that the streak lines from the iteration averaged simulations are not uniform and undulating, indicating that the region near the vehicle centreline is likely to be unsteady [77].

Figure 4.11 Orthographic projection of wake structures behind the Ahmed body for $\alpha=25^\circ$. Stream slices are contoured by velocity magnitude/ U_∞ overlaid with streak lines on each plane. Path lines are released from one side edge of the slant surface. The separated region is outlined with an iso-surface of $U/U_\infty=0$ coloured by velocity magnitude/ U_∞ .

Behind the vehicle, for $\alpha=25^\circ$, two distinct recirculation regions are present on the body centreline. In Region III, as α increases, the top recirculation bubble becomes more dormant due to the increased downwash on the body centreline fed by the C-pillar vortices. Consequently, the rear separation region is shorter. From the streak line patterns on the vehicle rear end, it is difficult to determine the wake structures. However as can be seen by taking slices in Figure 4.12 for $\alpha=25^\circ$, the separation bubble stretches further downstream near the sides of body than on the centreline. This is partially due to domination of the shear layers from the sides of the body, which have not been significantly affected by increasing α . Consequently, the centres of the recirculation region on the XZ-plane are located further away from the body while centres of recirculation of the XY-plane on the body centreline are closer to the body due to net downwash from the slant surface. This is not shown with the iso-surface of U/U_∞ .

Figure 4.12 Orthographic projection of wake structures behind the Ahmed body for $\alpha=25^\circ$. Slices are contoured by vorticity magnitude (0-1000s) overlaid with stream lines.

As the slant angle is increased to $\alpha=30^\circ$, the streak line patterns on the slant surface indicate separation on the entire surface except underneath the C-pillar vortex. On the body centreline, all the flow is reversed and streak lines on the XY plane indicate the rear and slant separation bubbles have merged. However, there are still separate regions of reversed flow on the slant surface and rear surface indicated by the iso-surface of U/U_∞ . A strong C-pillar vortex is present on the edges of the slant surface keeping the flow attached. Of note is the region of reversed flow inside the C-pillar vortex which is discussed in Chapter 6.

Figure 4.13 Orthographic projection of wake structures behind the Ahmed body for $\alpha=30^\circ$. Stream slices are contoured by velocity magnitude/ U , overlaid with streak lines on each plane. Path lines are released from one side edge of the slant surface. The separated region is outlined with an iso-surface of $U/U_\infty=0$ coloured by velocity magnitude/ U .

Behind the vehicle, streak lines on the body centreline indicate that the two recirculation regions are not present at high α . However, slices taken off centre the line in Figure 4.14 show that the upper recirculation region is more dominant.

Figure 4.14 Orthographic projection of wake structures behind the Ahmed body for $\alpha=30^\circ$. Stream slices are contoured by v/v_∞ , overlaid with streak lines. The XY plane is offset from the centreline of the body.

4.3.5 Region IV

Region IV occurs after the transition to a large separated wake for $\alpha > \alpha_c$. As can be seen in Figure 4.15, the wake is no longer attached to the slant surface and a full separation bubble exists. This is similar to what was observed for Region I. An upper and lower recirculation region is present with the upper recirculation region encompassing the slant surface. On the slant surface, the iteration averaged streak lines are not uniform indicating that the flow is highly varying inside the separation bubble. The streamlines released from the edge of the slant surface indicates that the C-pillar vortex has failed to form. The iso-surface of U/U_∞ indicating reversed flow shows even on the sides of the slant surface, the flow has separated.

Figure 4.15 Orthographic projection of wake structures behind the Ahmed body for $\alpha=35^\circ$. Stream slices are contoured by velocity magnitude/ U_∞ , overlaid with streak lines on each plane. Path lines are released from one side edge of the slant surface. The separated region is outlined with an iso-surface of $U/U_\infty=0$ coloured by velocity magnitude/ U_∞ .

4.3.6 Surface Pressure Near Slant Surface

To help correlate the flow structure within the different regimes with the forces exerted on the body, pressure profiles on the upper surfaces the Ahmed body are examined. Shown in Figure 4.17 and Figure 4.18 are streamwise cuts of the surface pressure distribution on the top and slant surface of the body on the model centreline, and on the top edge near the C-pillar. The locations where the surface pressure distribution are taken are indicated in Figure 4.16.

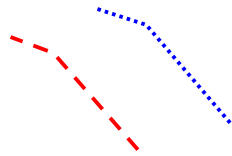


Figure 4.16 Location of surface pressure profile distribution for $Z=0$ (blue dotted line) and $Z=0.194$ (red dashed line).

For all slant angles, the pressure peaked at the top of the slant surface due to the abrupt change in geometry at the top of slant surface. The C_p on the slant surface was almost zero in Region I. Due to the formation of a small separation bubble on the slant surface in Region II, the pressure distribution is no longer zero on the slant surface and peaks at $C_p \approx 0.02$. The distinguishing difference between Region II and Region III is the location and magnitude of C_p on the slant surface. As can be seen for $\alpha=20^\circ$ and $\alpha=22^\circ$, the peak location of C_p on the slant surface is approximately midway along the slant surface. This is compared with $25^\circ < \alpha < 30^\circ$, where the peak C_p is higher and constant independent of α , and the location of the peak C_p has moved further upstream. Region I is similar to Region II with $C_p \approx 0$ due to the large separation bubble covering the slant surface.

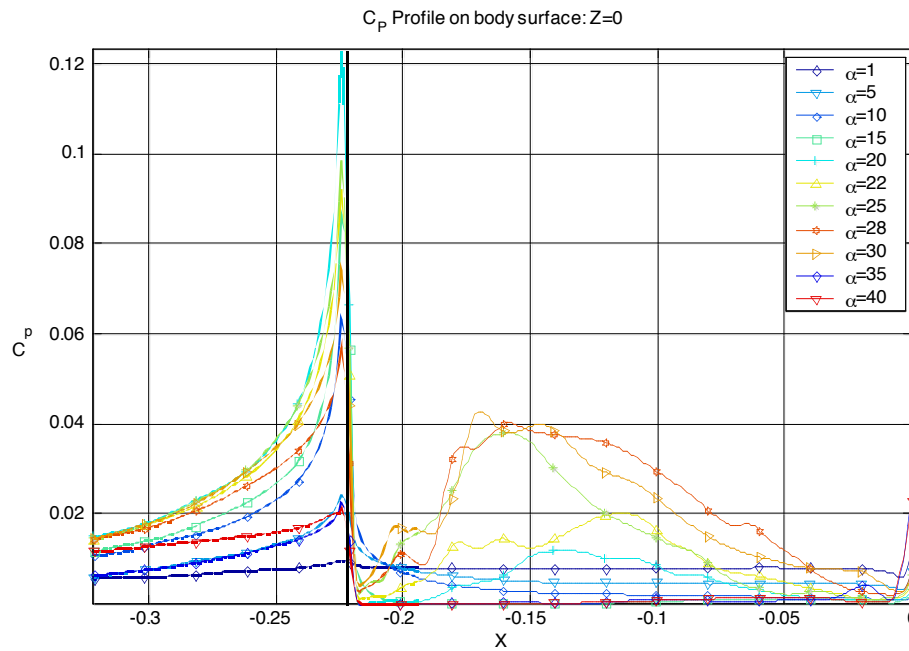


Figure 4.17 Profiles of surface C_p for slant angles as indicated, at $Z=0$ as indicated in Figure 4.16 (blue dotted line). The maximum C_p occurs for $\alpha=20^\circ$, while on the slant surface, the peak C_p occurs for $\alpha \approx 30^\circ$.

The pressure distribution on the side edge of the slant surface is heavily influenced by the presence of the C-pillar vortex. For all α , the peak C_p on the top edge of the slant surface is higher than the peak C_p at $Z=0$ (note the different y scale between Figure 4.17 and Figure 4.18). The C_p distribution along the slant surface indicates that peak C_p occurs at $\alpha=22^\circ$ which is the start of Region II whereas the peak drag on the body occurred at the transition between Region III and Region IV. This indicates that the strength of the vortex is strongest at $\alpha=22^\circ$.

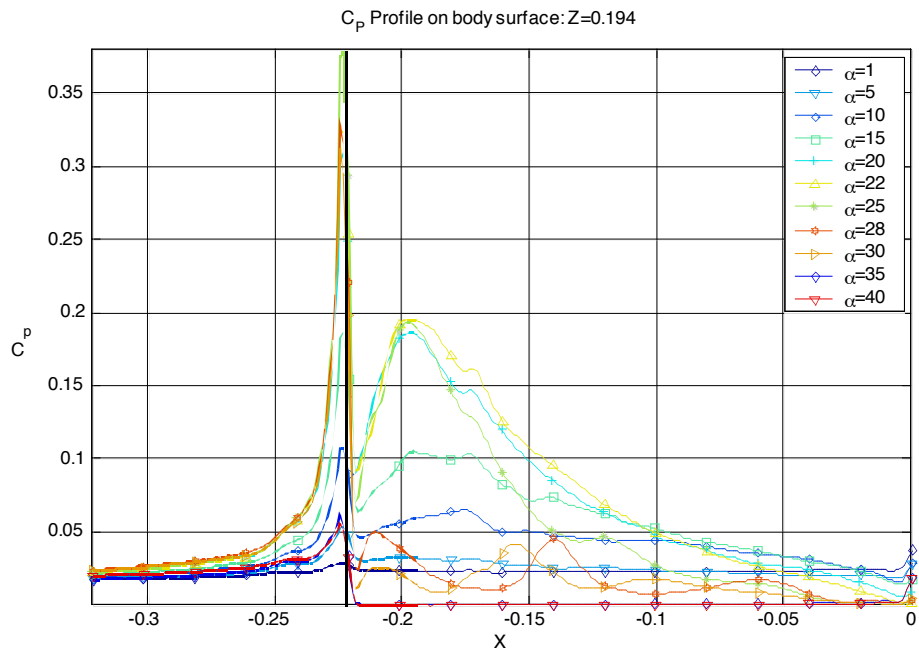


Figure 4.18 Profiles of surface C_p for slant angles as indicated at $Z=0.194$ as indicated in Figure 4.16 (red dashed line). The maximum C_p occurs at $\alpha=25^\circ$, while on the slant surface, the peak C_p on the slant surface occurs for $\alpha \approx 22^\circ$.

This can also be seen in Figure 4.19, which shows the pressure distribution on the top edge of the slant surface for various α along the z -axis. The peak C_p for a given slant angle on the top slant edge occurs on the side of the body as opposed to the centreline. The peak C_p occurs for $\alpha=25^\circ$ and $\alpha=26^\circ$, which is localised near the edge of the body. The highest mean C_p for the entire slant edge occurs for $\alpha=22^\circ$ where the high C_p is distributed along the top edge. The mean C_p across the top of the slant edge increases to $\alpha=22^\circ$ as α increases. It then becomes highly localised near the side edge, which is the formation point of the C-pillar vortex. This remains constant until $\alpha_c=30^\circ$, when C_p suddenly decreases but remains constant for $\alpha>30^\circ$.

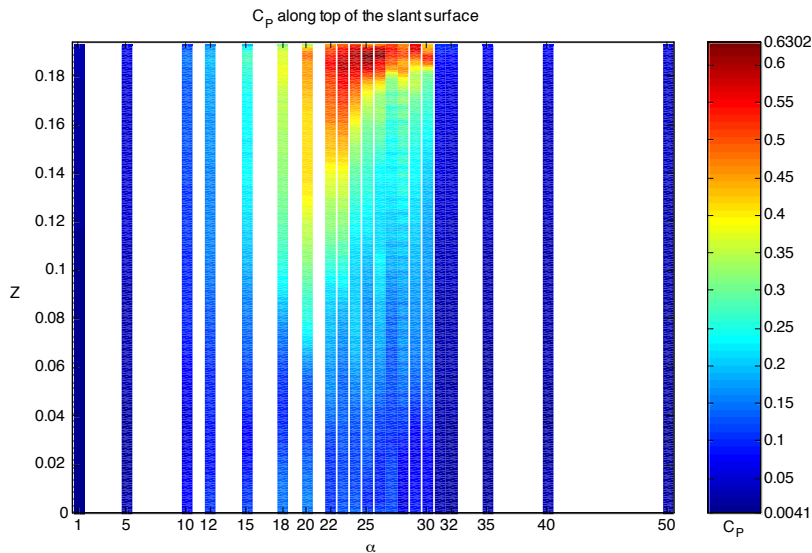


Figure 4.19 Pressure distribution along the top edge of the slant surface for different slant angles. The peak C_p on the top edge of the slant surface occurs for $\alpha=25^\circ$ on the edge of the body where the c-pillar is forming.

4.3.7 Rear separation bubble size

It was found that the rear separation bubble shape changed considerably in different regions. A slice of the rear separation bubble is shown in Figure 4.20 for various slant angles. The separation bubble is visualised with contours of vorticity magnitude on XZ planes at the midpoint of the rear surface. For $\alpha < 15^\circ$, the separation bubble on the centrelines stretches further downstream than in side regions of the wake. For $15^\circ < \alpha < 30^\circ$, the downwash from the slant surface causes the separation bubble to decrease near the vehicle centreline. There is relatively little change in size of the shear layers on the side of the body but as α increases, the size of the separation bubble at the vehicle centreline is reduced.

a. $\alpha=5^\circ$ b. $\alpha=10^\circ$ c. $\alpha=15^\circ$ d. $\alpha=20^\circ$ e. $\alpha=25^\circ$ e. $\alpha=30^\circ$

Figure 4.20 Progression of the rear separation bubble with increasing α . The XZ slice is located at the midpoint of the rear surface. Slices are contoured by vorticity magnitude (0-1000s) overlaid with stream lines.

The streamwise location of the centre of recirculation zones at three different spanwise locations for different slant angles is plotted in Figure 4.21. On the vehicle centreline at $Z=0$ (blue diamonds), the separation bubble vortex centre extends to $X=0.375$. Increasing α causes the separation bubble length to decrease until $\alpha=22^\circ$, where the separation bubble centre is located at $X=0.04$. Further increases in α have a negligible effect on the separation bubble centre on the vehicle centreline. On the edge of the body at $Z=0.1945$ (red circle), the location of the recirculation bubble initially moves towards the body. A local minimum is reached at $\alpha=12^\circ$, where further increases to α cause the sides of the separation to stretch slightly further downstream until the entire separation bubble is reduced for $\alpha>25^\circ$.

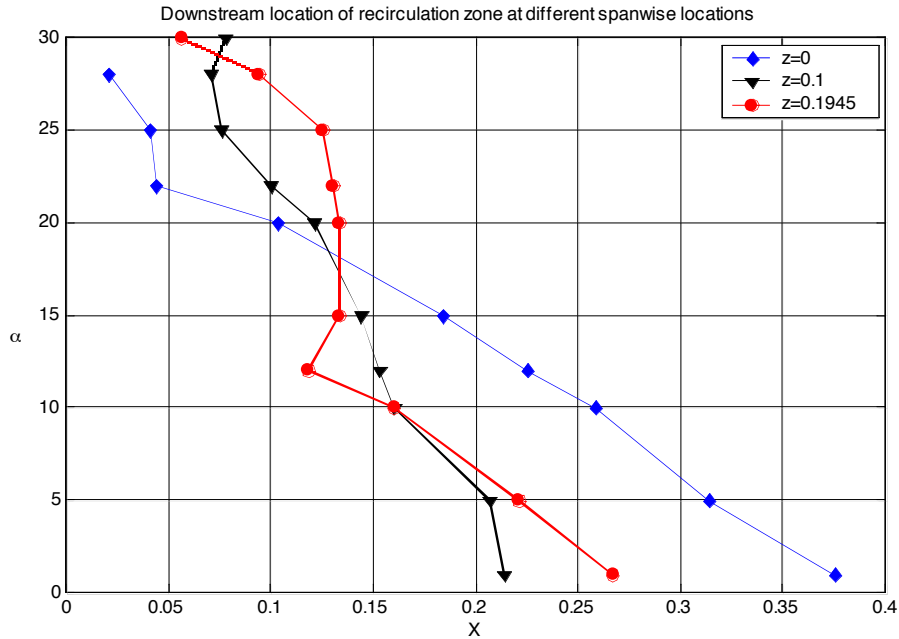


Figure 4.21 Downstream location of recirculation zones at different spanwise locations. $Z=0$ (blue diamond) is location of the top recirculation region on the vehicle centreline. The recirculation zone for $Z=0.1945$ was calculated from analysis of various recirculation regions on the XZ plane.

It is interesting to note that the size of the separation bubble is decreasing for increasing α up until $\alpha=12^\circ$ which coincides with the slant angle for minimum drag on the Ahmed body. For $\alpha>15^\circ$, the centres of the separation bubble vortices are located further downstream than the centres on the body centreline.

The general profile of the separation bubble is indicated in Figure 4.22 with iso-surface of C_{TP} . The separation region changes from a large separation region (a) to a region with two distinctive peaks on the edges. This is possibly due to the influence of the shear layers and the c-pillar vortex on the side extending the sides of the separation bubble. The induced downwash causes the separation bubble to be smaller on the body centreline.

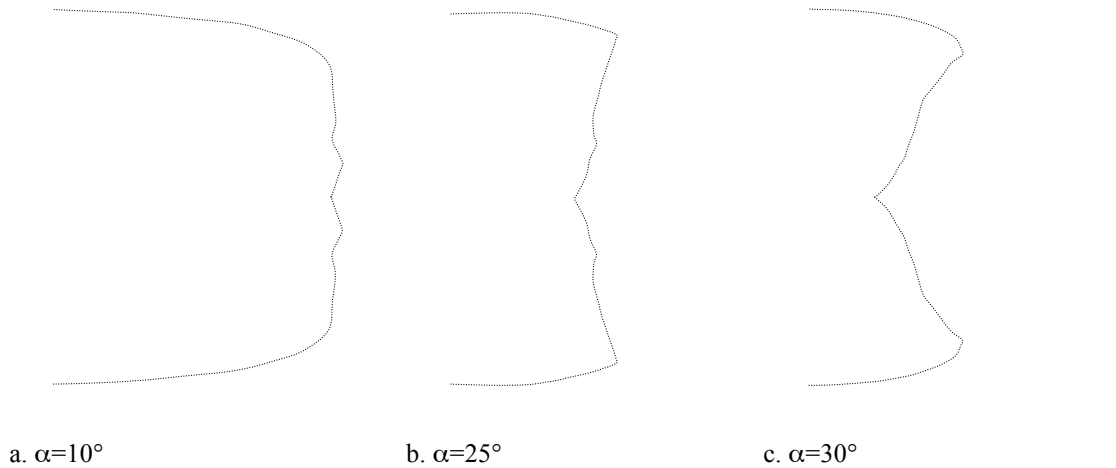


Figure 4.22 Top view of iso-surface of $C_{TP}=0$ coloured by U/U_∞ behind the body for $\alpha=10^\circ$ (a), $\alpha=25^\circ$ (b) and $\alpha=30^\circ$ (c) indicating the general profile of the separation bubble.

4.3.8 Conclusion

For varying slant angle on the Ahmedbody, four flow regions were identified with characteristic flow structures. Region I ($\alpha < 15^\circ$) is characterised by the flow being attached to the slant surface. A small separation bubble formed for Region II ($15^\circ < \alpha < 22^\circ$). In Region III ($22^\circ < \alpha < 30^\circ$), the flow on the slant surface is primarily separated except for the region which is influenced by the downwash induced by the C-pillar vortices. A large separation bubble adjacent to the slant and rear region of the Ahmed body, with no C-pillar vortices present, characterised the flow field for Region IV ($\alpha > 30^\circ$).

The strongest C_p occurred on the vehicle centreline for $\alpha=20^\circ$ at the top of the slant surface in Region II. Further increases to α decreased the peak C_p as the flow separated from the slant surface. This caused an overall stronger pressure on the slant surface, which caused the increase in drag. On the edge of the slant surface, the high C_p at $\alpha=22^\circ$ indicates that the C-pillar vortex is strongest.

In the near wake region behind the body, the separation bubble changes shape considerably as α is varied. For increasing α , the separation bubble changes from a round bubble to a separation bubble with the sides extending further downstream on the body centreline. As α approaches $\alpha=30^\circ$, a separation bubble exists with the edges of the bubble extending further downstream than at the body centreline. This is due to the downwash on the vehicle centreline making the separation bubble smaller while on the sides, the bubble is extended due to the influence of the c-pillar vortex and shear layer on the vehicle sides.

4.4 Experimental Comparison

In the following section, data from experiments will be compared with current numerical simulations. Experimental data are taken from Lienhart et al. [14] for $\alpha=25^\circ$ and $\alpha=35^\circ$, at $Re=2.86 \times 10^6$. For more details regarding the experiments, refer to Section 2.1.

The four parameters compared are the velocity profiles on the vehicle centreline ($Z=0$) above the slant surface, velocity profiles on the vehicle centre downstream of the model, spanwise sections of flow in the body wake, and pressure distributions on slant and rear surfaces of the body.

4.4.1 Wake structures near slant surface

Profiles of U velocity are shown in Figure 4.23 for $\alpha=25^\circ$ along the vehicle centreline with numerical simulation profiles in red with markers and profiles from experiments in black. Data for the numerical simulations were taken slightly off the centreline at $Z=0.025$ since on the centreline, there were some discrepancies of the velocity field (Figure 4.11) as a result of using a symmetric boundary condition to reduce the mesh size and increase the overall resolution of the model. As can be seen, for $\alpha=25^\circ$, both the experimental and numerical simulations indicate that the flow has separated from the top of the slant surface and is reattaching lower down. The boundary layer on the top of the body is larger than the boundary layer from the experiments.

Figure 4.23 Boundary layer profile above the slant surface at $Z=0$ on the XY plane for $\alpha=25^\circ$. Red marked line indicates data from numerical simulations while black solid line indicates data from experiments from Lienhart et al. [14]

However, the separation bubble in the simulations is longer, reattaching at 59% of slant length (Figure 4.24a). The experimental data indicate that the separation bubble

reattaches at 49% of the slant length (Figure 4.24b). Drouin [19] from experiments found the separation bubble to extend to approximately 54% of the slant length. The oil / soot streak flow visualisations (Figure 3.42) indicate that the length of the separation bubble fluctuates and does not have a steady reattachment length with the flow structures very unsteady in the separation bubble. Most simulations using RANS have over predicted the size of the separation bubble [15, 20, 31]. However, the main features of the flow structure are still present with the separation bubble forming over the upper section of the slant surface.

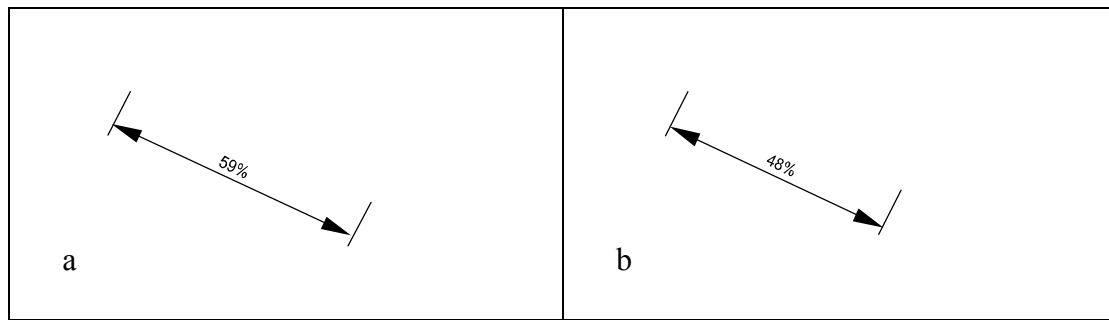


Figure 4.24 Stream lines and velocity vectors from numerical simulations (a) and experimental data [14] (b) for $\alpha=25^\circ$ at $Z=0$ on the XY plane. The separation bubble computed from simulations is slightly larger than those observed in experiments.

At $\alpha=35^\circ$, the flow has completely detached from the slant surface. This leads to a single, significantly larger, recirculation region within the wake. As can be seen in Figure 4.25, the numerical simulations show very similar results to the experimental data. For both $\alpha=25^\circ$ and $\alpha=35^\circ$, the boundary layer profile on the top of the body, before the slant surface, is similar. The inflection point for the u velocity profiles (dotted line) is in good agreement. In the shear layer separating the recirculation region from the outer flow, the wake deficit is slightly larger in the numerical simulations.

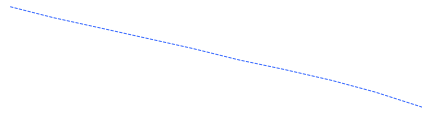


Figure 4.25 Boundary layer profile above the slant surface at $Z=0$ on the XY plane for $\alpha=35^\circ$. Red marked line indicates data from numerical simulations while black solid line indicates data from experiments from Lienhart et al. [14]. The blue dotted line represents the inflection point for the u -velocity profiles from numerical simulations.

The experimental streamline visualisations on the vehicle centreline in Figure 4.26 indicate a secondary separation bubble in the wake above the slant surface (b) which was not observed in the simulations (a).

a

b

Figure 4.26 Stream lines and velocity vectors from numerical simulations (a) and experimental data [14] (b) for $\alpha=35^\circ$ at $Z=0$ on the XY plane. Both sets of data show the wake separating from the top of the slant surface and not reattaching.

Figure 4.27 shows a comparison of the flow field using spanwise cuts. At the top of the slant surface (Figure 4.27a), the numerical simulations are similar to the experimental data. However, the experiments show an increased U/U_∞ at the top of the slant surface. Further down the slant surface (Figure 4.27 b, c), the simulated spanwise velocity near the C-pillar is not as high as that in the experiments. In addition, since the separation bubble in the simulation is larger, the downwash near the centreline is weaker than the experiments. On the spanwise plane collinear with the rear surface, the c-pillar vortices are clearly visible in both the experiments and numerical simulations. The U velocity of the C-pillar vortex is slower in simulations, whereas in the experiments, the axial velocity of the C-pillar vortex is near U_∞ with

the centre of the vortex moving further inboard. However, with the lack in resolution in the experiments, it is difficult to analyse the finer points of the behaviour of the C-pillar vortex.

a. $X=-0.138$

b. $X=-0.088$

c. $X=-0.038$

d. $X=0.0$

Figure 4.27 Comparison of spanwise slices of the flow field above the slant surface for $\alpha=25^\circ$ for (a) $X=-0.138$, (b) $X=-0.088$, (c) $X=-0.038$, (d) $X=0.0$. The left side of each figure is the data from the simulations compared with data from the experiments on the right side. Figures are coloured by contours of U/U_∞ overlaid with velocity vectors.

For $\alpha=35^\circ$, the spanwise slices in Figure 4.28 indicate that the wake has separated for the entire width of the slant surface. As can be seen in Figure 4.28a, the velocity vectors indicate that the spanwise velocity is very uniform in the experiments while in the simulations, the w velocity is stronger. However the shape of the separation bubble compares well with the experiments.

a. $X=-0.088$ b. $X=0.0$

Figure 4.28 Comparison of spanwise slices of the flow field above the slant surface for $\alpha=25^\circ$ for (a) $X=-0.088$, (b) $X=0.0$. The left side of each figure is the data from the simulations compared with data from the experiments on the right side. Figures are coloured by contours of U/U_∞ overlaid with velocity vectors.

4.4.2 Wake structures in the body wake.

Further comparisons were made between the numerical simulations and experiments of the flow structures behind the Ahmed body for $\alpha=25^\circ$ and $\alpha=35^\circ$. Velocity vectors on the body centreline ($Z=0$) are shown in Figure 4.29 for $\alpha=25^\circ$. Figure 4.31 compares the experiments with the simulations for $\alpha=35^\circ$.

For $\alpha=25^\circ$, both the experimental and numerical wake structures have the same overall pattern with a recirculation region behind the body with two spanwise vortices present. The recirculation region in the experiments is stronger just behind the body. This can be seen by the increased velocity vectors between the centres of spanwise vortices. Further downstream, the velocity fields are the very similar. However, it appears there is a greater wake deficit in the simulations with $U \rightarrow U_\infty$ occurring further downstream.



Figure 4.29 Velocity vectors on the vehicle centreline ($Z=0$) for $\alpha 25^\circ$ from simulation (a) and experiment (b). Dots indicate focus and saddle points in the wake region for comparison.

The spanwise cuts shown in Figure 4.29 are located in the wake behind the body with an outline of the body shown for reference. Near the body at $X=+0.80$ (Figure 4.30a), the C-pillar vortices are visible but not well defined in the experiments. The vortex centre calculated by the centre of recirculation of the spanwise velocity vectors is lower in the experiments and the axial velocity is still near to U_∞ . At $X=+0.2$ (Figure 4.30b), the experimental C-pillar vortex has a similar axial velocity compared with the simulations. The simulation shows the vortex merging with the separation bubble on the rear surface. By $X=+0.5$ shown in Figure 4.30c, the simulations compare well with the experimental data with two counter rotating vortices in the wake causing a net downwash on the vehicle centreline. However, The vortex is larger in the simulations.

a. $X=0.080$

b. $X=+0.2$

c. $X=+0.5$

Figure 4.30 Comparison of spanwise slices of the flow field downstream of the body for $\alpha=25^\circ$ for (a) $X=0.08$, (b) $X=0.2$, (c) $X=0.5$. The left side of each figure is the data from the simulations compared with data from the experiments on the right side. Figures are coloured by contours of U/U_∞ overlaid with velocity vectors.

At $\alpha=35^\circ$, the large separation bubble is present in both the simulations and experiments as shown on Figure 4.31. The recirculation region observed in the experiments stretches further downstream with the centres of recirculation further away from the body. However, it appears that the flow recovers more quickly in the experiments since the wake deficit profile at $X=0.55$ is similar to simulations where the recirculation bubble is not as large. Experimental velocity vectors indicate that the under body flow in the experiments is increased with a stronger velocity profile near the ground behind the body. This is due in part to a smaller boundary layer in experiments, so there is a greater mass flow rate under the vehicle.



Figure 4.31 Velocity vectors on the vehicle centreline ($Z=0$) for $\alpha=35^\circ$ from simulation(a) and experiment(b). Dots indicate focus and saddle points in wake region for comparison.

The spanwise cuts downstream in Figure 4.32 indicate that the separation bubble encompassed the entire width of the vehicle. Near the body at $X=+0.80$ (Figure 4.32a), there is a streamwise vortex and net downwash which is not visible in the experiments until $X=+0.2$ (Figure 4.32b). However, the centre of recirculation is higher and further away from the vehicle centreline. At $X=+0.5$ (Figure 4.32c), the two counter rotating vortices are in a similar position and the magnitude of the circulation is slightly stronger in the simulations.



Figure 4.32 Comparison of spanwise slices of the flow field downstream of the body for $\alpha=35^\circ$ for (a) $X=0.08$, (b) $X=0.2$, (c) $X=0.5$. The left side of each figure is the data from the simulations compared with data from the experiments on the right side. Figures are coloured by contours of U/U_∞ overlaid with velocity vectors.

4.4.3 Surface Pressure

Figure 4.33 and Figure 4.34 show comparisons of pressure distributions on rear surfaces from experiments and numerical simulations. The surfaces from the rear region of the Ahmed body were shown in Figure 3.49. Numerical data are shown on the positive Z side of the body while experimental data are shown on the negative Z side of the body. For $\alpha=25^\circ$, the numerical simulations are in good agreement with the experimental data with the footprint from the C-pillar vortex clearly visible. However, the magnitude of C_p has a higher peak suction in the experimental data. A high suction force across the top of the slant surface was not observed in the simulations. The presence of the larger separation bubble in the numerical simulations can be observed with the larger surface area on slant surface with $C_p < 0.6$. For $\alpha=25^\circ$, the C_N for the slant surface was similar. This could be due to the larger surface area on the slant surface with $C_p < 0.6$ being offset by the higher peak suction at the top of the slant surface and from the C-pillar vortex.

Figure 4.33 The C_p of rear, slant and partial side surfaces for $\alpha=25^\circ$. The left side of body is the C_p from the simulations while the right side is the C_p from the experiments.

For $\alpha=35^\circ$, the peak suction on the rear region of the body was not as strong with the minimum suction being $C_p=-0.31$ compared with $C_p=-0.4$ for $\alpha=25^\circ$. The main differences between the pressure distributions are near the body centreline where C_p is higher in the simulations and on the sides of the Ahmed body. The difference of C_p near the vehicle centreline could be due to some adverse effects of the symmetry boundary condition. However, due to the small range of C_p on surfaces (Range= $\Delta 0.2$ for $\alpha=35^\circ$, $\Delta 1.4$ for $\alpha=25^\circ$) this difference between simulations and experiments is not substantial.

Figure 4.34 The C_p of rear, slant and partial side surfaces for $\alpha=35^\circ$. The left side of body is the C_p from the simulations while the right side is the C_p from the experiments.

4.4.4 Surface Topology

The surface topology on the slant surface is compared with streak line visualisations from experiments to determine how the critical points compare. Streamlines from simulations were calculated using the velocity field for the slant surface coordinate system and then superimposed on the images of the surface skin friction patterns or time-averaged streamlines from PIV data (Drouin et al. [19]). In Figure 4.35, a comparison is made for $\alpha=25^\circ$. In Figure 4.35a, the positive bifurcation line correlates well with the streak line patterns. Due to the effect of the symmetry condition in the simulations, it is difficult to determine the length of the separation bubble but the simulation reattachment location is longer than in the experiments. The recirculation region indicated by the streamlines near the top corners of the slant surface is difficult to locate in the experiments. In Figure 4.35b, the recirculation region is further inboard than the simulations. As the data from Drouin et al. are off the body, the size of the separation bubble has a significant effect on the location of the recirculation region on a plane parallel to the slant surface.

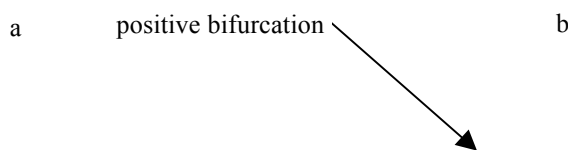


Figure 4.35 Surface Streamlines for $\alpha=25^\circ$ overlayed on experimental streak lines from (a) Lienhart and Becker [13] and (b) Drouin et al. [19]

The major difference between the simulations and experiments at $\alpha=30^\circ$ is the lack of the negative bifurcation line that is evident on the side of the slant surface in Figure 4.36. The streak line positive bifurcation line is evident. It appears that the separation bubble reattaches in Figure 4.36a, while there is no reattachment on the centreline in Figure 4.36b. The detached flow region was described by Vio et al. [22] as D-like in shape, with a central tail at its base, which appears similar to numerical simulations.

a
b
positive bifurcation
negative bifurcation

Figure 4.36 Surface Streamlines for $\alpha=30^\circ$ overlaid on experimental streak lines from (a) Sims-Williams (conducted by Dominy) [17] and (b) Vio et al. [22]

Initially it was considered that the discontinuous streamlines on the body centreline were due to the limiting effects of the symmetry condition on the spanwise velocity. In Figure 4.36, a similar pattern occurred with reversed flow on the body centreline.

The line indicating the edge of the separation bubble in Figure 4.36(a) can be misleading since it is the point at which the force of the reversed flow is in equilibrium with the force of gravity on the visualisation medium.

In both streak line visualisations and the numerical streamlines, reversed flow existed on the body centreline, contrary to Ahmed et al. (Figure 3.38), who reported that the separation bubble reattached to the slant surface. However, the Re of flow visualisations was reduced and discrepancies could be due to Reynolds Numbers effects.

4.5 Conclusion

Overall, the numerical simulations compare reasonably well with current numerical simulations with the essential flow structures captured. The numerical streamlines appear to be consistent with experimental streak lines except for the lack of the negative bifurcation line at $\alpha=30^\circ$.

At $\alpha=25^\circ$, the simulation separation bubble on the slant surface reattached, but was larger than the separation bubble observed in experiments. It appears that the C-pillar vortex has a reduced U/U_∞ along the vortex centreline which was not found in the experiments. Downstream of the body, the recirculation region was stronger. The pressure distribution on the rear portion of the Ahmed body is similar with the C-pillar vortex footprint clearly visible on the slant surface. However, the suction peak is not as strong.

The separated region for $\alpha=35^\circ$ compared better with the experimental data. The velocity profiles over the slant surface have the same inflection point (Figure 4.25) with the separation bubble behind the body slightly smaller. The spanwise velocity field is not as uniform as the experiments. The C_p on the rear surface appears to be stronger in the simulations, which could be an effect of the symmetry boundary condition. However, the $\Delta C_p=0.2$ for $\alpha=35^\circ$ emphasises minor differences in C_p , which are not evident for $\alpha=25^\circ$.

Chapter 5 Effect of Aspect Ratio

5.1 Introduction

The effect of vehicle aspect ratio (the representative ratio between the vehicle width and other geometric parameters) on the wake structures and drag of a vehicle has not been previously investigated in detail. This is somewhat due to the fact that vehicle width is dictated by road lane width regulations. However, subtle geometry changes have been shown to have a significant effect on the wake structures of automotive type geometries in ground effect [5].

Hoerner [78] examined the effects of height-to-span ratio of rectangular flat plates and cylinders at $Re=1 \times 10^5$. Above a critical ratio (height/span=0.6), the C_D was not affected by the change in aspect ratio. However, below the critical ratio, the increased three-dimensionality of the wake increased C_D dramatically.

Kurtz [79] undertook a limited study of the effect of vehicle aspect ratio for the design of electric and hybrid vehicles, with rounded corners and a blunt trailing edge. For the two ground clearances examined, for $0.6 \leq \text{height/width} \leq 0.9$, there was an increase in C_D . For higher ground clearances, it was found that there was linear increase in C_D with aspect ratio while for the lower ground clearances, there was a quadratic increase in C_D with AR.

Williams et al. [80] examined the effect of vehicle aspect ratio (height/width) on geometries similar to commercial vans by increasing the height of the body. For experiments on smooth radiused rectangular boxes with the same frontal area, it was found that the C_D was essentially constant for all geometries considered. However, for geometries with rough under-bodies, the C_D was higher for lower aspect ratio bodies, which had a larger under-body surface area. For all geometries considered, the bodies were essentially square-back vehicles with no slant surface.

Hucho [10] considered the effect of vehicle aspect ratio when comparing vehicles to finite length aircraft wings to determine the sources of drag. On aircraft wings, drag can be broken down into components of profile drag and induced drag from the wing tip vortices. The theory is only valid for high aspect ratio wings where the two components can be considered independently. Due to small aspect ratios of vehicles

compared with aircraft wings, Hucho concluded that it is not possible to isolate the effect of the vortex field.

Examination of aircraft wings by Abbot and Downhoff [81], for different aspect ratios ($\text{span}^2/\text{wing area}$), found that the maximum C_L for a given angle of attack increases with aspect ratio. For aspect ratios greater than 6, there is less variation of maximum C_L with AR. High-aspect ratio wings were found to have higher lift-curve slopes and lower C_D than wings of low aspect ratio, indicating a better lift/drag (LD) ratio for high-aspect ratio wings.

To determine the effect of the vehicle Aspect Ratio (AR), the vehicle width was modified. The Aspect Ratio is defined in Eqn 3.1 as:

$$AR = \frac{\text{Body Width}}{\text{Slant Length}} \quad \text{Eqn 5.1}$$

The slant length is used as the parameter to non-dimensionalise the aspect ratio as opposed to using the body height or body length. The C-pillar vortices are considered the critical flow structures. If the slant surface could be considered analogous to an aircraft wing at varying Angle of Attack, then the slant length would be analogous to the wing chord.

The vehicle AR was varied to determine how the overall shape of the body in ground effect affected the body forces. Of particular interest was the interaction between the C-pillar vortices on each side of vehicle and their influence on separation on the slant surface. This could affect the critical slant angle (α_c) where the wake fully separates from the slant surface. If there is a large variation in α_c for different AR, this could indicate that there are other factors affecting α_c beside the slant angle that have not been investigated.

For the parameter space study, the AR was varied between AR=1 to AR=2.5 which equates to a body width of 0.222 and 0.555 respectively if considering the full size Ahmed body used in experiments. The standard Ahmed body used in previous experiments is AR=1.75 (body width=0.389). For each AR, the slant angle was varied between $\alpha=1^\circ$ to $\alpha=40^\circ$. All simulations were undertaken at $Re=2.86 \times 10^6$.

In the following sections, because of the large number of aspect ratios investigated, the parameter space study of the forces will be broken into two sections. The first considers low aspect ratio bodies ($AR < 1.75$), defined as bodies narrower

than the standard Ahmed body, and the second is for high aspect ratio bodies ($AR > 1.75$). Body forces will be examined for different regions of the Ahmed body and then correlated with the wake structures.

5.2 Body forces

The pressure and viscous forces on different regions of the Ahmed body are examined for varying body aspect ratios. The overall forces, and forces on the rear sections of the model, will be examined as the AR and α are varied.

5.2.1 Low AR

5.2.1.1 Overall Forces

The overall C_D and C_L for the low AR bodies are shown in Figure 5.1. The profiles for all AR are similar since the C_D and C_L are non-dimensionalised against the cross-sectional area of the model. The C_D and C_L do not show that the overall drag and lift increase with increasing AR. Often the $C_D A$ ($C_D \times$ cross sectional area) is used for comparison of different geometries to gauge their effectiveness in overcoming aerodynamic drag[82] for comparison between dissimilar geometries. However, due to the similarity of all geometries examined, C_D is a likely to be a good indicator of the change in the wake flow structures.

In Section 4.2.1, the minimum overall C_D on the body for $AR=1.75$, occurred at $\alpha \approx 10-12^\circ$. A similar slant angle is evident for bodies with $AR < 1.75$, where minimum C_D occurs at $\alpha \approx 10^\circ$ (no data point at $\alpha=12^\circ$). However, below $AR < 1.25$, the C_D is almost constant between $5^\circ < \alpha < 10^\circ$, with the location of minimum drag less distinct than for higher aspect ratios. For $AR=1.0$, the critical slant angle (α_c), where the C_D is maximum occurs at $\alpha_c=34^\circ$ before a significant decrease in C_D . Above the critical slant angle, there is a corresponding decrease in C_L for $\alpha > \alpha_c$.

When the AR is increased from $AR=1.0$, the α_c for a given AR decreases. At $AR=1.1$, α_c is reduced to $\alpha_c=33^\circ$. At $AR=1.25$, α_c is reduced further to $\alpha_c=32^\circ$. For $1.25 \geq AR \geq 1.5$, maximum C_D occurs at $\alpha_c=32^\circ$, while for $1.6 \geq AR \geq 1.75$, the critical slant angle is reduced to $\alpha_c=30^\circ$. Also evident is that for $\alpha > \alpha_c$, where there is a large separated region in the wake, the C_D is higher for the lower AR bodies. The change in C_D at the critical slant angle is greater with increasing AR. This indicates that for lower AR bodies, the wake structures are stronger since the drag structures are

normalised by the cross-sectional area. This could possibly be due to the shear layers on the sides of the body having a more significant influence on the rear separation bubble for the narrower models.

The distinction between the different locations of α_c can be made clearer by plotting profiles of C_L , as opposed to C_D , since there is a significant decrease in lift at α_c . As was found for $AR=1.75$ (Section 4.2.1), for $0^\circ \geq \alpha \geq 15^\circ$, there is a linear increase in C_L , which plateaus until α_c is reached. For increasing AR , the C_L decreases slightly for increasing AR .

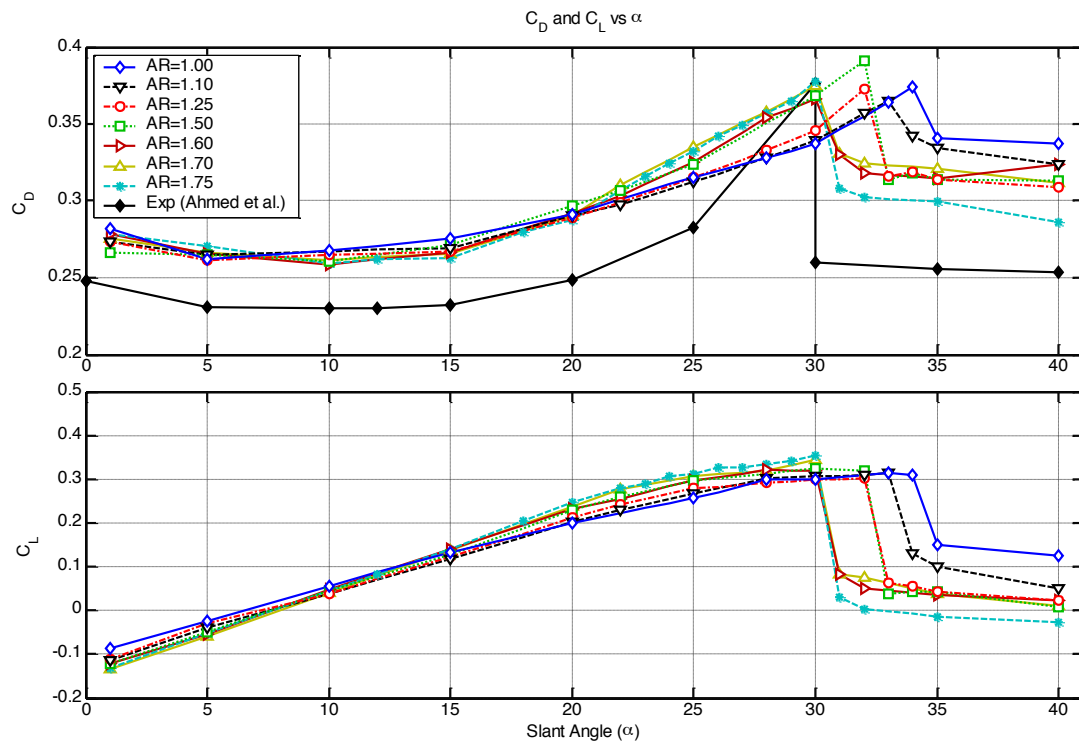


Figure 5.1 The total C_D and C_L for low AR Ahmed Bodies. Profiles of C_D and C_L vs. α are shown for $1.0 \leq AR \leq 1.75$. Experimental C_D data from Ahmed et al. [5] is included for comparison. Markers with solid fill indicate measurements from experimental data.

5.2.1.2 Lift to drag ratio

The LD ratio for low AR bodies is illustrated in Figure 5.2. Decreasing the AR does not affect the LD ratio significantly with the maximum LD ≈ 0.9 . The LD ratio decreases with AR for $\alpha \leq 10^\circ$, while for $10^\circ < \alpha \leq \alpha_c$, the LD ratio increases with AR due to the increase in lift. The LD ratio is higher for lower AR bodies since C_D decreases with AR for $\alpha > \alpha_c$. For $AR \leq 1.5$, the peak LD ratio does not occur at α_c , but occurs slightly lower, at $25^\circ \geq \alpha \geq 28^\circ$. This indicates that near α_c , the C_L is increasing at a higher rate than C_D as the slant angles increases.

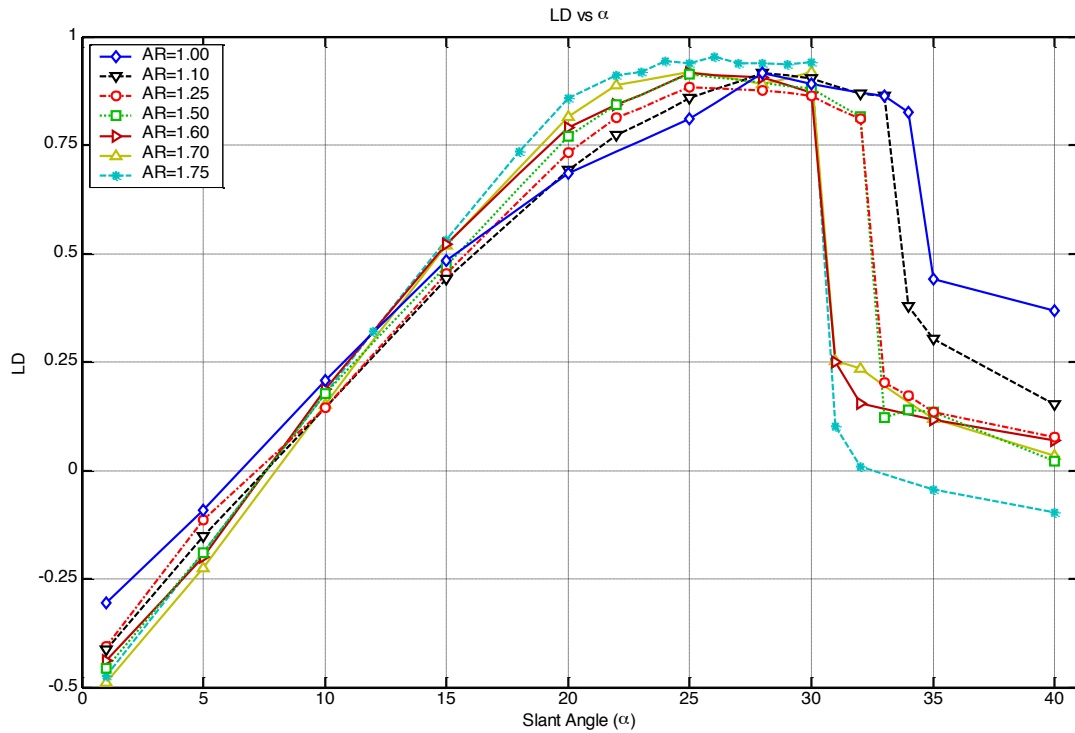


Figure 5.2 Profiles of the Lift to Drag (LD) ratio vs. α for $1.0 \leq AR \leq 1.75$. Markers with solid fill indicate measurements from experimental data.

5.2.1.3 Breakdown of surface

Figure 5.3 illustrates C_D profiles for the rear and slant surfaces, and C_L for the slant surface for $AR \leq 1.75$. As was seen with the standard Ahmed body, the C_D from the front and side surface were relatively constant for all α and are therefore not shown in the figure, in order to decrease clutter.

The overall profiles for low AR are similar to $AR=1.75$, which were discussed in Section 4.2.3. Up until $\alpha=\alpha_c$, C_D on the rear surface of the Ahmed body decreases for increasing α , due to the decreasing surface area on the rear surface levelling off near α_c . Above α_c , there is a net increase in the C_D on the rear surfaces of the body even though the surface area has reduced further. For the lower AR bodies, there is considerably less drag on the rear surfaces near α_c .

The sharp decrease in C_D at α_c in Figure 5.1 is due to a reduced C_D on the slant surface of the model. The change in C_D (ΔC_D) at the critical slant angle on the slant surface increases with AR. The ΔC_D in Figure 5.1 at $\alpha=\alpha_c$ is primarily due to the large ΔC_D on the slant surface but is offset by the increased ΔC_D on the rear surface. The slant angle in which the C_D profile starts to plateau decreases with AR. For $AR \leq$

1.1, the C_D on the rear surface is level for $30^\circ \leq \alpha \leq 32^\circ$, whereas for $1.6 \leq AR \leq 1.75$, the C_D is constant at $22^\circ \leq \alpha \leq 30^\circ$.

On the slant surface, there is a linear increase in C_L for all AR between $1^\circ < \alpha < 15^\circ$ in Region I (Section 4.3.2). Similar to $AR=1.75$, the linear increase in C_L with α no longer holds as $\alpha \rightarrow \alpha_c$. For the lower AR bodies investigated ($AR \leq 1.25$), the change in the drag profile between Region I and Region II is not as distinct for larger AR bodies ($1.25 > AR \geq 1.75$), indicating that the slant separation bubble on the slant surface has a smaller influence on the narrower bodies.

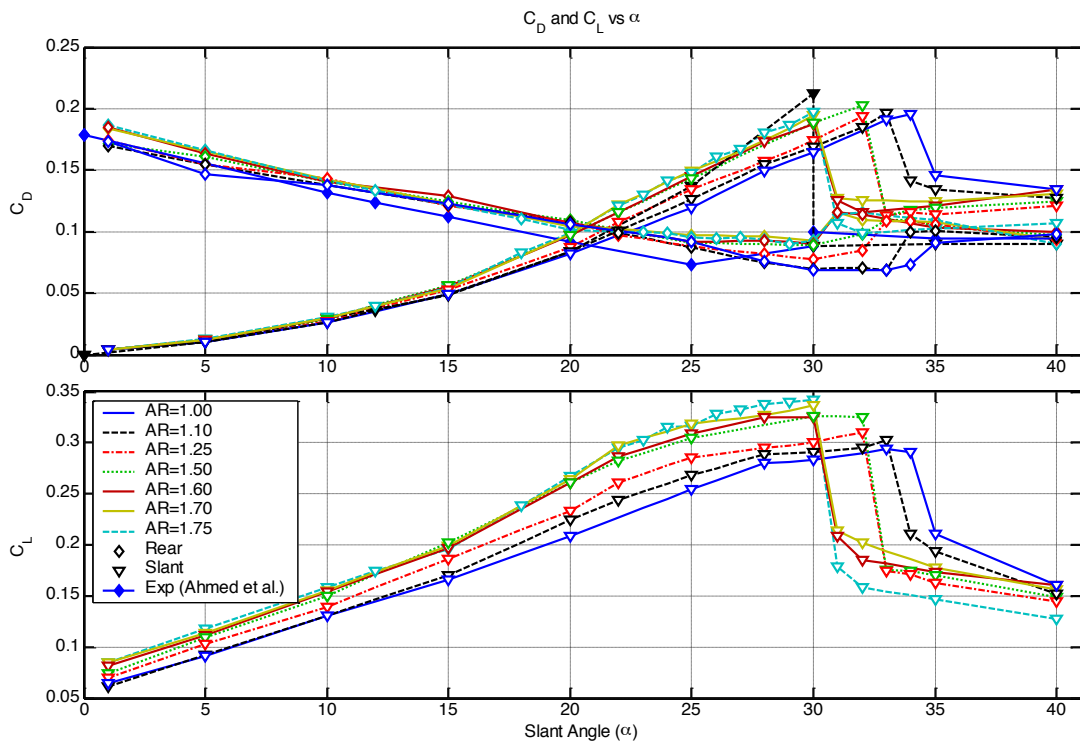


Figure 5.3 Profiles of the C_D and C_L on the slant and rear surface on the Ahmed body for Low AR bodies. Profiles of C_D and C_L vs. α are shown for $1.0 \leq AR \leq 1.75$. Markers with solid fill indicate measurements from experimental data.

5.2.1.4 C_N (slant surface)

The coefficient of normal force (C_N) on the slant surface is plotted in Figure 5.4. This helps to isolate the (effect of the) change in wake structures from the geometric changes to the body. The C_N for $\alpha < \alpha_c$ increases with AR, while above $\alpha > \alpha_c$, the C_N decreases with AR as was found with the C_L in Figure 5.3. In region I (Section 4.3.2) there is a linear increase of C_N with α . For a given slant angle, the C_N varies by $C_N \approx 0.025$ as the AR increases from $AR=1.0$ up to $AR=1.75$. The increased AR leads to an increase in C_N , since a higher portion of the slant surface is creating lift without the influence of the C-pillar vortex.

For $\alpha > 15^\circ$, a more pronounced non-linear relationship between C_N and α occurs as the AR is increased, indicating that more complex structures occur on the slant surface up to $AR=1.75$. At $AR=1.5$, α_c changes from $\alpha_c=32^\circ$ for $AR=1.5$, to $\alpha_c=30^\circ$ for $AR > 1.5$. At this transition point, the C_N for $\alpha=30^\circ$, $AR=1.5$ coincides with C_N for $\alpha=30^\circ$, $AR=1.6$. The C_N profiles for $AR=1.5$ and $AR=1.6$ are similar except for the location of α_c , indicating that a slight change in AR has a considerable effect on α_c .

In Section 4.2.4, C_N was used to define the different types of flow regimes on the slant surface. In Figure 5.4, the distinction between Region I and Region II occurs at $\alpha \approx 15^\circ$ and does not vary considerably with AR. However, not all aspect ratios show that the change in the gradient occurs at $\alpha=15^\circ$, with some AR ($AR=1.25$, 1.5) indicating a change in gradient at $\alpha < 15^\circ$. The transition to Region III from Region II does appear to change with AR. The transition point (marked with a “+”) occurs at higher slant angle for decreasing AR with the transition location decreasing from $\alpha=28^\circ$ at $AR=1.0$ down to $\alpha=22^\circ$ at $AR=1.25$. The transition point between Region II and Region III remains constant at $\alpha=22^\circ$ for $AR \geq 1.25$.

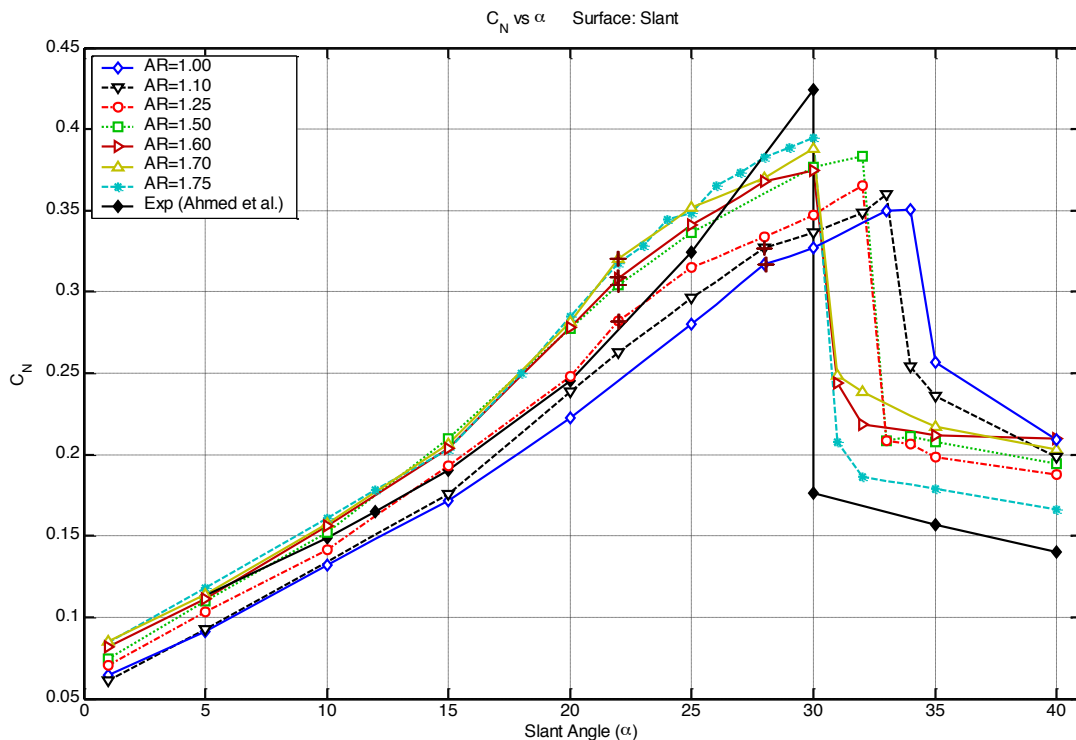


Figure 5.4 The C_N of the slant surface for low AR bodies. Profiles of C_N vs. α are shown for $1.0 \leq AR \leq 1.75$. The transition between Region II and Region III is indicated with +. Markers with solid fill indicate measurements from experimental data.

5.2.2 High AR

5.2.2.1 Overall Forces

The C_D and C_L of the entire body for the high aspect ratio bodies ($AR > 1.75$) is shown in Figure 5.5. The location of minimum C_D occurs at $\alpha = 10^\circ$ and is more distinctive than those for the low AR bodies (no simulations were undertaken at $\alpha = 12^\circ$). For $AR \geq 2.0$, the minimum C_D increases from $C_{D=0.265}$ to $C_{D=0.275}$, but remains at $\alpha = 10^\circ$. The location of α_c , which occurs at $\alpha = 30^\circ$ for $AR = 1.75$ reduces as the body becomes wider, continuing the trend found with low AR bodies. For $1.8 \leq AR < 2.0$, α_c reduces from $\alpha_c = 30^\circ$ to $\alpha_c = 29^\circ$. For $AR \geq 2.25$, α_c again reduces to $\alpha = 25^\circ$, leading to a considerably different C_D profile with the peak C_D reduced by $\Delta C_D \approx 0.035$ from $AR = 1.75$. The drag profile above the critical slant angle for the high AR bodies does not vary smoothly with further increases with α . This indicates that although the flow has separated from the slant surface, there are sizeable fluctuations causing the iteration-averaged wake to have considerable uncertainty. However, it does appear that the C_D for $\alpha > \alpha_c$ increases with AR, in contrast to low AR bodies.

The reduction of α_c as the AR increases is clearer with the profiles of C_L at different AR shown in Figure 5.5. Apart for $AR \geq 2.25$, the C_L profile $\alpha < \alpha_c$ does not vary considerably with AR, with the maximum $C_L \approx 0.325$. The C_L for $AR \geq 2.25$ increases with AR, with the peak lift of $C_L \approx 0.4$ for $AR = 2.5$, $\alpha_c \approx 25^\circ$. Past α_c , the C_L slowly decreases with neutral or negative lift on the body. Since the strong lift force on the slant surface is not present at $\alpha > \alpha_c$, down force is created from the Venturi effect of the body in ground effect. As was found in Section 4.2.1, the minimum drag at $\alpha = 12^\circ$, is mainly due to a geometric effect of the decreasing rear base surface area.

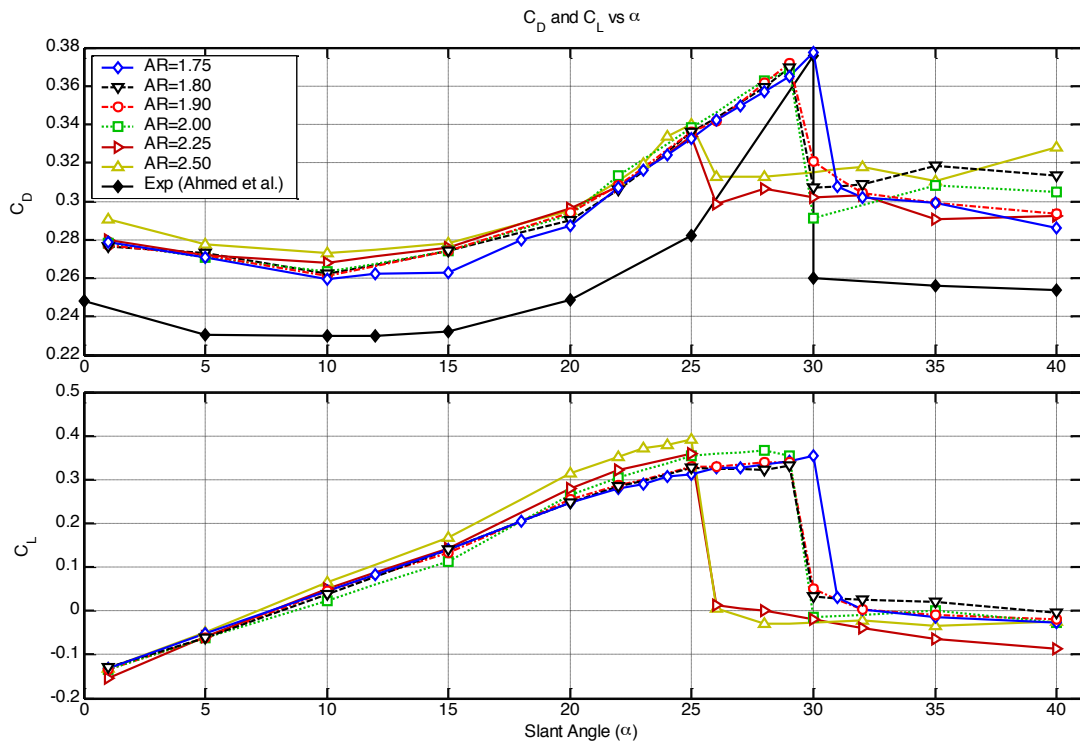


Figure 5.5 The total C_D and C_L for the high AR Ahmed bodies. Profiles of C_D and C_L vs. α are shown for $1.75 < AR \leq 2.5$. Experimental C_D data from Ahmed et al. [5] is included for comparison. Markers with solid fill indicate measurements from experimental data.

5.2.2.2 Lift to drag ratio

The LD ratio for the high aspect ratio bodies in Figure 5.6 asymptotes as $\alpha \rightarrow \alpha_c$. The LD ratio for $AR > 1.75$ does not vary much except for $AR \geq 2.25$, where the LD increases due to the increased lift on the bodies. The peak LD ratio does not coincide with α_c , since the lift asymptotes near α_c while C_D increases up to α_c . This causes the peak C_D for a given AR to occur at $2^\circ - 4^\circ$ less than α_c .

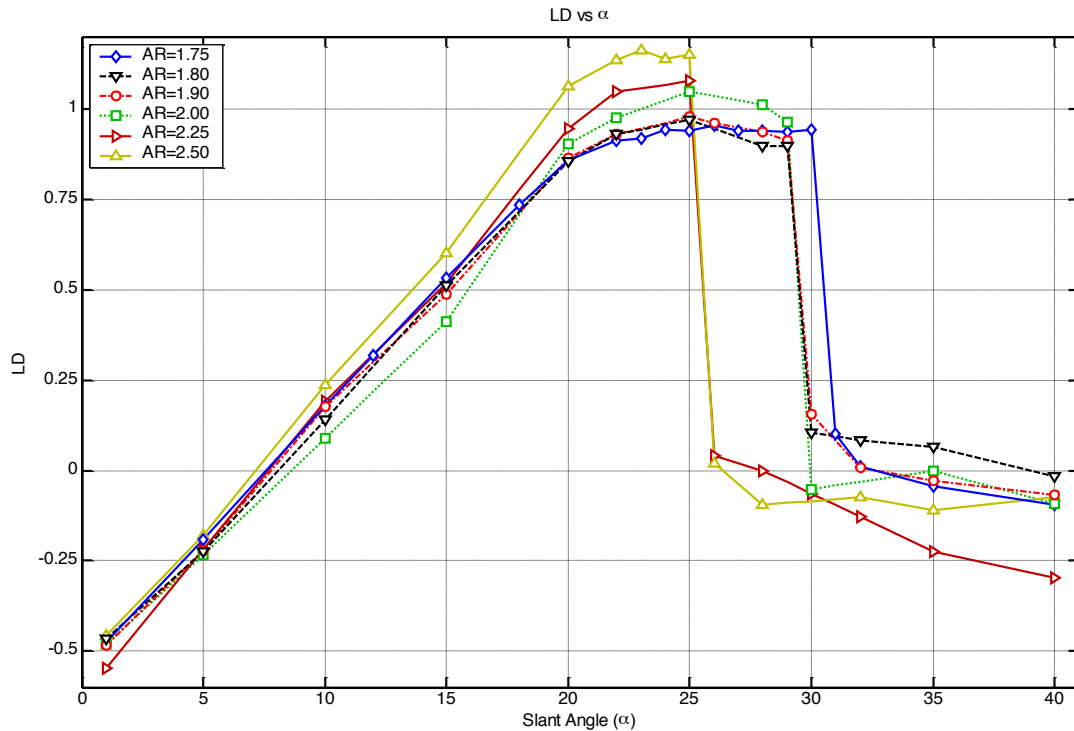


Figure 5.6 Profiles of the Lift to Drag (LD) ratio vs. α for $1.75 \leq AR \leq 2.5$.

5.2.2.3 Break down of forces from different surfaces

Figure 5.3 shows the C_D for the rear and slant surface, and the C_L for the slant surface. Similarly to $AR=1.75$, the C_D on the rear surface decreases as α increases up to α_c . Above α_c , the C_D on rear surfaces also increases as the wake structure changes to a large separated wake structure. For $AR \geq 2.25$ at $\alpha=25^\circ$, there is a significant increase in C_D of the same order of magnitude as the decrease in C_D on the slant surface. As a result, the overall decrease in C_D at α_c is not as significant as for $AR=1.75$.

The C_D on the slant surface for all AR increases with α in a fashion similar to $AR=1.75$ up until α_c , except for the location of α_c . However, the C_D does increase slightly with AR for a given slant angle, especially in Region II and Region III.

The profiles of C_L on the slant surface are similar to those found with the overall C_L (Figure 5.5). For $\alpha < \alpha_c$, the C_L increases slightly as AR increases but is not considerable. The decrease in C_L for $\alpha > \alpha_c$ is due to the geometric effects of increasing α which decreases the contribution of lift from the slant surface. The variations on C_D at $\alpha > \alpha_c$ in Figure 5.5 is not found in C_L , since there is no lift force

on the rear surface of the model and the C_L is predominately due to the variation of lift on the slant surface.

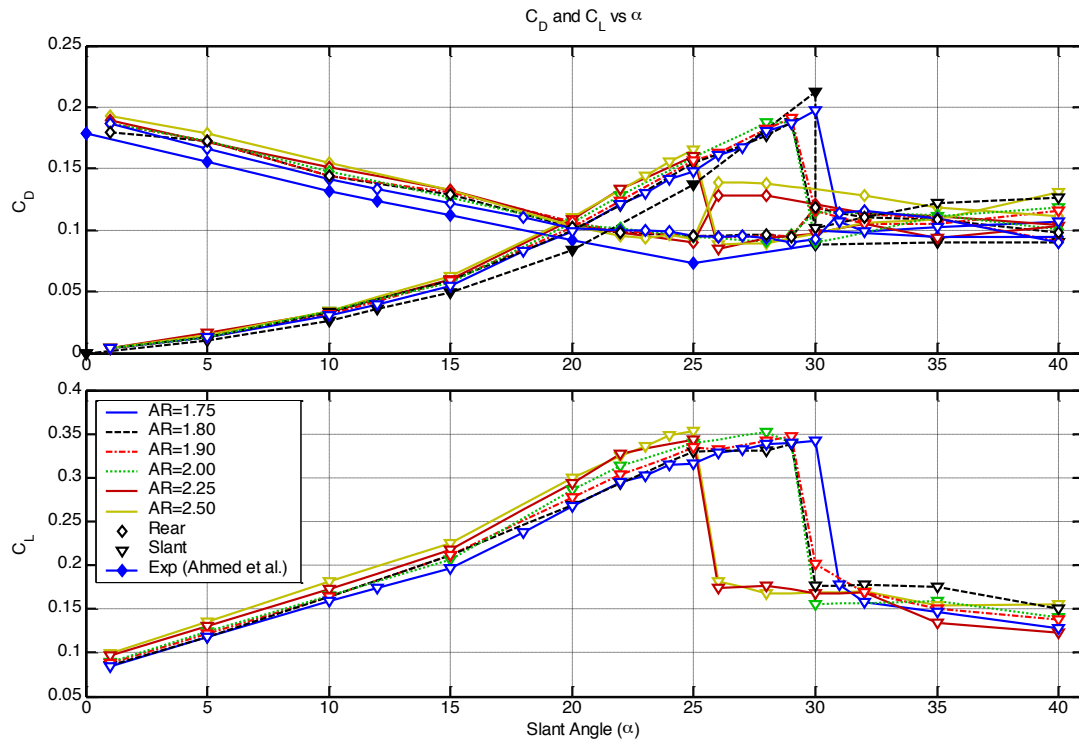


Figure 5.7 Profiles of the C_D and C_L on the slant and rear surface on the Ahmed body for high AR bodies. Profiles of C_D and C_L vs. α are shown for $1.75 \leq AR \leq 2.5$. Markers with solid fill indicate measurements from experimental data.

5.2.2.4 C_N slant

The C_N of the slant surface is shown in Figure 5.8 for high AR bodies. For $\alpha \leq 15^\circ$, there is an approximately linear relationship between C_N and α denoting Region I. In Region II, at $15^\circ \leq \alpha \leq 22^\circ$, the gradient of the C_N profile increases but still remains approximately linear. Above $\alpha=22^\circ$, the linear relationship no longer holds with the C_N still increasing up to α_c , where a significant decrease in normal force occurs at α_c . There is no significant change in C_N for $1.8 \leq AR \leq 1.9$, but above $AR \geq 2.0$, C_N increases for all $\alpha < \alpha_c$.

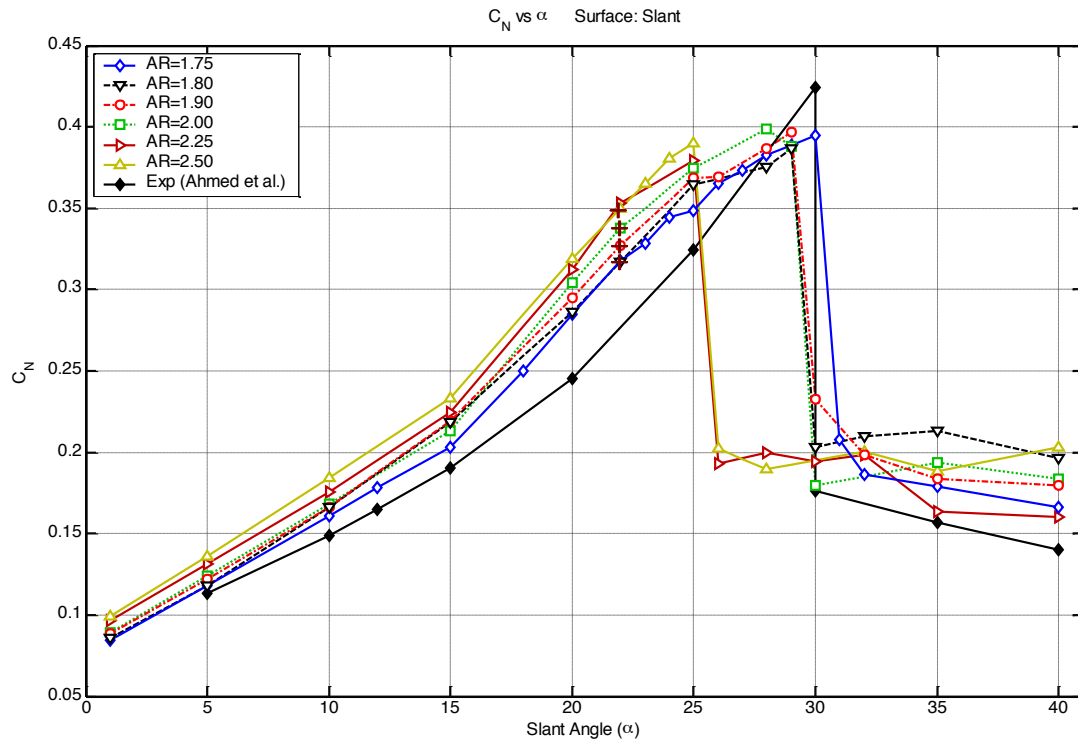


Figure 5.8 The C_N of the slant surface for High AR bodies. Profiles of C_N vs. α are shown for $1.75 \leq AR \leq 2.5$. The transition between Region II and Region III is indicated with +. Markers with solid fill indicate measurements from experimental data.

Due to the large change in α_c between $2.00 < AR < 2.25$, two additional aspect ratios ($AR=2.10, 2.20$) were investigated to determine how the α_c changes in this region. Figure 5.9 shows C_N for $22^\circ \leq \alpha \leq 32^\circ$ for the high AR bodies. Contrary to what is shown in Figure 5.8, above $AR=2.00$ there is not a dramatic drop in α_c to $\alpha_c=25^\circ$, but instead α_c decreases to $\alpha_c=28^\circ$ at $AR=2.10$ and then another reduction to $\alpha_c=26^\circ$ at $AR=2.20$. The large change of $\Delta\alpha_c$ of 4° in Figure 5.9 is due to the large change in AR.

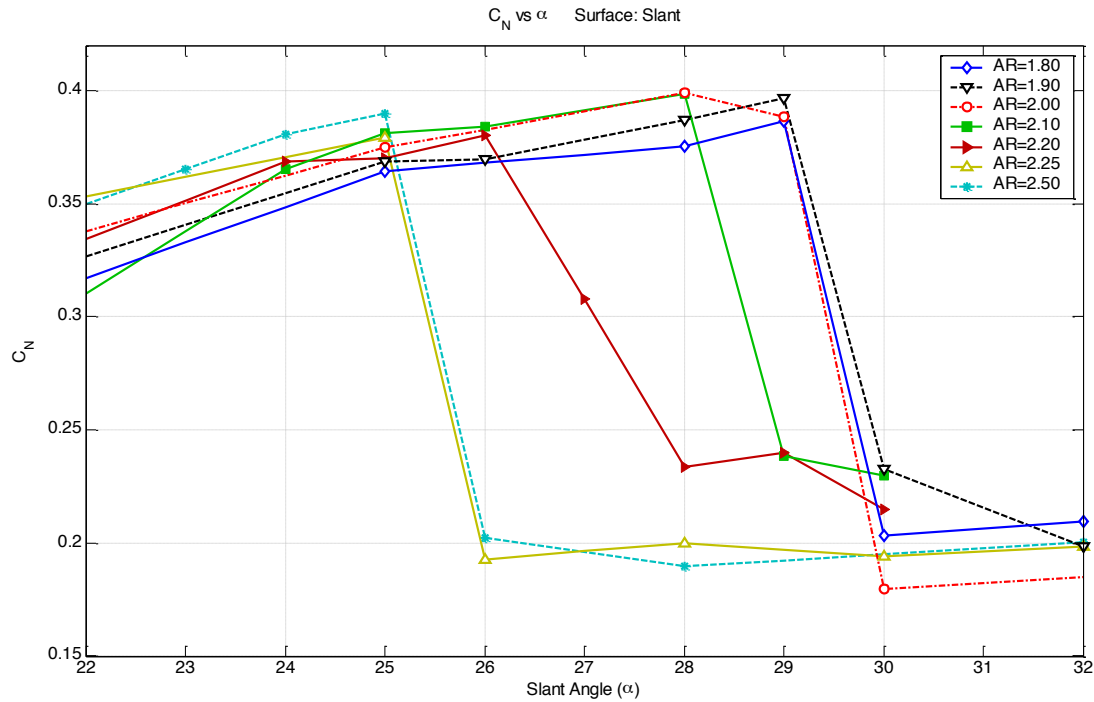


Figure 5.9 The C_N of the slant surface for high AR bodies with $AR=2.1$ and $AR=2.2$ added. Profiles of C_N vs. α are shown for $1.8 \leq AR \leq 2.5$. The sharp transition of α_c above $AR=2.0$ appears to be a gradual change to $\alpha_c=25^\circ$ at $AR=2.25$.

5.2.3 Effect of Aspect Ratio

In this section, the effect of AR on different components of the drag and lift forces from different regions of the Ahmed body will be examined.

Figure 5.10 shows contours of C_D for the entire body for all aspect ratios investigated. Contours indicate that the lowest C_D for a given AR occurs at $\alpha \approx 10^\circ$, and for the lower aspect ratios ($AR \leq 1.25$), changes in α do not result in a significant change in C_D for $5^\circ \leq \alpha \leq 15^\circ$. Also evident is the optimum AR and slant angle for minimum C_D for a given frontal area, which occurs at $\alpha=12^\circ$, $1.5 \geq AR \geq 1.75$.

Clearly visible is the ridge of increasing C_D as $\alpha \rightarrow \alpha_c$ for a given AR. For the aspect ratio range investigated, α_c decreases from $\alpha_c=34^\circ$ at $AR=1.0$ to $\alpha_c=25^\circ$ at $AR=2.5$. Generally, the C_D at α_c decreases with increasing AR. However, for situations where α_c is constant for a change in AR, the C_D increases with AR. This indicates that the C_D in Region III increases with AR for a given slant angle, but increasing AR also causes α_c to reduce.

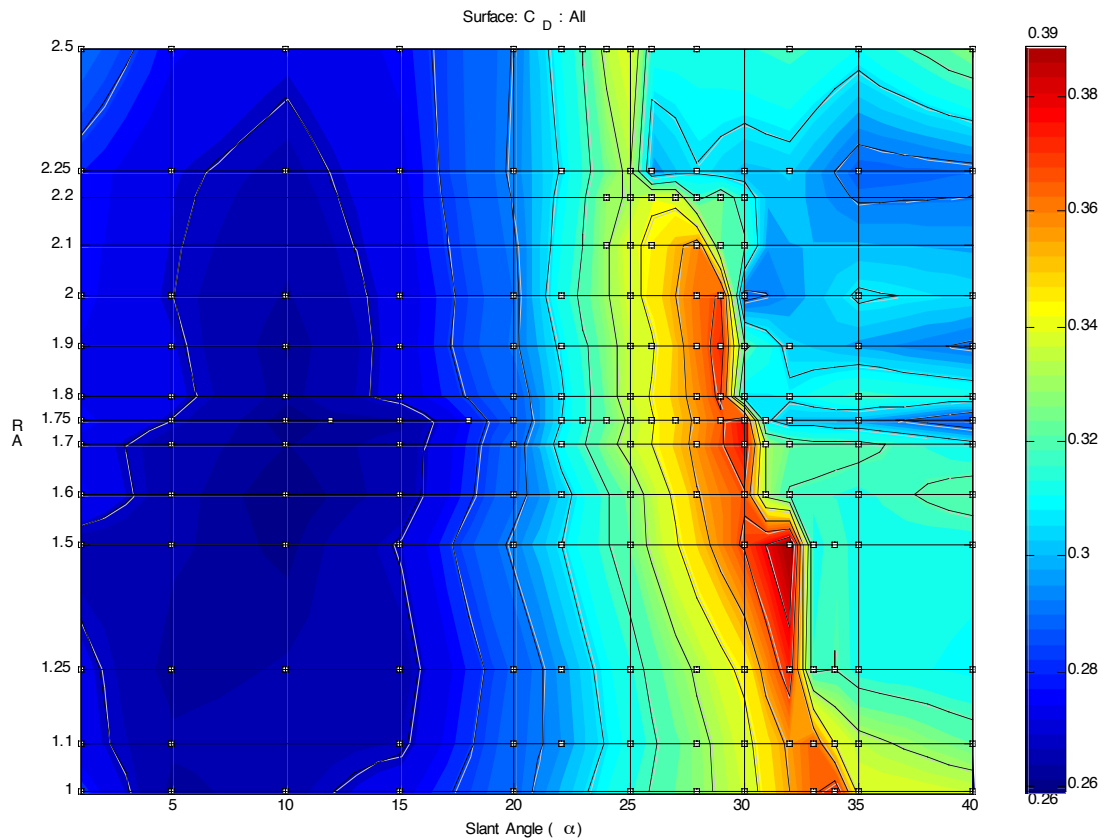


Figure 5.10 Contours of the total C_D on the entire Ahmed body for $1.0 < AR < 2.5$, $1 \leq \alpha \leq 40^\circ$. Dots indicate the locations of data points.

It is also of interest to show how the forces change with AR without normalising the drag with the cross-sectional area. Figure 5.11 shows the drag calculated for the Ahmed body at $Re=2.86 \times 10^6$ (40m/s inlet velocity at normal scale). The AR has a greater influence on the drag compared with α due to the increased surface area of the model with increasing AR. However, the effect of α on the drag is still evident. The maximum drag occurs for $AR=2.5$, $\alpha=25^\circ$, with the minimum drag occurring at $AR=1.0$, $5^\circ \leq \alpha \leq 15^\circ$ where the cross-sectional area is smallest. In region I, where the flow is attached to the slant surface, there is a linear increase in drag with AR, which is not continued to higher slant angles. In Region IV, there is also a linear increase in drag with a separated wake. However, the increase is not as consistent as for Region I.

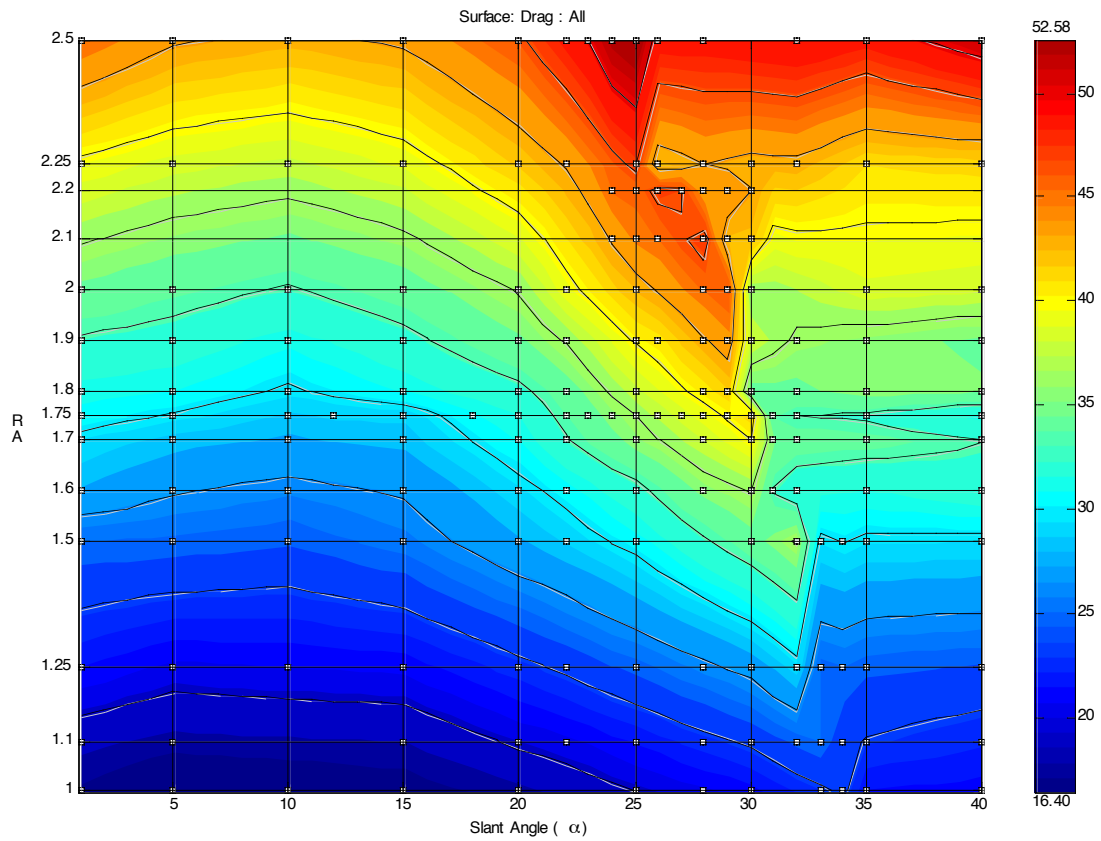


Figure 5.11 Contours of the total drag on the entire Ahmed body for $1.0 < AR < 2.5$, $1 \leq \alpha \leq 40^\circ$. Dots indicate the locations of data points.

The Overall C_L on the body in Figure 5.12 indicates that apart from the change of the critical slant angle, the C_L does not vary significantly with aspect ratio. In region III, the C_L increases with AR but not significantly.

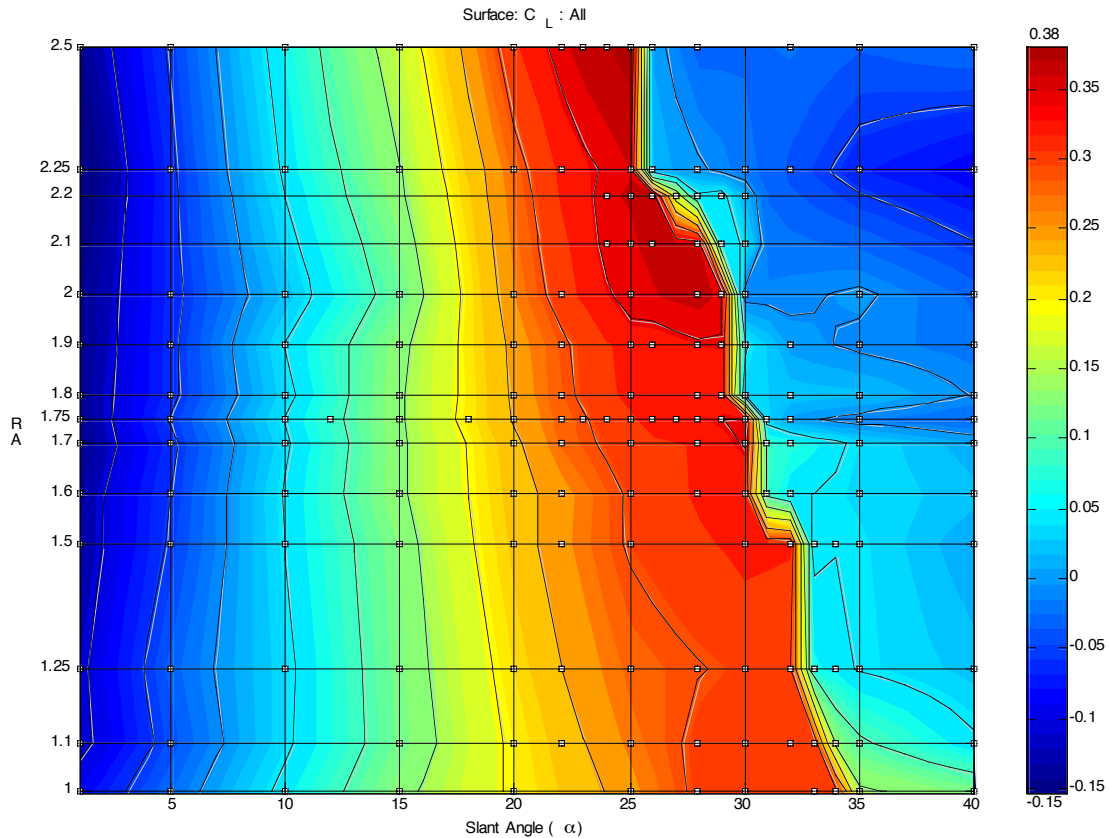


Figure 5.12 Contours of the total C_L on the entire Ahmed body for $1.0 < AR < 2.5$, $1 \leq \alpha \leq 40^\circ$. Dots indicate the locations of data points.

The C_N from the slant surface in Figure 5.13 has a very similar structure to the C_L in Figure 5.12. The location of α_c appears to decrease approximately linearly with AR. However, due to the sudden decreases over a small range of aspect ratios, it is unlikely to be such a simple relationship. It is more likely to be a critical parameter in the flow structures on the slant surface that causes the decrease in α_c , since the most significant change to the flow structure occurs adjacent to the slant surface.

Unlike the C_L in Region I, the C_N is not constant for a given slant angle. The contours in Figure 5.13 show that for a given α , the C_N increases. This results in a higher C_N on the slant surface with an increasing α when the AR increases. Due to the decrease in C_N at α_c , this results in the highest C_N occurring for $1.9 \leq AR \leq 2.1$, just before complete separation, as opposed to the strongest C_N occurring at the highest AR. Due to the variation in C_N at $\alpha = \alpha_c$, this indicates that the transition is not due to a critical normal force that causes the transition to a large separated wake.

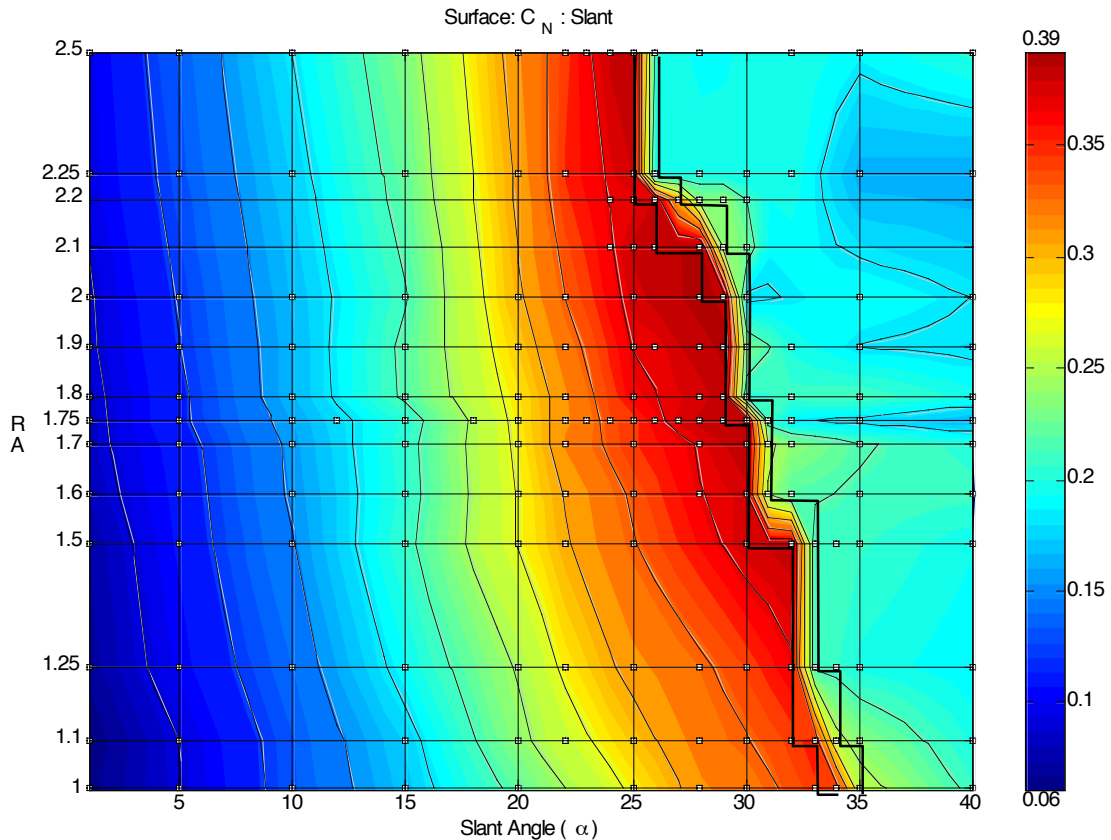


Figure 5.13 Contours of the total C_N on the slant surface of the Ahmed body for $1.0 < AR < 2.5$, $1 \leq \alpha \leq 40^\circ$. Dots indicate the locations of data points. Black lines indicate the transition from Region III to Region IV.

5.3 Wake Structures

5.3.1 Low AR bodies

The changes in the wake structure are examined for low aspect ratio vehicles, with AR varied from $1.0 \leq AR \leq 1.75$. To examine the wake structures for the low AR bodies, $AR=1.1$ is used here as a typical example of how the wake structures change with AR.

5.3.1.1 Region I

The flow structure for $\alpha=5^\circ$ shown in Figure 5.14 indicates that the underlying flow structure for $AR=1.1$ is not significantly different to that for $AR=1.75$. A large separation bubble exists behind the body, with a large region of reversed flow. The centres of recirculation on the body centreline are located close to the top and bottom shear layers emanating from the body.

On the slant surface, the flow is attached to the slant surface across the entire width. The streak lines on the slant surface indicate that the small α creates a vortex.

However, the streamlines released from the slant surface indicate that the C-pillar vortex does not form past the end of the body. At higher slant angles, the C-pillar vortex forms in Region I.

Figure 5.14 Orthographic projection of wake structures behind the Ahmed body for AR=1.1 $\alpha=5^\circ$. Stream slices are contoured by velocity magnitude/ U , overlaid with streak lines on each plane. Path lines are released from one side edge of the slant surface. The separated region is outlined with an iso-surface of $U/U_\infty=0$, coloured by velocity magnitude/ U .

The path lines in Figure 5.15 for $\alpha=1^\circ$ show the structure of the rear separation bubble clearly. The path lines released from the slant surface are entrained into the rear separation bubble. Inside the toroidal vortex structure, the streamlines are fed from the top recirculation zone to the bottom recirculation zone. The view from the rear of the body shows how the top spanwise vortex is linked to the bottom spanwise vortex via the side recirculation regions.

Figure 5.15 Path lines released from the slant surface coloured by Z-location of release point for AR=1.1, $\alpha=1^\circ$. Path lines indicate the structure of the torroidal vortex structure on rear region of body.

5.3.1.2 Region II

For AR=1.1, $\alpha=15^\circ$, a region of separated flow exists on the slant surface. As can be seen in Figure 5.16, the C-pillar vortex has formed on the edge and the flow remains attached to the sides of the slant surface. The separated region on the slant surface only occurs on the central portion and reattaches on the centreline of the body before the end of the slant surface. The streak lines on the slant surface indicate two recirculation regions inside the separation bubble. The rear separation region has reduced significantly in size behind the model, with the top recirculation region dominating the flow as opposed to Region I where the top and bottom recirculation regions are approximately equal.

Figure 5.16 Orthographic projection of wake structures behind the Ahmed body for AR=1.1, $\alpha=15^\circ$. Stream-slices are contoured by velocity magnitude/ U , overlaid with streak lines on each plane. Path lines are released from one side edge of the slant surface. The separated region is outlined with an iso-surface of $U/U_\infty=0$ coloured by velocity magnitude/ U .

Path lines released from the slant surface in Figure 5.17 show the size and shape of the slant separation bubble. Streamlines indicate that the flow is entrained mainly from the sides of the bubble and recirculates inside until it is ejected along the centreline. Downstream of the body, the C-pillar vortex dissipates in the wake and two counter-rotating vortices form from the downwash on the centreline.

Figure 5.17 Orthographic projection of wake structures behind the Ahmed body for AR=1.1, $\alpha=20^\circ$. Stream slices are contoured by velocity magnitude/ U , overlaid with streak lines on each

plane. Streamlines are released from one side edge of the slant surface. The separated region is outlined with an iso-surface of $U/U_\infty=0$ coloured by velocity magnitude/ U_∞ .

5.3.1.3 Region III

In Region III, there is separation from the entire top edge of the slant surface with the C-pillar vortex reattaching the flow on the sides, compared with Region II where only a small separation bubble exists. For $AR=1.1$, $\alpha=25^\circ$ in Figure 5.18, the separation bubble on the slant surface reattaches on the body centreline.

Figure 5.18 Orthographic projection of wake structures behind the Ahmed body for $AR=1.1$ $\alpha=25^\circ$. Stream slices are contoured by velocity magnitude/ U_∞ overlaid with streak lines on each plane. Path lines are released from one side edge of the slant surface. The separated region is outlined with an iso-surface of $U/U_\infty=0$ coloured by velocity magnitude/ U_∞ .

The streamlines released from the slant surface for $AR=1.2$, $\alpha=25^\circ$ in Figure 5.19 show the difference in the slant separation bubble. After the flow is entrained in the separation bubble, it progresses along the core of the spanwise vortex in the slant separation bubble until flow is ejected into the top of the C-pillar vortex. The dark blue streamline, which is released near the body centreline is present in the C-pillar. In contrast to Region II, there does not appear to be any flow ejected from the slant separation bubble on the body centreline.

Figure 5.19 Path lines released from the slant surface coloured by Z-location of release point for AR=1.1, $\alpha=25^\circ$. The dark blue path lines released near centreline of the body are entrained into the C-pillar vortex.

In Figure 5.20, the streak lines on the slant surface the 3D path lines are compared between AR=1.1, $\alpha=25^\circ$ and AR=1.75, $\alpha=25^\circ$. The path lines released from the C-pillar were not influenced significantly by changes in aspect ratio. The angle of the bifurcation line indicates that the area influenced by the C-pillar vortex has not changed. The streak lines on the surface show that the separation bubble stretches further downstream as the body widens. However, for the same position, relative to the edge of the body, the separation bubble is similar in size. The streak lines intersecting the dotted line on the diagram, which is relative to the edge of the body, are similar. Therefore, the main change in the flow structures between different low aspect ratio bodies for $\alpha=25^\circ$ occurs on the centre region of the body.

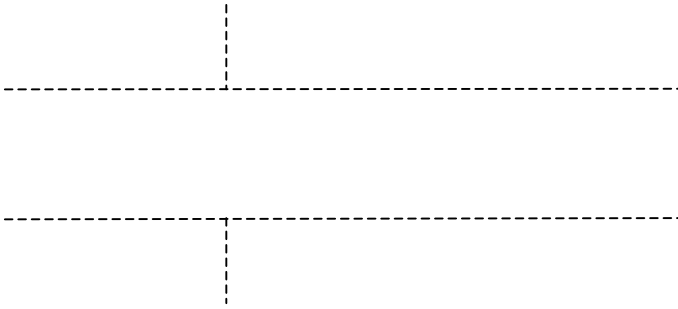


Figure 5.20 Comparison of the size of the slant separation bubble between AR=1.1, $\alpha=25^\circ$ and AR=1.75, $\alpha=25^\circ$. Black dotted lines are included for reference and are relative to the edge of the body to indicate a common reference point for comparison.

At the critical slant angle ($\alpha_c=33^\circ$) for AR=1.1 in Figure 5.21, the wake is highly three dimensional with strong streamwise C-pillar vortices. Even for the higher slant angles, the length of the separation bubble does not change significantly from $\alpha=25^\circ$ to $\alpha=34^\circ$. The streak lines on the centreline do not show smooth reattachment to the slant surface due to the strong three-dimensionality of the flow structures on the slant surface. Behind the model, the rear separation bubble reaches a minimum size due to the significant downwash on the centreline. Unlike AR=1.75, the rear separation bubble is significantly shorter on the centreline compared with its edges.

Figure 5.21 Orthographic projection of wake structures behind the Ahmed body for AR=1.1 $\alpha=33^\circ$. Stream slices are contoured by velocity magnitude/ U_∞ overlaid with streak lines on each plane. Path lines are released from one side edge of the slant surface. The separated region is outlined with an iso-surface of $U/U_\infty=0$ coloured by velocity magnitude/ U_∞ .

5.3.1.4 Region IV

Above α_c at $\alpha=34^\circ$, for $AR=1.1$, the flow has separated from the slant surface. In contrast to the wake structure for separated flow at $AR=1.75$, there is still a strong downwash behind body on the centreline. Streak lines on the slant surface indicate total separation and the C-pillars vortices are non-existent. In the wake, two strong counter-rotating vortex structures are present. Their presence in the wake causes the high drag (Figure 5.1) relative to $\alpha > \alpha_c$ for $AR=1.75$, where there were no strong counter-rotating vortices in the wake.

Figure 5.22 Orthographic projection of wake structures behind the Ahmed body for $AR=1.1$, $\alpha=34^\circ$. Stream slices are contoured by velocity magnitude/ U_∞ overlaid with streak lines on each plane. Path lines are released from one side edge of the slant surface. The separated region is outlined with an iso-surface of $U/U_\infty=0$ coloured by velocity magnitude/ U_∞ .

Figure 5.23 shows a progression of the wake structure for $\alpha \geq \alpha_c$ using the iso-surface of $C_{TP}=0$, coloured by C_p . At $\alpha=\alpha_c=34^\circ$, the C-pillar vortices extend from the edge of the slant surface, with the slant separation bubble clearly indicated. Above $\alpha > \alpha_c$ for $AR=1.1$ in Figure 5.23b, the separated region encompasses the entire rear surface of the body. Even though the C-pillar vortex has not formed, there is a strong shear layer stretching downstream from the edge of the slant surface. On the centreline, the strong downwash shortens the rear separation bubble. When α is increased to $\alpha=40^\circ$ in Figure 5.23d, the downwash on the centre has reduced, increasing the size of the separation bubble on the centreline even though it still extends further downstream on the sides of the body. However even at $\alpha=40^\circ$, two counter-rotating structures exist in the wake from the body.

AR=1.1 $\alpha=25^\circ$ AR=1.1 $\alpha=33^\circ$ AR=1.1 $\alpha=34^\circ$ AR=1.1 $\alpha=40^\circ$

Figure 5.23 Comparison of the wake structure for various AR

5.3.2 High AR bodies

5.3.2.1 Region I

Figure 5.24 shows the wake structure for Region I for high AR bodies. There is no separation from the slant surface, which is similar to the lower AR bodies examined. The major change in the wake structure for higher AR bodies is the increased size of the separation bubble in the body wake. Compared with AR=1.75, $\alpha=5^\circ$, the iso-surface of $U/U_\infty=0$ in Figure 4.8, the maximum downstream position is $x \approx 0.4$ compared with AR=2.5, $\alpha=5^\circ$, where the iso-surface extends downstream to $X=0.45$. It is only really the width of the rear separation bubble which increases with AR.

Figure 5.24 Orthographic projection of wake structures behind the Ahmed body for AR=2.5 $\alpha=5^\circ$. Stream slices are contoured by velocity magnitude/ U_∞ overlaid with streak lines on each plane. Path lines are released from one side edge of the slant surface. The separated region is outlined with an iso-surface of $U/U_\infty=0$ coloured by velocity magnitude/ U_∞ .

The Iso-surface of $U/U_\infty=0$ indicates that the rear separation bubble does not extend to the outer sides of the model. In Figure 5.25, it can be seen that this is due to the inboard position of the centre of recirculation since there is only reversed flow between the two centres of recirculation. The location of centres of recirculation on the XY plane is located further away from rear end of body compared with the centres of recirculation on the XZ plane.

Figure 5.25 Orthographic projection of planes of vorticity magnitude for AR=2.5 $\alpha=5^\circ$. Planes are overlaid with stream lines indicate the recirculation regions.

5.3.2.2 Region II

The major difference between Region I and Region II is the existence of a separation bubble on the slant surface of the model. Figure 5.26 shows the flow visualisation for AR=2.5, $\alpha=15^\circ$, where a small region of separated flow is present on the slant surface. This is in contrast to most other aspect ratios where the flow is still attached at $\alpha=15^\circ$. The C-pillar vortex appears to be of similar strength to lower aspect ratio bodies at $\alpha=15^\circ$ (Figure 5.16), while the rear separation bubble has also decreases in length significantly compared with Region I.

Figure 5.26 Orthographic projection of wake structures behind the Ahmed body for $AR=2.5$, $\alpha=15^\circ$. Stream slices are contoured by velocity magnitude/ U , overlaid with streak lines on each plane. Path lines are released from one side edge of the slant surface. The separated region is outlined with an iso-surface of $U/U_\infty=0$ coloured by velocity magnitude/ U .

A significant difference is that the slant separation bubble has separated from the base of the slant surface rather than the top of the slant surface. Inside the separation bubble, two recirculation focus points exist from the reversed flow on the body centreline, which is connected to rear separation bubble. A significant portion of the slant surface, which is attached still exists and is not influenced by the C-pillar vortex structure. Compared with $AR=2.5$, $\alpha=20^\circ$, in Figure 5.27, the flow structures on the slant surface have changed, with the separation bubble separating from the top of the slant surface. The focal points inside the separation bubble have moved outwards and towards the top of the slant surface similar to the separation bubble at $AR=1.75$, $\alpha=25^\circ$ (Figure 4.11).

Figure 5.27 Orthographic projection of wake structures behind the Ahmed body for $AR=2.5$, $\alpha=20^\circ$. Stream slices are contoured by velocity magnitude/ U , overlaid with streak lines on each plane. Path lines are released from one side edge of the slant surface. The separated region is outlined with an iso-surface of $U/U_\infty=0$ coloured by velocity magnitude/ U .

Figure 5.28 shows the top view of path lines released from the slant surface for $AR=2.5$, $\alpha=15^\circ$ (a) and $\alpha=20^\circ$ (b). The path lines show the considerable change in the flow structure with a larger recirculation in the separation bubble at $\alpha=20^\circ$. There is significantly more entrainment of the flow from the sides of the bubble for $\alpha=20^\circ$ compared with $\alpha=15^\circ$. Also visible is the existence of a secondary recirculation zone inside the separation bubble near the body centre for $\alpha=15^\circ$ (Figure 5.28a).

(a)

(b)

Figure 5.28 Top view of path lines released from the slant surface for $AR=2.5$, $\alpha=15^\circ$ (a) and $\alpha=20^\circ$ (b). Path lines are coloured by Z release location.

The top view of contours of vorticity magnitude and the streamlines in Figure 5.29 at the Y midpoint of the rear surface for $AR=2.5$, $\alpha=15^\circ$ and $\alpha=20^\circ$ show the rear separation bubble also changes shape for the small change in α . In Region I, the iso-surface of $U/U_\infty=0$ did not extend to the sides of the rear surface, while in Figure 5.27,

the separation bubble is shorter, but extends to the sides of the slant surface. The centre of recirculation determined by the streamlines on the XZ plane indicate that the recirculation centre has moved away from the body centreline into the shear layer regions on the side of the model. While the contours of vorticity magnitude indicate that the strength of the shear layers on the sides of the body have increased and extend further downstream from the body. This indicates that the rear separation bubble has changed from a toroidal vortex structure to a wake structure, which is dominated by two counter-rotating spanwise vortices with the C-pillar vortex affecting the sides of the rear separation bubble.

(a)

(b)

Figure 5.29 Top of planes of vorticity magnitude on the Y midpoint of the rear surface for AR=2.5, $\alpha=15^\circ$ (a) and $\alpha=20^\circ$ (b). Planes are overlaid with streamlines to indicate the recirculation regions.

It appears that within Region II, there are significant changes in the wake structure on the slant surface and behind the model. The C_N for AR=2.5 in Figure 5.8 indicates that $\alpha=15^\circ$ should be classified in Region I. However, since the wake has separated from the slant surface, it could be classified in Region II. The small separation bubble near body centreline does appear to change the C_N significantly.

5.3.2.3 Region III

The wake structure at AR=2.5, $\alpha_c=25^\circ$ in Region III is illustrated in Figure 5.30, just before total separation occurs on the slant surface. The separation bubble on the slant surface extends to virtually its entire width at the top. Due to the increased width of the slant surface, the separation bubble extends to the rear of the body, contrary to the smaller AR where the flow is still attached on the centreline at $\alpha=25^\circ$. The length of the iso-surface of $U/U_\infty=0$ has decreased significantly from $X \approx 0.5$ at $\alpha=5^\circ$ to $X \approx 0.2$ at $\alpha_c=25^\circ$. The downwash on the centreline does not appear to be as significant as that observed on lower aspect ratio bodies indicating that downwash is dependent on α as opposed to α relative to α_c .

Figure 5.30 Orthographic projection of wake structures behind the Ahmed body for $AR=2.5$, $\alpha=25^\circ$. Stream slices are contoured by velocity magnitude/ U , overlaid with streak lines on each plane. Path lines are released from one side edge of the slant surface. The separated region is outlined with an iso-surface of $U/U_\infty=0$ coloured by velocity magnitude/ U .

The path lines released from the slant surface for $AR=2.5$, $\alpha=25^\circ$ shown in Figure 5.31 illustrate the spanwise horseshoe vortex present on the slant surface. In contrast to the low aspect ratio bodies, there is no entrainment of fluid from the slant surface separation bubble into the C-pillar vortex at the formation point of the C-pillar vortex. In the wake, the majority of path lines in the rear separation bubble merge into the two counter-rotating structures in the wake.

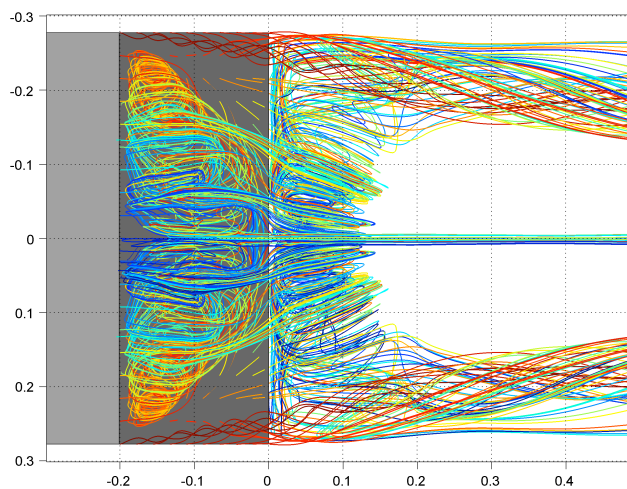


Figure 5.31 Path lines released from the slant surface coloured by Z-location of release point for $AR=2.5$, $\alpha=25^\circ$.

Figure 5.32 shows a comparison of the size of the separation bubble for $AR=2.5$ and $AR=1.75$ at $\alpha=25^\circ$, similar to Figure 5.20. Although the separation bubble is larger on the body centreline compared with $AR=1.75$, it can be seen that if the separation size bubble is compared relative to the edge of the body, the size of the separated regions are similar. This indicates that the length of the separation bubble is dependent on the AR of the vehicle, since the region of attached flow due to the influence of C-pillar vortex is constant at $\alpha=25^\circ$ (see section 5.4.3).

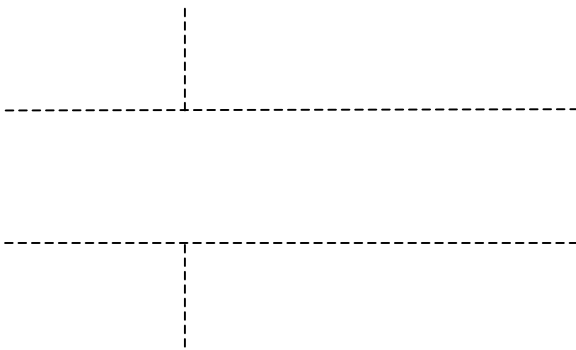


Figure 5.32 Comparison of the size of the slant separation bubble between $AR=2.5$, $\alpha=25^\circ$ and $AR=1.75$, $\alpha=25^\circ$. Black dotted lines are included for reference and are relative to the edge of the body.

5.3.2.4 Region IV

In Region IV for $AR=2.5$, full separation occurs across the slant surface creating a large separation bubble in the wake similar to Region I. As can be seen in Figure 5.33, for $AR=2.5$, $\alpha=26^\circ$, the path lines released from the side of the slant surface indicate that the C-pillar vortex has not formed and a shear layer exists on the side of the slant surface. However, the shear layer is still rolling up creating some localised downwash as indicated by the streamlines on the YZ plane collinear with the rear surface (marked with white box on Figure 5.33). Unlike the low AR bodies, the downwash along the body centreline has decreased considerably from $\alpha \leq \alpha_c$, allowing the separation bubble to extend further downstream. Streak lines on the slant surface indicate that the structures inside the slant surface are not uniform.

Figure 5.33 Orthographic projection of wake structures behind the Ahmed body for AR=2.5, $\alpha=26^\circ$. Stream slices are contoured by velocity magnitude/ U_∞ overlaid with streak lines on each plane. Path lines are released from one side edge of the slant surface. The separated region is outlined with an iso-surface of $U/U_\infty=0$ coloured by velocity magnitude/ U_∞ .

Increasing α in Region IV for AR=2.5 increases the size of the separation bubble behind the body as shown in Figure 5.34 for AR=2.5, $\alpha=40^\circ$. As can be seen by the in-plane streamlines on the YZ plane, the flow is more uniform inside the separation bubble. The streak lines on the slant surface are horizontal rather than vertical as has been observed in experiments for AR=1.75, $\alpha=35^\circ$ [14].

Figure 5.34 Orthographic projection of wake structures behind the Ahmed body for $AR=2.5$, $\alpha=40^\circ$. Stream slices are contoured by velocity magnitude/ U , overlaid with streak lines on each plane. Path lines are released from one side edge of the slant surface. The separated region is outlined with an iso-surface of $U/U_\infty=0$ coloured by velocity magnitude/ U .

Path lines released from the rear surface at $AR=2.5$, $\alpha_c=40^\circ$ in Figure 5.35 indicate a toroidal vortex structure is present. It would be expected that as $\alpha \rightarrow 90^\circ$, the wake would transfer from a largely 2-dimensional wake to a structure with a toroidal type vortex structure. This transition back flow structure more reminiscent of Region I was not examined, but it appears that for $AR=2.5$, $\alpha=40^\circ$ is above this transition point.

Figure 5.35 Path lines released from the slant surface coloured by Z-location of release point for AR=2.5, $\alpha=40^\circ$.

Figure 5.36 shows the progression of the separation bubble for increasing α for AR=2.5, visualised by the iso-surface of $C_{TP}=0$ coloured by C_p . In Region II ($\alpha=20^\circ$) and Region III ($\alpha=25^\circ$), the development of the C-pillar vortex is clearly visible. At $\alpha=25^\circ$, the iso-surface of $C_{TP}=0$ indicates that the C-pillar vortex is interacting with the rear separation bubble. This makes it difficult to track the C-pillar vortex from the slant surface downstream because beyond the rear of the body the C-pillar merges with the rear separation bubble. Further downstream, two counter-rotating vortices are present in the wake. In Figure 5.36d, the large separation bubble visible with the folding in of the shear layer in the wake is evident as a groove in the top of the iso-surface of C_{TP} for $\alpha=26^\circ$.

a. AR=2.5 $\alpha=5^\circ$ b. AR=2.5 $\alpha=20^\circ$ c. AR=2.5 $\alpha=25^\circ$ d. AR=2.5 $\alpha=26^\circ$

Figure 5.36 Iso surface of C_{TP}

5.4 Effect of aspect ratio

5.4.1 Change in downwash

Flow visualisations in the previous sections indicated an increase in downwash in the wake region of the Ahmed body as $\alpha \rightarrow \alpha_c$ for all AR examined. To quantify the change in downwash, the mass flow rate (\dot{m}) of the wake passing through a control volume (CV) is calculated as outlined in Figure 5.37. The CV is parallel to the XZ plane with limits in the X direction of $0 \leq X \leq 1$ while in the Z direction, CV extends to the edges of the Ahmed body ($-\text{width}/2 \leq Z \leq +\text{width}/2$). The CV is varied in the Y direction in order to locate the plane at which the strongest downwash occurs in the vehicle wake. To clarify, due to the coordinate system, a strong downwash is indicated by a negative \dot{m} so a strong downwash is a highly negative \dot{m} .

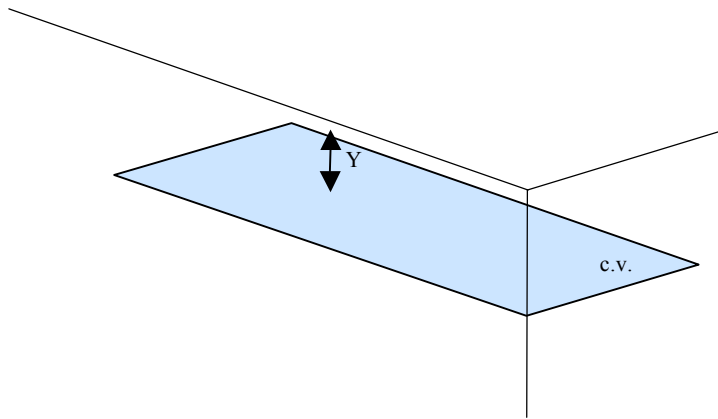


Figure 5.37 Diagram indicating the location of the control volume plane used to calculate the mass flow rate and hence the downwash in the wake region of the Ahmed body. The plane is adjusted in the Y direction to determine where the peak downwash occurs.

Figure 5.38 shows contours of the \dot{m} at different Y planes calculated at different slant angles for $AR=1.75$. These indicate that the overall downwash in the wake region increases with α up to $\alpha=\alpha_c$. At $\alpha=5^\circ$, the strongest downwash occurs near the top of the Ahmed body ($Y=0.288$) while there is a positive \dot{m} (up-wash) near the bottom the Ahmed body. Flow visualisation by Ahmed [7] indicated an overall up-wash in the wake at $\alpha=5^\circ$. The location of the CV with strongest downwash decreases and the minimum \dot{m} decreases with increasing α up to $\alpha=\alpha_c$ indicated by the dashed line. The decreasing \dot{m} is consistent with the increasing lift on the body (Figure 5.12) due to the increasing vertical momentum transferred to the fluid from the slant surface. At $\alpha_c=30^\circ$, the location of maximum downwash occurs at $Y \approx 0.177$, which is a plane coincident with the bottom edge of the slant surface. This indicates that as the fluid flows over the slant surface, the vertical momentum of the fluid increases until the base of the slant surface, where it reaches a maximum since beyond the slant surface, there is nothing to add additional momentum to the fluid. After separation from the slant surface at $\alpha>\alpha_c$, the downwash decreases, with the \dot{m} profile similar to $\alpha=5^\circ$ with up-wash near the ground. The dotted black line indicates the CV plane with the $\dot{m} = 0$. This shows that for $18^\circ \leq \alpha < \alpha_c$, throughout the entire wake region except for very close to the ground boundary layer, there is an overall downwash in the wake. x

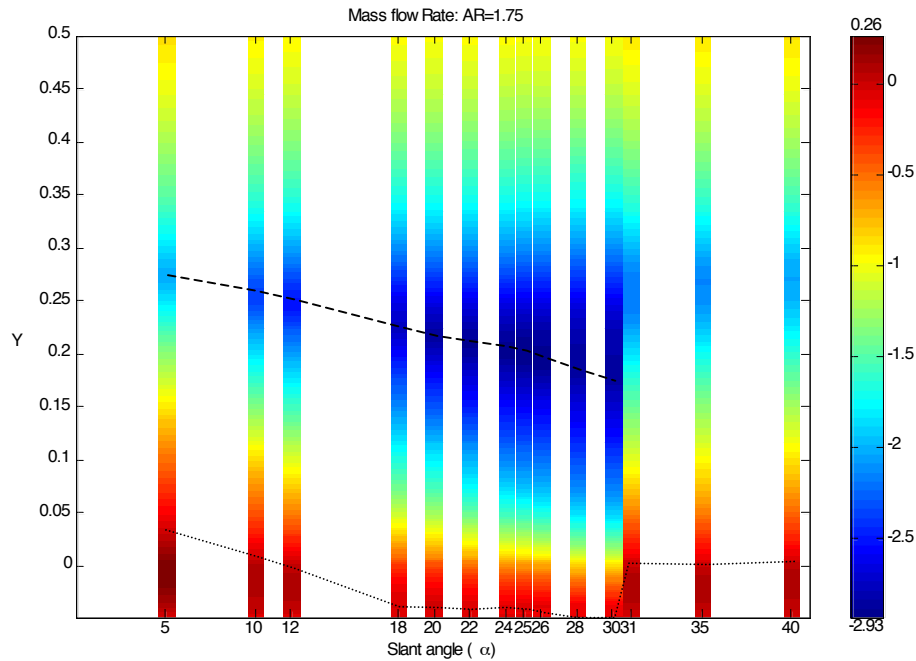


Figure 5.38 Bands of the \dot{m} at different Y planes calculated at different slant angles for $AR=1.75$. The dashed lines indicates the Y location of strongest downwash for a given α , while the dotted line indicated the Y location where $\dot{m} = 0$.

To compare different AR, the minimum \dot{m} , or strongest downwash, was calculated for each simulation. Since a larger CV is used for the higher AR, the \dot{m} increases and gives a misleading impression when comparing different AR. Therefore, \dot{m} was divided by the CV area to normalise the results between different aspect ratios. Figure 5.39 shows the normalised minimum \dot{m} for the parameter space. The \dot{m} decreases with increasing m for $\alpha < \alpha_c$ indicating a stronger downwash on the higher AR bodies. As shown in 5.4.2, the size of the C-pillar vortex is not a function of AR. Therefore for the higher AR bodies, there is a larger region between the C-pillar vortices where there is a downwash due to the C-pillar vortices so there is a lower minimum \dot{m} . Similar to the profiles of C_L , there is a linear change in \dot{m} in Region I and II, while in Region III, the \dot{m} plateaus until $\alpha = \alpha_c$. Increasing α in Region III does not necessarily increase the \dot{m} , which is most likely due to an increasing separation bubble on the slant surface decreasing the downwash in the wake since the flow is not attached to the slant surface. At $AR=1.1$, above $\alpha = \alpha_c$, it was found that the two counter-rotating structures were still present in the wake region of the body. It was expected that the downwash would be stronger for the low AR bodies. However, the higher than expect \dot{m} is due to up-wash caused by the two counter-

rotating vortices in the wake, which is compensating the increased downwash on the centreline.

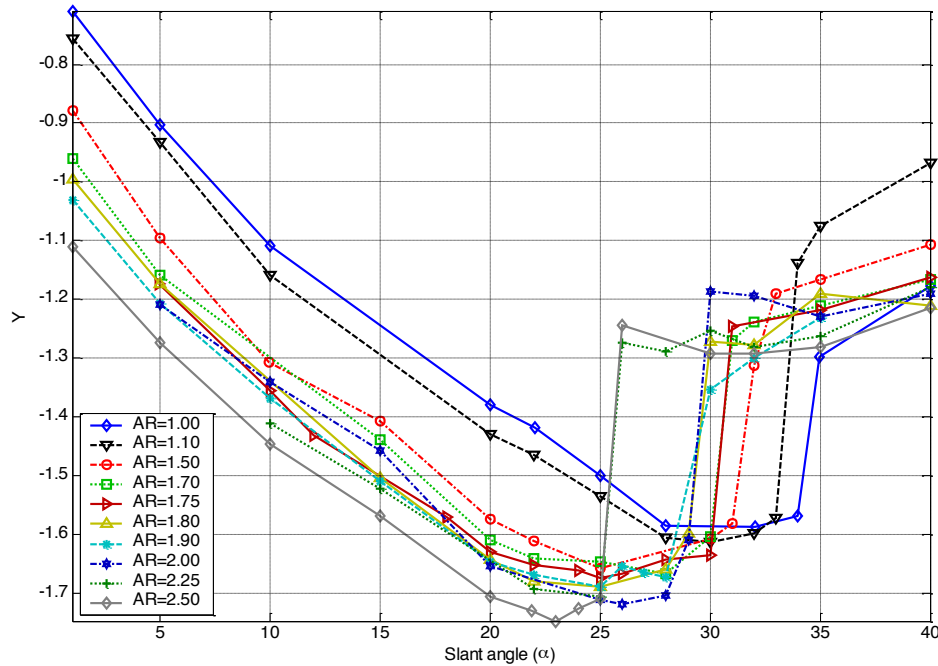


Figure 5.39 Minimum normalised \dot{m} for different AR as a function of α . Results indicate that the strongest downwash in the wake region of the Ahmed body occurs for the high AR bodies.

If only a very small control volume along the centreline is considered ($-0.001 \leq Z \leq +0.001$, $0 \leq X \leq 1$), only the downwash from the two counter-rotating vortices is calculated. Figure 5.40 shows \dot{m} along the centreline of the Ahmed body for the parameter space covered. In contrast to Figure 5.39, which includes up-wash from the C-pillar vortex, the low AR bodies have the strongest downwash on the centreline of the model. There appears to be a linear decrease in the \dot{m} along the centre with α until $\alpha = \alpha_c$. The downwash is considerably reduced for $AR > 2.0$ where the $\dot{m} \approx -0.02$ is approximately half of that for $AR = 1.0$ ($\dot{m} \approx -0.0375$). In region IV for $AR \leq 1.1$ ($\alpha > \alpha_c$), the large drop off in downwash experienced with $AR = 1.75$ is not evident. Instead, \dot{m} increases linearly as α increases.

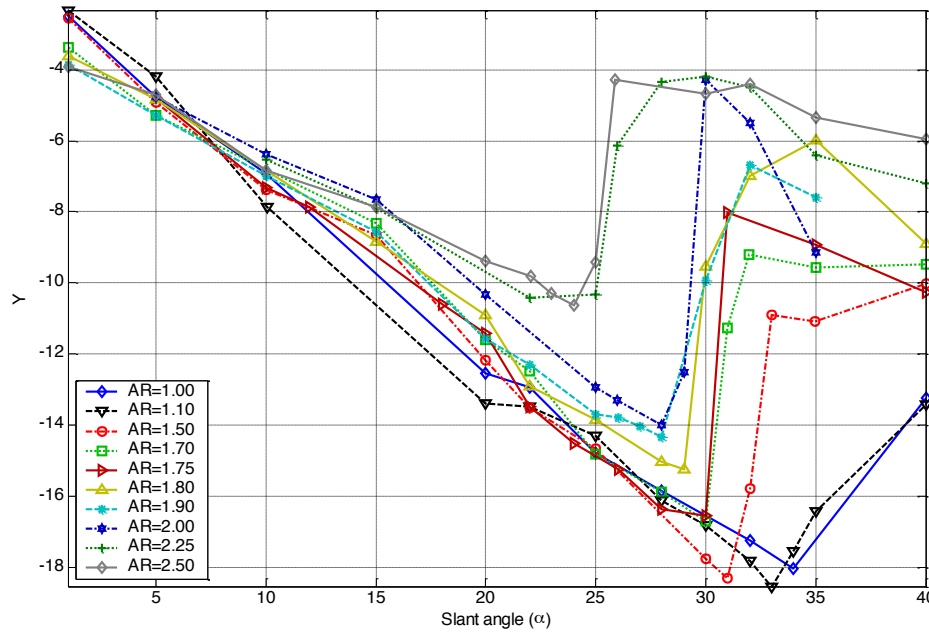


Figure 5.40 Normalised \dot{m} on the centreline region of the wake (CV: $-0.001 \leq Z \leq +0.001$, $0 \leq X \leq 1$). On the centreline region, the strongest downwash occurs for the lowest AR bodies.

The difference between AR=1.1 and AR=1.75 is clearly indicated in Figure 5.41, which shows \dot{m} along the centreline of the body at different slant angles. In Figure 5.41a, \dot{m} decreases gradually to $\alpha_c = 33^\circ$, then gradually increases again. In Figure 5.41b, there is a sudden increase in \dot{m} at $\alpha = \alpha_c$, indicating a lack of downwash on the centreline compared with $\alpha \leq \alpha_c$.

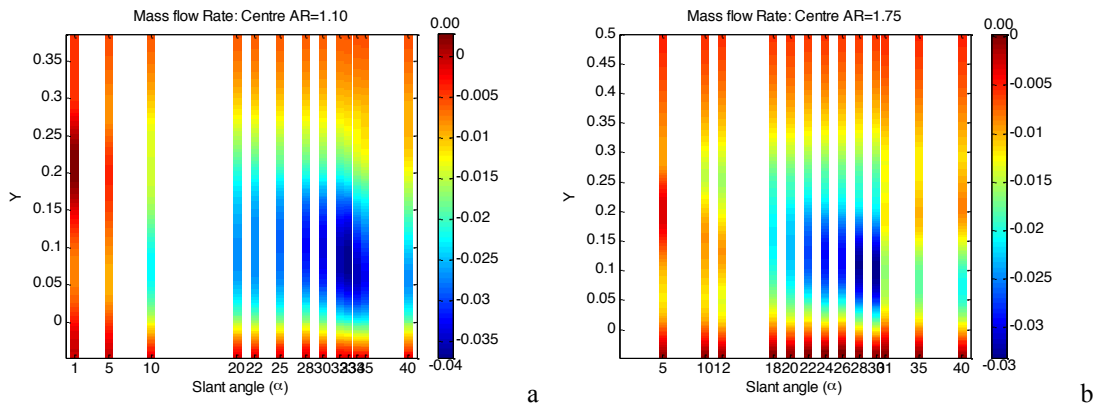


Figure 5.41 Bands of normalised centreline \dot{m} for AR=1.1 (a) and AR=1.75 (b).

In this section, the effect of the downwash in the wake of the Ahmed body has been quantified to demonstrate the change in the wake structure. The peak downwash occurs on a plane coincident with the bottom edge of the slant surface. It was found that the highest AR bodies had the strongest downwash for $\alpha \leq \alpha_c$. However, this takes into account the up-wash caused by the two counter-rotating vortices in the

wake. If only the downwash on the centreline is considered, then downwash decreases with increasing α .

5.4.2 Portion of slant surface with separated flow

In Section 5.2.1 and 5.2.2, the portion of the slant surface that was separated appeared to be dependent on AR for a given α . Flow visualisations indicated that the C-pillar vortex strength did not change with AR because the same area of the slant surface had attached flow. To quantify this observation, the region where reversed flow ($U/U_x < 0$) occurred was determined by finding the largest contour on the slant surface where $U/U_x = 0$.

Figure 5.42 shows the contours of $U/U_x = 0$ for AR=1.75 on the slant surface. The coordinate system used is relative to the slant surface as outlined in Section 6.2. It was found that even though using a symmetry boundary condition did not influence the C_D and C_L , it does have an effect on the velocity field near the model centreline. The dotted lines indicate the likely contour of the separated region.

For AR=12°, the separated region is only on the centreline of the slant surface and extends to the base of the slant surface ($Z=0.222$). As $\alpha \rightarrow \alpha_c$, the separated region becomes wider at the top of the slant surface, while at the bottom, the region becomes narrower due to increasing influence of the C-pillar vortex. For $\alpha \geq 25^\circ$, the edge profile of the vortex does not increase with α indicating that the region in which the C-pillar influences the attached flow of the slant surface does not increase with α . Although near the centreline of the body, the separation bubble extends further down the slant surface with increasing α .

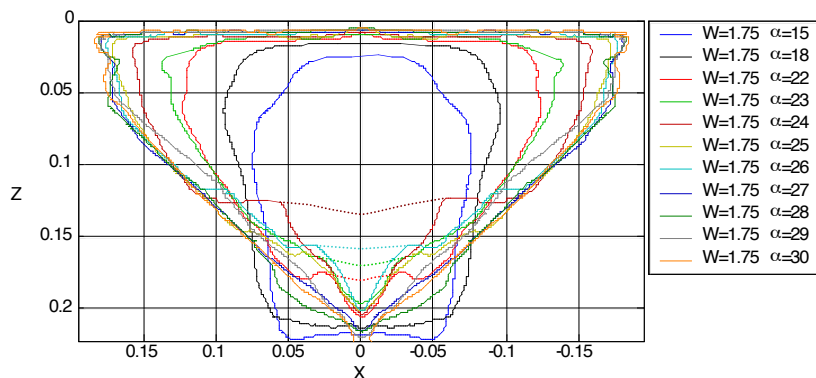


Figure 5.42 Contours of $U/U_x = 0$ on the slant surface for various α for AR=1.75. Refer to Section 6.2 for coordinate system used. The side profile of the separated region appears to be similar for $\alpha \geq 25^\circ$.

The edge profile of the separated region for $AR=1.1$ and $AR=2.5$ is shown in Figure 5.43 with the X coordinate relative to the edge of the slant surface. For the high and low AR investigated, the edge profile of the separated surface asymptotes towards a common profile with increasing α . At $AR=1.1$, the edge profiles are similar for $\alpha > 25^\circ$, while for $AR=2.5$, edge profiles are similar for $\alpha > 24^\circ$. It appears that for $\alpha < 25^\circ$, the separated region is still increasing with α , but for $\alpha \geq 25^\circ$, the separated region is limited by the C-pillar vortex keeping the flow attached to the slant surface.

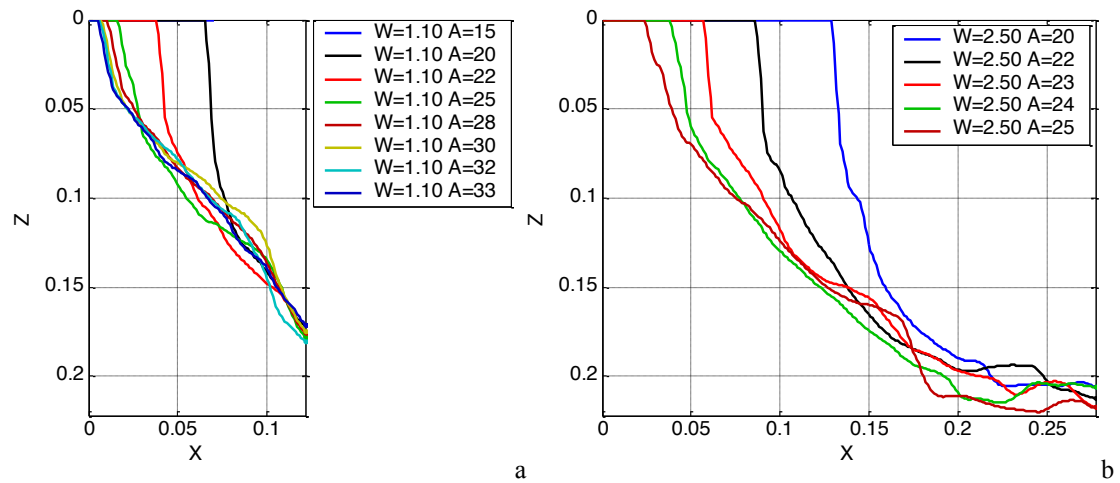


Figure 5.43 Edge profiles of $U/U_\infty = 0$ on the slant surface for $AR=1.1$ (a) and $AR=2.5$ (b). For both AR , the edge profile of the separated region appears to be similar for $\alpha \geq 25^\circ$.

Figure 5.44 shows the edge profiles for various AR at $\alpha=25^\circ$ with the X coordinate relative to the edge of the body. Apart from the increased size of the separation bubble with increasing AR , the contour of U/U_∞ is similar near the formation point of the C-pillar vortex structure ($X=0, Z=0$). The length of the separation bubble appears to be dependent on the AR since the profile is similar for all AR . At $AR=1.0$, the separated region extends to $Z \approx 0.11$ before it reaches the centreline of the model, whereas for $AR=2.5$, the separation bubble reaches the bottom of the slant surface.

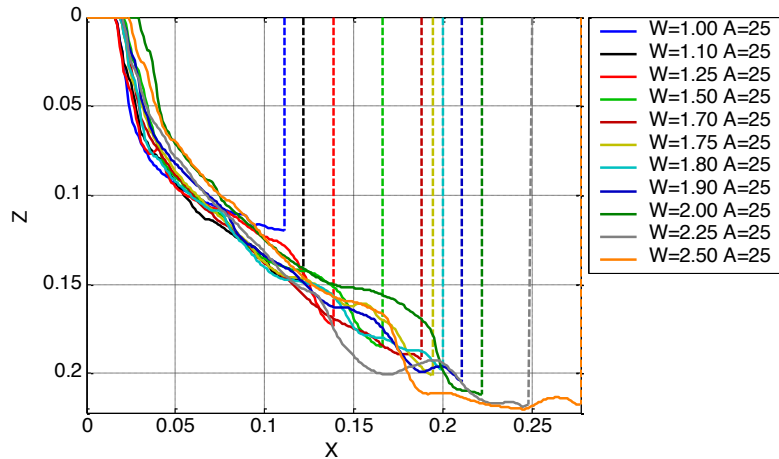


Figure 5.44 Edge profile of contour of U/U_∞ at $\alpha=25^\circ$ for all various AR. Dotted lines indicated the centreline of Ahmed body for a given AR. Profiles for AR=25° near the formation point of the C-pillar vortex are constant for $\alpha=25^\circ$.

These results indicate that for $\alpha \geq 25^\circ$, the effect of C-pillar vortex does not appear to be increasing in size and influencing a larger region of the slant surface. The size of the separation bubble appears to be dependent on the AR of the body for a given slant angle. Ahmed [5] hypothesised that the cause for the transition is due to the merging of the rear and slant separation bubbles. This does not hold for low AR bodies where there is no merging of the separated regions before the transition to large separation bubble and decreased drag.

5.4.3 Separation bubble size

In Section 4.3.7, the shape of the rear separation bubble was found to change with α for AR=1.75. Determining the shape of the rear separation bubble due to the complex interaction of C-pillar vortex with the rear separation bubble is difficult. One method examined to reveal the shape of the separation bubble was to create a surface by releasing path lines from known separation points on the Ahmed body. In Figure 5.45, the surface created by the path lines released from the edge of rear surface for AR=1.75 shows the evolution of the rear separation bubble for $\alpha \leq \alpha_c$. At $\alpha=20^\circ$ (Figure 5.45b), the surface shows the size reduction of the rear separation bubble from $\alpha=5^\circ$ (Figure 5.45a). For $20^\circ \leq \alpha \leq 30^\circ$, on the sides of the separation surface, it is difficult to distinguish between the rear separation bubble and the two counter-rotating streamwise vortices. Along the centreline, the decrease in the size of the separation bubble is evident as $\alpha \rightarrow 30^\circ$ (Figure 5.45d).

a. AR=1.75 $\alpha=5^\circ$ b. AR=1.75 $\alpha=20^\circ$ c. AR=1.75 $\alpha=25^\circ$ d. AR=1.75 $\alpha=30^\circ$

Figure 5.45 Orthographic projection of the separation surface created by releasing path lines from perimeter of the rear surface for AR=1.75, $\alpha=5^\circ$ (a), $\alpha=20^\circ$ (b), $\alpha=25^\circ$ (c) and $\alpha=30^\circ$ (d). Stripes on the separation surface indicate the distance the flow has travelled from the release location.

Figure 5.46 shows how the wake structure changes between $\alpha=\alpha_c$ and $\alpha>\alpha_c$ for different AR. The separation surface is created by releasing path lines from the rear and slant surface. At AR=1.1 (Figure 5.46 a, b), the wake separates from the slant surface, but streamwise vortices are still present for $\alpha>\alpha_c$. At AR=1.1, $\alpha=34^\circ$, the shear layer from the side of the slant surface folds into the wake. The evolution of the wake structures for $\alpha>\alpha_c$ for increasing AR (Figure 5.46 b, d, e) indicates that the downwash on the centreline of the body decreases with increasing AR. At AR=1.75, the formation of counter-rotating streamwise vortices is present, but at AR=2.5, there appears to be no evidence of downstream vortices forming.

a. AR=1.1 $\alpha=33^\circ$ b. AR=1.1 $\alpha=34^\circ$ c. AR=1.75 $\alpha=30^\circ$ d. AR=1.75 $\alpha=31^\circ$ e. AR=2.5 $\alpha=25^\circ$ f. AR=2.5 $\alpha=26^\circ$

Figure 5.46 Orthographic projection of a comparison of the wake structure for $\alpha=\alpha_c$ and $\alpha>\alpha_c$ for AR=1.1 (a, b), AR=1.75 (c, d) and AR=2.5 (e, f). The separation surface is created by releasing path lines from the perimeter of the slant and rear surface. Stripes on the separation surface indicate the distance the flow has travelled from the release location.

To quantify the change in the rear separation bubble shape for different AR, instead of monitoring the location of centres of the recirculation zone (Section 4.3.7) or the examining the separation surface created by path lines, the shape of the total pressure=0 (C_{TP}) iso-surface is used. The C_{TP} gives a good indication of the extension of the wake on sides of the rear separation bubble and gives a better indication than using contours of $U/U_\infty=0$, which only captures the reversed regions in separation bubble. To compare between different models, iso-surface of $C_{TP}=0$ was calculated similar to Figure 4.22. Then for a given Z location, the maximum downstream location of the iso-surface was determined. Care was taken to ensure the iso-surface created by the streamwise vortices was not included.

Shown in Figure 5.47 is the maximum downstream location of $C_{TP}=0$ for the $AR=1.75$ for different slant angles. At $\alpha=5^\circ$, the rear separation bubble extends considerably far downstream. However, it quickly decreases as $\alpha \rightarrow \alpha_c$. Above $\alpha=20^\circ$, the separation bubble extends further downstream on the sides of the separation bubble compared with the centreline as was found in Section 4.3.7. The wake reverts back to a large separation bubble for $\alpha > \alpha_c$ with the separation bubble similar from $31^\circ \leq \alpha \leq 40^\circ$.

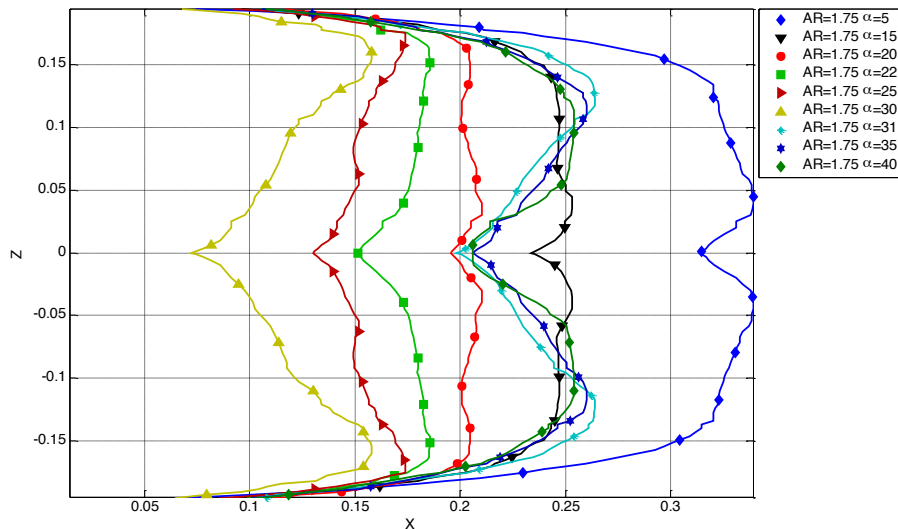


Figure 5.47 Profiles of rear separation bubble for $AR=1.75$ for various α . Profile of separation bubble is determined by locating the maximum downstream location of contour of $C_{TP}=0$ for a given Z location.

At $AR=1.10$, the max downstream location separation bubble using the iso-surface of $C_{TP}=0$ is shown in Figure 5.48. The separation bubble is shorter at $\alpha=5^\circ$ compared with $\alpha=5^\circ$ with $AR=1.75^\circ$, due to the reduced rear surface area on the low AR body. The separation bubble rapidly decreases as $\alpha \rightarrow \alpha_c$ from the reduction in rear surface area. However, unlike $AR=1.75$, at $\alpha_c=34^\circ$, the downstream distance across the entire span is relatively constant, with the sides of the separation bubble not extending further downstream. At $\alpha > \alpha_c$, the separation bubble structure is substantially different since the presence of two counter-rotating streamwise vortices cause a low region of C_{TP} inside the separation bubble and as a result, two peaks are present in the separation bubble profile. For further increases in α , this feature is relieved and the wake appears to be reverting back to similar structure observed for $\alpha > \alpha_c$ at $AR=1.75$. However, at $AR=1.1$ $\alpha=40^\circ$, the wake still has not reverted back to a large

separation bubble indicating the presence of counter-rotating streamwise structures at high α .

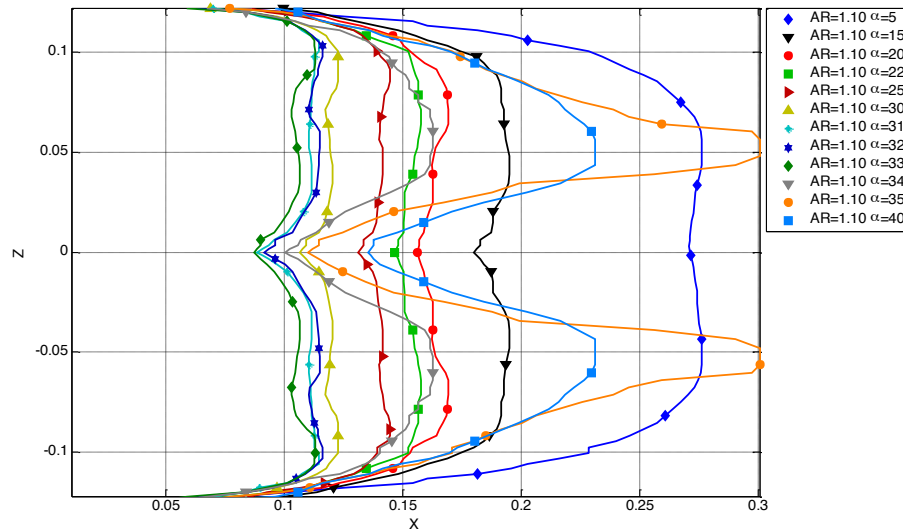


Figure 5.48 Profiles of rear separation bubble for AR=1.10 for various α . Profile of separation bubble is determined by locating the maximum downstream location of contour of $C_{TP}=0$ for a given Z location.

At AR=2.5 in Figure 5.49, the separation bubble at $\alpha=5^\circ$ extends a similar distance downstream for AR=1.75, in contrast to the increase in the separation bubble from AR=1.1 \rightarrow 1.75. This could indicate that in Region I, beyond a certain AR, the size of the separation bubble is controlled by the shear layers from the top and bottom of the slant surface as opposed to the shear layers from the sides of the rear surface. It stands to reason, that for an infinite AR Ahmed body, the size separation bubble would not keep increasing. The size of the separation bubble reduces to $\alpha_c=25^\circ$, where on the centreline, the separation bubble is shorter than on the sides of the domain indicating the influence of the C-pillar vortices on the rear wake. At $\alpha>\alpha_c$, the separation bubble is constant and extends downstream to $X \approx 0.275$, which is slightly greater than AR=1.75 ($X \approx 0.25$).

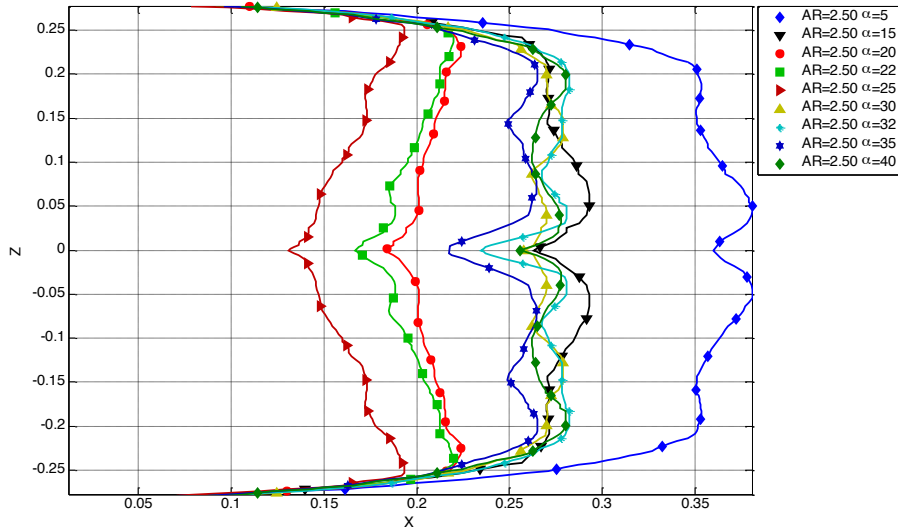


Figure 5.49 Profiles of rear separation bubble for AR=2.5 for various α . Profile of separation bubble is determined by locating the maximum downstream location of contour of $C_{TP}=0$ for a given Z location.

To compare the effect of the AR on the size of the rear separation bubble, the location of the maximum downstream location of $C_{TP}=0$ is calculated for $\alpha=5^\circ$ (Region I), $\alpha=25^\circ$ (Region III) and $\alpha=35^\circ$ (Region IV). In Region I in Figure 5.50, the increase in AR causes the separation bubble to extend further downstream. For $1.5 \leq AR \leq 2.0$, the separation bubble increases by $\Delta X \approx 0.25$. However, for $2.0 \leq AR \leq 2.5$, there is no substantial increase in separation bubble size, indicating that for $AR \geq 2.0$, the separation bubble downstream distance is constant with AR.

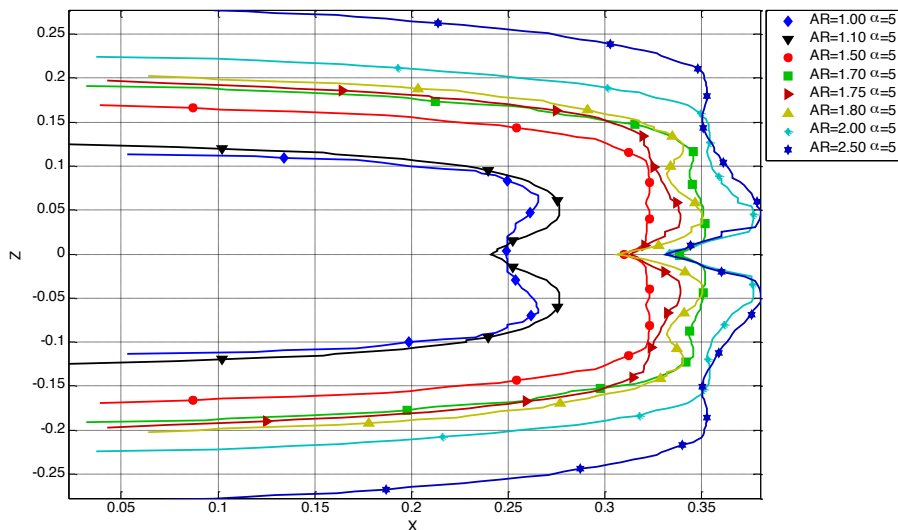


Figure 5.50 Profiles of rear separation bubble for $\alpha=5^\circ$ for various AR in Region I. Profile of separation bubble is determined by locating the maximum downstream location of contour of $C_{TP}=0$ for a given Z location.

The profiles of the separation bubble for $\alpha=25^\circ$ in Region II shown in Figure 5.51 indicate a similar structure of the separation bubble for all AR considered. However, on the sides of the separation bubble the separation bubble extends further downstream with AR, on the centreline, the separation bubble size is relatively constant for all AR. This indicates that even though the separation bubble is increasing downstream with AR, on the centreline, the downwash from the slant surface limits how far the separation bubble extends.

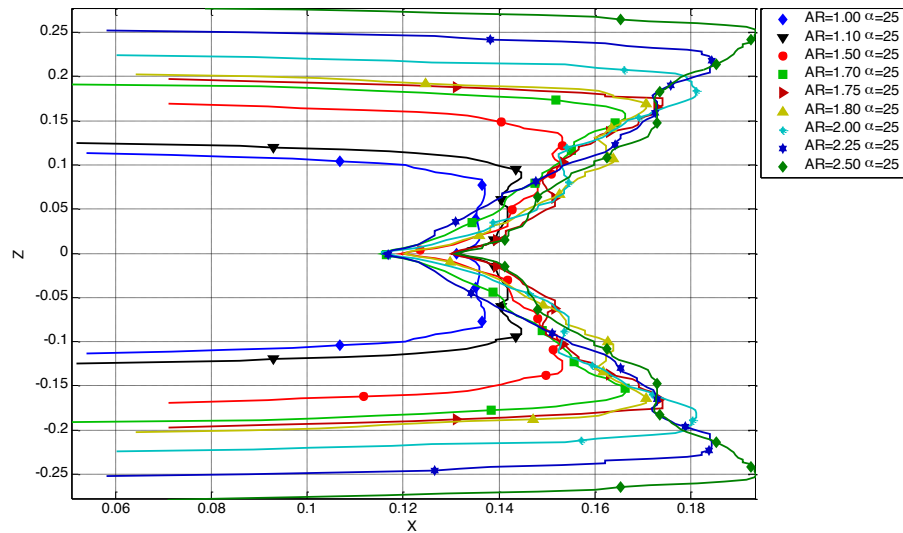


Figure 5.51 Profiles of rear separation bubble for $\alpha=25^\circ$ for various AR in Region III. Profile of separation bubble is determined by locating the maximum downstream location of contour of $C_{TP}=0$ for a given Z location.

In Region IV in Figure 5.52, the variation in the maximum downstream distance for different AR at $\alpha=35^\circ$, is not as large as in Region III. Since a large separation bubble is present, Region IV does not experience the influence of the streamwise vortices. Apart from $AR \leq 1.25$, the maximum downstream location varies from $X \approx 0.25$ at $AR=1.5$ to $X \approx 0.275$ at $AR=2.5$. On the centreline, the strength of the two counter-rotating streamwise vortices in wake decreases with increasing AR. This is visible by the increase in the downstream position of the separation bubble on the centreline.

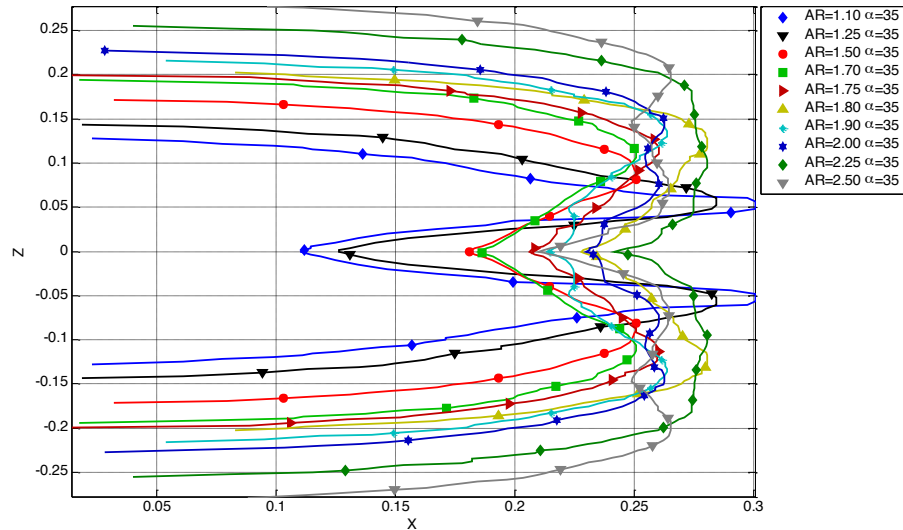


Figure 5.52 Profiles of rear separation bubble for $\alpha=35^\circ$ for various AR in Region I. Profile of separation bubble is determined by locating the maximum downstream location of contour of $C_{TP}=0$ for a given Z location.

5.4.4 Downstream effects

Two counter-rotating streamwise structures appear in the wake region of the Ahmed body, caused in part from the downwash on the centreline and from the C-pillar vortices. To quantify the effect of the AR and α on the wake structures, the strength of the streamwise vortices was analysed by calculating circulation (Γ) using different spanwise slices of streamwise vorticity. Circulation is calculated by integrating the streamwise vorticity of the over the entire spanwise plane of the domain. Shown in Figure 5.53 are contours of Γ as a function of downstream location for AR=1.75. In the rear wake, Γ increases for all the wake increases $\alpha \rightarrow \alpha_c$, when the Γ decreases for $\alpha > \alpha_c$. For a given α , Γ increases downstream to a maximum and then decreases. The location of the maximum Γ occurs closer to Ahmed body as $\alpha \rightarrow \alpha_c$ due to the increased strength of the two counter-rotating streamwise vortices.

Beyond the end of the model, Γ for a given α should remain constant for an ideal vortex except for the effects of diffusion. However, since Γ is calculated in a domain near the body, and diffusion exists in the wake, Γ does not remain constant with X .

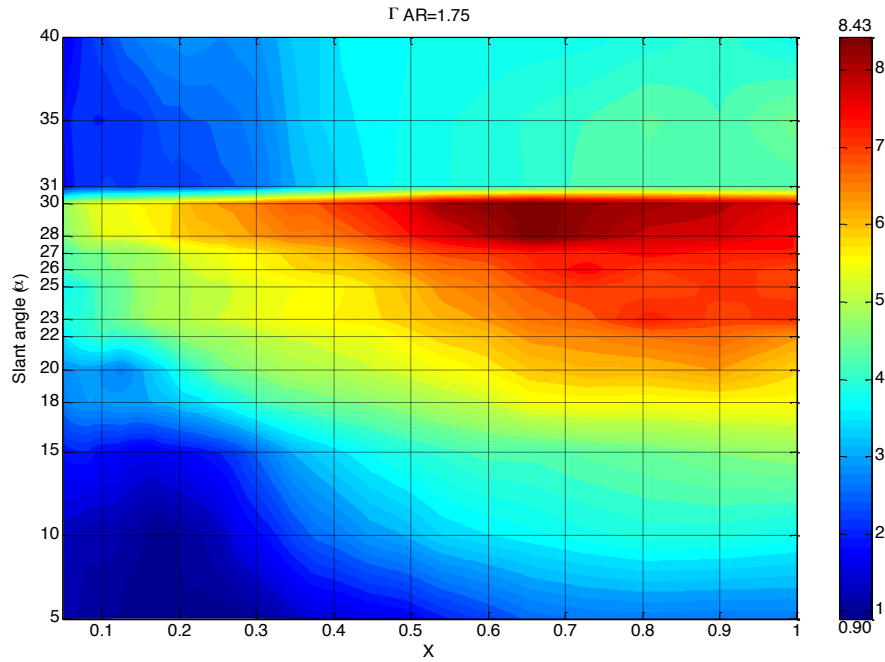


Figure 5.53 circulation for AR=1.75

Figure 5.54 shows contours of Γ for AR=1.1 and AR=2.5 for various α . In Figure 5.54a, the location of maximum Γ in the wake occurs closer to the rear end of the body. At $\alpha > \alpha_c$, Γ does not decrease as significantly at $\alpha = \alpha_c$, since strong streamwise vortices are still present. At AR=2.5 in Figure 5.54b, the location of maximum Γ for a given α occurs further downstream near $X \approx 1.0$. $\int \Gamma$

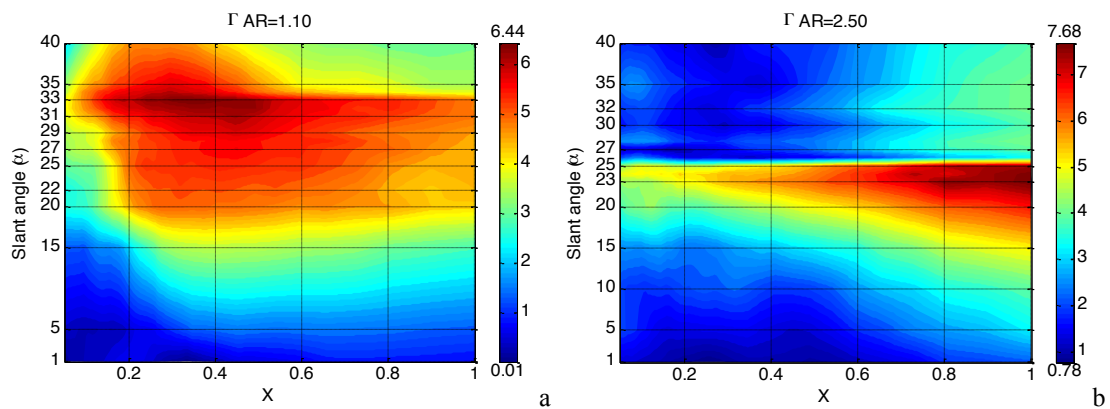


Figure 5.54 Circulation as a function of downstream distance and slant angle for AR=1.1 and AR=2.5.

To compare between different AR, $\bar{\Gamma} = \int_0^1 \Gamma dx / \int_0^1 dx$ is calculated for each simulation as shown in Figure 5.55. This corresponds to the spatially-averaged circulation for the near wake region. As $\alpha \rightarrow \alpha_c$ for a given AR., the strength of the $\bar{\Gamma}$ increases, while at $\alpha > \alpha_c$, $\bar{\Gamma}$ decreases significantly. In Region I, the variation

between AR is similar indicating the same strength of the downstream structures. In Region III, there is a larger variation in $\bar{\Gamma}$ where large downwash exists and the two counter-rotating vortices are present in the wake, The strongest $\bar{\Gamma}$ occurs for AR=1.75 at $\alpha=\alpha_c$. This is in contrast to section 5.4.1, where \dot{m} is a maximum at AR=2.5, whereas on the centreline, \dot{m} is maximum at AR=1.0. This indicates that the strength of the counter-rotating vortical structures in the wake increase as AR \rightarrow 1.75. However, due to the decreasing α_c with increasing AR, the circulation in the wake does not increase further for AR>1.75.

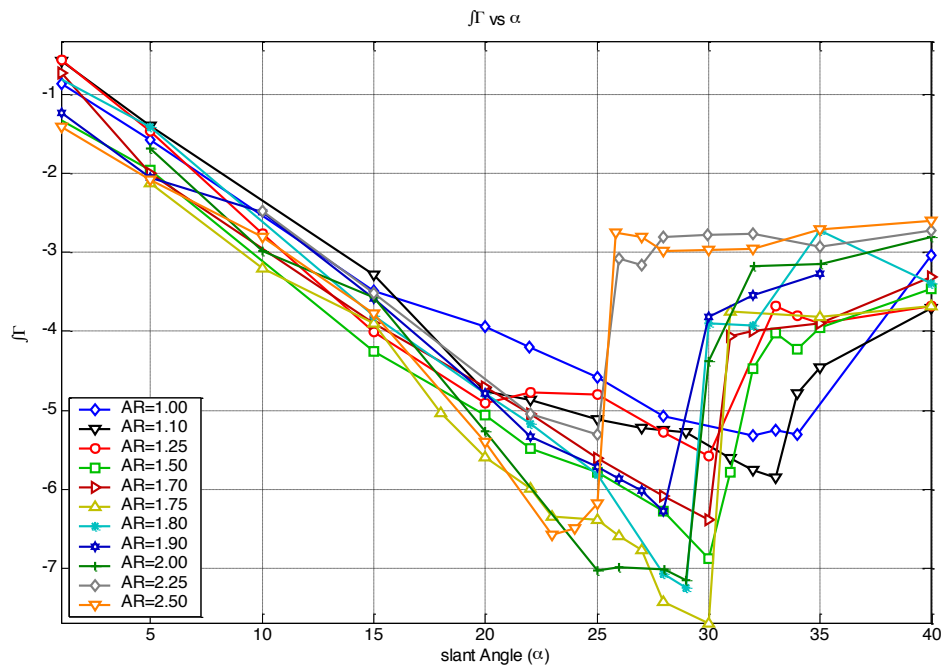


Figure 5.55 $\bar{\Gamma}$ of the near wake for different AR.

5.5 Conclusion

In this chapter, which examined the wake structures for the Ahmed body, the effect of the body aspect ratio has been determined for $1.0 \leq AR < 2.5$. The most significant effect found from varying AR is the change in location of α_c , where the wake structures change from a wake dominated by the C-pillar vortices, to a large separation bubble encompassing the slant and rear surface. For the standard Ahmed body (AR=1.75) $\alpha_c=30^\circ$, while α_c increases to $\alpha_c=34^\circ$ for AR=1.0, and reduces to $\alpha_c=25^\circ$ for AR=2.5. The change in location of α_c represents the location of maximum C_D for a given AR which results in a lower peak C_D for AR>1.75, since $\alpha_c < 30^\circ$.

In Region I, the wake is characterised by a large rear separation bubble with an internal toroidal vortex structure (Figure 5.15), with attached flow on the slant surface

and weak C-pillar vortices. There is little variation in C_D for low AR bodies, while for $AR > 1.75$, C_D does increase but it is not significant considering the large increase in cross-sectional area. Increasing the aspect ratio of the body from $AR = 1.0$, the rear separated region extends further downstream. However, above $AR = 1.5$, the length of the separation bubble does not increase substantially compared with the increase of AR. It stands to reason that above a certain AR, the separation bubble should not increase since the length of the separation bubble will be determined by the shear layer emanating from the top and bottom of the Ahmed body. This study indicates that for $AR > 1.5$, the length of the separation bubble is independent of AR. The Γ downstream of the Ahmed body for $AR = 1.1$ is more dependent on α rather than AR (Figure 5.55).

Region II is characterised by the presence of a small separation bubble forming near the centreline on the slant surface, which results in a slightly higher C_D for a given α . However, in Region II, C_D still increases linearly with α . Analysis of the C_N indicates that Region I occurs for $0^\circ < \alpha < 15^\circ$. However, for some AR, a small separation bubble on the slant surface was found for $\alpha = 15^\circ$, even though the C_N gradient did not increase. Visualisations for $AR = 2.5$ indicate that initial separation on the slant surface occurs from the base of the slant surface for high AR bodies rather than from the top edge of the slant surface (Figure 5.26). The formation of a small separation bubble on the slant surface for $\alpha \approx 15^\circ$ is likely to be sensitive to small fluctuations upstream of the slant surface. For small increases in α above $\alpha = 15^\circ$, the bubble separates from the top slant surface and reattaches before the end of the slant surface (Figure 5.28). The increase of α from region I to region II decreases the length of the rear separation bubble substantially. There is change in the shape of the rear separation bubble observed for high AR bodies, where the wake changes from a torroidal vortex to a structure dominated by two counter-rotating spanwise vortices. The vertical component of the torroidal vortex is replaced by a stronger shear layer emanating from the sides of the rear surface.

As $\alpha \rightarrow \alpha_c$ in Region III, the C_D for a given AR reaches a maximum with the peak C_D occurring for $AR = 1.5$, $\alpha = 32^\circ$. For a given α , C_D increases with AR, whereas for $AR > 1.5$ the variation of C_D with AR is smaller. The C_D on the rear surface plateaus as $\alpha \rightarrow \alpha_c$, while the C_D on the slant surface increases with α .

In Region III, the flow is separated across the entire width of the top of the slant surface. However the C-pillar vortices keep the flow attached on the side regions of the slant surface. For low AR bodies, path lines released from the slant surface indicate that the C-pillar and slant separation bubble are linked, since flow from the centreline of the model migrates along the spanwise vortex in the slant separation bubble and is then entrained into the C-pillar vortex (Figure 5.19). For higher AR bodies, the flow visualisations indicate that the slant separation bubble and C-pillar vortices are not linked (Figure 5.31).

An important observation, is the size and location of the C-pillar vortex which appears to be relatively unaffected by the change in AR in Region III. Examination of the separated region at $\alpha=25^\circ$ indicates that the same region near the side of the slant surface is attached (Figure 5.44). The width of the attached region on the side of the slant surface is similar for a given distance from the top of the slant surface. Therefore, for larger AR bodies, the surface area of the attached region is greater due to the increased width of the slant surface. The length of the slant separation bubble is dependent on the AR, since for increasing AR, the separation bubble can extend further down the slant surface before it reaches the centreline. This is the downstream limit of the slant separation bubble since C-pillar vortices exist on both side edges of the slant surface.

The downwash from the slant surface, assisted by C-pillar vortices, has a large influence on rear separation bubble in Region III (see section 5.4.3). It is found that the downwash in the wake limits the length of the separation bubble on the centreline. On the edges of the model, the separated region extends further downstream with increasing AR since the length of the rear separation bubble still increases with AR; however, the downwash limiting the size of the separation bubble is not as significant as the C-pillar vortex is present on the sides of the model. This results in the rear separation bubble extending further downstream as $AR \rightarrow 2.5$, while at the centreplane the length of the separated region determined by the iso-surface of $C_{TP}=0$ remains constant.

The sudden decrease in C_D at $\alpha > \alpha_c$ occurs for all AR examined between Region III and Region IV, although for $AR \geq 2.25$, C_D at $\alpha_c=25^\circ$ is not as high compared with $AR=1.75$, and the decrease in C_D at $\alpha > \alpha_c$ is not as large. For lower AR bodies, the

reduction of C_D is also reduced because C_D is higher due to presence of two counter-rotating streamwise vortices. However, the wake has separated from the slant surface and the C-pillar vortices found for $\alpha < \alpha_c$ are not present. Visualisations of the flow field indicate that instead of the shear layer rolling up into a vortex, it appears to fold over due to the downwash still present leading to the counter-rotating vortices. For increasing AR, the strength of the counter-rotating streamwise vortices in the wake decreases as evidenced by the decreasing downwash on the body centreline (Figure 5.40), and the reduction of Γ in the wake. The separated region at the rear of the body is relatively constant in the wake with increasing AR except for low AR bodies, where the downwash decreases the length of the separation bubble on the centreline.

Chapter 6 C-Pillar Vortex Structure

6.1 Introduction

To determine the mechanism that causes the flow transition at the critical slant angle (α_c), detailed analysis focusing on the C-pillar vortex was undertaken. After transition at $\alpha > \alpha_c$, the C-pillar vortex is no longer a dominant feature of the flow field. Up to now, the mechanism for the transition to a fully separated wake has not been clear. Ahmed et al. [5] concluded that the transition to low drag at $\alpha = 30^\circ$ was due to the merging of the separation bubbles on the slant surface and on rear the surface. The same conclusions were reached by Giovannini [83] in his research on flow control on the Ahmed body.

An alternative mechanism is the one proposed for the phenomenon of vortex breakdown (Section 3.9), which has been observed on delta wings. For fastback shaped automotive geometries, the C-pillar vortices delay the total separation of the slant surface. The C-pillar vortex starts to *break down* as α approaches the critical slant angle (α_c). Increasing α moves the location of vortex breakdown closer to the top of the slant surface. For $\alpha > \alpha_c$, the vortex would burst instantaneously if it were to form, resulting in the flow evolving into a fully separated wake.

Hucho [10, 11, 84] has briefly mentioned that the transition is due to the C-pillar vortices lifting off and/or bursting at the critical slant angle, causing a large separated wake. Han[25] concluded that vortex breakdown was the mechanism causing the wake transition at α_c but this was not pursued further.

Investigations by Sims-Williams [17] examined the possibility of vortex breakdown occurring behind automotive geometries. His investigations found that vortex breakdown does not occur behind the Ahmed body or Rover 200 model. No evidence was found of sudden growth of vortices and reversed flow along the vortex core. However, only the wake past the rear of the vehicle was analysed. As reported by Sims-Williams, Sedney[85] hypothesised that the mechanism for transition on the Morel body was due to vortex breakdown which was present in the wake of a Honda Accord [86].

Recent numerical simulations by Menter and Kuntz [69] showed signs of vortex breakdown in flow visualisations. Unsteady DES simulation was carried out for $\alpha=25^\circ$ showing that the maximum side force (Z axis) coincided with the asymmetric flow field, with only one C-pillar vortex showing signs of vortex breakdown. Flow visualisation in Figure 6.1 using iso-surfaces of total pressure shows the C-pillar vortex exhibiting signs of spiral vortex breakdown.

Figure 6.1 Iso-surfaces of total pressure coloured by eddy viscosity for $\alpha=25^\circ$. This flow field was calculated using information from DES simulations. The C-pillar flow structures indicate signs of the vortex breakdown on the closest side on the body. [87]

Although vortex breakdown has been suggested as a potential mechanism that causes the transition to a large separated wake on simplified automotive geometries, it has yet to be investigated in detail. In this chapter, the structure of the C-pillar vortex is analysed for different slant angles for the standard Ahmed body and for other aspect ratios. The methods used to determine the location of the vortex and data collection methods are discussed. Analysis of the vortex structure shows the presence of vortex breakdown and the effect on wake structures. The various criteria (Section 3.9.4) used in the prediction of vortex breakdown are compared based on simulation results.

6.2 Vortex core location

The C-pillar vortex is formed from the rolling up of the boundary layer as it separates from the sides of the slant surface. In order to characterise this vortex, spanwise cuts of the flow field were made at multiple streamwise locations above the slant surface and in the near wake. On each spanwise cut, the vortex centre was found and various other flow parameters such as the maximum swirl velocity of the vortex

were determined. Originally the spanwise cuts were made on the YZ planes to characterise the C-pillar vortex. This was acceptable for a small α , but not for a high α , since vortices primarily follow the slant surface. For the analysis, the reference frame is rotated to be relative to the slant surface as shown in Figure 6.2. In this case, the rotated X-Y plane is normal to the slant surface and the vortex was tracked downstream in the Z direction. The velocity field was rotated to follow the slant surface reference frame.

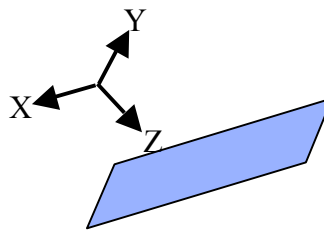


Figure 6.2 Coordinate system used relative to slant surface for the analysis of vortex breakdown.

Finding the centre of a vortex is a non-trivial problem, even for relatively simple situations where the vortex is strong relative to other vortex structures and its general location is known. Robinson [88] provided a definition of a vortex by specifying the conditions for detecting swirling flows:

A vortex exists when instantaneous streamlines mapped into a plane normal to the vortex core exhibit a roughly circular or spiral pattern when viewed from a reference frame moving with the centre of the vortex core.

As summarised by Jiang et al. [89], there are a variety of methods to find the core of a vortex. The simplest methods, such as the Maximum Vorticity method [90] and the Predictor–Corrector Method [91], look for local maxima and minima of the vorticity pressure fields. These methods are Galilean invariant since the vorticity field is examined but the Maximum Vorticity method does not work well for regions that contain shear layers. Other more complex methods, such as the Swirl Parameter

Method [91], the λ_2 method [92] and the Eigenvector method [93], examine the eigenvalues of the velocity gradient tensor to determine the presence of a vortex. These are based on critical-point theory which asserts that the eigenvalue and eigenvectors of the velocity gradient tensor, evaluated at a critical point, define the local flow pattern about that point. The Eigenvector method has been used successfully on aircraft at high angles of attack to detect bursting of leading edge vortices as shown in Figure 6.3, similar to this investigation

a

b

Figure 6.3 Flight test of a F/A-18C showing dispersion of smoke resulting from vortex burst [94] (a) compared with vortex cores extracted from transient CFD simulations. Near the vortex burst, the Eigenvalue method has difficulty detecting the vortex core location [95] and special consideration is required for the boundary layers.

Various methods were employed to determine the vortex centre using spanwise cuts of the flow field since the generalised direction of the swirl axis was known. Typical spanwise cuts of different characterisation of the flow field above the slant surface for $\alpha=30^\circ$ at $Z=0.12$ measured from the top of the slant surface are shown in Figure 6.4. Only one side of the body was examined.

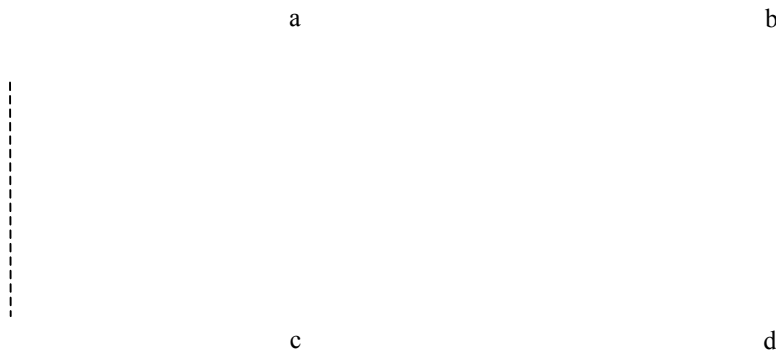


Figure 6.4 Typical spanwise slice of the pressure (a), vorticity (b), imaginary eigenvalue (c) and axial velocity (d) fields above the slant surface clearly outlining the C-pillar vortex. Streamlines indicate in-plane velocity field. The dotted line indicates the location of the edge of the body.

As described by Robinson [88], in-plane streamlines exhibit a roughly circular pattern. The rolling of the shear layer from the side of the slant surface is visible with contours of vorticity (Figure 6.4b), with the vortex centre identified by the region of low pressure (Figure 6.4a). Since the velocity field is not Galilean invariant, it is not possible to use the streamlines to locate the vortex centre unless the velocity field is viewed from the vortex reference frame. However, this requires prior knowledge of the orientation of the vortex. This is therefore not a generally acceptable method to determine the vortex centre even though, in Figure 6.4, the centre of the streamlines is close to the centre of the low pressure region.

Since the location of the vortex is relatively well defined, complex methods such as the Eigenvector method or Predictor-Corrector method were not required. The four methods investigated to determine the vortex centre are the pressure method, vorticity method, axial velocity method and the eigenvalue method. The last examines the imaginary component of the eigenvalue from the in-plane gradient tensor. In each case, the spanwise cut of the flow field was analysed to find either a minima or maxima in the parameter of interest.

The initial method used to investigate the position of the vortex centre was the vorticity method. This method had difficulties in distinguishing between the shear layer and the vortex centre. As can be seen in Figure 6.4b, the peak vorticity is

located in the shear layer and not in the centre of the vortex. Therefore, considerable filtering would be required to avoid detecting a peak location in the shear layer rolling up around the vortex centre. This was also the case with the eigenvalue method. Furthermore, it was not possible to track vortices near the slant surface due to the calculation of the gradient tensor. The minimum location found (which determines the vortex centre) using the pressure method and axial velocity method correlated well with the perceived vortex centre location as can be seen in Figure 6.4. However, since the axial velocity is not Galilean invariant, care must be taken to ensure that the cut plane is normal to the vortex axis. However, the pressure method does not need to take into account the velocity components. The pressure minimum is a good indicator of a vortex centre and was used in the Predictor Corrector method which searches for pressure minima on planes normal to the vorticity vector.

The calculated paths of the C-pillar vortex using the different tracking methods for $\alpha=30^\circ$ are shown in Figure 6.5. It can be seen that there is considerable shifting in the calculated centre using the vorticity method. This is due to the influence of the shear layer affecting calculations. For $Z=0.1$, both the eigenvalue method and vorticity method are tracking the shear layer instead of the vortex centre. However, it appears that the axial velocity and pressure method are tracking the centre of the vortex. For analysis of the C-pillar vortices, the pressure method was used to determine the location of the vortex centre.

Figure 6.5 Comparison of different vortex tracking methods used to track the C-pillar vortex above the slant surface. Both the eigenvalue method and vorticity method tracked the shear layer instead of the vortex centre. The pressure method appeared to give the most accurate path of the vortex centre since it did not track the shear layer.

6.3 Methods

Vortex tracking was carried out for all simulations where flow visualisations indicated the presence of the C-pillar vortex in the range $10^\circ < \alpha < \alpha_c$. For each simulation, the vortex was tracked using the pressure method since initial examinations found this method to be the most reliable. After the vortex core path was located, data were collected along the vortex centreline. In addition, data were collected on lines radiating from the calculated vortex centre in all four compass directions for calculation of the swirl velocity and changes in pressure distribution inside the vortex as indicated in Figure 6.6. In general, only N and S directions were considered since the W direction was influenced by the shear layer from the side of the body and the E direction was dependent on the size of the slant separation bubble.

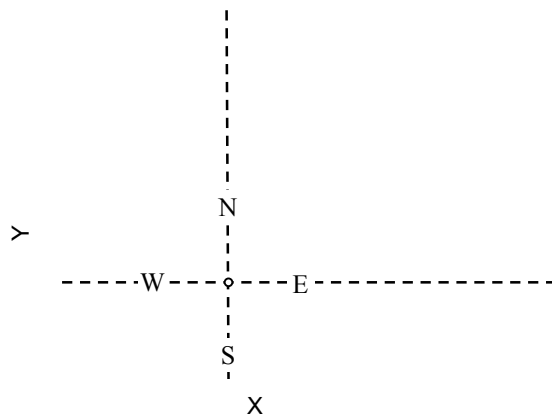


Figure 6.6 Schematic indicating the compass direction used to take slices of the C-pillar vortex.

6.4 Standard Ahmed body

Simulations for the standard Ahmed body indicated that the C-pillar vortices were breaking down with regions of reversed flow in the vortex core. This can be seen in Figure 6.7 using iso-surfaces of total pressure for various slant angles up to $\alpha=30^\circ$. For $\alpha=27^\circ$ (Figure 6.7c), an expansion of the C-pillar vortex, that was not present at lower α is visible (Figure 6.7a). It must be noted that these visualisations and simulations are iteration averaged so the C-pillar vortex is smoothed out. This makes vortex breakdown more difficult to determine since it is a time-dependent phenomena.

a. AR=1.75 $\alpha=20^\circ$ b. AR=1.75 $\alpha=25^\circ$ c. AR=1.75 $\alpha=27^\circ$ d. AR=1.75 $\alpha=30^\circ$

Figure 6.7 Iso-surface of total pressure ($C_{TP}=0$) coloured by pressure above the slant surface for $\alpha=20^\circ$ (a), $\alpha=25^\circ$ (b), $\alpha=27^\circ$ (c) and $\alpha=30^\circ$ (d).

6.4.1 Location of vortex core

The location of the centre of the C-pillar vortex was tracked from the top of the slant surface as it progressed downstream using the coordinate system defined in Figure 6.2. Figure 6.8 shows the location of the vortex centre in the YZ plane. This indicates how far the vortex is from the slant surface. Note that the vortex has been tracked past the end of the slant surface, which ends at $Z=0.222$.

As the vortex forms from the edge of the body, the core vortex moves further away from the slant surface as it progresses downstream. For increasing α , the slope of the vortex path increases relative to the slant surface, which is mainly due to the increasing slant angle. For small α , the vortex is not detected until a distinct low pressure zone is formed. At $\alpha=10^\circ$, the formation point of the vortex occurs at $Z\approx 0.075$ indicating that the vortex does not form at the top of the slant surface. The formation point of the vortex moves towards the top of the slant surface as $\alpha\rightarrow 20^\circ$. There is a clear change in vortex core location as α increases for $\alpha<25^\circ$, whereby the location of the vortex core does not move away from the slant surface as α increases. For $\alpha<25^\circ$, Figure 6.8 indicates a linear increase in the slope of the vortex centreline

relative to the slant surface, but for $\alpha > 25^\circ$, the location of the vortex is still increasing but not consistently with α .

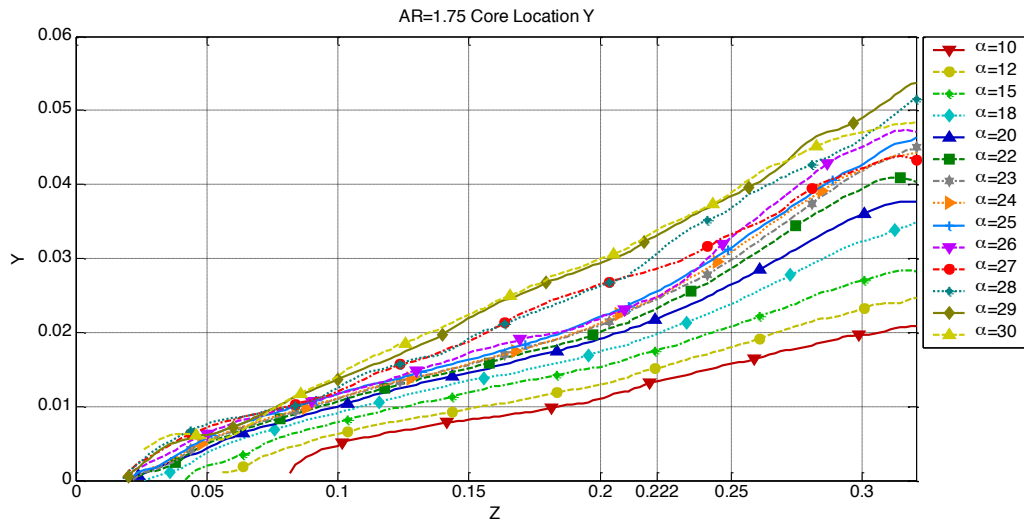


Figure 6.8 Location of core axis in the YZ plane for AR=1.75, which indicates the location the vortex above the slant surface.

This is better illustrated in Figure 6.9, which shows the Y location of the C-pillar vortex at Z=0.2 with respect to α . For $\alpha \leq 25^\circ$, the linear increase of Y at Z=0.2 with α is evident. Above $\alpha > 25^\circ$, the location of the C-pillar vortex is quite inconsistent, but still increases as $\alpha \rightarrow \alpha_c$. For $\alpha > \alpha_c$, the C-pillar vortex is not present in the wake.

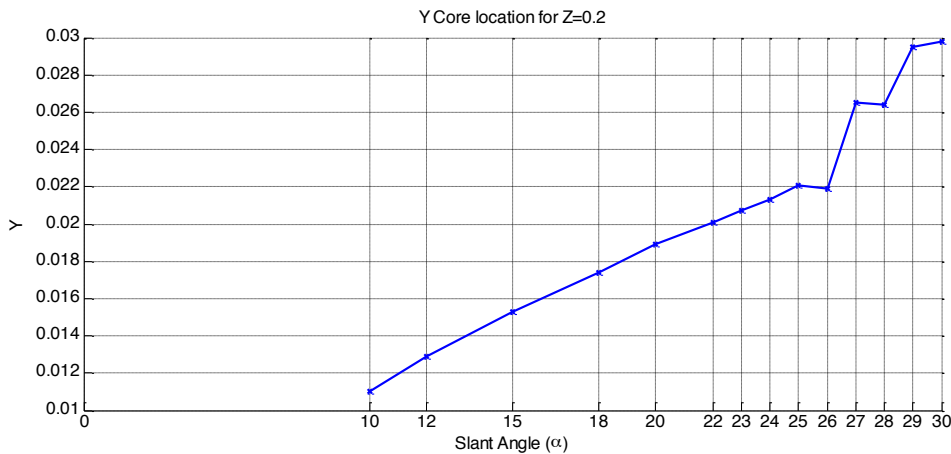


Figure 6.9 Location of the vortex axis in the Y-plane for different α at Z=0.2 for AR=1.75. The profile indicates that there is a linear change in the vortex position as $\alpha \rightarrow 25^\circ$.

It was observed in Section 4.3 that for increasing α , the vortex moves further inboard away from the side edge of the body as the vortex strength increases. Figure 6.10 shows the path of the vortex in the XZ plane with X=0 being the edge of the body. Similar to the Y location in Figure 6.8, the slope of the centreline of the C-pillar increases as $\alpha \rightarrow 25^\circ$, indicating that the vortex is moving inwards towards the

centreline of the body. For $\alpha > 25^\circ$, there is less variation in the change of location of the centreline.

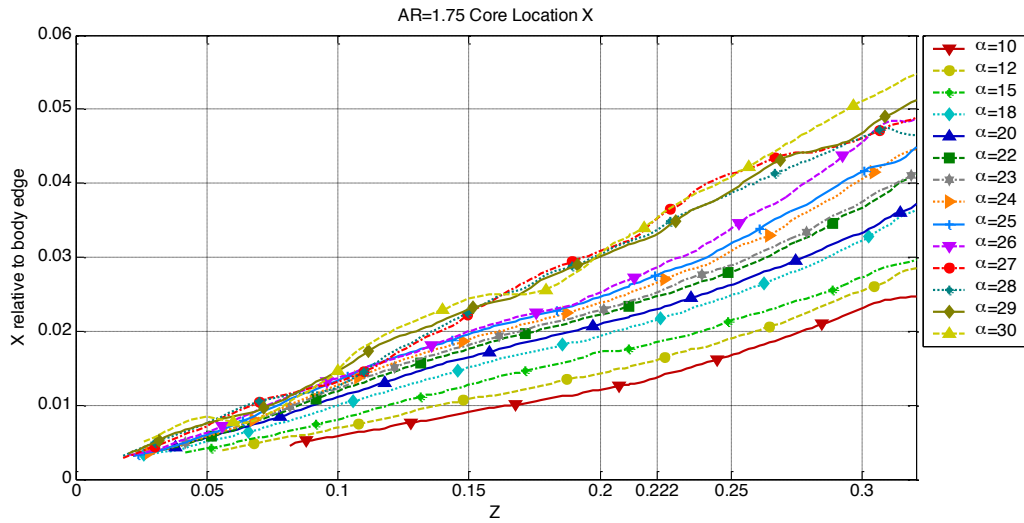


Figure 6.10 Location of vortex axis in the XZ plane for AR=1.75, which indicates how far inward the C-pillar vortex is located relative to the edge of the slant surface.

After the vortices move past the end of the slant edge, they appear to twist inwards towards the vehicle centreline, while for $Z < 0.222$, the centreline profile is more linear. Since the shear layer from the side of the slant surface is feeding the C-pillar vortex, the position of the vortex is relative to the edge of the body. However, past the body in the wake, the downwash on the centreline causes the twist towards the centreline since the vortex is no longer being fed by the shear layer.

For $\alpha > 24^\circ$, there is very little variation in the onset location of the vortex near the top of the slant surface, similar to that observed in Figure 6.10.

6.4.2 C-pillar Vortex Size

Flow visualisations of vortices exhibiting vortex breakdown show signs of expansion of the vortex core. The vortex radius (r_c) calculated using the location of $V_{\theta_{\max N}}$ is shown in Figure 6.11 as the C-pillar vortex grows in the Z direction. There is a general linear growth rate of the vortex as $\alpha \rightarrow 25^\circ$. At $\alpha = 25^\circ$, the expansion rate of r_c at $Z > 0.175$ is significantly larger than the expansion rate for $\alpha = 24^\circ$. The black solid lines in Figure 6.11 differentiate the two expansion rates for C-pillar vortices for $\alpha = 25^\circ$. For $\alpha > 25^\circ$, the vortices have a higher expansion rate than was found for $\alpha = 24^\circ$. The location at which the higher expansion rate occurs earlier in the development of the C-pillar vortex as α increases, is $\alpha > 24^\circ$.

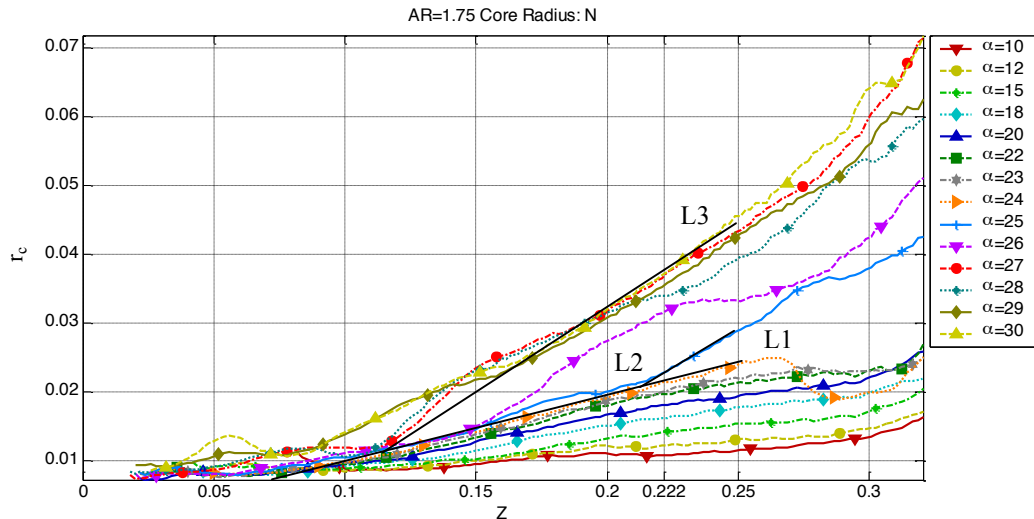


Figure 6.11 The radius of the C-pillar vortex (r_c) for AR=1.75. For $\alpha \leq 24^\circ$, there is a linear increase in r_c with Z , while for $\alpha > 25^\circ$, r_c has a linear piecewise profile, where the core of the vortex expands after the vortex has formed.

To simplify the change in the vortex radius with Z , the profile is defined with the lines L1, L2 and L3 (Figure 6.11). There is a linear increase in r_c with α up until the radius size is similar to L1 for $\alpha < 24^\circ$. At $\alpha = 25^\circ$, the profile changes into a piecewise linear profile combining L1 and L2. Further increasing α causes the intersection of L1 and L2 to occur closer to the top of the slant surface ($Z=0$) until the profile of r_c is a piecewise profile of L1 and L2. Above $\alpha > 24^\circ$, L1 remains constant. This simplified explanation suggests that the radius of vortex at $\alpha > 25^\circ$ has a sudden expansion as the vortex forms on the slant surface. For further increase in α , this expansion occurs closer to the formation point of the vortex.

Figure 6.12 shows contours of V_θ which determines r_c in the YZ plane along the axis of the C-pillar vortices for $\alpha = 24^\circ$ and $\alpha = 26^\circ$. Solid lines indicate the location of the vortex axis while the dotted lines indicate the location of $V_{\theta_{\max N}}$ and $V_{\theta_{\max S}}$. As can be seen, there is a clear difference in the swirl velocity profiles at $Z=0.2$ with an increased region of low V_θ near the vortex axis. The effect increases the radial distance where $V_{\theta_{\max}}$ occurs relative to the vortex axis, increasing r_c .

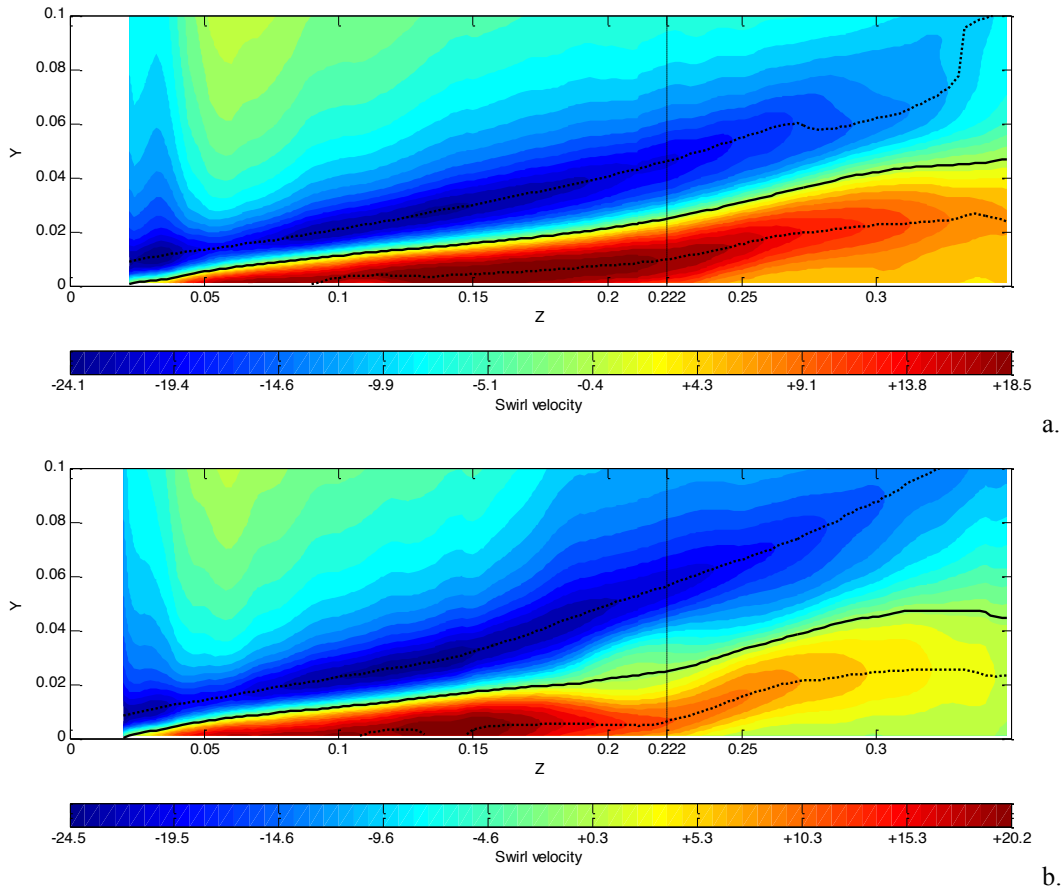


Figure 6.12 Contours of swirl velocity (V_0) on the NS plane for $AR=1.75$, $\alpha=24^\circ$ (a) and $\alpha=26^\circ$ (b). For $\alpha=26^\circ$, a region of $V_0 \approx 0$, increasing the radius of the C-pillar vortex.

6.4.3 Pressure Profiles along Vortex Core

Figure 6.13 shows profiles of the negative static pressure coefficient ($-C_p$) along the vortex axis for various slant angles. As seen with r_c , there are two distinct regions characterised by a change in patterns at $\alpha=24^\circ$.

At the formation point of the C-pillar vortex, $-C_p$ increases from $-C_p \approx 0.3$ at $\alpha=10^\circ$ to $-C_p \approx 1.1$ at $\alpha=24^\circ$. The $-C_p$ at the formation points remains relatively constant as for $\alpha \geq 25^\circ$. Profiles of C_p on the edge of the slant surface in Section 4.3.6 found that C_p was strongest as $\alpha \rightarrow 25^\circ$ and remained strong until $\alpha = \alpha_c$. As the vortex forms on the slant surface, an adverse pressure exists along the vortex axis with $-C_p \rightarrow 0$ as the vortex progresses downstream. For $\alpha \leq 24^\circ$, the adverse pressure gradient along the vortex core decreases gradually, while for $\alpha > 25^\circ$, there is a distinct decrease in $-C_p$ where the adverse gradient steepens. The region where the pressure gradient is steeper is located closer to the top of the slant surface as $\alpha \rightarrow 30^\circ$.

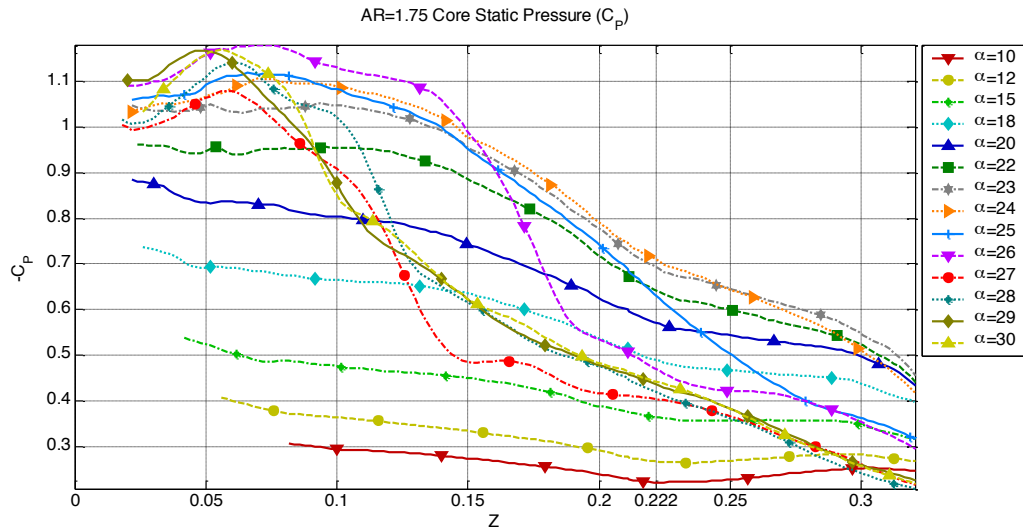


Figure 6.13 Coefficient of static pressure ($-C_p$) along the vortex axis for AR=1.75 for $10^\circ \leq \alpha \leq 30^\circ$.

To simplify, the change in $-C_p$ with α , $1/0.222 \int_0^{0.222} -C_p dz$ is calculated for slant angle and normalised by the integral length in Figure 6.14. This is effectively the mean C_p for the C-pillar vortex. These results indicate that the overall $-C_p$ in the vortex is strongest at $\alpha=24^\circ$ and then decreases and becomes constant for $\alpha > 27^\circ$.

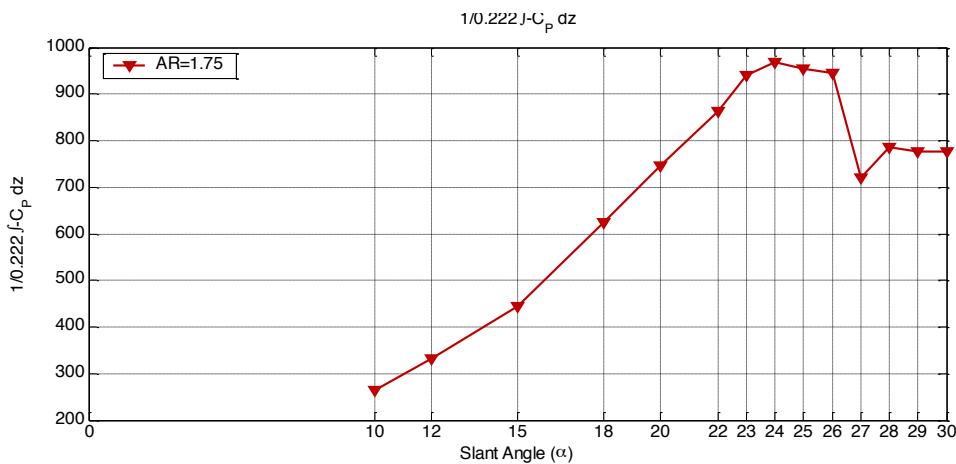


Figure 6.14 The $\int -C_p$ normalised by the integration length to show the overall change in pressure with α for AR=1.75

As can be seen in Figure 6.15, there is a clear distinction between the two regions at $\alpha > 24^\circ$ when examining the profile of the coefficient of dynamic pressure (C_{DP}). For $\alpha=10^\circ$, the C_{DP} after the formation of the vortex, from $Z=0.1$ to $Z=0.222$, is relatively constant. Downstream of the end of the body, C_{DP} increases due to an increase in $V_{x(axis)}$ along the velocity core. As $\alpha \rightarrow 24^\circ$, the C_{DP} increases near the formation point of the vortex and decreases to $C_{DP} \approx 0.45$ at the end of the slant surface

indicating that $V_{x(\text{axis})}$ is decreasing as the vortex progresses downstream. At $\alpha=25^\circ$, the C_{DP} peaks at $C_{DP}\approx 0.8$ but at $Z>0.15$, the C_{DP} gradient is steeper compared with $\alpha<24^\circ$, and decreases considerably to $C_{DP}<0.1$ past the end of the body. This decrease in C_{DP} is due to a decrease in axial velocity on the vortex centreline. For higher $\alpha(>25^\circ)$, the Z -location where $C_{DP}<0.1$ occurs further upstream in the formation of the vortex.

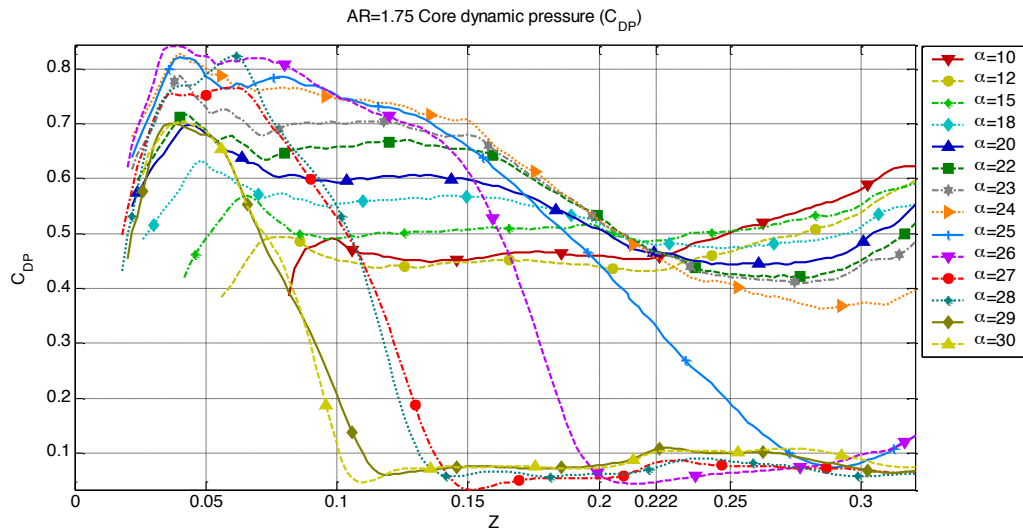


Figure 6.15 Coefficient of dynamic pressure (C_{DP}) along the vortex axis for $AR=1.75$ for $10^\circ\leq\alpha\leq 30^\circ$.

Figure 6.16 is the Z location where $C_{DP}=0.1$, which is an indicator of the location of the vortex breakdown moving closer to the top of the slant surface. After the initial breakdown at $\alpha=25^\circ$, the location of $C_{DP}=0.1$ appears to asymptote to $Z\approx 0.1$ as $\alpha\rightarrow 30^\circ$. However, this does not indicate the exact location of vortex breakdown but shows how the location changes as α increases. The actual location of the beginning of vortex breakdown is closer to the top of the slant surface as $\alpha\rightarrow\alpha_c$, since by the time $C_{DP}\approx 0.1$, the vortex breakdown has already been initiated.

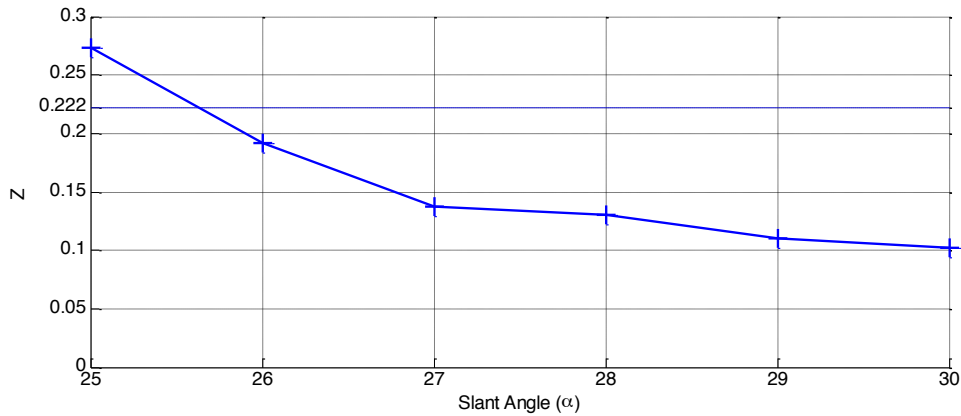


Figure 6.16 the Z location where $C_{DP} \approx 0.1$ for $AR=1.75$, $25^\circ \leq \alpha \leq 30^\circ$.

The change in the location of vortex breakdown is shown in Figure 6.17, using the iso-surface of $C_{DP}=0.1$ for different slant angles at $AR=1.75$. At $\alpha=26^\circ$ (Figure 6.17a), the region in the C-pillar vortex where $C_{DP}<0.1$ occurs near the base of the slant surface. This region moves up the slant surface as $\alpha \rightarrow 30^\circ$. Since the simulations are iteration averaged, there still exists considerable variation between simulations, such as the significantly larger region of $C_{DP} \approx 0.1$ for $\alpha=27^\circ$ (Figure 6.17b), but the region of vortex breakdown is still apparent. Further downstream past the slant surface, the iso-surface of $C_{DP}=0.1$ shows the expansion of the C-pillar vortex as it interacts with the rear separation bubble. The shape of the iso-surface suggests that the breakdown is a bubble type rather than spiral type.

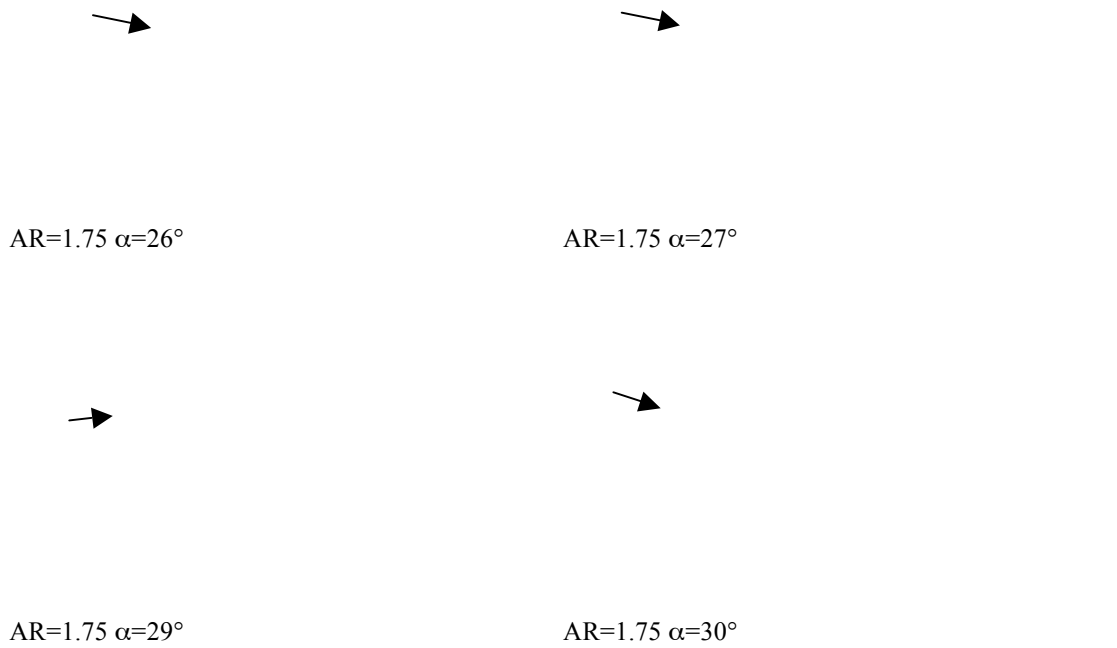


Figure 6.17 Iso-surface of $C_{DP}=0.1$ coloured by C_{TP} above the slant surface for $\alpha=26^\circ$ (a), $\alpha=27^\circ$ (b), $\alpha=28^\circ$ (c) and $\alpha=30^\circ$ (d) at $AR=1.75$. The region where the vortex expands and $C_{DP}=0.1$ is indicated by the arrows.

The change of negative total pressure ($-C_{TP}$) for $AR=1.75$ and $10^\circ \leq \alpha < 30^\circ$ is shown in Figure 6.18. For $\alpha \leq 24^\circ$, after the initial formation of the vortex, $-C_{TP}$ gradually decreases as the vortex progresses downstream. Since C_{DP} is decreasing while C_p is increasing with downstream distance, the gradient of $-C_{TP}$ is lower, but $-C_{TP}$ still decreases as the vortex progresses downstream.

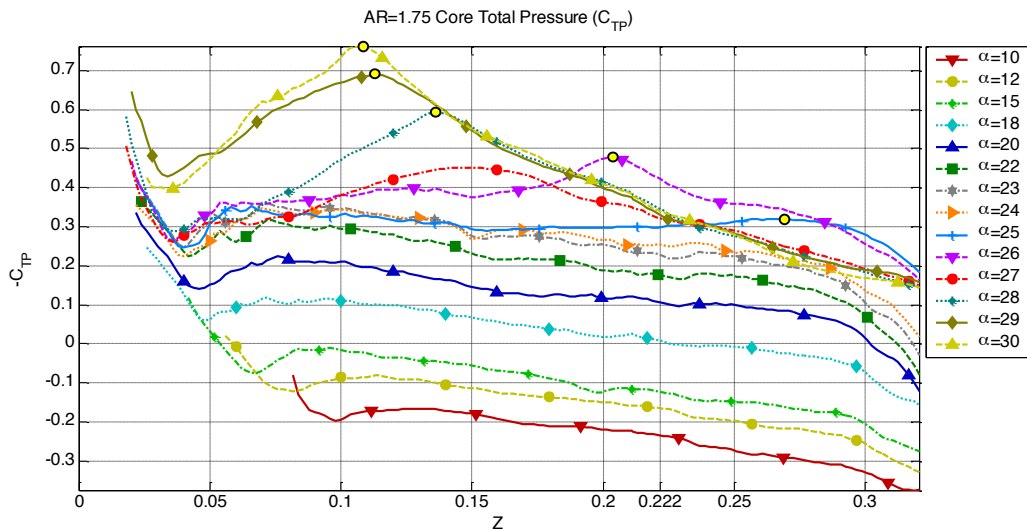


Figure 6.18 Coefficient of total pressure ($-C_{TP}$) along the vortex axis for $AR=1.75$ for $10^\circ \leq \alpha \leq 30^\circ$. The location of peak $-C_{TP}$ along the vortex axis is indicated by \circ .

At $\alpha=25^\circ$, due to the gradual decrease in C_{DP} with increasing α , $-C_{TP}$ is constant for the length of the vortex. At $\alpha>25^\circ$, the sudden decrease in C_{DP} causes $-C_{TP}$ to increase along the vortex. The peak in $-C_{TP}$ coincides with the location where C_{DP} reaches a minimum, since before breakdown, C_{DP} decreases the overall C_{TP} . This peak occurs closer to the top of the slant surface as $\alpha\rightarrow 30^\circ$. Past the location of maximum $-C_{TP}$, the contribution of $C_{DP}\approx 0$, so $-C_{TP}$ is mainly comprised of $-C_p$. Since $-C_p$ past the breakdown has a similar profile, $-C_{TP}$ past the breakdown for $\alpha\geq 27^\circ$ along the vortex core is similar.

6.4.4 Core Axial velocity

In Figure 6.19, the $V_{x(\text{axis})}$ is shown at the vortex axis for different slant angles at $AR=1.75$. For $\alpha\geq 25^\circ$, the $V_{x(\text{axis})}$ decreases to $V_{x(\text{axis})}<0.1$ showing the rapid deceleration of the vortex core. Regions of reversed flow are not well indicated due to the averaging of the flow field and streamwise movement of the vortex breakdown location. However, there exists a definite decrease in axial velocity on the vortex centreline for $\alpha\geq 25^\circ$. For $\alpha=27^\circ$, a region of reversed flow occurs for $0.15<Z<0.2$. As the major velocity component at the vortex core is $V_{x(\text{axis})}$, the profiles of C_{DP} (Figure 6.15) are similar to the profiles of $V_{x(\text{axis})}$.

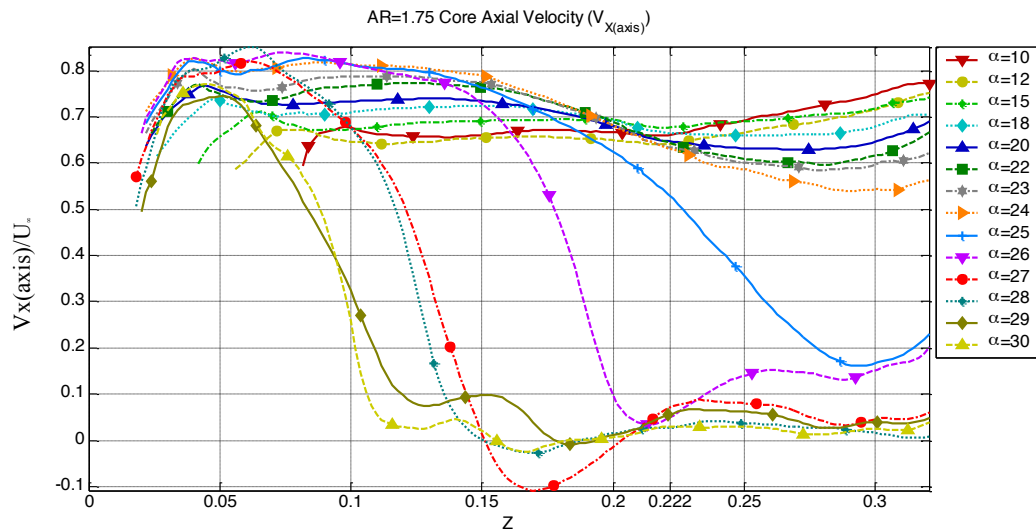


Figure 6.19 $V_{x(\text{axis})}$ along the C-pillar vortex axis for $AR=1.75$ for $10^\circ\leq\alpha\leq 30^\circ$. For regions where the vortex breakdown exists, $V_{x(\text{axis})}/U_0$ drops significantly.

6.4.5 Core Vorticity

The streamwise vorticity ($|\omega_z|$) along the vortex is shown in Figure 6.20 for $AR=1.75$. For all the simulations, the highest $|\omega_z|$ occurs at the formation point of the vortex indicating the highest swirl flow in the vortex core. $|\omega_z|$ then decreases as the C-pillar vortex forms the shear layer on the side of the slant surface. For $\alpha < 25^\circ$, the maximum $|\omega_z|$ increases with α , indicating that the vortex is increasing in strength as $\alpha \rightarrow 23^\circ$, where the peak $|\omega_z|$ in the vortex occurs. For $23^\circ \geq \alpha \geq \alpha_c$, the maximum $|\omega_z|$ is relatively constant at the formation point of the C-pillar vortex. For $\alpha > 25^\circ$, the gradual decrease of $|\omega_z|$ with Z changes and there is a local minimum in $|\omega_z|$. This minimum occurs earlier in the formation of the vortex as $\alpha \rightarrow \alpha_c$, indicating a sudden change in the structure of the C-pillar vortex.

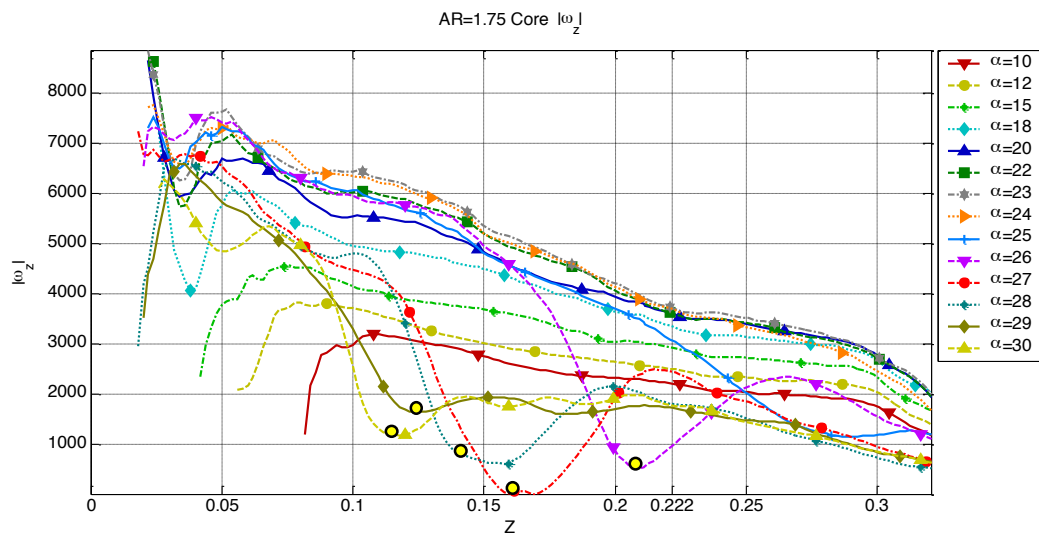


Figure 6.20 Profiles of $|\omega_z|$ along the C-pillar vortex axis for $AR=1.75$ for $10^\circ \leq \alpha \leq 30^\circ$. For regions where the vortex expands, $|\omega_z|$ decreases to a minimum indicated by \circ .

6.4.6 Swirl parameter

The swirl parameter (S) has been used as an indicator of vortex breakdown occurring in the flow field (Section 3.9.4.2). However, S is usually calculated at a location upstream of vortex breakdown as an indicator to determine the likelihood of vortex breakdown occurring in the flow field. In this situation, the location of the vortex breakdown is determined by monitoring the evolution of the vortex as it forms over the slant surface. The critical swirl parameter (S^*) is taken as $S^* \approx 1.37$ (Section 3.9.4.2). S_N which is calculated using $V_{\theta(\max)_N}$ is shown in Figure 1.21. The initial

high S_N at the formation point of the vortex is due to low $V_{x(axis)}$. For $\alpha \leq 24^\circ$, S_N increases due to increasing $V_{\theta(max)_N}$ as the slant angle increases. The peak value of $S_N=0.8$ at $\alpha=24^\circ$ at the end of the slant surface before it decreases as the vortex strength decreases due to interaction with the wake region behind the Ahmed body. However, at $\alpha=25^\circ$, $S_N > 1.4$ at $Z \approx 0.26$ which is past the end of the slant surface. This shows that the C-pillar vortex is starting to break down behind the body. As $\alpha \rightarrow 30^\circ$, $S_N > 1.37$ occurs earlier in the formation of the vortex. The same trends were found when using S_S as can be seen in Figure 6.22.

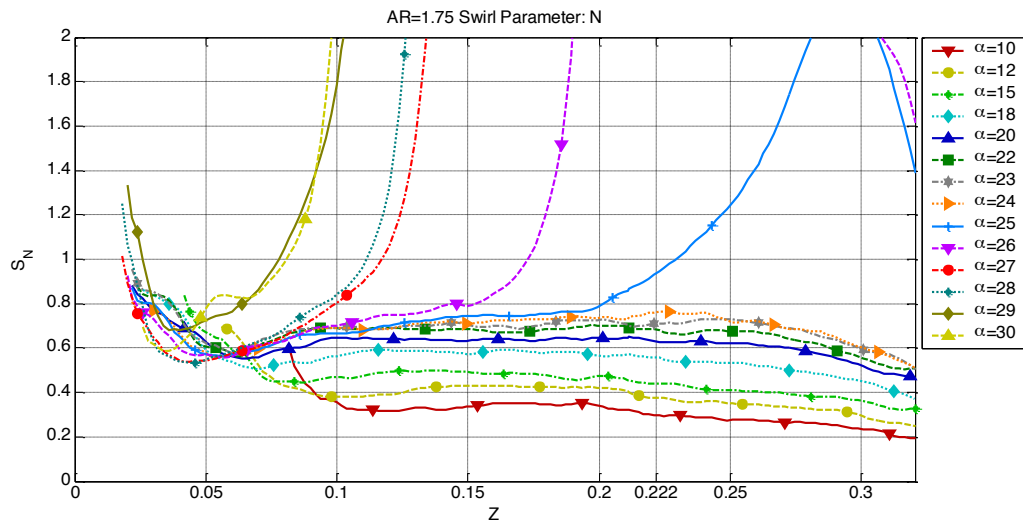


Figure 6.21. The Swirl parameter (S_N) calculated from $V_{\theta(max)_N}$ for $AR=1.75$ $10^\circ \leq \alpha \leq 30^\circ$. S_N exceeding $S^*=1.37$ is used as the criterion to quantify the location of vortex breakdown.

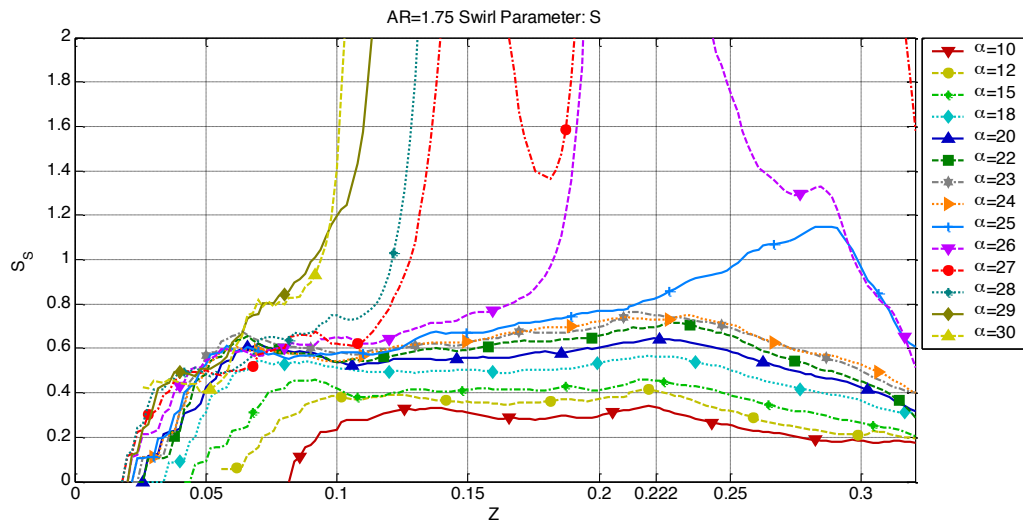


Figure 6.22. The Swirl parameter (S_S) calculated from $V_{\theta(max)_S}$ for $AR=1.75$ $10^\circ \leq \alpha \leq 30^\circ$. S_S exceeding $S^*=1.37$ is used as the criterion to quantify the location of vortex breakdown.

6.4.7 Helix Angle

Hall [60] reported that vortex breakdown would follow if the helix angle (γ) in the flow field exceeded $\gamma \approx 50^\circ$. Figure 6.23 shows the maximum γ calculated along the north-south slice of the velocity field through the core of the vortex. At $\alpha \leq 25^\circ$, after the initial formation of the vortex, the maximum γ is relatively constant in the vortex. The location where the maximum γ along the vortex axis occurs along the vortex axis is closer to the formation point with increasing α . For $\alpha > 25^\circ$, $\gamma > 50^\circ$, which indicates that vortex breakdown occurs at $\alpha = 26^\circ$ and not $\alpha = 25^\circ$ as was shown using the S^* criteria. The transition to $\gamma > 50^\circ$ is quite sudden, indicating an abrupt change in the shape of the vortex. In the region where S_N exceeds 1.4 for $\alpha = 25^\circ$ as shown in Figure 6.21, γ decreases.

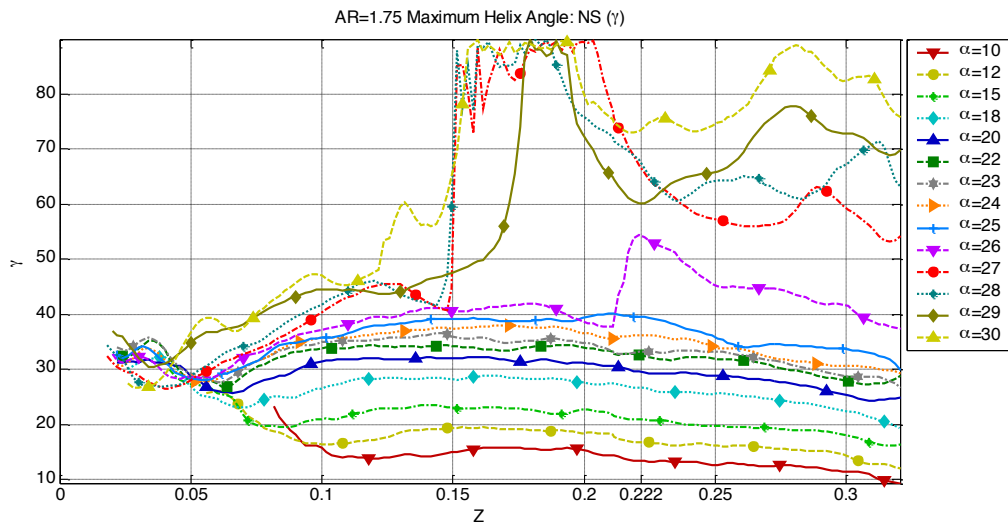


Figure 6.23 The maximum helix angle (γ) in the NS plane for $AR=1.75$, $10^\circ \leq \alpha \leq 30^\circ$. Maximum $\gamma > 50^\circ$ is used as the criteria to determine if the C-pillar vortex breaks down.

Of more significance are the contours of γ taken on the ZY plane through the vortex core before and after the occurrence of vortex breakdown. The breakdown location is clearly visible in the comparison between γ for $\alpha = 24^\circ$ (Figure 6.24) and $\alpha = 28^\circ$ (Figure 6.25). For $\alpha = 24^\circ$, the peak γ occurs at the north edge of the vortex with no clear changes in the structure of the vortex as it progresses downstream and past the slant surface.

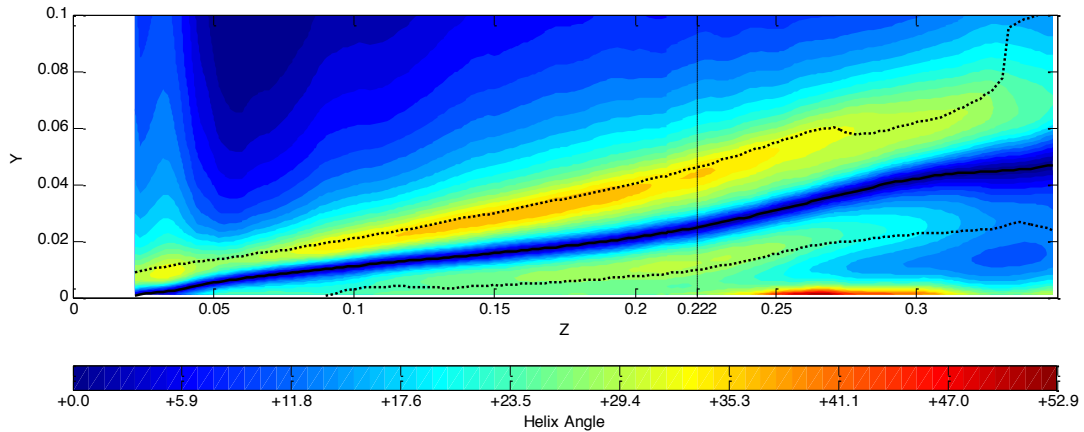


Figure 6.24 Contours of Helix angle (γ) on the NS plane for $AR=1.75$, $\alpha=24^\circ$ showing no significant changes in the C-pillar vortex as it progresses downstream.

For $\alpha=28^\circ$ (Figure 6.25), γ increases dramatically near the vortex core at $Z \approx 0.15$. The change in γ shows a distinct bubble region forming with the peak contours of γ occurring near the vortex core. Since the V_θ is normalised by $V_{\theta(\text{axis})}$, γ is always zero along the vortex centreline. Downstream of $Z \approx 0.15$, contours of γ are not constant indicating that the structure has not stabilised.

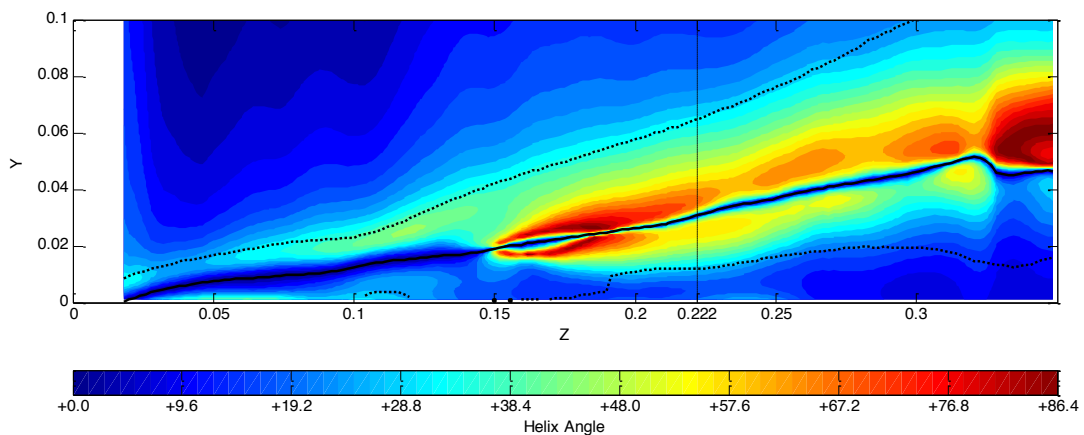


Figure 6.25. Contours of Helix angle (γ) on the NS plane for $AR=1.75$, $\alpha=28^\circ$ showing significant changes in the C-pillar vortex as it progresses downstream at $Z \approx 0.15$.

6.4.8 Core Gradient

Experiments [96] show that the result of vortex breakdown is the expansion of the vortex core. As a result, the gradient of V_θ at the vortex centre is significantly different after vortex breakdown as shown schematically in Figure 6.26. The swirl velocity core gradient,

$\frac{\partial V_\theta}{\partial Y_{(\text{axis})}}$, was calculated along the vortex axis with higher

gradients indicating a vortex with stronger swirl velocity around the vortex centre.

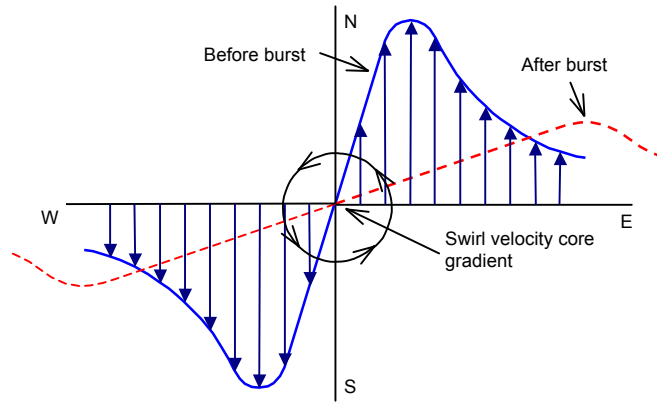


Figure 6.26 Schematic of vortex gradient [96] before breakdown (blue solid line) and after vortex breakdown (red dotted) line indicating a decrease in the core gradient.

Figure 6.27 shows the swirl velocity core gradient calculated from $V_{\theta_{NS}}$. For all slant angles, the highest swirl velocity gradient occurs at the formation point of the vortex and the swirl velocity gradient decreases as the vortex expands downstream. For $\alpha \leq 25^\circ$, there is a gradual decrease in the swirl velocity gradient. However, for $\alpha > 25^\circ$, a local minima (marked with dots) exists indicating a rapid change in vortex shape.

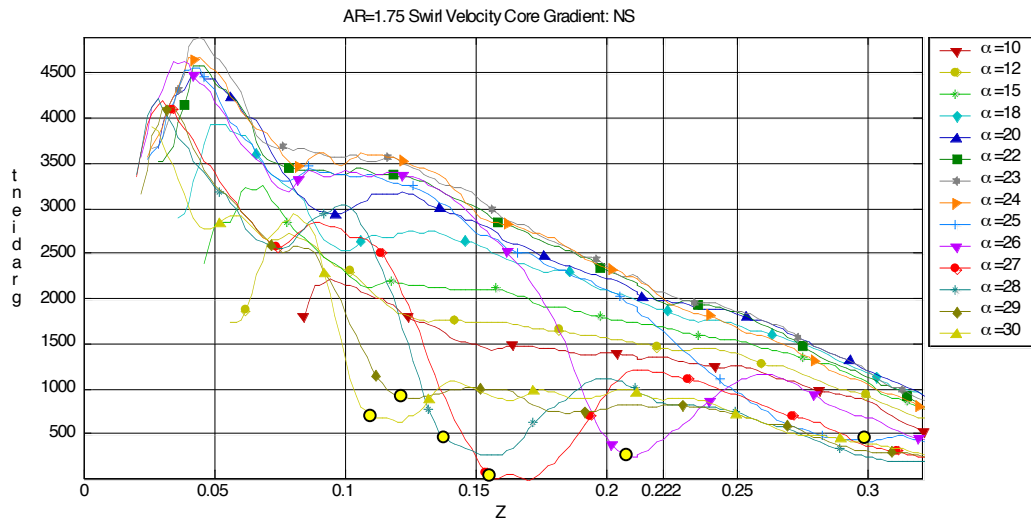


Figure 6.27 The swirl velocity core gradient taken in the NS plane for $AR=1.75$, $10^\circ \leq \alpha \leq 30^\circ$. For regions where the vortex expands, the core gradient decreases to a minimum indicated by \circ .

The swirl velocity core gradient calculated using $V_{\theta_{EW}}$ is shown in Figure 6.28. Similar results were found with a local core gradient minimum in the formation of the vortex. The location of the minima for each α coincides closely with the local minima in Figure 6.27. The value of the local minima is also similar in both the NS

and in the EW directions indicating that the expansion of the vortex core occurs radially.

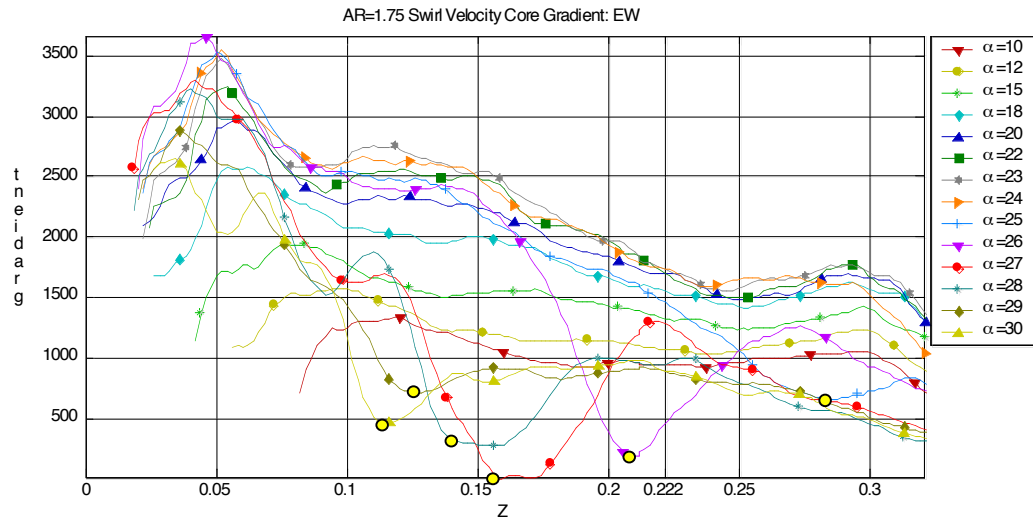


Figure 6.28 The swirl velocity core gradient taken in the EW plane for $AR=1.75$, $10^\circ \leq \alpha \leq 30^\circ$. For regions where the vortex expands, the core gradient decreases to a minimum indicated by \circ .

6.5 Effect of Aspect Ratio on Vortex Breakdown

In the analysis of the C-pillar vortex for $AR=1.75$, simulations indicate that as $\alpha \rightarrow \alpha_c$, the location of vortex breakdown occurs closer to the formation point of the vortex. This is a positive indication that the mechanism for the transition to a large separated wake at $\alpha > \alpha_c$ is due to the breakdown of the C-pillar vortex.

In section Section 5.2.3, the value of α_c decreases with increasing AR. To support the claim that the transition at α_c is due to the bursting of the C-pillar vortex so close to the top of the slant surface as to prevent the formation of the C-pillar vortex, analysis of the C-pillar vortex was undertaken for different AR. By examining the effect of vortex breakdown for different AR, it should be possible to determine if α or α relative to α_c is the critical parameter that affects the presence of vortex breakdown. With the additional parameter, a better understanding of how the C-pillar vortex structure changes can be examined.

6.5.1 Low Aspect Ratio Bodies

To examine the effect of vortex breakdown on low AR bodies, $AR=1.1$ is considered to investigate the change in the C-pillar vortex as $\alpha \rightarrow \alpha_c$. Simulations indicate for $AR=1.1$, vortex breakdown is present for $29^\circ \leq \alpha \leq 33^\circ$, compared with $AR=1.75$ where breakdown is present for $25^\circ < \alpha < 30^\circ$.

6.5.1.1 Core Position

The location of the vortex axis is shown in Figure 6.29 and Figure 6.30 in the YZ plane and XZ plane, respectively. In Regions I & II, where no large separated regions exist on the slant surface, the slope of the C-pillar vortex axis increases as $\alpha \rightarrow \alpha_c = 33^\circ$. Similar to $AR=1.75$, where there is a linear increase in the location of the axis in the X and Y plane for $\alpha < 24^\circ$, there is a linear increase up to $\alpha < 27^\circ$ for $AR=1.1$. In comparison to the case of $\alpha=30^\circ$ and $AR=1.75$, just before total breakdown of the C-pillar vortex at $Z=0.2$, the vortex for $AR=1.1$ and $\alpha=30^\circ$ is closer to the slant surface. Interestingly, the location of the C-pillar vortex at $Z=0.2$ for $AR=1.1$ and $\alpha=33^\circ$ is similar to the case of $AR=1.75$ and $\alpha=30^\circ$, indicating that the position of the C-pillar vortex at α_c does not appear to vary with AR. This suggests that the relation between the C-pillar vortex and α_c is more important than the actual slant angle of the body, since α_c varies. If the position of the C-pillar is due to α , then it would be expected

that the C-pillar vortex would be further away from the slant surface at $\alpha=33^\circ$ compared with $\alpha=30^\circ$.

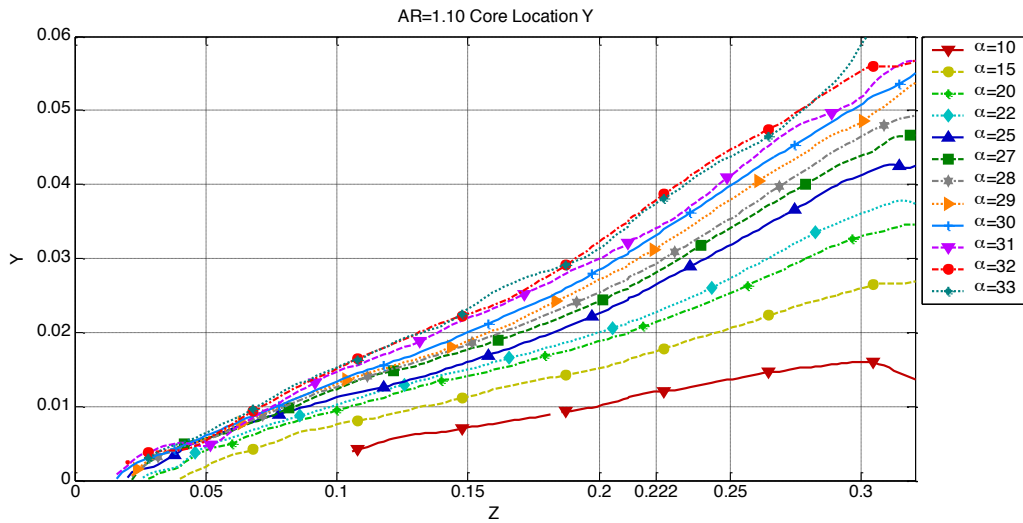


Figure 6.29 Location of vortex axis in the YZ plane for AR=1.1, which indicates the location the vortex above the slant surface.

Figure 6.30 shows the location of the C-pillar vortex relative to the side edge of the slant surface, for a given α . In this figure, the location of the C-pillar vortex is closer to the side edge of the body, indicating that for low AR bodies, the C-pillar vortex is influenced by the AR. This is due to the lower slant surface area. As a result, the C-pillar vortices are located closer to the side edges of the slant surface.

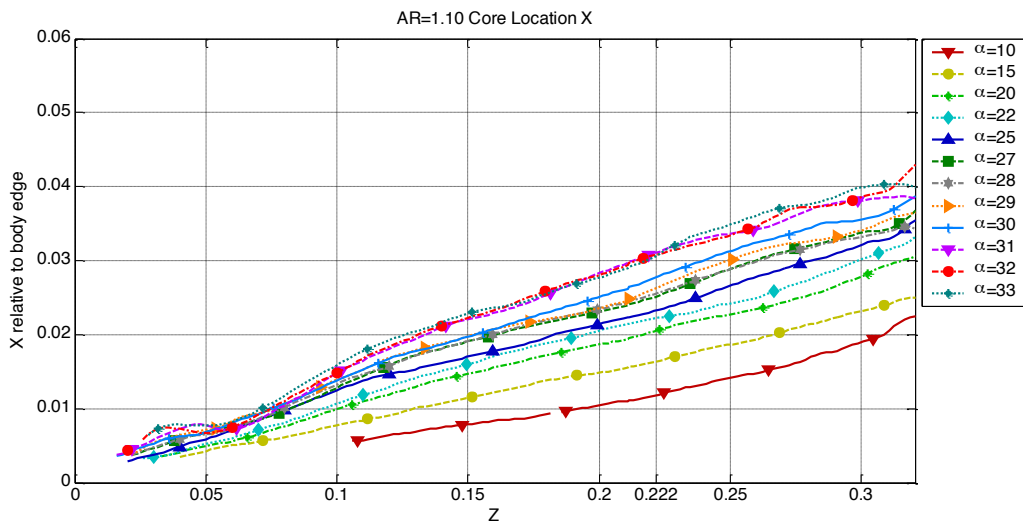


Figure 6.30 Location of vortex axis in the XZ plane for AR=1.1, which indicates how far inward the C-pillar vortex is located relative to the edge of the slant surface.

6.5.1.2 Core radius

Due to the reduced surface area on the slant surface for AR=1.1, the r_c of the C-pillar vortex is more likely to be influenced by the AR since the C-pillar vortex takes

up a greater portion of the slant surface. Figure 6.31 shows r_c for AR=1.1 calculated from the location of $V_{\theta_{\max N}}$ (Section 3.9.4.2). The variation found of r_c with Z for AR=1.75 (Figure 6.11) is present but is not as abrupt for the AR=1.1. The transition from the linear radial increase with X to a linear piecewise profile occurs at $\alpha=29^\circ$, compared with $\alpha=25^\circ$ for AR=1.75. The reason for the small increase of r_c for $\alpha>31^\circ$ at $X<0.05$ near the formation location is due to the small dip of the core at that location, shown in Figure 6.29, increasing r_c relative to the Y increase of the vortex axis. Past the end of the body ($Z>0.222$), there is a larger variation in r_c due to its interaction with the wake structures downstream, which gives a false impression of r_c , especially for $\alpha=27^\circ$. Here the decrease of r_c is due to a small decrease in the location of $V_{\theta_{\max N}}$ from the change of shape of the C-pillar vortex.

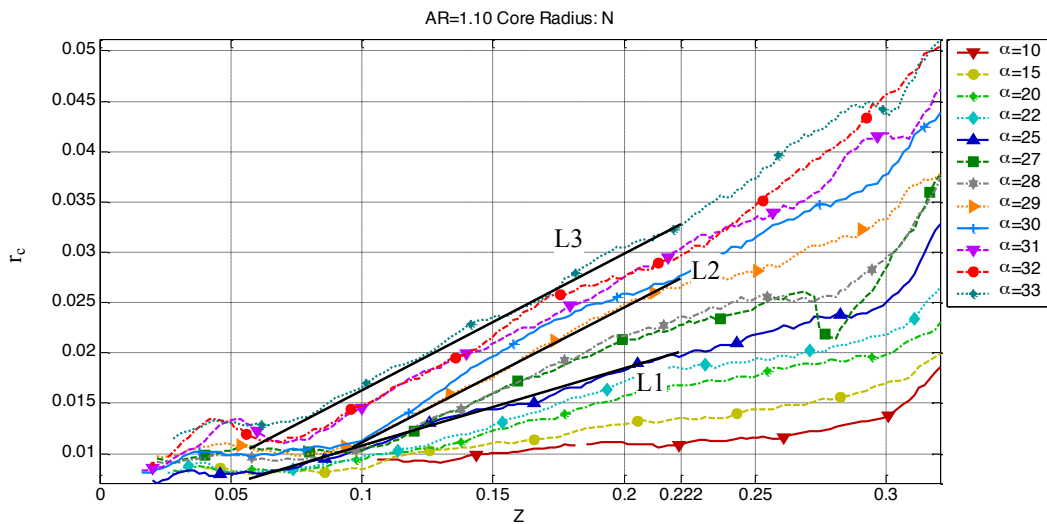


Figure 6.31 The radius of C-pillar vortex (r_c) for AR=1.1. For $\alpha \leq 24^\circ$, there is a linear increase in r_c with Z, while for $\alpha > 25^\circ$, r_c has a linear piecewise profile, where the core of the vortex expands after the vortex has formed. L1-L3 are described Section 6.4.2.

The change in r_c is outlined in Figure 6.32. This figure shows contours of V_θ through the core of the vortex with the region of interest highlighted by a rectangular box. In Figure 6.32a, V_θ is constant along the vortex core. However, at $\alpha=29^\circ$ (Figure 6.32b), there is an increase in the extent of the region of $V_\theta \approx 0$ near the vortex axis, which increases r_c since $V_{\theta_{\max N}}$ is pushed further away from the vortex axis. The location of the expansion on the centreline of the vortex occurs earlier in the formation of the C-pillar vortex at $\alpha=28^\circ$ (Figure 6.32c), until at $\alpha=33^\circ$ (Figure

6.32d), the expansion of the vortex occurs at $Z \approx 0.075$, near the top of the slant surface.

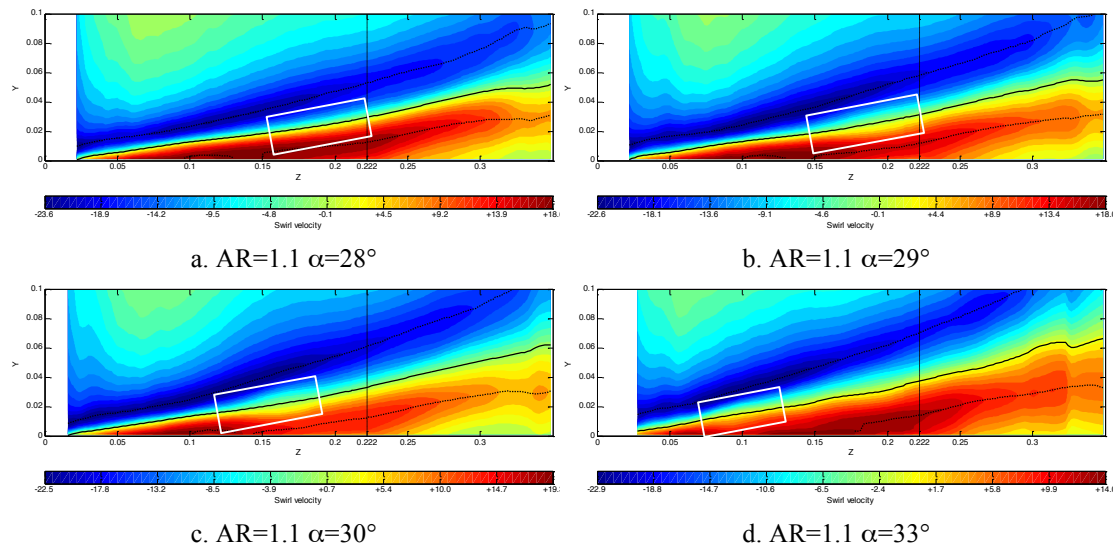


Figure 6.32 Contours of swirl velocity (V_θ) on the NS plane for AR=1.1, $\alpha=28^\circ$ (a), $\alpha=29^\circ$ (b), $\alpha=30^\circ$ and $\alpha=33^\circ$. The black box indicates the region where there is an increase of the extent of the region of $V_\theta \approx 0$ on the axis centerline.

6.5.1.3 Core Pressure

Figure 6.33 shows profiles of $-C_p$ along the vortex axis for $10^\circ \leq \alpha \leq 33^\circ$ at AR=1.1. Similar to AR=1.75, as α increases, $-C_p$ inside the vortex increases with the strongest $-C_p$ at the formation point of the vortex. As the C-pillar vortex progresses along the slant surface, $-C_p$ decreases towards $C_p=0$, which is evident for all slant angles. The profiles of $-C_p$ for $\alpha > 29^\circ$ show that the adverse pressure gradient increases as the vortex progresses, with the location of the maximum pressure gradient occurring closer to the top of the slant surface. For $\alpha \geq 31^\circ$, there is little variation of $-C_p$ with α , indicating a similar vortex structure, with breakdown occurring near the formation point of the C-pillar vortex.

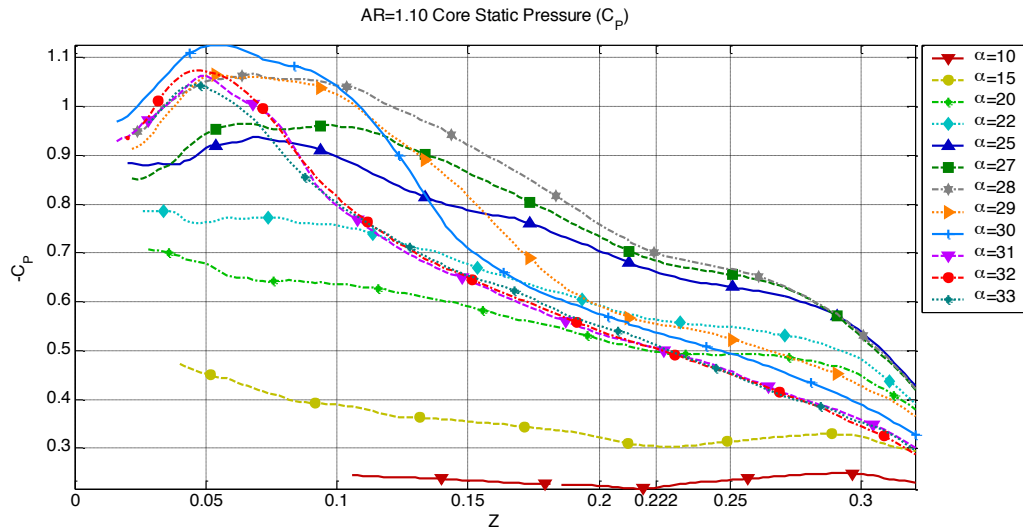


Figure 6.33 Coefficient of static pressure ($-C_p$) along the vortex axis for $AR=1.1$ for $10^\circ \leq \alpha \leq 33^\circ$.

For $AR=1.75$ in section 6.4.3, the C_{DP} , which is comprised mainly of $V_{x(axis)}$, decreased considerably at the breakdown location. As can be seen in Figure 6.36, the C_{DP} for $AR=1.1$ exhibits a sudden decrease to $C_{DP} \leq 0.1$ at the location of the vortex breakdown. This location where $C_{DP} \approx 0.1$ for $\alpha \geq 29^\circ$ occurs closer to the top of the slant surface with increasing α . In comparison with Figure 6.15 for $AR=1.75$, the value of C_{DP} at $Z \approx 0.222$ was similar if breakdown was not evident. However, for $AR=1.1$, while for $\alpha \leq 25^\circ$, $C_{DP} \approx 0.45$ at $Z \approx 0.222$, C_{DP} for $27^\circ \leq \alpha < 28^\circ$ is considerably less but does not approach $C_{DP} \approx 0.1$. For $27^\circ \leq \alpha < 28^\circ$, although there is a decrease in C_{DP} indicating a decrease of $V_{x(axis)}$, S_N does exceed the threshold for vortex breakdown to occur.

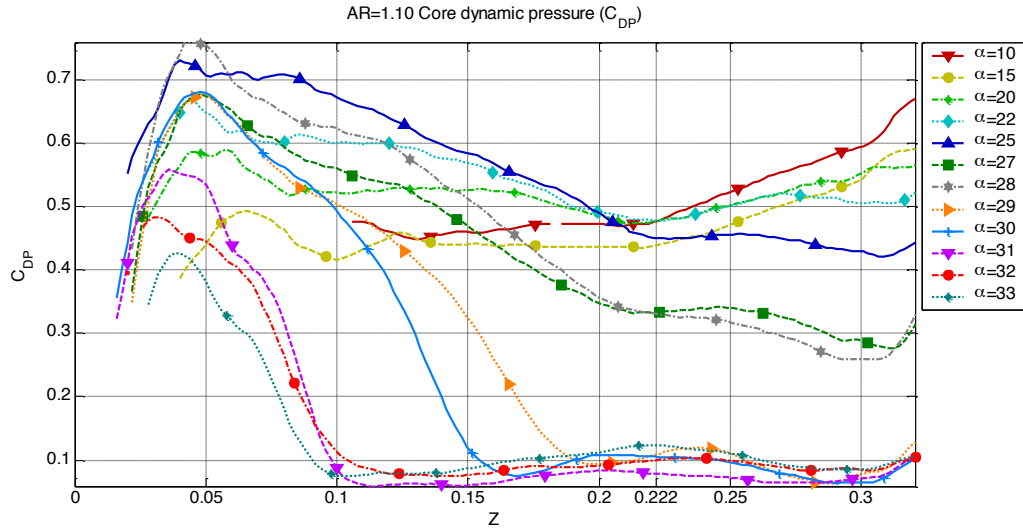


Figure 6.34 Coefficient of dynamic pressure ($-C_{DP}$) along the vortex axis for AR=1.1 for $10^\circ \leq \alpha \leq 33^\circ$.

Profiles of $-C_{TP}$ for AR=1.1 in Figure 6.35 exhibit the presence of breakdown along the vortex core. The increased region of C_{DP} near the formation location of the C-pillar vortex, decreases C_{TP} for $\alpha > 29^\circ$, which leads to a maximum of C_{TP} at the location of vortex breakdown. Past the change in $-C_{TP}$ at formation point of the C-pillar vortex, the $-C_{TP}$ increases to a maximum downstream (marked with \circ in Figure 6.35); beyond this location, $-C_{TP}$ consists mainly of $-C_p$. The location of maximum $-C_{TP}$ occurs at $Z \approx 0.18$, which is closer to the top of the slant surface with increasing α , where at $\alpha_c = 33^\circ$, the maximum $-C_{TP}$ occurs at $Z \approx 0.09$.

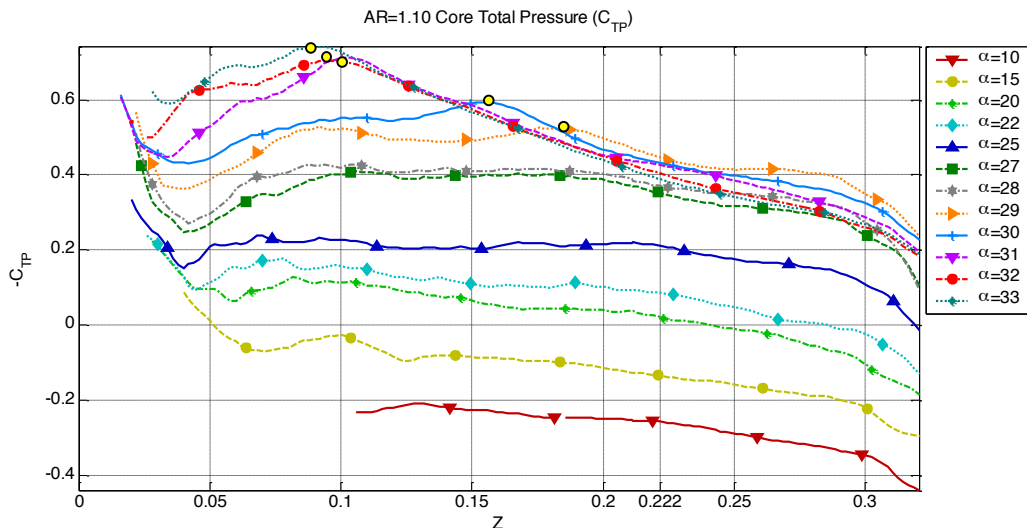


Figure 6.35 Coefficient of total pressure ($-C_{TP}$) along the vortex axis for AR=1.1 for $10^\circ \leq \alpha \leq 33^\circ$. The location of peak $-C_{TP}$ along the vortex axis is indicated by \circ .

For AR=1.75 in section 6.4.3, the C_{DP} which is comprised mainly of $V_{x(axis)}$ decreased significantly at the breakdown location. As can be seen in Figure 6.36, the C_{DP} for AR=1.1 exhibits a sudden decrease to $C_{DP} \leq 0.1$ at the location of the vortex breakdown. This location, where $C_{DP} \approx 0.1$ for $\alpha \geq 29^\circ$, is closer to the top of the slant surface with increasing α . In comparison with Figure 6.15 for AR=1.75, the value of C_{DP} at $Z \approx 0.222$ was similar if breakdown was not evident. However, for $\alpha \leq 25^\circ$ at AR=1.1, C_{DP} at the base of the slant surface $C_{DP} \approx 0.45$ but for $27^\circ \leq \alpha < 28^\circ$ C_{DP} is considerably less but does not approach $C_{DP} \approx 0.1$. For $27^\circ \leq \alpha < 28^\circ$, although there is a decrease in C_{DP} showing a reduction of $V_{x(axis)}$, S_N does exceed the threshold for vortex breakdown to occur.

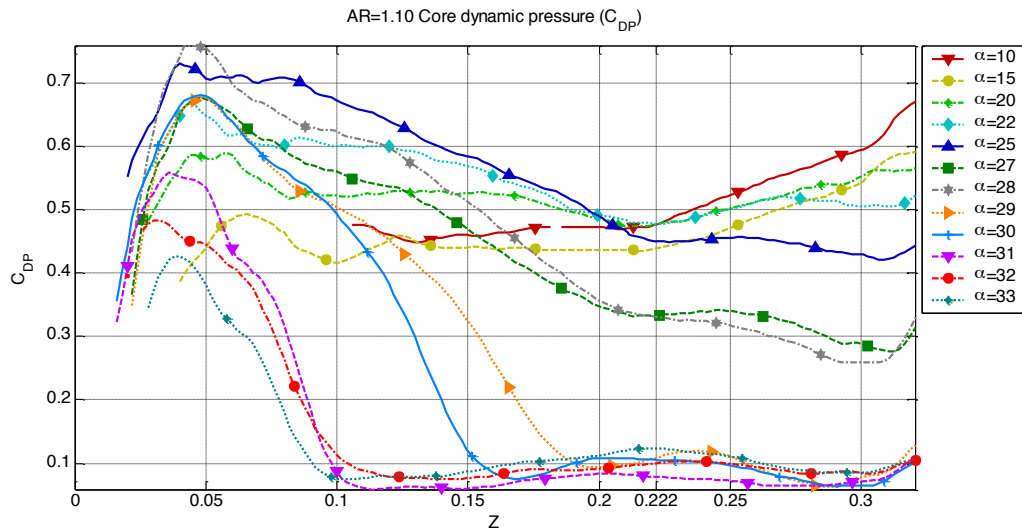


Figure 6.36 Coefficient of dynamic pressure (C_{DP}) along the vortex axis for AR=1.1 for $10^\circ \leq \alpha \leq 33^\circ$.

6.5.1.4 Core Axial velocity

Figure 6.37 plots $V_{x(axis)}$ for AR=1.10 for $10^\circ \leq \alpha < 33^\circ$. This shows a clear transition in profile at $\alpha = 28^\circ$. For $\alpha \leq 28^\circ$, along the axis, there is a gradual decrease of $V_{x(axis)}$ along the entire length of the $V_{x(axis)} > 0.4$. At $\alpha \approx 22^\circ$, which is the junction between Region II and Region III, the gradient of $V_{x(axis)}$ changes from a positive gradient for $Z > 0.1$ to a negative gradient for $\alpha > 28^\circ$. In Region II, the C-pillar is weaker and as the vortex dissipates in the wake, $V_{x(axis)} \rightarrow U_\infty$.

At $\alpha > 28^\circ$, there is a sudden decrease in $V_{x(axis)}$ which occurs earlier in the formation of the vortex for increasing α although the flow is not reversed. There is

also a corresponding decrease in the maximum $V_{x(\text{axis})}$ for a given slant angle for $\alpha > 28^\circ$, indicating that the entire axial velocity of the vortex decreases with $\alpha \rightarrow \alpha_c$. Similarly near α_c , $V_{x(\text{axis})}$ along the entire axis decreases, making the vortex more likely to breakdown.

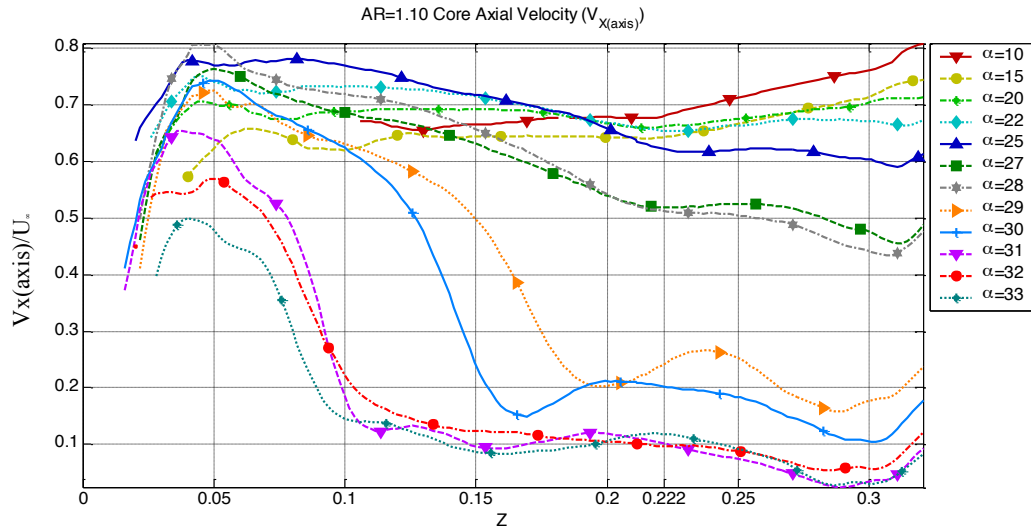


Figure 6.37 $V_{X(\text{axis})}$ along the C-pillar vortex axis for $AR=1.1$ for $10^\circ \leq \alpha \leq 33^\circ$. For regions where the vortex breakdown exists, $V_{X(\text{axis})}/U$ drops significantly.

6.5.1.5 Core vorticity

Figure 6.38 shows the change in absolute streamwise vorticity ($|\omega_z|$) along the core axis for $AR=1.1$. As $\alpha \rightarrow 25^\circ$, the maximum $|\omega_z|$ along the core of the vortex increases to a maximum of $|\omega_z| \approx 7000s$ which occurs for $\alpha=25^\circ$ near the formation point of the vortex. For $\alpha > 28^\circ$, there is a local minimum on $|\omega_z|$ as the vortex forms. The location of the minimum $|\omega_z|$ occurs closer to the top of the slant surface with increasing α . After the position of $|\omega_z|$, there is no recovery of $|\omega_z|$ back to levels found for $\alpha \leq 28^\circ$ for a given downstream distance, indicating that the vortex has changed structure and the rotation around the vortex core has decreased.

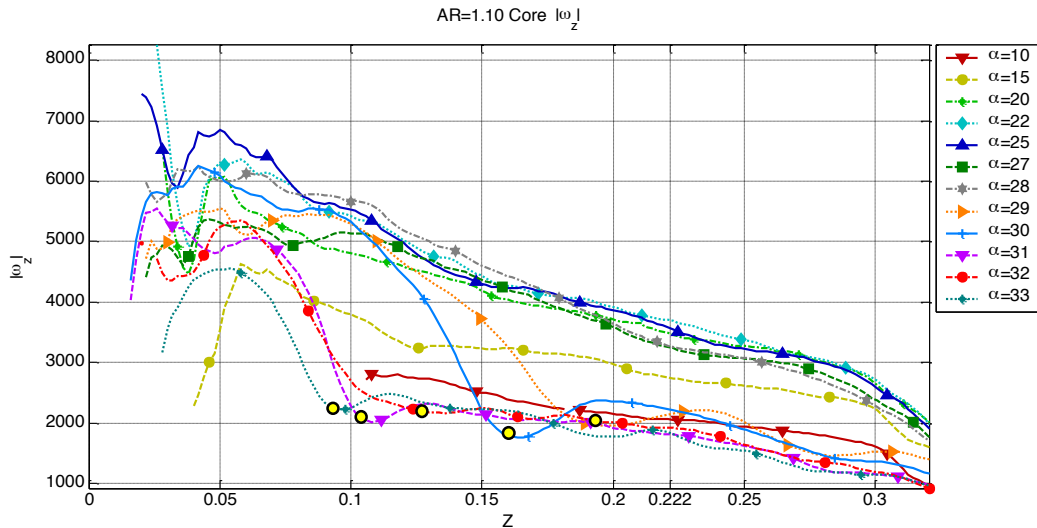


Figure 6.38 Profiles of $|\omega_z|$ along C-pillar vortex axis for $AR=1.1$ for $10^\circ \leq \alpha \leq 33^\circ$. For regions where the vortex expands, $|\omega_z|$ decreases to a minimum indicated by \circ .

6.5.1.6 Swirl parameter

To determine the existence of vortex breakdown for $AR=1.1$, S_N is plotted in Figure 6.39 for the slant angles examined. For $\alpha \leq 28^\circ$, the S_N does not exceed $S^* \approx 1.37$ at any location along the C-pillar vortex. For $AR > 28^\circ$, as the vortex progresses downstream, $S^* \approx 1.37$ is exceeded. For $\alpha = 29^\circ$, $S^* \approx 1.37$ at $Z \approx 0.16$, which decreases to $Z \approx 0.07$ for $\alpha = 33^\circ$. Compared with $AR=1.75$, where $S^* > 1.37$ for $25^\circ \geq \alpha \geq 30^\circ$, vortex breakdown is not evident until a higher α as predicted by the decrease in $V_{x(axis)}$.

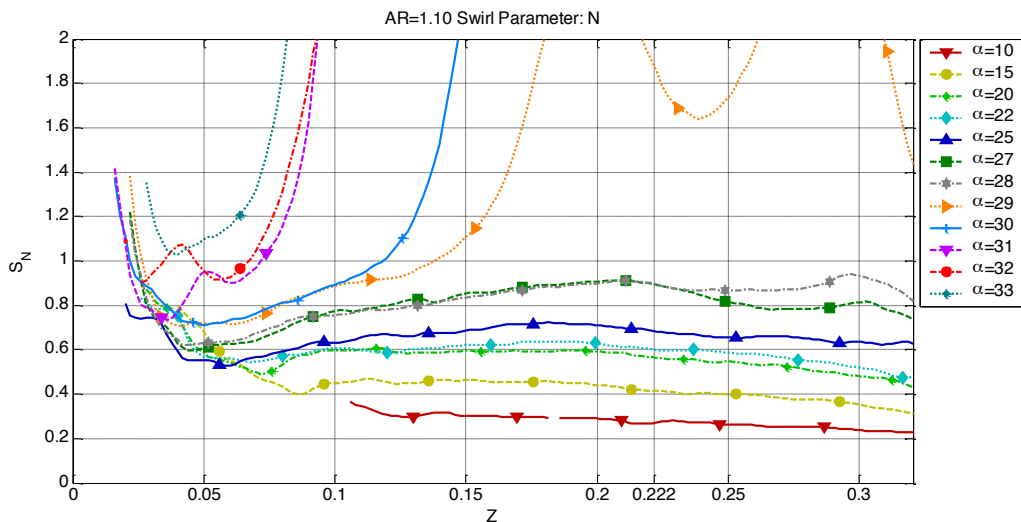


Figure 6.39 The Swirl parameter (S_N) calculated from $V_{0(max)N}$ for $AR=1.1$ $10^\circ \leq \alpha \leq 33^\circ$. S_N exceeding $S^*=1.37$ is used as the criterion to quantify the location of vortex breakdown.

6.5.1.7 Helix angle

The maximum helix angle (γ) for a given Z location for $AR=1.1$ is shown in Figure 6.40. Contrary to the S_N , $\gamma > 50^\circ$ for $\alpha > 31^\circ$, which implies that in the range $29^\circ \leq \alpha \leq 30^\circ$, vortex breakdown is not predicted to occur. The location where $\gamma > 50^\circ$, occurs past the end of the slant surface for $\alpha = 31^\circ$ and 32° , whereas the S^* and decrease in axial velocity along the centreline predicts vortex breakdown to occur closer to the top of the slant surface. However, 50° is a rule of thumb and not a precisely determined critical value.

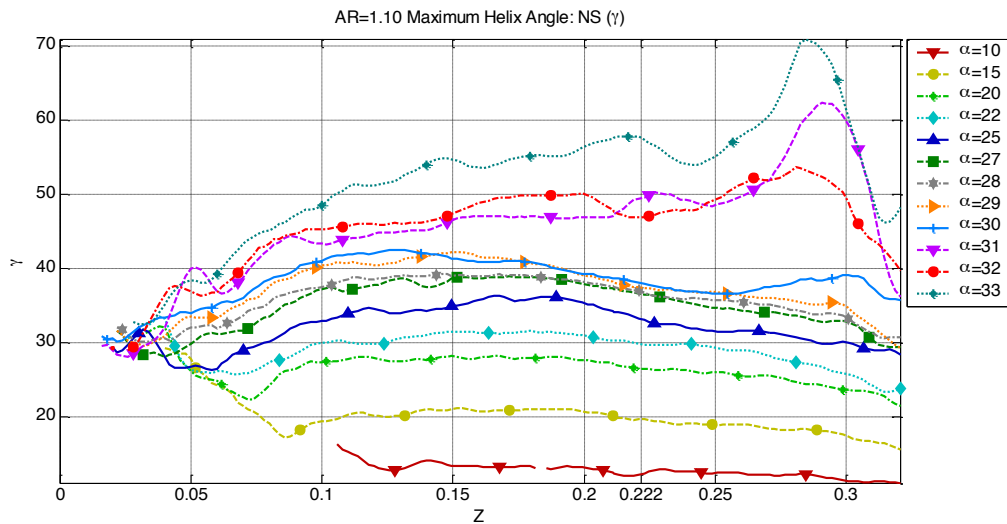


Figure 6.40 The maximum helix angle (γ) in the NS plane for $AR=1.1$, $10^\circ \leq \alpha \leq 33^\circ$. Maximum $\gamma > 50^\circ$ is used as the criteria to determine if the C-pillar vortex breaks down.

This difference can be seen in Figure 6.41, which shows contours of the γ along a NS slice through the core of the vortex. While for $\alpha=28^\circ$ (Figure 6.41a) and $\alpha=29^\circ$ (Figure 6.41b), the maximum γ occurs mid way down the slant surface, but does not exceed $\gamma = 50^\circ$. For α where $\gamma > 50^\circ$ such as $\alpha=30^\circ$ (Figure 6.41c) and $\alpha=33^\circ$ (Figure 6.41d), an abrupt change in vortex occurs past the end of the slant surface signalling a change in vortex structure. However, substantial decrease in $V_{x(\text{axis})}$ which is usually associated with vortex breakdown occurs near the formation point of the vortex structure. This is different to $\alpha=28^\circ$, $AR=1.75$, where the abrupt change in the C-pillar vortex occurs at roughly the same location where $S_N > S^*$.

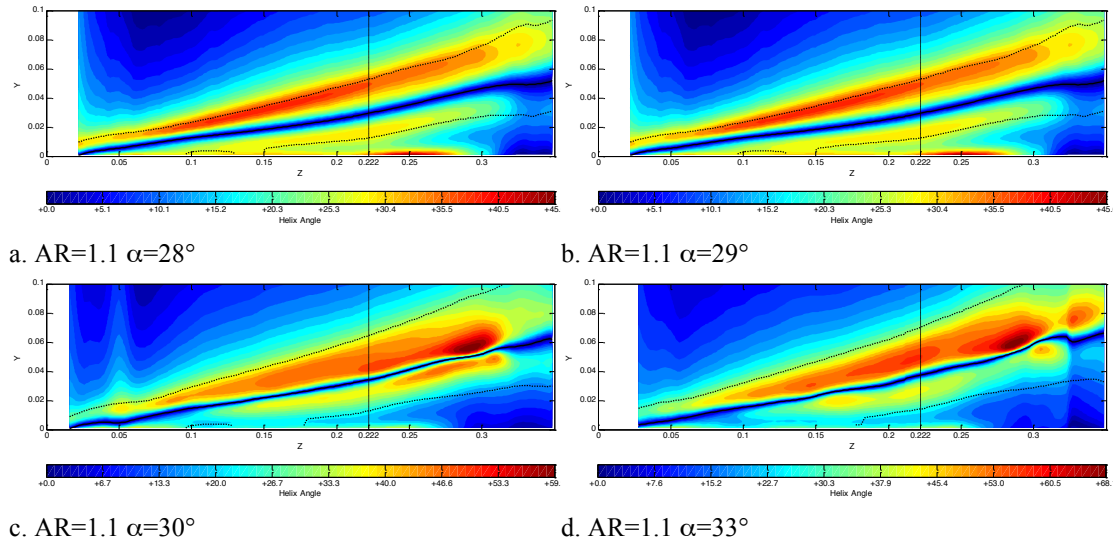


Figure 6.41 Contours of Helix angle (γ) on the NS plane for $AR=1.1$, $\alpha=28^\circ$ (a), $\alpha=29^\circ$ (b), $\alpha=30^\circ$ (c) and $\alpha=33^\circ$ (d). While γ does not predict the initial location of the breakdown, γ indicates the change of the vortex structure.

6.5.1.8 Core Gradient

The core gradient taken in the NS plane shown in Figure 6.42 reveals a decrease in the core gradient due to the decrease in V_θ near the axis core as a result of the expansion of the vortex. The decrease in the core gradient occurs for $\alpha=29^\circ$ at $Z \approx 0.2$ and is marked with a dot. The location of minimum gradient occurs closer to the top of the slant surface as $\alpha \rightarrow 33^\circ$, indicating a significant reduction in the swirl velocity of vortex core similar to $|\omega_z|$.

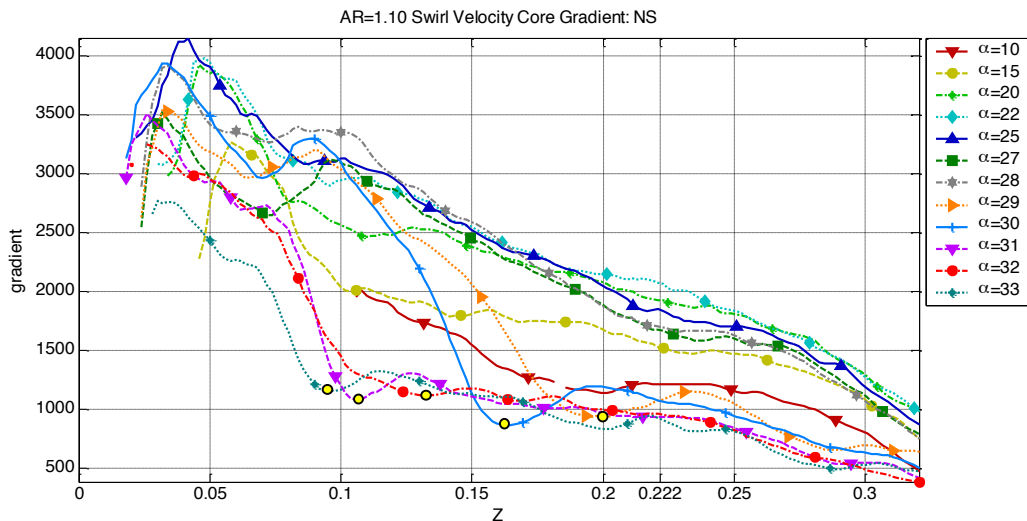


Figure 6.42. The swirl velocity core gradient taken in the NS plane for $AR=1.1$, $10^\circ \leq \alpha \leq 33^\circ$. For regions where the vortex expands, the core gradient decreases to a minimum indicated \circ .

6.5.2 High Aspect Ratio Bodies

The location of the vortex core burst point leading up to the complete breakdown of the C-pillar vortex for $\alpha > \alpha_c$ is not as distinct for $AR=2.5$ as in the previous cases ($AR \leq 1.75$). For $AR=2.5$, evidence of vortex breakdown is only present for $\alpha = \alpha_c = 25^\circ$, while for $AR=1.1$ and $AR=1.75$, breakdown is present for $\alpha < \alpha_c$.

6.5.2.1 Core Location

The location of the vortex core in the Y-plane is shown in Figure 6.43. In comparison to $AR=1.75$, the location of the vortex core for $\alpha=25^\circ$ has a similar profile with an almost linear increase in Y as the vortex forms over the slant surface. Unlike $AR=1.75$, there is no distinct change in the location of the vortex centre in the YZ plane as $\alpha \rightarrow \alpha_c$.

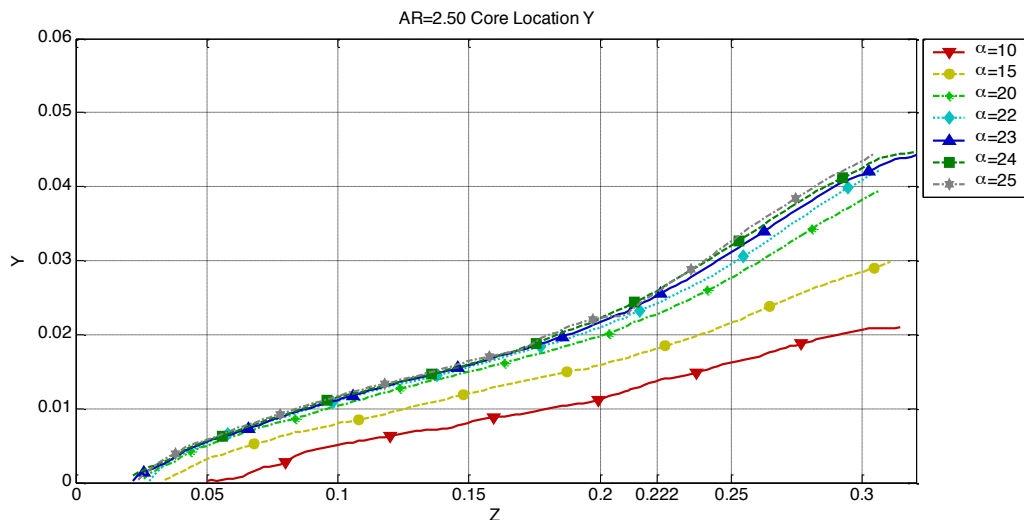


Figure 6.43 Location of core axis in the YZ plane for $AR=2.5$, which indicates the location the vortex above the slant surface.

The X-location of the C-pillar vortex relative to the edge of the body, in Figure 6.44, is shown up to $\alpha_c=25^\circ$. As for the Y-plane, the location of the vortex in the X-plane is similar to $AR=1.75$. There is a slight increase in the location of the C-pillar vortex, indicating that the vortex has moved further inboard with an increase in AR ; however, this is not a significant change in the vortex location.

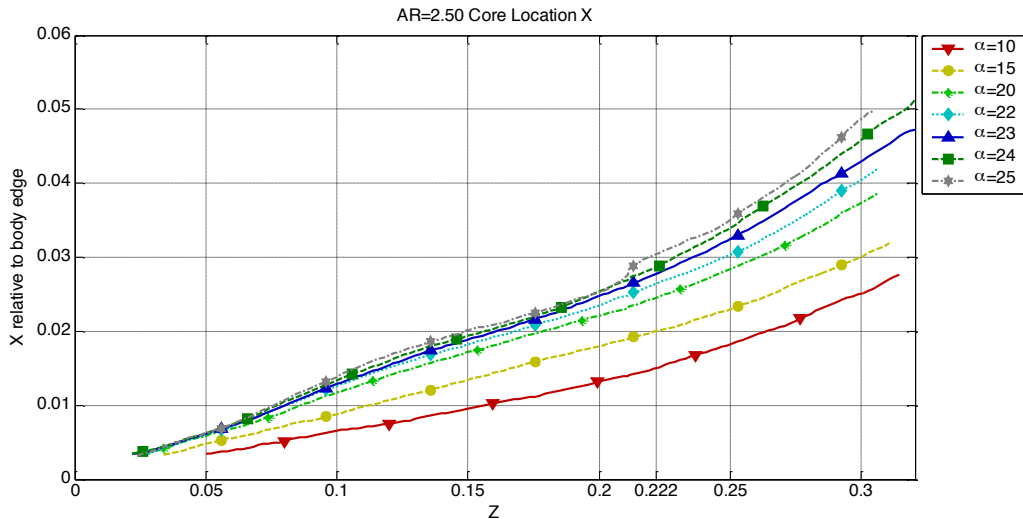


Figure 6.44 Location of vortex axis in the XZ plane for AR=2.5, which indicates how far inward the C-pillar vortex is located relative to the edge of the slant surface.

6.5.2.2 Core Radius

The core radius (r_c) calculated from $V_{\theta_{max N}}$ for AR=2.5 is outlined in Figure 6.45. For $\alpha < 25^\circ$, there is a linear increase in r_c with respect to Z for increasing α . At $\alpha = 25^\circ$, the profile of C-pillar vortex changes to piecewise linear profile with the gradient of r_c increasing at $Z \approx 0.125$. Past the end of the slant surface ($Z > 0.222$), the sudden decrease of r_c is due to the decrease in location of $V_{\theta_{max N}}$ as shown in Figure 6.46a.

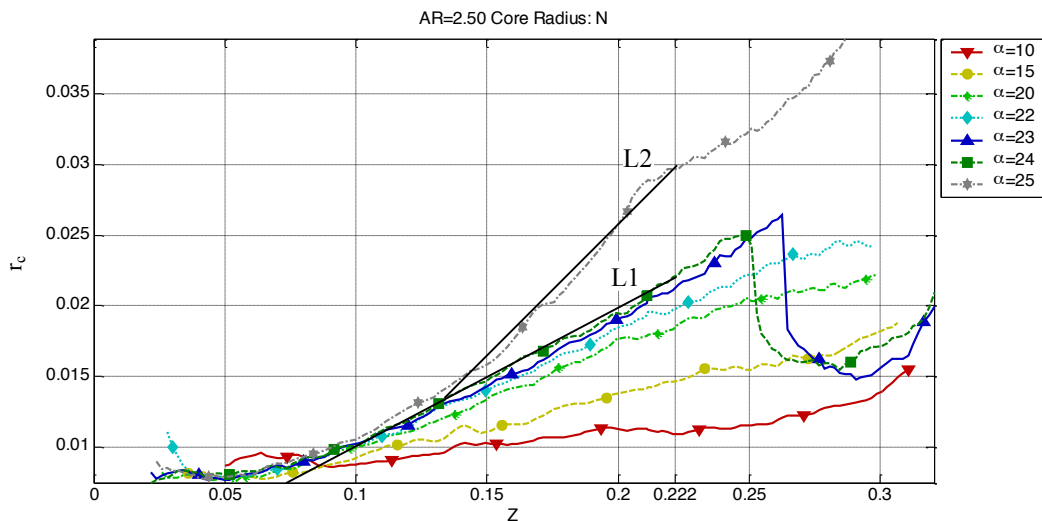


Figure 6.45 The radius of C-pillar vortex (r_c) for AR=2.5. For $\alpha \leq 24^\circ$, there is a linear increase in r_c with Z, while for $\alpha = 25^\circ$, r_c has a linear piecewise profile, where the core of the vortex expands after the vortex has formed.

The change of r_c between $\alpha=24^\circ$ and $\alpha=25^\circ$ for AR=2.5 is shown in Figure 6.46 using contours of V_θ in the NS plane along the vortex axis. The profile for $\alpha=24^\circ$ (Figure 6.46a) shows that the C-pillar vortex changes as it progresses downstream. However, at $\alpha=25^\circ$ (Figure 6.46b), r_c increases due to the increased region of $V_\theta \approx 0$ near the vortex centreline at $Z > 0.175$.

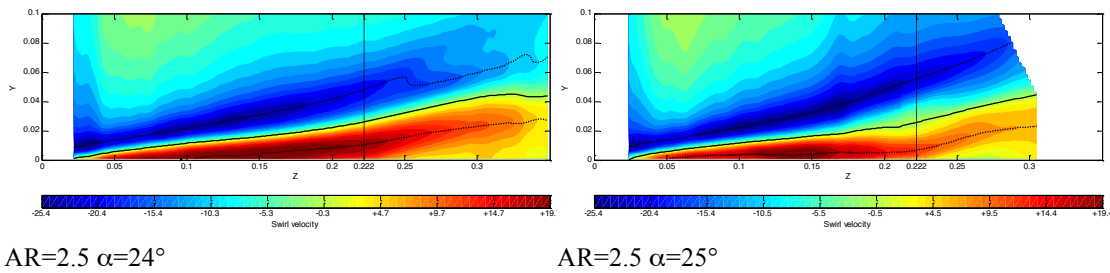


Figure 6.46 Contours of swirl velocity (V_θ) on the NS plane for AR=2.5, $\alpha=24^\circ$ (a) and $\alpha=25^\circ$ (b). For $\alpha=25^\circ$, a region of $V_\theta \approx 0$ appears, increasing the size of the C-pillar vortex.

6.5.2.3 Pressure

The profiles of $-C_p$ at AR=2.5 for various slant angles are shown in Figure 6.47. For increasing α , the $-C_p$ of the vortex increases as observed for AR=1.75. Even with the large increase in AR, the profiles of $-C_p$ for $\alpha < 25^\circ$ are similar, although $-C_p$ for a given α for AR=2.5 is higher compared with AR=1.75. At $\alpha=25^\circ$ where vortex breakdown is present for both aspect ratios, the location where the $-C_p$ decreases occurs earlier in the formation of the C-pillar vortex above the slant surface.

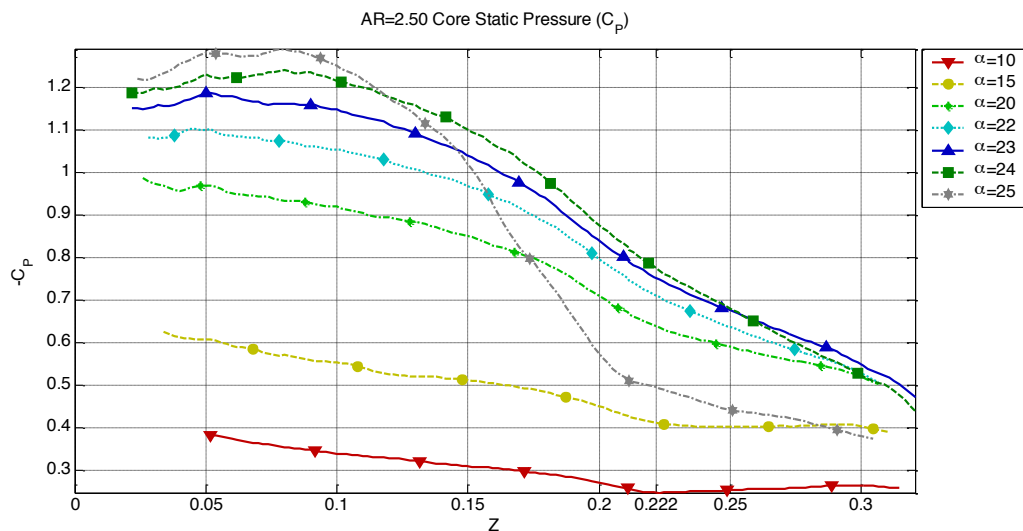


Figure 6.47 Coefficient of static pressure ($-C_p$) along the vortex axis for AR=2.5 for $10^\circ \leq \alpha \leq 25^\circ$.

The C_{DP} for AR=2.5 in Figure 6.48 shows a significant reduction in C_{DP} for $\alpha=25^\circ$ where there is a marked reduction in the axial velocity along the vortex core. Similar

to $AR=1.75$, C_{DP} at the base of the slant surface for $\alpha \leq 24^\circ$ is unchanged for all angles at $C_{DP} \approx 0.45$. The region where $0.1 < C_{DP} < 0.45$ at $Z \approx 0.222$ for $AR=1.1$ was not observed for the higher AR bodies.

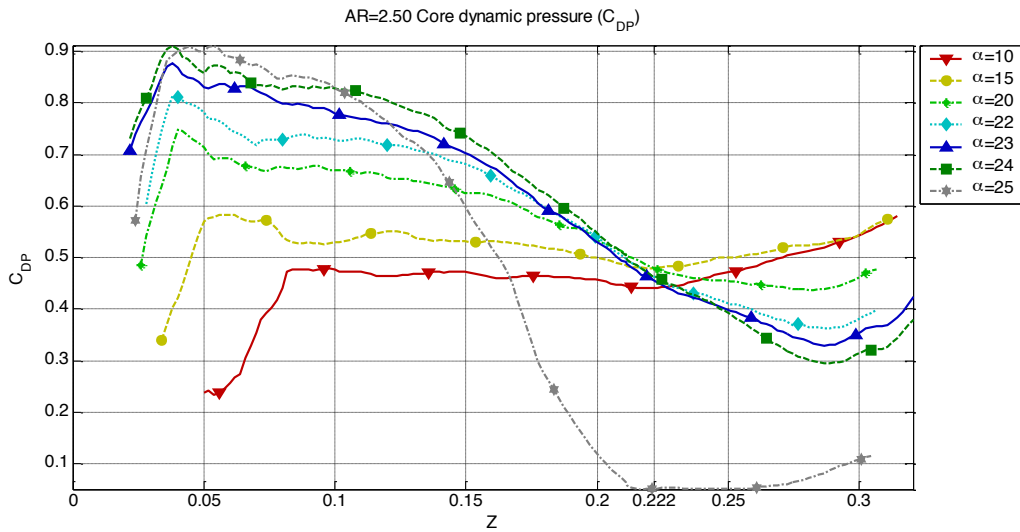


Figure 6.48 Coefficient of dynamic pressure (C_{DP}) along the vortex axis for $AR=2.5$ for $10^\circ \leq \alpha \leq 25^\circ$.

Profiles of $-C_{TP}$ in Figure 6.49 for $AR=2.5$ initially appear different to $AR=1.1$ (Figure 6.18) and $AR=1.75$ (Figure 6.35). These differences are due to the fact that only one slant angle exists where the vortex breaks down for $AR=2.5$. For $AR=1.75$, $\alpha=25^\circ$, $-C_{TP}$ is relatively constant along the entire slant surface, while for $AR=2.5$, $\alpha=25^\circ$, the location of the breakdown is noted by the slight increase of $-C_{TP}$ at $Z \approx 0.18$.

Since $C_{TP} = C_{DP} + C_P$, the increasing C_P cancels out the decreasing C_{DP} along the vortex axis for $\alpha \leq 24^\circ$, leaving almost a constant C_{TP} throughout the formation of the vortex. However, for $\alpha=25^\circ$, C_{DP} reduces the $-C_{TP}$ before breakdown of the vortex, and after breakdown, $-C_{TP}$ mainly consists of the $-C_P$ component since $C_{DP} \approx 0$.

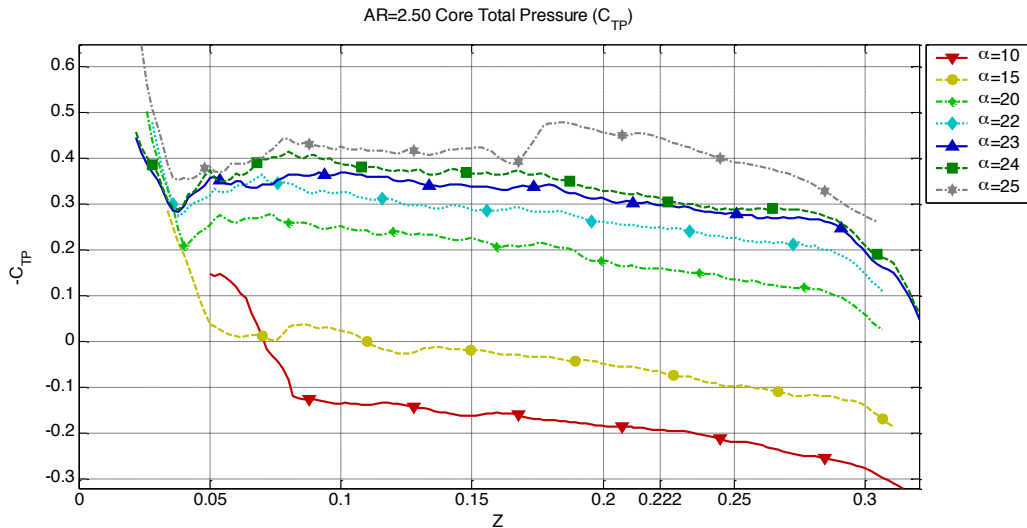


Figure 6.49 Coefficient of total pressure ($-C_{TP}$) along the vortex axis for $AR=2.5$ for $10^\circ \leq \alpha \leq 25^\circ$.

6.5.2.4 Axial Velocity

The profiles of $V_{x(axis)}$ for $AR=2.5$ in Figure 6.50 near the base of the slant surface at $Z \approx 0.222$ are found to be similar. For $AR \leq 15^\circ$, $V_{x(axis)}$ along the axis of vortex is steady and increases slightly past the end of the body. For $20^\circ \leq \alpha \leq 24^\circ$, $V_{x(axis)}$ decreases after the initial formation of the vortex and decreases further past the end of the slant surface, resulting in similar $V_{x(axis)}$ at $Z \approx 0.222$. For $\alpha = 25^\circ$, there is a substantial decrease in $V_{x(axis)}$ indicating the breakdown of the vortex core, with $V_{x(axis)}$ starting to decrease at $Z \approx 0.1$ and the minimum $V_{x(axis)}$ coinciding with the rear of the slant surface. Even though profiles of S_N in Figure 6.52 indicate vortex breakdown at $Z \approx 0.175$, Figure 6.50 indicates that $V_{x(axis)}$ is starting to decrease closer to formation point of the vortex.

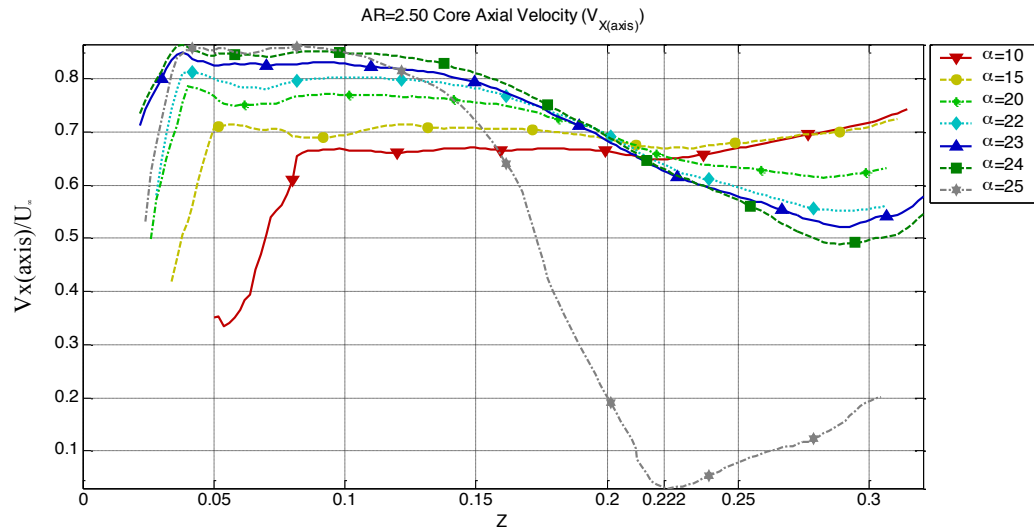


Figure 6.50 $V_{x(\text{axis})}$ along the C-pillar vortex axis for $AR=2.5$ for $10^\circ \leq \alpha \leq 25^\circ$. For regions where the vortex breakdown exists, $V_{x(\text{axis})}/U_{\infty}$ drops significantly.

6.5.2.5 Vorticity

The change in the structure of the C-pillar vortex for $AR=2.5$ is shown in profiles of $|\omega_z|$ in Figure 6.51. As $\alpha \rightarrow \alpha_c$, $|\omega_z|$ on the centreline of the vortex increases with AR , with the maximum $|\omega_z|$ occurring between $\alpha=24^\circ$ to 25° . This is similar to $AR=1.75$, where the maximum $|\omega_z| \approx 7000$ occurs for $23^\circ \leq \alpha \leq 26^\circ$. For $\alpha_c=25^\circ$, the profile of $|\omega_z|$ along the vortex axis shows $|\omega_z|$ slowly decreasing from the maximum value at the beginning of the vortex. There is a sudden decrease of $|\omega_z|$ from $Z \approx 0.15$ until it reaches a minimum at $Z \approx 0.222$, which coincides with the location of minimum $V_{x(\text{axis})}$. This indicates that at the location of breakdown, the sudden expansion of the core reduces all components of the velocity field.

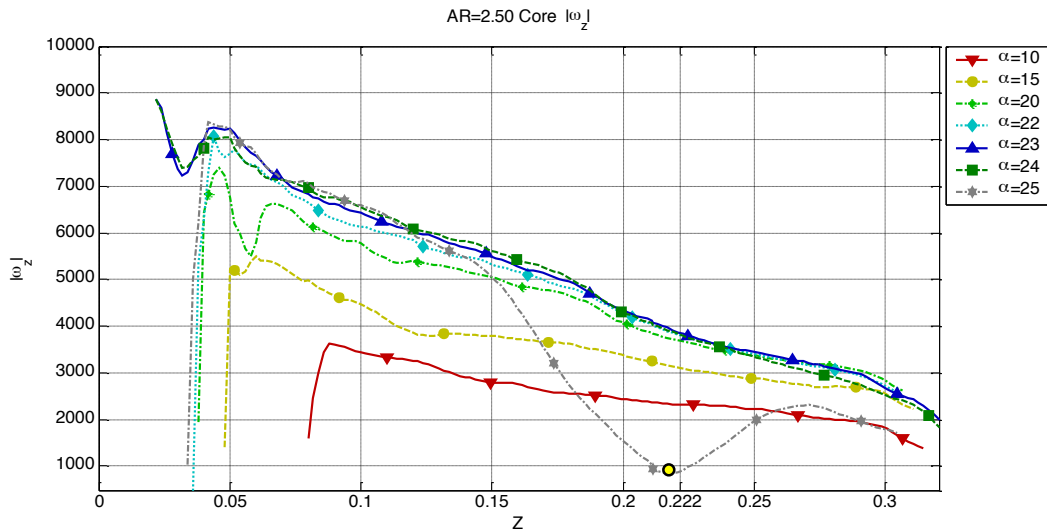


Figure 6.51 Profiles of $|\omega_z|$ along C-pillar vortex axis for $AR=2.5$ for $10^\circ \leq \alpha \leq 25^\circ$. For regions where the vortex expands, $|\omega_z|$ decreases to a minimum indicated by \circ .

6.5.2.6 Swirl Velocity

To determine the location of vortex breakdown, S_N is calculated along the vortex axis for $AR=2.5$. As can be seen, for $\alpha \leq 24^\circ$, S_N is constant for the entire length of the vortex, implying $V_{x(axis)}$ and $V_{\theta_{max}N}$ are decreasing at similar rates. For $\alpha=25^\circ$, $S_N > S^*$ at $Z \approx 0.175$ indicating that the vortex is bursting.

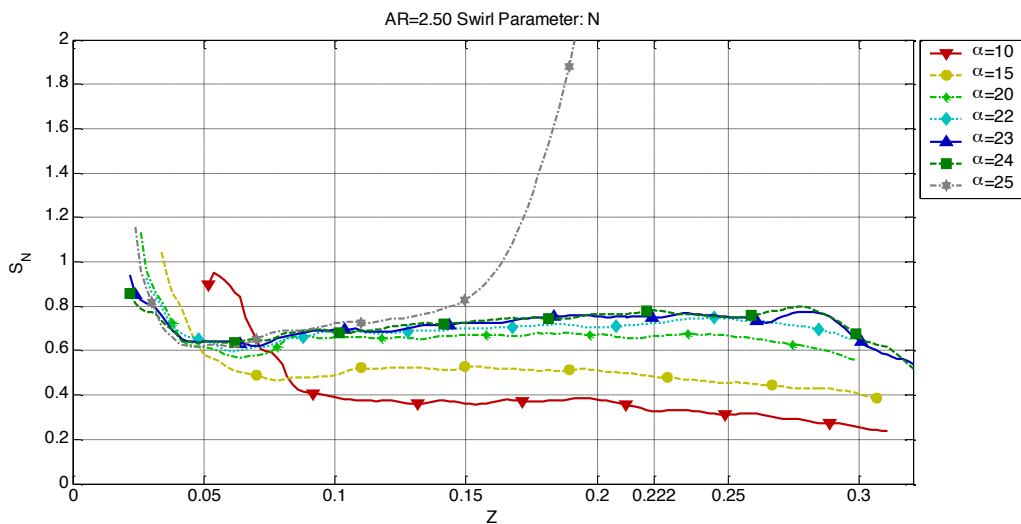


Figure 6.52 The Swirl parameter (S_N) calculated from $V_{\theta_{(max)N}}$ for $AR=2.5$, $10^\circ \leq \alpha \leq 25^\circ$. S_N exceeding $S^*=1.37$ is used as the criterion to quantify the location of vortex breakdown.

6.5.2.7 Helix angle

The maximum γ for $AR=2.5$ in Figure 6.53 indicates a similar result for S_N with the only vortex breakdown shown for $\alpha=25^\circ$. As was found for $AR=1.1$, the predicted location of vortex breakdown is different compared with the downstream

location using S^* as vortex breakdown criteria. For $\alpha=25^\circ$, $AR=2.5$, the location of vortex breakdown is at $Z\approx 0.21$ compared with $Z\approx 0.175$ using S^* , which coincides with the location of minimum $|\omega_z|$ and $V_{x(\text{axis})}$ along the vortex axis.

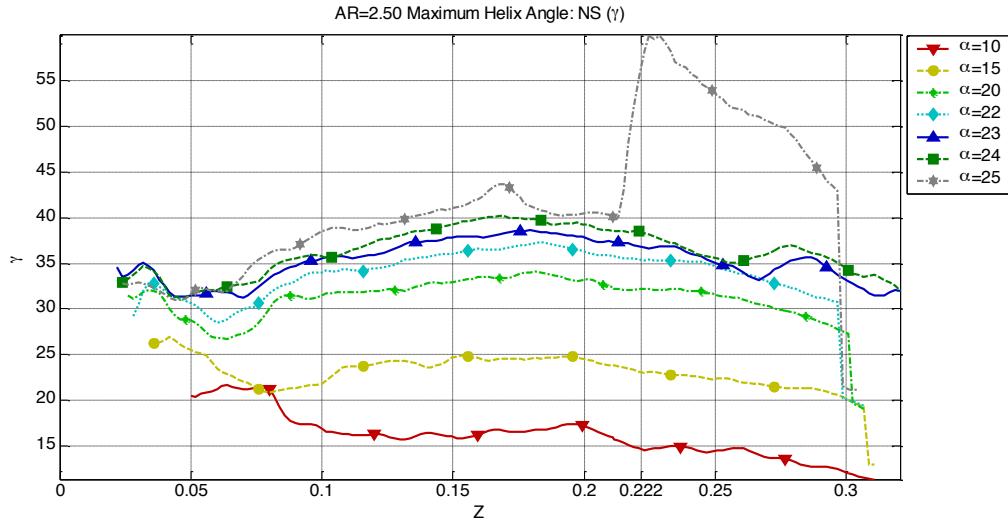


Figure 6.53 The maximum helix angle (γ) in the NS plane for $AR=2.5$, $10^\circ \leq \alpha \leq 25^\circ$. Maximum $\gamma > 50^\circ$ is used as the criteria to determine C-pillar vortex break down.

Profiles of γ , along a NS slice along the vortex axis in Figure 6.54, show the distinct change in maximum γ occurring at the end of the slant surface ($Z\approx 0.222$). However, before the significant change in the vortex structure upstream at $Z\approx 0.175$, there is a local maximum of γ on the north side of the vortex core which coincides with the predicated location for vortex breakdown using $S_N > S^*$ as the prediction method. The second significant change in the structure of the vortex core at $Z\approx 0.222$ is the appearance of the vortex breakdown further upstream when $V_{x(\text{axis})}$ begins to decrease. Therefore, using S^* is a better indicator of breakdown rather than maximum γ since S^* indicates the beginning of vortex breakdown rather than the outcome.

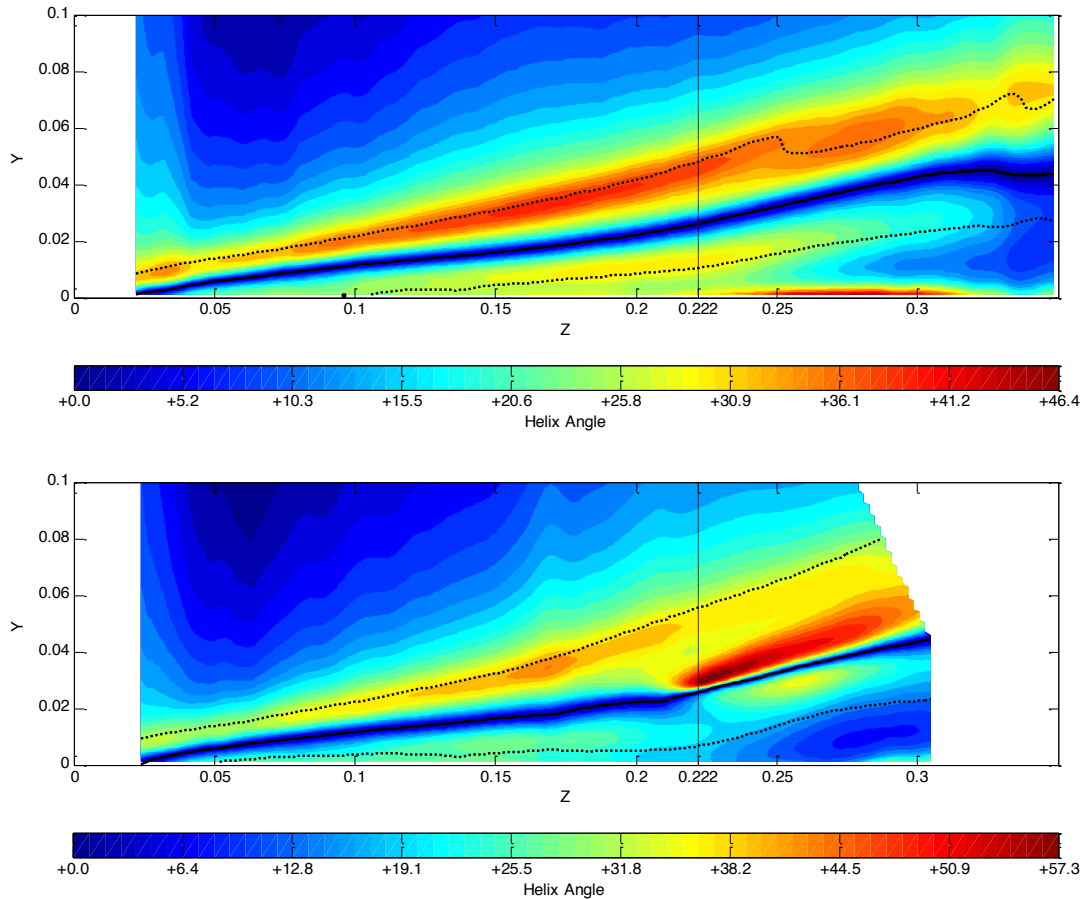


Figure 6.54 Contours of Helix angle (γ) on the NS plane for $AR=1.75$, $\alpha=24^\circ$ (a) and $\alpha=25^\circ$ (b) showing the change in the C-pillar vortex when vortex breakdown is present.

6.5.2.8 Core Gradient

The core gradient for $AR=2.5$, as shown in Figure 6.55, reveals the location of expansion and corresponding decrease in V_θ occurring for $\alpha=25^\circ$. The gradient profile for $\alpha=25^\circ$ links together the differences found using S_N and maximum γ in the vortex core. At $Z \approx 0.175$, where the $S_N > S^*$, there is a sudden change in the profile with the slope of the core gradient decreasing. At $Z \approx 0.222$, profiles of maximum γ indicate that the vortex has changed structure which is where the minimum core gradient occurs for $\alpha=25^\circ$. The differences in the Z location of S^* and maximum γ in the flow field are due to predicting different features of the C-pillar vortex. The swirl parameter indicates the initiation point where the C-pillar vortex starts to burst while the location of $\gamma > 50^\circ$ indicates the location of the breakdown of the vortex, where $V_{x(\text{axis})}$ and V_θ are a minimum.

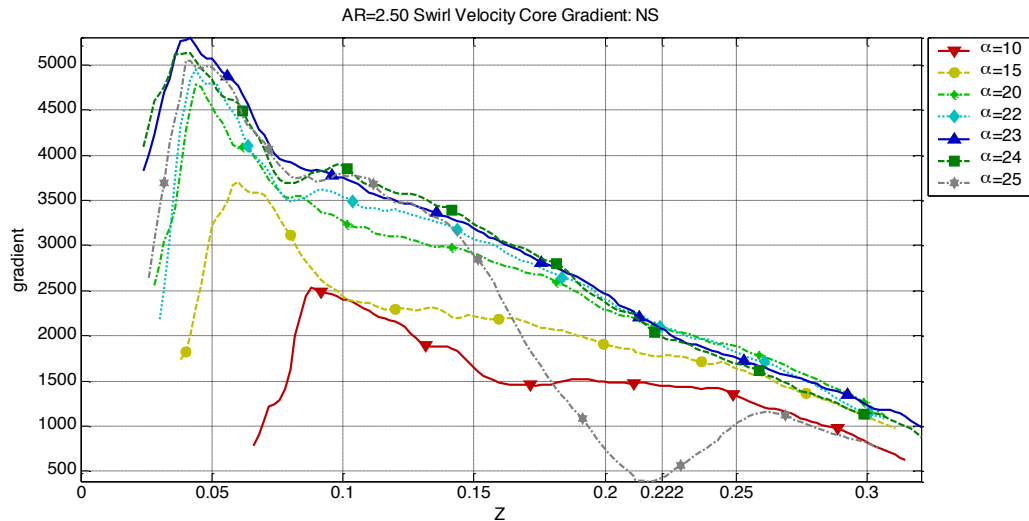


Figure 6.55 The swirl velocity core gradient taken in the NS plane for $AR=2.5$, $10^\circ \leq \alpha \leq 25^\circ$. For regions where the vortex expands, the core gradient decreases to a minimum indicated by \circ .

6.5.3 Effect of Aspect Ratio on the C-pillar Vortex

In this section, the effect of AR on the C-pillar vortex is examined by looking at different flow parameters. As was found in section 6.4 and 6.5, the AR has a considerable effect on the slant angle at which vortex breakdown is initiated and the location where the flow gradients are too high for the C-pillar vortex to form ($\alpha > \alpha_c$). To quantify the effect of AR on the C-pillar vortex, the location, size and strength are examined as well as the location of vortex breakdown using S^* .

6.5.3.1 Location of C-pillar vortex

For the low AR bodies, it was observed that the location of the C-pillar vortex relative to the edge of the slant surface ($X=0$ is slant surface edge) varied for constant α , compared with the standard Ahmed body and high AR bodies. Figure 6.56 shows the location of the vortex axis at $Z=0.2$ in the XY plane (Figure 6.2). The different line types represent various AR while the symbols indicate different slant angles. For $\alpha \geq 25^\circ$ and all AR, there is considerable variation in the location of the C-pillar vortex due to the presence of breakdown.

The locations of C-pillar vortex for $AR \geq 1.5$ are similar for a given α , with the location of the axis relative to the body edge for $\alpha < 25^\circ$ being constant. However, for $AR < 1.5$, the vortex axis for a given slant angle is located closer to the edge of the body. This indicates that for low AR bodies, the proximity of the C-pillar vortices on each side of the slant surface and the slant surface separation bubble affects their location and causes the vortices to be located closer to the slant surface. For the

higher AR bodies, the influence between the two C-pillar vortices is less and as a result, the vortex is able to follow a path, which would be the path of a vortex for an infinite span Ahmed body.

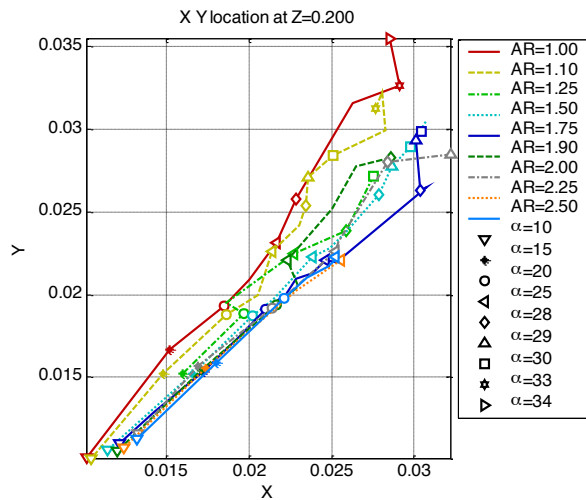


Figure 6.56 Location of C-pillar vortex for at $Z=0.2$ for different AR in the XY plane. Symbols indicate slant angle.

6.5.3.2 Radius of vortex

As was discussed in Sections 6.4.2, 6.5.1.2 and 6.5.2.2, above a certain α for a given AR, there is a sudden expansion of the vortex core, indicating the presence of vortex breakdown. The vortex radius, r_C , is shown in Figure 6.57 for different AR at $Z=0.2$. As can be seen for $AR=1.0$ and 1.1 , the vortex radius does not expand until $\alpha > 28^\circ$. The expansion of the vortex core for $AR \geq 1.25$ occurs at $\alpha > 25^\circ$. At $AR=1.75$, the expansion of the vortex core occurred past the end of the slant surface so it is not shown. Also shown in Figure 6.57 is that r_C for $\alpha < 25^\circ$ is relatively constant for all AR, while r_C generally increases with AR for $\alpha > 25^\circ$, indicating that the magnitude of the vortex breakdown increases with AR.

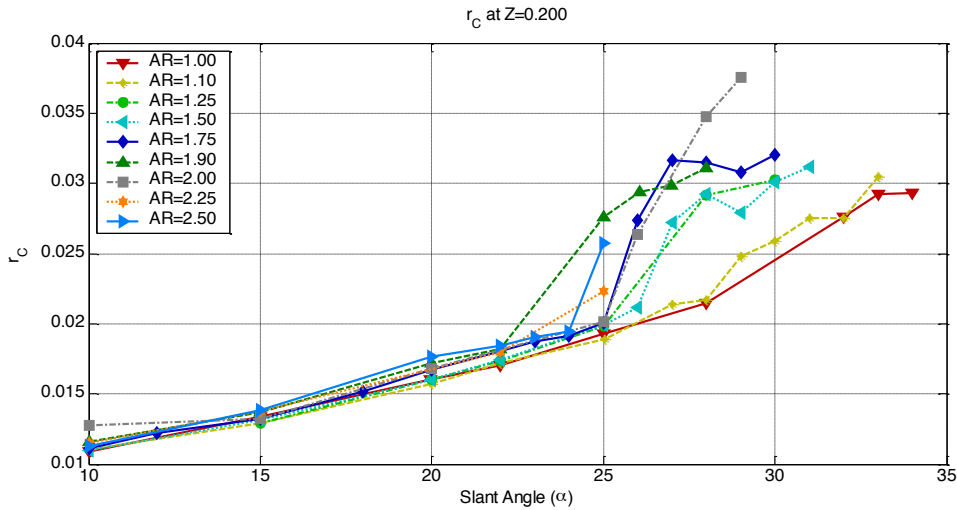


Figure 6.57 Radius of the C-pillar vortex (r_c) for different AR calculated at $Z=0.2$.

6.5.3.3 Pressure of vortex

To quantify the changes in C_p for the standard Ahmed body, $1/0.222 \int_0^{0.222} C_p dz$ was calculated in Figure 6.14. Figure 6.58 plots $\int C_p dz$ for various AR. For a given slant angle, $\int C_p dz$ decreases with AR indicating that the strength of the vortex is increasing with AR. For $AR=1.00$ and $AR=1.10$, the minimum $\int C_p dz$ occurs at $\alpha \approx 28^\circ$ while for $AR > 1.25$, the minimum $\int C_p dz$ occurs between $\alpha \approx 24$ to 25° , indicating that the strength of the C-pillar vortex is dependent on AR since the slant angle in which the minimum occurs $\int C_p dz$ decreases with increasing AR.

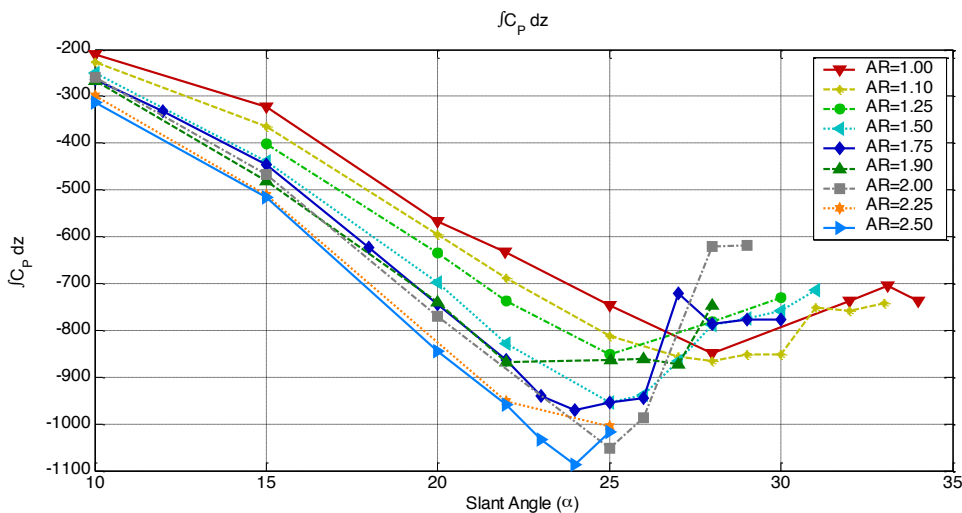


Figure 6.58 $\int C_p dz$ normalised by the integration length as indicator of overall C_p of the C-pillar vortex for different AR. The strength of C-pillar vortex increases with AR with peak $\int C_p dz$ occurring for $\alpha \approx 24^\circ$.

6.5.3.4 Location of vortex breakdown

For the current set of numerical simulations, $S_N > S^*$ was used as the criterion to quantify the existence and location of the breakdown of C-pillar vortex. Other parameters examined earlier to determine vortex breakdown, such as maximum $\gamma > 50^\circ$, $C_{DP} \approx 0.1$ or the location of minimum core gradient, do indicate the presence of vortex breakdown. However, maximum γ does not indicate the initial point and minimum core gradient requires user input to confirm location of the vortex breakdown, making it difficult to automate.

Figure 6.59 is the parameter space map showing which simulations indicate the presence of vortex breakdown. Figure 6.60 shows the Z location where $S_N > 1.37$ for different AR. For simulations where vortex breakdown is detected, the slant angle in which breakdown is detected decreases with increasing AR. For $AR \leq 1.1$, breakdown occurs for $\alpha \geq 29^\circ$ which decreases to $\alpha = 25^\circ$ for $AR > 2.0$. Simulations indicate that for $\alpha < 25^\circ$, breakdown is not encountered at any AR. As discussed in section 6.5.4, $V_{\theta_{\max N}}$ increases with AR. Therefore for $AR \rightarrow \infty$, eventually $S_N > S^*$ for $\alpha \geq 25^\circ$ and the wake structure would switch to a complete separation wake structure without vortex breakdown detected for any slant angle. In Section 5.2.2.4, for $2.0 \leq \alpha < 2.25$, there was a gradual decrease of α_c as $AR \rightarrow 2.25$. It would be expected that there would be a corresponding decrease in the range at which breakdown occurs from $26^\circ \leq \alpha \leq 29^\circ$ at $AR = 2.0$ to $\alpha = 25^\circ$ at $AR = 2.25$.

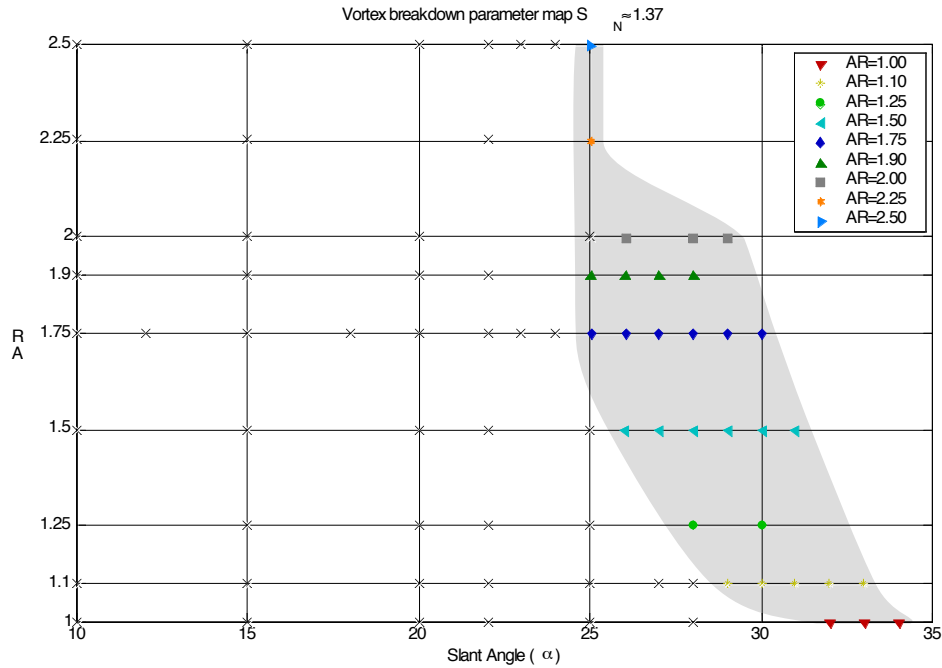


Figure 6.59 Parameter space map indicating simulations where vortex breakdown is detected ($S_N > S^*$). Crosses indicate simulations where the C-pillar vortex exists but no breakdown is present.

The downstream location of breakdown shown in Figure 6.60, shows that for a given AR, the location of breakdown occurs closer to the top of the slant surface as was observed for AR=1.1 (Figure 6.39) and AR=1.75 (Figure 6.21). For lower AR bodies, the location of breakdown is closer to the top of the slant surface. For AR=1.0, for $33^\circ \leq \alpha < 34^\circ$, breakdown occurs at $Z < 0.1$, which is a narrow band compared with AR=1.1, where breakdown occurs for $0.075 < Z < 0.175$. For AR > 1.75, $S_N \approx 1.37$ is located further away from the top of the slant surface, with the location of vortex breakdown closer to the base of the slant surface. For AR where breakdown is present at $\alpha = 25^\circ$, the location of breakdown is closer to the top of the slant surface with increasing AR. These results suggest that breakdown on low AR bodies is less sensitive to changes in α since breakdown occurs over a larger range compared with $AR \geq 2.25$, where for a small change of α either side of $\alpha = 25^\circ$, vortex breakdown is not present.

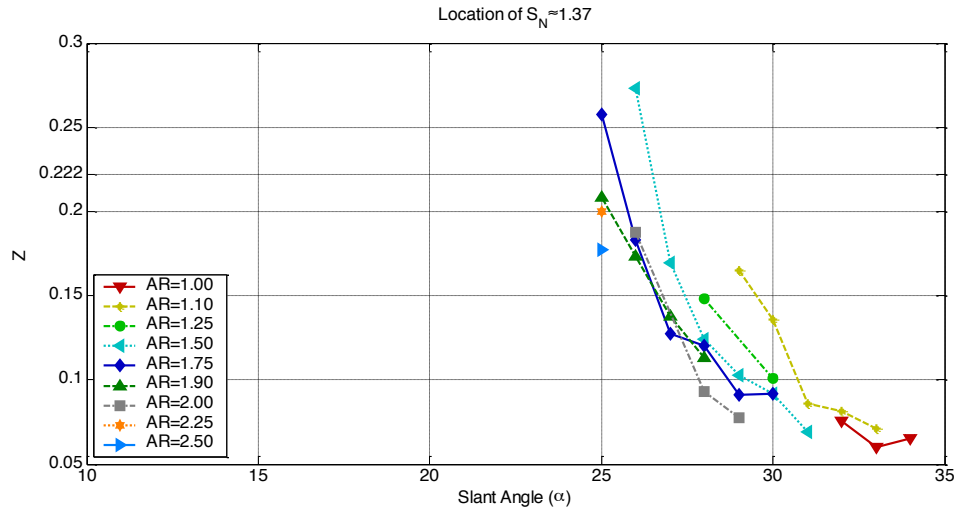


Figure 6.60 Location of the C-pillar vortex breakdown predicted using $S_N \approx 1.37$ for different AR. For increasing AR, breakdown of the vortex decreases $\alpha \rightarrow \alpha = 25^\circ$.

6.5.4 Mechanism for change of α_c

Simulations indicate that the mechanism for the transition to a fully separated wake structure at $\alpha > 30^\circ$ for the standard Ahmed body ($AR = 1.75$) is due to the total breakdown of the C-pillar vortex. They also indicate that vortex breakdown is present for $25^\circ \leq \alpha \leq 30^\circ$, with the location of the breakdown occurring earlier in the formation of the vortex as $\alpha \rightarrow \alpha_c$. For $\alpha > \alpha_c$, if a C-pillar vortex was to form, S would exceed S^* at the formation point of the vortex and breakdown would immediately occur, leading to the absence of the C-pillar vortex for $\alpha > \alpha_c$. This in turn leads to a wake structure with full separation across the entire slant surface.

In Figure 6.19, there was a sustainable decrease in $V_{x(\text{axis})}$ at the location of the vortex breakdown which leads to S_N exceeding $S^* \approx 1.37$. Profiles of $V_{\theta_{\max N}}$ shown in Figure 6.61 which is used for the calculation of S_N , reveals that $V_{\theta_{\max N}}$ increases with α . This in turn increases S_N if $V_{x(\text{axis})}$ is constant. Therefore, as $\alpha \rightarrow 30^\circ$, S_N increases as indicated in Figure 6.21. For $\alpha > 25^\circ$, the variation of $V_{\theta_{\max N}}$ for a given Z location is not substantial and does not explain why the breakdown occurs downstream and migrates forward with increasing α since the $V_{\theta_{\max N}}$ magnitude reduces with downstream distance. If $V_{x(\text{axis})}$ is also used for the calculation of S_N for $\alpha < 25^\circ$, $V_{x(\text{axis})}$ past the end of the slant surface decreases as $\alpha \rightarrow \alpha_c$. As a result, S_N increases downstream along the vortex axis which eventually causes S_N to exceed S^* . For

$S_N > S^*$, the vortex cannot recover and a substantial decrease of $V_{x(axis)}$ occurs along the vortex leading to the C-pillar vortex bursting.

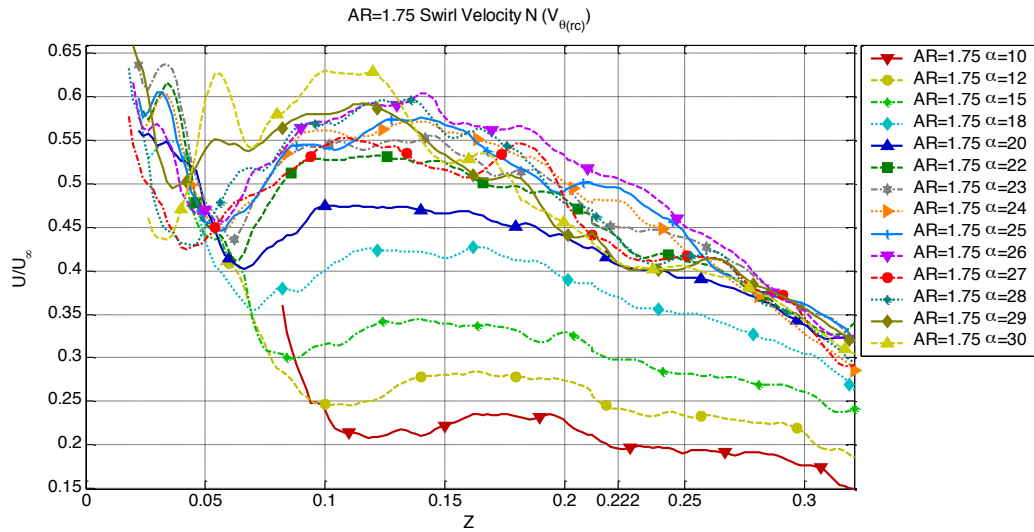


Figure 6.61 The swirl velocity (V_0) for $AR=1.75$ as a function of the Z location, which shows that the overall V_0 increases with α .

To determine the effect of AR on vortex breakdown, $\alpha=25^\circ$ is used for comparison between AR since it is possible to examine the entire AR parameter space. Profiles of $V_{\theta_{max N}}$ for $\alpha=25^\circ$ at various AR are illustrated in Figure 6.62, which shows that $V_{\theta_{max N}}$ for a given downstream location above the slant surface increases with AR . The increasing $V_{\theta_{max N}}$ causes S_N to increase and as a result, the C-pillar vortex is more likely to breakdown for a small decrease in $V_{x(axis)}$ as the vortex progresses downstream since the swirl velocity is stronger relative to the axial velocity.

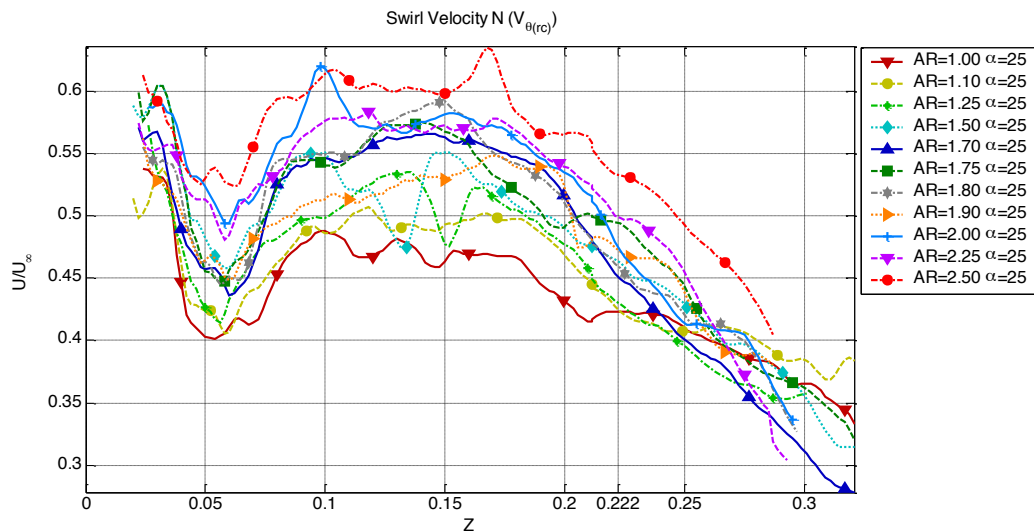


Figure 6.62 The swirl velocity (V_0) for $\alpha=25^\circ$ as a function of the Z location for various AR , which shows that the overall V_0 increases with AR .

Profiles of $V_{x(\text{axis})}$ for $\alpha=25^\circ$ for different AR are shown in Figure 6.63. For $AR \leq 1.25$, $V_{x(\text{axis})}$ above the slant surface is smaller compared with $V_{x(\text{axis})}$ for $AR > 1.5$. In comparison to $V_{\theta_{\max N}}$, the variation of $V_{x(\text{axis})}$ in regions where vortex breakdown is not present for a given downstream location is smaller over the AR range, indicating that it is the increase in $V_{\theta_{\max N}}$ with AR that causes vortex breakdown to occur at a lower α .

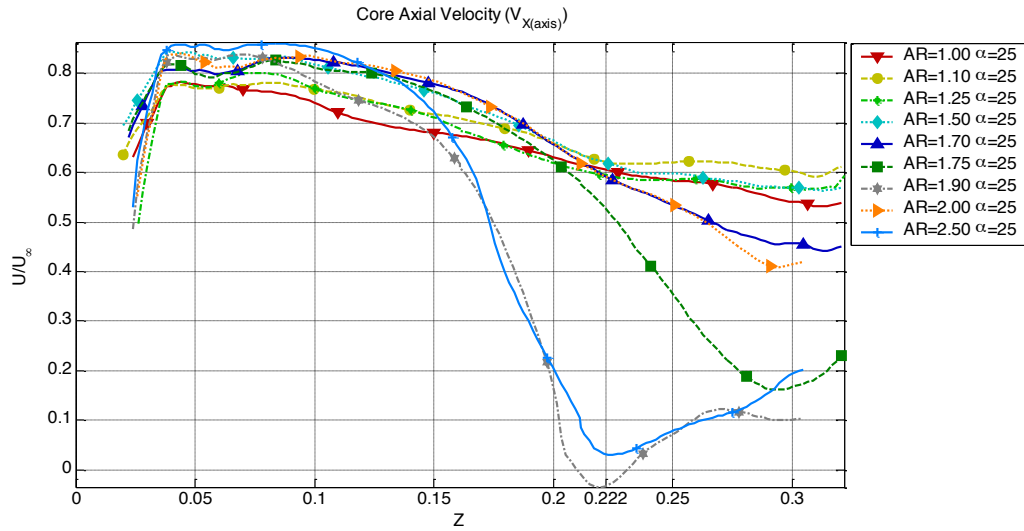


Figure 6.63 The core axial velocity ($V_{X(\text{axis})}$) for $\alpha=25^\circ$ as a function of the Z location for various AR, which shows that the overall $V_{X(\text{axis})}$ decreases past the slant surface with increasing AR.

6.6 Conclusion

In this chapter, the C-pillar vortex emanating from the side edges of the slant surface was examined to determine how α and AR affect the vortex structure. Simulations indicate that as $\alpha \rightarrow \alpha_c$, vortex breakdown occurs, leading to the complete separation over the slant surface. For $AR=1.75$, simulations suggest that the vortex starts to break down past the slant surface at $\alpha=25^\circ$ and then as $\alpha \rightarrow 30^\circ$, the location of the breakdown occurs earlier in the formation of the slant surface. For all AR examined, for $\alpha < 25^\circ$, the vortex location and r_c increase linearly with the Z -location. For $\alpha \geq 25^\circ$, r_c has a piecewise linear profile due to the expansion of the vortex core. This expansion is due to the increased region of $V_\theta \approx 0$ near the vortex core (Figure 6.12) moving the location of $V_{\theta_{\max N}}$ away from the vortex core. Profiles of C_p along the vortex core show that the pressure along the vortex core decreases indicating that the strength of the vortex is increasing until $\alpha \approx 25^\circ$, where the C_p at the formation

point of the vortex for $25^\circ < \alpha < 30^\circ$ is relatively constant. Overall, consideration of the integral $\int C_p dz$ shows that at $\alpha \approx 24^\circ$, the vortex has the lowest overall C_p . Past the beginning of the vortex, the $-C_p$ rapidly decreases when breakdown occurs. Profiles of C_{DP} show clearly the change in the structure when the C-pillar vortex breaks down with the C_{DP} decreasing to $C_{DP} \approx 0.1$. This is due to the significant decrease in $V_{x(\text{axis})}$ along the vortex axis. Due to iteration averaging of the flow field to determine a mean flow field, reversed flow inside the vortex is usually not present.

Of the various methods used to quantify vortex breakdown, the swirl parameter was found to be the best method to predict the location where the vortex core expands. As shown for $AR=2.5$, $\alpha=25^\circ$, $S_N > S^*$ indicates where the C-pillar vortex starts to expand while the location where $\gamma > 50^\circ$ shows the location of maximum expansion, where $V_{x(\text{axis})} \rightarrow 0$. This is clearly indicated with profiles of the core gradient and $|\omega_z|$ which show that the change of the $|\omega_z|$ gradient ($Z \approx 0.15$ for $AR=2.5$, $\alpha=25^\circ$) occurs when $S_N > S^*$, while minimum $|\omega_z|$ indicates the maximum expansion of the vortex ($Z \approx 0.21$).

Examination of S_N for different AR suggests that change of vortex breakdown with AR is due to the increase of $V_{\theta \max N}$ with AR , while the variation of $V_{x(\text{axis})}$ with AR is negligible in comparison. As a result, α_c reduces with increasing AR . For aspect ratios where vortex breakdown is present in the C-pillar vortex but the flow is still attached, the decrease of the Z -location of core expansion is due to decreasing $V_{x(\text{axis})}$ along the core axis. There is a larger decrease in $V_{x(\text{axis})}$ with increasing α leading to the location of vortex breakdown being closer to the formation point of the vortex.

Simulations indicate that the mechanism for the transition to a fully separated wake structure at $\alpha > \alpha_c$ is due to the flow field near the formation point exceeding the swirl parameter criteria for a stable vortex, and as a result, the C-pillar vortex fails to develop. This is indicated by the location of the breakdown occurring closer to the top of the slant surface as $\alpha \rightarrow \alpha_c$.

Chapter 7 Wake Analysis

7.1 Introduction

In previous chapters, the forces on different surfaces of the Ahmed body were analysed. With this information, it is possible to make a qualitative analysis of which flow structures are responsible for the change in body forces as the slant angles change. However, it is not possible to pinpoint the different wake structures affecting the drag. Instead of examining the pressure on the body surfaces, a wake survey is undertaken to determine the change in streamwise momentum of the flow passing the body, leading to an enhanced understanding of the drag mechanism in vehicle wakes. The wake survey was first used by Onorato et al. [97] in the study of a notchback car configuration. Experiments were conducted on a 1/5 scale model vehicle at $Re=2.0 \times 10^6$ to determine the effect of trunk length on the drag structures. Pressure and velocity vector measurements were conducted on spanwise slices downstream to calculate the drag using momentum theory and compared with force balance measurements. The calculated drag was found to be in good agreement with the drag measured from the wind tunnel balance. Analysis of the spanwise velocity field in the wake was found to be effective in determining the change in drag structures when the trunk length was modified. This method was also considered for use on the Ahmed body [19, 97-99] but not undertaken in the literature available.

Due to the low aspect ratio of vehicles, it has not been possible to isolate induced drag from profile drag, as has been carried out on aircrafts [10]. Chometon and Laurent [100] examined the wake of a finite aspect ratio airfoil through downstream velocity surveys. The purpose of this study was to clarify the vortex drag component from momentum theory in comparison with induced drag described by Prandtl [101]. They found that vortex drag accounted for half the value of the induced drag and proposed that the induced drag included a viscous term for the production and dissipation of the rolling vortex that was not included in the vortex drag term. This was later examined by Ardonceau and Amani [102] on a similar geometry. A finer grid spacing and larger domain for the calculation of vortex drag was used in their wake survey. As a result, there was a 2.91% discrepancy between the induced drag and vortex drag in comparison to 57.25% difference found by Chometon and Laurent.

However, there were discrepancies in Ardonceau and Amani's calculations which will be discussed in Section 7.2.

In the following sections, the momentum theorem used by Onorato will be explained. This will then be applied to the data from numerical simulations on the wake structures of the Ahmed body. The standard Ahmed body, and low aspect ratio and high aspect ratio bodies will be examined to pinpoint the flow structures influencing drag and how changes in geometry affect the wake.

7.2 Method

7.2.1 Momentum Theory

The application of the momentum theory method to calculate the drag on the Ahmed body is described in this section. A schematic of the stream tube surrounding the body is shown in Figure 7.1. Section A_1 is a stream tube cross-section located far upstream in the free stream flow ahead of the model. Section A_2 is the measurement plane (YZ plane) in the wake of the model. It is assumed that the stream tube is large enough for the pressure on the external surface of the stream tube to be equal to the free stream pressure.

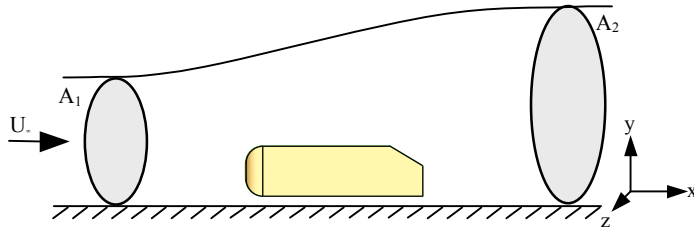


Figure 7.1. Stream tube around Ahmed body

The drag coefficient from momentum theory is shown below

$$\begin{aligned}
 C_x = & + \frac{1}{S} \iint_{A_2} \left(\frac{P_{t_1} - P_{t_2}}{1/2 \rho V_{x_1}^2} \right) dy dz && \text{(pressure loss, } C_{PL}) \\
 & - \frac{1}{S} \iint_{A_2} \left(1 - \frac{V_{x_2}}{V_{x_1}} \right)^2 dy dz && \text{(Longitudinal velocity loss, } C_{LVL}) \\
 & + \frac{1}{S} \iint_{A_2} \left[\left(\frac{V_{y_2}}{V_{x_1}} \right)^2 + \left(\frac{V_{z_2}}{V_{x_1}} \right)^2 \right] dy dz && \text{(vortex drag, } C_{VD}),
 \end{aligned} \tag{Eqn 7.1}$$

where P_t is the total pressure, ρ is the density, S is the cross-sectional area of the Ahmed body, and V_x , V_y , V_z are the components in the velocity components in the x, y and z directions, respectively. This can also be rewritten in terms of total drag instead of drag coefficient as shown in Eqn 7.2.

$$\begin{aligned}
 F_x = & + \iint_{A_2} (P_{t_1} - P_{t_2}) dy dz && \text{(pressure, } F_{PL}) \\
 & - \frac{\rho V_{x_1}^2}{2} \iint_{A_2} \left(1 - \frac{V_{x_2}}{V_{x_1}} \right)^2 dy dz && \text{(Longitudinal velocity, } F_{LVL}) \\
 & + \frac{\rho V_{x_1}^2}{2} \iint_{A_2} \left[\left(\frac{V_{y_2}}{V_{x_1}} \right)^2 + \left(\frac{V_{z_2}}{V_{x_1}} \right)^2 \right] dy dz && \text{(vortex drag, } F_{VD})
 \end{aligned} \tag{Eqn 7.2}$$

The pressure term represents the total pressure loss. As $Re \rightarrow \infty$, this term is reduced to zero [102]. The bottom line in Eqn 7.1(C_{PL}) is the free stream dynamic pressure. The longitudinal velocity term represents the velocity loss contribution in drag. For flow with no separation, this term can be assumed to be negligible since the wake deficit is minimal. However, contrary to Roumeas et al. [99], this term cannot be assumed to be negligible for bluff bodies with separated wakes. In the region where a wake deficit is present, the longitudinal velocity term decreases the overall drag. The third term represents vortex drag, which is associated with rotational kinetic energy of the flow. This term is linked to the presence and strength of streamwise vortices. The total sum of these terms gives the overall C_D (Eqn 7.1) or total force (Eqn 7.2). However, the location of portions of each component of Eqn 7.1 is dependent on the streamwise location of A_2 but the total force is not dependent on the location of the measurement plane.

As was discussed in section 7.1, Ardonceau and Amani [102] found that the vortex drag correlated well with the induced drag on a finite aircraft wing, and differences found by Chometon and Laurent [100] were due to integration errors using a coarse grid. Ardonceau and Amani stated that the kinetic energy of the vortex pattern was represented by $C_{LVL}+C_{VD}$ and not C_{VD} alone. However, in their calculations of C_{LVL} they used a slightly different formula.

$$C_{LVL} = \frac{1}{S} \iint_{A_2} \left[1 - \left(\frac{V_{x_2}}{V_{x_1}} \right)^2 \right] dy dz \quad \text{Eqn 7.3}$$

It was found that when Eqn 7.3 was used, the total drag was dependent on the streamwise location of the measurement plane indicating that momentum was not conserved. This suggests that the C_{LVL} term should not be incorporated into the kinetic energy of the vortex pattern.

Since discrepancies exist in the formulation of the momentum equation, attempts were made to find the original source given by Onorato et al. [97] but to no avail. Subsequent derivations of the formula indicate discrepancies in both versions given in the literature. Implementation of the version derived by Onorato matched well with force measurements from the pressure distribution on the slant and rear surface and location of the measurement plane did not effect the calculated C_D .

This method has also been used by other researchers [6, 11, 19, 103-105] to examine the wake. Cogotti [103, 104] implemented this technique at the Pininfarina Aerodynamic and Aeroacoustic Research Centre to create a “micro drag maps” of the vehicle wake to understand how and where the car aerodynamic drag is generated with success.

7.2.2 Implementation

To determine the momentum integral for the wake region of the Ahmed body, spanwise cross sections of the wake at different streamwise locations were calculated. The measurement plane was sequentially moved from a location before the slant surface to a location downstream of the body ($X=1.0$). At each location, the flow field was linearly interpolated onto a fine uniform mesh to calculate the momentum integral. In Figure 7.2, the C_D for each component of the momentum integral at different streamwise locations for $AR=1.75$, $\alpha=30^\circ$ is plotted. The beginning of the slant surface is located at $X=-0.192$. If the line for total C_D is considered, the

contribution of the slant surface as well as the contribution of the rear surface to the overall C_D can be determined. The contribution of the slant surface is calculated by the change of total drag from $X = -0.1$ to $X = 0$. However, this takes into account the relatively small contribution of the momentum loss through viscous drag on side and underside regions in the corresponding X range. The contribution of the rear surface to the total drag is the sudden increase in drag at $X = 0$. The total C_D of the Ahmed body would approximately be the maximum value of total drag which occurs at $X > 0$. However, this is not exact since the body is in ground effect and the ground boundary is stationary. There is momentum loss due to the boundary layer on the ground, which should increase the overall C_D . Since the C_D of the rear and slant surfaces is calculated by a change in C_D , the effect of the momentum loss from the ground boundary should be constant.

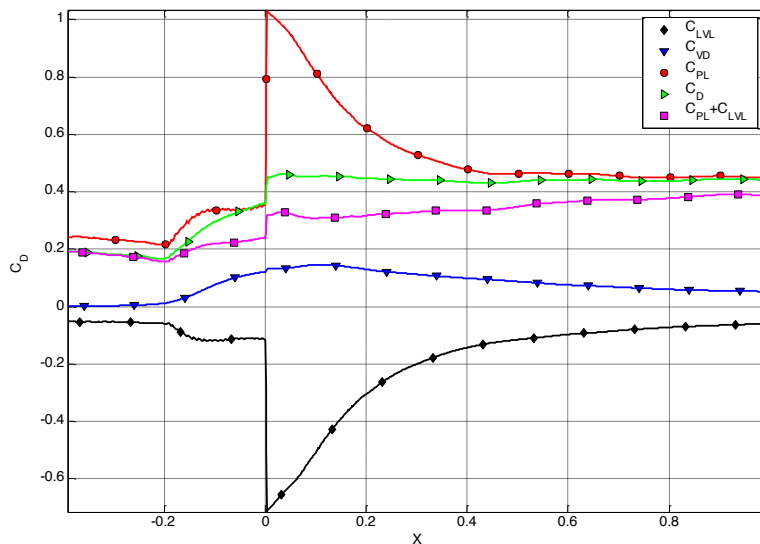


Figure 7.2 Typical drag plot

In addition to calculating the C_D at a particular streamwise location, the three components of the momentum equation were integrated onto a discretized grid to create a “drag map” of the wake to gain an insight of where the structures responsible for the drag occur. Figure 7.3 is a 3D representation of the drag map of the measurement plane downstream of the Ahmed body ($AR=1.75$, $\alpha=20^\circ$) coloured by the intensity of the total drag. The drag from the C-pillar vortices is evident as well the wake deficit in the rear separation bubble.

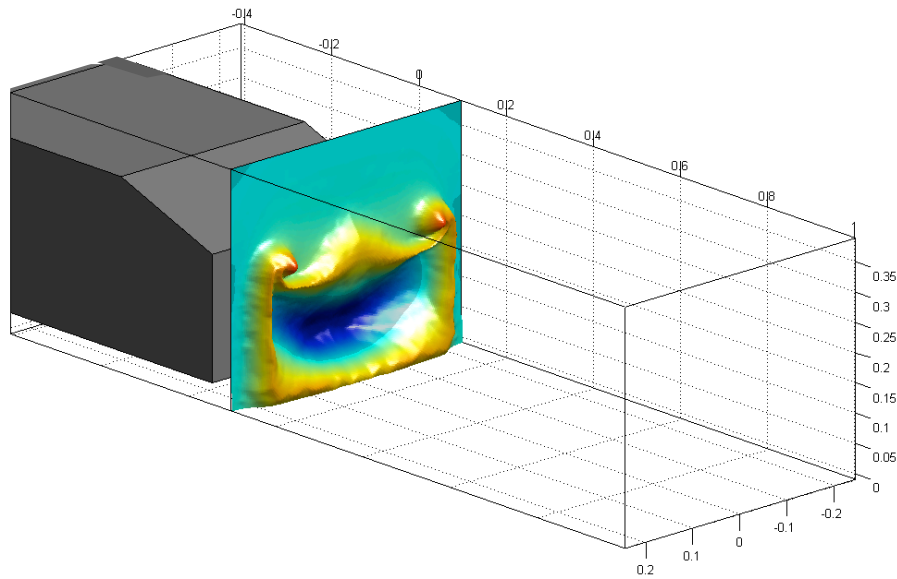


Figure 7.3 3D representation of the drag map of the measurement plane downstream of the Ahmed body ($AR=1.75$, $\alpha=20^\circ$) coloured by the intensity of the total drag.

7.2.3 Resolution study

Before calculating the momentum integral to determine the C_D from the simulations, a resolution study was undertaken to determine the influence of the domain limits and grid density required for integration. The resolution study was undertaken for $AR=1.75$, $\alpha=30$.

7.2.3.1 Grid Density

The mesh density required for the integration of the momentum integral was examined at four streamwise locations at $X=-0.192$ (top of slant), $X=-0.005$, $X=+0.005$ and $X=+0.5$. The grid spacing was varied from 0.001 up to 0.05 with corresponding total C_D calculated. Figure 7.4 shows the calculated C_D for the different grid densities investigated.

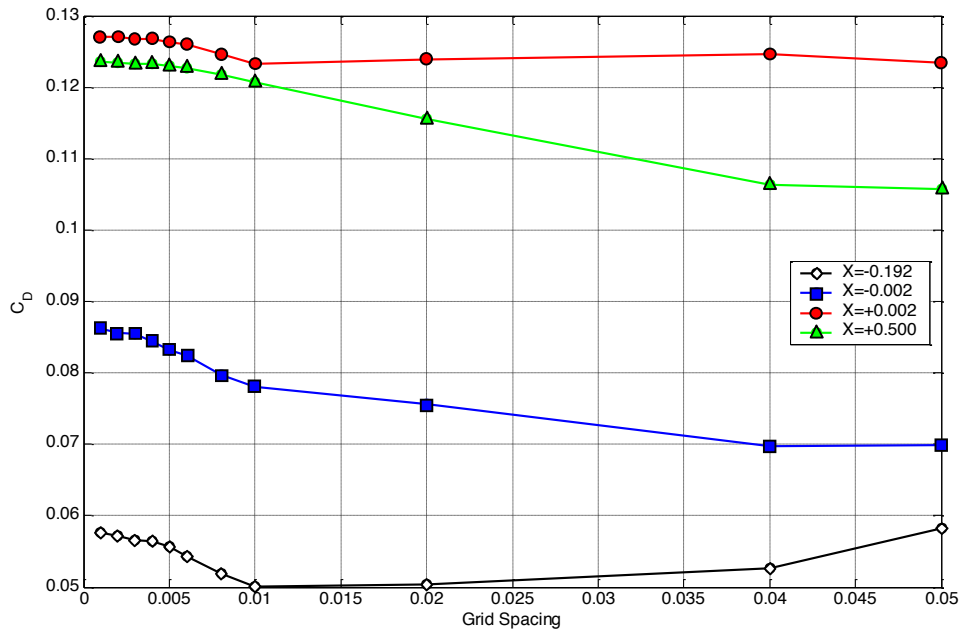


Figure 7.4. Effect grid spacing on the C_D calculated on different measurement planes.

In general, for the smaller mesh spacing, the C_D increased towards a constant value as more flow features were captured. For the higher mesh spacing, errors were incurred due to the integration window overlapping the position of the Ahmed body.

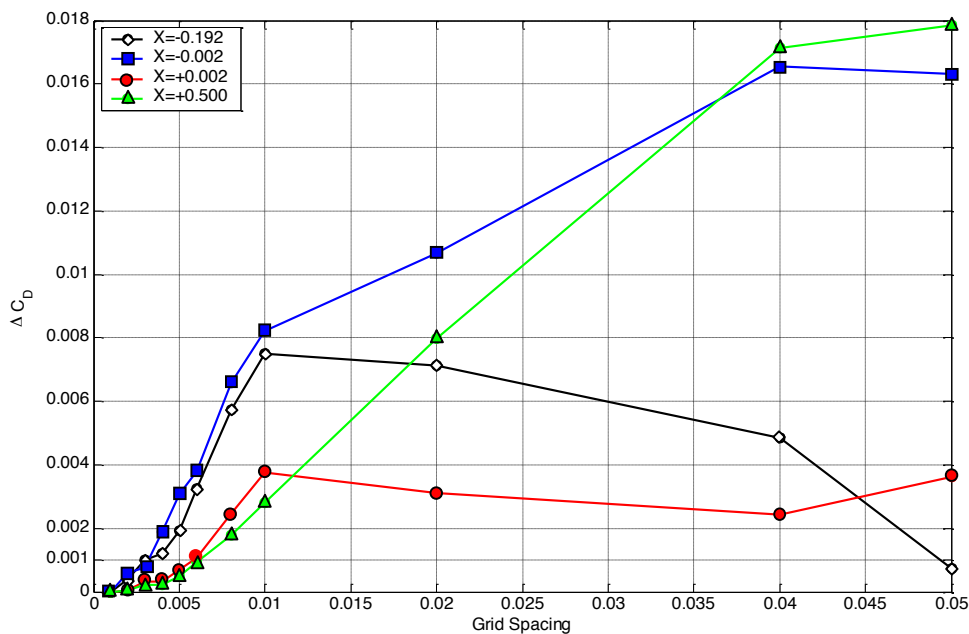


Figure 7.5 ΔC_D of the grid spacing measured at different measurements planes relative to grid spacing=0.001.

The change in C_D relative to the smallest grid spacing used (grid spacing=0.001) is plotted in Figure 7.5. For a change of C_D at all streamwise locations less than $\Delta C_D=0.001$, a grid spacing of 0.002 is required.

7.2.3.2 Domain limits

The domain size required for calculation of the momentum integral was examined to ensure that C_D was independent of mesh size. The stream tube considered for the analysis needs to be large enough so that the pressure on the perimeter of the stream tube was equal to the free stream pressure. As the cross-sectional area of the stream tube increases, the drag should asymptote to a constant value as there is no contribution to the drag from the free stream velocity. For bodies not in the free stream and in ground effect, this is more difficult because it is harder to isolate the momentum loss from the body from the momentum loss due to the ground. Figure 7.6 shows the drag map and U/U_∞ downstream of the Ahmed body ($AR=1.75$, $\alpha=30^\circ$). Only half the model is illustrated. The influence of the ground boundary layer on the drag is evident especially away from the body. This is a consequence of using larger grid spacing away from the body creating a larger boundary layer. Increasing the area of the stream tube used for the momentum integral would capture more of the momentum loss due to the ground.

Figure 7.6 Typical spanwise slice of the calculated C_D (a) and U/U_∞ (b) showing the influence of the ground boundary layer for $AR=1.75$ $\alpha=30^\circ$. The change of domain size to calculate the integration limits is shown the spanwise slice of U/U_∞ .

The domain size was adjusted in the Y and Z directions in increments of 0.01. This measurement labelled the offset distance is relative to the limits of the Ahmed

body so when domain size is the same cross-section as the Ahmed body, the offset distance is zero. In the Z direction, the offset distance was varied from $Z=0.189$ to $Z=0.8945$, while Y domain was adjusted from $Y=0.288$ to $Y=0.9880$ at the same time as indicated in Figure 7.6.

The C_D of the total drag at different streamwise locations for $AR=1.75$ $\alpha=30^\circ$ is plotted in Figure 7.7. For increasing domain size, there is an increase in C_D for all streamwise locations as a larger region is used for the integration. It appears that the gradients for an offset distance in excess of 0.35 are similar for all slices indicating that the momentum loss from the ground plane is relatively constant throughout the domain. However, this makes it difficult to determine the domain size required.

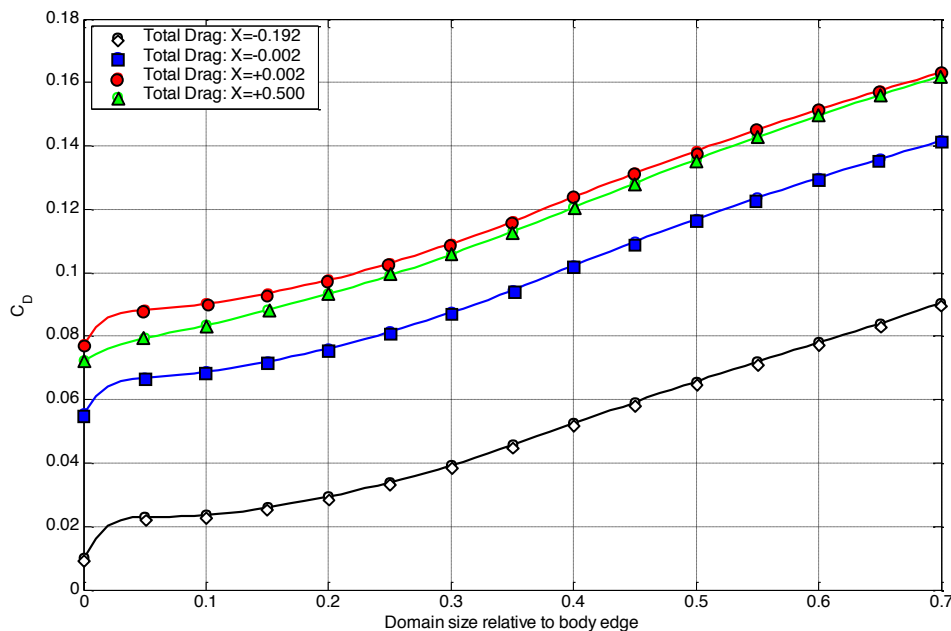


Figure 7.7 Total C_D at different spanwise locations for changing domain size relative to the body extents. For larger domain sizes, the momentum loss from the ground is included in the total C_D making it difficult to determine where the C_D asymptotes.

If the vortex drag component of C_D is used to determine the domain size, it isolates the effect of the ground boundary layer since it only contributes to wake deficit and pressure loss. The C_D of the vortex drag plotted in Figure 7.8 at the same streamwise locations indicates that C_D plateaus for increasing domain size.

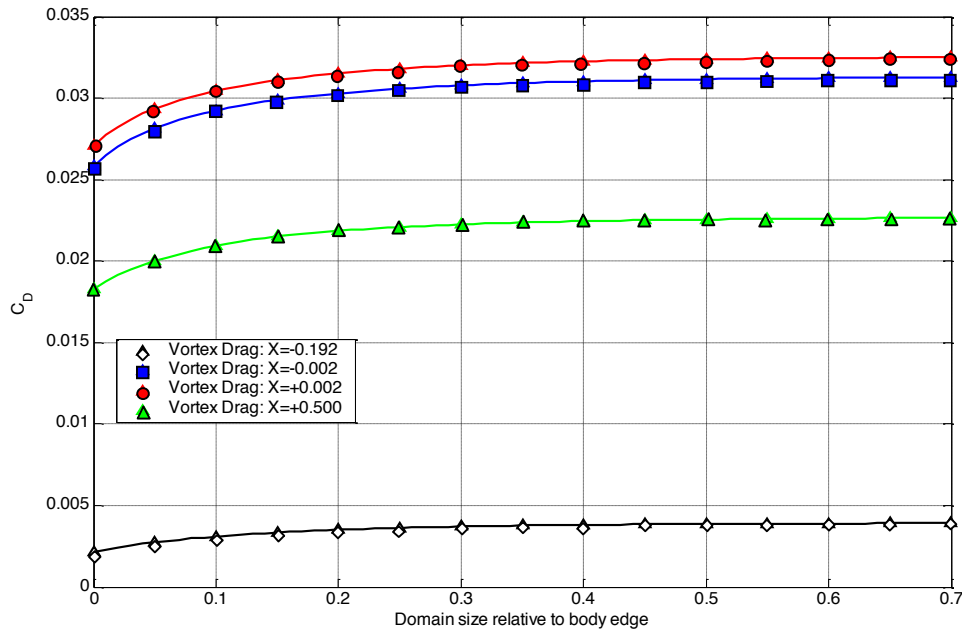


Figure 7.8 C_D of the vortex drag at different spanwise locations for changing domain size relative to the body extents. For increasing domain sizes, the vortex drag C_D asymptotes indicating that far away from the body, the spanwise velocity field has negligible influence on the momentum loss.

The ΔC_D relative to the largest domain size examined is outlined in Figure 7.9. The largest ΔC_D occurs at $X \approx 0$, which would be expected since the C-pillar vortex at that location is the strongest in the flow field. To ensure the $\Delta C_D \leq 0.001$ for streamwise locations, the domain should be set at least with an offset distance > 0.2 from side and top of the Ahmed body.

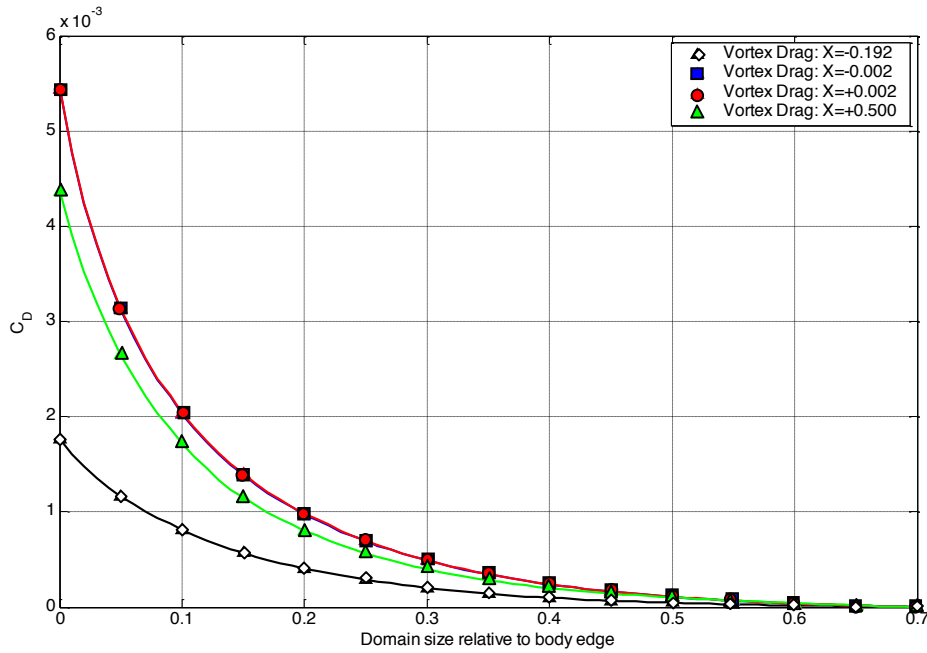


Figure 7.9 Vortex drag contribution to C_D relative to the largest domain size examined (offset distance=0.7). For offset distance >0.2 , the $\Delta C_D < 0.001$.

7.2.4 Comparison with Surface Forces

To verify the accuracy of the momentum method, the drag calculated using momentum theory is compared with the drag calculated directly from the surface pressure and surface viscous stresses. Figure 7.10 shows C_D calculated at different streamwise locations for $\alpha=5, 20, 25, 30$ and 35 . For all slant angles, the total C_D is over predicted, primarily due to the momentum loss from the ground boundary layer. Before the start of the slant surface the C_D is relatively similar for all α , but considerably different over the slant surface. At $X=0$, the highest drag occurs for $\alpha=30^\circ$, which correlates well with C_D in Section 4.2.1 from the surface forces.

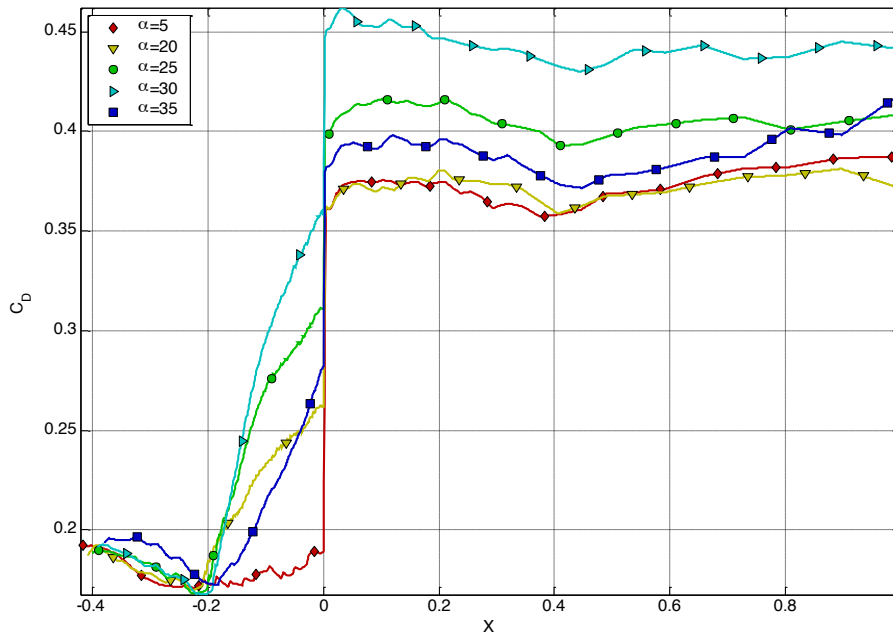


Figure 7.10 The calculated C_D for AR=1.75 for $5^\circ \leq \alpha \leq 35^\circ$ using the momentum equation at different streamwise locations.

For each slant angle, the contribution of the slant surface region is calculated by the change in total C_D at measurement planes at the top of the slant surface and at the base of the slant surface. The C_D of the rear surface is determined by calculating C_D just before and after the slant surface. (Section 3.2). These are compared with the calculated C_D of the rear and slant surfaces from the pressure and viscous forces from the simulations in Figure 7.11. Both the C_D contributions from both the rear and slant surfaces are in good agreement with the calculated C_D from the surfaces. However the C_D of the rear and slant surface is slightly under predicted for $20^\circ < \alpha < 30^\circ$.

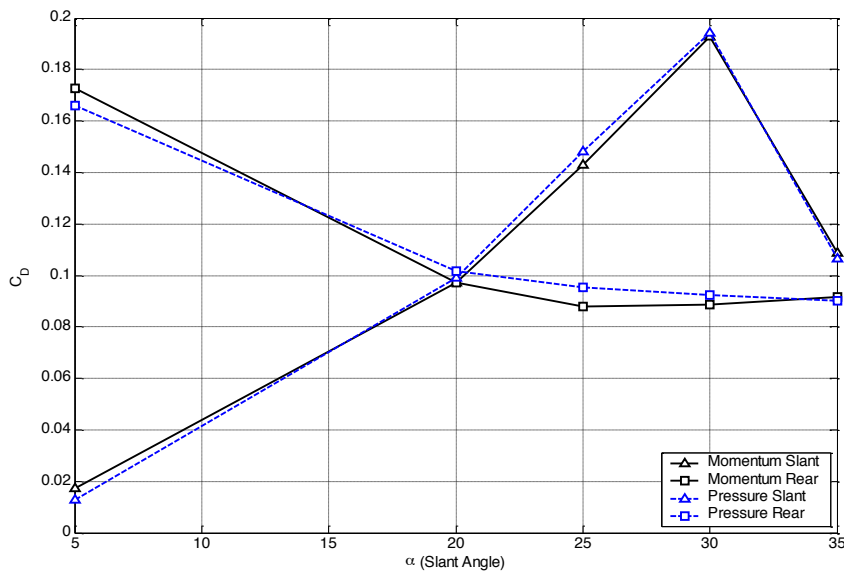


Figure 7.11 Comparison of the C_D calculated from momentum equation and from the pressure and viscous forces using on the slant and rear surfaces for AR=1.75 $5^\circ \leq \alpha < 35^\circ$.

These results indicate that the calculation of C_D from the momentum method is possible but care must be taken to ensure that the effects from ground boundary layer are taken into account. By summing the C_D of the rear and slant surface, it is possible to determine the drag profile for changing α since, as discussed in Section 4.2.3, the contribution from the front and side surfaces is relatively constant.

7.3 Results

In this section, the momentum theory is used to analyse the wake structures and pinpoint sources of drag in the wake region of the Ahmed body. A detailed analysis of the change in wake structure with α for $AR=1.75$ is carried out to determine how different flow structures contribute to the overall drag. The effect of AR is examined to demonstrate how the C_D is affected by changes in AR .

7.3.1 Standard Ahmed body

7.3.1.1 Change in C_D in X direction

The C_D of the different components calculated from the momentum theory are shown in Figure 7.12 for $AR=1.75$, $\alpha=30^\circ$. The C_D is the sum of the streamwise velocity, pressure and vortex drag coefficients. The $C_{PL}+C_{LVL}$ term represents the summation C_{LVL} and C_{PL} of the momentum loss due to non-rotational effects.

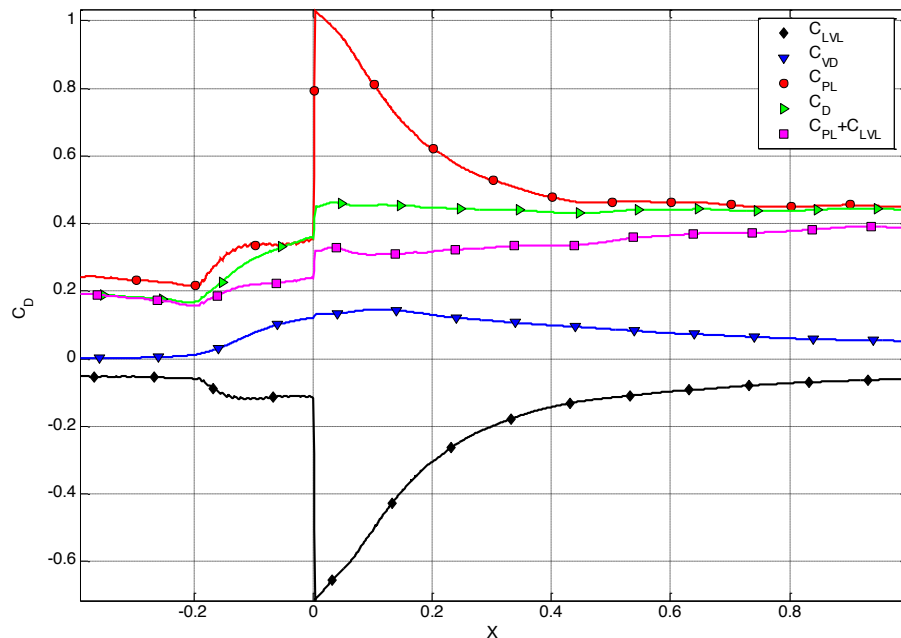


Figure 7.12 Different components the momentum equation for $AR=1.75$, $\alpha=30^\circ$. The $C_{PL}+C_{LVL}$ term represents the summation C_{LVL} and C_{PL} of the momentum loss due to non-rotational effects.

Before the top of the slant surface, all components are quite constant. Losses due to pressure and the boundary layer on the body are already present with $C_{VD} \approx 0$ indicating that the flow field has a negligible rotational component.

Across the slant surface, the C_{VD} increases associated with the formation of the C-pillar vortices and the associated downwash on the slant surface. The gradual increase in C_{VD} is in contrast to C_{PL} , where there is an initial increase at the top of the slant surface and then it plateaus. This is due to the pressure loss from the separation on the slant surface. The reversed flow on the slant surface also decreases C_{LVL} in a similar fashion.

At the rear surface of the vehicle, a large spike occurs in C_{PL} , which is counteracted by C_{LVL} . This is due to increased surface area with stronger negative total pressure causing drag. Across the rear surface, C_{VD} remains constant.

Behind the body, the C_{PL} quickly decreases and the C_{LVL} increases to a constant value in the far wake. This indicates that at $X > +1.0$, the major flow field characteristics that cause the drag on the body have stabilised. Interestingly, C_{VD} peaks at a location behind the body and not above the slant surface. This is thought to be mainly due to the large downwash on the centreline of the body. As the two counter-rotating vortices dissipate in the wake, the C_{VD} for the downstream flow decreases.

In the wake downstream of the model, the C_{LVL} is still negative due to the presence of a wake deficit from the bluff body. In the far wake, $|C_{LVL}| \approx |C_{VD}|$, and as a result the terms tend to cancel each other out. The main contribution to the overall C_D is that of C_{PL} , which is almost equal to C_D at $X = +0.9$.

7.3.1.2 C_D of slant and rear surfaces using the momentum equation.

The effect of the drag components on the slant surface is illustrated in Figure 7.13. The C_{PL} and C_{LVL} in Figure 7.13b increase gradually until $\alpha = \alpha_c$, where there is a significant increase and decrease, respectively. For $\alpha > \alpha_c$ the drag on the slant surface is dominated by C_{PL} and C_{LVL} . Due to its magnitude, it is difficult to determine the effect of C_{VD} for $\alpha < \alpha_c$. Since C_{LVL} and C_{PL} have a roughly equal but opposite profile, they are summed together in Figure 7.13a to represent the component drag not due to

vortex drag. At the $\alpha=\alpha_c$, the transition to a lower C_D is due to a sudden decrease in C_{VD} while $C_{PL}+C_{LVL}$ remains relatively constant across the transition.

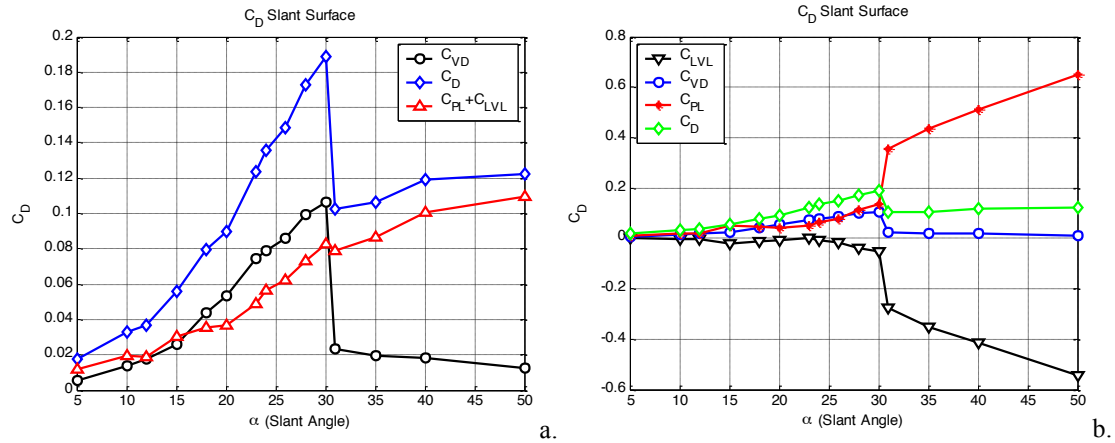


Figure 7.13 The components of the momentum equation and total C_D on the slant surface. C_D , C_{VD} and $C_{PL}+C_{LVL}$ are shown in Figure a since the magnitude of C_{VD} and C_{LVL} mask the change of C_D in Figure b.

On the rear surface in Figure 7.14b, the C_{LVL} and C_{PL} increase and decrease respectively, as the slant angle is increased. There is relatively little change in C_{PL} at α_c . This decrease is proportional to the reduction in area of the rear surface with increasing α . The increase in C_D that occurred on the rear surface at α_c is primarily due to an increase in C_{VD} (Figure 7.14a). However, this only contributes a small portion of the overall C_D on the rear surface since the $C_{PL}+C_{LVL}$ is greater.

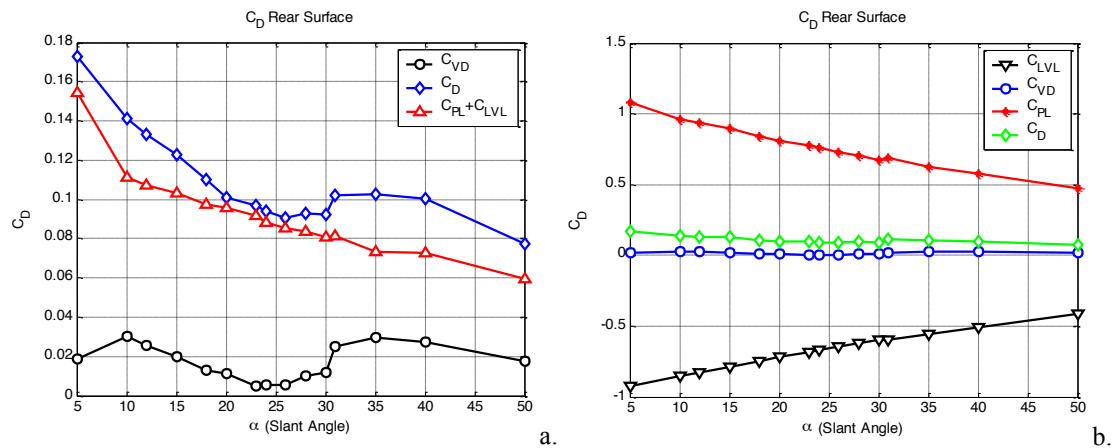


Figure 7.14 The components of the momentum equation and total C_D on the rear surface. C_D , C_{VD} and $C_{PL}+C_{LVL}$ are shown in Figure a since the magnitude of C_{VD} and C_{LVL} mask the change of C_D in Figure b.

7.3.1.3 Effect of slant angle

The change in total C_D for different α is shown in Figure 7.15 for AR=1.75. The increase in C_D for $\alpha=12^\circ \rightarrow 30^\circ$ is from $C_D \approx 0.35$ up to $C_D \approx 0.45$. The C_D past the rear of the body is constant with $C_D \approx 0.375$ for $\alpha > \alpha_c$. The C_D calculated behind the

body ($X>0$) does not vary significantly with downstream location past the end of the model as expected since there are no surfaces creating more losses in the flow except for the ground boundary. The increase in overall C_D from the slant surface is in the region of $-0.2>X>0$ for $15^\circ<\alpha<30^\circ$. After total flow separation from the slant surface at $\alpha>\alpha_c$, the contribution to the drag is still higher than for $\alpha<15^\circ$.

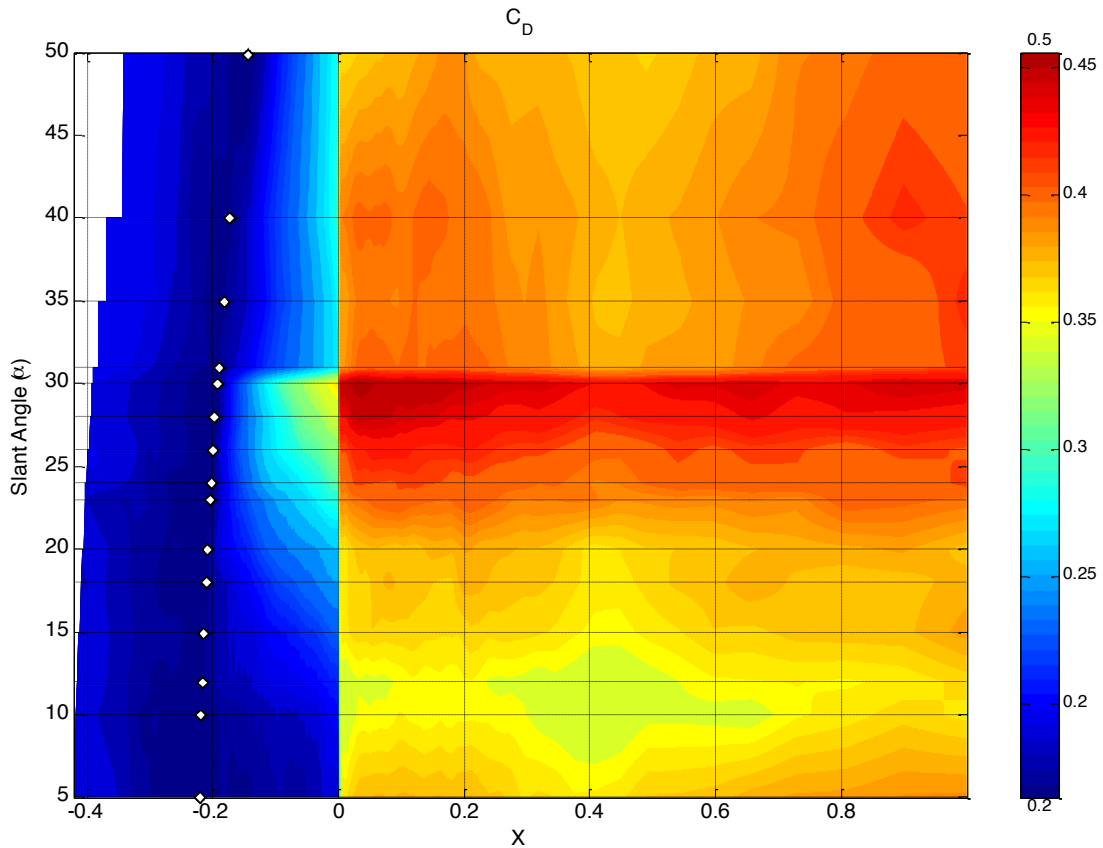


Figure 7.15 Contours of C_D at different streamwise locations for $AR=1.75$, $5^\circ \leq \alpha \leq 50^\circ$. The top of the slant surface is indicated by the symbol \diamond .

The change in C_{VD} with α at different spanwise locations is outlined in Figure 7.16 where the top of the slant surface is indicated by the symbol \diamond . Along the slant surface region, C_{VD} increases as $\alpha \rightarrow \alpha_c$ before a sudden decrease occurs at $\alpha > \alpha_c$. For $\alpha > \alpha_c$, there is an absence of C_{VD} indicating an absence in streamwise vortices and strong downwash in the wake on the body centreline. Downstream of the body ($X>0$), for all slant angles, a peak in the vortex drag occurs. The location of the peak C_{VD} (indicated by the dashed line) moves towards the rear of the body as α approaches α_c . This change of the separation bubble size on the centreline with respect to α is similar Section 4.3.7. The increased downwash from the slant surface caused by the C-pillar vortices causes the strongest C_{VD} in the wake, and not above

the slant surface. This is because as the separation bubble closes, there is an increase in downwash (increase in-plane YZ velocity magnitude) above the separation bubble, which contributes to the C_{VD} in the wake. In effect, the separation bubble is helping to contribute to increased vortex drag. However, this cannot be considered in isolation since C_D after the end of the body remains constant, and the C_{VD} decreases the contribution of $C_{PL}+C_{LVL}$ to the overall C_D . The location of the peak C_{VD} for $\alpha > \alpha_c$ is similar to the position for small slant angles, indicating that the influence of the separation bubble on C_{VD} for small AR is similar to that for $\alpha > \alpha_c$. The C_{VD} is larger in the far wake downstream, indicating the presence of stronger streamwise vortices as α approaches α_c . The increased C_{VD} in the far wake does not begin to increase until $\alpha > 15^\circ$ (which was observed in Section 4.3.3), where path lines released from the side of the slant surface formed a C-pillar vortex but further downstream, the vortex was not well defined by the path lines.

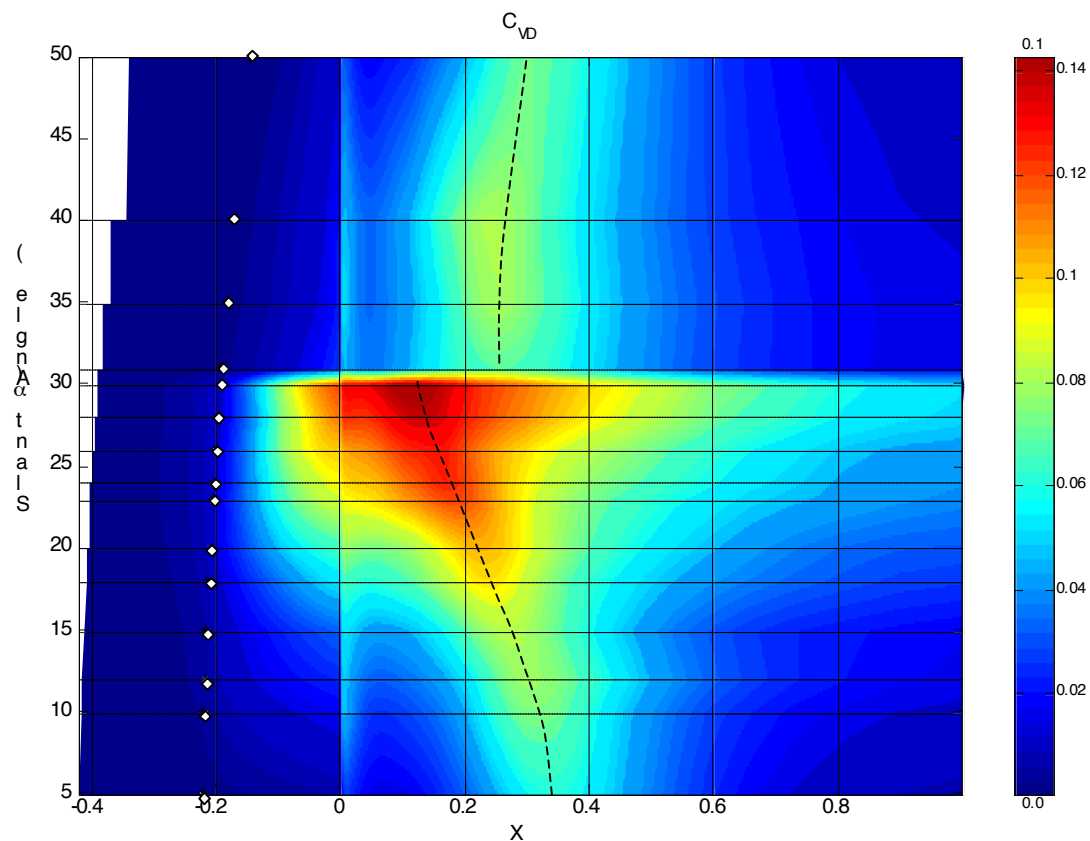


Figure 7.16 Contours of C_{VD} at different streamwise locations for $AR=1.75$, $5^\circ \leq \alpha \leq 50^\circ$. The top of the slant surface is indicated by \diamond .

The contribution of pressure loss (C_{PL}) as illustrated in Figure 7.17, is significantly influenced by α . For small slant angles and $\alpha > \alpha_c$, the contribution to the total drag behind the body is considerable. This is due to two factors, one being the decreasing contribution of C_{PL} behind the body, which is due to the decreasing size of the rear separation bubble as $\alpha \rightarrow \alpha_c$, and the other being the sudden increase in C_{PL} at $\alpha = \alpha_c$. In Figure 7.14b, the contribution of C_{PL} from the rear surface decreases with α due to the reducing rear surface area and corresponding separation bubble. This decreases C_{PL} for $X > 0$ since the smaller separation bubble has smaller pressure losses. The C_{PL} decreases as $\alpha \rightarrow \alpha_c$, but in this same slant angle range, the increase in C_{PL} from the slant surface (see Figure 7.13b) does not increase significantly. For $\alpha > \alpha_c$, the separation bubble on the slant surface suddenly increases C_{PL} on the slant surface, which increases with α . The increase of C_{PL} on the slant surface adds to the overall C_{PL} in the wake and this results in a higher C_{PL} for $X > 0$. As a result, the pressure loss for the separated wake at $\alpha > \alpha_c$ is due to the increased separation bubble size. For bodies just below $\alpha = \alpha_c$, the contribution of pressure loss to the overall C_D is minimal compared with $\alpha > \alpha_c$.

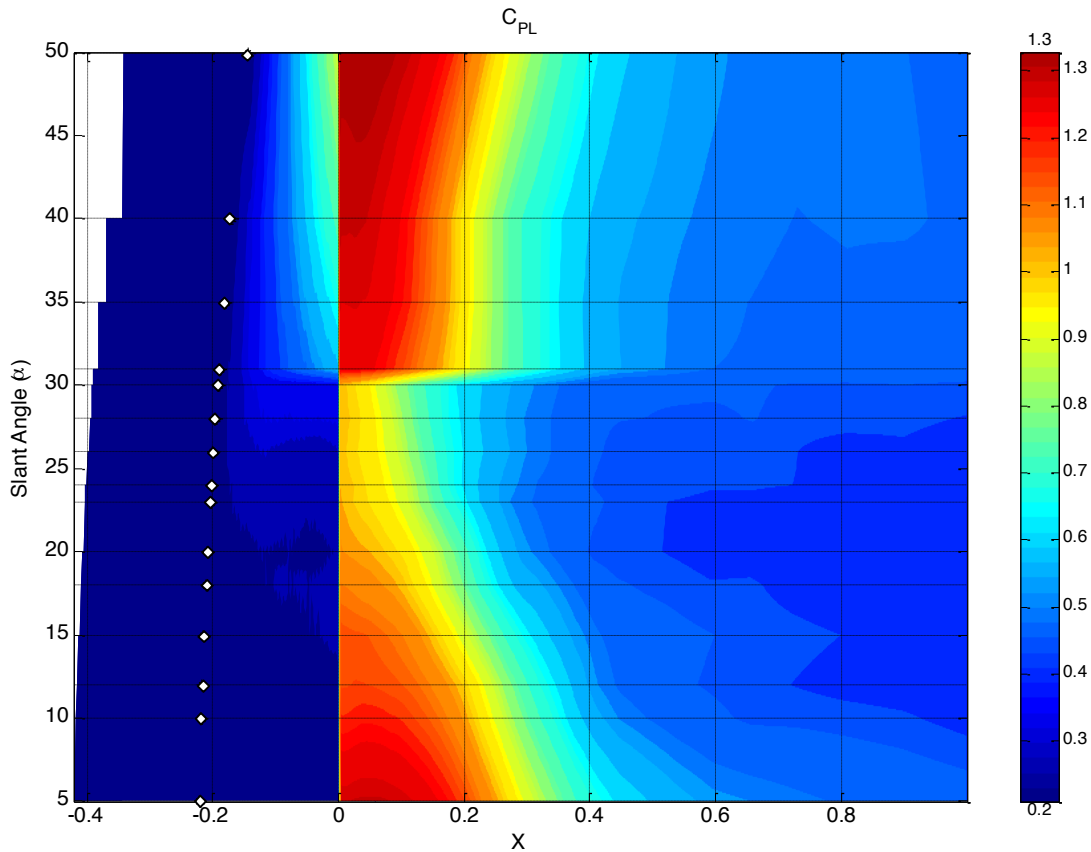


Figure 7.17 Contours of C_{PL} at different streamwise locations for $AR=1.75$, $5^\circ \leq \alpha \leq 50^\circ$. The top of the slant surface is indicated by \diamond .

The effect of the longitudinal velocity loss (C_{LVL}) shown in Figure 7.18 has a similar profile to C_{PL} . The strongest loss in streamwise velocity occurs for slant angles with regions in the wake where $U \ll U_\infty$. Since the C_{LVL} term is the negative integral of a squared term, the fact that reversed flow could be present is irrelevant since the C_{LVL} is relative to U_∞ . On the front region of the body where the flow velocity increases due to curvature, and $U > U_\infty$, this term would be positive. For $\alpha < 15^\circ$, $C_{LVL} < 0$ on the body ($X < 0$) is due to $U < U_\infty$ in the boundary layer on the body and on the ground. The C_{LVL} further decreases on the slant surface for $\alpha > 15^\circ$ caused by the small separation bubble on the slant surface. The C_{LVL} decreases (more negative) as the size of the separation bubble increases on the slant surface due to the region of stronger reversed flow. Behind the body, the regions with largest wake deficit have the lowest C_{LVL} . For $15^\circ < \alpha < 30^\circ$ where the strongest C_{VD} occurs in the far wake, C_{LVL} is higher than for slant angles without strong streamwise vortices. This indicates that the wake recovers back to free stream ($U = U_\infty$) for wake structures without strong streamwise vortices.

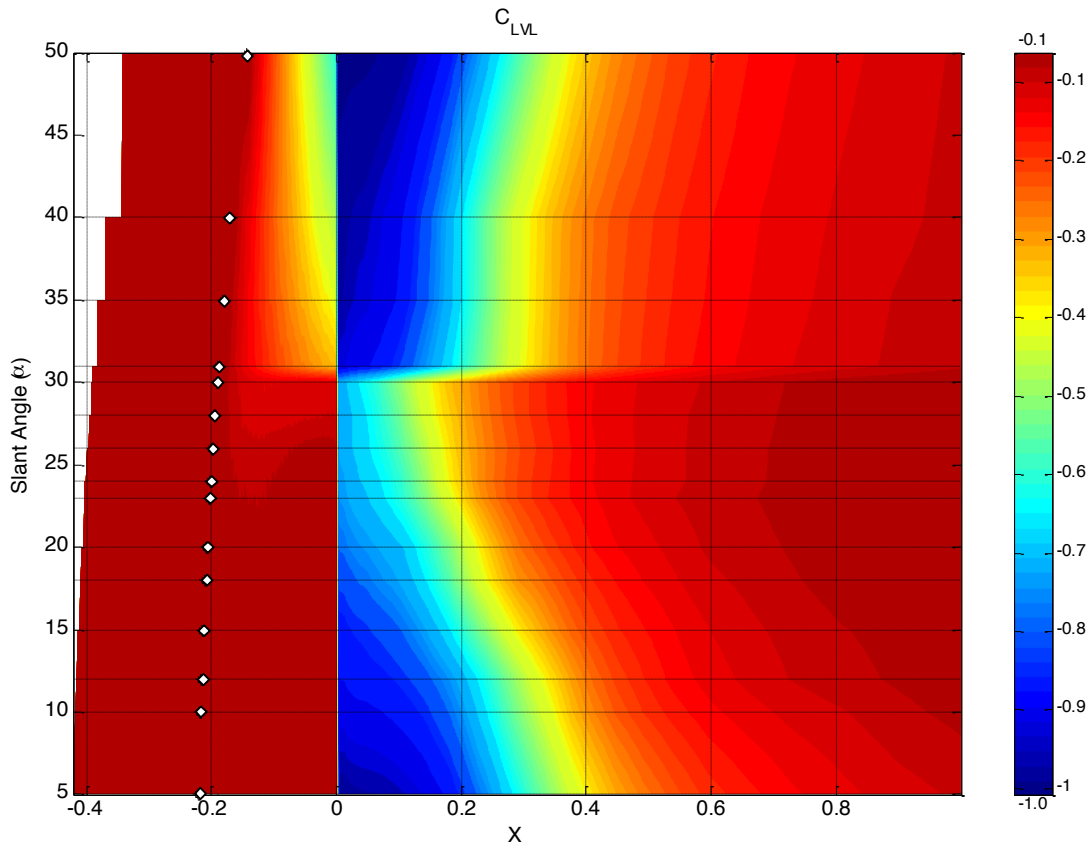


Figure 7.18 Contours of C_{LVL} at different streamwise locations for $AR=1.75$, $5^\circ \leq \alpha \leq 50^\circ$. The top of the slant surface is indicated by \diamond .

The percentage of the contribution of C_{VD} to the total C_D is shown in Figure 7.19. As $\alpha \rightarrow \alpha_c$, the C_{VD} comprises a larger percentage of the total C_D due to the presence of the C-pillar vortex creating stronger downwash. At $\alpha=30^\circ$, C_{VD} contributes up to 33% of the total drag. On the slant surface, C_{VD} contributes a larger portion of the total C_D than in the wake behind the body at $\alpha=30^\circ$. The rear separation bubble mainly contributes to C_{PL} and C_{LVL} , decreasing the percentage contribution of C_{VD} even though C_{VD} is at its maximum behind the body and not on the slant surface. At $\alpha > \alpha_c$, C_{VD} contributes up to 20% of the drag, but this occurs downstream of the body from the folding of the shear layer into the separation bubble causing a localised region of downwash (Section 4.3.5) shown in Figure 7.23.

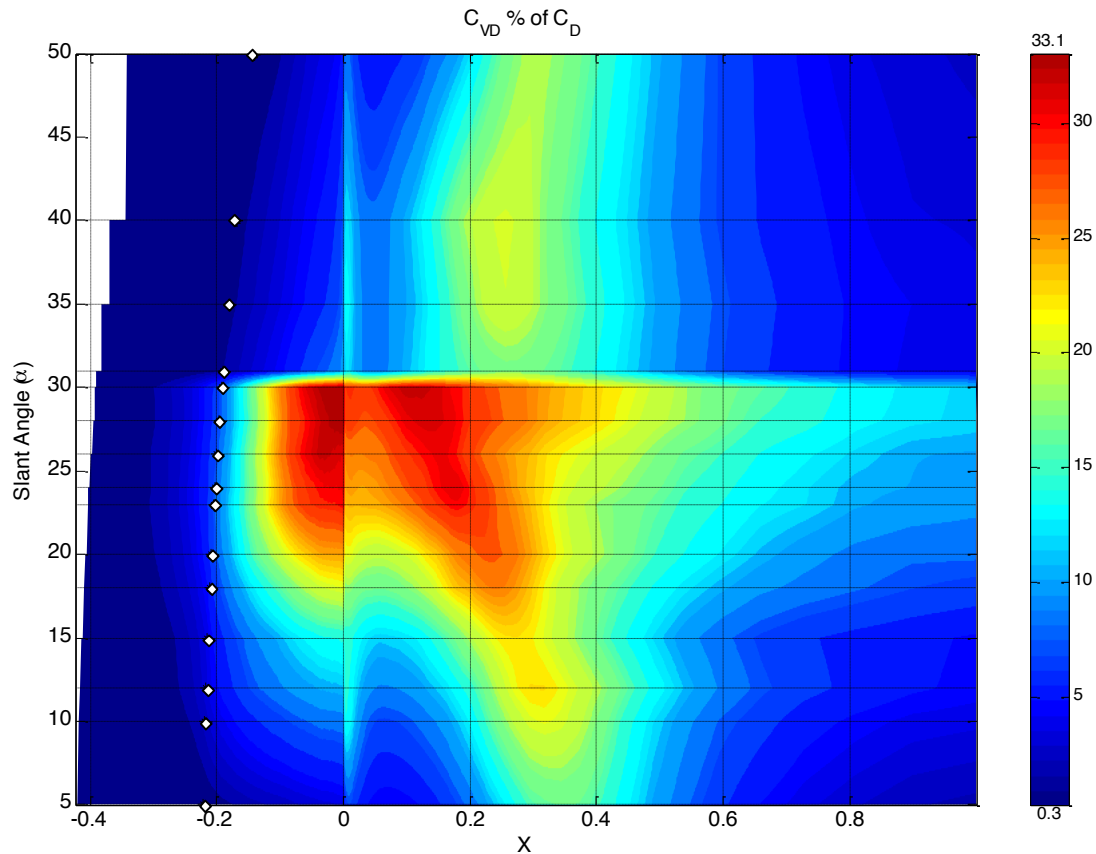


Figure 7.19 Contours of the percentage of C_{VD} of C_D at different streamwise locations for $AR=1.75$, $5^\circ \leq \alpha \leq 50^\circ$. The top of the slant surface is indicated by \diamond .

7.3.1.4 Spatial analysis

To locate the flow structures causing the drag in the wake, the different components of the momentum equation are integrated onto a discretized domain. In this section, the wakes for three different slant angles ($\alpha=15^\circ$, 30° and 35°) are examined at different streamwise locations indicated in Figure 7.20.

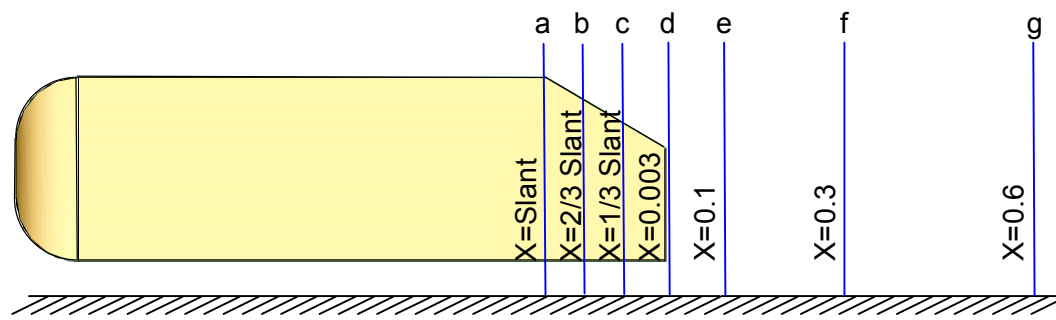


Figure 7.20 Location of streamwise planes used for the spatial analysis of the wake.

The streamwise distribution of the momentum equation and the total drag for $AR=1.75$, $\alpha=15^\circ$ is shown in Figure 7.21 for the different streamwise locations. At the top of the slant surface (Figure 7.21a), the main contribution to C_D is due to C_{PL} . The longitudinal velocity loss on the body side exists but the boundary layer is quite

small. Contours of the local C_{VD} indicate that upstream of the slant surface, the C-pillar is influencing the flow field causing the flow to have a spanwise velocity component. Contours of C_D show that the drag caused by the ground boundary layer at all streamwise locations is mainly comprised of C_{PL} . On the slant surface (Figure 7.21 b & c), the small separation bubble causes C_{LVL} to decrease and C_{PL} to increase. However, due to C_{PL} and C_{LVL} cancelling each other out, the strongest C_D on the slant surface occurs in the shear layer above the small separation bubble. The increased contribution of the C-pillar vortex is visible on the sides of the slant surface. Beyond the end body, the overall C_{VD} increases (Figure 7.16) to a maximum at $X \approx 0.3$ for $\alpha=15^\circ$. This increase in C_{VD} does not occur inside the C-pillar vortex but is due to the induced downwash caused by the C-pillar vortex closer to the centreline of the body (Figure 7.21f). The C-pillar vortex contributes to C_D by increasing C_{PL} at the vortex centre.

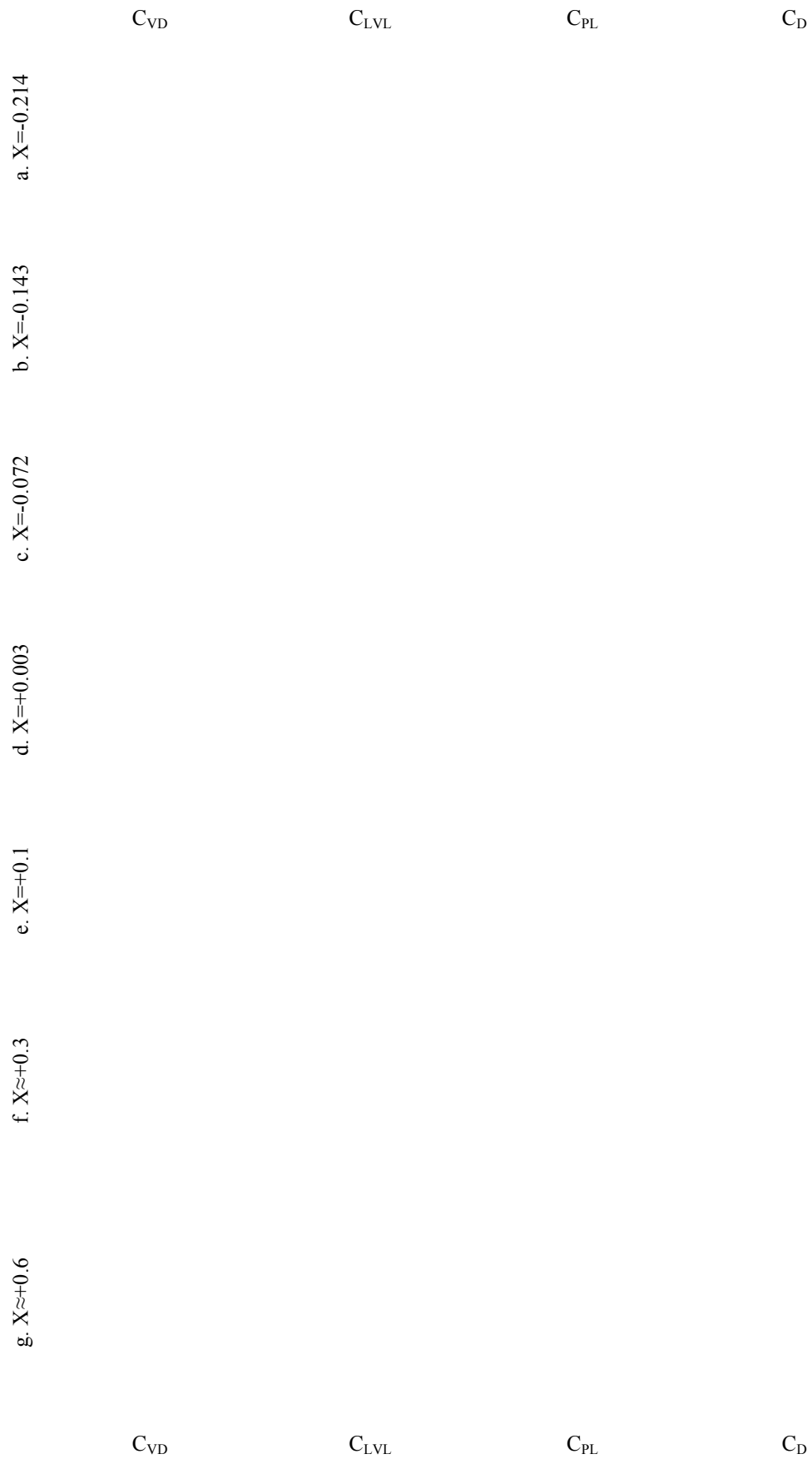


Figure 7.21 Contours of spanwise slices of C_{VD} , C_{LVL} , C_{PL} and C_D for $AR=1.75$, $\alpha=15^\circ$, at different streamwise locations.

The cross-sectional distribution of the different drag components for $AR=1.75$, $\alpha=30^\circ$ is shown in Figure 7.22. Of interest at $\alpha=30^\circ$, is the contribution of the C-pillar vortex to the overall C_D . At the top of the slant surface, the viscous losses due to the boundary layer are visible in the contours of the C_{PL} , contributing to the overall drag on the body.

Near the top of the slant surface (Figure 7.22b), there is separation over the entire width, except on the sides, where the C-pillar vortex exists. Inside the C-pillar vortex, the increased C_{PL} is due to the low pressure at the vortex centre. On the remaining slant surface, the separation bubble causes strong drag in the form of pressure losses. However, this is compensated by the longitudinal velocity losses from the reversed flow in the separation bubble. Nevertheless, the overall C_D near the top of the slant surface indicates that the highest C_D occurs in the shear layer and in the core of the C-pillar vortex.

At two-thirds of the slant surface along (Figure 7.22c), the C_{PL} inside the vortex core is still high while the C_{PL} inside the separation bubble decreases. This is compensated by the increased surface area of the separation bubble. Due to the velocity deficit inside the C-pillar vortex, the C_{LVL} compensates the C_{PL} , which results in the highest C_D occurring on the edge of the vortex structure. The highest vortex drag occurs where the in-plane velocity magnitude is a maximum, which on the slant surface, occurring on the inside edge of the C-pillar vortex, where the swirl velocity is maximum at the vortex radius (Section 3.9). The swirl velocity approaches zero at the vortex centre. Therefore, inside the vortex C_{VD} is negligible.

At the back of the body (Figure 7.22d), the total C_{PL} increase at $X=0$ in Figure 7.12 is due to the increased surface area on the rear surface (Figure 7.22d). In comparison with $AR=1.75$, $\alpha=15^\circ$, the maximum C_{PL} increases from $C_{PL}=0.004$ to $C_{PL}=0.006$, which occurs inside the C-pillar vortex. The total C_D indicates that the strongest regions of drag occur above the slant surface. Of note is the increased C_{VD} in the shear layer region on the side and under side region of the body. The C_D is not high relative to the region above the slant surface or the rear surface, but this spread occurs over a large surface area causing a considerable increase in the drag. Downstream of the body inside the separation bubble, the drag mainly occurs on the edges of the separation bubble. In the centre of the separation bubble, the C_D is negative due to the strong reversed flow.

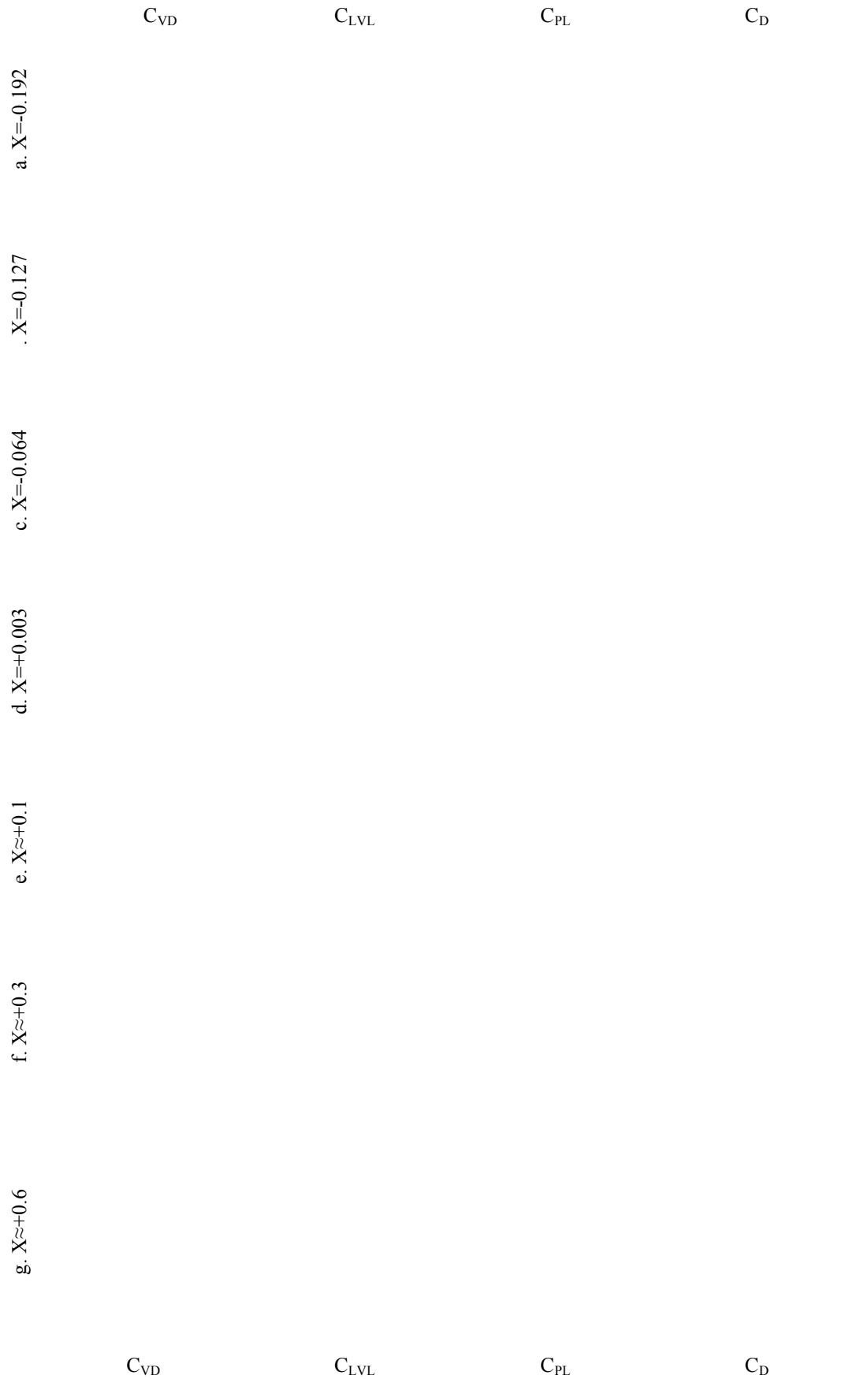


Figure 7.22 Contours of spanwise slices of C_{VD} , C_{LVL} , C_{PL} and C_D for $AR=1.75$, $\alpha=30^\circ$, at different streamwise locations.

The C-pillar vortex causes C_{VD} to peak at $X=0.1$ (Figure 7.22e) due to the larger region of downwash, even though the peak C_{VD} is higher at $X=0.003$ (Figure 7.22d). Past the separation bubble, C_{VD} is still present on the inside of the two counter-rotating vortices in the wake caused by the downwash on the centreline. In the far wake (Figure 7.22g), maximum C_D occurs at the centre of the streamwise vortex, due to the pressure loss in the core.

The distribution of C_D for $AR=1.75$, $\alpha=35^\circ$ in Figure 7.23 is significantly different to that for $AR=1.75$, $\alpha=30^\circ$ (Figure 7.22), due to the large separated wake region. Above the slant surface, the wake is dominated by the C_{PL} and C_{LVL} with the absence of C_{VD} contributing to the overall C_D . The highest C_D occurs in the shear layer of the separation bubble and on the boundary layers on the sides of the body. Inside the separated region above the slant surface, C_{PL} is uniform but C_{LVL} is uneven, resulting in fluctuations of the C_D over the span of the slant surface. On the plane collinear with the rear of the body (Figure 7.23d), C_{VD} contributes to overall C_D , but not to the same extent as at $\alpha=30^\circ$ (maximum of $C_{VD}=0.00035$ compared with $C_{VD}=0.0022$). On the rear surface, there is an increase in C_{VD} due to the increased Y velocity along the rear surface from the recirculation of the separation bubble. This region of high C_{VD} is not found further downstream. However, there is a region of C_{VD} emanating from the top corner of the slant surface, which can be tracked downstream. This region is due to an increased in-plane velocity outside the separated region induced by the separation bubble causing some downwash as it closes. Further downstream, C_D is predominately due to pressure loss with downwash on the body centreline contributing to the overall drag.

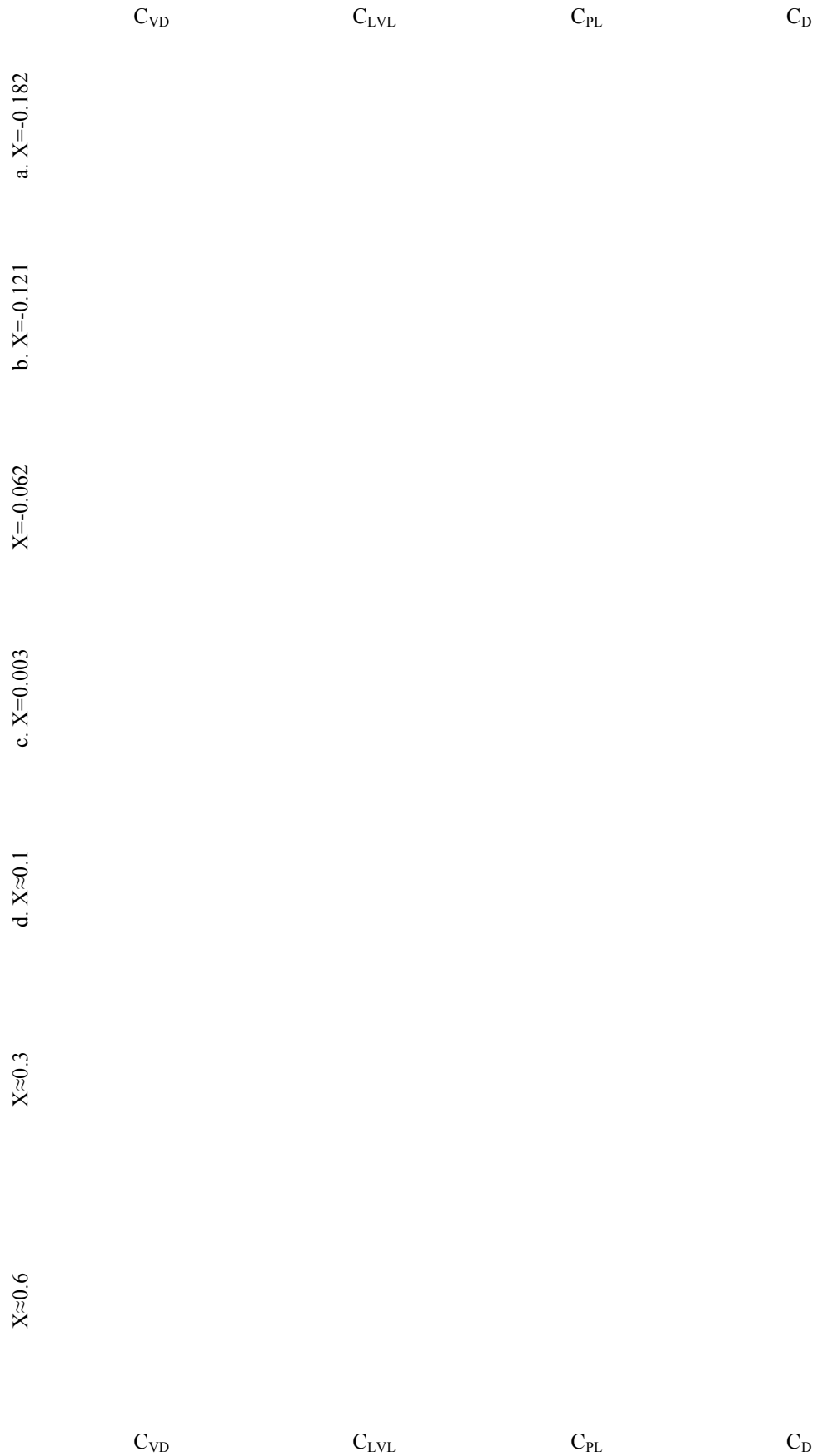


Figure 7.23 Contours of spanwise slices of C_{VD} , C_{LVL} , C_{PL} and C_D for $AR=1.75$, $\alpha=35^\circ$, at different streamwise locations.

7.3.2 Effect of AR on drag structures

The effect of the vehicle aspect ratio on the wake structures is examined in this section. The separate components of the momentum equation are analysed to determine how they affect the overall C_D of the body for different AR. To simplify the parameter space, not all aspect ratios were considered for the analysis since in the previous sections a small number of aspect ratios have provided an adequate representation. The aspect ratios examined were AR=1.1, 1.5, 1.75, 2.0 and 2.5.

7.3.2.1 Drag calculations on the slant and rear surface

Figure 7.24 shows the C_D calculated for the slant surface and rear surface of the Ahmed body using the pressure and viscous forces (Section 4.2.3), and the change in momentum on the fluid for the different AR. In general, C_D calculated using the momentum equation compares well with the calculated C_D from the surface pressures. The C_D calculated from the momentum equation is under predicted but this could be improved by using a larger control volume with a finer mesh.

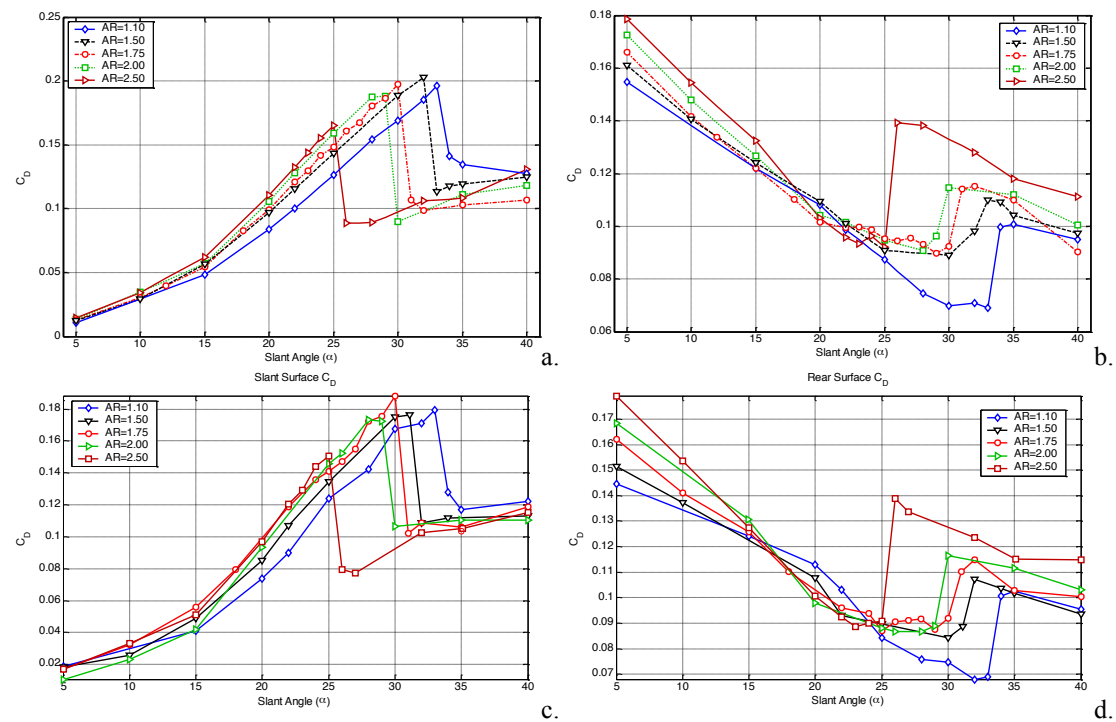


Figure 7.24 The calculated C_D on the slant surface using the surface pressure and viscous drag (a), the momentum equation (b); and on the rear surface using the surface pressure and viscous drag (c) and the momentum equation (d).

The individual contributions to the momentum on the slant and rear surface are shown in Figure 7.25. As can be seen, the considerable change of C_D at α_c on the slant surface is due to the reduction of the C_{VD} (Figure 7.25a), while $C_{LVL}+C_{PL}$

increases with α . For a given α , $|C_{PL}| > |C_{LVL}|$ and therefore $C_{PL} + C_{LVL}$ increases with α . However, there is a sudden change in C_{PL} and C_{LVL} at α_c , but the terms cancel each other out negating their effect on the overall C_D at α_c .

On the rear surface (Figure 7.24b), C_D decreases as $\alpha \rightarrow \alpha_c$, when C_D increases at $\alpha = \alpha_c$. The increase of C_D on the rear surface is due to the increase in $C_{PL} + C_{LVL}$ as shown in Figure 7.25b. Of note is the increase in magnitude of C_{PL} and C_{LVL} (Figure 7.25d) compared with the slant surface due to the presence of the separation bubble on the rear surface. On higher AR bodies, the increase of C_D at α_c on the rear surface is greater than for the lower AR bodies. The breakdown of the C_D in Figure 7.25c indicates that at α_c , there is an increase in $C_{PL} + C_{LVL}$. However, the increase for $AR=1.1$ and $AR=2.5$ on the rear surface is similar at α_c . The increased ΔC_D is due to the increased ΔC_{VD} at α_c on the higher AR bodies, which was not present at $AR=1.1$ at $\alpha = \alpha_c$, while the C_{VD} increases by $\Delta C_{VD} \approx 0.026$ for $AR=2.5$. This indicates that for the higher AR bodies, when the wake separates from the slant surface, the spanwise velocity increases in magnitude near the rear surface of the body. This could be due to increased velocity inside the recirculation bubble. For the low AR bodies, at α_c , there are still considerable streamwise vortices in the wake after separation from the slant surfaces shown by the smaller decrease in C_{VD} on the slant surface at $\alpha = \alpha_c$ (Figure 7.25a).

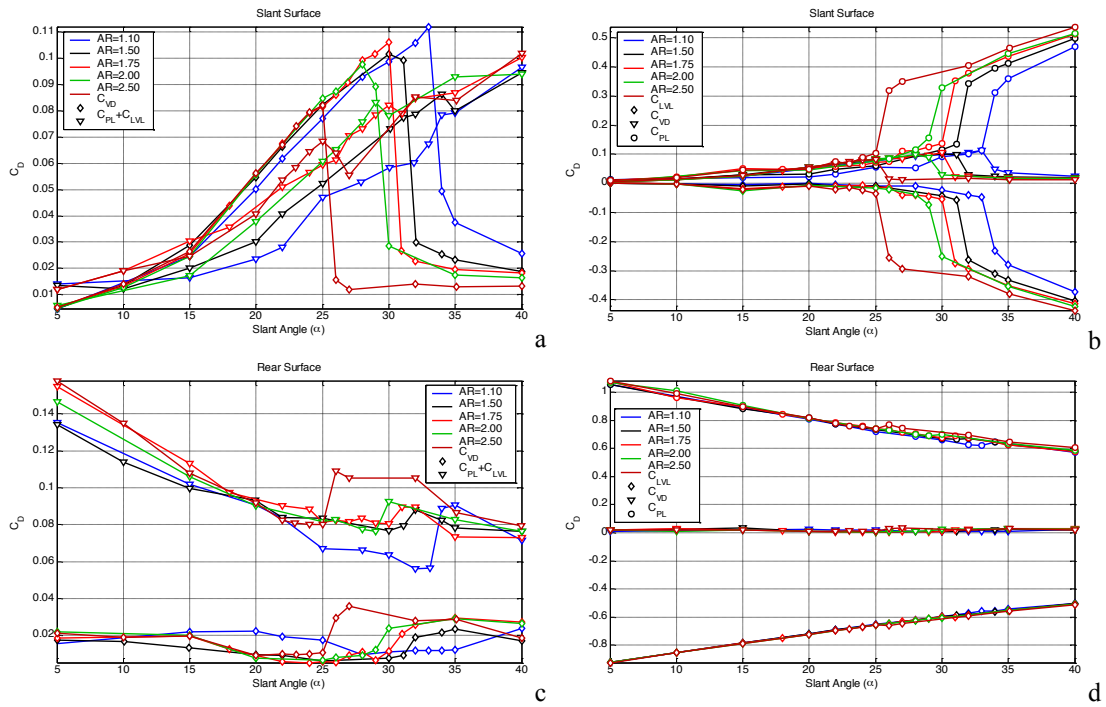


Figure 7.25 Individual components of the momentum equation calculated for the slant surface (a, b) and the rear surface (c, d).

7.3.2.2 Streamwise change in momentum equation with AR

To compare the effect of the AR on the momentum equation, different streamwise locations ($X=-0.222, -0.005, +0.005$ and $+0.5$) are considered to determine how the different components of the momentum equation change in the wake.

Figure 7.26 shows C_{VD} and $C_{PL}+C_{LVL}$ at $X=-0.222$, which is before the slant surface for all slant angles. The C_D for all AR does not change significantly with α . The lower AR bodies have a higher C_D before the slant surface, which is due to $C_{PL}+C_{LVL}$. The C_D on the low AR is higher since such bodies have a higher surface area/area ratio, but if the actual drag is compared, the higher AR bodies have higher drag due to the increased surface area with greater pressure and longitudinal velocity loss. C_{VD} exists before the slant surface but is insignificant compared with $C_{PL}+C_{LVL}$. However, the C_{VD} increases with AR due to the increase in spanwise velocity magnitude near the centreline of the body as shown in Figure 7.27.

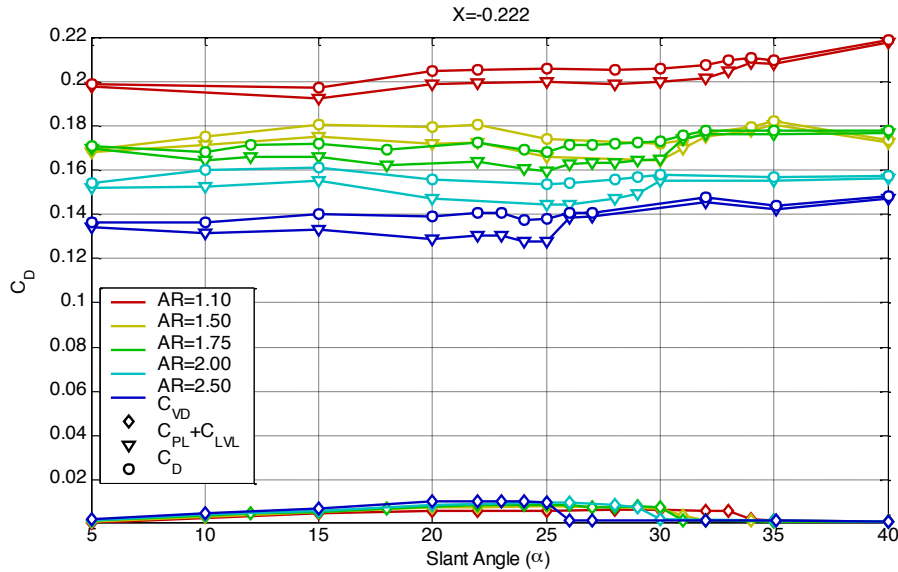


Figure 7.26 Components of the momentum equation at $X=-0.222$ for various AR.

a

b

Figure 7.27 Comparison of the C_{VD} before the slant surface for AR=1.1(a) and AR=2.5 (b) for $\alpha=25^\circ$. Contours indicate that for the higher AR bodies, the increase in C_{VD} is due to higher spanwise velocity magnitude near the corner of the body.

Prior to the end of the slant surface, at $X=-0.005$ in Figure 7.28, the overall C_D has increased primarily due to the increase in C_{VD} . For a given α , the C_D on the lower AR bodies is higher, due to the higher C_{PL} and C_{LVL} found at $X=-0.222$ although $C_{PL}+C_{LVL}$ has increased for all AR from $X=-0.222$. The $C_{PL}+C_{LVL}$ increases with α for all AR and does not change significantly at α_c , unlike C_{VD} . For $\alpha < \alpha_c$, the C_{VD} for all AR are similar, indicating that the C_{VD} , which is primarily due to the C-pillar vortex causing downwash on the centreline, does not increase with AR. This matches Section 5.4.2, where it was found that the footprint from the C-pillar vortex near the top of the slant surface does not increase with AR. The C_{VD} increases slightly for the higher AR bodies but this is mainly due to the higher C_{VD} before the top of the slant surface. At $\alpha=\alpha_c$, C_{VD} reduces considerably which diminishes the overall C_D at $X=-0.005$.

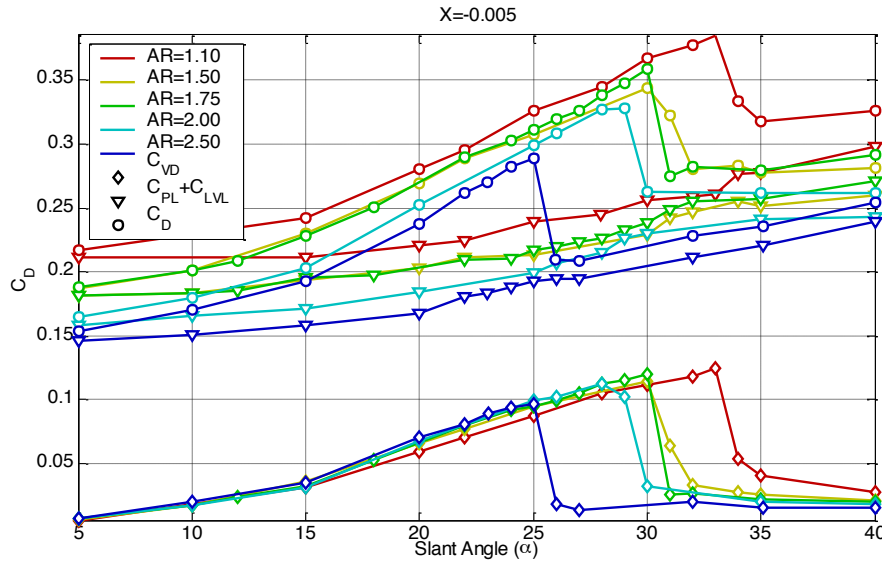


Figure 7.28 Components of the momentum equation at $X=-0.005$ for various AR.

Just past the rear end of the body at $X=+0.005$ in Figure 7.29, there is a sudden increase in overall C_D which is due to the increase in $C_{PL}+C_{LVL}$ in the region adjacent to the rear surface of the Ahmed body. The C_{VD} has increased slightly compared with $X=-0.005$. After separation at $\alpha > \alpha_c$, the low AR bodies have a higher C_{VD} but it is not significantly higher compared with the high AR bodies.

The lower AR bodies have the strongest $C_{PL}+C_{LVL}$ but the profile for a given AR has changed from $X=-0.005$ (Figure 7.28). $C_{PL}+C_{LVL}$ in Figure 7.29 approaches a minimum value as $\alpha \rightarrow \alpha_c$, where $C_{PL}+C_{LVL}$ increases with α for $X=-0.005$. $C_{PL}+C_{LVL}$ increases suddenly past the back of the body from the pressure losses on the rear surface of the model. The losses in this region are greater for bodies with low AR since the rear surface area is larger. As a result, for a given AR, as $\alpha \rightarrow \alpha_c$ $C_{PL}+C_{LVL}$ decreases. On the other hand, $C_{PL}+C_{LVL}$ increases for $\alpha > \alpha_c$ due to a change in the wake structure with increased pressure losses from the larger separation region.

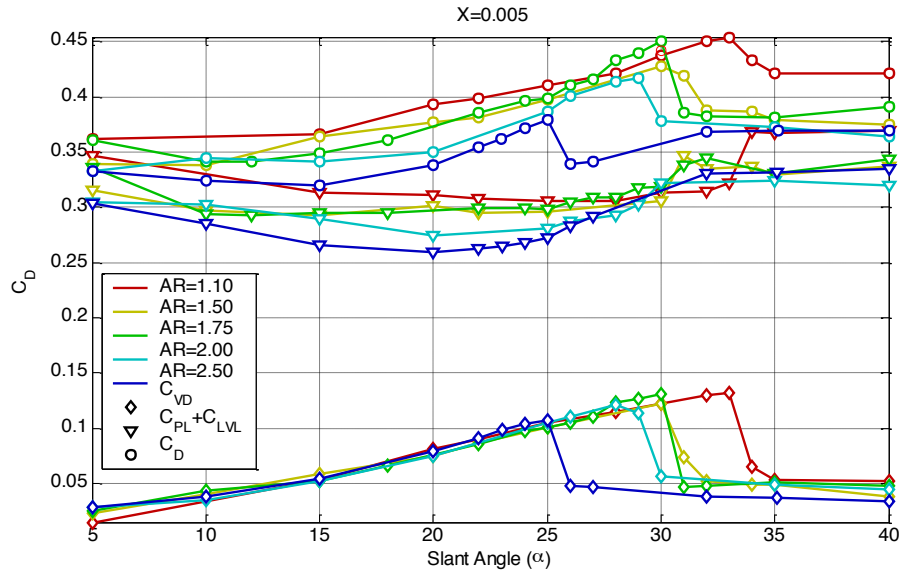


Figure 7.29 Components of the momentum equation at $X=+0.005$ for various AR.

Figure 1.30 shows that C_{VD} has decreased for all AR in the wake at $X=+0.5$. Compared with $X=+0.005$ where the strongest C_{VD} occurs for $AR=1.1$ at $X=+0.5$, the bodies with the highest C_{VD} are those in the middle of the AR range ($AR=1.75$). This indicates that even though low AR bodies have strong streamwise vertical structures near the body, they dissipate more quickly compared with higher AR bodies. The highest AR body examined ($AR=2.5$) has little change in C_{VD} between $X=+0.005$ and $X=+0.5$ for $\alpha > \alpha_c$, whereas C_{VD} for $\alpha < \alpha_c$ has decreased. For bodies with strong C_{VD} present near the bodies, the value decreases downstream. Since, in theory, C_D at $X=0.005$ and $X=0.5$ should remain constant, there is an increase in pressure loss as the streamwise vortices dissipate. The overall C_D does not change after the body but, as can be seen in Figure 7.12, the components of the momentum equation change with downstream distance beyond the body, while C_D remains constant.

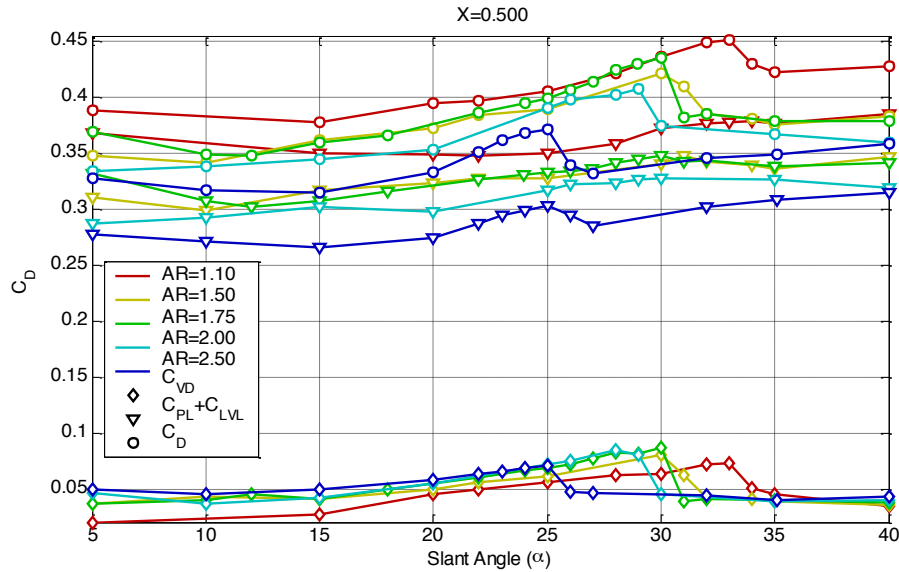


Figure 7.30 Components of the momentum equation at $X=+0.5$ for various AR.

7.3.2.3 Wake visualisations

To compare the effect of AR on the flow structures, visualisations of the different components of the momentum equation are considered at different locations downstream of the body for AR=1.1, 1.75 and AR=2.5, for $\alpha=25^\circ$.

Figure 7.31 compares contours of C_D between the three aspect ratios at different X locations. Before the slant surface at $X=-0.21$ (Figure 7.31a), the highest C_D occurs on the surface of the model. As a result, the cross-sectional surface area increases with AR, and for AR=2.5, there are greater drag losses. At 1/3 of the way down the slant surface at $X=-0.134$ (Figure 7.31b), the C_D from the C-pillar vortex is visible. For all AR, C_D in the C-pillar region appears to be similar. The shear layer cutting the separation bubble has a similar magnitude. However, the increased width on the larger AR bodies creates an overall higher drag. Past the end of body at $X=+0.005$ (Figure 7.31c), the region of C_D corresponding to the C-pillar vortex comprised of a larger area. However, the magnitude of C_D is lower compared with the lower AR bodies. It would be expected that the larger surface area with decreased C_D for AR=2.5 would compensate for a smaller vortex. The magnitude of the C_D from the separation bubble is similar above the remaining area of the slant surface, except the overall C_D increases since the size of that separated bubble is larger for the higher AR bodies. The C_D s adjacent to the rear surface for all AR are similar. Further downstream at $X=+0.1$ (Figure 7.31d), which encompasses the rear separation bubble, C_D in the vortex core is highest for AR=1.1 and becomes less concentrated with

increasing AR. The C_D for the higher AR bodies is higher in the separated bubble. However, C_D in this region is negative indicating that the separation bubble is not contributing to the drag. This is due to the negative C_{LVL} from the reversed flow in the separation bubble. Beyond, the separation bubble in the wake at $X=+0.5$ (Figure 7.31e), the region of drag associated with the two counter-rotating streamwise vortices in the wake increases with AR. Its location relative to the edge of the body is constant.

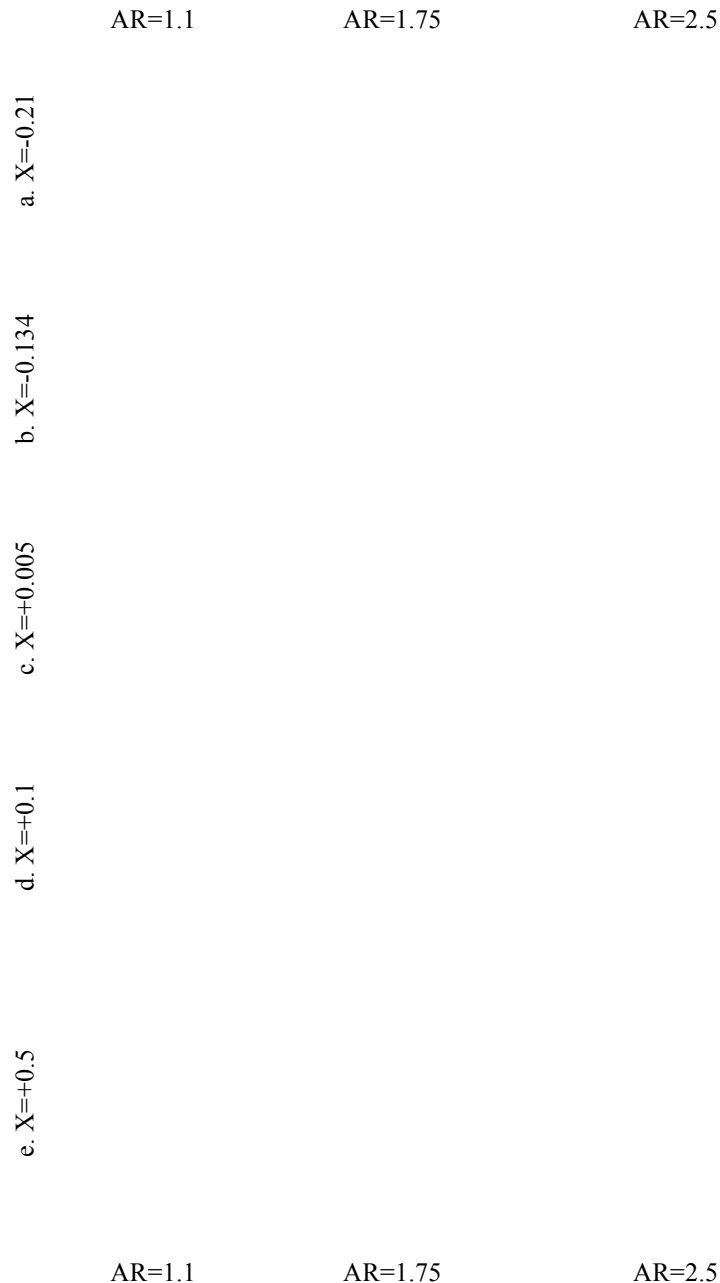


Figure 7.31 Contours of spanwise slices of C_{VD} at various streamwise locations for AR=1.1, AR=1.75 and AR=2.5 for $\alpha=25^\circ$

Figure 7.32 shows streamwise slices of C_{VD} at different downstream locations for $AR=1.1, 1.7$ and 2.5 at $\alpha=25^\circ$. Before the slant surface, C_{VD} is negligible relative to downstream levels. At $1/3$ from the top of the slant surface in Figure 7.32b, the increased spanwise velocity from the C-pillar vortex increases with AR . While there is an increased area of strong C_{VD} , the magnitude of C_{VD} is higher. Beyond the end of the Ahmed body at $X=+0.005$ (Figure 7.32c), the maximum magnitude of C_{VD} is similar for all AR . However, the area of strong C_{VD} is larger for the higher AR bodies. The profile of C_{VD} near the vortex edge is similar for all AR . The increased area of C_{VD} might be due to a larger downwash above the slant surface because of the larger void created by the higher AR bodies. At $X=+0.1$ (Figure 7.32d), the maximum C_{VD} in the wake has decreases for the larger AR body, indicating that for low AR bodies, the C-pillar vortex undergoes less dissipation in the wake region compared with high AR bodies at $\alpha=25^\circ$. This can also be seen at $X=+0.5$ (Figure 7.32e), where there is a region of strong C_{VD} compared with the wider bodies. This causes a stronger downwash on the centre. The strong downwash on the centreline for low AR bodies was also found in Section 5.4.1. For high AR bodies, the contours of C_{VD} indicate that the spanwise velocity decreases rapidly downstream of the model compared with the lower AR bodies.

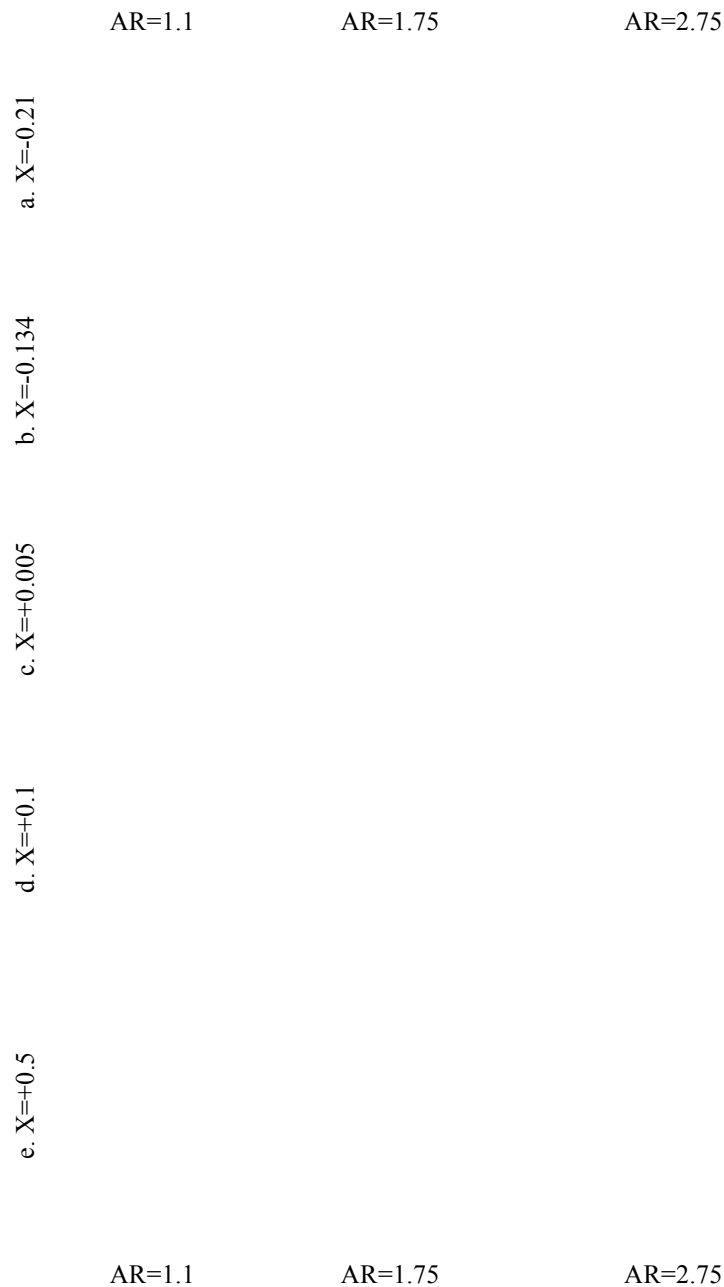


Figure 7.32 Contours of spanwise slices of C_{VD} at various streamwise locations for $AR=1.1$, $AR=1.75$ and $AR=2.5$ for $\alpha=25^\circ$

7.4 Conclusion

In this chapter, the wake structures for the Ahmed body have been analysed using the momentum equation to locate the sources of drag and how they change with α and AR . By evaluating the separate contributions from integrating the momentum equation over control volumes with different streamwise locations, it is possible to determine the contribution of drag from the slant surface and rear surface. However, considerable care is required to ensure that the C_D due to the ground boundary condition is not included in the drag of the Ahmed body.

Figure 7.13a shows that the reduction in C_D at α_c is due to a reduction in C_{VD} . As C_{LVL} decreases and C_{PL} increases, they effectively cancel each other out. On the rear surface, $C_{PL}+C_{LVL}$ decreases with increasing α due to the reducing area of the rear surface. The increase in drag at α_c found on the rear surface is due to an increase in C_{VD} .

Analysis of the effect of α on drag indicates the presence of a peak C_{VD} for a given α past the end of the body ($X>0$). This is associated with increased downwash due to the closing of the rear separation bubble increasing the downwash generated by the C-pillar vortices. At $\alpha=\alpha_c$, C_{VD} contributes up to 33% of the total drag on the Ahmed body, which reduces to approximately 10 % for $\alpha>\alpha_c$ when the C_{VD} is calculated just beyond the end of the body.

The contours of C_{VD} , C_{LVL} , C_{PL} and C_D in Figure 7.21→Figure 7.23 show the regions in the wake that contribute to high drag. Before the slant surface, C_D is due to pressure loss and longitudinal velocity loss in the boundary layer on the surface of the model. Over the slant surface where a slant separation bubble exists, contours of C_D indicate that the highest drag occurs in the shear layer region of the bubble. Inside the slant separation bubble, the main losses are from the C_{PL} . On the side of the separation bubble inside the C-pillar vortex, the main source of drag is pressure loss inside the vortex. However, the C-pillar vortex creates a region of high C_{VD} on the inside of the vortex. The peak C_D coincides with the radius of the vortex where the swirl velocity is the highest. The strongest C_D downstream of the body occurs on the edges of the rear separation bubble. Inside the separated region, C_D is negative due to a strong C_{LVL} . For flows with two counter-rotating streamwise vortices present in the far wake, C_D can be primarily associated with pressure losses in the vortex core. For $\alpha>\alpha_c$, the main losses in the wake are from C_{PL} , which originates from the shear layers of the separation bubble that encompasses the slant and rear surface.

When the AR of the body is varied, $C_{PL}+C_{LVL}$ increases with AR on the slant due to the increased size of the slant separation bubble. The peak C_{VD} for the five aspect ratios considered indicate that C_{VD} does not change considerably with AR. On the rear surface, the increase in C_D at $\alpha=\alpha_c$ is due to the increase in C_{VD} since the increase of $C_{PL}+C_{LVL}$ is similar for all AR examined. The higher C_D on side surfaces on low AR bodies are due to the higher surface area/cross sectional area ratio. However,

$C_{PL}+C_{LVL}$ also increases with surface area. On the slant surface, it was found that C_{VD} for $\alpha < \alpha_c$ does not vary with AR and the $C_{PL}+C_{LVL}$ increases with α for all AR. Spanwise slices of C_{VD} for various AR indicate that the increase in C_{VD} with AR is due to the increased downwash on the inside of the C-pillar vortex. This is due to the large area for downwash to occur between the C-pillar vortices.

Chapter 8 Unsteady Simulations

8.1 Introduction

In this chapter, unsteady simulations are undertaken to examine the unsteady nature of the wake structures behind the Ahmed body. For flows at high Re , the flow fields are unsteady and contain high turbulence levels. In the past, the time averaged flow structures were examined to gain an insight into the wake structures. Now, however, as the technology of both experimental and numerical research has improved, there is a much greater emphasis in examining the internal nature of unsteady flow structures.

While Ahmed et al. [5] examined the effect of the mean flow structures, recent research by Sims-Williams [17, 106, 107] and Vio [22, 108] has involved experiments on the unsteady flow structures in the wake of the Ahmed body. Also recently, large computational simulations of unsteady simulations have been performed on the Ahmed body [35, 75, 106, 109, 110].

Experiments by Vio et al. [22, 108] examined the unsteady structures for an Ahmed body at $\alpha=30^\circ$ experimentally. They found that the rear surface of the Ahmed body exhibited levels of unsteadiness with high frequencies linked to both high and low pressure regions on the rear and slant surface. However, the auto-spectral density functions showed a single dominant shedding frequency of $0.36 \leq St < 0.39$. (Strouhal number based on free stream velocity and the square root of the model frontal area). Most energy was found on the rear base rather than the slant surface, with the cross-spectral phase estimate on the rear base indicating alternating shedding from the top and bottom of the rear surface similar to a Von Karman vortex street. The energy from the auto-spectral density functions from pressure taps within the impingement region of the C-pillar vortex showed a small spectral peak, indicating unsteadiness present in the C-pillar vortex. Vio speculated that the C-pillar vortices, which are relatively stable, are buffeted by the unstable flow behind the body.

Sims-Williams and Duncan [106] reported on experimental and numerical experiments on the Ahmed body at $\alpha=25^\circ$, 27.5° and 30° . In the experiments, the strongest spectral peak occurred near the base of the rear surface with $St=0.58$ for $\alpha=27.5^\circ$ and $St=0.52$ for $\alpha=30^\circ$. This equates to a real time frequency of 40Hz and

43Hz, respectively, at 25m/s free stream velocity. The spectral peak found by Vino et al. [22] occurred at $St \approx 0.39$, which translates to a real time frequency of 41Hz at 35m/s. However, Vino found that St did not vary significantly with Re ($St=0.36-0.39$ for free stream velocity 20-35m/s), for an Ahmed body at $\alpha=30^\circ$. Other experiments by Sims-Williams [17] found the $St=0.49$ for $\alpha=20^\circ$ and $St=0.5$ at $\alpha=22^\circ$ for a two-dimensional Ahmed body (end plates on edge of body to stop C-pillar vortices). On three dimensional bodies, $St \approx 0.58$ for $\alpha=27.5^\circ$ and $St \approx 0.35$ for $\alpha=30^\circ$.

From these data it is difficult to distinguish a trend since there appears to be considerable variation in the calculated St for $\alpha=30^\circ$. This is not surprising since the flow structures approaching α_c are very sensitive to the flow conditions with intermittent switching between flow states. However data for $\alpha < 30^\circ$ suggest that the St increases with α .

Figure 8.1 shows an instantaneous image of the contours of total pressure on the centreplane of the Ahmed body at $\alpha=25^\circ$ calculated using PowerFLOW (Lattice Boltzmann method) from Sims-Williams and Duncan [106]. The simulations showed that the shear layer emanating from the top of the slant surface is unsteady with larger oscillations in the wake. The pumping frequency of the far wake appeared to be consistent with experimental results of $St=0.52$ for $\alpha=30^\circ$ [106].

Figure 8.1 Instantaneous contours of total pressure on the centreline of the Ahmed body at $\alpha=25^\circ$ calculated using PowerFLOW [106].

Analysis of these simulations was further expanded by Duncan et al. [111], in which the wake was deconstructed using different frequency bands to determine the frequencies present. The low frequency band in Figure 8.2a ($< 100\text{Hz}$) shows dominant shedding in the wake occurs from the vortex shedding from the bottom of the rear surface. The high frequency shedding between 100 Hz and 1000 Hz occurs in the “shear-layer” vortices (Kelvin-Helmholtz instability) emanating from the top of the slant surface.

a.

b.

Figure 8.2 Visualisations of the energy of low frequency fluctuations (<100Hz) (a) and the broadband Fourier reconstruction of pressure fluctuations at frequencies between 100 Hz and 1000 Hz, (b) along the body centreline for $\alpha=25^\circ$ [111].

Krajnović and Davidson [109, 110] conducted large eddy simulations (LES) simulations on the Ahmed body for $\alpha=25$ at $Re=3.1 \times 10^4$, which is lower than the current investigation. They found an extremely complex flow that contained a large variety of time and length scales. The instantaneous flow visualisations showed the shear layer on the slant surface shedding spanwise vortices, with the vortices inside the recirculation region moving upstream. As vortices shed downstream, they are tilted so they shed towards the centreline. Wassen and Thiele [75] demonstrated for the low Re using LES that, depending on the grid resolution, the wake is either attached or separated. This indicates that higher resolution is required for LES simulations for higher Re and it also suggests that even at $\alpha=25^\circ$, both attached and separated wake structures are possible.

Gilhome et al. [112] investigated the time dependent nature of the shedding structures on the back of a notchback vehicle (Ford AU Falcon) with the slant angle of the rear window $\approx 27^\circ$. Experiments showed the presence of a low shedding frequency associated with the large scale shedding from the rear of the body, and another higher frequency associated with the shedding of the reattachment zone on the deck lid of the body (Figure 8.3). Gilhome hypothesised that the shedding from the window results in shedding of hair-pin vortices. The presence of the deck-lid causes the separation bubble on the centreline to reattach and reduces the adverse gradient in the C-pillar vortices.

Figure 8.3 Proposed shedding structures from a notchback vehicle with hair-pin vortices shed from the centre-line [112].

In this chapter the unsteady flow structures of the standard Ahmed body are examined. Due to the large computational requirements for the unsteady simulations, only limited slant angles are considered ($\alpha=10,22,25,28,30$ and 35). The resolution study for the unsteady time step was presented in Section 3.6.1.3.

To justify the use of time independent data for the parameter space study, the average flow fields of time dependent simulations are compared with the mean time independent simulations. To gain an insight into the unsteadiness of the flow, the time histories of the drag and lift body forces are analysed. Also, the unsteady wake structures are visualised to get a better insight into the wake structures. Finally, the frequency spectrum of the total pressure in the wake is investigated to determine the frequencies associated with the different wake structures.

8.2 Time averaged simulations

8.2.1 Introduction

In the previous chapters, iteration-averaged data from time steady simulations was used to examine the wake structures, sources of drag and the occurrence of vortex breakdown in the C-pillar vortex. To justify the use of iteration-averaged (IA) data, the visualisations of the flow field are compared with the iteration-averaged (TA) data from the unsteady simulations. Unsteady simulations were not used for the parameter space study due to the extremely long computational run time required (10-20 times longer than steady simulations).

8.2.2 $\alpha=10^\circ$, AR=1.75

The comparison of the flow structures between IA and TA simulations in Region I is shown in Figure 8.4 for AR=1.75, $\alpha=10^\circ$. In both simulations, the flow is attached to the slant surface, with a large separation bubble present in the wake. The flow patterns on the slant surface are slightly different near the body centreline, with surface streak lines, twisting in towards the centreline. Unsteady visualisations (Movie 9.3) indicate that although the flow lines twist towards the centre, no separation or significant unsteadiness is present on the slant surface, with a stable C-pillar vortex. At the rear of the Ahmed body, the size of the separation bubble is slightly larger for the IA solutions but has the same overall structure.

Figure 8.4 Comparison of the wake structures at $\alpha=10^\circ$, AR=1.75 between iteration averaged (a) and time averaged simulations (b). Refer to Section 4.3.1 for figure description.

8.2.3 $\alpha=22^\circ$ AR=1.75

The slant separation bubble on the slant surface is similar for both IA and TA simulations at $\alpha=22^\circ$ as illustrated in Figure 8.5. The separation reattaches on the centreline at a similar location to the foci points on the slant surface. On the body centreline, the structures appear to be more influenced by the imposed symmetry boundary condition on the IA solutions, with the rear region of reversed flow slightly different between simulations. However, away from the centreline, there are no significant discrepancies between the IA and TA simulations. The C-pillar vortex does not vary between IA and TA simulations.

Figure 8.5 Comparison of the wake structures at $\alpha=22^\circ$, $AR=1.75$ between iteration averaged (a) and time averaged simulations (b). Refer to Section 4.3.1 for figure description.

8.2.4 $\alpha=25^\circ$, $AR=1.75$

At $\alpha=25^\circ$ in Figure 8.6, the slant separation bubble size predicted by the TA solution is larger and extends further down the slant surface. However, the flow is still attached to the slant surface. In the rear region, the IA simulation predicted that the region of reversed flow near the edges of the model would encompass a larger region of the rear surface, while the TA simulation indicates that the mean flow is more uniform. This could be due to the large sample size used to calculate the mean flow field for the unsteady simulations (>700 data sets).

Visualisations of the mean flow field for the time dependent simulations do not indicate the presence of the breakdown of the C-pillar vortex past the end of the slant surface. Subsequent investigation of the unsteady flow field indicates that for $\alpha=25^\circ$, as the solution steps forward in time, the vortex breakdown observed in the IA simulation dissipates although initially present (Movie 9.24). This indicates that the onset of vortex breakdown for a given slant angle, especially past the end of the slant surface, is sensitive to changes in the flow field.

Figure 8.6 Comparison of the wake structures at $\alpha=25^\circ$, $AR=1.75$ between iteration averaged (a) and time averaged simulations (b). Refer to Section 4.3.1 for figure description.

8.2.5 $\alpha=28^\circ$, AR=1.75

In Figure 8.7, the IA simulations are compared with the TA simulations at $\alpha=28^\circ$. In this region, the C-pillar vortex breaks down above the slant surface at $X\approx-0.05$. While the iteration averaged simulations indicate regions of reversed flow inside the C-pillar vortex, this is not shown in TA simulations. However, unsteady visualisations in Movie 9.36 indicate the presence of reverse flow inside the vortex core. This is also confirmed by unsteady visualisations of $C_{DP}=0.1$ in Movie 9.34. Due to the larger number of frames used for the TA simulations, the flow field is more uniform with the iso-surface $U/U_\infty=0$ representing the region of reversed flow on the slant surface smoother. This iso-surface also indicates that on the centreline, the slant separation bubble is larger. Downstream of the body, the downwash along the centre is marginally stronger but the rear separation bubble is similar.

Figure 8.7 Comparison of the wake structures at $\alpha=28^\circ$, AR=1.75 between iteration averaged (a) and time averaged simulations (b). Refer to Section 4.3.1 for figure description.

As has been previously mentioned, this study used simulations using a symmetrical boundary condition along the centreline of the Ahmed body to reduce computation requirements. For unsteady simulations with highly unstable wakes, this is not ideal. To verify that the symmetry boundary condition did not have a large effect on the

results, a simulation using the full model was undertaken.

Figure 8.8 Time averaged wake structure $\alpha=28^\circ$ AR=1.75 of the full model (no symmetry boundary condition on centreline). Refer to Section 4.3.1 for figure description.

8.2.6 $\alpha=30^\circ$, AR=1.75

In contrast to $\alpha=25^\circ$, at $\alpha=30^\circ$, the TA flow in Figure 8.9a, indicates that the vortex breakdown in the C-pillar vortex is larger. This is indicated by the larger iso-surface of $U/U_\infty=0$ along the vortex core, which almost extends to the formation point of the C-pillar vortex. Contours of normalised velocity magnitude in the rear view indicate that the vortex core is larger at the end of the slant surface due to the increased region of reduced velocity magnitude (mainly comprised of $V_{X(\text{axis})}$). This results in a stronger downwash on the centreline indicated by the in-plane streamlines on the symmetry plane. Although there are slight variations between the IA and TA simulations, the key flow features have not altered significantly to allow the use of the IA simulations for the analysis of the flow field. Vino et al. [22] integrated the streamlines along the centreline of the Ahmed body from the time averaged velocity field. The streamlines indicate that the rear separation bubble on the centreline is very short extending to $X=0.15$, which is similar to the IA and TA simulations.

Figure 8.9 Comparison of the wake structures at $\alpha=30^\circ$, $AR=1.75$ between iteration averaged (a) simulations and time averaged simulations (b). Refer to Section 4.3.1 for figure description.

8.2.7 $\alpha=35^\circ$, $AR=1.75$

Both the IA and TA simulations at $\alpha=35^\circ$ (Figure 8.10) indicate that the wake has separated from the slant surface and a large separation bubble exists. The rear separation bubble extends the same distance downstream for both simulations. The location of the top recirculation region indicated by the path lines on the symmetry plane in the TA simulation is not shown in the IA simulation. This results in a small change in the shape of the iso-surface of $U/U_\infty=0$. The three-dimensional path lines released from the edge of the slant surface indicate that more flow is entrained into the rear separation bubble.

Figure 8.10 Comparison of the wake structures at $AR=1.75$ $\alpha=5^\circ$ between iteration averaged (a) simulations and time averaged simulations (b). Refer to Section 4.3.1 for figure description.

8.2.8 Conclusion

The comparison between the iteration averaged simulations used for the parameter space study and the time averaged simulations from time dependent simulations compare well for $AR=1.75$. Simulations were compared for a variety of slant angles which simulate all the types of flow fields found in the wake in the parameter space study. Even though there are slight differences between the IA and TA simulations which are to be expected (different number of points used to average), the key flow features and structures compare well. The largest difference found occurred for $\alpha=30^\circ$

in the C-pillar vortex, which shows the vortex breakdown in the TA simulations was larger. This could be possibly due to the larger fluctuations the location of breakdown in the C-pillar vortex in the IA simulations, and the averaging smoothed out the region of breakdown.

8.3 Body Forces

To achieve a better understanding of the unsteady nature of the wake structures, the body forces for the time dependent simulations for the Ahmed body are investigated in this section. Due to the long computational times required, only a short time span is considered. However, because of the high frequency nature of the wake, this time span appears to be sufficient to capture the wake features.

The unsteady C_D and C_L for the entire body for $AR=1.75$ $10^\circ \leq \alpha \leq 35^\circ$ is shown in Figure 8.11. This demonstrates the extremely unsteady nature of the wake structure. As can be seen, for all α considered, the C_D and C_L oscillate about a mean value with a high frequency unsteadiness present, indicating that unsteadiness is not due to the wake evolving. The iteration averaged solution was used as a base for these simulations and was run for 0.1s of simulation time before data collection.

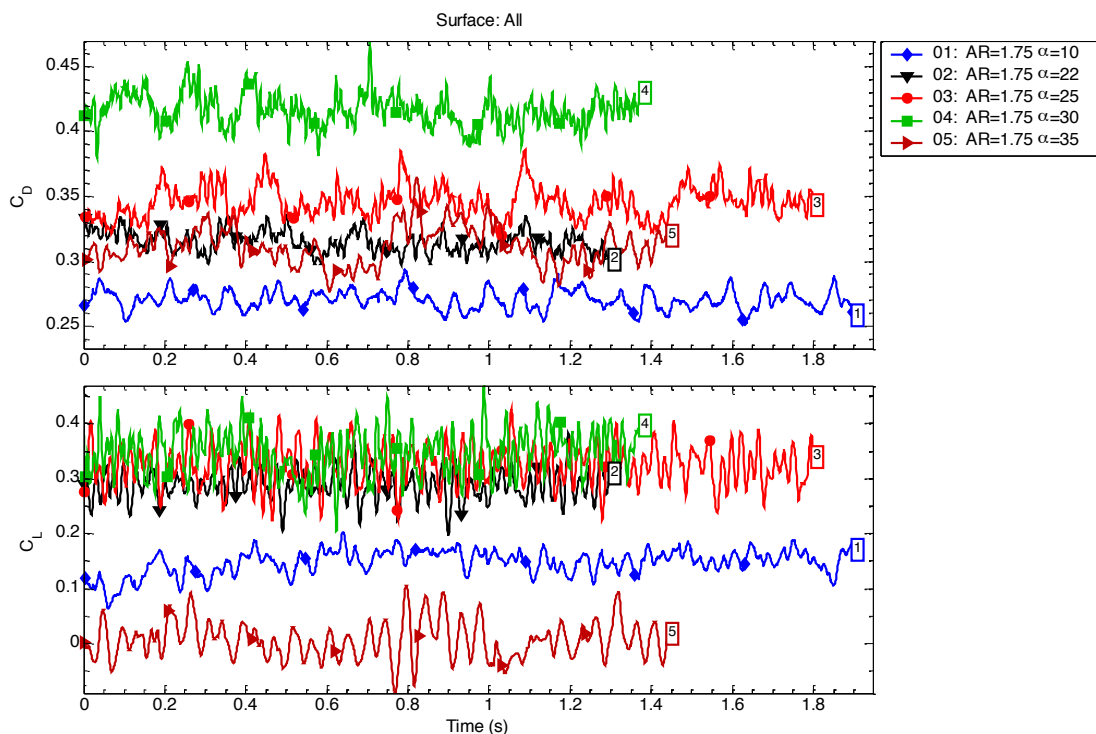


Figure 8.11 The time dependent C_D and C_L of the entire Ahmed body for $\alpha=10^\circ$, 22° , 25° , 30° and 35° for $AR=1.75$.

To determine the frequencies of the force history on the Ahmed body, a Fast Fourier Transform (FFT) of the C_D and C_L history was conducted. Due to the limited length of the data collection, the frequency spectrum is not as comprehensive as it could be because longer time histories are required for a more accurate FFT. However, the frequency spectrum is still able to show the key features of the wake. The frequency is non-dimensionalised by using the Strouhal Number (St) which is calculated using the square root of body cross sectional area and the free stream velocity as reference values.

The frequency spectrum of the C_D and C_L history of the forces from all surfaces of the Ahmed body is illustrated in Figure 8.12. It is evident that for the slant angle examined, the frequency spectrum is both complex and noisy with multiple frequencies present on the surfaces of the model and with different flow structures near various regions of the model. A trend that is evident is that for $22^\circ \leq \alpha \leq 30^\circ$, where a separation bubble is evident on the slant surface, the frequency spectrum of the C_L has higher frequencies present compared with $\alpha=10^\circ$ and 20° . The energy in these frequencies is smaller in the frequency spectrum of C_D .

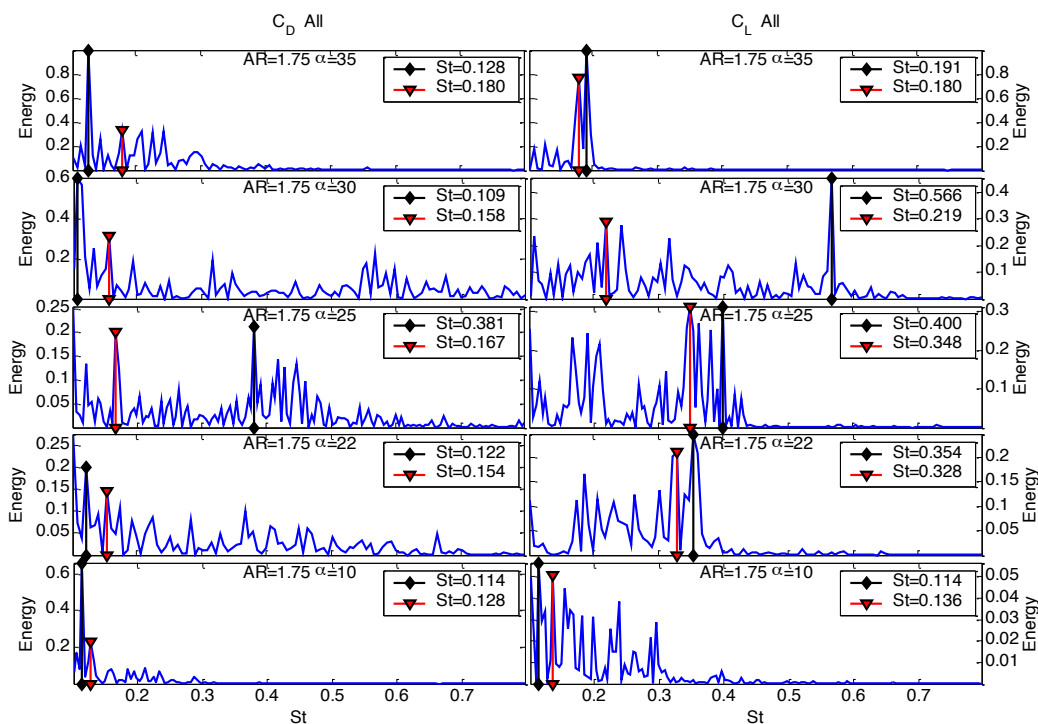


Figure 8.12 The frequency spectrum of the entire Ahmed body calculated from the C_D (left column) and the C_L (right column).

To identify which spectral peaks are associated with which surfaces, the drag and lift history of $AR=1.75$, $\alpha=30^\circ$ of all surfaces is considered in Figure 8.13 (refer to

Section 3.2 for region definitions). The fluctuations found in C_D in Figure 8.11 are primarily due to the fluctuations on the slant and rear surface. On the front and side surfaces, the C_D is relatively constant. However, C_L of the side surface does fluctuate which is the cause of the different frequency spectrum of the C_L and C_D in Figure 8.12. In addition, the C_L of the rear surface ≈ 0 so the frequency spectrum from C_L on this surface is not applicable. Since the C_D and C_L of the slant surface are just different components of the normal force, the frequency spectrum should be the same.

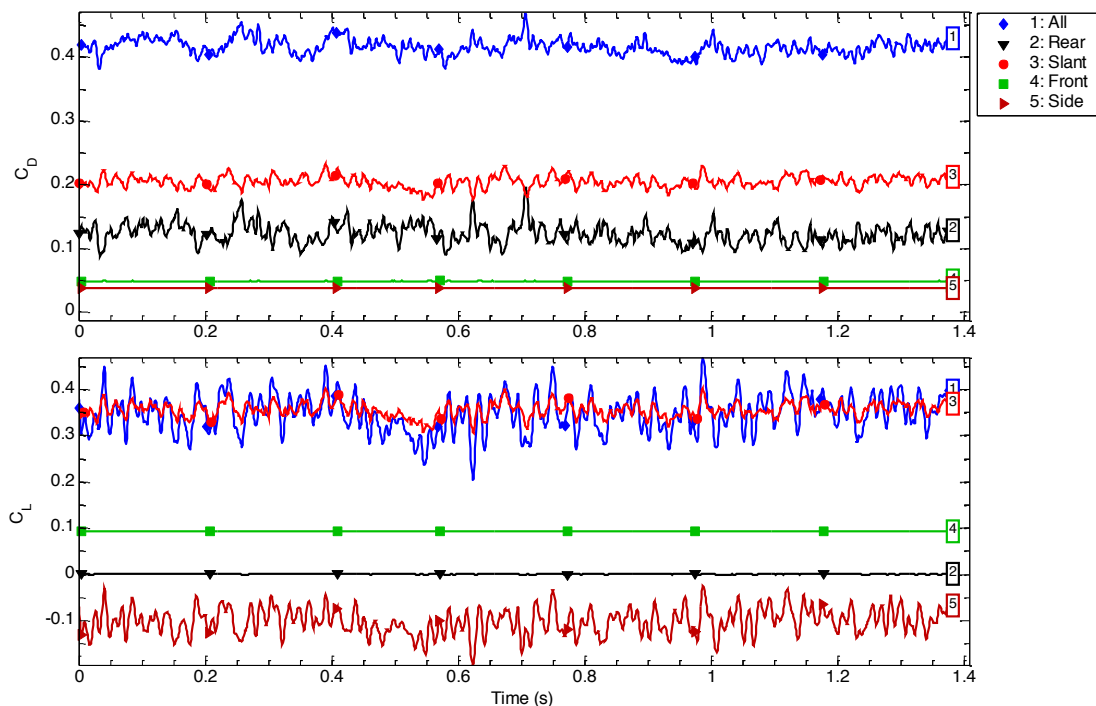


Figure 8.13 The unsteady C_D and C_L on all surfaces of the Ahmed body at $\alpha=30^\circ$, $AR=1.75$. (refer to Section 3.2 for region definitions)

The frequency spectrum of the C_D and C_L for $AR=1.75$, $\alpha=30^\circ$ for all surfaces is shown in Figure 8.14. The C_D frequency spectrum confirms that the frequencies present on the entire model are due to rear and slant surface, while the front and side surface do not contribute. Alternately, the C_L frequency spectrum is mainly comprised of the side surface spectrum with contributions from the slant surface spectrum. The two peak frequencies found on all surfaces are present on the slant and side surfaces. This makes the analysis of the front regions of the Ahmed body redundant, while analysis of the entire body difficult, due to the extra noise created by the side surfaces. The return spectrum from the slant surface using C_L or C_D is similar, since both time histories originate from the same surface. Thus, for the analysis of the frequency history on the slant surface, only the C_D history is used.

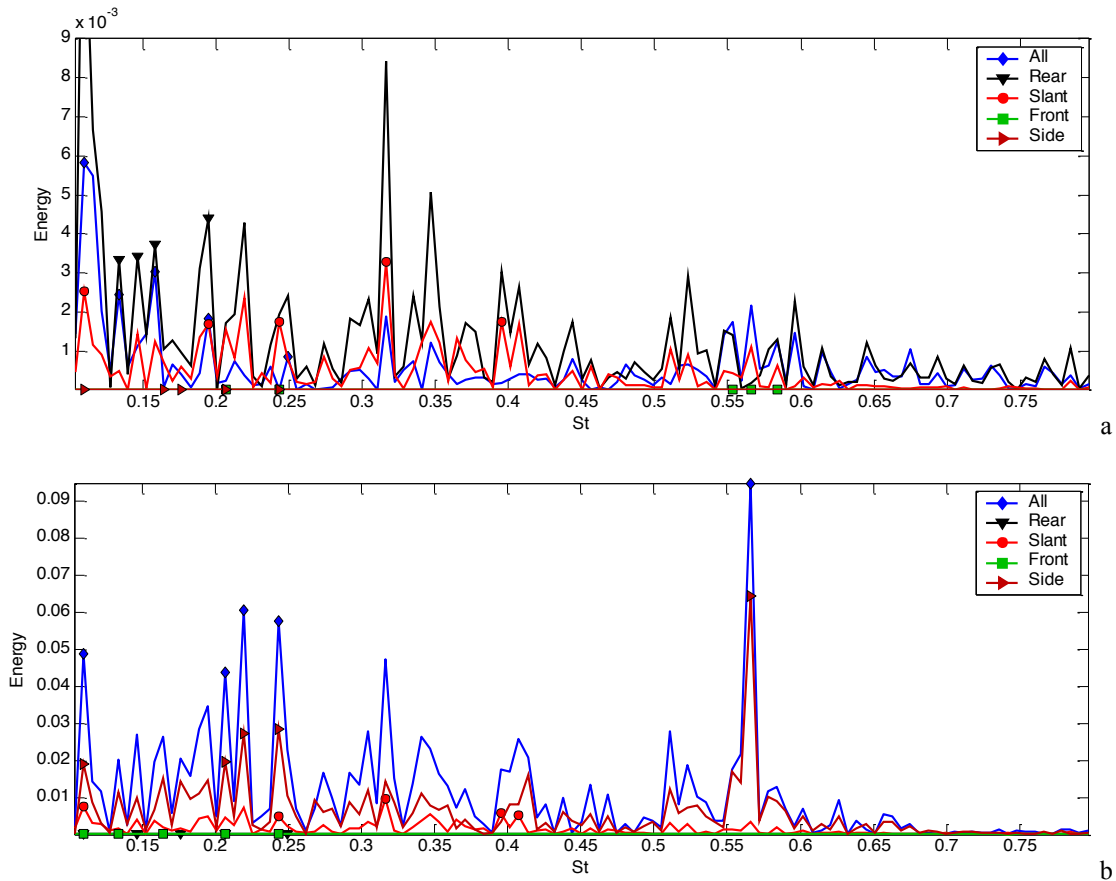


Figure 8.14 The frequency spectrum from C_D (a) and C_L (b) on the entire model and on individual surfaces. Refer to Section 3.2 for surface definitions.

The frequency spectrum of the C_D history for $AR=1.75$ $10^\circ \leq \alpha \leq 35^\circ$ for the slant surface is shown in Figure 8.15 and the rear surface in Figure 8.16. Although this analysis could be more accurate with more data for the FFT, they still given an indication of the effect of α on unsteady wake structures.

On the slant surface in Figure 8.15, the spectrum for all slant angles is dominated by low frequencies. When the flow is attached to the slant surface at $\alpha=10^\circ$, the frequency spectrum is relatively low frequencies with the strongest frequency occurring at $St=0.154$. When the wake separates from the slant surface, the frequency spectrum indicates higher frequencies present on the slant surface. As $\alpha \rightarrow 30^\circ$, the energy in these frequencies increases while there is still the peak at $St \approx 0.18$. The frequency spectrum at $\alpha=30^\circ$ shows that above the slant surface, the wake structure is quite chaotic with multiple spectral peaks present.

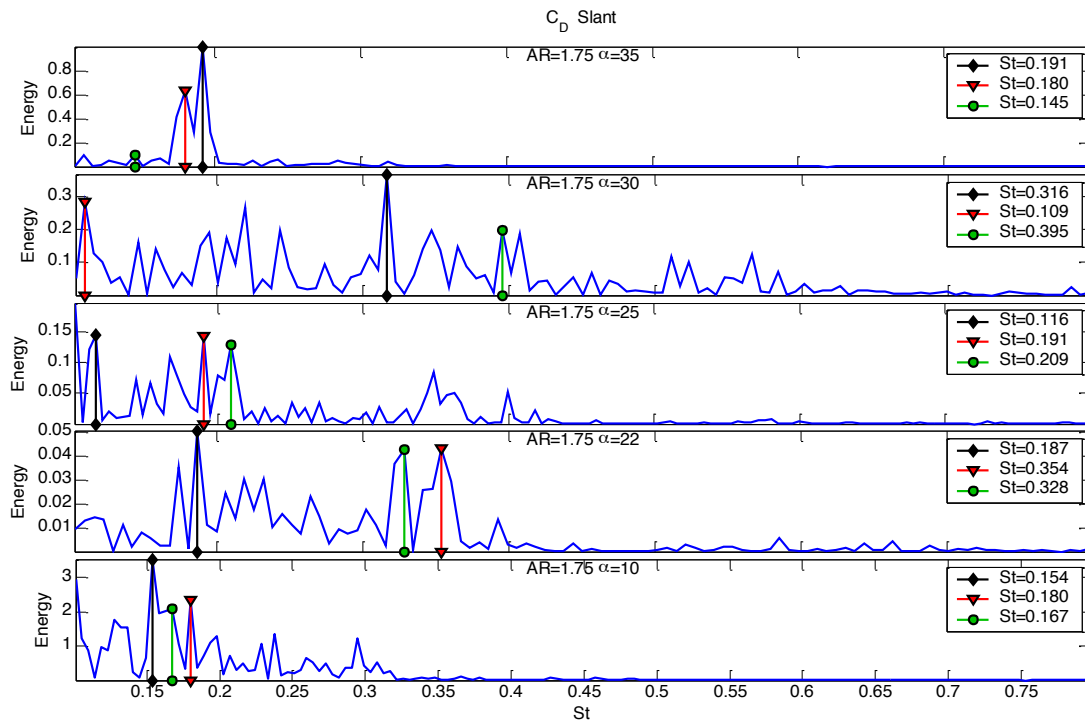


Figure 8.15 Frequency spectrum of the slant surface calculated from the C_D history for $\alpha=10^\circ$, 22° , 25° , 30° and 35° .

In contrast to the slant surface, the frequency spectrum on the rear surface in Figure 8.16 is less complex. The energy in the frequencies found at $St \approx 0.35$ is lower compared with the lower frequencies. For regions where flow is separated from the slant surface at $22^\circ \leq \alpha \leq 30^\circ$, the effect of the flow structures on the slant surface affect the spectrum on the rear surface.

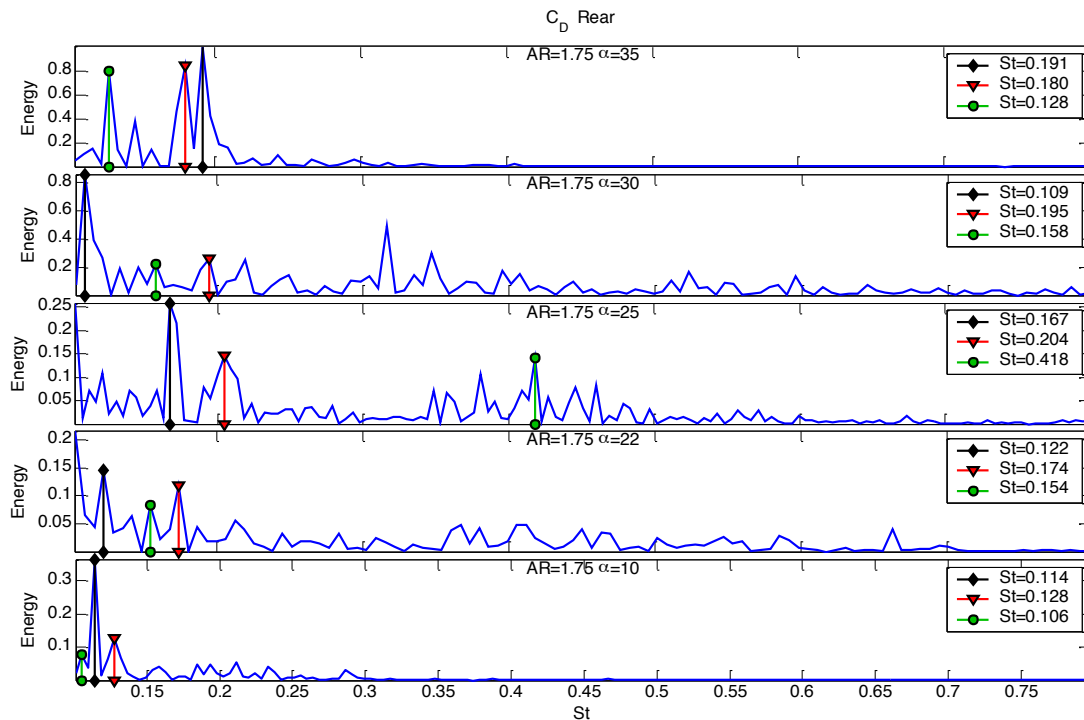


Figure 8.16 Frequency spectrum of the rear surface calculated from the C_D history for $\alpha=10^\circ$, 22° , 25° , 30° and 35° .

As discussed, Sim-Williams and Duncan [106] found at $\alpha=25^\circ$, that the peak shedding frequency occurred at $St \approx 0.52$ numerically while Vino et al. [22] found the shedding frequency at $\alpha=30^\circ$ reduced to $St=0.39$ [22]. The frequency spectrum does not show a distinct shedding frequency, but the frequencies in this range between $\alpha=25^\circ$ and $\alpha=30^\circ$ appear to decrease as α increases. The energy in the low frequency spectrum makes this difficult to quantify.

Although the analysis of the frequency spectrum of the body provides some insight into the unsteady wake structures, the information it provides is limited. Perhaps with longer run times, the resolution of the spectrum could be improved.

8.4 Unsteady Simulations

In this section, the unsteady nature of the wake structures is examined using flow visualisations on the rear portion of the Ahmed body. To reduce the computational requirements of the simulations, a symmetrical boundary condition was used. This is not ideal for unsteady simulations. However, as is shown in Section 8.2.5, the symmetrical boundary condition does not appear to adversely affect the time averaged flow field. For all visualisations, unless otherwise stated, the flow field is mirrored along the body centreline.

To aid visualisation of the unsteady flow structures in the wake region of the Ahmed body, flow visualisations are provided in the form of movies on the DVD provided. In the document, instantaneous images of the flow structures are used to indicate flow patterns with links to the corresponding unsteady visualisations. All movies slow down the flow field considerably at 5 frames per second. Each frame corresponds to a $\Delta t=0.002\text{s}$ of real time flow with visualisations approximately 1s of real time flow.

8.4.1 $\alpha=10^\circ$, AR=1.75

The wake structures for region I are shown using AR=1.75, $\alpha=10^\circ$ as a typical example of the flow structures. In contrast to the time averaged flow which indicates a large stable separation bubble in the rear region of the Ahmed body, instantaneous images of C_{TP} along the body centreline indicate that there is vortex shedding present in the wake region as shown with a time series in Figure 8.17. The contours of C_{TP} and in-plane streamlines indicate that vortices are forming on the top and bottom of the rear region of the Ahmed body and shedding alternatively. This creates oscillations in the wake region with the wake flapping in the Y direction as opposed to discrete spanwise vortices shed downstream in the wake.

Figure 8.17 Time series of slices of contours of C_{TP} overlaid with in-plane streamlines on the body centreplane for $\alpha=10^\circ$, $AR=1.75$. The time series for $t=0.500s$ (a), $t=0.512s$ (b) and $t=0.532s$ shows vortices shedding alternatively from the top and bottom of the rear of the slant surface (Movie 9.1).

The wake structure inside the separation bubble is still a toroidal type vortex structure with the top and bottom spanwise shedding vortices linked together. However the location of side components of the toroidal vortex structure are relatively stable.

Flow visualisation of the iso-surface $C_{TP}=0$ (Figure 8.18) indicates that the shedding region occurs mainly along the centreline of the body. However, on the side regions, the separation bubble and shear layer separating from the edge of the slant surface are steady close to the rear surface.

a. $t=0.500s$ b. $t=0.512s$ c. $t=0.532s$

Figure 8.18 Series of instantaneous iso-surface of $C_{TP}=0$ coloured by C_p for $\alpha=10^\circ$ at $t=0.500s$ (a), $t=0.512s$ (b) and $t=0.532s$ showing the wake shedding along the centreline (Movie 9.5).

The downwash on the centre-line of the body causes the formation of counter-rotating streamwise vortices in the wake. The alternating shedding of vortices inside the rear separation bubble causes the position of the end of the separation bubble to fluctuate quite strongly as shown in Movie 9.5. During the downwards movement of the end of the separation bubble towards the ground, the increased downwash increases the strength of the two counter rotating streamwise vortices (Movie 9.8). The fluctuations in the streamwise vortices are evident from examining the visualisations of the iso-surface of $|\omega_x|=500$ in Movie 9.7.

On the slant surface, the iso-surface of $|\omega_x|=500$ (Movie 9.7) indicates that the C-pillar vortex on the slant surface is stable. However, the fluctuations downstream affect the pressure distribution on the slant surface, even though the flow is attached to the slant surface as shown in Movie 9.5.

8.4.2 $\alpha=22^\circ$, $AR=1.75$

At $AR=1.75$, $\alpha=22^\circ$, the separation from the centreline region of the slant surface creates a substantially different wake structure compared with the time-average solution (Figure 8.5). On the slant surface in Figure 8.19, instead of the separation bubble being quite stable, the flow visualisation indicates that the shear layer emanating from the top of the slant surface is unstable above the separated region of the slant surface.

a. $t=0.104s$ b. $t=0.110s$ $t=0.116s$

Figure 8.19 Top view of the instantaneous flow field above the slant surface using iso-surface of $\|\omega\|=1500s$ (top row) and $|\omega_x|=1500s$ (bottom row) for $t=0.104s$ (a), $t=0.110s$ (b) and $t=0.116s$ (c). Unsteady visualisations of the data are shown in Movie 9.20 and Movie 9.19.

Due to the large velocity gradient in the shear layer, the shear layer becomes unstable and spanwise vortices are forming and shedding (referred to as a Kelvin-Helmholtz instability) as shown by iso-surfaces of $|\omega_x|=1500s$ in Movie 9.19. The time-averaged solution smoothes out the fluctuations on the slant surface, resulting in the slant separation bubble similar to what happens over a backwards facing step [113]. Due to the influence of the C-pillar vortex, the unsteady vortex structures above the slant surface move towards the centreline as they progress down the slant surface. Because of the turbulent nature of the flow structures, the spanwise vortices break up and twist, and quickly become incoherent. Although the iso-surface of $U/U_* = 0$ indicates the flow structures are moving downstream, inside the slant separation bubble, the flow is still reversed. The iso-surface of $|\omega_x|=500$ in Movie 9.18 indicates that there are low frequency structures moving upstream inside the separation bubble but are easily masked by the higher frequency shedding of the Kelvin-Helmholtz instability.

Although the time averaged flow structures indicate that the slant separation bubble reattached before the end of the slant surface, this is misleading since the unsteady flow visualisations (Movie 9.19) show that the vortices shed from the top of the slant surface propagate the entire length of the slant surface. Downstream of the

slant surface, the time averaged flow suggest, that the flow is attached to the slant surface, while the unsteady iso-surface of U/U_∞ shows that there are substantial regions of separated flow as shown in Figure 8.20. However, to the sides of the slant separation bubble, the wake is still attached due to the influence of the C-pillar vortex. Since the region where the C-pillar vortex keeps the flow attached to the slant surface increases with downstream distance along the slant surface, this causes the width of the slant separation bubble to decrease. The “squeezing” of the slant separation bubble in effect causes the spanwise vortices to change orientation as they propagate downstream. This rotation of the vortex cores changes the U/U_∞ component of the vortex to decrease and when the flow is averaged, it indicates that the wake is attached past the slant surface. The change in orientation of the vortex core can be seen in Figure 8.19.

a. $t=0.126s$ b. $t=0.132s$ c. $t=0.138s$

Figure 8.20 Top view of the Iso-surface of $U/U_\infty=0$ showing the region of separated flow on the slant surface at $t=0.126s$ (a), $t=0.132s$ (b) and $t=0.138s$ (c). Unsteady flow visualisation are shown in Movie 9.16.

The vortices shed from the top of the slant surface propagate downstream to interact with the rear separation bubble as shown in Figure 8.21 using an iso-surface of $C_{TP}=0$. The interaction of the vortices from the slant surface with the lower frequencies unsteadiness of the rear separation bubble causes the wake to be a lot more unstable compared with $AR=1.75$, $\alpha=22^\circ$.

a. $t=0.120s$ b. $t=0.126s$ c. $t=0.132s$

Figure 8.21 Isometric view the Iso-surface of $C_{TP}=0$ for $\alpha=22^\circ$, $AR=1.75$ at $t=0.120s$ (a), $t=0.126s$ (b) and $t=0.132s$ (c) showing the vortices from the slant surface interacting with the rear separation bubble. Unsteady visualisation of the flow structures are shown in Movie 9.15.

As opposed to $\alpha=22^\circ$, where most of the shedding occurs from the top and bottom of the rear separation bubble, at $\alpha=22^\circ$, the entire rear separation bubble is unstable. This is evident in Figure 8.22, which shows an instantaneous image of the vorticity magnitude ($\|\omega\|$) on the XZ plane at $Y=0.1$. In Figure 8.22a, the vertical components of the toroidal vortex structure is evident, while for Figure 8.22b, which shows vortices shed from the sides of the rear are more unstable.

Figure 8.22 Contours of $\|\omega\|$ on XZ plane at $Y=0.1$ for $\alpha=10^\circ$, $AR=1.75$ (top half) at $t=0.5s$ and $\alpha=22^\circ$, $AR=1.75$ (bottom half) at $t=0.138s$. The rear separation bubble change in the structure with vortex shedding from the side of the rear surface at $\alpha=22^\circ$ (bottom half). The unsteady flow visualisation is shown in Movie 9.11.

Similar to $\alpha=22^\circ$, there is a large vertical oscillation of the wake structures from the vortex shedding of the rear separation bubble. However the wake structure is more complex due to vortices shed from the slant surface interacting with the vortex shedding from the rear separation bubble. The largest oscillations are still from the alternating vortex shedding from the rear separation bubble which is evident in the change in pressure on the ground boundary layer in Figure 8.23 using an iso-surface of $\|\omega\|=500s$.

a. $t=0.104s$

b. $t=0.110s$

c. $t=0.116s$

Figure 8.23 Isometric view of the rear region of the Ahmed body at $\alpha=22^\circ$, $AR=1.75$ with isosurface of $\|\omega\|=500s$ which shows the influence of vortex shedding on the ground boundary layer in the wake region. The unsteady flow visualisation is shown in Movie 9.18.

The C-pillar vortices are affected by the vortex shedding. Past the end of the rear surface, the C-pillar vortex interacts with the rear wake structures. The iso-surface of $|\omega_x|=500s$, in Movie 9.17, shows the C-pillar starting to become unstable and oscillate. Close to the body, there are no indications of vortex breakdown but the iso-surface of $C_{DP}=0.1$ in Figure 8.24 suggests in regions where the C-pillar occurs downstream, vortex breakdown appears to occur intermittently at $X\approx 0.25$. However, since this does not occur close to the body, it does not affect the separation from the slant surface.

Figure 8.24 Side view of an iso-surface of $C_{DP}=0.1$ coloured by C_{TP} for $\alpha=22^\circ$, $AR=1.75$ at $t=0.138s$ showing signs of the vortex breaking down at $X\approx 0.2$. The unsteady visualisation is shown in Movie 9.14.

8.4.3 $\alpha=25^\circ$, $AR=1.75$

With the increase in α to $\alpha=25^\circ$, the vortex breakdown that is evident in the iteration averaged solution is initially present, as shown by visualising an iso-surface of $C_{DP}=0.1$ in Figure 8.25. However, as the solution progresses forward in time, the region of $C_{DP}=0.1$ in the core of the C-pillar vortex disappears, indicating that the C-pillar vortex has not broken down (bottom half). When vortex breakdown is not present, the vortex is still unstable and fluctuates past the end slant surface from the shedding of the rear separation bubble.



Figure 8.25 Comparison of an iso-surface of $C_{DP}=0.1$ for $\alpha=25^\circ$, $AR=1.75$ at $t=0.088s$ (top half) and $t=0.364s$ (bottom half). At the start of the simulation, the surface marked with an arrow indicates the region where $C_{DP}=0.1$ inside the C-pillar vortex. The unsteady visualisation is shown in Movie 9.24.

Similar to the case of $\alpha=22^\circ$, the shear layer from the top of the slant surface is unstable and breaks up into spanwise vortices which in turn, form turbulent structures. Among the structures present on the slant surface, hair-pin vortices are shed from the slant surface visualised in Figure 8.26 using an iso-surface of $\|\omega\|=1500s$. This is similar to shedding observed by Gilhome et al. [112] on notchback vehicles, but the hair-pin structures are more localised compared with larger structures observed on a notchback back. Flow visualisations of contours of vorticity magnitude indicate that the frequency of the wake structure is different to the shedding frequency of the rear separation bubble (see Section 8.5.3).

Figure 8.26 Shedding of hair-pin vortices from the slant surface visualised by iso-surface of $\|\omega\|=1500$ coloured by C_{TP} for $\alpha=25^\circ$, $AR=1.75$. The three plots are for $t=0.142s$, $t=0.164s$ and $t=0.186s$. The unsteady visualisation is shown in Movie 9.30.

Although the mesh used for this simulation is not as dense as that performed by Krajnović and Davidson [109, 110], (Figure 3.79) in the current simulations Re is substantially higher, the unsteady wake structures are similar. The shear layer emanates from the top of the slant surface, shedding vortices, which move towards the centreline as they migrate downstream. Experiments by Drouin et al. [19] also showed that the instantaneous wake structures on the centreline are unsteady while the C-pillar vortex is relatively stable.

8.4.4 $\alpha=28^\circ$, $AR=1.75$

The unsteady wake structures at $\alpha=28^\circ$ clearly shows the breakdown of the C-pillar vortex as it progresses downstream from the top of the slant surface. As discussed in Section 6.4.3, the iso-surface of $C_{DP}=0.1$ is a good indicator of where the vortex breaks down. As can be seen in Figure 8.27, a region of $C_{DP}=0.1$ occurs inside the region where the C-pillar vortex exists, showing breakdown. The unsteady visualisation of the iso-surface of $C_{DP}=0.1$ in Movie 9.24 shows that the C-pillar vortex is unstable after breakdown. The influence of the C-pillar on C_{TP} on the slant surface in Movie 9.52 shows that the C_{TP} is relatively constant on the slant surface, but after breakdown, there are large fluctuations present.

Figure 8.27 Top view of the iso-surface of $C_{DP}=0.1$ coloured by C_{TP} for $\alpha=28^\circ$, $AR=1.75$ at $t=0.274s$ showing the region of vortex breakdown of the C-pillar vortex.

In the simulations, the location of breakdown initially remains constant but then starts to fluctuate along the vortex axis. However, on average the start of the iso-surface of $C_{DP}=0.1$ remains at $X=-0.05$. The structure of the iso-surface suggests that the breakdown is a bubble type breakdown with a spiral tail in the wake (Section 3.9).

In Figure 8.28, which shows an iso-surface of $\|\omega\|=1500s$, the shear layer from the side of the slant surface still rolls around the core even though it is unstable.

Figure 8.28 Isometric view of an iso-surface of $\|\omega\|=1500$ coloured by C_{TP} for $\alpha=28^\circ$ AR=1.75, at $t=0.356s$. Even after the C-pillar vortex has broken down, the shear layer from the edge of the slant surface still wraps around the vortex core somewhat masking the breakdown inside.

The unsteady flow field of C_{TP} for the full Ahmed body at $\alpha=28^\circ$, AR=1.75 shows that the instantaneous wake is not symmetrical about the centreline as is to be expected for a highly turbulent flow. Similar to the symmetrical simulation on the slant surface, the separated region along the centreline is most unstable with vortices formed in the shear layer. The shedding of hair-pin type vortices is present in the wake and is not a result of running a symmetric simulation, as shown in Figure 8.29.

Figure 8.29 Top view of an instantaneous iso-surface of $\|\omega\|=1500$ coloured by C_{TP} on full model (no symmetry boundary condition) for $\alpha=28^\circ$, AR=1.75 at 0.074s.

Vino [114] speculated that a possible shedding mechanism could be the alternating shedding of the wake from alternating sides of the body. The unsteady visualisation of the iso-surface of $C_{TP}=0$ in Movie 9.55, shows that the shedding downstream of the body is roughly symmetrical although the contours of $\|\omega\|$ along the XZ plane in Figure 8.30 show that the shear layers on either side of the body are not rolling up in unison. Due to the short run time of this simulation, there might not be sufficient time for this to occur. However, simulations indicate that it is shedding along the centreline of the body that influences the wake structure downstream so this is more likely to lead to a symmetrical shedding structure downstream of the body. There does not appear to be a large difference between the full model and simulations, which use a symmetric boundary condition along the body centreline. However, there are not enough data to undertake a spectral analysis of the wake frequencies to confirm this.

Figure 8.30 Top view of contours of $\|\omega\|$ overlaid with in-plane pathlines on a XZ plane at $Y=0.1$ showing the shedding of side edge vortices are not symmetrical.

8.4.5 $\alpha=30^\circ$, AR=1.75

The wake structures at $AR=1.75$, $\alpha=30^\circ$ are very unstable for the entire slant surface including the C-pillar vortex. Flow visualisations using contours of vorticity magnitude on the centreline in Figure 8.31, indicate the spanwise vortices rolling from the top of the slant surface are significantly larger compared with lower AR and due to the larger slant angle, move downstream relative to U_∞ as opposed to moving along the slant surface.

Figure 8.31 Contours of $\|\omega\|$ overlaid with in-plane streamlines along the centreline of the body for $\alpha=30^\circ$, AR=1.75. Unsteady flow visualisation is shown in Movie 9.43.

The flow visualisations using an iso-surface of $|\omega_x|$ in Figure 8.32 shows the C-pillar vortex is unstable on the slant surface. The C-pillar vortex is breaking down close to the formation point at the top of the slant surface which results in the wake downstream of the C-pillar vortex becoming very unstable.

Figure 8.32 Iso-surface of $|\omega_x|=1500$ (a) and $|\omega_x|=500$ (b) for $\alpha=30^\circ$, $AR=1.75$ at $t=0.484s$. Unsteady visualisation is shown in Movie 9.49 and Movie 9.48 respectively.

In Movie 9.44, the iso-surface of $C_{DP}=0.1$ indicates that the location of vortex breakdown occurs near the top of the slant surface and fluctuates quite considerably along the vortex core axis. The unsteady flow visualisation indicates that vortex breakdown initially occurs near the top of the slant surface. If the location of the expansion of the vortex core moves downstream, this is not sustained for long and a new breakdown occurs near the top of the slant surface separate from the expansion that moved downstream along the vortex core. The instantaneous iso-surface of $\|\omega\|=1500s$ in Figure 8.33 indicates that it is a bubble type breakdown with a large swirling tail occurring downstream of the breakdown.

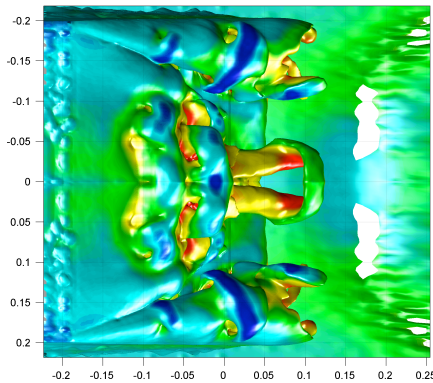


Figure 8.33 Top view of iso-surface of $\|\omega\|=1500$ (a) and $\|\omega\|=500$ (b) for $\alpha=30^\circ$, $AR=1.75$ at $t=0.252s$ coloured by C_{TP} showing a spiral pattern in the breakdown of the C-pillar vortex. Unsteady flow visualisations are shown in Movie 9.50 and Movie 9.48 respectively.

Time averaged flow indicates that the separation bubble stretches further downstream on the sides of the Ahmed body compared with the centre. The shape of the rear separation bubble was quantified by using the iso-surface of $C_{TP}=0$ in Section 5.4.3. Unsteady flow visualisations of iso-surface $C_{TP}=0$ (Movie 9.45) indicate that the separation bubble on the centreline is shorter, but there is significant vortex

shedding occurring so the shape of the rear separation bubble is constantly evolving. On the sides of the rear surface, the mean length of the separation bubble extends further downstream. The remnants of the C-pillar vortex after the breakdown merge with the rear separation bubble, which extends the bubble even further downstream. The side structures of rear separation bubble shed downstream into the two counter rotating vortices. The unsteady visualisations of offset slices of C_{TP} (Movie 9.45) show the oscillations of the two counter rotating structures downstream of the body.

8.4.6 $\alpha=35^\circ$, $AR=1.75$

The most significant change apart from the wake structures between $\alpha=30^\circ$, $AR=1.75$ and $\alpha=35^\circ$, $AR=1.75$ is that the shedding frequency of the wake structure has substantially reduced. The unsteady visualisation of $\|\omega\|=1500s$ (Figure 8.34) shows a shear layer extending off the top and sides of the slant surface. The shear layer does not appear to break up as a result of a Kelvin-Helmholtz instability, but the shear layer sheds at a frequency similar to the vortex shedding from the rear separation bubble. The spanwise vortices shed from the slant surface interact with the larger scale unsteadiness downstream of the body (Movie 9.46).

Figure 8.34 Side view and rear view of iso-surface of $\|\omega\|=1500$ for $\alpha=35^\circ$, $AR=1.75$ at $t=0.164s$, showing that the shear layer extends from the sides and top of the slant surface. Unsteady visualisation is shown in Movie 9.60.

As opposed to $\alpha=10^\circ$, $AR=1.75$, the sides of the rear separation bubble are unsteady, but the largest oscillations of the rear separation bubble occur on the centreline of the body. As the vortices shed from the top of the separation bubble, they entrain the flow from the sides of the separation causing the two counter rotating vortices in the wake as shown in the visualisation of the unsteady iso-surface of

$C_{TP}=0$ (Movie 9.55). This action destroys the spanwise nature of the vortices shed from the top of the slant surface as the downwash on the centreline twists the flow structures. Unsteady contours of $C_{TP}=0$ on the centreline in Figure 8.35 indicate that there is alternating shedding from the top and bottom of the separation bubble.

Figure 8.35 Side view of contours of C_{TP} on the body centreline for $\alpha=35^\circ$, $AR=1.75$ at $t=0.092s$ (a), $t=0.104s$ (b) and $t=0.138s$ (c) showing vortex shedding from the top and bottom of the rear separation bubble. The unsteady flow visualisation is shown in Movie 9.51.

The unsteady surface streak lines on the slant surface in Movie 9.53, show that on the slant surface, there is not a large variation in flow patterns compared with off the slant surface where the vortex shedding is occurring. The rate of change of the surface streak line patterns is slow compared with the unsteadiness in the wake. Downstream of model in Movie 9.52, the contours of C_{TP} overlaid with in-plane streamlines on a YZ plane at $X=0.5$, the shedding wake structure is quite complex. This can be seen in the series of instantaneous images on the same plane in Figure 8.36. During the shedding cycle, two sets of counter rotating vortices are present in

the wake, with one pair created with the up wash cycle of the separation bubble and the other created by the downwash cycle.

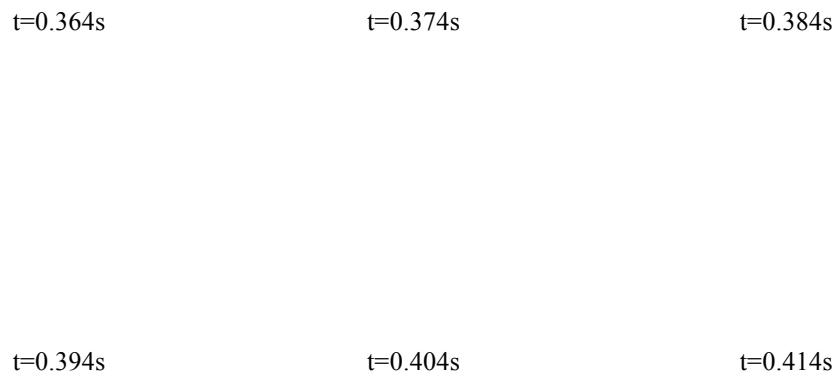


Figure 8.36 A series of instantaneous flow visualisations of contours of C_{TP} overlaid with in-plane pathlines on YZ plane at $X=0.5$ showing the unsteady wake structures nature of the counter-rotating streamwise vortices.

8.5 Frequency analysis

In this section, the frequency spectrum of the wake region is examined to determine the dominant frequencies associated with vortex shedding from the rear region of the Ahmed body. This is to quantify the unsteady structure since the frequency analysis of the body forces did not give a clear indication of the unsteady wake structures.

In the wake, the time history of the C_{TP} ([106, 111]) was collected at discrete locations in the domain. For each point in the domain on a given plane with a constant X , Y or Z coordinate, the frequency spectrum was calculated to determine the power of various frequencies. Sampling window of at least 1024 points was used with multiple sampling bin used to provide a more accurate spectrum. Data was sampled for at least 2s, which is small compared with experiments. For a given plane, the frequency spectrum of each location was added together to determine which frequencies are dominant in that location of the wake. Therefore, the frequency spectrums shown below are likely to be more complex compared with the frequency spectrum at a discrete point since multiple frequencies are present along a plane.

For example, to calculate the frequency spectrum on the body centreline, the power of each location in the wake is summed and then normalised by the highest power in the domain. The frequency spectrum for $\alpha=10^\circ$ is shown in Figure 8.37, which shows a distinctive peak at $St=0.295$ where St is the Strouhal number. The Strouhal number is normalised by the free stream velocity and the square root of the body cross sectional area as done in other studies [22, 106]. For a given spectrum, the energy of the given frequency is calculated to determine spatially where that frequency has strongest energy to determine what flow structures are associated with it. The associated energy on the centreline for $\alpha=10^\circ$ with $St=0.295$ among other frequencies is shown in Figure 8.38. For the analysis at each slant angle examined, three planes are used to determine wake frequencies, which are an XY plane at $Z=0.0$ along the body centreline and two YZ planes at $X=0$ and $X=0.5$.

8.5.1 $\alpha=10^\circ$, $AR=1.75$

The frequency spectrum along the body centreline is shown in Figure 8.37, which shows a distinct frequency present at $St=0.295$ with multiple lower frequencies present. The unsteady wake structure are visualised in Movie 9.1 which shows that the dominant frequency is due to the shedding of the rear separation bubble as observed in Section 8.4.1. The spectrum also shows that a number of other frequencies are present, but there is an absence of high frequencies which are present at higher slant angles.

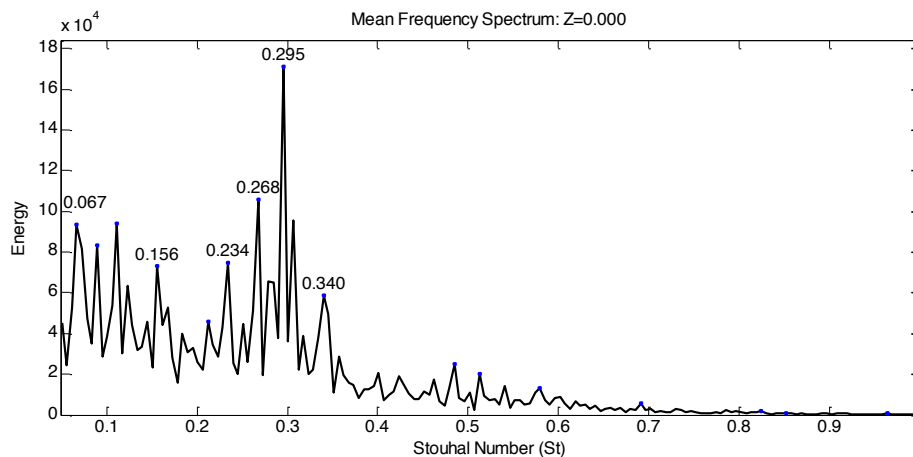


Figure 8.37 Energy frequency spectrum for $\alpha=10^\circ$, $AR=1.75$ on a XY plane at $Z=0$.

The corresponding energy of four distinct frequencies is shown in Figure 8.38. In Figure 8.38a, the strongest energy associated at $St=0.067$ occurs in the shear layer emanating from the top of the rear surface and is present downstream of the model.

However, the frequency of this structure is too low to be associated with the vortex shedding from the top of the rear separation bubble. Due to the long period of the structure, it is difficult to determine the associated structure in Movie 9.1. However, the dominant frequency at $St=0.295$ in Figure 8.38c is associated with the shedding of the vortices from the bottom of the rear surface and the large oscillations past the end of the rear separation bubble. Due to the energy of the downstream oscillations correlating with the shedding of the bottom vortex, this suggests that the wake structure driving the downstream vortex shedding is the bottom spanwise vortex on the rear surface. The spectral peaks at $St=0.268$ (Figure 8.38b) and $St=0.340$ (Figure 8.38d) occur in the shear layer on the top of rear separation bubble. This indicates that shedding from the top edge of the rear surface contains multiple high and low frequencies.

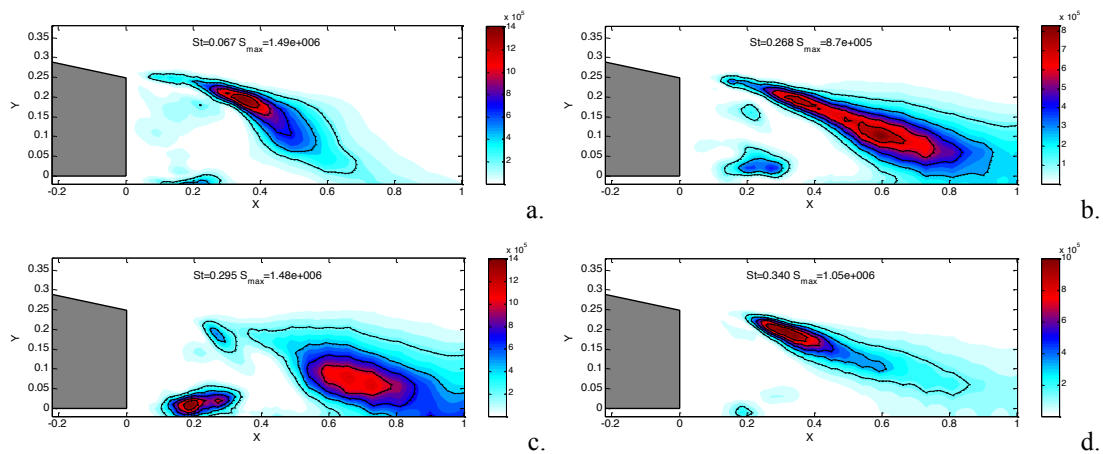


Figure 8.38 Contours of the energy of various frequencies along the centreline for $\alpha=10^\circ$, $AR=1.75$ for $St=0.067$ (a), $St=0.268$ (b), $St=0.295$ (c) and $St=0.340$ (d).

The frequency spectrum along the body centreline is shown in Figure 8.39, which shows a large spectrum of low frequency structures. The unsteady wake structure on this surface is visualised in Movie 9.1. However, compared with the frequency spectrum at the centreline, there is far less energy in the spectrum since the flow is attached on the slant surface and flow is relatively stable.

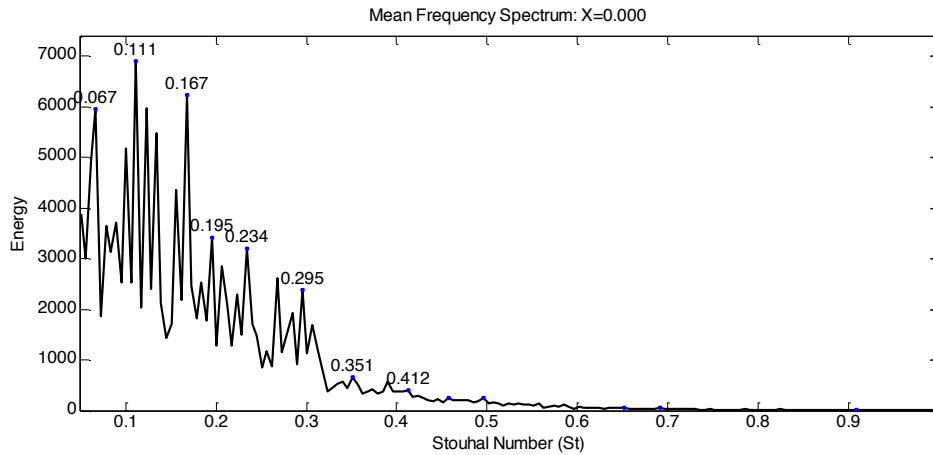


Figure 8.39 Energy frequency spectrum for $\alpha=10^\circ$, $AR=1.75$ on a YZ plane at $X=0$.

Figure 8.40 shows the energy of discrete frequencies on a plane collinear with the rear end of the Ahmed body. At $St=0.067$ in Figure 8.40a, the highest energy occurs on the centreline above the slant surface, with no energy in the region where the C-pillar vortex is present. The spectral peak at $St=0.111$ (Figure 8.40b) and $St=0.295$ (Figure 8.40c) occur on the underside of the Ahmed body. $St=0.295$ is shown in Figure 8.38 to be associated with the shedding of the bottom portion of the rear separation bubble.

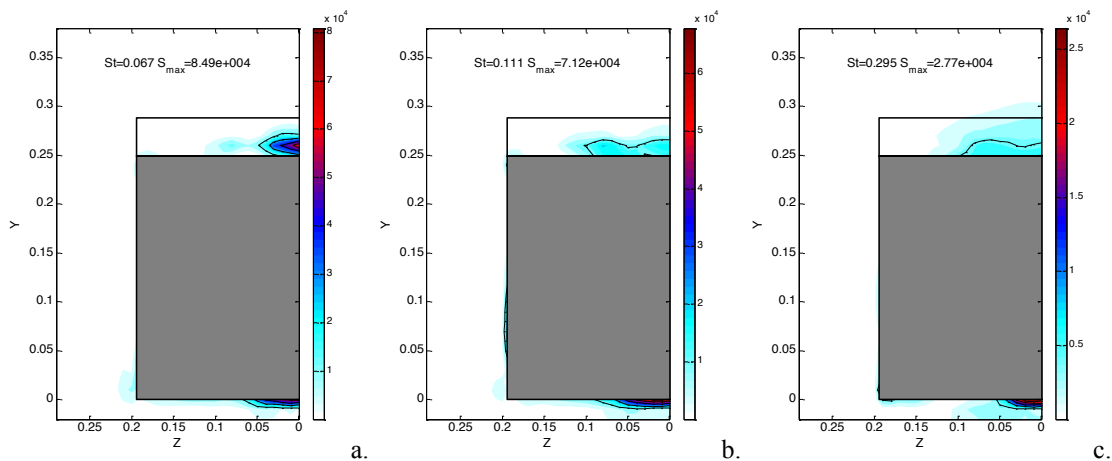


Figure 8.40 Contours of the energy of various frequencies on a plane collinear with the rear surface for $\alpha=10^\circ$, $AR=1.75$ for $St=0.067$ (a), $St=0.111$ (b) and $St=0.295$ (c).

The frequency spectrum downstream of the body at $X=0.5$ is shown in Figure 8.39, which shows a strong peak at $St=0.295$ and another lower peak at $St=0.111$. The unsteady wake structures on this surface are visualised in Movie 9.1. Clearly, the dominant frequency downstream of the model is the frequency associated with the large oscillations in the wake.

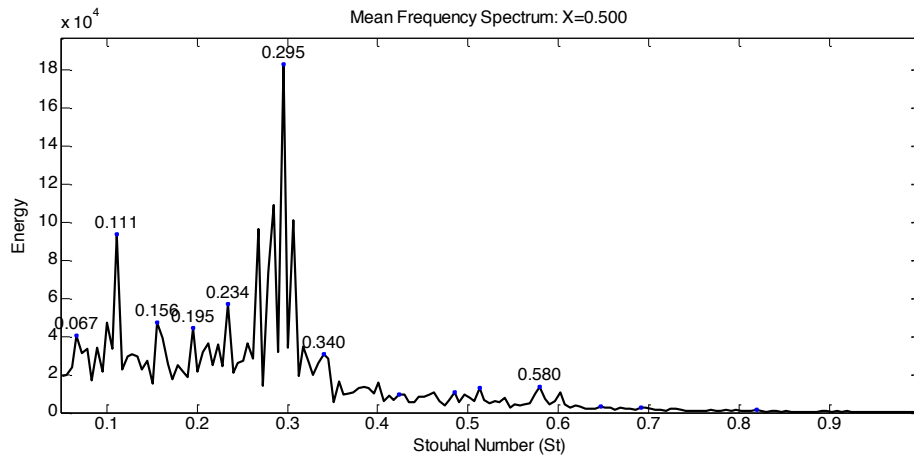


Figure 8.41 Energy frequency spectrum for $\alpha=10^\circ$, $AR=1.75$ on a YZ plane at $X=0.5$.

The energy associated with $St=0.111$ and $St=0.039$ on a YZ plane at $X=0.5$ shown is Figure 8.42. The energy of $St=0.039$ is associated with counter rotating streamwise vortex structures. The power associated with $St=0.111$, as shown in Figure 8.42, occurs near the ground plane underneath the location of the counter rotating streamwise vortices. While the power of this structure is less and the St is lower compared with counter rotating streamwise vortices, the unsteady visualisations in Movie 9.2 indicate that the spanwise vortex developed on the ground plane forms in the upwards motion of the oscillations of the wake. The vortex formed on the ground plane moves slower downstream than that associated of the oscillations in the wake. That is to say, the period that it takes the structure to move past a location is higher compared with the period from the oscillations in the wake even though the upwash of the oscillations forms the structure upstream.

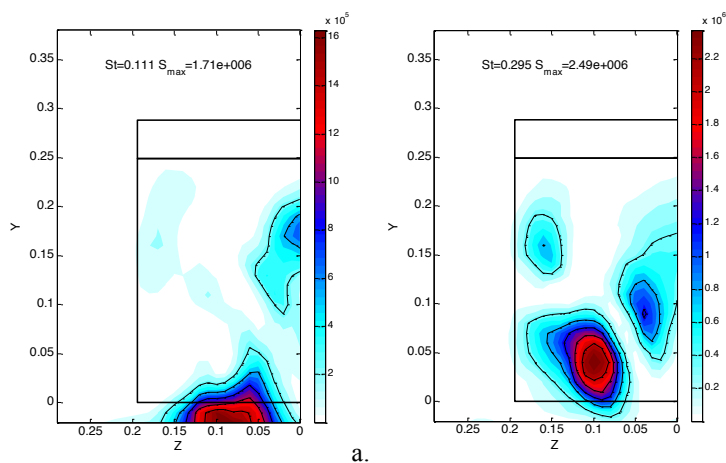


Figure 8.42 Contours of the energy of various frequencies on a YZ plane at $X=0.5$ for $\alpha=10^\circ$, $AR=1.75$ for $St=0.111$ (a) and $St=0.295$ (b)

8.5.2 $\alpha=22^\circ$, AR=1.75

The frequency spectrum along the body centreline for $\alpha=22^\circ$ is shown in Figure 8.43, which shows that the spectrum is more complex compared with $\alpha=10^\circ$. The unsteady wake structure on this surface is visualised in Movie 9.11. Due to the vortex shedding on the slant surface, multiple high frequency ($St > 0.358$) peaks exist, but the lower frequency peaks dominate the frequency spectrum. Compared with $\alpha=10^\circ$ (Figure 8.37), the peak energy is less but is spread over a broader spectrum.

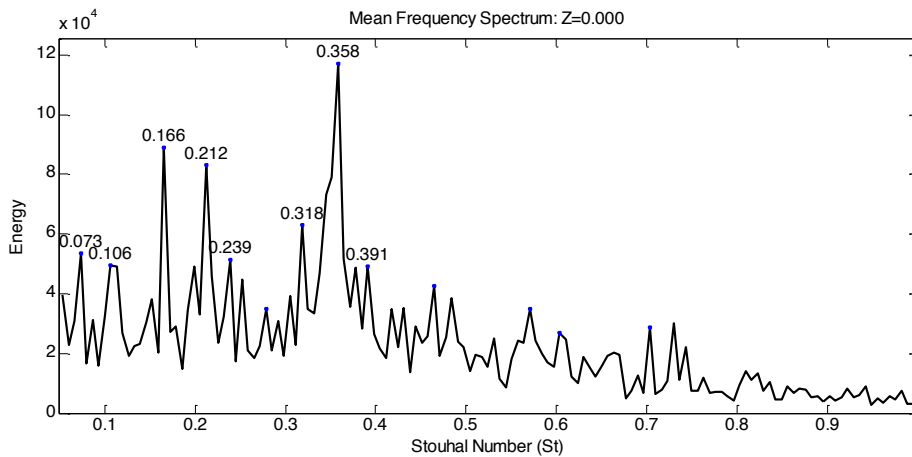


Figure 8.43 Energy frequency spectrum for $\alpha=22^\circ$, AR=1.75 on a XY plane at Z=0.

The corresponding energy of the discrete frequencies is shown in Figure 8.44 for $St=0.166$ (a), $St=0.212$ (b), $St=0.358$ (c) and $St=0.391$ (d). Figure 8.44a shows that the peak at $St=0.166$ occurs mainly in the top of the rear separation bubble. The unsteady flow visualisations in Movie 9.15 indicate that along the centreline, the wake structure is very unstable due to the rolling up and shedding of the shear layer. Although a relatively low frequency is found in the shear layer, it is masked by the highly unsteady turbulent structures in the flow visualisation. The peak frequency at $St=0.212$ (b) and $St=0.391$ (c) also occur in the top shear layer indicating the energy is spread over a large frequency range. The location of the spectral peak for $St=0.358$ (Figure 8.44c), which is associated with the unsteadiness in the far wake, occurs at the top and bottom of the rear surface again indicating that the rolling up of the bottom vortex is the dominant feature controlling the shedding of the rear separation bubble.

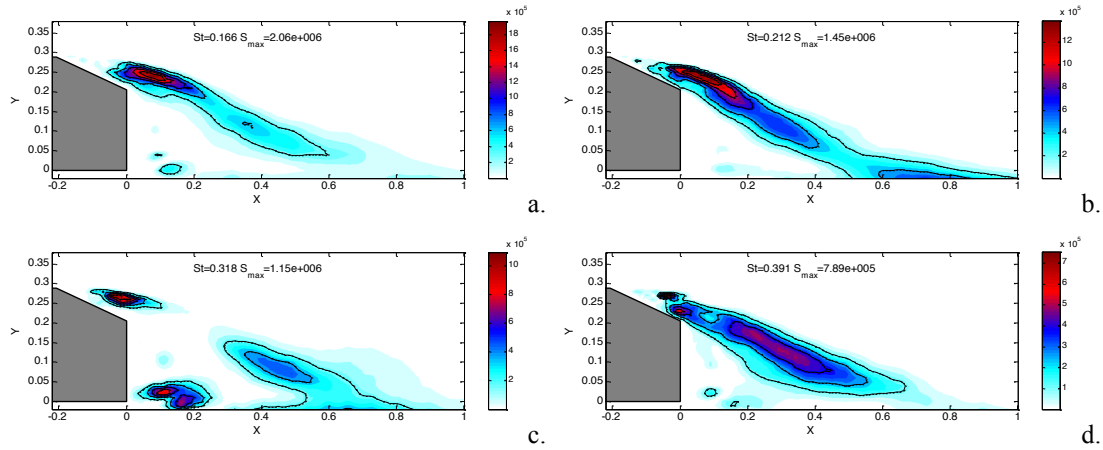


Figure 8.44 Contours of the energy of various frequencies along the centreline for $\alpha=22^\circ$, $AR=1.75$ for $St=0.166$ (a), $St=0.212$ (b), $St=0.318$ (c) and $St=0.391$ (d).

On a plane collinear with the rear end of the body, the frequency spectrum in Figure 8.45 shows the multiple peak frequencies present. The frequency spectrum is quite broad indicating that the wake contains a number of different frequencies. The unsteady wake structure on this surface visualised in Movie 9.11 reveals that the largest fluctuations occur on the centreline while the C-pillar vortex is relatively stable.

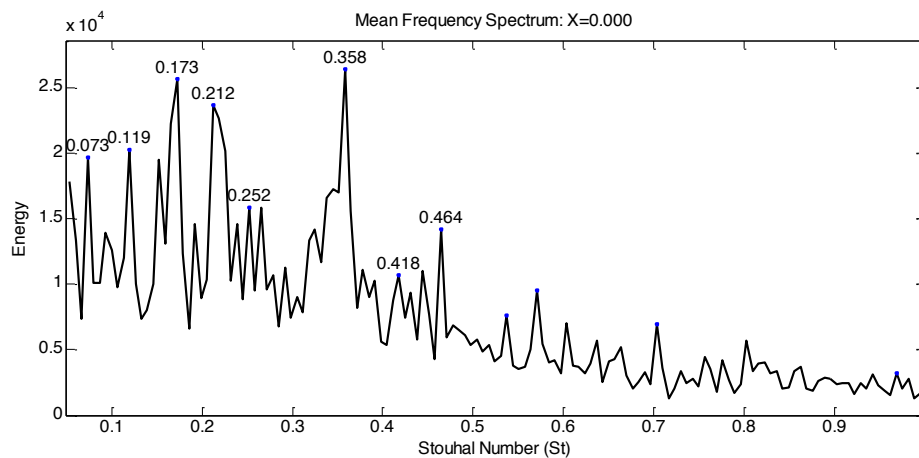


Figure 8.45 Energy frequency spectrum for $\alpha=22^\circ$, $AR=1.75$ on a YZ plane at $X=0$.

This is confirmed in Figure 8.46, which shows the spatial location of three peak spectra found on the YZ plane collinear with the rear of the body. Even the lower frequency of $St=0.173$ (Figure 8.46a) and the most dominant frequency of $St=0.358$ (Figure 8.46b) occur on the centreline region of the Ahmed body, confirming that at $\alpha=22^\circ$, the C-pillar is stable. The spatial location of the three frequencies in Figure 8.46 show that higher frequencies occur closer to the centreline.

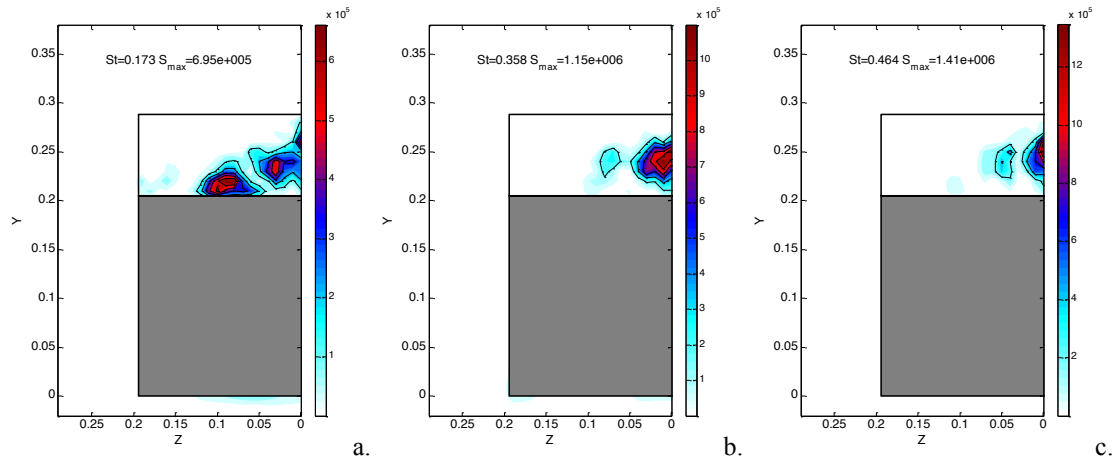


Figure 8.46 Contours of the energy of various frequencies on a plane collinear with the rear surface for $\alpha=22^\circ$, $AR=1.75$ for $St=0.173$ (a), $St=0.358$ (b) and $St=0.464$ (c).

The frequency spectrum on a YZ plane downstream at $X=0.5$ in Figure 8.47 is significantly different to the spectrum closer to the body (Figure 8.45), with the peak at $St=0.358$ significantly larger than the other spectra present. The unsteady wake structure visualised on this surface in Movie 9.12 shows that the two counter rotating vortices in the wake fluctuate considerably from the shedding on the centreline.

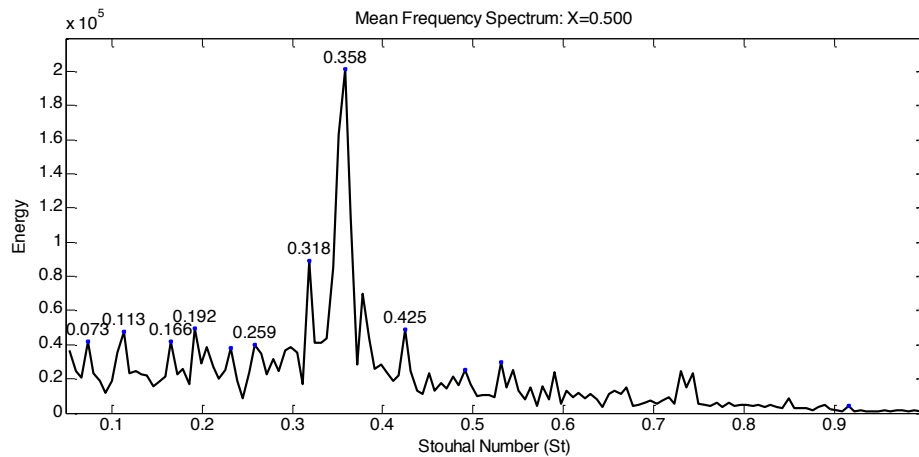


Figure 8.47 Energy frequency spectrum for $\alpha=22^\circ$, $AR=1.75$ on a YZ plane at $X=0.5$.

The spatial spectrum of the dominant frequency in Figure 8.48b indicates that the spectrum of the major frequency correlates with the location of the mean of the two counter rotating vortices in the wake. For other spectral peaks at $St=0.318$ (Figure 8.48a) and $St=0.425$ (Figure 8.48c), they are present near the location of the streamwise vortex. These results indicate that the shedding of the spanwise vortex from the bottom of the rear surface causes the primary shedding in the wake downstream of the counter-rotating streamwise vortices since this is the dominant frequency downstream.

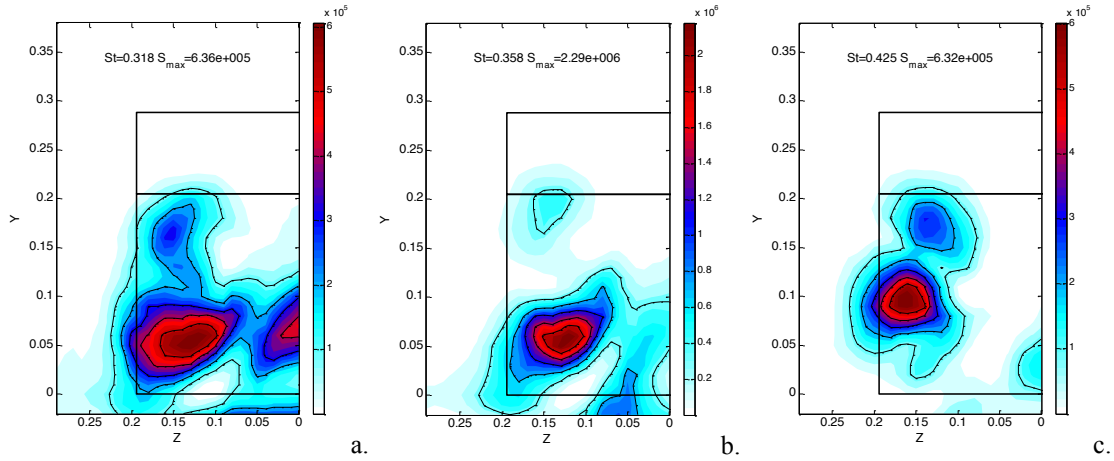


Figure 8.48 Contours of the energy of various frequencies on a YZ plane at X=0.5 for $\alpha=22^\circ$, AR=1.75 for St=0.318(a), St=0.358(b) and St=0.425(c).

8.5.3 $\alpha=25^\circ$, AR=1.75

A general trend observed is that as $\alpha \rightarrow \alpha_c$, the wake structures are more turbulent along the centreline of the Ahmed body. This is evident in Figure 8.49 which shows the frequency spectrum calculated along the body centre for $\alpha=25^\circ$. Similar to the lower slant angles, the peak frequency occurs at St=0.351, but there are more peaks across the spectrum. The unsteady visualisation of the C_{TP} on the centreline in Movie 9.21 shows sustainable shedding from the slant surface interacting with the shedding from the rear surface. The dominant shedding at St=0.351 is more evident downstream.

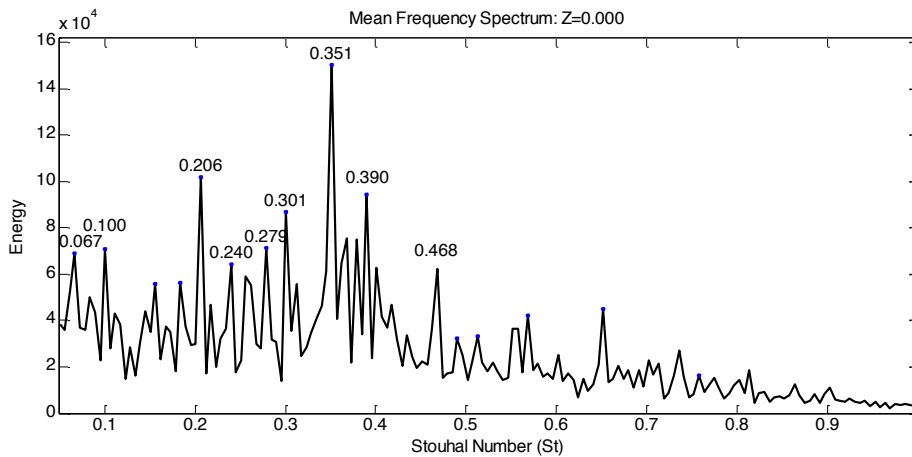


Figure 8.49 Energy frequency spectrum for $\alpha=25^\circ$, AR=1.75 on a XY plane at Z=0.

The associated energy associated with the different peak frequencies are shown in Figure 8.50. These results show that the shear layer emanating from the top of the slant surface is highly unsteady. The figure indicates that before the shear layer starts to shed, a low frequency is present and as the vortices shed downstream, the

frequency increases as the structures get progressively smaller. In Figure 8.50c, the dominant spectral peak of $St \approx 0.35$ found at lower slant angles is still present.

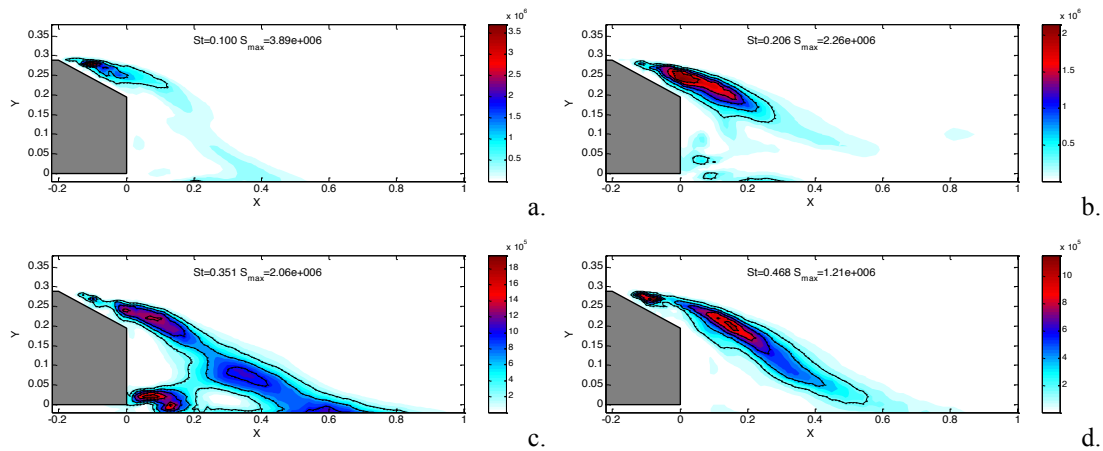


Figure 8.50 Contours of the energy of various frequencies along the centreline for $\alpha=25^\circ$, $AR=1.75$ for $St=0.1$ (a), $St=0.206$ (b), $St=0.351$ (c) and $St=0.468$ (d).

The frequency spectrum on the plane collinear with the rear surface of the body at $\alpha=25^\circ$ in Figure 8.51 shows that the frequency with the highest energy is $St=0.206$. The peak $St=0.084$ is not found on the centreline spectrum. The unsteady visualisation of C_{TP} on this plane shown in Movie 9.21 indicates that there are some fluctuations in the C-pillar vortex region.

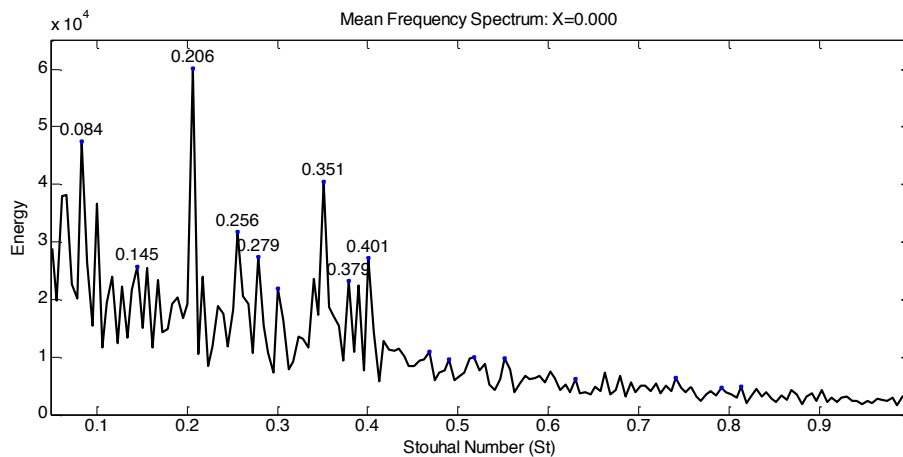


Figure 8.51 Energy frequency spectrum for $\alpha=25^\circ$, $AR=1.75$ on a YZ plane at $X=0$.

The energy at $St=0.084$, $St=0.206$ and $St=0.351$ on this plane is shown in Figure 8.52, which shows that the highest energy of these frequencies occurs near the centreline in the separated region. The energy at $St=0.084$ in Figure 8.52a shows a small region of energy near the axis of the C-pillar vortex, showing that the C-pillar is starting to oscillate. However, this is masked by the greater energy in the unsteadiness near the centreline of the slant surface.

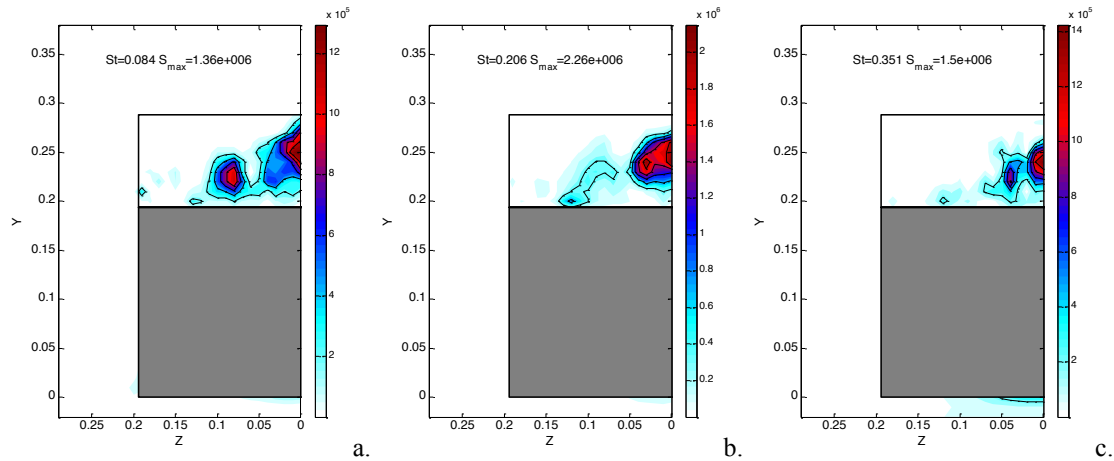


Figure 8.52 Contours of the energy of various frequencies on a plane collinear with the rear surface for $\alpha=25^\circ$, $AR=1.75$ for $St=0.085$ (a), $St=0.206$ (b) and $St=0.351$ (c).

Further downstream on a YZ plane at $X=0.5$, the spectral peak at $St=0.084$ is present but the energy in this frequency is small compared with $St=0.351$, due to the shedding at the base of the slant surface. The unsteady flow visualisations in Movie 9.22 on the same plane indicate that the wake is more unsteady compared with $\alpha=22^\circ$. At $\alpha=22^\circ$ in Figure 8.48, the frequency at $St=0.351$ contained most of the energy at $X=0.5$, while for $\alpha=25^\circ$, multiple frequencies are present past the end of the separation bubble.

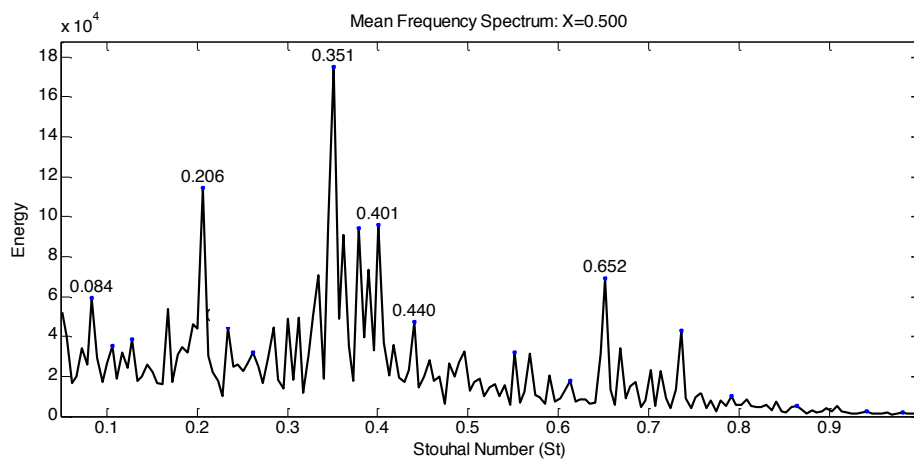


Figure 8.53 Energy frequency spectrum for $\alpha=25^\circ$, $AR=1.75$ on a YZ plane at $X=0.5$.

The energy of different frequencies at $X=0.5$ shows that the different spectral peaks occur in different regions near the centre of the counter-rotating vortex structures. Although the energy for $St=0.351$ is higher compared with the other frequencies present, they cannot be discounted since they are still relatively strong. The unsteady flow visualisations in Movie 9.22 show that the streamwise vortex does

not oscillate about a common location, indicating that the structures shed from the Ahmed body are more complex.

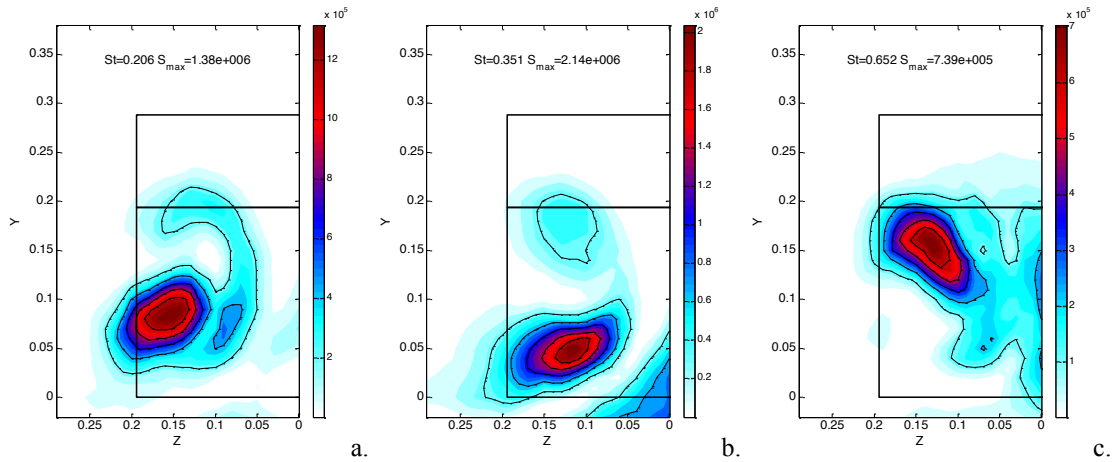


Figure 8.54 Contours of the energy of various frequencies on a YZ plane at $X=0.5$ for $\alpha=25^\circ$, $AR=1.75$ for $St=0.206$ (a), $St=0.351$ (b) and $St=0.652$ (c).

8.5.4 $\alpha=30^\circ$, $AR=1.75$

The frequency spectrum along the body centreline at $\alpha=30^\circ$ is outlined in Figure 8.55, which shows multiple distinct frequencies present along the centreline. The highest peak occurs at $St=0.437$, which is higher compared with the other slant angles which all showed the strongest peak at $St\approx 0.35$. The unsteady visualisations of the C_{TP} on the centreline in Movie 9.41 reveal that the shedding from the top of the rear surface rather than the bottom of the rear surface is dominating the shedding of the wake downstream, in contrast to the lower slant angles examined.

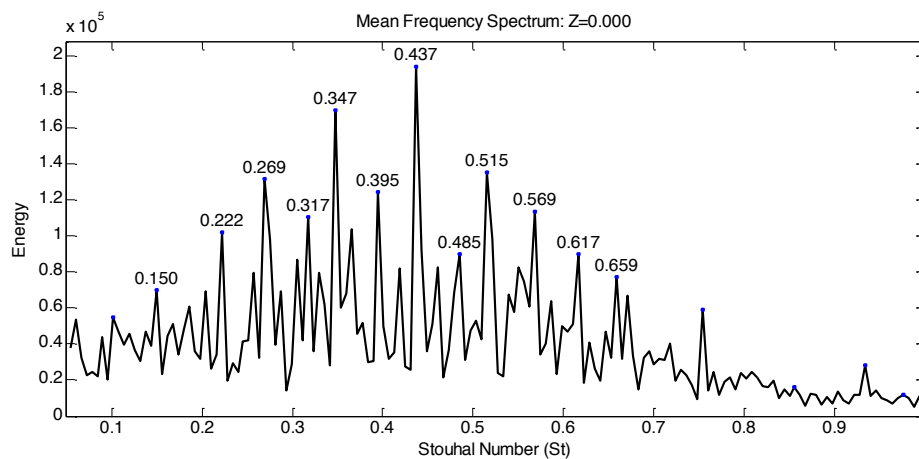


Figure 8.55 Energy frequency spectrum for $\alpha=30^\circ$, $AR=1.75$ on a XY plane at $Z=0$.

This is confirmed in Figure 8.56 which shows the energy for discrete frequencies in the wake. The peak frequency at $St=0.437$ in Figure 8.56c occurs in the unsteady shear layer emanating from the slant surface. The only spectral peak found near the

base of the rear surface occurred for $St=0.659$, which is considerably higher compared with the other slant angles. At $\alpha=30^\circ$, the size of the rear separation bubble is considerably shorter along the centreline due to the strong downwash from the slant surface, so it is not too surprising that this influences which region controls the vortex shedding.

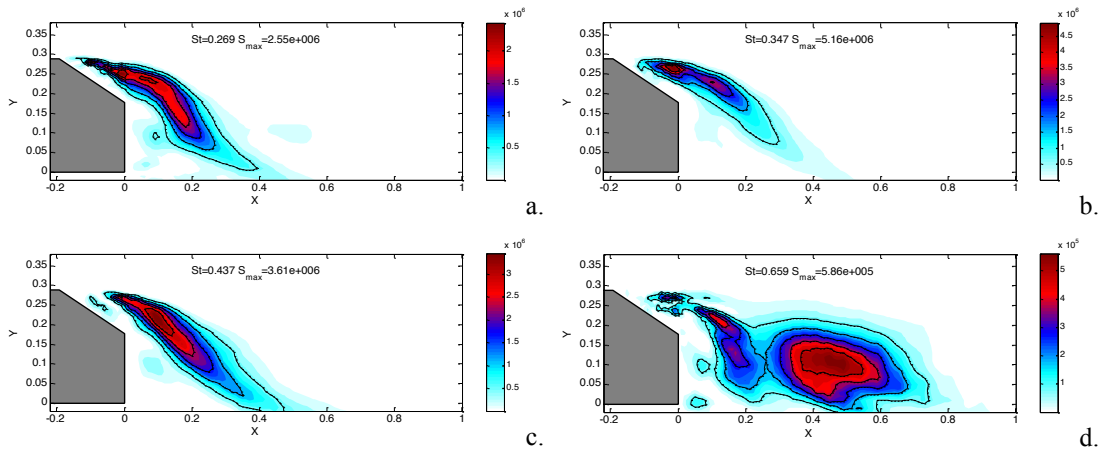


Figure 8.56 Contours of the energy of various frequencies along the centreline for $\alpha=30^\circ$, $AR=1.75$ for $St=0.269$ (a), $St=0.347$ (b), $St=0.437$ (c) and $St=0.659$ (d).

Surprisingly, on the plane collinear with the rear surface, there is a dominant frequency present at $St=0.347$ as shown in Figure 8.57. This frequency is close to the dominant frequency present at lower slant angles. The unsteady visualisation of C_{TP} on this plane in Movie 9.41 shows shedding along the centreline. The flow field in the region where the C-pillar vortex passes through the plane is also very unsteady and the frequencies of the structures appear to be higher than near the centreline.

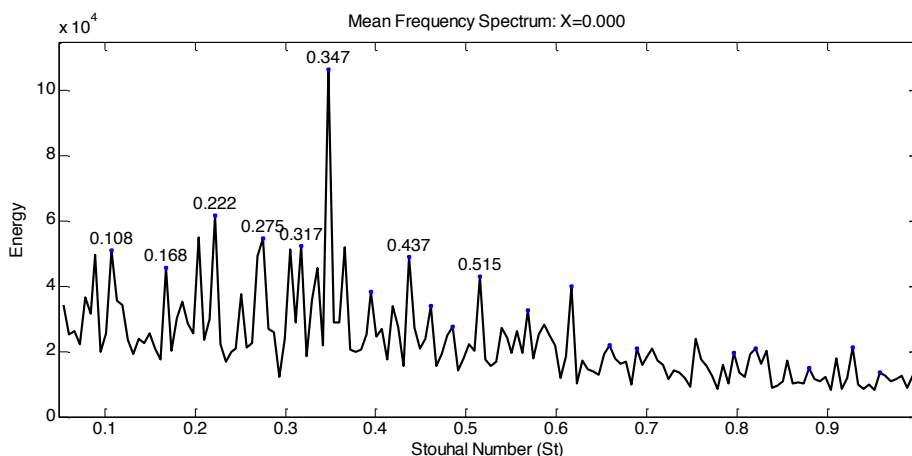


Figure 8.57 Energy frequency spectrum for $\alpha=30^\circ$, $AR=1.75$ on a YZ plane at $X=0$.

The energy of three discrete frequencies is mapped onto the YZ plane at $X=0$ in Figure 8.58. The peak frequency of $St=0.347$ shown in Figure 8.58b occurs near the

centreline of the body along with the other spectral peaks found. In Figure 8.58c, the region where the C-pillar exists is isolated, the peak frequency that occurs is $St=0.820$. The location of this energy is present appears to be on the edge of the C-pillar vortex as opposed to the core axis, which is similar to observations made by Sim-Williams and Duncan [106].

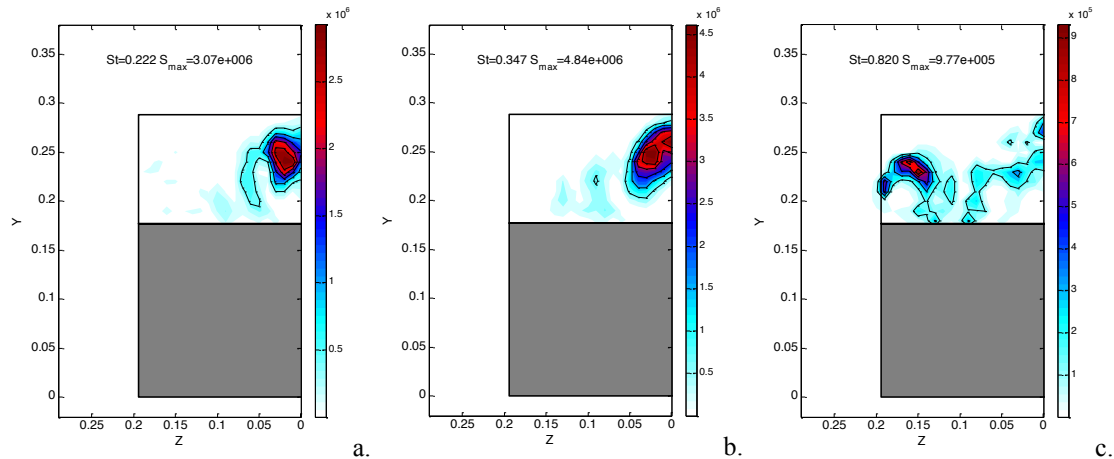


Figure 8.58 Contours of the energy of various frequencies on a plane collinear with the rear surface for $\alpha=30^\circ$, $AR=1.75$ for $St=0.222$ (a), $St=0.347$ (b) and $St=0.820$ (c).

Downstream at $X=0.5$ in Figure 8.59, the frequency spectrum downstream of the body appears to contain multiple frequencies and appears to be dominated by higher frequencies than those previously observed. The peak frequency of $St=0.565$ is near to the frequency found for the shedding frequency of the vortices shed from the base of the slant surface. This indicates that even when the near wake is dominated by the shedding from the slant surface, downstream, it is still the shedding from the base of the slant surface which is more important. The unsteady visualisations in Movie 9.42 indicate that the wake structure is very unsteady and it is difficult to identify and confirm a periodic shedding pattern.

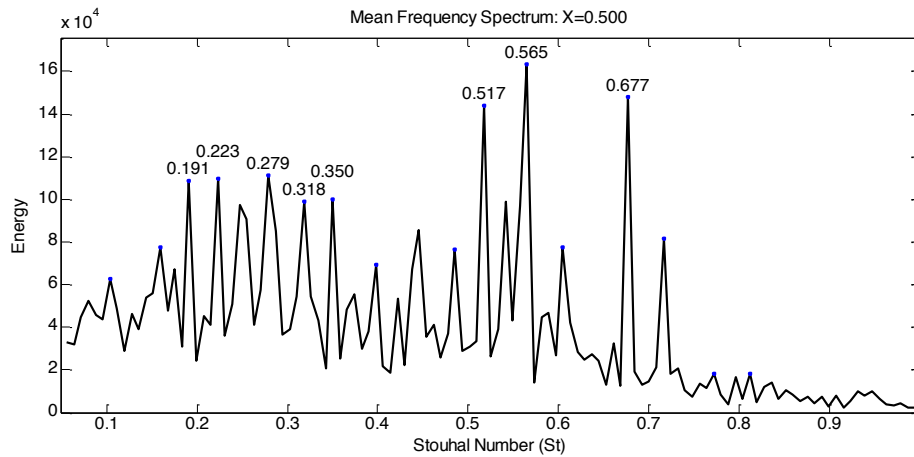


Figure 8.59 Energy frequency spectrum for $\alpha=30^\circ$, $AR=1.75$ on a YZ plane at $X=0.5$.

The energy of discrete frequencies on a YZ plane at $X=0.5$ in Figure 8.60 show the locations of the different high frequencies found to occur in different regions of the wake. The location of the time-averaged counter rotating streamwise vortex is dominated by the shedding from the base of the rear surface of $St=0.565$ (Figure 8.60b). The location of the higher frequency of $St=0.677$ in Figure 8.60c occurs in a higher location and could be due to the influence of the C-pillar vortex which is very unstable.

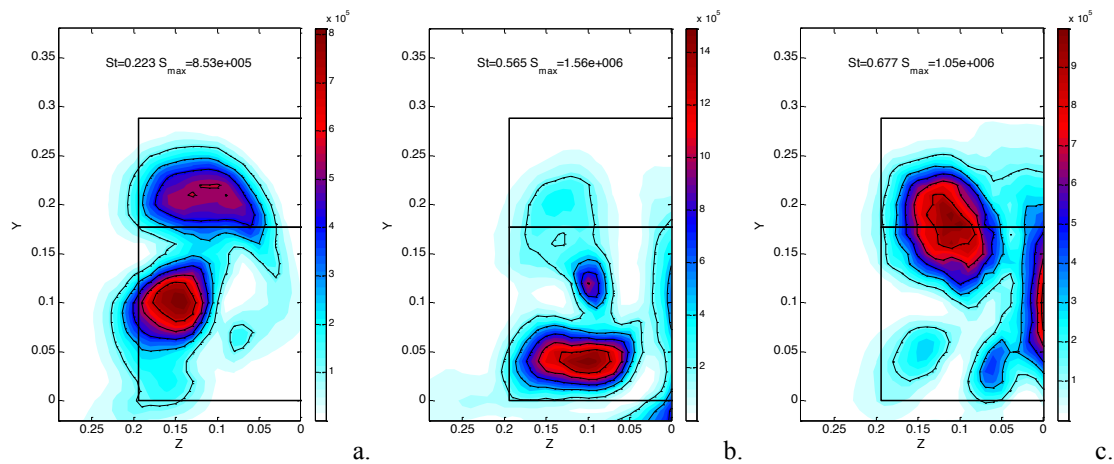


Figure 8.60 Contours of the energy of various frequencies on a YZ plane at $X=0.5$ for $\alpha=30^\circ$, $AR=1.75$ for $St=0.223$ (a), $St=0.565$ (b) and $St=0.677$ (c).

8.5.5 $\alpha=35^\circ$, $AR=1.75$

As shown in section 8.4.6, the unsteady wake structure after complete separation from the slant surface is massively different. This is also shown in the frequency spectrum of the body centreline for $\alpha=35^\circ$ in Figure 8.61. The peak frequency is significantly lower compared with simulations where the wake structure is attached to the slant surface. The spectrum overall is considerably less noisy with only two

distinct frequencies present and there is a lack of high frequency noise. The unsteady visualisations of C_{TP} along the body centreline in Movie 9.51 show there is vortex shedding evident in the wake and the overall change in the flow field is quite slow.

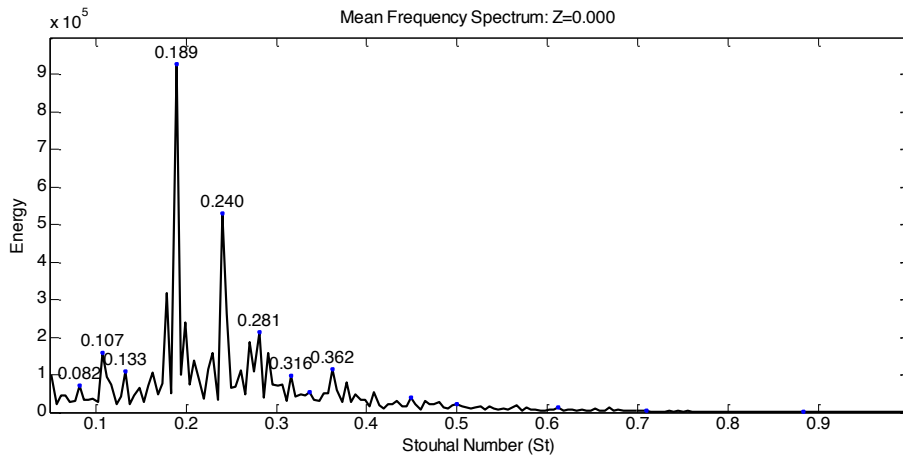


Figure 8.61 Energy frequency spectrum for $\alpha=35^\circ$, $AR=1.75$ on a XY plane at $Z=0$.

The energy of various frequencies in Figure 8.62 shows that most of the energy is located past the end of the separation bubble. The peak frequency of $St=0.189$ contains a lot of energy in the downstream region as opposed to close to the slant surface. A spectral peak exists near the base of the slant surface for $St=0.189$ indicating that it is still the shedding from the base of the rear surface that influences the wake structures. However the energy distribution for $St=0.107$ also shows a peak coinciding with base of the rear surface.

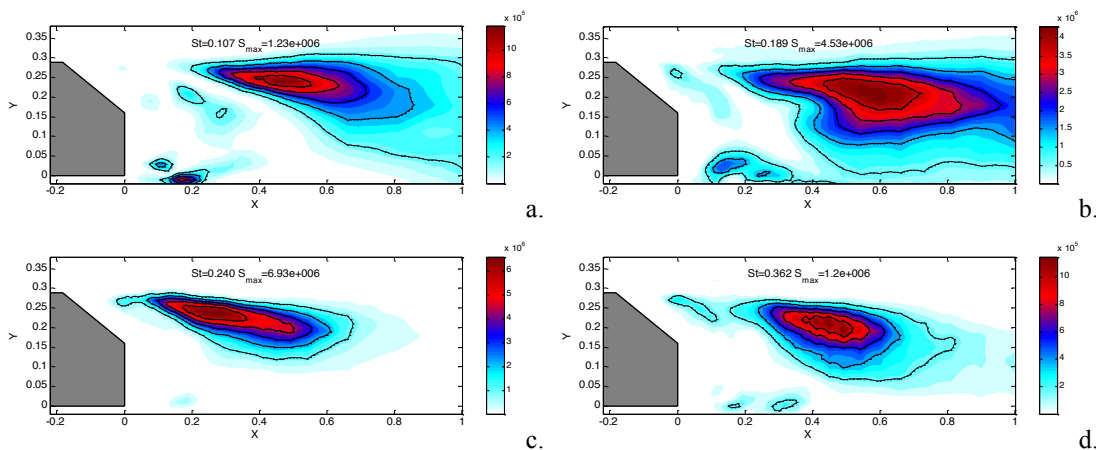


Figure 8.62 Contours of the energy of various frequencies along the centreline for $\alpha=35^\circ$, $AR=1.75$ for $St=0.107$ (a), $St=0.189$ (b), $St=0.240$ (c) and $St=0.362$ (d).

On the plane collinear with the base of the slant surface in Figure 8.63, the same spectral peak is found. The unsteady visualisations in Movie 9.51 reveal that most of the unsteadiness in this plane occurs in the shear layer emanating from the top and sides of the slant surface.

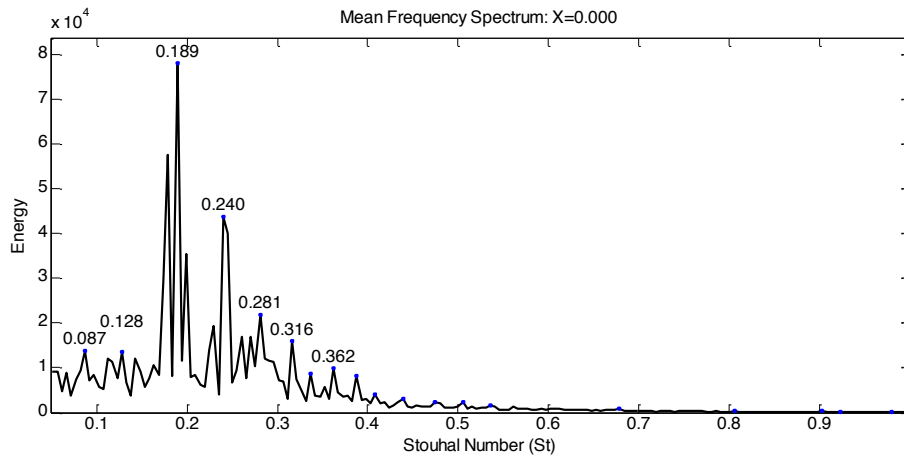


Figure 8.63 Energy frequency spectrum for $\alpha=35^\circ$, $AR=1.75$ on a YZ plane at $X=0$.

This is confirmed in Figure 8.64 which shows the distribution of energy for $St=0.087$, $St=0.189$ and $St=0.240$ on the plane collinear with the rear surface. The peak frequency of $St=0.189$ (Figure 8.64b) is located in the region where the C-pillar vortex used to exist, and the unsteadiness is most likely due to the interaction of the shear layer on the top of the slant surface interacting with the shear layer on the side of the slant surface. The higher frequency peak of $St=0.240$ (Figure 8.64c) occurs in the shear layer near the centreline and is more visible in the unsteady visualisations (Movie 9.58).

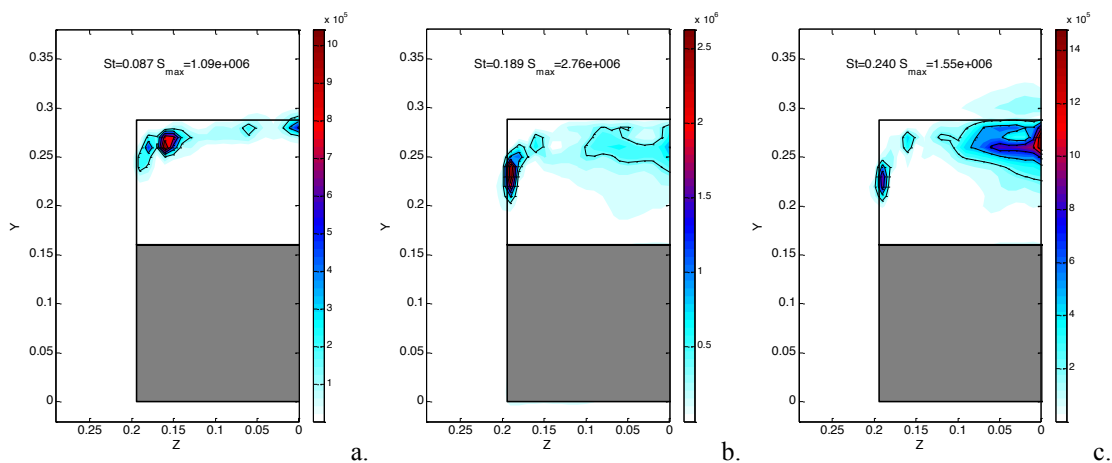


Figure 8.64 Contours of the energy of various frequencies on a plane collinear with the rear surface for $\alpha=35^\circ$, $AR=1.75$ for $St=0.087$ (a), $St=0.189$ (b) and $St=0.240$ (c).

Downstream of the body at $\alpha=35^\circ$, only one dominant frequency is present as shown in Figure 8.65. While other spectral peaks exist, the dominant frequency is $St=0.190$. The unsteady wake structure visualised using C_{TP} on the YZ plane at $X=0.5$ indicates a complex wake structure of streamwise C-pillar vortices shedding with large oscillations as discussed above.

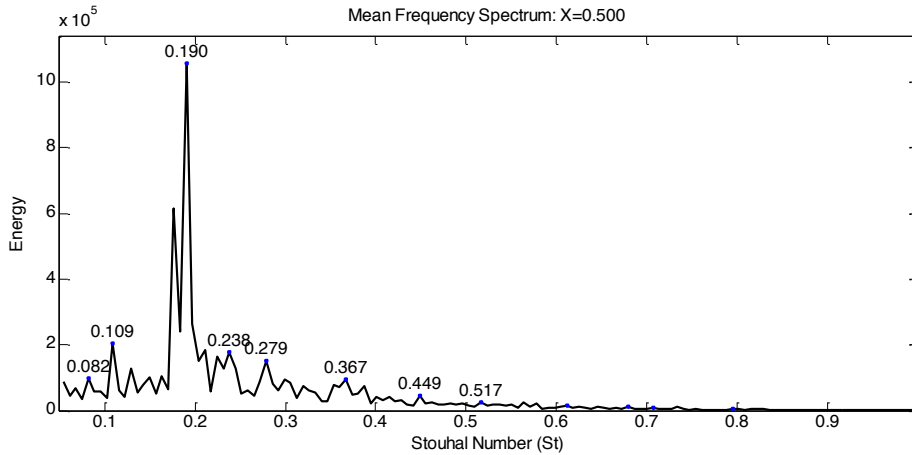


Figure 8.65 Energy frequency spectrum for $\alpha=35^\circ$, $AR=1.75$ on a YZ plane at $X=0.5$.

The energy of the wake structures at $St=0.109$, $St=1.90$ and $St=0.279$ on the YZ plane at $X=0.5$ is shown in Figure 8.66. The wake structure for $St=0.190$ in Figure 8.66b shows that most energy is in the region where the time-averaged counter rotating streamwise vortices exist. The energies of the other frequencies at $St=0.109$ (Figure 8.66a) and $St=0.279$ (Figure 8.66c) occur on the centreline near the top of the slant surface. This shows that the effect of the shedding from the slant surface carries downstream even though there are larger structures in the wake.

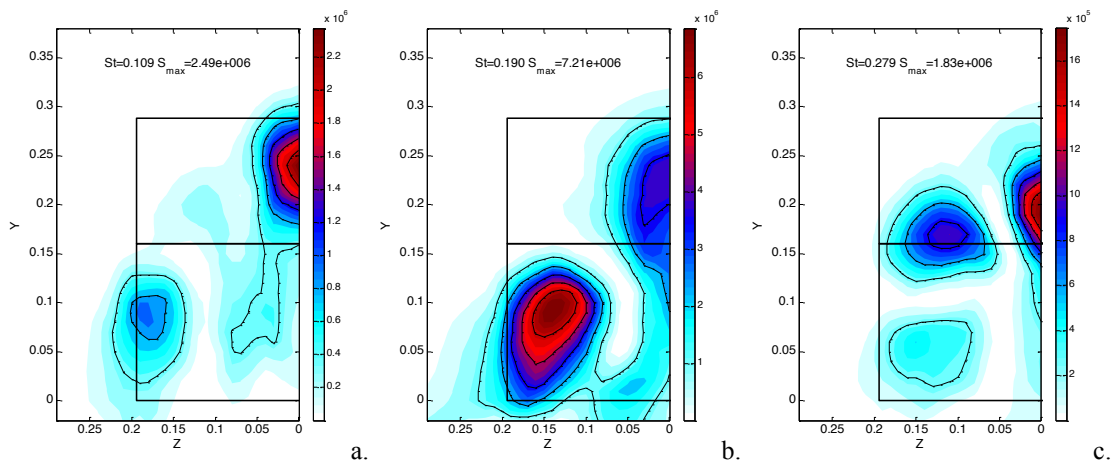


Figure 8.66 Contours of the energy of various frequencies on a YZ plane at $X=0.5$ for $\alpha=35^\circ$, $AR=1.75$ for $St=0.109$ (a), $St=0.190$ (b) and $St=0.279$ (c).

8.6 Conclusion

In this chapter, the unsteady wake structures for the Ahmed body ($AR=1.75$) have been examined for comparison with the time-independent simulations used in previous chapters. A detailed analysis of the wake structures has been undertaken and the frequency spectra of the wakes have been examined.

In comparison with the time independent simulations, the time averaged flow field of time dependent simulations are very similar. No large variations in the wake structure were observed for the slant angles considered which cover the various flow regions defined in Section 4.3. Across all the α considered, the time-averaged flow structures were smoother than the iteration averaged simulations since more samples were used to calculate the mean flow field and there appeared to be greater downwash along the centreline. The time-averaged solution at $\alpha=30^\circ$ (Figure 8.9) revealed that the vortex breakdown was stronger compared with the time independent simulations. The comparison of a full model and a symmetrical simulation at $\alpha=28^\circ$ showed that the symmetry plane did not adversely influence the flow field.

The frequency analysis of the drag and lift body forces was not successful. It is difficult to quantify any frequencies present in the wake. This is most likely due to the fact that the body forces are effectively averaging the wake structure forces over an area so any periodic structures are masked. For example, if the base of the slant surface is shedding alternatively from the top and bottom of the rear surface, the drag forces on the rear surface do not experience the alternating shedding as a location in the flow would experience. However, the analysis of the frequency spectrum did show the higher frequency structures present when the flow was partially separated from the slant surface with multiple frequencies present (Figure 8.15).

The visualisations of the wake structures in Section 8.4 give a better insight into the unsteady nature of the wake structures for various α at $AR=1.75$. The flow visualisations at $\alpha=10^\circ$ showed that shedding occurs near the centreline of the body while on the side regions, the rear separation bubble is relatively steady. The toroidal vortex structure present in the rear separation bubble is diminished as $\alpha=10^\circ \rightarrow 22^\circ$. This is most likely due to the increased alternating shedding from the top and bottom of the rear surface changing the rear separation bubble, which results in a shear layer emanating from the sides of the rear surface at $\alpha=22^\circ$ (Figure 8.22).

The flow structures on the slant separation bubble at $\alpha=22^\circ$ are significantly different compared with the time-averaged flow structures. The shear layer emanating from the top of the slant surface is unstable with vortices shed downstream. Even though the time-averaged flow indicates that the separation bubble reattaches, the spanwise vortices shedding past the end of the slant separation and interact with

the rear separation bubble. Even though the length of the separation bubble on the slant surface is used as a measure of the accuracy of various numerical methods, the unsteady simulations indicate that the size of the separation bubble fluctuates. At $\alpha=22^\circ$, the iso-surfaces of $C_{DP}=0.1$ (Figure 8.24) indicate intermittent vortex breakdown past the end body as the C-pillar vortex interacts with the wake structure.

At $\alpha=25^\circ$, the vortex breakdown occurred closer to the slant surface. However, as the unsteady solution progresses, the C-pillar no longer breaks down indicating that at $\alpha=25^\circ$, the C-pillar vortex is at the limit of breaking down for $AR=1.75$. On the slant surface, the vortices shed from the shear layer are forced towards the centreline because of the presence of the C-pillar vortex. This twisting motion helps create hair-pin vortex structures off the slant surface as observed by Gilhome et al. [112].

These structures increase in strength due to stronger recirculation in the region on the slant surface at $\alpha=28^\circ$. The C-pillar vortex also exhibits signs of vortex breakdown over the slant region at $X\approx-0.05$, with the iso-surface of $C_{DP}=0.1$ (Figure 8.27) showing a bubble type breakdown with a spiral tail. The unsteady simulations using a full model showed that the wake were roughly symmetrical about the centreline.

The vortex breakdown observed in the time dependent simulations is stronger with a larger core size than that observed for the time independent simulations. The unsteady visualisations indicate that the C-pillar is breaking down near the top of the slant surface and the structures shed from the C-pillar are very unsteady. The short rear separation bubble along the centreline observed in the time independent simulations is similar to the computed unsteady flow field and the experimental results by Vio [22, 108]. Downstream of the body, the wake structures are not coherent and the downwash causes large oscillations.

Although the wake structure at $\alpha=35^\circ$ also shows large oscillations, since a large separation bubble exists and the highly unsteady C-pillar vortices have burst, there is more coherent large scale shedding. Both the upwash movement and downwash movement of the separation bubble create counter rotating streamwise vortices downstream of the body.

The frequency analysis of the wake structures provides a much greater insight into shedding structures behind the Ahmed body. For all slant angles, multiple

frequencies are present in the wake which is to be expected for a turbulent flow. For slant angles, where the wake was attached to or fully separated from the slant surface ($\alpha=10^\circ$ and 35°), the frequency spectrum was less noisy and one dominant shedding frequency is present. As found by Sim-Williams [17], the dominant shedding frequency found downstream is linked to the shedding from the base of the rear surface. This was true for all slant angles investigated except for $\alpha=35^\circ$. The simulations indicate that the dominant frequency of the shedding in general increases as $\alpha \rightarrow \alpha_c$. The dominant shedding frequency at $\alpha=25^\circ$ is lower ($St=0.351$ compared with $St=0.52$) than those found numerically by Duncan [106, 111]. However the numerical simulations were based on frequency spectrum data from higher slant angles and no experimental frequency spectrum data was provided for $\alpha=25^\circ$.

The frequency spectrum for $\alpha=30^\circ$ is considerably more complex than the spectrum found from the experiments. This is partially due to the limited sampling size of two seconds of simulation time compared with large samples possible from experiments. Above the slant surface, a dominant frequency of $St \approx 0.347$ was found while downstream, the dominant frequency associated with the shedding from the base of the slant surface was higher at $St \approx 0.565$. Experimental data from different researchers [22, 106, 107] showed quite a large spread in data of the calculated St for $\alpha=30^\circ$ making it difficult to compare to experiments predictions. High frequencies are associated with the periphery of the C-pillar vortex (Figure 8.64). Vio [22] observed an unsteadiness present in the core of the C-pillar vortex which was thought to be due to the buffeting from the separation bubble downstream. No spectral peaks were found for simulations with no vortex breakdown, so it may be possible that this buffeting could be an indicator of the vortex bursting.

After the wake has separated from the top of the slant surface at $\alpha=35^\circ$, the dominant frequency is associated with the shedding from the top of rear separation bubble as opposed to the shedding from the base of the rear surface. The shedding frequency is considerably lower at $St=0.189$ with most of the energy in the large scale oscillation of the wake. Figure 8.64 shows that the shedding is initiated from the unsteadiness in the separated shear from the top and side of the slant surface.

Chapter 9 Conclusion

The main objectives of the research outlined and discussed in the introduction of this thesis were:

1. Development of a strategy to obtain accurate numerical solutions, including development of an appropriate numerical grid, choice of turbulence model and selection of near-optimal solution parameters such as turbulence options and unrelaxation parameters.
2. Characterisation of the effect of the Ahmed body slant angle on the flow.
3. Characterisation of the effect of the vehicle aspect ratio on the wake structures.
4. Examination of the C-pillar vortex structure and the conditions leading to vortex breakdown.
5. Pinpointing the wake structures that cause the drag using momentum theory.
6. Examination of the unsteady wake structures for the Ahmed body.

This chapter will discuss the conclusions found from the investigation associated with each objective and finally suggest topics for future work in this field.

9.1 Strategy for numerical simulations

In Chapter 2, an approach to obtain useful numerical solutions was developed. It was difficult to find fully-converged solutions using the steady flow solver despite considerable effort spent modifying the under-relaxation parameters and other solution parameters; however, the solutions from the time-independent simulations fluctuated around a mean solution in reasonable agreement with solutions from the time-dependent simulations (see further discussion below). Since the flow is very sensitive to small changes in the body geometry, at least over parts of the slant angle range, it is perhaps not surprising that different numerical strategies could have a significant effect on the simulations. In particular, for some slant angles, it was found that the wake had a tendency to progress to a fully separated wake, while experiments indicated that the flow was still attached to the slant surface. This behaviour has been

observed in the numerical simulations of other researchers [20]. It is difficult to determine whether such discrepancies are a result of a component of the numerical method, such as the turbulence model, due to the restricted grid size used for the simulations, or perhaps even differences between the conditions in the experiments and the numerical simulations. The grid resolution study did not find a large variation in the computed flow structure. Significant time and effort was employed in cycles of refining and optimising the grid, testing different turbulence models, and comparing a representative sample of predictions with experimental results before the final governing numerical parameters were chosen. In particular, it was necessary to determine the minimum acceptable grid size and grid-point distribution, the appropriate turbulence model including options such as the wall treatment, acceptable relaxation parameters and the simulation time adequate for iteration-averaging. While the predictions are not a perfect match to available experimental results, trends in parameters such as the drag variation with slant angle and surface friction pattern, are well-predicted.

An investigation of run-time simulation parameters was conducted at various slant angles to ensure that predictions were not dependent on slant angle. For the $k\omega$ -SST and realizable- $k\epsilon$ turbulence models, it was found that the solution was sensitive to the initial conditions and the number of iterations for which the code was run. For simulations near the critical slant angle, the flow field appeared to be bistable. If the simulation was stopped when the residuals first started to asymptote, the predicted flow field was similar to that from the high drag regime, while longer run times saw the solution evolve further to have a wake structure similar to that of the low drag regime with a large separation bubble. This phenomenon was observed when using the $k\omega$ -SST and realizable- $k\epsilon$ turbulence models but not when using the RSM turbulence model. Possibly this suggests that turbulence models based on an isotropic turbulent viscosity are not well suited for simulations of this type.

Although the RSM turbulence model appeared to be better suited, there were other difficulties. Due to the sensitive nature of the flow field, the solutions could not be converged to a steady state. Instantaneous visualisations of the flow field indicated wake flow structures similar to unsteady flow structures from the time-dependent solver. For a time-independent solver, it is difficult to theoretically justify oscillating solutions as representative of true time-dependent behaviour. However, the drag and

lift history indicated that the solution oscillated about a mean value. As a result, the flow field was sampled over a large number of iterations (iteration averaged) and a (iteration-)mean flow field produced. The qualitative wake flow features and quantitative drag measurements compared well with the experimental trends as the slant angle was varied. To verify the relevance of the simulations, time-dependent simulations were also performed. The time-averaged data from these simulations compared well with the iteration-averaged simulations. Given this, and since steady simulations were much less expensive computationally, iteration-averaged simulations were used for the bulk of the parameter space studies.

9.2 Effect of slant angle

As part of the parameter space study, detailed analysis of the effect of the slant angle (α) was undertaken. Although these studies have been carried out in the past, both experimentally [5] and numerically [15], they have only taken data at a small number of locations. This study examined the Ahmed body for a higher number of slant angles.

The overall body forces on the Ahmed body compare well to experimental results [1] and show a similar trend as α is varied (Figure 4.1). Similar to other numerical simulations [15, 27, 31], C_D is over predicted but this is mainly due to an over prediction in the forces on the front portion of the body (Figure 4.5). The C_D on the slant and rear surfaces compares reasonably well with the experimental data. However, given the limited number of data points by Ahmed et al. [5] at which the contributions of individual surfaces are calculated, it is difficult to verify if local variations are realistic in the simulations.

The minimum C_D found in the simulations and experiments at $\alpha \approx 12^\circ$ is not correlated with a minimum C_D contribution from any particular surface. It is due to the geometric effect of changing α , which reduces the C_D on the rear surface (decreasing the surface area). There is a corresponding increase in C_D on the slant surface for increasing α , which results in the local minimum C_D occurring at $\alpha \approx 12^\circ$.

The coefficient of normal force (C_N) from the slant surface (Figure 4.6) was used as a guide to identify changes in the flow structures since this region undergoes the largest variation with α and is directly affected by the C-pillar vortices. The simulations predict an approximate piece-wise linear profile of C_N for $1^\circ \leq \alpha < 22^\circ$,

which encompasses Region I and II. (Details of flow structures common to each region are given below). For $22^\circ \leq \alpha \leq 30^\circ$, C_N in Region III still increases, but the linear dependence on α is lost. At the critical slant angle (α_c), C_N is a maximum, and there is a sudden decrease for $\alpha > 30^\circ$. Past α_c , C_N in Region IV decays slowly until $\alpha = 50^\circ$. Simulations were not conducted for $50^\circ < \alpha < 90^\circ$.

Four regions were identified from the drag and lift forces, and from the flow visualisations in the analysis of the wake structures. These are defined as Region I through to Region IV and are distinguished by the change in C_N profile in Figure 4.6.

In Region I, the flow is attached to the slant surface with a large separation bubble extending downstream. A small increase in α has a significant effect on the length of the rear separation bubble.

In Region II, a small stable separation bubble was observed on the slant surface. This separation bubble is only present in the central region of the slant surface and then reattaches again. Streaklines on the slant surface indicate two recirculation regions inside the separation bubble. The rear separation bubble changes from a toroidal type vortex structure to one where the spanwise vortices on the rear surface are more dominant. The unsteady visualisation for $\alpha = 22^\circ$ in 8.4.2 indicated that the wake was more unsteady with the increase of α , and the shear layers emanating from the sides of the rear surface were oscillating.

The major difference that occur from Region II to III is that the wake separates for almost the entire width of the top of the slant surface. However, the C-pillar vortices keep the wake attached to the edges of the slant surface. The rear separation bubble is considerably shorter as $\alpha \rightarrow \alpha_c$ due to the strong downwash along the body centreline. Analysis of the wake structure indicates that for $\alpha > 20^\circ$, the sides of the rear separation bubble extend further downstream than on the centreline. The presence of the C-pillar vortices and the shear layers from the sides of the slant surface makes the separation bubble extend further downstream near the sides of the body, while the downwash along the centreline dramatically shortens the bubble. Streamline plots by Vino et al. [22] also showed a small rear separation bubble along the centreline. Profiles of surface C_P along the centreline indicate that the peak C_P occurs at $\alpha = 20^\circ$, just before the wake starts to separate from the top of the slant surface. The C_P near the edge of the slant surface is influenced by the C-pillar vortex and peaks later at

$\alpha=25^\circ$, just as the C-pillar vortex starts to breakdown. For $25^\circ < \alpha \leq 30^\circ$, the C-pillar starts to undergo vortex breakdown due to the increase in the vortex swirl velocity. The location of the breakdown occurs closer to the formation point of the C-pillar vortex as $\alpha \rightarrow 30^\circ$, leading to the transition to a fully separated wake.

Past α_c in Region IV, the C-pillar vortex does not form and the flow separates from the top of the slant surface. This results in a large separation bubble encompassing the slant and rear surface. As opposed to the C-pillar forming, the shear layers from the sides of the slant surface fold over the top of the rear separation bubble since there is still downwash along the centreline but it is significantly reduced from $\alpha < \alpha_c$.

The comparison with experimental data in Section 8.2 shows that the numerical simulations compare well with the experimental data from Lienhart et al. [13, 14]. At $\alpha=25^\circ$, the velocity profiles indicate that the separation bubble is larger, but as was shown in Section 8.4.3, the wake structure above the slant surface is very unsteady with shear-layer vortices shedding downstream. This leads to considerable variation in the reattachment length. The spanwise slices of U/U_∞ showed a slight variation of the structure of the C-pillar vortex, showing that the C-pillar vortex at $\alpha=25^\circ$ is not as well defined as in the numerical simulations. The unsteady simulations showed that the C-pillar vortex was very sensitive to breakdown and while the steady simulations indicated breakdown was present, the C-pillar vortex is likely to have a higher U/U_∞ , closer to the experimental results.

For $\alpha=35^\circ$, the separation bubble is of a size and shape similar to the experiments along the body centreline. Both the simulations and experiments indicate the presence of streamwise vortices downstream of the body past the rear separation bubble.

9.3 Effect of Aspect Ratio

Chapter 5 examined the effect of the body aspect ratio on the wake structures for the Ahmed body for $1.0 \leq AR < 2.5$. The most significant effect found from varying AR is the change in location of α_c , where the wake structures change from a wake dominated by the C-pillar vortices to a large separation bubble encompassing the slant and rear surface. For the standard Ahmed body ($AR=1.75$), $\alpha_c=30^\circ$. For the range of AR investigated, α_c increases to $\alpha_c=34^\circ$ for $AR=1.0$, and reduces to $\alpha_c=25^\circ$ for

AR=2.5. The location of α_c represents the location of maximum C_D for a given AR and results in a lower peak C_D for AR>1.75, since $\alpha_c < 30^\circ$. Since the location of α_c can be correlated with total breakdown of the C-pillar vortex, the decrease of α_c with AR does not decrease smoothly and is sensitive to changes in α_c . It is likely that since the C-pillar vortex is bistable at AR=1.75, there will be a variation in the location of α_c for other AR. However, for AR>2.0, it is likely that the location of the α_c will not vary significantly, since the transition from attached flow to a separated wake is quite sudden. Examination of the C-pillar vortex in Section 6.5.2 showed vortex breakdown only occurs at one slant angle.

There is little variation in C_D for low AR bodies in Region I, while for AR>1.75, C_D does increase but it is not significant considering the large increase in cross-sectional area. For AR=1.75, the transition between Region I and II occurs for $15^\circ < \alpha < 20^\circ$. However, for some AR, a small separation bubble on the slant surface was found for $\alpha = 15^\circ$, even though the C_N gradient did not increase, indicating that the small separation bubble on the slant surface has a minimal effect on drag. In Region III, C_D for a given AR reaches a maximum with the peak C_D occurring for AR=1.5 and $\alpha = 32^\circ$. For a given α , C_D increases with AR, whereas for AR>1.5 the variation of C_D with AR is smaller. The C_D on the rear surface plateaus as $\alpha \rightarrow \alpha_c$, while the C_D on the slant surface increases with α . C_N at α_c increases for $1.0 \leq AR \leq 1.75$, while C_N at α_c for AR>1.75 does not vary appreciably, indicating that the AR does not change C_D much with wider vehicles. However, the total drag does increase with AR due to the larger frontal area.

The largest change in C_D between Region III and Region IV occurs in the middle of the AR range. Since the location of α_c is lower relative to AR=1.75 for high AR bodies, the change at the transition is small. For the low AR bodies, the change in C_D is also reduced due to the presence of two counter-rotating streamwise vortices. This means that the C_D in Region IV is higher relative to the standard Ahmed body (AR=1.75).

Visualisations for AR=2.5 indicate that initial separation on the slant surface occurs from the base of the slant surface for high AR bodies rather than from the top edge of the slant surface. The formation of a small separation bubble on the slant surface for $\alpha \approx 15^\circ$ is likely to be sensitive to small fluctuations upstream of the slant

surface. For small increases in α above $\alpha=15^\circ$, the bubble separates from the top slant surface and reattaches before the end of the slant surface (Figure 5.28). In Region III, the flow is separated across the entire width of the top of the slant surface with the C-pillar vortices keeping the flow attached on the sides of the slant surface. For low AR bodies, flow visualisations suggest that the C-pillar and slant separation bubble are linked with the flow from the slant separation entrained into the C-pillar vortex. For higher AR bodies, the flow visualisations indicate that the slant separation bubble and C-pillar vortices are not linked.

An observation made for $\alpha=25^\circ$ is the region on the slant surface which remains attached is relatively unaffected by varying in AR. The width of the attached region on the side of the slant surface is similar for a given distance from the top of the slant surface. Therefore, for larger AR bodies, the surface area of the attached region is greater due to the increased width of the slant surface. The length of the slant separation bubble is dependent on the AR, since for increasing AR, the separation bubble can extend further down the slant surface before it reaches the centreline.

Simulations showed that the length of the rear separation bubble increases with AR. However, since the downwash in the wake limits the length of the separation bubble on the centreline, on the edges of the model the separated region extends further downstream with increasing AR. This results in the rear separation bubble extending further downstream as $AR \rightarrow 2.5$, while on the centreplane the length of the separated region does not vary to such a large extent.

For low AR bodies past the critical slant angle, counter-rotating streamwise vortices are present in the wake, with a strong downwash still present. Flow visualisation indicates that the shear layers from the sides of the slant surface fold over due to the downwash. For increasing AR, the strength of the counter-rotating streamwise vortices in the wake decreases as evidenced by the reduction of Γ in the wake. Except for low AR bodies, the size of the rear separation bubble downstream is constant and independent of AR.

9.4 Structure of C-pillar vortex and vortex breakdown

The structure of the C-pillar vortex emanating from the top corners of the slant was examined to determine how α and AR affect the vortex structure. Simulations indicate that as $\alpha \rightarrow \alpha_c$, vortex breakdown occurs, leading to complete separation over

the slant surface. For $AR=1.75$, simulations suggest that the vortex starts to break down past the slant surface at $\alpha=25^\circ$ and then as $\alpha \rightarrow 30^\circ$, the location of the breakdown occurs earlier on the slant surface.

Of the various methods used to quantify vortex breakdown, the swirl parameter was found to be the best method to predict the location where the vortex core expands. $S_N > S^*$ indicates where the C-pillar vortex starts to expand while the helix angle $\gamma \approx 50^\circ$ shows the location of maximum expansion, where $V_{x(\text{axis})} \rightarrow 0$. However, $\gamma \approx 50^\circ$ is only a guide, making it difficult to use it as a criterion for breakdown. The expansion of the vortex core was shown by examining core gradient (gradient of what?) and $|\omega_z|$, which shows that the gradient of the swirl velocity decreased as the size of the vortex expands at the breakdown location.

Examination of S_N for different AR suggests that the change of vortex breakdown with AR is due to the increase of $V_{\theta_{\max N}}$ with AR , while the variation of $V_{x(\text{axis})}$ with AR is negligible in comparison. As a result, α_c reduces with increasing AR . For aspect ratios where the vortex breakdown is present in the C-pillar vortex but the flow is still attached, the decrease of the Z -location of core expansion is due to decreasing $V_{x(\text{axis})}$ along the core axis. There is a larger decrease in $V_{x(\text{axis})}$ with increasing α leading to the location of vortex breakdown being closer to the formation point of the vortex.

Simulations indicate that the mechanism for the transition to a fully separated wake structure at $\alpha > \alpha_c$ is due to the flow field near the formation point exceeding the swirl parameter criterion for a stable vortex and, as a result, the C-pillar vortex fails to develop. This is indicated by the location of the breakdown occurring closer to the top of the slant surface as $\alpha \rightarrow \alpha_c$.

9.5 Sources of drag in the wake

The flow field for the Ahmed body was analysed using the momentum equation to locate the sources of drag in the wake. By evaluating the separate contributions from integrating the momentum equation over control volumes, sources of pressure loss (C_{PL}), longitudinal velocity loss (C_{LVL}) and vortex drag (C_{VD}) were identified. It was possible to calculate the contribution of drag from the slant and rear surface, but considerable care is required to ensure that the C_D due to the ground boundary

condition is not included. This method is better suited to identify sources of drag (especially C_{VD}) rather than for calculating the overall drag on a body.

The analysis shows that the reduction in C_D at α_c is due to a reduction in C_{VD} . At $\alpha=\alpha_c$, C_{VD} contributes up to 33% of the total drag on the Ahmed body, which reduces to approximately 10 % for $\alpha>\alpha_c$. Analysis of the effect of α on drag indicates the presence of a peak C_{VD} for a given α past the end of the body ($X>0$). This is associated with increased downwash due to the closing of the rear separation bubble increasing the downwash generated by the C-pillar vortices.

Contours of C_{VD} , C_{LVL} , C_{PL} and C_D were taken at different downstream regions to identify structures in the wake contributing to the body drag. Simulations show that before the slant surface, C_D is due to pressure loss and longitudinal velocity loss in the boundary layer on the surface of the model. Over the slant surface where a slant separation bubble exists, contours of C_D indicate that the highest drag occurs in the shear layer region of the bubble. Inside the slant separation bubble, the main losses are from the C_{PL} . On the side of the separation bubble inside the C-pillar vortex, the main source of drag is pressure loss inside the vortex. However, the C-pillar vortex creates a region of high C_{VD} on the inside edge of the vortex. The strongest C_D downstream of the body occurs on the edges of the rear separation bubble. For flows with two counter-rotating streamwise vortices present in the far wake, C_D is primarily associated with pressure losses in the vortex core. For $\alpha>\alpha_c$, the main losses in the wake are from C_{PL} , which originates (what is originating?) from the shear layers of the separation bubble.

When the AR of the body is varied, $C_{PL}+C_{LVL}$ increases with AR on the slant due to the increased size of the slant separation bubble. The peak C_{VD} for the five aspect ratios considered indicate that C_{VD} does not change significantly with AR. This results in the portion of C_{VD} from the total C_D decreasing with increasing AR. Spanwise slices of C_{VD} for various AR indicate that the increase in C_{VD} (small relative to C_{PL} and C_{LVL}) with AR is due to the increased downwash on the inside of the C-pillar vortex.

9.6 Unsteady wake structures

The unsteady wake structures for the Ahmed body ($AR=1.75$) were examined for comparison with the time-independent simulations. A detailed analysis of the wake structures was undertaken and the frequency spectra of the wakes were examined.

The structure of the time-averaged flow field of the time-dependent simulations compared well with that from the time-independent simulations. No large variations in the wake structure were observed for the slant angles covering the various flow regions considered. The time-averaged solution at $\alpha=30^\circ$ revealed that the vortex breakdown was stronger compared with the time-independent simulations.

The frequency analysis of the drag and lift body forces was not conclusive. It is difficult to quantify any frequencies present in the wake. This is most likely due to the fact that the body forces result from effectively averaging the wake structure forces over an area so any periodic structures are masked.

The visualisations of the wake structures gave a better insight into their unsteady nature. The flow visualisations at $\alpha=10^\circ$ showed that shedding occurs near the centreline of the body while on the side regions, the rear separation bubble is relatively steady. The toroidal vortex structure present in the rear separation bubble is diminished as $\alpha=10^\circ \rightarrow 22^\circ$. The flow structures on the slant separation bubble at $\alpha=22^\circ$ are significantly different compared with the time-averaged flow structures. The shear layer emanating from the top of the slant surface is unstable with vortices released and shed downstream. Even though the time-averaged flow indicates that the separation bubble reattaches, the spanwise vortices are shed past the end of the slant separation and interact with the rear separation bubble. Visualisations indicated intermittent vortex breakdown past the end of the body as the C-pillar vortex interacts with the wake structure. As the unsteady solution evolves for $\alpha=25^\circ$, the region of breakdown in the C-pillar vortex disappears indicating that the C-pillar vortex is at the limit of breaking down for $AR=1.75$. The vortices shed from the shear layer at the top of the slant surface are forced towards the centreline because of the presence of the C-pillar vortex. The C-pillar vortex exhibits signs of bubble-type vortex breakdown with a spiral tail breakdown over the slant region at $X \approx -0.05$. This location moves towards the top of the slant surface as $\alpha \rightarrow \alpha_c$ and the wake after breakdown is highly unsteady. When the C-pillar vortex does not form at $\alpha=35^\circ$,

there is large-scale shedding from the separation bubble and the structures are more coherent.

The frequency spectrum of the wake structures provided a better insight into the shedding structures behind the Ahmed body rather than drag and lift history. For all slant angles, multiple frequencies are present in the wake which is to be expected for a turbulent flow. For slant angles where the wake was attached to, or fully separated from, the slant surface ($\alpha=10^\circ$ and 35°), the frequency spectrum was less noisy and one dominant shedding frequency was present. As found by Sim-Williams [17], the dominant shedding frequency found downstream is linked to the shedding from the base of the rear surface. This was true for all slant angles investigated except for $\alpha=35^\circ$. The simulations indicate that the dominant frequency of the shedding in general increases as $\alpha \rightarrow \alpha_c$. The dominant shedding frequency at $\alpha=25^\circ$ is lower ($St=0.351$ compared with $St=0.52$) than that found numerically by Duncan [106, 111]. The frequency spectrum for $\alpha=30^\circ$ is considerably more complex than the spectrum found from the experiments, perhaps partially due to the limited sampling length. Above the slant surface, a dominant frequency was $St \approx 0.347$, while downstream, the dominant frequency associated with the shedding from the base of the slant surface was higher at $St \approx 0.565$. Experimental data [22, 106, 107] showed quite a large spread making it difficult to directly compare simulations with experiments. High frequencies are associated with the periphery of the C-pillar vortex (Figure 8.64). After the wake has separated from the top of the slant surface at $\alpha=35^\circ$, the dominant frequency is associated with the shedding from the top of rear separation bubble as opposed to the shedding from the base of the rear surface.

9.7 Future Work

As a result of this numerical investigation, the following areas have been identified for further research.

7. Due to the already large size of the parameter space of this study, the effect of Reynolds number and inflow turbulence was not investigated. The variation found between some experimental data could be due to Reynolds number effects and varying levels of free-stream turbulence intensity. Numerical or experimental studies at a variety of slant angles would be useful to quantify

these effects, especially since most automotive vehicles on the road experience higher levels of turbulence than those common to wind tunnel testing. Although extensive experiments have been carried out by Vaino et al [22], it is difficult to quantify different effects using only one slant angle.

8. Since simulations indicate that the C-pillar vortex appears to be the dominant flow feature that affects the wake structures, it is surprising that only limited research has been conducted on the structure of the vortex as it forms from the edge of the slant surface. Further research using more accurate simulation methods such as LES is required to confirm the presence of vortex breakdown. Thus far, experiments have not indicated the presence of vortex breakdown. One reason could be due to the fact that it is difficult to measure the flow structures of the C-pillar vortex. Due to the sensitivity of the structure, intrusive flow measurement methods could adversely affect the flow structures.
9. This study showed the time-averaged flow is considerably different to the unsteady wake flow. This is an area that could be expanded with future studies. A more comprehensive investigation will contribute to understanding the unsteady flow structures on automotive geometries which could lead to more aerodynamic efficient vehicles.
10. The momentum equation was shown to be an effective method for pinpointing structures in the wake which cause the drag. Although more complex, this could be applied to unsteady data to quantify how the unsteady flow structures affect the drag measurements.
11. One of the most beneficial areas of research is to examine methods of further reducing the drag on automotive geometries. This could either be done using active or passive methods of drag reduction. The Ahmed body is a geometry with strong wake structures caused by the presence of C-pillar vortices, so different methods of controlling the C-pillar vortex could be examined to reduce the overall drag of the body. This is an area which is already starting to expand [115, 116]. The Ahmed body could also be modified to simulate notch back geometries by examining the effect of the deck lid geometry on the wake structures and linking it to experiments by Gilhome [117]. This would

be more beneficial than defining a new geometry since a considerable knowledge base already exists for the Ahmed body.

References

1. Strachen, R.K., Knowles, K., and Lawson, N.J. *A CFD and Experimental Study of an Ahmed Reference Model*. In *Proceedings of the 2004 SAE International Congress*. 2004. Detroit.
2. Watkins, S. and Vio, G. *On Vehicle Spacing and its Effect on Drag and Lift*. In *Fifth International Colloquium on Bluff Body Aerodynamics & Applications*. 2004. Ottawa, Canada.
3. Graysmith, J.L., Baxendale, A.j., Howell, J.P., and Haynes, T. *Comparison between CFD and Experimental results for the Ahmed Body*. In *RAeS Conference on Vehicle Aerodynamics*. 1994. Loughborough.
4. Ramm, G. and Hummel, D. *A Panel Method for the Computational of the Flow around Vehicles Including Side-edge Vortices and Wake*. In *3rd International Conference, Innovation and Reliability in Automotive Design and Testing*. 1992. Florence, Italy.
5. Ahmed, S.R., Ramm, G., and Faltin, G. *Some Salient Features of the Time-Averaged Ground Vehicle Wake*. In *Automobile Aerodynamics; Wakes, Wind Effect, Vehicle Development. Papers presented at the 1984 SAE International Congress and Exposition*. 1984. Detroit, MI, Engl: SAE, Warrendale, PA, USA.
6. Cogotti, A., *Wake Surveys of Different Car-Body Shaped with Coloured Isopressure Maps*. SAE (Society of Automotive Engineers) Transactions, 1984. **840302**: p. 85-93.
7. Ahmed, S.R., *Influence of Base Slant on the Wake structure and drag of road vehicles*. Journal of fluids Engineering, 1983. **105**: p. 429-434.
8. Ahmed, S.R., *Wake structure of Typical Automobile Shapes*. Journal of fluids Engineering, 1981. **103**: p. 162-169.
9. Buchheim, R., Deutenbach, K.-R., and Lückhoff, H.-J. *Necessity and Premises for reducing the Aerodynamic Drag of Future Passenger Cars*. In *SAE Technical Paper Series 810185*. 1981. Detroit, USA.
10. Hucho, W.-H., *Aerodynamics of Road Vehicles*. 1990, Cambridge: University Press.

11. Hucho, W.-H. and Sovran, G., *Aerodynamics of Road Vehicles*. Annual Review of fluid Mechanics, 1993. **25**: p. 485-537.
12. Le Good, G. and Garry, K.P., *On the Use of Reference Models in Automotive Aerodynamics*. SAE (Society of Automotive Engineers) Transactions, 2004. **2004-01-1308**: p. 375-400.
13. Lienhart, H. and Becker, S. *Flow and Turbulence Structure in the Wake of a Simplified Car Model*. In *SAE 2003 World Congress*. 2003. Detroit, Michigan.
14. Lienhart, H., Stoots, C., and Becker, S. *Flow and Turbulence in the Wake of Simplified Car Model (Ahmed Model)*. In *DGLR Fach Symp. der AG STAB*. 2000. Stuttgart.
15. Gilliéron, P. and Chometon, F. *Modelling of Stationary Three-Dimensional Separated Air Flows around an Ahmed Reference Model*. In *Third International Workshop on Vortex Flows and Related Numerical Methods III, ESIAM*. 1999. Toulouse, France.
16. Morel, T. *The Effect of base slant on the flow pattern and drag of three-dimensional bodies with blunt ends*. In *Aerodynamic Drag Mechanisms of Bluff Bodies and Road Vehicles*. 1976. Warren, USA: Plenum Press.
17. Sims-Williams, D.B., *Self-Excited Aerodynamic Unsteadiness Associated with Passenger Cars*, in *School of Engineering*. 2001, University of Durham.
18. Dominy, R.G., *Private communication with*, D.B. Sims-Williams, Editor. 1995.
19. Drouin, V., Giovanni, A., and Gillieron, P. *Topology and characterisation of the vortical near-wake flow over a simplified car model*. In *Symposium of Bluff Body Wakes and Vortex-Induced Vibrations*. 2002. Port Douglas, Australia.
20. Guilmineau, E. *Computational Study of Flow Around a Simplified Car Body*. In *Fifth International Colloquium on Bluff Body Aerodynamics & Applications*. 2004. Ottawa, Canada.
21. Spohn, A. and Gillieron, P. *Flow Separations Generated by a Simplified Geometry of an Automotive Vehicle*. In *Congrès IUTAM Symposium on Unsteady Separated Flows*. 2002. Toulouse, France.
22. Vino, G., Watkins, S., Mousley, P., Watmuff, J., and Prasad, S., *Flow structures in the near-wake of the Ahmed model*. *Journal Of Fluids and Structures*, 2005. **20**: p. 673-695.

23. Ahmed, S.R. and Hucho, W.H. *The Calculation of the Flow Field Past a Van with the Aid of a Panel Method*. In *SAE (Society of Automotive Engineers) Transactions*, 770390. 1977. Warrendale, Pa.
24. Buchheim, R., Rohe, H., and Wustenberg, H. *Experiences with Computational Fluid Mechanics in Automotive Aerodynamics*. In *2nd International ATA Symposium, Use of Supercomputers in the European Automotive Industry*. 1988. Turin, Italy.
25. Han, T., *Computational analysis of three-dimensional turbulent flow around a bluff body in ground proximity*. *AIAA Journal*, 1989. **27**(9): p. 1213-1219.
26. Hashiguchi, M., Kawaguchi, K., Yamasake, R., and Kuwahara, K. *Computational Study of the Wake Structure of a Simplified Ground-Vehicle with Base Slant*. In *SAE (Society of Automotive Engineers) Transactions*. 1989.
27. Makowski, F.T., *Fluent/UNS simulation of the Ahmed Body W/30-Deg Base Slant Angle*. 1997, Fluent Deutschland GmbH. p. 34.
28. Makowski, F.T. and Kim, S. *Advances In External-Aero simulation of Ground Vehicles Using the Steady RANS Equations*. In *SAW World Congress*. 2000. Detroit, USA.
29. Basara, B. and Jakirlic, S. *Flow Around a Simplified Car Body (Ahmed Body): Description of Numerical Methodology*. In *9th ERCOFTAC/IAHR Workshop of Refined Turbulence Modelling*. 2001. Darmstadt, Germany.
30. Guilmineau, E. and Queutey, P. *Simulation of flow around a simplified car body*. In *9th ERCOFTAC/IAHR Workshop of Refined Turbulence Modelling*. 2001. Darmstadt, Germany.
31. Braun, M. and Lanfrit, M. *Simulation of the Ahmed Body*. In *9th ERCOFTAC/IAHR Workshop of Refined Turbulence Modelling*. 2001. Darmstadt, Germany.
32. Hinterberger, C. and Rodi, W. *Case 9.4: (Ahmed Body) Flow around a simplified car body LES with wall functions*. In *9th ERCOFTAC/IAHR Workshop of Refined Turbulence Modelling*. 2001. Darmstadt, Germany.
33. Ouhlos, O., Khier, W., Liu, Y., and K, H. *Test case 9.4: Flow around a simplified car body*. In *9th ERCOFTAC/IAHR Workshop of Refined Turbulence Modelling*. 2001. Darmstadt, Germany.
34. Craft, T., Gant, S., Iacovides, H., Launder, B., and Robinson, C. *Computational study of the flow around the "Ahmed" Car Body (Case 9.4)*. In *9th*

- ERCOFTAC/IAHR Workshop of Refined Turbulence Modelling*. 2001. Darmstadt, Germany.
35. Kapadia, S., Roy, S., and Wurtzler, K. *Detached Eddy Simulation over a reference Ahmed car model*. In *41st Aerospace Sciences Meeting and Exhibit*. 2003. Reno, Nevada: American Institute of Aeronautics and Astronautics.
 36. Kapadia, S., Roy, S., Vallero, M., Wurtzler, K., and Forsythe, J. *Detached eddy simulation over a reference ahmed car model*. In *ERCOFTAC Workshop, Direct and Large-Eddy Simulation-V*. 2003. Technical University of Munich Garching, Germany.
 37. Krajnovic, S. and Davidson, L. *Large-Eddy Simulation of the Flow Around Simplified Car Model*. In *SAE World Congress*. 2004. Detroit, USA.
 38. Peckham, D.H. and Atkinson, S.A., *Preliminary results of low speed wind tunnel tests on a gothic wing of aspect ratio, 1.0*, in *Aeronautical Research Council Technical Report, TN No. Aero. 2504, C. P. No. 508*. 1957.
 39. Chok, C., Parameswaran, S., Sun, R., and Gleason, M., *Numerical investigation of the effects of base slant on the wake pattern and drag of three-dimensional bluff bodies with a rear blunt end*. *Journal of Wind Engineering and Industrial Aerodynamics*, 1994. **51**(3): p. 269-285.
 40. Leibovich, S., *Vortex Stability and Breakdown: Survey and Extension*. *AIAA Journal*, 1983. **22**(9): p. 1192-1206.
 41. Leibovich, S., *The Structure of vortex Breakdown*. 1978. **10 L2**: p. 221-246.
 42. Delery, J., *Aspects of Vortex Breakdown*. *Prog. Aerospace Sci*, 1994. **30**: p. 1-59.
 43. Mitchell, A.M. and Delery, J., *Research into vortex breakdown control*. *Progress in Aerospace Sciences*, 2001. **37**(4): p. 385-418.
 44. Lucca-Negro, O. and O'Doherty, T., *Vortex breakdown: a review*. *Progress in Energy and Combustion Science*, 2001. **27**(4): p. 431-481.
 45. Mununga, L., *Confined Flow Vortex Breakdown Study And Modeling of Mixing in a Stirred Vessel*, in *Mechanical Engineering*. 2005, Monash Univeristy: Melbourne.
 46. Spall, R.E. and Gatski, T.B., *A criterion for vortex breakdown*. *Physics of Fluids*, 1987. **30**(11): p. 3434-3440.

47. Benjamin, B.T., *Theory of vortex breakdown phenomenon*. Journal of Fluid Mechanics, 1962. **14**(4): p. 593-629.
48. Jones, J.P., *The breakdown of vortices in separated flow*, in *Report 140*. 1960, University of Southampton, USA.
49. Sarpkaya, T., *Vortex breakdown in swirling conical flows*. AIAA Journal, 1971. **9**(9): p. 1792-1799.
50. Sarpkaya, T., *On stationary and travelling vortex breakdowns*. Journal of Fluid Mechanics, 1971. **45**(3): p. 545-559.
51. Faler, J.H. and Leibovich, S., *An experimental map of the internal structure of a vortex breakdown*. Journal of Fluid Mechanics, 1978. **86**: p. 313--335.
52. Lambourne, N.C. and Bryer, D.W., *The Bursting of Leading Edge Vortices; Some Observations and Discussion of the Phenomenon*. Aeronautical Research Council, 1961. **R&M 3282**.
53. Poisson-Quinton, P. and Erlich, E., *Hypersustentation et équilibrage des ailes élancées (Hyperlift and balancing of slender wings)*. NASA TT-F-9523, 1964.
54. Su, W., Liu, M., and Liu, Z. *Topological Structures of Separated Flows About a Series of Sharp Edged Delta wings at Angles of Attack up to 90*. In *Proceedings of the IUTAM Symposium*. 1989. Cambridge.
55. Earnshaw, P.B. and Lawford, J.A., *Low-speed wind-tunnel experiments on a series of sharp-edged delta wings*, in *Aeronautical Research Council No 3424*. 1964.
56. Earnshaw, P.B., *Measurements of vortex-breakdown position at low speed on a series of sharp edged symmetrical models*, in *RAE Technical Report, No 64047*. 1964.
57. Menke, M., Yang, H., and Gursul, I., *Experiments on the unsteady nature of vortex breakdown over delta wings*. Experiments in Fluids, 1999. **27**(3): p. 262-272.
58. Gordnier, R.E. and Visbal, M.R., *Computation of the aeroelastic response of a flexible delta wing at high angles of attack*. Journal Of Fluids and Structures, 2004. **19**: p. 785-800.
59. Pascal, P., *Contribution a l'etude d'un écoulement tourbillonnaire en fluide incompressible*. 1992, Université Louis Pasteur: Strasbourg.

60. Hall, M.G., *Vortex Breakdown*. Annual Review of fluid Mechanics, 1972. **4**: p. 195-218.
61. Bossel, H., *Vortex Breakdown flowfield*. Physics of Fluids, 1969. **12**(3): p. 609-628.
62. Brown, G.L. and J.M., L., *Axisymmetric vortex breakdown. Part 2: Physical mechanism*. Journal of Fluid Mechanics, 1990. **221**: p. 553-576.
63. Thompson, M.C., Hourigan, K., and Sheridan, J., *Three-dimensional instabilities in the wake of a circular cylinder*. Experimental Fluids Science, 1996. **12**: p. 190-196.
64. Johnson, S., Hourigan, K., and Thompson, M.C., *Low Frequency Structures in the wake of Elliptical Cylinders*. European Journal of Mechanics B/Fluids, 2003. **22**(5/6): p. 229-239.
65. Johnson, S., Hourigan, K., and Thompson, D. *Low Frequency Unsteadiness in the Wake of Elliptical Cylinders*. In *Conference on Bluff Bodies and Vortex Induced Vibration 3*. 2002. Port Douglas, Queensland.
66. Versteeg, H.K. and Malalasekera, W., *An introduction to Computational Fluid Dynamics, The finite volume method*. 1995, Harlow, England: Prentice Hall.
67. Patanker, S.V. and Spalding, D.B., *A Calculation Procedure for Heat, Mass and Momentum Transfer in Three-dimensional Parabolic Flows*. Int. J. Heat Mass Transfer, 1972. **15**: p. 1787.
68. Wilcox, D.C., *Turbulence Modelling for CFD*. 1993, Griffin Printing: Glendale.
69. Menter, F.R., *Two-Equation Eddy-Viscosity Turbulence Models for Engineering Applications*. AIAA Journal, 1994. **32**(8): p. 1598-1605.
70. Fluent, *Fluent 6.1 User Guide*. 2003, Lebanon: Fluent Inc.
71. Launder, B.E. and Spalding, D.B., *The Numerical Computation of Turbulent Flows*. Computer Methods in Applied Mechanics and Engineering, 1974. **3**: p. 269-289.
72. Fluent, *Gambit User Guide*. 2003, Lebanon: Fluent Inc.
73. Okada, M., Sheridan, J., and Thompson, M.C. *Effect of width-to-height ratio on wake structures of simplified vehicle geometry*. In *Fourth Conference on Bluff Body Wakes and Vortex-Induced Vibrations*. June, 2005. Santorini, Greece.

74. Bearman, B. *Measurements of transverse forces on cylinders undergoing vortex-induced vibration*. In *Fourth Conference on Bluff Body Wakes and Vortex-Induced Vibrations*. June, 2005. Santorini, Greece.
75. Wassen, E. and Thiele, F. *Numerical Investigation of the Unsteady Wake Structures behind a Generic Vehicle*. In *Fourth Conference on Bluff Body Wakes and Vortex-Induced Vibrations*. June, 2005. Santorini, Greece.
76. Vio, G., Watkins, S., Mousley, P., Watmuff, J., and Prasad, S. *The Unsteady Near-Wake of a Simplified Passenger Car*. In *15th Australasian Fluid Mechanics Conference*. 2004. Sydney, Australia.
77. Scotto d'Apollonia, A., Granier, B., Amalric, B., and Debaty, P. *Early Design Stage Simulation Process for External Aerodynamics at PSA Peugeot Citroen*. In *1st European Automotive CFD Conference*. 2003.
78. Hoerner, S.F., *Fluid Dynamic Drag*. 1965, Brick Town: Hoerner Fluid Dynamics.
79. Kurtz, D., *Aerodynamic design of electric and hybrid vehicles: A guidebook (JPL publication)*. 1980, Pasadena: Jet Propulsion Lab.
80. Williams, J., Barlow, J., and Ranzenbach, R. *Experimental Study of CD Variation With Aspect Ratio*. In *SAE Technical Paper Series 2001-01-1040*. 1999.
81. Abbot, I.H.D., A.E., *Theory of Wing Sections*. 1959, New York: Dover Publications.
82. Tamai, G., *The Leading Edge. Aerodynamic Design of Ultra-streamlined Land Vehicles*. 1999, Cambridge, USA: Robert Bentley.
83. Giovannini, A., *Personal Communication Re Mechanism for transition on the Ahmed Body*, S. Johnson, Editor. 2003: Melbourne.
84. Hucho, W.H. *Aerodynamic of Road Vehicles - a Challenge for Computation Fluid Dynamics*. In *1st European Automotive CFD Conference*. 2003. Bingen, Germany.
85. Sedney, R. *A Flow Model for the Effect of a Slanted Base on Drag, Aerodynamics of Transportation*. In *ASME-CSME Conference, Niagara Falls*. 1979.
86. Goh, E.K., *An Experimental Study into the Time-Dependent Characteristics of a Road Vehicle Wake Flow*, in *Department of Aeronautics*. 1994, Imperial College: London.

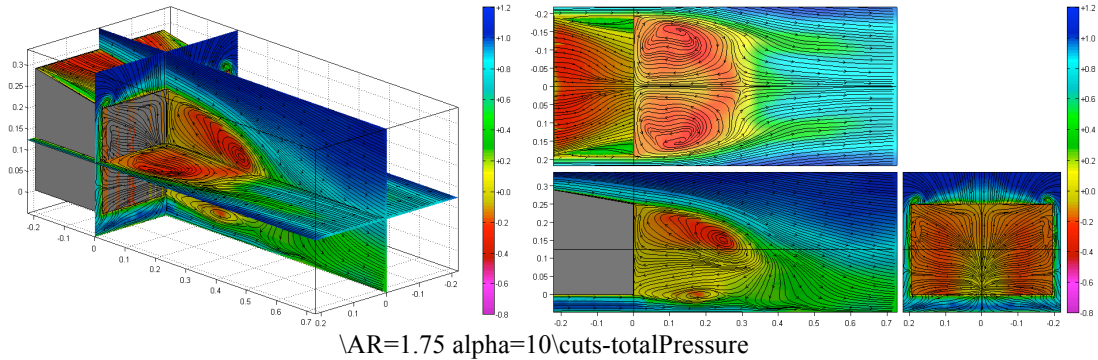
87. Menter, F.R. and Kuntz, M. *Adaptation of Eddy-Viscosity Turbulence Models to Unsteady Separated Flow Behind Vehicle*. In *The aerodynamics of heavy vehicles: Trucks, Buses and Trains*. 2002. California.
88. Robinson, S.K., *Coherent Motions in the Turbulent Boundary Layer*. Annual Review of fluid Mechanics, 1991. **23**: p. 601-639.
89. Jiang, M., Machiraju, R., and Thompson, D., *Detection and Visualization of Vortices*, in *Visualization Handbook*, C.J.a.C. Hansen, Editor. 2005, Academic Press. p. 295-309.
90. Strawn, R.C., Kenwright, D.N., and Ahmad, J., *Computer visualizations of Vortex Wake Systems*. AIAA Journal, 1999. **37**(4): p. 511-512.
91. Banks, D.C. and Singer, B.A., *A Predictor-Corrector Technique for Visualising Unsteady Flow*. IEEE Trans. on Visualisation and Computer Graphics, 1995. **1**(2): p. 151-163.
92. Jeong, J. and Hussain, F., *On the identification of a vortex*. Journal of Fluid Mechanics, 1995. **285**: p. 69-94.
93. Sujudi, D. and Haines, R. *Identification of Swirling Flow in 3D Vector Fields*. In *AIAA 12th Computation Fluid Dynamics Conference Paper*. 1995.
94. NASA, *F-18 HARV smoke and tuff visualization*. 1989, Dryden Flight Reseach Center.
95. Kenwright, D.N. and Haines, R., *Automatic vortex core detection*. IEEE Computer Graphics and Applications, 1998. **18**(4): p. 70-74.
96. McCormick, B., *Aerodynamics, Aeronautics and Flight Mechanics, 2nd Edition*. Vol. New York. 1995, New York: John Wiley and sons inc.
97. Onorato, M., Costelli, A.F., and Garrone, A., *Drag Measurement through Wake Analysis*. SAE (Society of Automotive Engineers) Transactions, 1984. **840302**: p. 85-93.
98. Beaudion, J.F., Aider, J.L., and Wesfreid, J.E. *Drag reduction of a 3D bluff body using vortex generators*. In *Fourth Conference on Bluff Body Wakes and Vortex Induced Vibrations*. 2005. Santorini, Greece.
99. Roumeas, M., Gillieron, P., and Kourta, A. *Analyze and control of the near-wake flow around a simplified car geometry*. In *Fourth Conference on Bluff Body Wakes and Vortex Induced Vibrations*. 2005. Santorini, Greece.

100. Chometon, F. and Laurent, J., *Study of three dimensional separated flows, relation between induced drag and vortex drag*. 9, 1990. **5**(437-455).
101. Kroo, I., *Drag Due to Lift: Concepts for Prediction and Reduction*. Annual Review of Fluid Mechanics, 2001. **33**: p. 587-617.
102. Ardonceau, P. and Amani, G., *Remarks on the relation between lift induced drag and vortex drag*. European Journal of Mechanics B/Fluids, 1992. **11**(4): p. 455-460.
103. Cogotti, A. *Flow-Field Surveys Behind Three Squareback Car Models Using a New 'Fourteen-Hole Probe'*. In *SAE Congress*. 1987. Detroit.
104. Cogotti, A. *A Strategy for Optimum Surveys of Passenger-Car Flow Fields*. In *SAE Congress*. 1989. Detroit.
105. Cogotti, A. *The Evolution of the Performance on an Automotive Wind Tunnel*. In *Fifth International Colloquium on Bluff Body Aerodynamics & Applications*. 2004. Ottawa, Canada.
106. Sims-Williams, D.B. and Duncan, B.D. *The Ahmed Model Unsteady Wake: Experimental and Computational Analyses*. In *Proceedings of the 1998 SAE International Congress & Exposition, Feb 23-26 1998*. 2002. Detroit, MI, USA: SAE, Warrendale, PA, USA.
107. Sims-Williams, D.B. and Dominy, R.G. *Experimental investigation into unsteadiness and instability in passenger car aerodynamics*. In *Proceedings of the 1998 SAE International Congress & Exposition, Feb 23-26 1998*. 1998. Detroit, MI, USA: SAE, Warrendale, PA, USA.
108. Vio, G., Watkins, S., Mousley, P., Watmuff, J., and Prasad, S. *The Unsteady Near-Wake of a Simplified Passenger Car*. In *15th Australasian Fluid Mechanics Conference*. December, 2004. Sydney, Australia.
109. Krajnovic, S. and Davidson, L., *Flow around a simplified car, part 1: large Eddy simulation*. Transactions of the ASME. Journal of Fluids Engineering, 2005. **127**(5): p. 907-18.
110. Krajnovic, S. and Davidson, L., *Flow around a simplified car, part 2: understanding the flow*. Transactions of the ASME. Journal of Fluids Engineering, 2005. **127**(5): p. 919-28.
111. Duncan, B.D., Sengupta, R., Mallick, S., Shock, R., and Sims-Williams, D.B. *Numerical Simulation and Spectral Analysis of Pressure Fluctuations in Vehicle Aerodynamic Noise Generation*. In *SAE 2002 World Congress & Exhibition*. 2002. Detroit, USA.

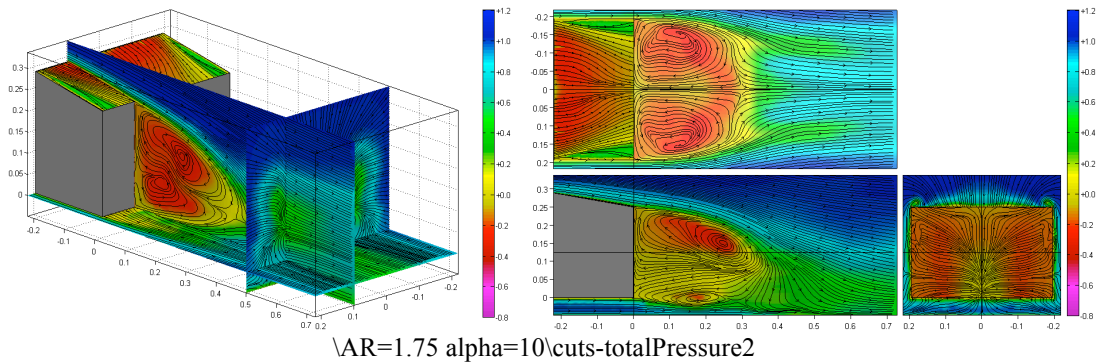
112. Gilhome, B.R., Saunders, J.W., and Sheridan, J. *Time-averaged and Unsteady Near-Wake Analysis of Cars*. In *SAE Technical Paper Series 2001-01-1040*. 2001. Detroit, USA.
113. Driver, D.M., *Time-Dependent Behaviour of a Reattachign Shear-layer*. *AIAA Journal*, 1987. **25**(7): p. 914-919.
114. Vino, G., *Personal Communication Re Structure of unsteady shedding*, S. Johnson, Editor. 2004: Ottawa, Canada.
115. Aider, J.L., Beaudoin, J.F., and Wesfreid, J.E. *Drag Reduction of a 3D Bluff Body Using Vortex Generators*. In *Fourth Conference on Bluff Body Wakes and Vortex-Induced Vibrations*. June, 2005. Santorini, Greece.
116. Guilmineau, E. and Duvigneau, R. *Drag Reduction by Flow Control for the Ahmed Body*. In *Fourth Conference on Bluff Body Wakes and Vortex-Induced Vibrations*. June, 2005. Santorini, Greece.
117. Gilhome, B.R., *Unsteady and Time-Averaged Near-Wake Flow Over the Rear of Sedan Automobiles*, in *Mechanical Engineering*. 2002, Monash University: Melbourne.

Movies

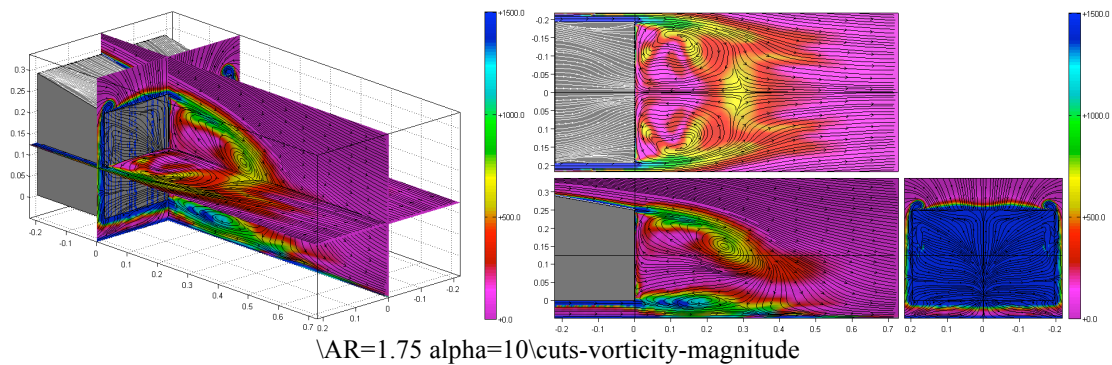
AR=1.75 $\alpha=10^\circ$



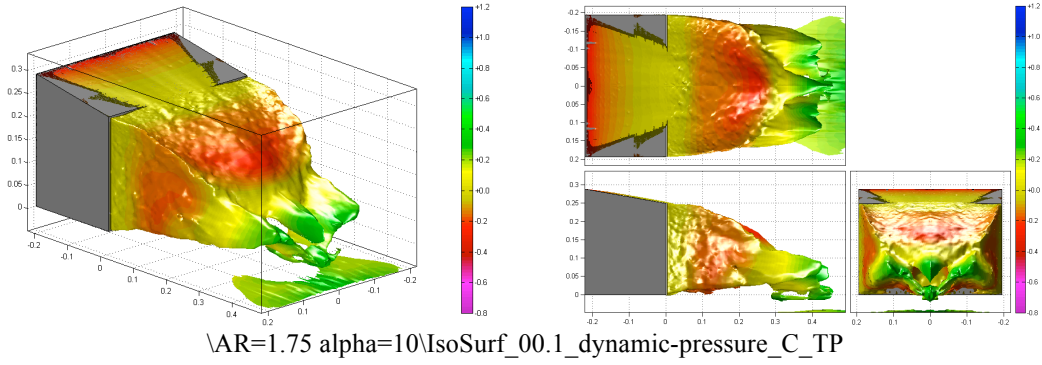
Movie 9.1 $\alpha=10^\circ$, AR=1.75. Unsteady visualisation using slices of C_{TP} and in plane streamlines on planes located at $X=0$, $Y=0.1$ and $Z=0$. Flow structures on the slant surface are visualised by surface streaklines and contours of C_{TP} .



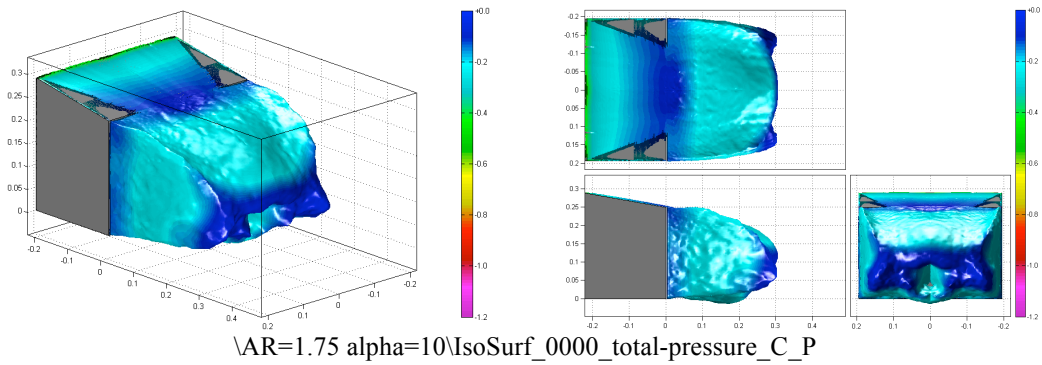
Movie 9.2 $\alpha=10^\circ$, AR=1.75. Unsteady visualisation using slices of C_{TP} and in plane streamlines on planes located at $X=0.5$, $Y=0.0$ and $Z=0.09$. Flow structures on the slant surface are visualised by surface streaklines and contours of C_{TP} .



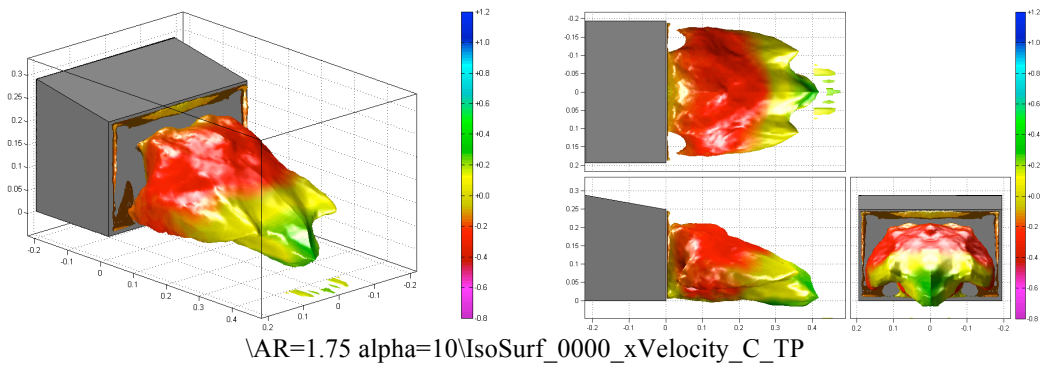
Movie 9.3 $\alpha=10^\circ$, AR=1.75. Unsteady visualisation using slices of $\|\omega\|$ and in plane streamlines on planes located at $X=0$, $Y=0.1$ and $Z=0$. Flow structures on the slant surface are visualised by surface streaklines.



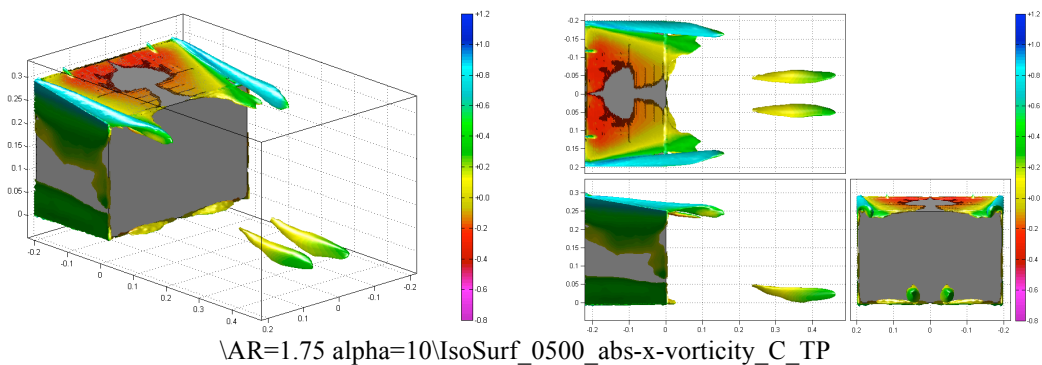
Movie 9.4 $\alpha=10^\circ$, AR=1.75. Iso-surface of $C_{DP}=0.1$ coloured by C_{TP} .



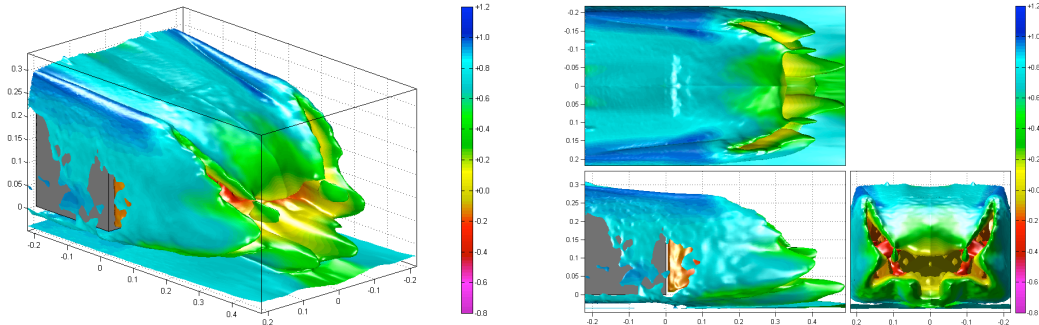
Movie 9.5 $\alpha=10^\circ$, AR=1.75. Iso-surface of $C_{TP}=0.0$ coloured by C_P .



Movie 9.6 $\alpha=10^\circ$, AR=1.75. Iso-surface of $U/U_\infty=0.0$ coloured by C_{TP} .

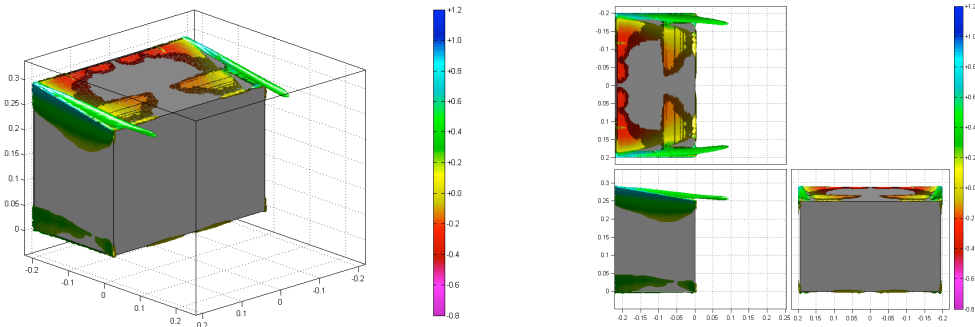


Movie 9.7 $\alpha=10^\circ$, AR=1.75. Iso-surface of $|\omega_x|=500s$ coloured by C_{TP} .



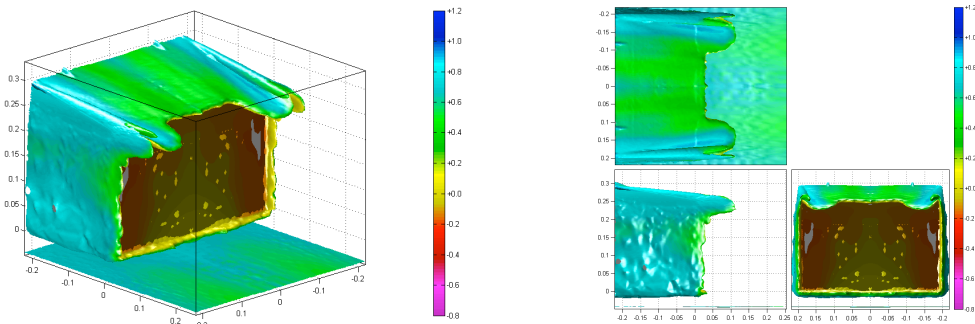
\AR=1.75 alpha=10\IsoSurf_0500_vorticity_magnitude_C_TP

Movie 9.8 $\alpha=10^\circ$, AR=1.75. Iso-surface of $\|\omega\|=500$ s coloured by C_{TP} .



\AR=1.75 alpha=10\IsoSurf_1500_abs-x-vorticity_C_TP

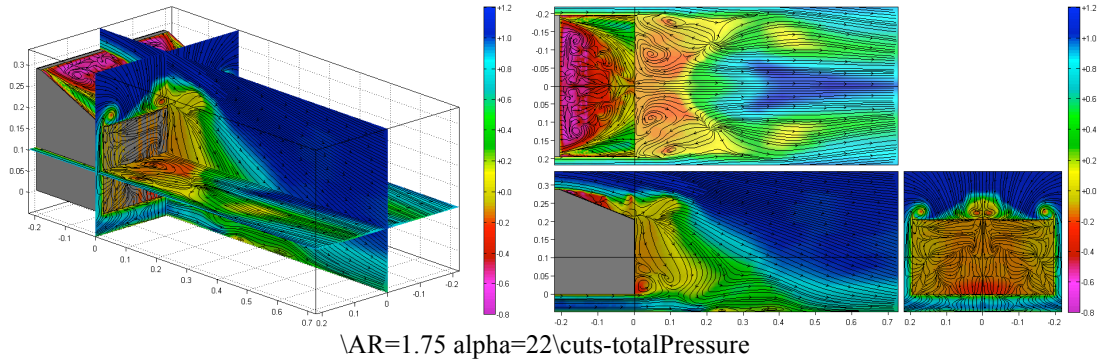
Movie 9.9 $\alpha=10^\circ$, AR=1.75. Iso-surface of $|\omega_x|=1500$ s coloured by C_{TP} .



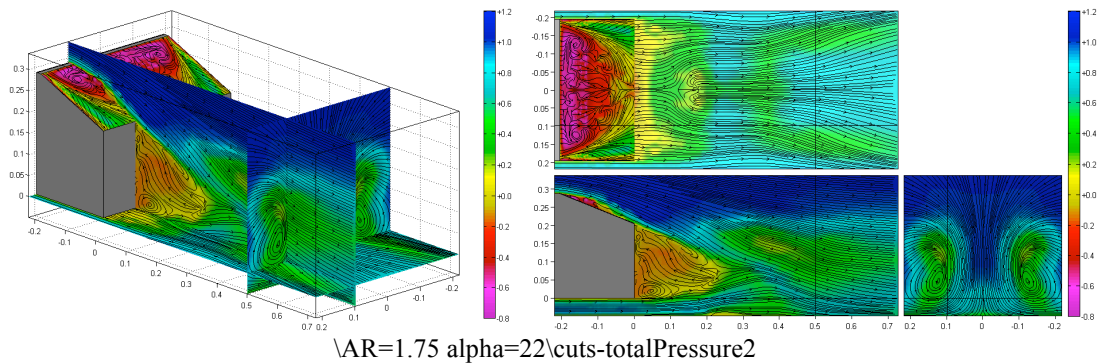
\AR=1.75 alpha=10\IsoSurf_1500_vorticity_magnitude_C_TP

Movie 9.10 $\alpha=10^\circ$, AR=1.75. Iso-surface of $\|\omega\|=1500$ s coloured by C_{TP} .

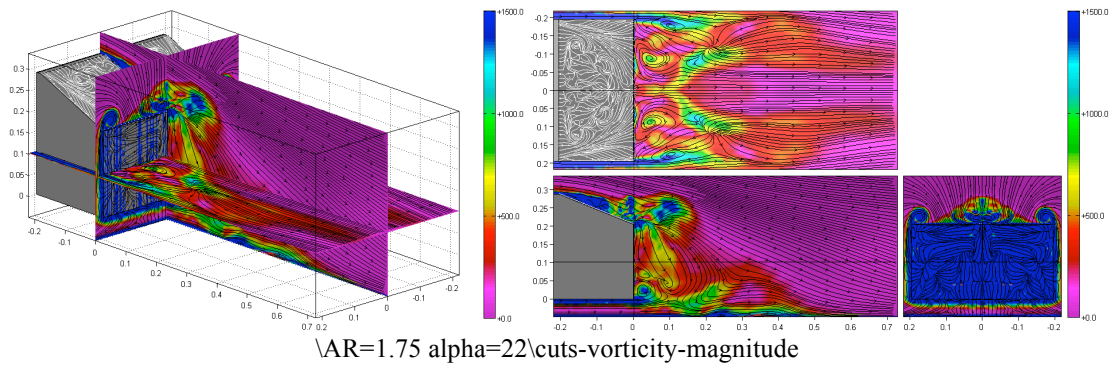
AR=1.75 $\alpha=22^\circ$



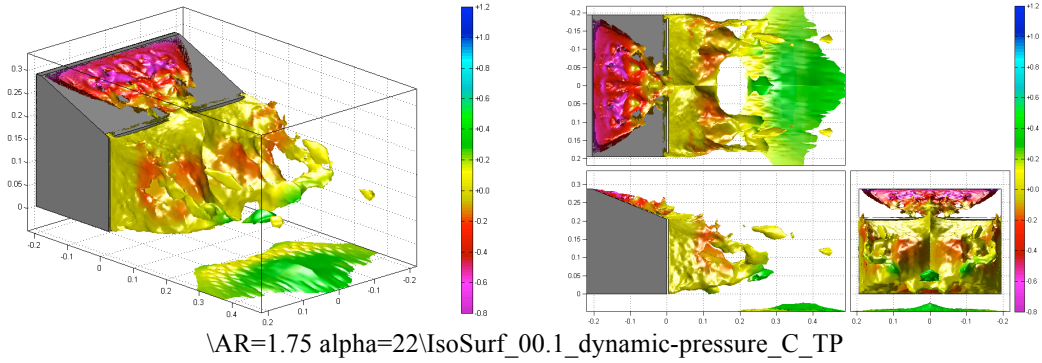
Movie 9.11 $\alpha=22^\circ$, AR=1.75. Unsteady visualisation using slices of C_{TP} and in plane streamlines on planes located at $X=0$, $Y=0.1$ and $Z=0$. Flow structures on the slant surface are visualised by surface streaklines and contours of C_{TP} .



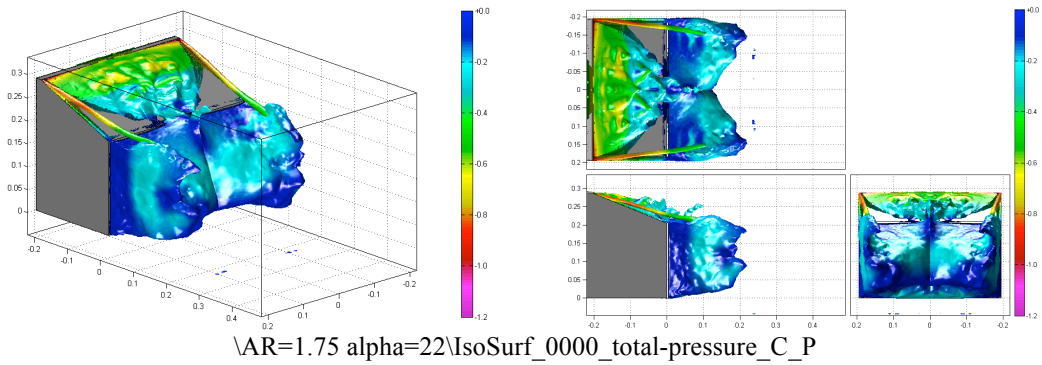
Movie 9.12 $\alpha=22^\circ$, AR=1.75. Unsteady visualisation using slices of C_{TP} and in plane streamlines on planes located at $X=0.5$, $Y=0.0$ and $Z=0.09$. Flow structures on the slant surface are visualised by surface streaklines and contours of C_{TP} .



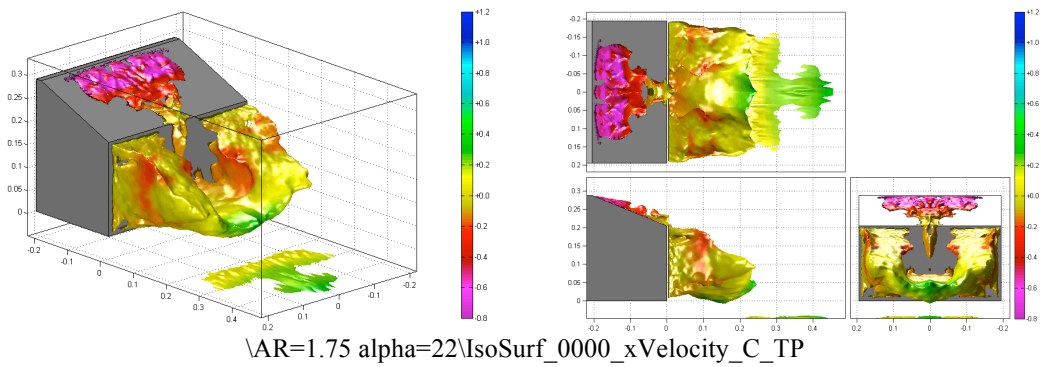
Movie 9.13 $\alpha=22^\circ$, AR=1.75. Unsteady visualisation using slices of $\|\omega\|$ and in plane streamlines on planes located at $X=0$, $Y=0.1$ and $Z=0$. Flow structures on the slant surface are visualised by surface streaklines.



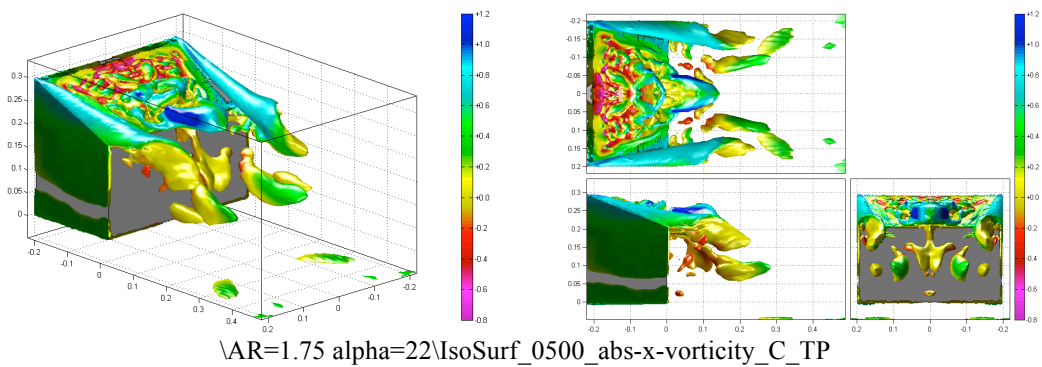
Movie 9.14 $\alpha=22^\circ$, AR=1.75. Iso-surface of $C_{DP}=0.1$ coloured by C_{TP} .



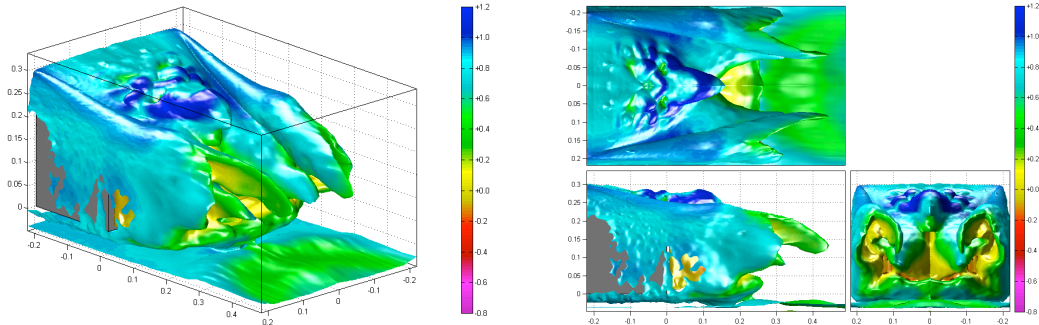
Movie 9.15 $\alpha=22^\circ$, AR=1.75. Iso-surface of $C_{TP}=0.0$ coloured by C_P .



Movie 9.16 $\alpha=22^\circ$, AR=1.75. Iso-surface of $U/U_\infty=0.0$ coloured by C_{TP} .

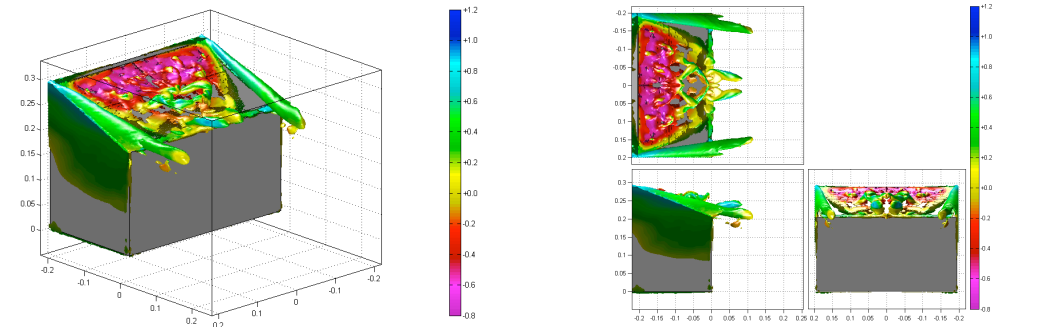


Movie 9.17 $\alpha=22^\circ$, AR=1.75. Iso-surface of $|\omega_x|=500s$ coloured by C_{TP} .



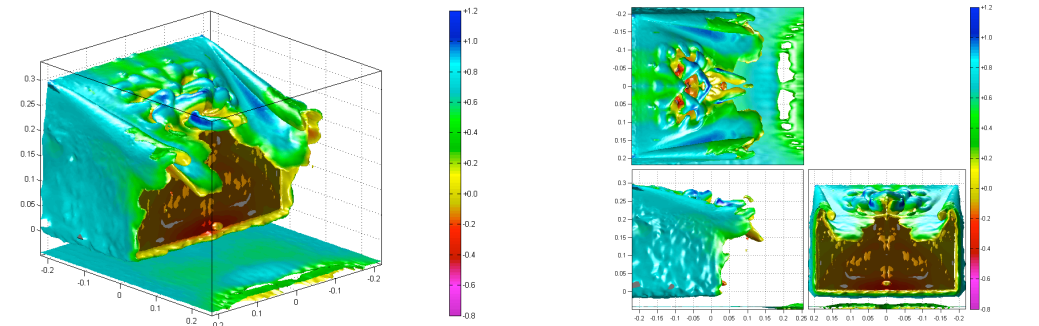
\AR=1.75 alpha=22\IsoSurf_0500_vorticity_magnitude_C_TP

Movie 9.18 $\alpha=22^\circ$, AR=1.75. Iso-surface of $\|\omega\|=500$ s coloured by C_{TP} .



\AR=1.75 alpha=22\IsoSurf_1500_abs-x-vorticity_C_TP

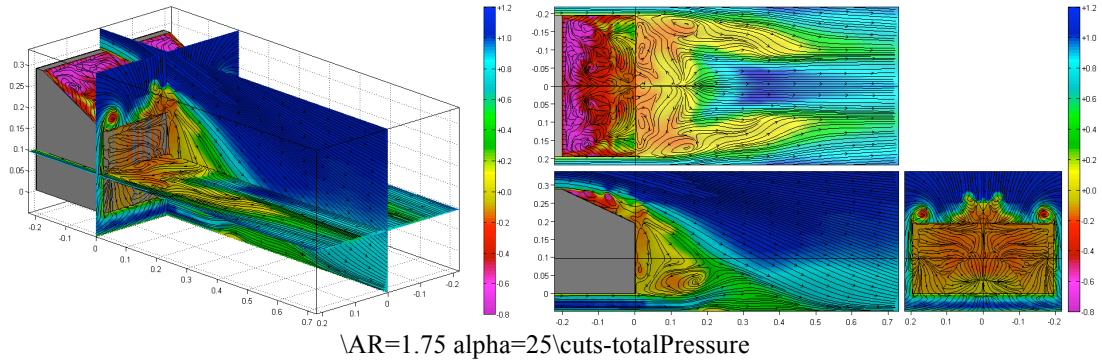
Movie 9.19 $\alpha=22^\circ$, AR=1.75. Iso-surface of $|\omega_x|=1500$ s coloured by C_{TP} .



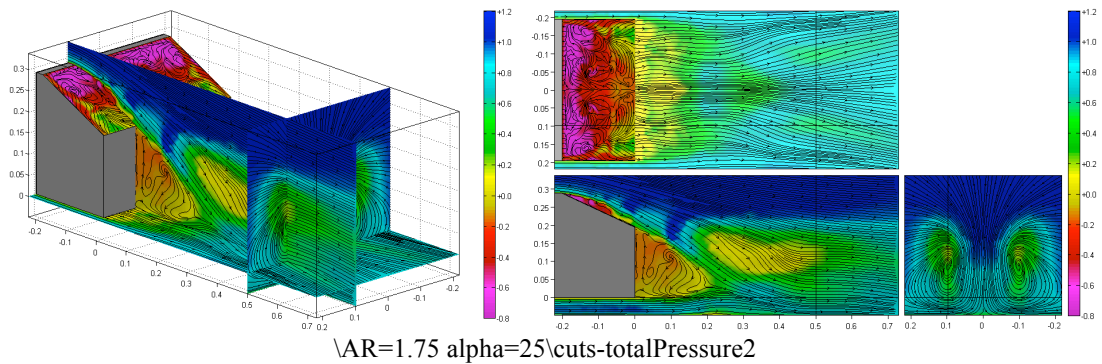
\AR=1.75 alpha=22\IsoSurf_1500_vorticity_magnitude_C_TP

Movie 9.20 $\alpha=22^\circ$, AR=1.75. Iso-surface of $\|\omega\|=1500$ s coloured by C_{TP} .

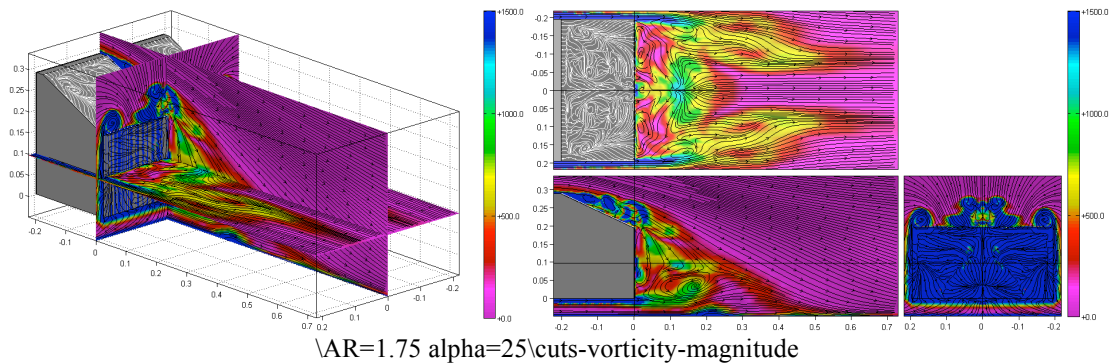
AR=1.75 $\alpha=25^\circ$



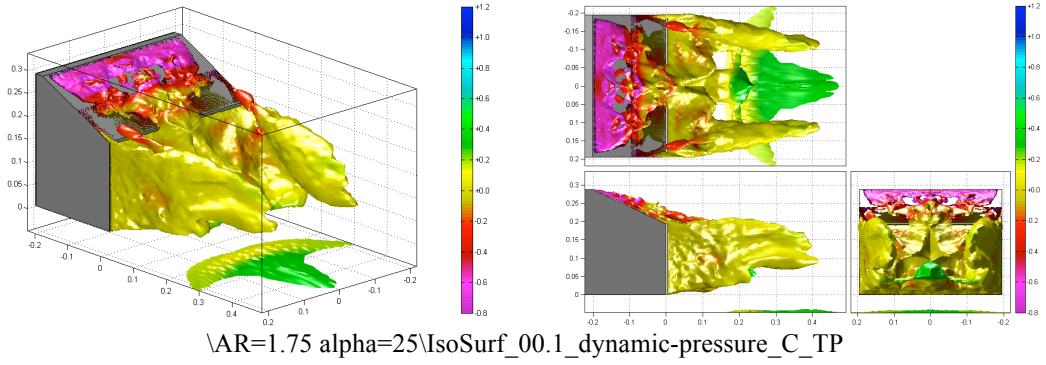
Movie 9.21 $\alpha=25^\circ$, AR=1.75. Unsteady visualisation using slices of C_{TP} and in plane streamlines on planes located at $X=0$, $Y=0.1$ and $Z=0$. Flow structures on the slant surface are visualised by surface streaklines and contours of C_{TP} .



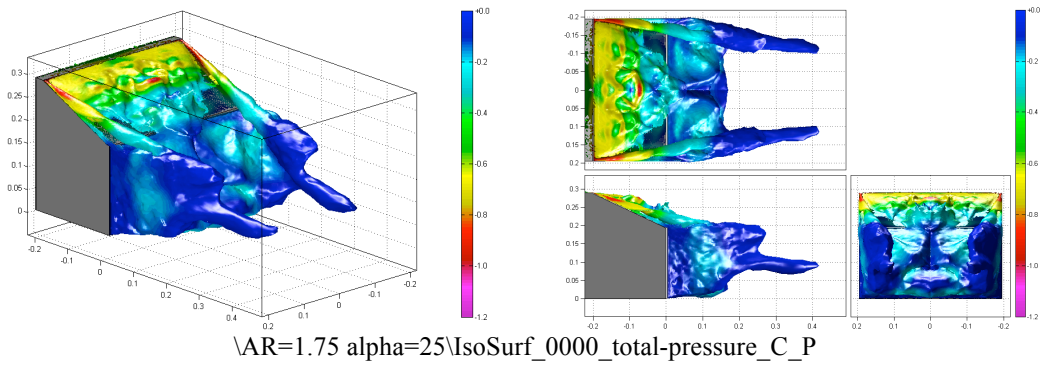
Movie 9.22 $\alpha=25^\circ$, AR=1.75. Unsteady visualisation using slices of C_{TP} and in plane streamlines on planes located at $X=0.5$, $Y=0.0$ and $Z=0.09$. Flow structures on the slant surface are visualised by surface streaklines and contours of C_{TP} .



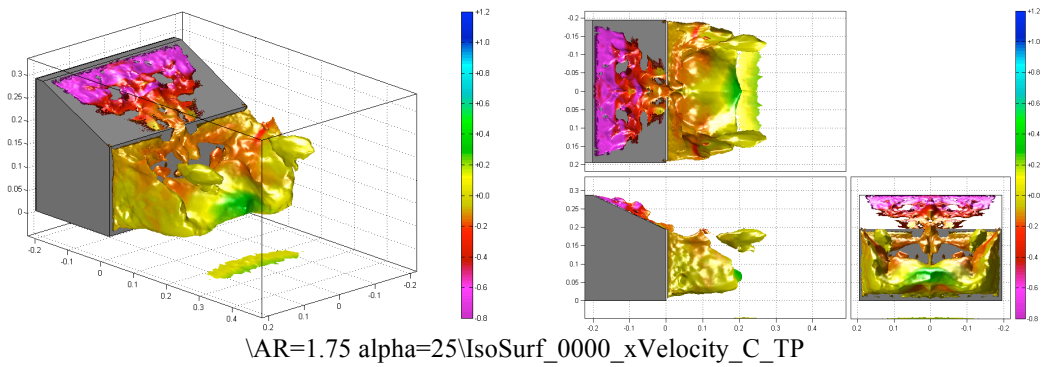
Movie 9.23 $\alpha=25^\circ$, AR=1.75. Unsteady visualisation using slices of $\|\omega\|$ and in plane streamlines on planes located at $X=0$, $Y=0.1$ and $Z=0$. Flow structures on the slant surface are visualised by surface streaklines.



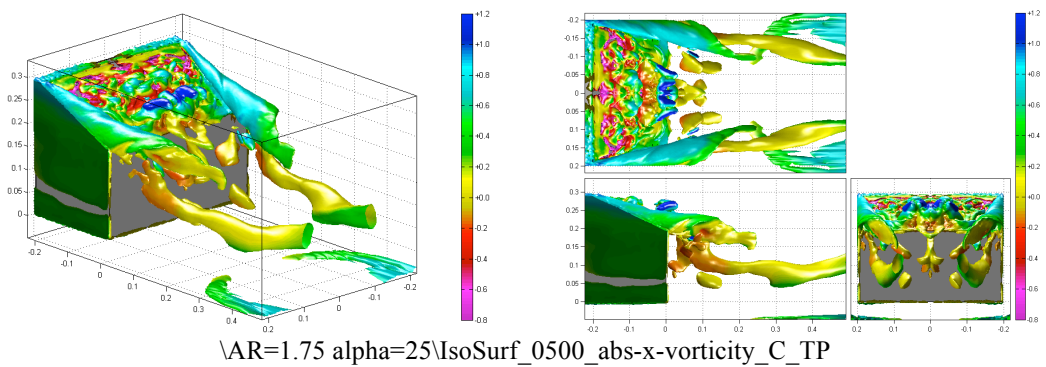
Movie 9.24 $\alpha=25^\circ$, AR=1.75. Iso-surface of $C_{DP}=0.1$ coloured by C_{TP} .



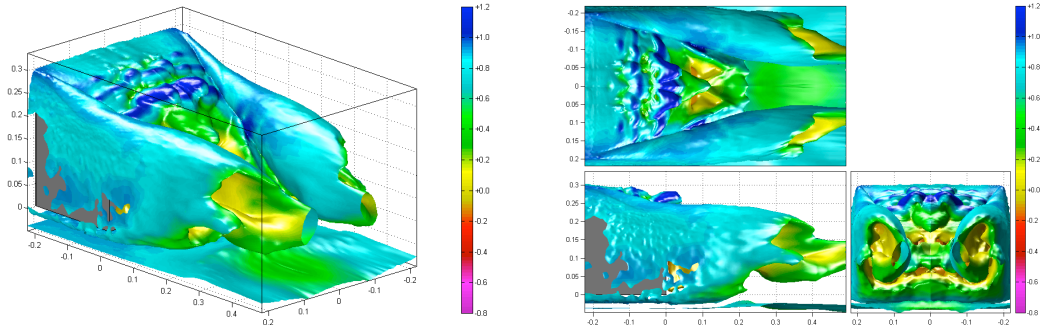
Movie 9.25 $\alpha=25^\circ$, AR=1.75. Iso-surface of $C_{TP}=0.0$ coloured by C_P .



Movie 9.26 $\alpha=25^\circ$, AR=1.75. Iso-surface of $U/U_\infty=0.0$ coloured by C_{TP} .

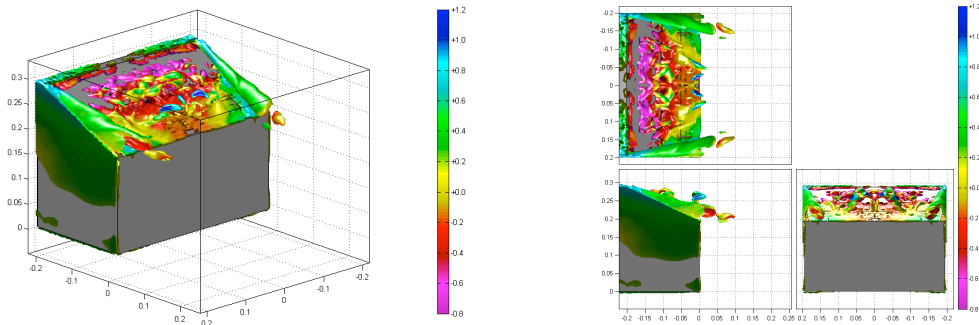


Movie 9.27 $\alpha=25^\circ$, AR=1.75. Iso-surface of $|\omega_x|=500s$ coloured by C_{TP} .



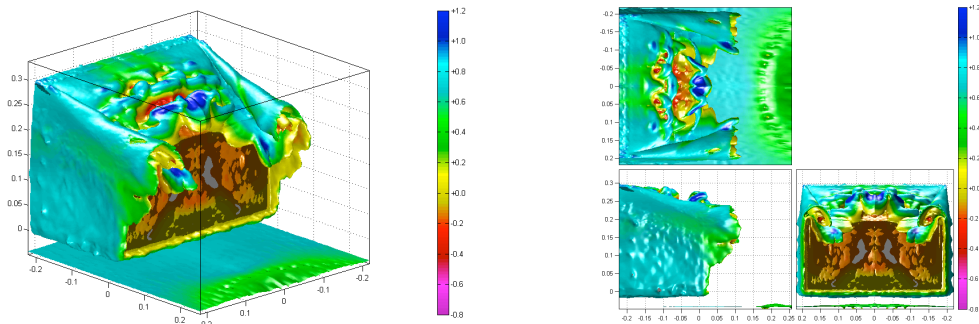
\AR=1.75 alpha=25\IsoSurf_0500_vorticity_magnitude_C_TP

Movie 9.28 $\alpha=25^\circ$, $AR=1.75$. Iso-surface of $\|\omega\|=500s$ coloured by C_{TP} .



\AR=1.75 alpha=25\IsoSurf_1500_abs-x-vorticity_C_TP

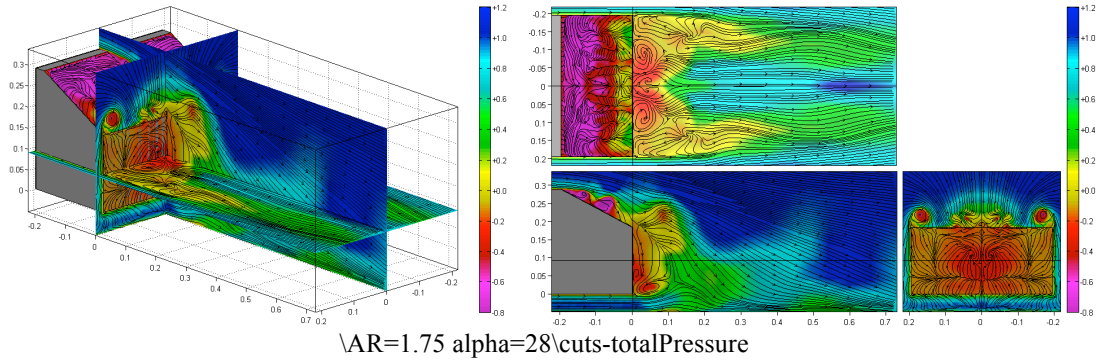
Movie 9.29 $\alpha=25^\circ$, $AR=1.75$. Iso-surface of $|\omega_x|=1500s$ coloured by C_{TP} .



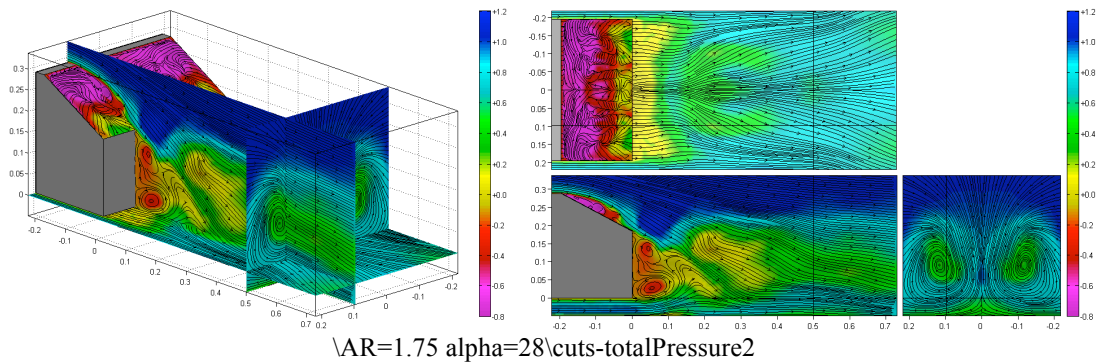
\AR=1.75 alpha=25\IsoSurf_1500_vorticity_magnitude_C_TP

Movie 9.30 $\alpha=25^\circ$, $AR=1.75$. Iso-surface of $\|\omega\|=1500s$ coloured by C_{TP} .

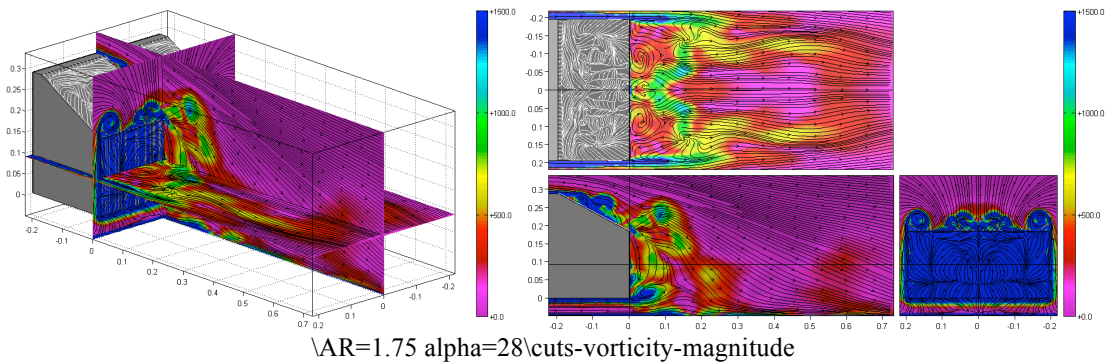
AR=1.75 $\alpha=28^\circ$



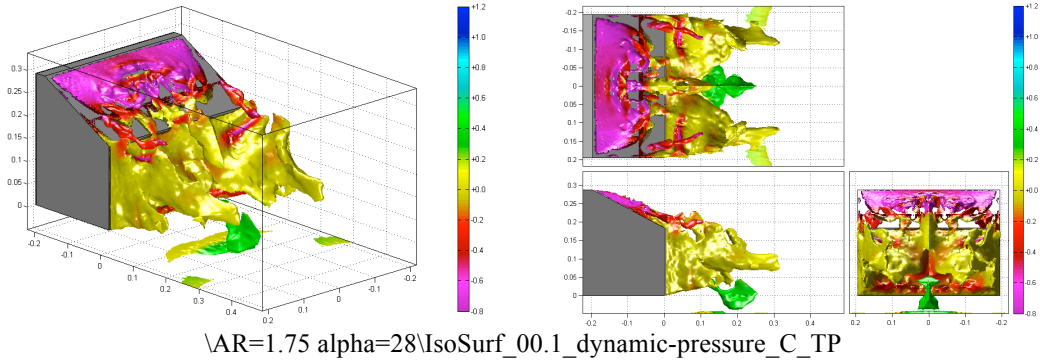
Movie 9.31 $\alpha=28^\circ$, AR=1.75. Unsteady visualisation using slices of C_{TP} and in plane streamlines on planes located at $X=0$, $Y=0.1$ and $Z=0$. Flow structures on the slant surface are visualised by surface streaklines and contours of C_{TP} .



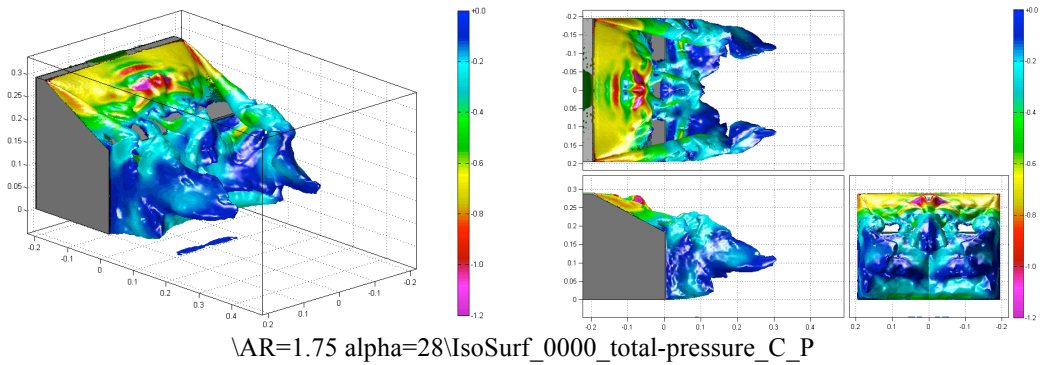
Movie 9.32 $\alpha=28^\circ$, AR=1.75. Unsteady visualisation using slices of C_{TP} and in plane streamlines on planes located at $X=0.5$, $Y=0.0$ and $Z=0.09$. Flow structures on the TP surface are visualised by surface streaklines and contours of C_{TP} .



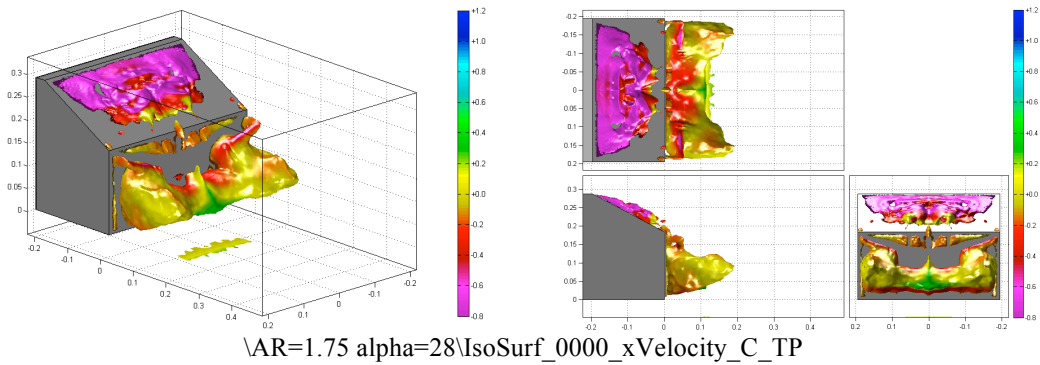
Movie 9.33 $\alpha=28^\circ$, AR=1.75. Unsteady visualisation using slices of $\|\omega\|$ and in plane streamlines on planes located at $X=0$, $Y=0.1$ and $Z=0$. Flow structures on the slant surface are visualised by surface streaklines.



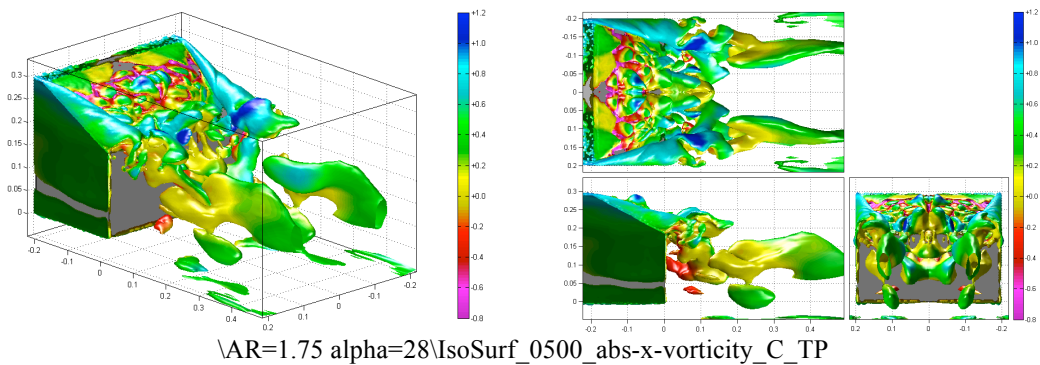
Movie 9.34 $\alpha=28^\circ$, AR=1.75. Iso-surface of $C_{DP}=0.1$ coloured by C_{TP} .



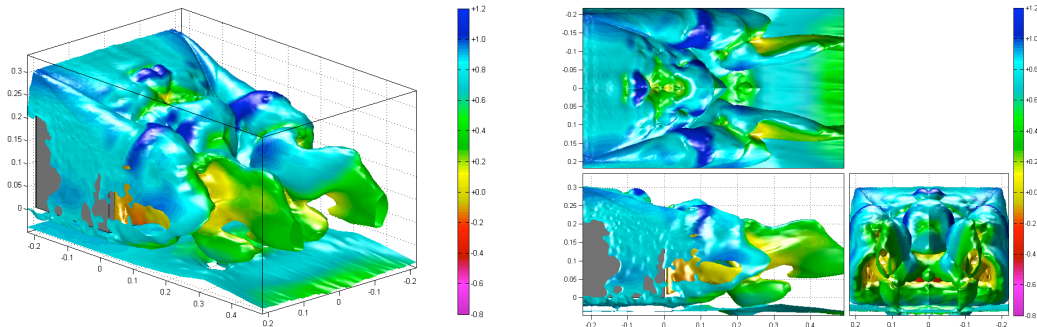
Movie 9.35 $\alpha=28^\circ$, AR=1.75. Iso-surface of $C_{TP}=0.0$ coloured by C_p .



Movie 9.36 $\alpha=28^\circ$, AR=1.75. Iso-surface of $U/U_\infty=0.0$ coloured by C_{TP} .

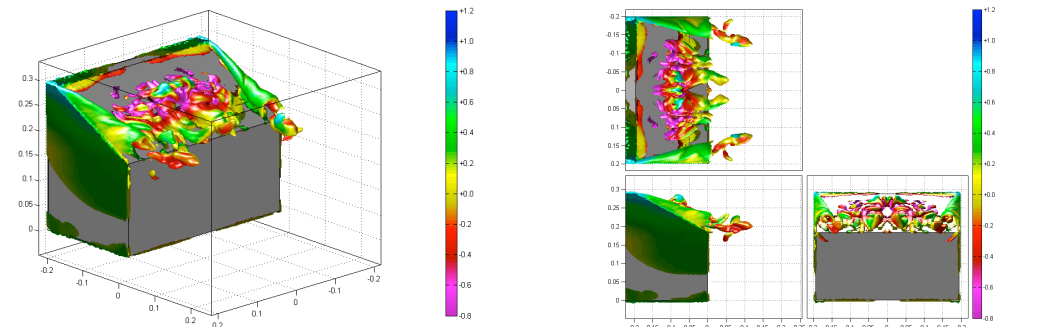


Movie 9.37 $\alpha=28^\circ$, AR=1.75. Iso-surface of $|\omega_x|=500s$ coloured by C_{TP} .



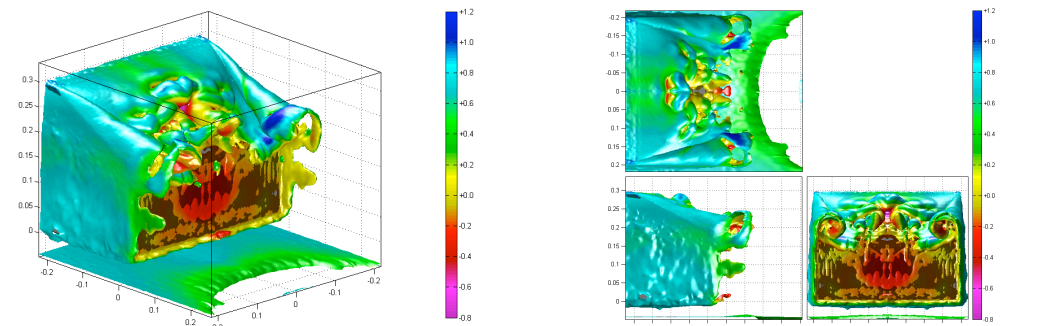
\AR=1.75 alpha=28\IsoSurf_0500_vorticity_magnitude_C_TP

Movie 9.38 $\alpha=28^\circ$, AR=1.75. Iso-surface of $\|\omega\|=500$ s coloured by C_{TP} .



\AR=1.75 alpha=28\IsoSurf_1500_abs-x-vorticity_C_TP

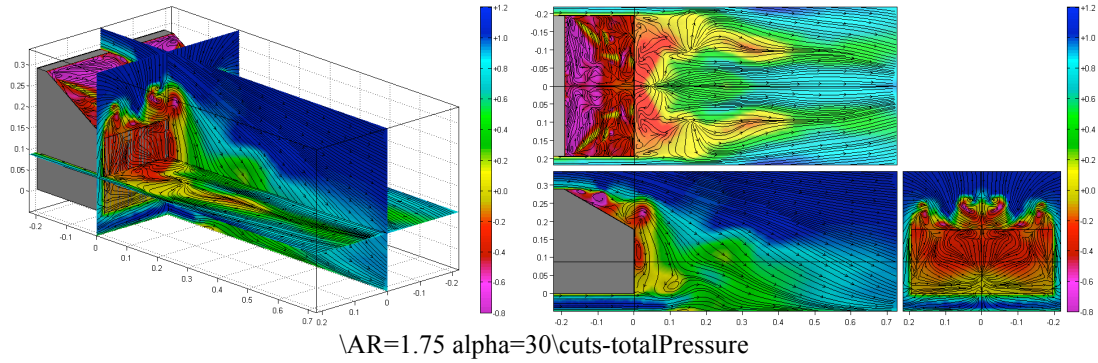
Movie 9.39 $\alpha=28^\circ$, AR=1.75. Iso-surface of $|\omega_x|=1500$ s coloured by C_{TP} .



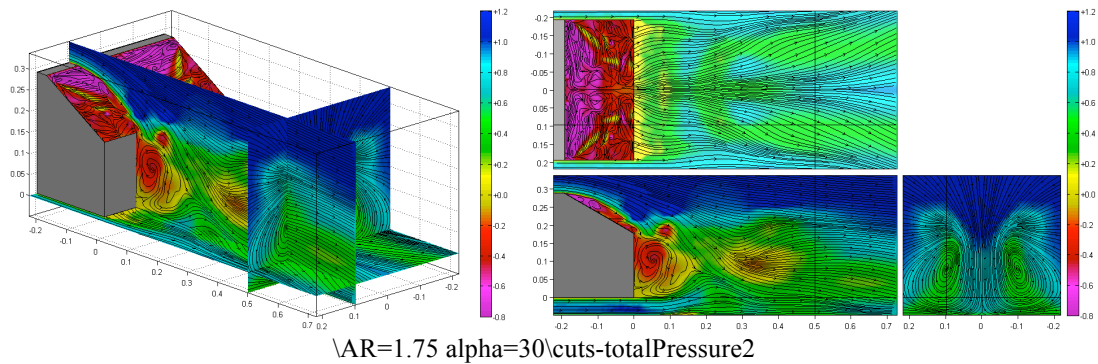
\AR=1.75 alpha=28\IsoSurf_1500_vorticity_magnitude_C_TP

Movie 9.40 $\alpha=28^\circ$, AR=1.75. Iso-surface of $\|\omega\|=1500$ s coloured by C_{TP} .

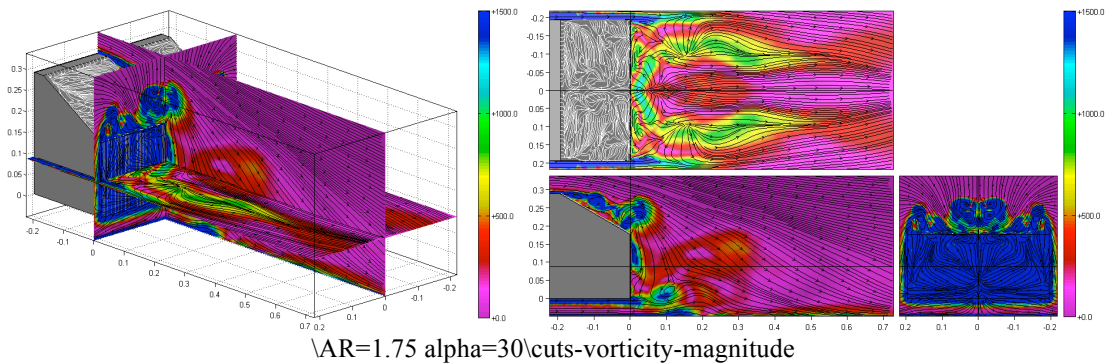
AR=1.75 $\alpha=30^\circ$



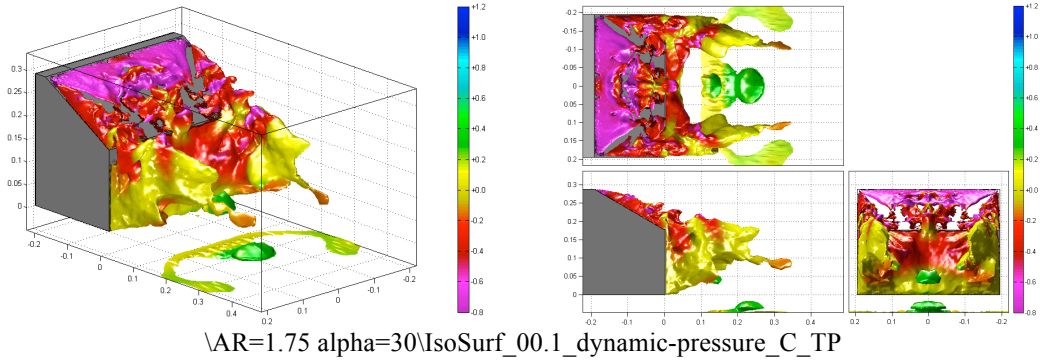
Movie 9.41 $\alpha=30^\circ$, AR=1.75. Unsteady visualisation using slices of C_{TP} and in plane streamlines on planes located at $X=0$, $Y=0.1$ and $Z=0$. Flow structures on the slant surface are visualised by surface streaklines and contours of C_{TP} .



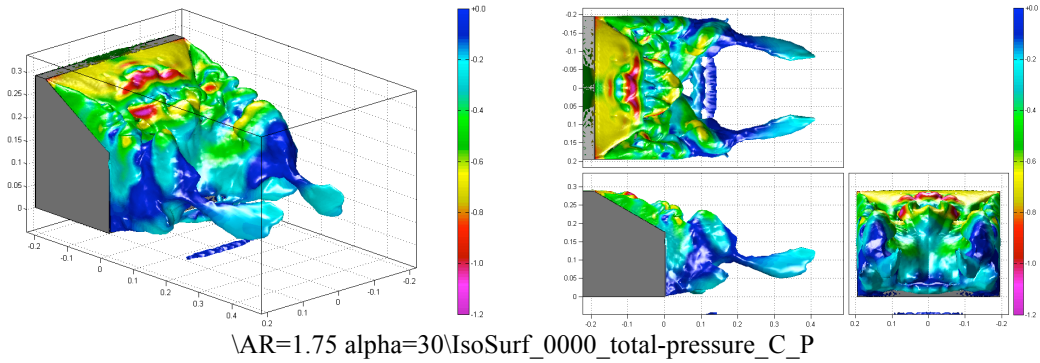
Movie 9.42 $\alpha=30^\circ$, AR=1.75. Unsteady visualisation using slices of C_{TP} and in plane streamlines on planes located at $X=0.5$, $Y=0.0$ and $Z=0.09$. Flow structures on the slant surface are visualised by surface streaklines and contours of C_{TP} .



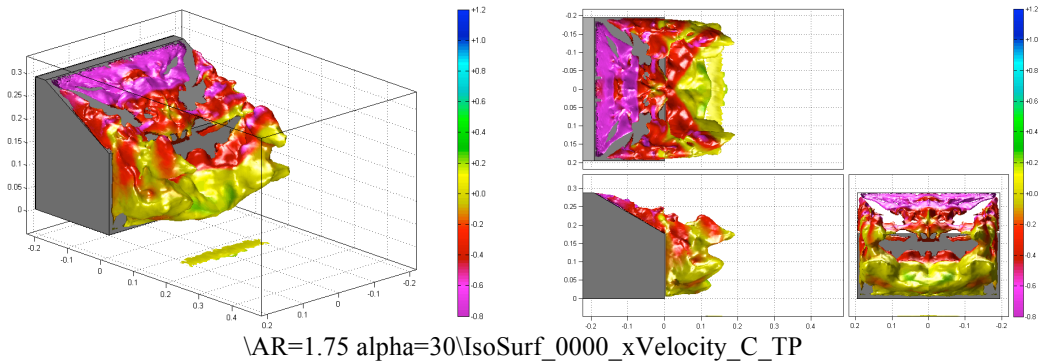
Movie 9.43 $\alpha=30^\circ$, AR=1.75. Unsteady visualisation using slices of $\|\omega\|$ and in plane streamlines on planes located at $X=0$, $Y=0.1$ and $Z=0$. Flow structures on the slant surface are visualised by surface streaklines.



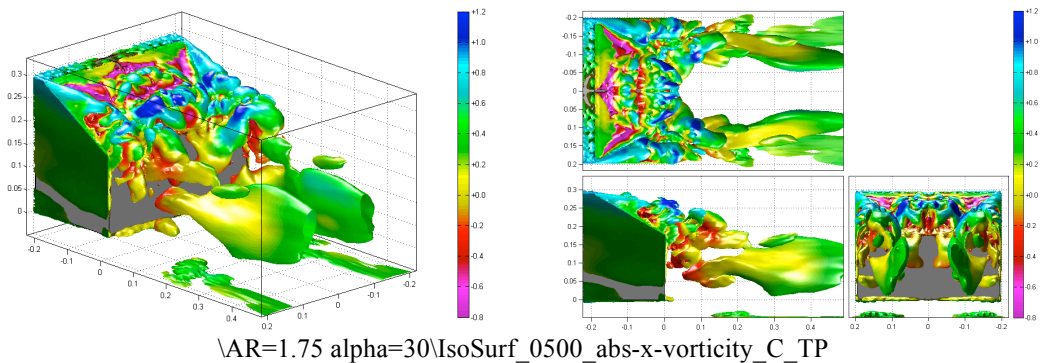
Movie 9.44 $\alpha=30^\circ$, AR=1.75. Iso-surface of $C_{DP}=0.1$ coloured by C_{TP} .



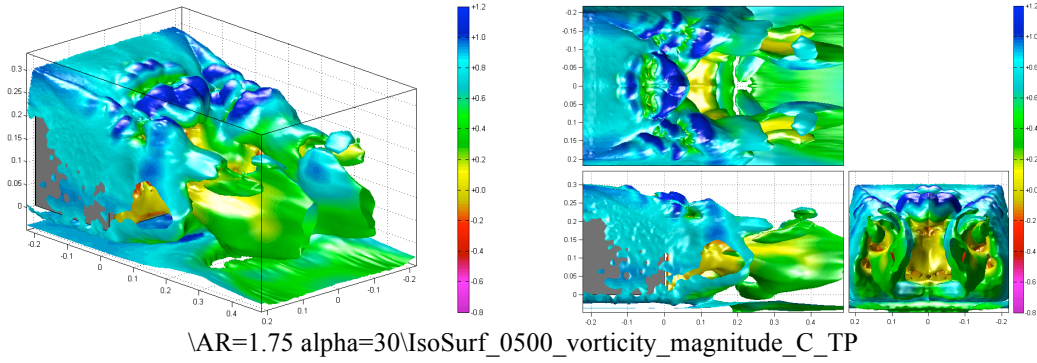
Movie 9.45 $\alpha=30^\circ$, AR=1.75. Iso-surface of $C_{TP}=0.0$ coloured by C_P .



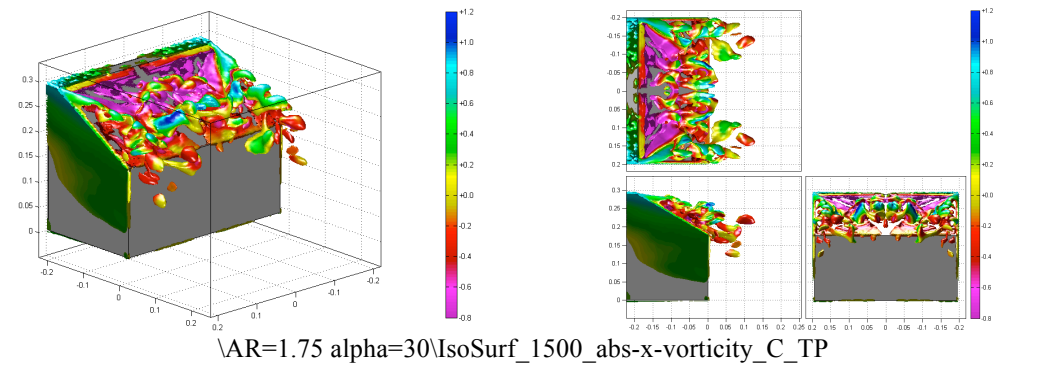
Movie 9.46 $\alpha=30^\circ$, AR=1.75. Iso-surface of $U/U_\infty=0.0$ coloured by C_{TP} .



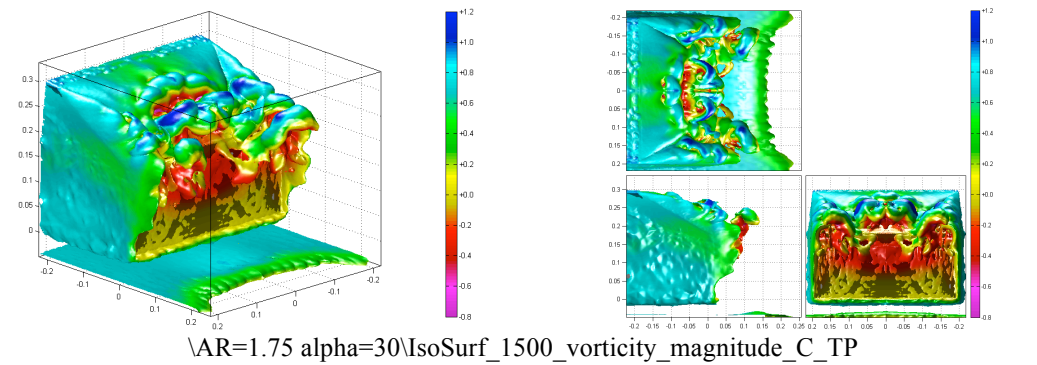
Movie 9.47 $\alpha=30^\circ$, AR=1.75. Iso-surface of $|\omega_x|=500s$ coloured by C_{TP} .



Movie 9.48 $\alpha=30^\circ$, AR=1.75. Iso-surface of $\|\omega\|=500$ s coloured by C_{TP} .

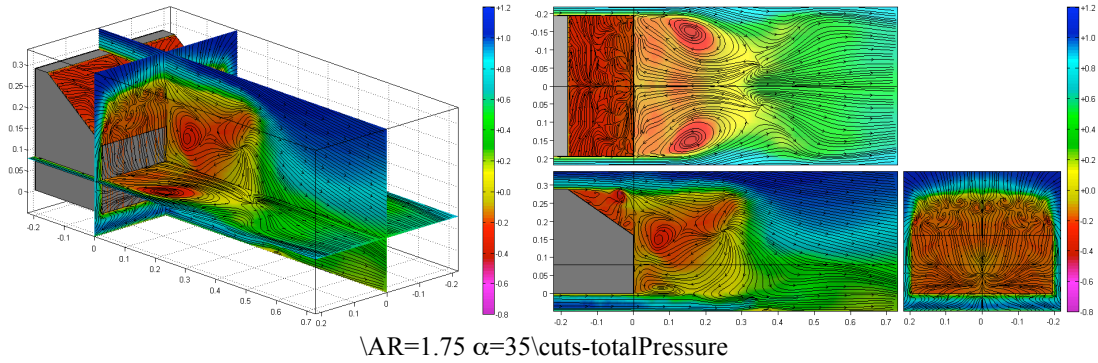


Movie 9.49 $\alpha=30^\circ$, AR=1.75. Iso-surface of $|\omega_x|=1500$ s coloured by C_{TP} .

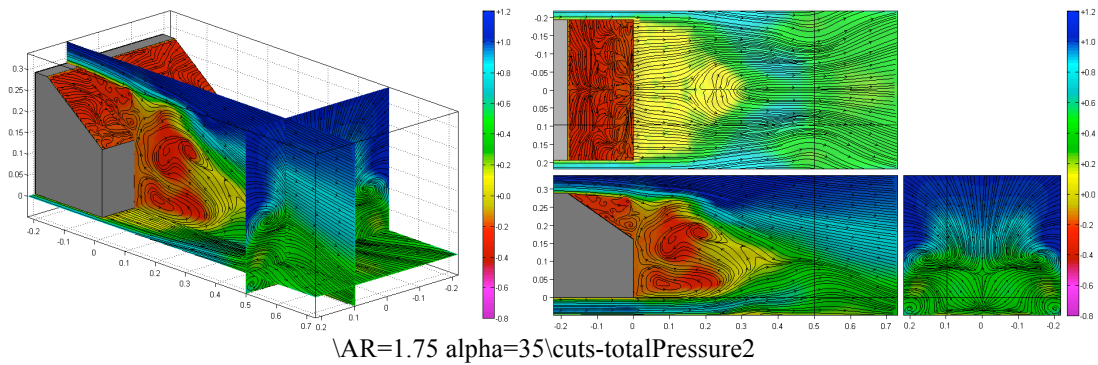


Movie 9.50 $\alpha=30^\circ$, AR=1.75. Iso-surface of $\|\omega\|=1500$ s coloured by C_{TP} .

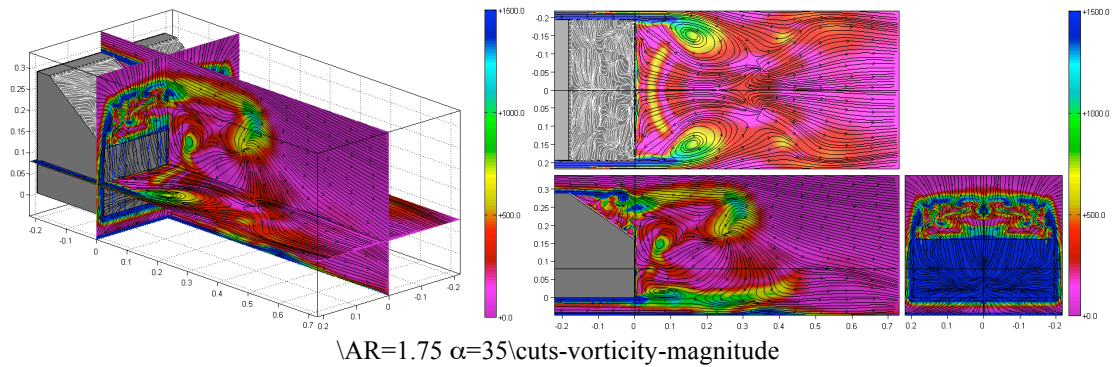
AR=1.75 $\alpha=35^\circ$



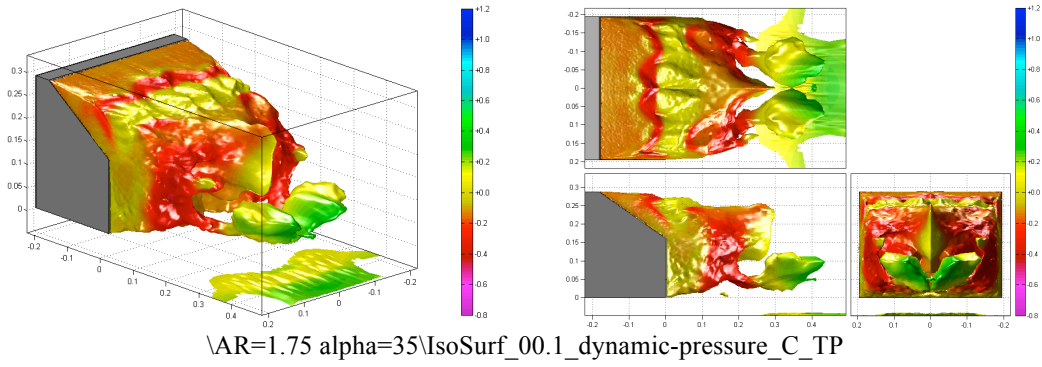
Movie 9.51 $\alpha=35^\circ$, AR=1.75. Unsteady visualisation using slices of C_{TP} and in plane streamlines on planes located at X=0, Y=0.1 and Z=0. Flow structures on the slant surface are visualised by surface streaklines and contours of C_{TP} .



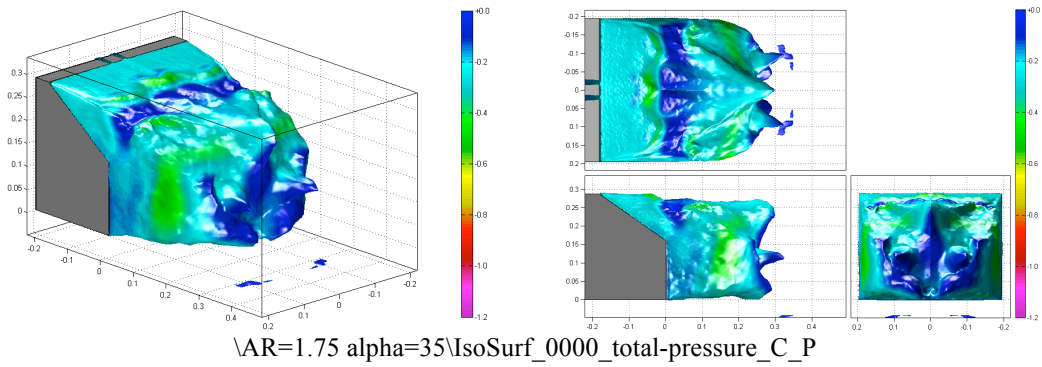
Movie 9.52 $\alpha=35^\circ$, AR=1.75. Unsteady visualisation using slices of C_{TP} and in plane streamlines on planes located at X=0.5, Y=0.0 and Z=0.09. Flow structures on the slant surface are visualised by surface streaklines and contours of C_{TP} .



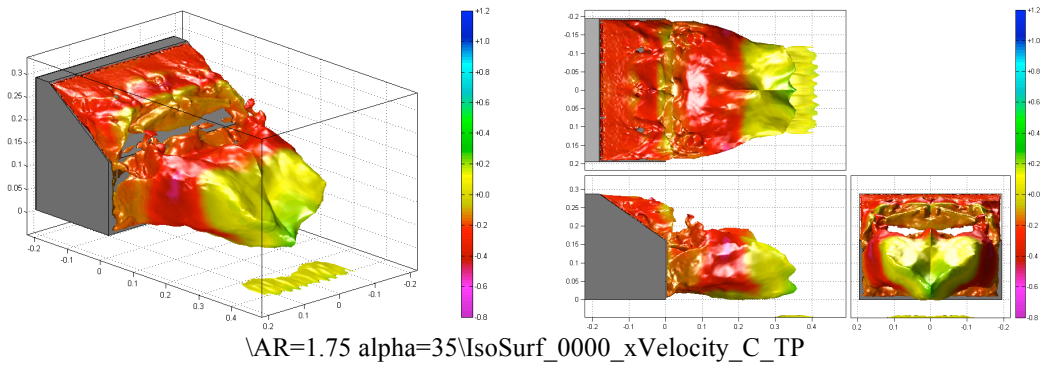
Movie 9.53 $\alpha=35^\circ$, AR=1.75. Unsteady visualisation using slices of $\|\omega\|$ and in plane streamlines on planes located at X=0, Y=0.1 and Z=0. Flow structures on the slant surface are visualised by surface streaklines.



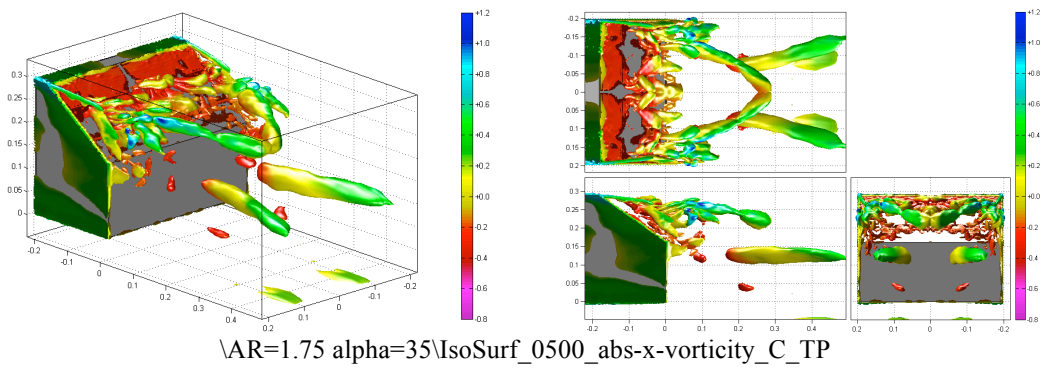
Movie 9.54 $\alpha=35^\circ$, $AR=1.75$. Iso-surface of $C_{DP}=0.1$ coloured by C_{TP} .



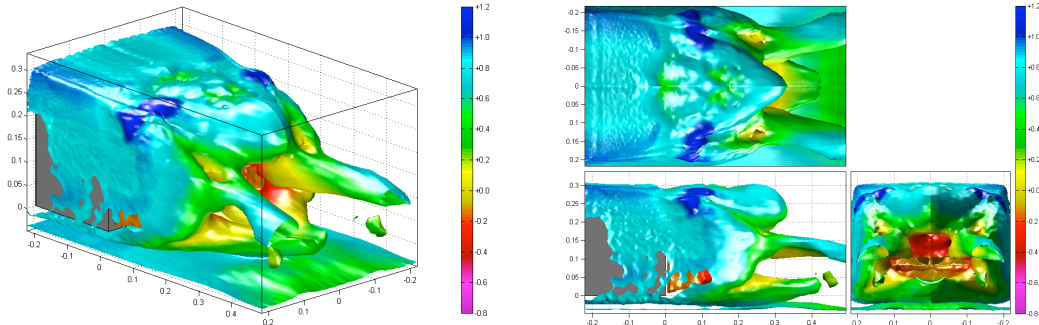
Movie 9.55 $\alpha=35^\circ$, $AR=1.75$. Iso-surface of $C_{TP}=0.0$ coloured by C_P .



Movie 9.56 $\alpha=35^\circ$, $AR=1.75$. Iso-surface of $U/U_\infty=0.0$ coloured by C_{TP} .

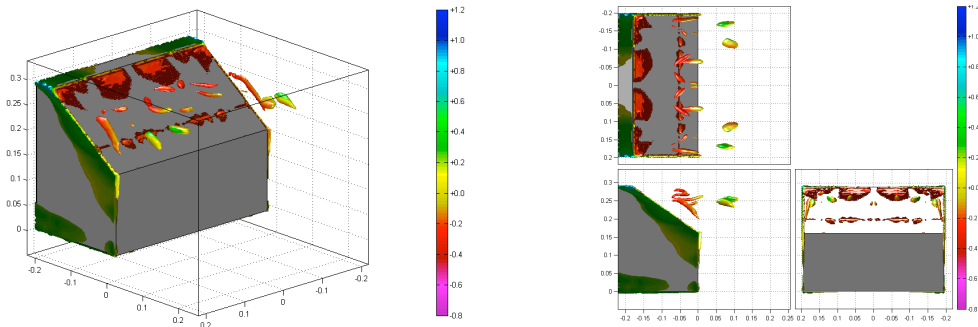


Movie 9.57 $\alpha=35^\circ$, $AR=1.75$. Iso-surface of $|\omega_x|=500s$ coloured by C_{TP} .



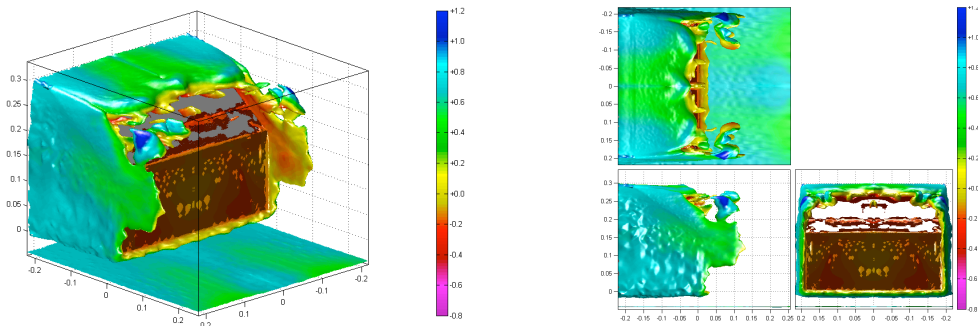
\AR=1.75 alpha=35\IsoSurf_0500_vorticity_magnitude_C_TP

Movie 9.58 $\alpha=35^\circ$, AR=1.75. Iso-surface of $\|\omega\|=500$ s coloured by C_{TP} .



\AR=1.75 alpha=35\IsoSurf_1500_abs-x-vorticity_C_TP

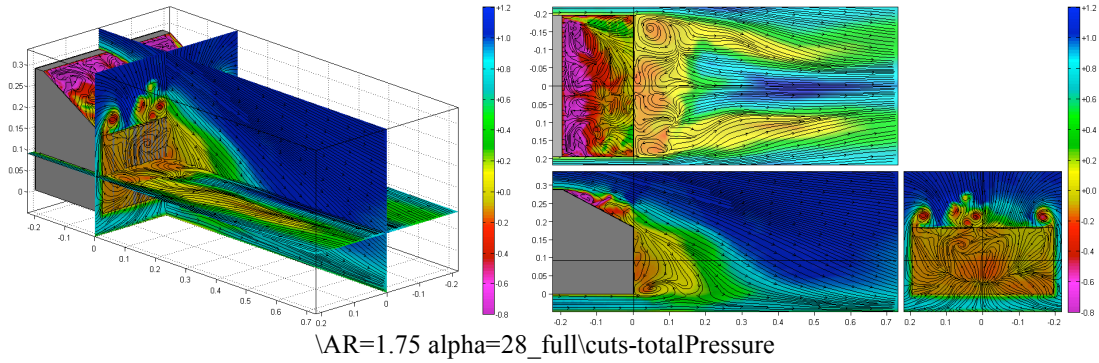
Movie 9.59 $\alpha=35^\circ$, AR=1.75. Iso-surface of $|\omega_x|=1500$ s coloured by C_{TP} .



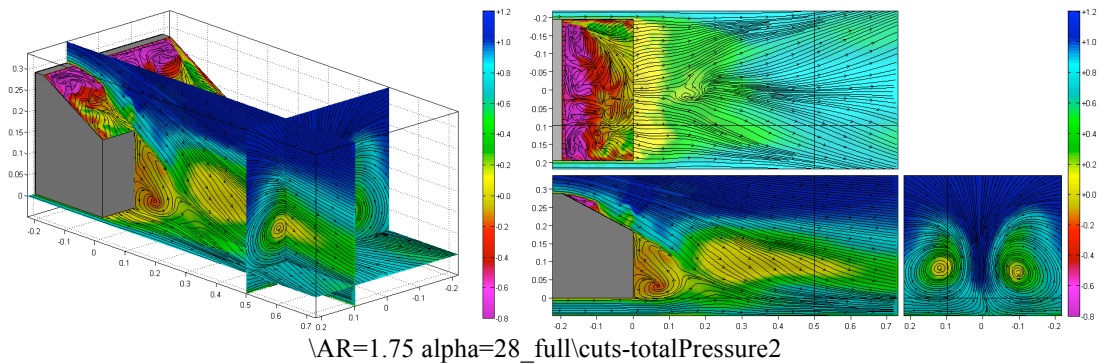
\AR=1.75 alpha=35\IsoSurf_1500_vorticity_magnitude_C_TP

Movie 9.60 $\alpha=35^\circ$, AR=1.75. Iso-surface of $\|\omega\|=1500$ s coloured by C_{TP} .

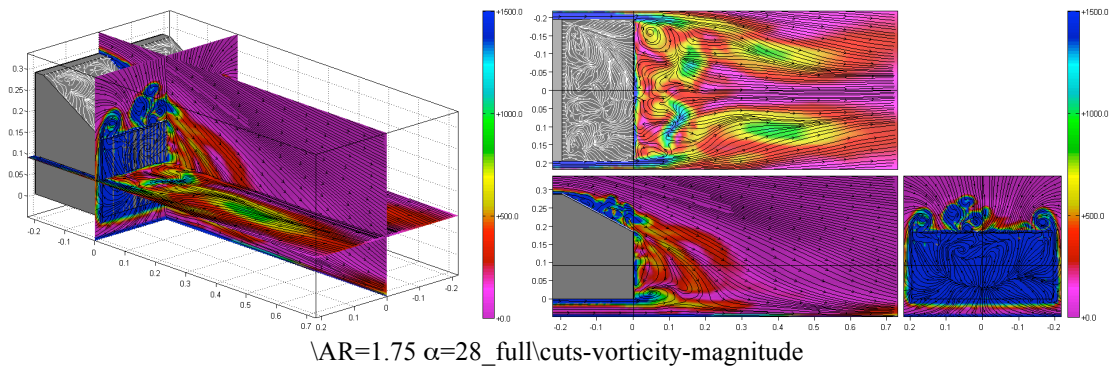
AR=1.75 $\alpha=28^\circ$ Full model



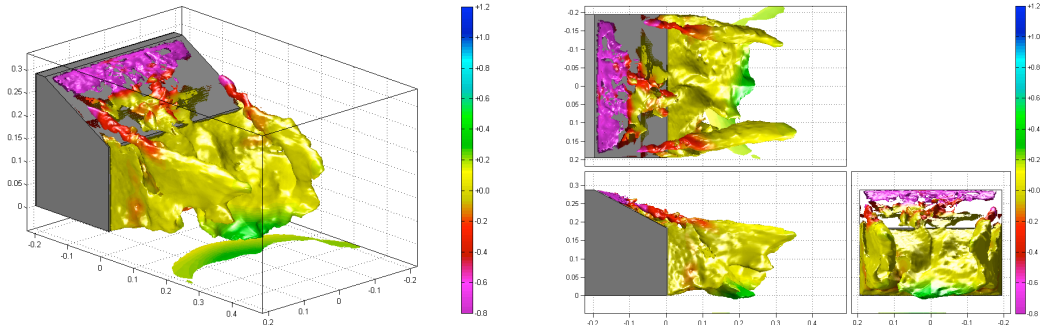
Movie 9.61 $\alpha=28^\circ$, AR=1.75 full model. Unsteady visualisation using slices of C_{TP} and in plane streamlines on planes located at $X=0$, $Y=0$ and $Z=0$. Flow structures on the slant surface are visualised by surface streaklines and contours of C_{TP} .



Movie 9.62 $\alpha=28^\circ$, AR=1.75 full model. Unsteady visualisation using slices of C_{TP} and in plane streamlines on planes located at $X=0.5$, $Y=0.0$ and $Z=0.09$. Flow structures on the slant surface are visualised by surface streaklines and contours of C_{TP} .

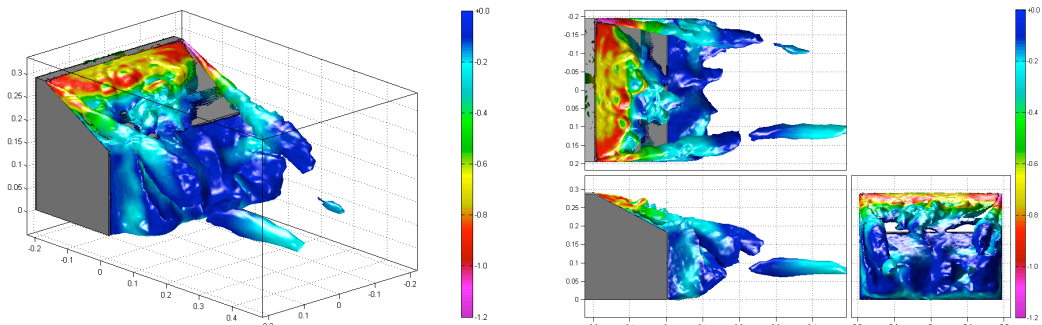


Movie 9.63 $\alpha=28^\circ$, AR=1.75 full model. Unsteady visualisation using slices of $\|\omega\|$ and in plane streamlines on planes located at $X=0$, $Y=0.1$ and $Z=0$. Flow structures on the slant surface are visualised by surface streaklines.



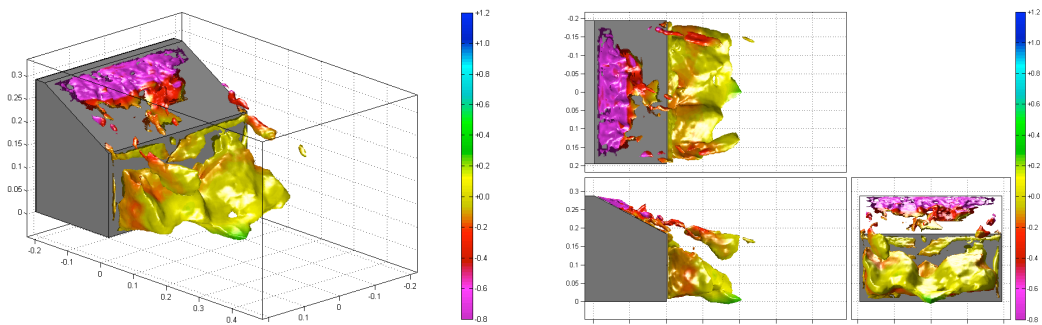
\AR=1.75 alpha=28_fullIsoSurf_00.1_dynamic-pressure_C_TP

Movie 9.64 $\alpha=28^\circ$, AR=1.75 full model. Iso-surface of $C_{DP}=0.1$ coloured by C_{TP} .



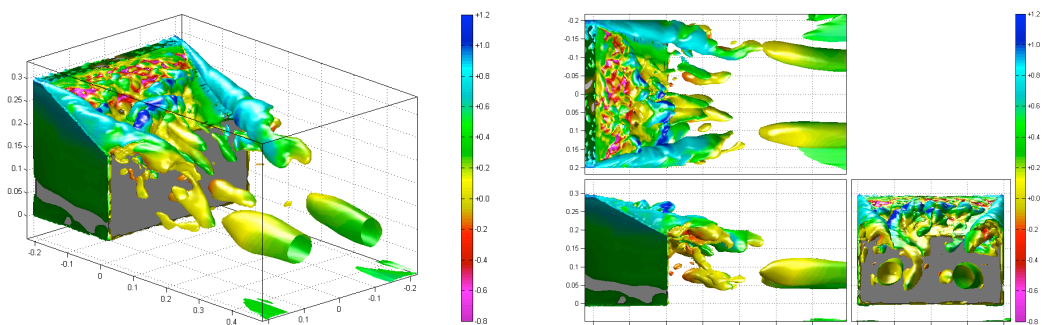
\AR=1.75 alpha=28_fullIsoSurf_0000_total-pressure_C_P

Movie 9.65 $\alpha=28^\circ$, AR=1.75 full model. Iso-surface of $C_{TP}=0.0$ coloured by C_P .



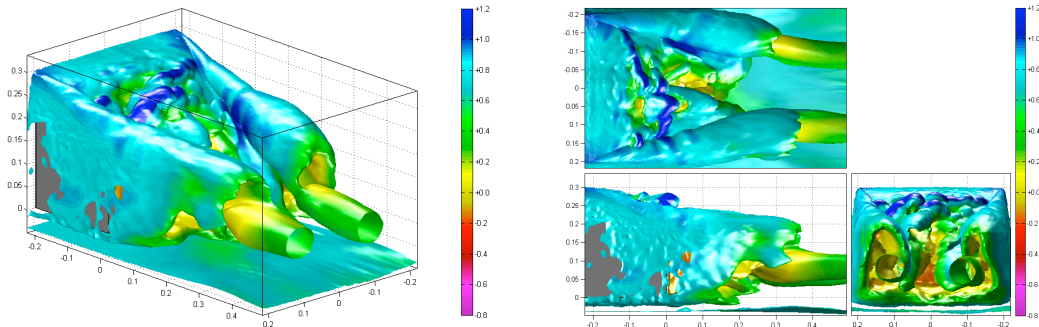
\AR=1.75 alpha=28_fullIsoSurf_0000_xVelocity_C_TP

Movie 9.66 $\alpha=10^\circ$, AR=1.75 full model. Iso-surface of $U/U_\infty=0.0$ coloured by C_{TP} .



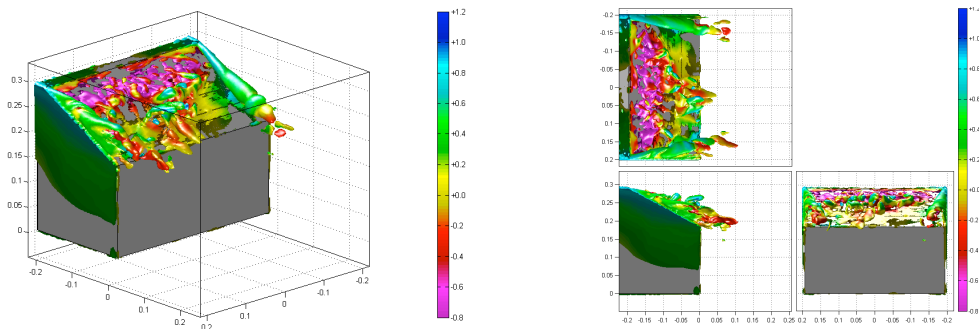
\AR=1.75 alpha=28_fullIsoSurf_0500_abs-x-vorticity_C_TP

Movie 9.67 $\alpha=28^\circ$, AR=1.75 full model. Iso-surface of $|\omega_x|=500s$ coloured by C_{TP} .



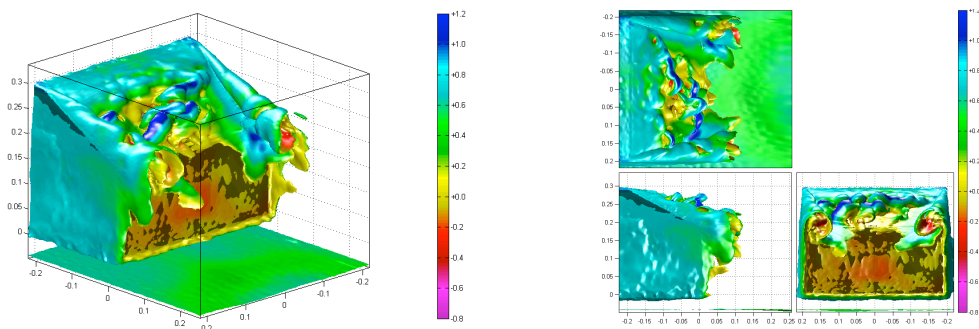
\AR=1.75 alpha=28_fullIsoSurf_0500_vorticity_magnitude_C_TP

Movie 9.68 $\alpha=28^\circ$, AR=1.75 full model. Iso-surface of $\|\omega\|=500$ s coloured by C_{TP} .



\AR=1.75 alpha=28_fullIsoSurf_1500_abs-x-vorticity_C_TP

Movie 9.69 $\alpha=28^\circ$, AR=1.75 full model. Iso-surface of $|\omega_x|=1500$ s coloured by C_{TP} .



\AR=1.75 alpha=28_fullIsoSurf_1500_vorticity_magnitude_C_TP

Movie 9.70 $\alpha=28^\circ$, AR=1.75 full model. Iso-surface of $\|\omega\|=1500$ s coloured by C_{TP} .